Synthesis, enzymatic recognition and antiviral properties of modified purine nucleosides

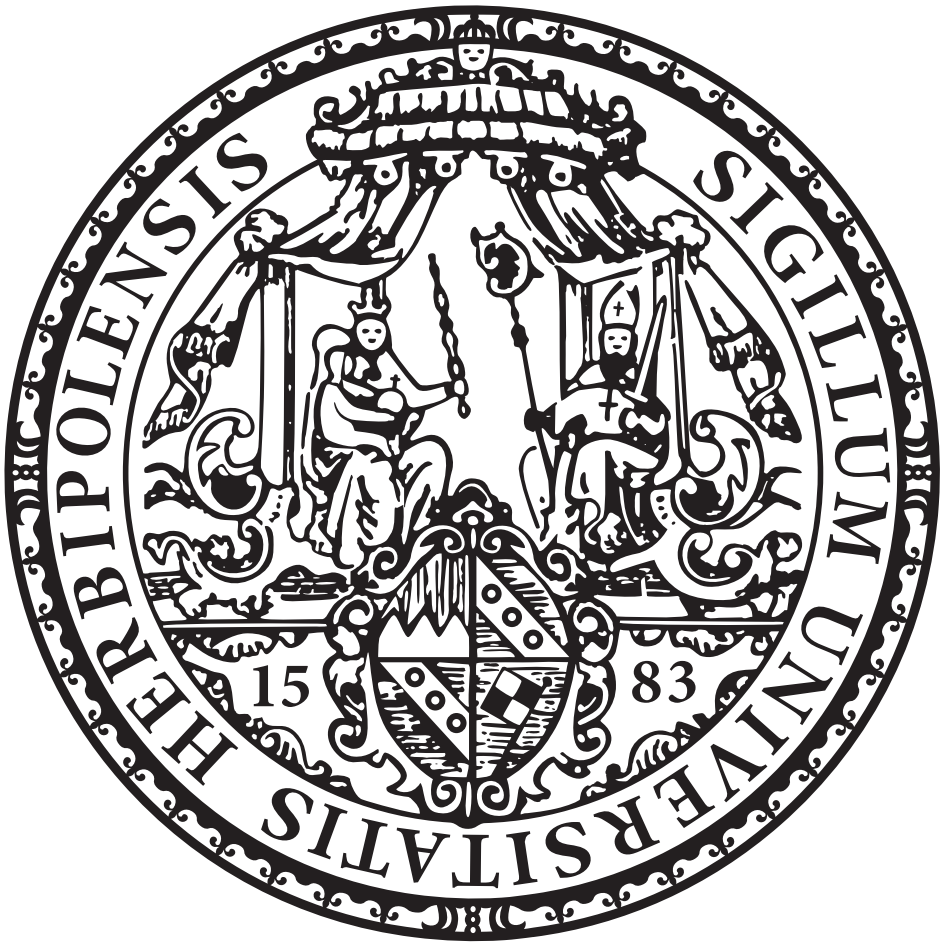

Dissertation zur Erlangung des naturwissenschaftlichen Doktorgrades der Julius-Maximilians-Universität Würzburg

vorgelegt von

Florian Seitz

aus Hofgeismar

Würzburg 2023

Eingereicht bei der Fakultät für Chemie und Pharmazie am:

13.03.2023

Gutachter der schriftlichen Arbeit:

1. Gutachter: Prof. Dr. Claudia Höbartner

2. Gutachter: Prof. Dr. Jürgen Seibel

Prüfer des öffentlichen Promotionskolloquiums:

1. Prüfer: Prof. Dr. Claudia Höbartner

2. Prüfer: Prof. Dr. Jürgen Seibel

3. Prüfer:

Datum des öffentlichen Promotionskolloquiums:

Doktorurkunde ausgehändigt am:

Für meine Familie

...and for MK; in lieu of a new element

Zuallererst gilt mein besonderer Dank meiner Doktormutter Prof. Dr. Claudia Höbartner für die Möglichkeit, meine Dissertation in ihrem Arbeitskreis anzufertigen. Vielen Dank für die Arbeit an einem so interessanten Thema und die Möglichkeit, dabei meine eigenen Ideen und Strategien einfließen zu lassen. Ebenfalls danke ich dir für deine stetige Bereitschaft zu Diskussionen sowie Hilfestellung bei Problemen und offenen Fragestellungen.

Prof. Dr. Jürgen Seibel danke ich für die Übernahme des Zweitgutachtens dieser Arbeit.

Weiterhin gilt mein Dank meinen Kooperationspartnern aus den Arbeitsgruppen von Prof. Dr. Patrick Cramer (Max-Planck-Institut für Multidisziplinäre Naturwissenschaften, Göttingen) und Prof. Dr. Markus Bohnsack (Universitätsmedizin Göttingen), insvesondere Dr. Jens Kretschmer und Nicole Kleiber für die Bereitstellung der in dieser Arbeit verwendeten m^6A Reader- und Eraser-Proteine.

Ebenfalls danke ich den aktuellen und ehemaligen Mitarbeitern unserer Analytik-Abteilungen; insbesondere Michaela Schraut und Sebastian Mayer für die Messung meiner Oligo-Proben sowie Dr. Juliane Adelmann für ihre Unterstützung bei der Methodenentwicklung von HPLC-MS-Analysen.

Stefanie Schmitt und Andreas Lange danke ich für die synthetische Unterstützung meiner Projekte. Besonderer Dank geht auch an Doris Feineis sowie Ann-Kathrin Lenz und Manuela Michel für ihre stetige Hilfsbereitschaft und tolle Unterstützung im Laboralltag.

Danke an die (aktuellen und ehemaligen) Mitglieder des AK Höbartner für die gute Arbeitsatmosphäre und Zusammenarbeit sowie die gemeinsamen Unternehmungen auch außerhalb der Uni. Hierbei geht mein besondere Dank an Julia, Carina (Ninchen-Bienchen) und Hermann sowie an Taku und Ai für die gemeinsamen Boulderabende.

Vielen Dank ebenfalls an meine Praktikanten und Bachelorstudenten Gerald, Willi, Paul, Max, Nora und Tina für die gute gemeinsame Zeit und die Unterstützung meiner Projekte.

Caro, Christine und besonders Julia danke ich für das Korrekturlesen meiner Arbeit.

Letztendlich möchte ich mich herzlich bei meiner Familie, meinen Freunden und ganz besonders bei Julia für ihre dauerhafte Unterstützung, ihr Verständnis, wenn ich mal wieder im Stress war, und generell die schöne Zeit außerhalb der Arbeit bedanken.

List of Publications

Parts of this thesis have been published (*authors contributed equally):

Kokic, G.*; Hillen, H. S.*; Tegunov, D.*; Dienemann, C.*, Seitz, F.*; Schmitzova, J.; Farnung, L.; Siewert, A.; Höbartner, C.; Cramer, P. Mechanism of SARS-CoV-2 polymerase stalling by remdesivir. *Nat. Commun.* **2021**, *12*, 279.

Contents

Abstract

RNA as one of the three main biopolymers of life fulfils a variety of indispensible functions in the storage of genetic information as well as in the regulation of cellular processes. Beyond the four canonical nucleobases as primary building blocks, a plethora of posttranscriptional modifications gives rise to the epitranscriptome as a second layer of information. In eukaryotic mRNA, the most abundant posttranscriptional modification is N^6-methyladenosine (m^6A). Being involved in a variety of regulatory processes and linked to the occurence of various diseases, m^6A and the proteins responsible for its biosynthesis, recognition and removal are highly relevant research subjects.

In the first part of this thesis, the concept of atomic mutagenesis was employed to gain novel mechanistic insights into m^6A recognition by human reader proteins and oxidative m^6A demethylation by human demethylase enzymes. In particular, non-natural m^6A atomic mutants featuring distinct steric and electronic properties were synthesized, subsequently converted into phosphoramidite building blocks and site-specifically incorporated into RNA oligonucleotides.

Fluorescence anisotropy measurements using these modified oligonucleotides revealed the impact of the atomic mutagenesis on the molecular recognition by the human m^6A readers YTHDF2, YTHDC1 and YTHDC2 and allowed to draw conclusions about structural prerequisites for substrate recognition. The integrity of the exocyclic methylamino substituent is crucial, whereas mutations of the purine heterocycle are partly tolerated.

The concept of atomic mutagenesis was further exploited to study the human m^6A demethylases FTO and ALKBH5. Substrate recognition and demethylation mechanism of these enzymes were analyzed by HPLC-MS and PAGE-based assays using the exquisite modified oligonucleotides synthesized in this work. These studies showed that FTO follows a classical stepwise oxidative pathway whereas ALKBH5-mediated demethylation involves a covalent RNA-enzyme intermediate.

The examined m^6A atomic mutants reduced demethylase activities by different degrees, with ALKBH5 being generally more tolerant toward substrate mutagenesis. General substrate binding, however, was unaffected. Aided by quantum-mechanical simulations, it was concluded that disruption of electrostatic interactions between substrate nucleoside and enzyme binding pocket affects the positioning of the nucleobase inside the active site and

impairs the correct alignment of the exocyclic methyl group with the catalytic center.

Modified nucleosides are not only utilized by nature to expand the genetic alphabet, but are also extensively researched as drug candidates. Due to the 2019 SARS-CoV-2 pandemic, especially antiviral nucleosides and prodrugs derived from them have gained increasing attention. In the second part of this thesis, the antiviral mechanism of the anti-SARS-CoV-2 drug remdesivir was investigated, which acts by causing delayed stalling of the viral RNA-dependent RNA polymerase (RdRp).

Novel phosphoramidite building blocks of the remdesivir nucleoside Rem were synthesized and site-specifically incorporated into RNA using solid-phase synthesis. Using these oligonucleotides, it was possible to construct defined RNA-RdRp complexes, the structures of which were elucidated by collaborators using cryogenic electron microscopy (cryo-EM). It was found that the 1'-cyano substituent causes Rem to act as a steric barrier of RdRp translocation.

This translocation barrier does not lead to complete inhibition, but can eventually be overcomeby the polymerase. Therefore, novel derivatives of Rem with potentially improved antiviral properties were designed. Two Rem analogs were synthesized and converted into nucleoside triphosphates, one of which was already subjected to activity test by collaborators. A third Rem derivative was obtained as an anomeric mixture, which needs to be separated for further investigations.

Besides its antiviral properties, also interesting spectroscopic properties of Rem were detected. Rem shows highly environment-sensitive fluorescence with intensities comparable to already established fluorescent nucleosides and may therefore be an interesting candidate for future applications as a fluorescent probe.

Zusammenfassung

Als eines der drei zentralen Biopolymere des Lebens erfüllt RNA eine Vielfalt unersetzlicher Funktionen in der Speicherung genetischer Informationen sowie in der Regulierung zellulärer Prozesse. Über die vier kanonischen Nukleoside als primäre RNA-Bausteine hinausgehend existiert eine Vielzahl posttranskriptioneller Modifikationen, die eine zweite Informationsebene, genannt das Epitranskriptom, aufbauen. Die häufigste posttranskriptionelle Modifikation in eukaryotischer mRNA ist N^6-Methyladenosin (m^6A). Dieses ist in eine Vielzahl regulatorischer Prozesse involviert und steht im Zusammenhang mit verschiedenen Krankheitsbildern, weshalb m^6A selbst sowie die Proteine, die für seine Biosynthese, Erkennung und Abbau verantwortlich sind, als hochgradig relevante Forschungsobjekte zählen.

Im ersten Abschnitt dieser Arbeit wurde das Konzept der atomaren Mutagenese genutzt, um neue Einblicke in die Erkennung von m^6A durch menschliche m^6A-bindende Proteine sowie in die oxidative Demethylierung von m^6A durch menschliche Demethylaseenzyme zu gewinnen. Hierbei wurden nicht natürlich vorkommende m^6A Atommutanten mit unterschiedlichen elektronischen und sterischen Eigenschaften synthestisiert, in Phosphoramiditbausteine umgewandelt und positionsspezifisch in RNA-Oligonukleotide eingebaut.

Durch Fluoreszenzanisotropie-Messungen mit diesen Oligonukleotiden wurden der Einfluss der Atommutagenese auf die molekulare Erkennung durch die menschlichen m^6A-bindenden Proteine YTHDF2, YTHDC1 und YTHDC2 untersucht. Die erhaltenen Ergebnisse ließen Rückschlüsse auf die strukturellen Voraussetzungen für die Erkennung eines Substrates zu. Das Vorhandensein eines exozyklischen Methylamino-Substituenten ist zwingend erforderlich, während Mutationen des heterozyklischen Purin-Grundgerüstes teilweise toleriert werden.

Das Konzept der atomaren Mutagenese wurde weiterhin zur Untersuchung der menschlichen m^6A-Demethylasen FTO und ALKBH5 verwendet. Die Substraterkennung und der Demethylierungsmechanismus dieser beiden Enzyme wurde durch HPLC-MS- und PAGE-basierte Analysen mit Hilfe der in dieser Arbeit synthetisierten modifizierten Oligonukleotide untersucht. Die experimentellen Befunde zeigten, dass FTO einem klassischen schrittweisen oxidativen Mechanismus folgt, während Demethylierung durch ALKBH5 über ein kovalentes RNA-Enzym-Intermediat abläuft.

Die untersuchten m^6A Atommutanten verringerten die Demethylase-Aktivitäten in un-

terschiedlichem Ausmaß, wobei ALKBH5 sich als allgemein toleranter gegenüber Mutagenese des Substrates herausstellte. Die generelle Bindung der Substrat-RNA wurde jedoch in keinem Fall beeinträchtigt. Unterstützt durch quantenmechanische Simulationen wurde geschlussfolgert, dass Störungen der elektrostatischen Wechselwirkungen zwischen Substrat-Nukleosid und Enzym die Positionierung der Nukleobase in der Bindungstasche beeinflussen und die korrekte Ausrichtung der exozyklischen Methylgruppe auf das katalytische Zentrum beeinträchtigen.

Modifizierte Nukleoside dienen nicht ausschließlich zur Erweiterung des genetischen Alphabets in der Natur, sondern werden auch als potentielle Wirkstoff-Kandidaten erforscht. Mit dem Aufkommen der SARS-CoV-2-Pandemie in 2019 rückten besonders antivirale Nukleoside und von ihnen abgeleitete Prodrug-Strukturen in den Fokus. Im zweiten Teil dieser Arbeit wurde der antivirale Wirkmechanismus des Anti-SARS-CoV-2-Wirkstoffes Remdesivir untersucht, der eine verzögerte Blockade der viralen RNA-abhängigen RNA-Polymerase (RdRp) bewirkt.

Neuartige Phosphoramidit-Bausteine des Remdesivir-Nukleosids Rem wurden synthetisiert und mittels Festphasensynthese positionsspezifisch in RNA eingebaut. Mit diesen Oligonukleotiden war es möglich, RNA-RdRp-Komplexe mit definierter Struktur zu konstruieren, deren Strukturen von Kooperationspartnern mittels Cryoelektronenmikroskopie (Cryo-EM) aufgeklärt wurden. Es wurde herausgefunden, dass der 1'-Cyano-Substituent dazu führt, dass Rem als sterische Blockade der RdRp-Translokation agiert.

Da diese Tranlokationsbarriere keine vollständige Inhibition bewirkt, sondern von der Polymerase überwunden werden kann, wurden neuartige Rem-Derivate mit potentiell verbesserten antiviralen Eigenschaften entworfen. Zwei Rem-Analoga wurden synthetisiert und in Nukleosid-Triphosphate umgewandelt. Eines dieser Triphosphate wurde bereits von Kooperationspartnern Aktivitätstests unterzogen. Ein drittes Derivat wurde als anomeres Gemisch erhalten, welches für weitere Untersuchungen separiert werden muss.

Neben seinen antiviralen Eigenschaften wurden auch interessante spektroskopische Eigenschaften von Rem festgestellt. Rem zeigt hochgradig umgebungsabhängige Fluoreszenz mit Intensitäten ähnlich bereits etablierten fluoreszenten Nukleosiden und ist daher ein interessanter potentieller Kandidat für zukünftige Anwendungen als Fluoreszenzsonde.

Introduction

1 Modified nucleosides in the epitranscriptome

Besides proteins, nucleic acids are one of the two central biopolymers of life. While DNA exists predominantly in form of the famous double helix (Figure 1A) and serves as a storage of genetic information, RNA comes in a much broader variety of shapes and functions. The most widely known representatives are the messenger RNA (mRNA), which is an intermediary transcript of DNA information, as well as the ribosomal RNA (rRNA) and transfer RNA (tRNA), which participate in translation of the information confered by mRNA into amino acid sequences. The vast majority of all transcribed RNAs, however, are not

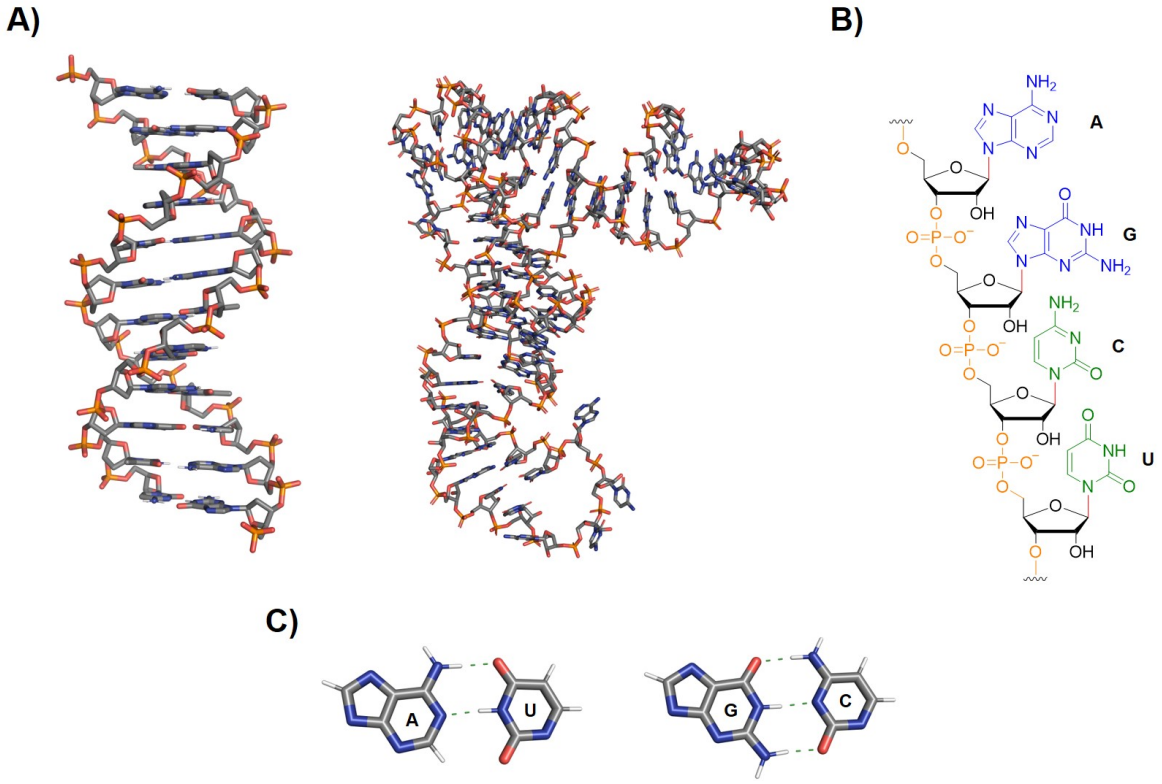

Figure 1: Structural features of nucleic acids. A) Structural models of B-form DNA double helix (left) and tRNA cloverleaf structure (right, human $tRNA^{Gly}$, PDB ID 5E6M). B) The linear RNA primary structure comprising the four canonical nucleosides A, G, C and U, which are connected *via* 3'–5'-phosphodiester bridges (orange). The four RNA nucleosides are formed by β-*N*-glycosidic linkages (red) between the N9 of purine nucleobases (blue) or the N1 of pyrimidine nucleobases (green) and the C1' of D-ribose (black). C) Watson-Crick base pairing between A and U (two H-bonds) and between G and C (three H-bonds).

actively involved in the translation process, but rather play roles in regulatory cellular processes. As an example, long non-coding RNAs (lncRNAs) regulate gene expression through interactions with transcription modulators, the RNA polymerase II or the template DNA

itself, while various types of small noncoding RNAs such as micro RNAs (miRNAs) and small interfering RNAs (siRNAs) play important roles in gene silencing, posttranscriptional modulation of gene expression and many more processes.[1,2]

Despite their diverse functions and partly highly complex and ordered secondary structures such as the tRNA cloverleaf (Figure 1A), all RNAs are built from only four basic building blocks (Figure 1B). The two purine nucleobases adenine and guanine as well as the two pyrimidine nucleobases cytosine and uracil are connected via β-*N*-glycosidic bonds at N9 (purines) or N1 (pyrimidines) to the C1'-atom of D-ribose, thereby forming the nucleosides adenosine (A), guanosine (G), cytidine (C), and uridine (U). These nucleosides are further connected via 3'–5'-phosphodiester bridges, yielding the linear primary structure of RNA oligo- or polymers. Assembly or folding of these linear strands into higher ordered structures is guided by specific pairwise hydrogen bonding interactions (Watson-Crick base pairing, Figure 1C) between purine and pyrimidine nucleobases (A=T and G≡C).

To provide the broad variety of RNA structures and functions with such a limited set of basic building blocks, nature utilizes a second layer of information to expand the available genetic code: a collection of more than 150 posttranscriptional chemical modifications of the nucleobase as well as the ribose structure gives rise to the so-called epitranscriptome.[3] Whereas naturally occuring chemical modification of the ribose is limited to 2'-position of the sugar, the landscape of nucleobase modifications is much more diverse (Figure 2). Most posttranscriptional modifications are installations of small substituents, such as methyl or acetyl groups; yet, also the introduction of larger substituents such as isopentenyl or methylcarbonylmethyl residues (e. g. in ms^2i^6A or mcm^5se^2U) is known. The class of hypermodified nucleobases even features introduction of amino acid substituents (e. g. N^6-threonylcarbamoyladenosine, t^6A, or lysidine, k^2C) or similarly bulky groups (queuosine, Q), often located at C7 of 7-deazapurine bases, or the overall alteration of the heterocyclic nucleobase skeleton (wybutosine, yW).[4] A notable mention in this context is the nucleoside pseudouridine (Ψ), which is a C-glycosidic isomer of uridine. Ψ retains the base pairing pattern of U while providing an additional H-bond donor function, which helps stabilize RNA structure through interactions with the phosphate backbone.[5]

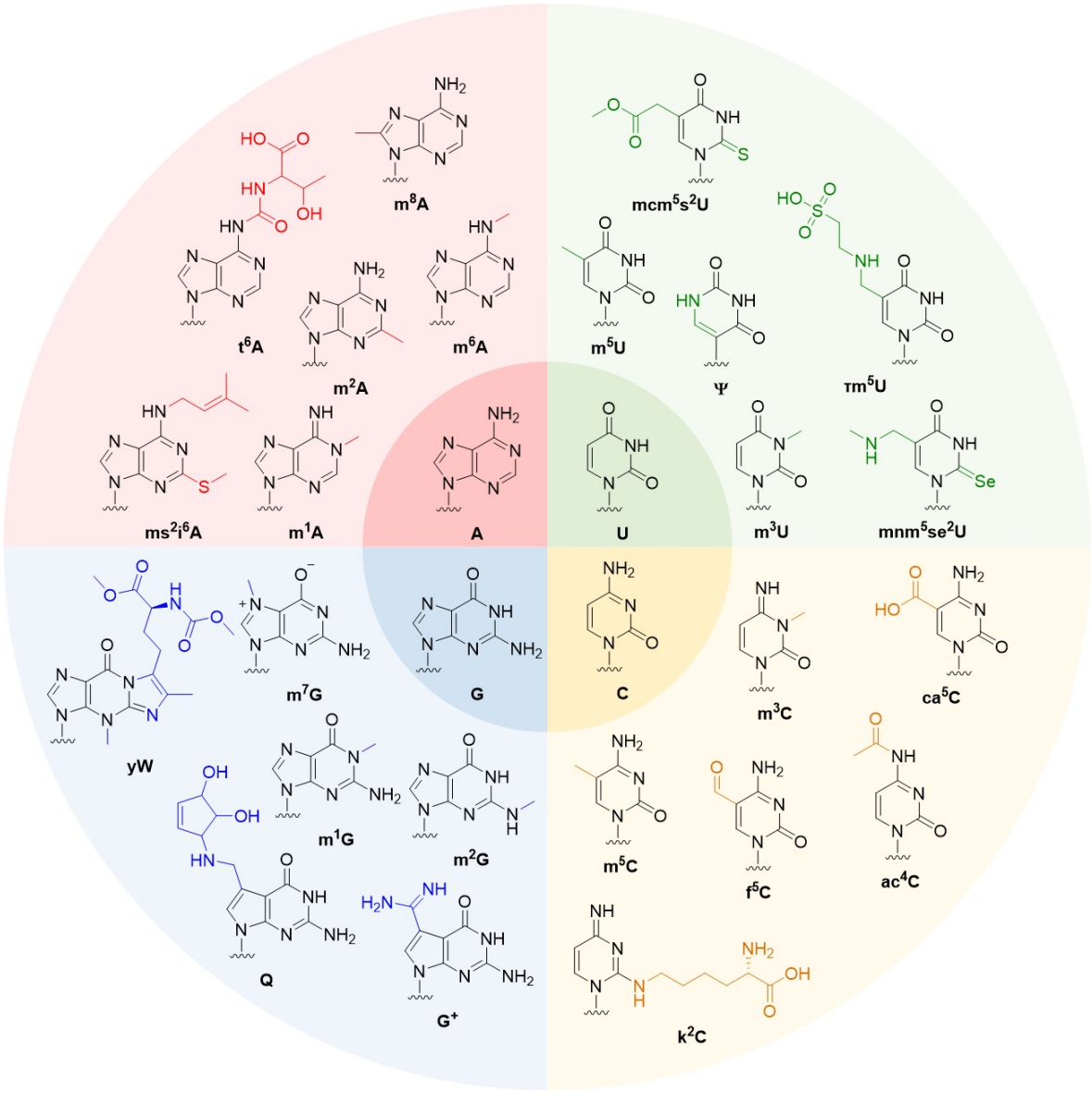

Figure 2: Natural nucleobase modifications. A vast variety of posttranscriptional nucleobase and ribose modifications gives rise to the epitranscriptome as a second layer of genetic information. This figure shows a selection of naturally occuring nucleobase modifications.[4,6]

The most extensively modified RNA species in the human organism is tRNA with ca. 10–15% of all nucleosides in tRNA being modified. This translates to about eight modification sites per tRNA molecule, many of which are located in or adjacent to the anticodon loop (Figure 3A).[4] Here, the presence of (hyper-)modified nucleosides at position 34 (wobble postition) and 37 expand codon recognition and enhance translation fidelity, for example by preventing frameshift events.[7–9] Modifications outside the anticodon loop mainly enhance tRNA stability and aid correct folding. A notable example is the presence of pseudouridine in the TΨC-loop, which enhances the interaction with the D-loop and increases the

tRNA melting temperature.[10,11] Some tRNA modifications have been shown to be involved in complex interdependences. As an example, installation of N^3-methylcytidine (m^3C) at position 32 of human mitochondrial (mt-)$tRNA^{Thr}$ and mt-$tRNA^{Ser(UCN)}$ by the methyltransferase enzyme METTL8 is dependent on the presence of t^6A or ms^2i^6A, respectively, at position 37.[12–14]

Other non-coding RNA species, such as snRNAs, are also known to be heavily modified; however, their modification sites and extent are not yet comprehensively mapped.[15] Thus, rRNA is frequently named as the second most highly modified class of RNAs, although with only ca. 2% the fraction of modified nucleosides is significantly lower than in tRNA.[16] The most abundant modifications in rRNA are 2'-*O*-methylated nucleosides (N_m) as well as pseudouridine sites. Together, these two modifications are about 10-fold more abundant than all other nucleoside modifications combined. 2'-*O*-Methylations and pseudouridinylations of rRNA are mostly introduced by small nucleolar ribonucleoproteins (sno-RNPs) consisting of a catalytic protein unit and a snoRNA which guides the enzyme to its target site *via* complementary base pairing. Unlike in tRNA, where modification sites have been found across all three loops, modifications in rRNA are clustered around functionally important sites such as the peptidyltransferase center and decoding site.[17] While deletion of single modifications often does not show any adverse effects, loss of multiple modifications sites has been shown to impact both ribosome folding and activity. The broadest variety of cellular defects has been reported for loss of three to five nucleoside modifications in the intersubunit bridge helix 69 in yeast, which include altered rRNA structure, reduced cellular rRNA levels and functional defects such as slower amino acid incorporation rates and higher stop codon readthrough.[18] Similar effects have been observed upon deletion of six Ψ-sites in the peptidyl transferase center, which highlights the importance of rRNA modifications, especially Ψ and N_m for ribosome function.[19]

In contrast to tRNA and rRNA, a comparably small variety of modified nucleosides has been detected in mRNA, with the main representatives being N^6-methyladenosine (m^6A), N^1-methyladenosine (m^1A), Ψ, 5-methylcytidine (m^5C), and 2'-*O*-methylated nucleosides; yet, the latter three lack in-depth mapping and functional characterization (Figure 3B).[20] While distribution and function of 2'-*O*-methylated nucleosides remain largely elusive, a prominent example is found in the 5' cap structure (Figure 3C). This general structural feature of mature mRNA consists of an N^7-methyl-guanosine (m^7G) linked to an N_m nucleoside (mostly A_m) *via* a 5'–5'-triphosphate linkage and is required to initiate translation.[21,22] The cap A_m may be further methylated to yield m^6A_m, a modification which stabilizes mRNA transcripts by providing resistance to the mRNA-decapping enzyme DCP2.[23,24]

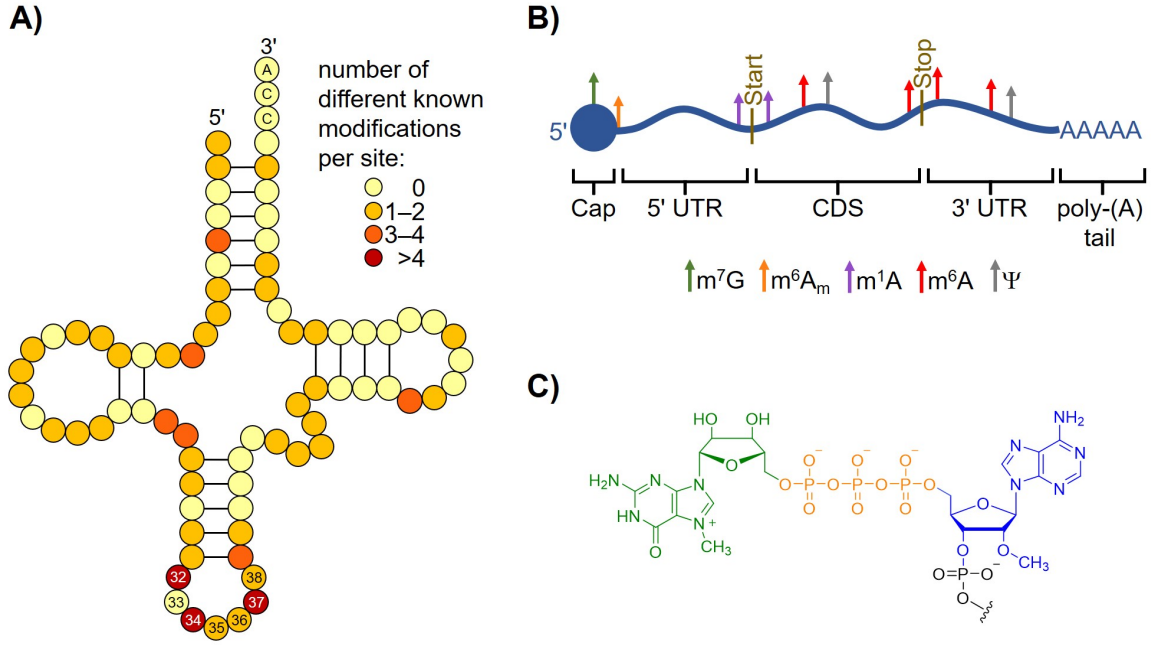

Figure 3: Modified nucleosides in RNA. A) Schematic 2D representation of a tRNA, showing the distribution of modified sites (detected across all three domains of life). Nucleoside positions are color-coded based on the number of different modifications found at the respective position. Position 34 (wobble position) and 37 often bear hypermodified nucleobases.[4] B) Localization of five prominent modified nucleosides (colored arrows) in mRNA.[20] Modifications are shown in regions of particular enrichment, but may as well be present in other sites within the mRNA sequence. C) The 5' cap structure consists of an m^7G nucleoside (green) linked to a 2'-*O*-methylated nucleoside (here A_m, blue) *via* a 5'–5'-triphosphate linkage (orange).

Pseudouridinylation of human mRNA occurs mainly inside coding sequences (CDSs) and 3' untranslated regions (3' UTRs).[25,26] Especially inside the CDS pseudouridinylation notably affects the genetic code. Conversion of uridine moieties inside stop codons enables stop codon readthrough, thereby converting the modified nonsense codons into sense codons coding for Ser, Thr, Tyr or Phe.[27] This observation suggests that pseudouridinylation of mRNA represents a way to expand the genetic code.

Although it is a prevalent modification in the epitranscriptome and well studied in tRNA and rRNA, m^1A was only in 2016 confirmed to be present in mRNA as well, and the m^1A methylome was mapped by two independent research groups.[28,29] Both studies reported a high abundance of m^1A sites (more than 900 and more than 7000 sites, respectively); this estimate was supported in a follow-up study by one of the authors (Li *et al.*), who found more than 700 m^1A sites in human mRNA.[28–30] Interestingly, the latter study reported that m^1A distribution differs between nuclear- and mitochondrial-encoded transcripts.[30] In nuclear-encoded mRNA, m^1A was found mainly present in the 5' UTR and the CDS, where

it clusters around the start codon. Presence of m^1A appeared to be positively correlated with the number of alternative translation initiation sites as well as with enhanced translation of methylated transcripts. In stark contrast, m^1A profiling of mt-mRNA revealed 22 of 23 modification sites to be located in the CDS, where they, owing to their interference with canonical Watson-Crick base pairing, decreased mitochondrial translation. Strikingly, a later work by Safra *et al.* used the same antibody for m^1A immunoprecipitation as the three aforementioned studies, but further confirmed their detected m^1A sites based on misincorporation rates of a special reverse transcriptase, which left the authors with a total number of only eight rather than 7000 methylation sites in human mRNA.[31] All of these sites were found in sequence contexts resembling the T-loop of tRNAs and are installed by the TRMT6/TRMT61A complex, which is also responsible for m^1A installation in tRNA. To elucidate the large discrepancy between the results of Safra *et al.* and the three previous publications, the raw data of the study by Li *et al.* were re-evaluated.[32] Here, a significantly reduced number of sites were assigned to m^1A in human mRNA, mainly due to the presence of redundant and mismapped reads in the original publication. Furthermore, the confirmed sites were found to be typically modified at very low levels. Overall, despite the initial reports stated otherwise, the more recent studies suggest a very low abundance of the m^1A modification across human mRNA.

The both most prevalent (on average more than three sites per molecule) and most extensively studied posttranscriptional modification in mRNA is N^6-methyladenosine.[33] Using m^6A-specific methylated RNA immunoprecipitation with next-generation sequencing (MeRIP-Seq) and other high-throughput m^6A mapping methods, m^6A sites have been found to be particularly enriched around stop codons and in 3' UTRs.[34] The presence of m^6A sites is recognized by a set of reader proteins which influence the cellular fate of their bound targets, resulting in enhanced translation efficiency, accelerated mRNA degradation and further effects.[35,36] Together with the dynamic nature of the m^6A modification (both writer and eraser enzymes have been identified) these features suggest adenosine N^6-methylation to be a means of cellular stress reponse by providing a metabolic fast-track route for certain transcripts.[37–39] Additionally, misregulation of cellular m^6A levels has been shown to be correlated with a variety of diseases such as myeloid leukemia and obesity.[40,41]

The manifold implications of the m^6A mRNA modification in regulatory as well as pathogenic processes have sparked massive interest in the investigation of the m^6A epitranscriptome as well as in the reader, writer and eraser proteins interacting with this modification. The biological role of m^6A and its interplay with writers, readers and erasers will therefore be discussed in further detail in Part I of this thesis. The work in this part will particularly

focus on the demethylation of m^6A by the two human demethylase enzymes FTO and ALKBH5. In brief, atomic mutagenesis of the native m^6A substrate, achieved by chemical synthesis, is utilized to systematically probe the importance of distinct structural features of the substrate for enzymatic recognition and activity. Additionally, the effect of substrate mutagenesis on the binding affinity of m^6A reader proteins from the YTH protein family is examined.

2 Modified nucleosides as antiviral agents

Being involved in the regulation of various cellular processes, modified nucleoside structures often present a suitable starting point for drug design. Especially in the field of anticancer

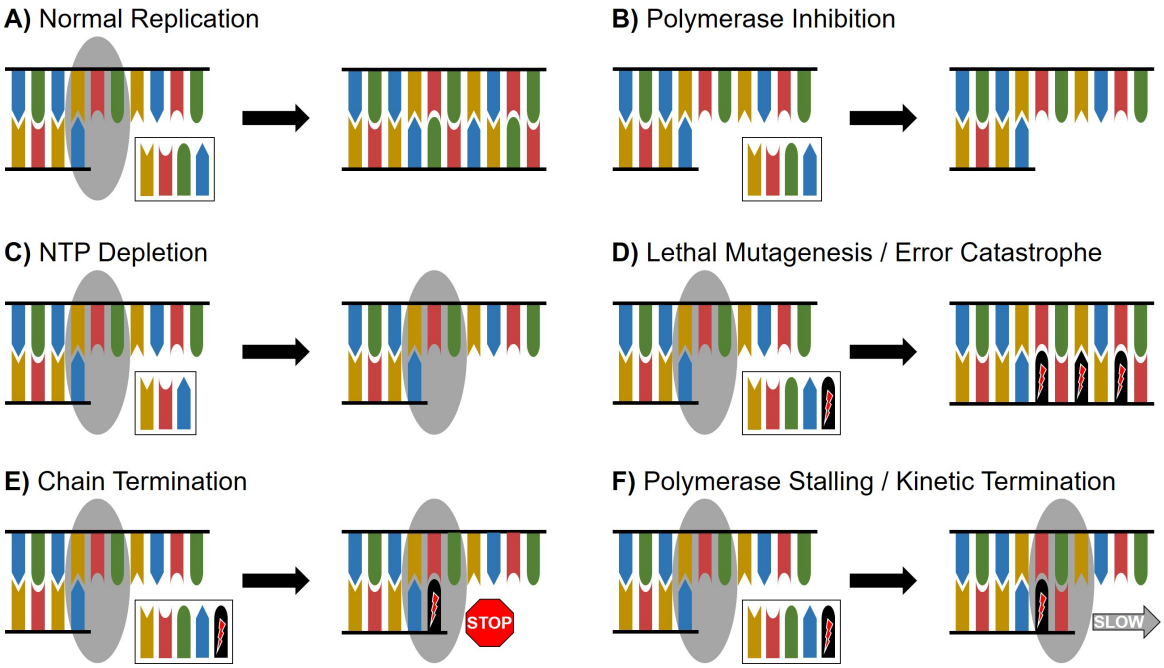

Figure 4: Mechanisms of action (MOAs) of antiviral nucleosides. A) Regular replication in absence of antiviral NTPs. B) Inhibition of the viral polymerase leading to inefficient replication. C) Inhibition of viral replication by depletion of canonical NTP stores. The antiviral nucleoside interferes with native NTP synthesis by inhibition of enzymes involved in their biosynthetic pathway. D) Lethal mutagenesis induced by incorporation of mutagenic NTPs. The ability to form base pairs with more than one cognate NTP leads to tranversion mutations, which accumulate over several replication cycles and lead to a fatal error catastrophe. E) Obligate chain termination following incorporation of an antiviral nucleoside lacking a 3'-OH group. F) Polymerase stalling or kinetic chain termination caused by incorporation of an antiviral nucleoside which renders further chain extension inefficient.[42,43] Colored sticks represent canonical NTPs, black sticks with red lightning flash depict the antiviral NTP. The viral polymerase is depicted as a grey oval, the available NTP pool is shown in a black box.

therapy and among antiviral therapeutics the number of nucleoside-based drugs is steadily increasing. Antiviral agents may in general act *via* two different mechanisms: they can either prevent the viral penetration of the cell membrane or the subsequent replication of the virus inside the host cell.[43] Due to their structural similarity to canonical nucleosides, antiviral nucleoside analogs fall into the second category and mainly interfere with viral DNA or RNA synthesis. Depending on their molecular structure, their detrimental effect on viral nucleic acid synthesis can arise from different mechanisms of action (Figure 4).[42,43]

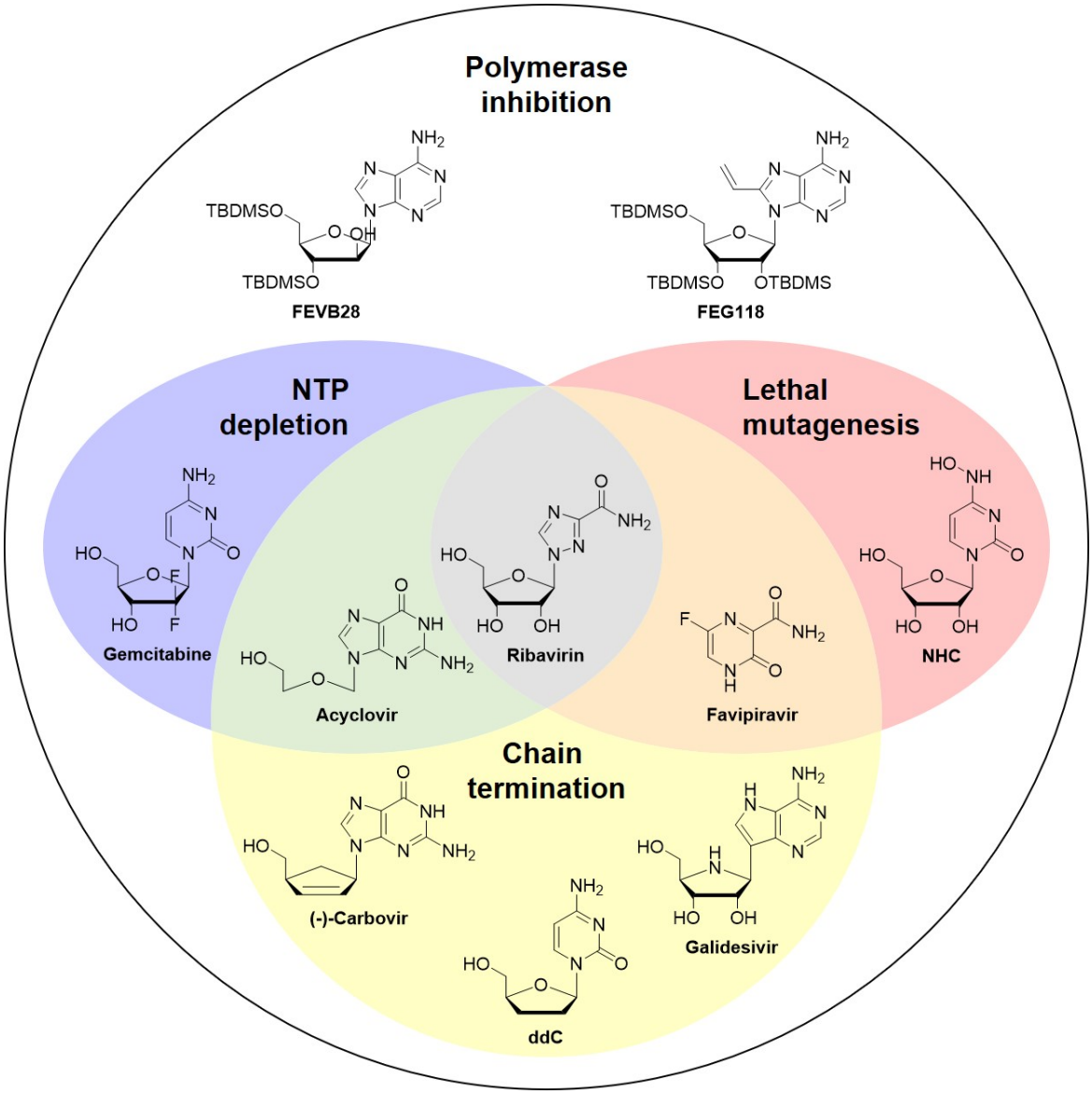

Figure 5: Examples of antiviral nucleoside analogs arranged according to their antiviral mechanism.

A common feature of antiviral nucleoside drugs is their competition with the canonical NTPs for the polymerase binding site. Because non-natural NTPs are commonly less effi-

ciently incorporated than their canonical counterparts, they inherently convey an inhibitory effect on the polymerase (Figure 4B). In addition, a few examples of antiviral nucleosides have been shown to exert a noncompetitive polymerase inhibition. Among these are the silylated adenosine analogs FEVB28 and FEG118 (Figure 5), which were shown to allosterically inhibit the bovine viral diarrheavirus polymerase through interaction with a binding site in proximity to the catalytic center.[44]

Apart from polymerase inhibition, three main MOAs can be distinguished: lethal mutagenesis, obligate or non-obligate/kinetic chain termination and depletion of cellular NTP pools. The latter (Figure 4C) exploits the structural similarity of the antiviral agents with natural NTPs or their synthetic precursors to competitively inhibit crucial enzymes in the NTP biosynthetic pathway; thus, the antivirals indirectly inhibit viral replication or transcription by lowering cellular NTP levels.[42] As an example, ribavirin (Figure 5) acts as an inhibitor of the inosine monophosphate dehydrogenase (IMPDH) and therefore leads to depletion of cellular GTP pools; this effect was found to be one of ribavirin's main MOAs against influenza virus.[45,46] Recently, it has been shown that not only the guanosine analog ribavirin, but also guanosine itself shows antiviral effects.[47] In the presence of high guanosine concentrations, Hepatitis C virus (HCV)-infected Huh-7.5 reporter cells displayed an increased GTP:GDP ratio. This GTP:GDP imbalance was found to reduce the fidelity of the HCV polymerase and resulted in an increased level of insertion and deletion mutations (indels). While there are several examples of antiparasitic and anticancer nucleoside drugs which alter NTP levels, e. g. allopurinol and 5-formyluracil, this MOA is rather rare among the group of antiviral nucleosides.[48,49] Here, a more common mechanism is the induction of lethal mutagenesis (Figure 4D).

To introduce mutations into the viral RNA, the antiviral NTP needs to be able to be incorporated opposite different template nucleosides. Antivirals of this category can therefore adopt two different anomeric or rotameric forms, as shown in Figure 6. As an example, ribavirin mostly acts as a G surrogate, yet rotation of the exocyclic amide functionality also enables base pairing with uridine.[46] An analogous rotameric equilibrium provides the basis for the antiviral activity of favipiravir.[50] N^4-hydroxycytidine (NHC), on the other hand, adopts two tautomeric forms which mimick the Watson-Crick faces of C and U, respectively.[51] Such mutagenic nucleosides can be incorporated opposite either of their base pairing partners during viral replication or transcription. Conversely, they can also serve as a template for incorporation of either cognate NTP. As a result, transition mutations are introduced, which accumulate over several replication cycles and ultimately result in lethal mutagenesis of the viral RNA, also known as error catastrophe.[46,52,53]

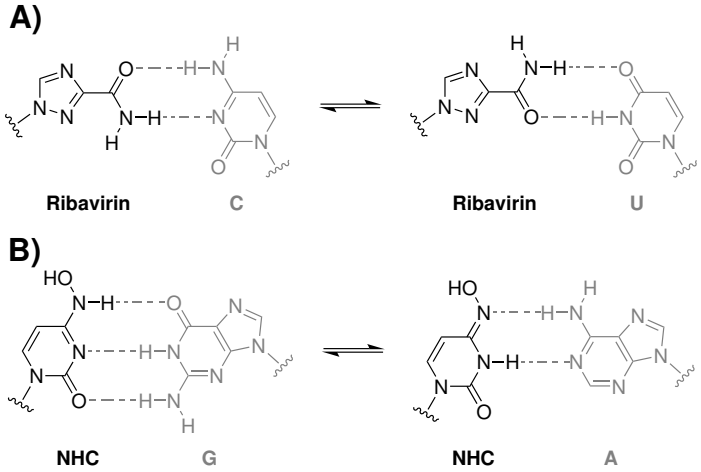

Figure 6: The mutagenic antiviral nucleosides ribavirin and NHC. A) The two rotamers of the ribavirin amide function form Watson-Crick base pairs with C and U, respectively.[46] B) The hydrogen bonding patterns of the amino (left) and imino (right) tautomers of NHC resemble C and U, and therefore allow base pairing with either G or A.[52]

The final class of nucleoside antivirals inhibits viral transcription or replication by termination of the polymerization process. Members of this class can be further categorized as either obligate or non-obligate chain terminators. Obligate chain terminators are incorporated into the viral RNA and inhibit further strand growth due to lack of a 3'-hydroxy function (Figure 4E). While already the canonical 2'-3'-dideoxynucleosides such as ddC show potent antiviral activity, e. g. against HIV, the design of obligate chain terminators has been expanded to include rigidified or even carbocyclic dideoxyribose-analogs such as in (-)-carbovir (Figure 5) for improved antiviral properties.[49] As another alternative to dideoxy-sugars, acyclic backbones have been implemented, which allow for better interactions with the viral polymerase binding sites due to their superior flexibility. This modification has led to prominent antivirals such as acyclovir (Figure 5) and the anti-HIV drug tenofovir.[49]

The term 'non-obligate chain terminators' describes nucleosides which do not lack the 3'-hydroxy group and therefore not inevitably cause chain termination; however, incorporation of these nucleosides into the viral RNA renders further RNA extension inefficient and ultimately results in polymerase stalling. A study on nucleosides inhibiting the hepatitis C viral polymerase found 2'-*C*-Me-modified nucleosides to be the most potent non-obligate chain terminators; combination with 7-deaza-nucleobases further improved their activity.[54] However, also C1'-substituted nucleosides and nucleosides with altered ribose structures, such as galidesivir (Figure 5), have shown activity based on this MOA.[55,56]

The global SARS-CoV-2 outbreak in 2019 further increased the interest in antiviral nucleosides and extensive studies aimed at repurposing and refining known nucleoside antivirals to rapidly provide treatment for the new pandemic. Especially amongst the mutagenic and chain-terminating nucleosides, promising candidates were identified; these will be discussed in further detail in part II of this thesis. This second part is centered around the antiviral adenosine analog remdesivir, which became the first FDA-approved anti-SARS-CoV-2 drug. In brief, the synthesis of a remdesivir phosphoramidite building block and its subsequent incorporation into RNA are used to investigate the mechanistic principles of remdesivir-induced stalling of the SARS-CoV-2 RNA-dependent RNA polymerase (RdRp). Based on the results of this study, the synthesis of remdesivir derivatives and their active triphosphate forms is described, aiming at an improved efficiency of remdesivir's polymerase stalling mechanism.

Part I

Probing substrate recognition of N^6-methyladenosine (m^6A) eraser and reader proteins using m^6A atomic mutagenesis

1 Background

Being the most prevalent posttranscriptional modification in eukaryotic mRNA, N^6-methyladenosine received special attention in the field of epitranscriptomics.[33] Especially the discovery that adenosine N^6-methylation is a reversible process and plays a role in regulatory cellular processes sparked interest in the proteome (writer enzymes, eraser enzymes and reader proteins; Figure 1.1) associated with this modification. These m^{6}A-interacting proteins and their biological relevance will be discussed in Section 1.2. Yet, a crucial prerequisite for understanding the m^{6}A interactome is the ability to site-specifically detect and quantify modified sites in cellular RNA. Therefore, Section 1.1 will cover an overview of methods which have been established for m^{6}A mapping and quantification.

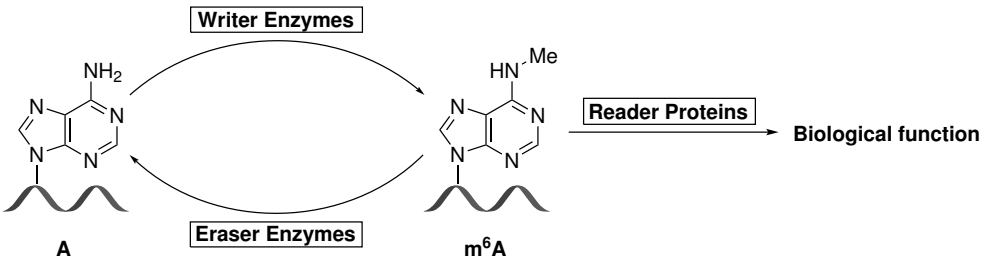

Figure 1.1: Schematic representation of the m^{6}A interactome. Adenosine in RNA is methylated by writer complexes using *S*-adenosylmethionine (SAM) as a cofactor. The methylation may be reverted by oxidative demethylation mediated by eraser enzymes. The m^{6}A modification is recognized by a set of reader proteins, which affect the cellular fate of their bound transcripts. The m^{6}A interactome will be discussed in further detail in Section 1.2.

1.1 Distribution and mapping of m^{6}A in mRNA

The great interest in function and cellular distribution of the m^{6}A modification led to the development of various methods for the detection, validation and quantification of adenosine methylation sites in RNA. The first high-throughput m^{6}A sequencing methods utilized m^{6}A-specific antibodies (Figure 1.2A). These techniques, termed m^{6}A-seq and MeRIP-Seq (methylated RNA immunoprecipitation with next-generation sequencing), involve digestion of the RNA of interest into fragments of ca. 100 nt length. Fragments containing one or more m^{6}A modifications are immunoprecipitated followed by next-generation sequencing. Plotting the frequency of sequencing reads for every position of the sequence results in peaks statistically centered around the m^{6}A site.[34,57]

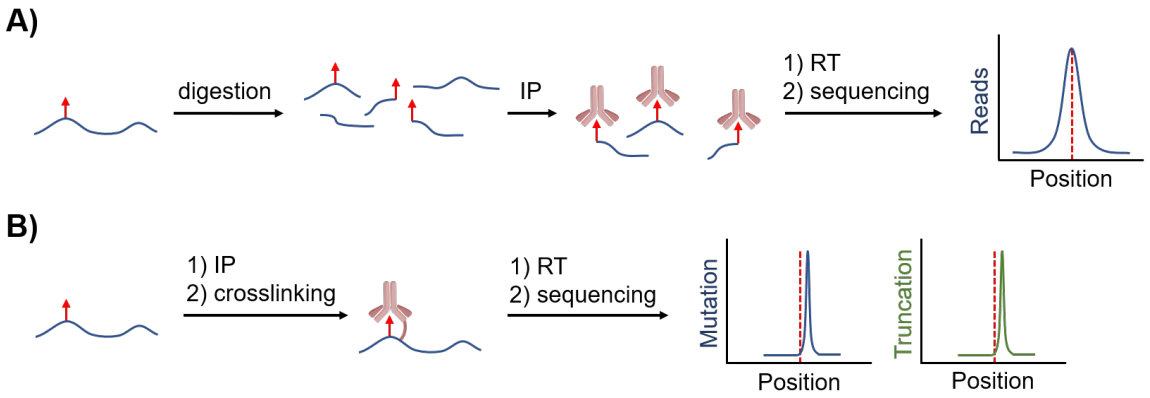

Figure 1.2: Schematic outline of antibody- and UV-crosslinking-mediated high-throughput mapping of m^6A sites (red arrows). A) m^6A mapping based on immunoprecipitation with m^6A-specific antibodies (m^6A-seq, MeRIP-Seq).[34,57] B) m^6A mapping using immunoprecipitation followed by photo-crosslinking (miCLIP, m^6A-CLIP).[58,59] Red dashed lines mark the position of the m^6A site.

Both methods suffer from low resolution (ca. 200 nt) and cannot detect the presence of more than one modification sites in close proximity, as they will be covered by the same m^6A peak. The resolution can be improved to 23 nt using a photo-crosslinking-assisted m^6A sequencing strategy (PA-m^6A-seq), where cells producing the target transcript are grown in medium supplemented with 4-thiouridine (s^4U).[60] Anti-m^6A antibodies can in this case be crosslinked to nearby s^4U sites *via* irradiation at 365 nm. These crosslinked sites are read as U instead of C in sequencing; the position of m^6A sites can therefore be more precisely determined based on the occurence of U-to-C mutations in proximity. Further method refinement resulted in the development of m^6A individual-nucleotide-resolution cross-linking and immunoprecipitation (miCLIP) and m^6A-CLIP, which enable UV-mediated crosslinking of the antibody to the target transcript even in absence of further modified nucleosides such as s^4U (Figure 1.2B).[58,59] Similar to PA-m^6A-seq, the target transcript is immunoprecipitated followed by crosslinking of RNA and antibody by UV irradiation. The crosslink causes frequent C-to-U mutations adjacent to the m^6A site during cDNA generation, accompanied by increased cDNA truncation. The thereby obtained mutation and truncation patterns at the adjacent position enable m^6A mapping at single-nucleotide resolution. However, there are still drawbacks to the antibody-based approaches: they usually require comparably large amounts of input RNA and rely on the use of costly antibodies. Additionally, the utilized antibodies are not completely specific for m^6A sites, but also bind to the structurally related m^6A_m.[61] Therefore, the development of antibody-free alternatives was desired.

An early, prominent example is site-specific cleavage and radioactive-labeling followed by ligation-assisted extraction and thin-layer chromatography (SCARLET).[62] Here, RNase H

cleavage of an RNA at a specific site is induced guided by a suitable RNA/2'-*O*-Me-RNA hybrid as complementary strand. After cleavage, the nucleotide of interest is located at the 5'-terminal end of the cleaved strand and can be radioactively labeled with a ^{32}P phosphate group. Subsequent release of the labeled nucleoside monophosphate followed by TLC analysis enables detection of the methylation status and quantification of the m^{6}A level at the probed site. While achieving single-nucleotide resolution, SCARLET is not suitable for high-throughput sequencing. Yet, it can be used to validate m^{6}A sites predicted by other methods, as well as to quantify the methylation extent of single sites. Quantification is required to fully characterize an m^{6}A site, as not each copy of an RNA transcript is methylated; the methylation extent of a site therefore presents an additional layer of gene regulation.[62,63]

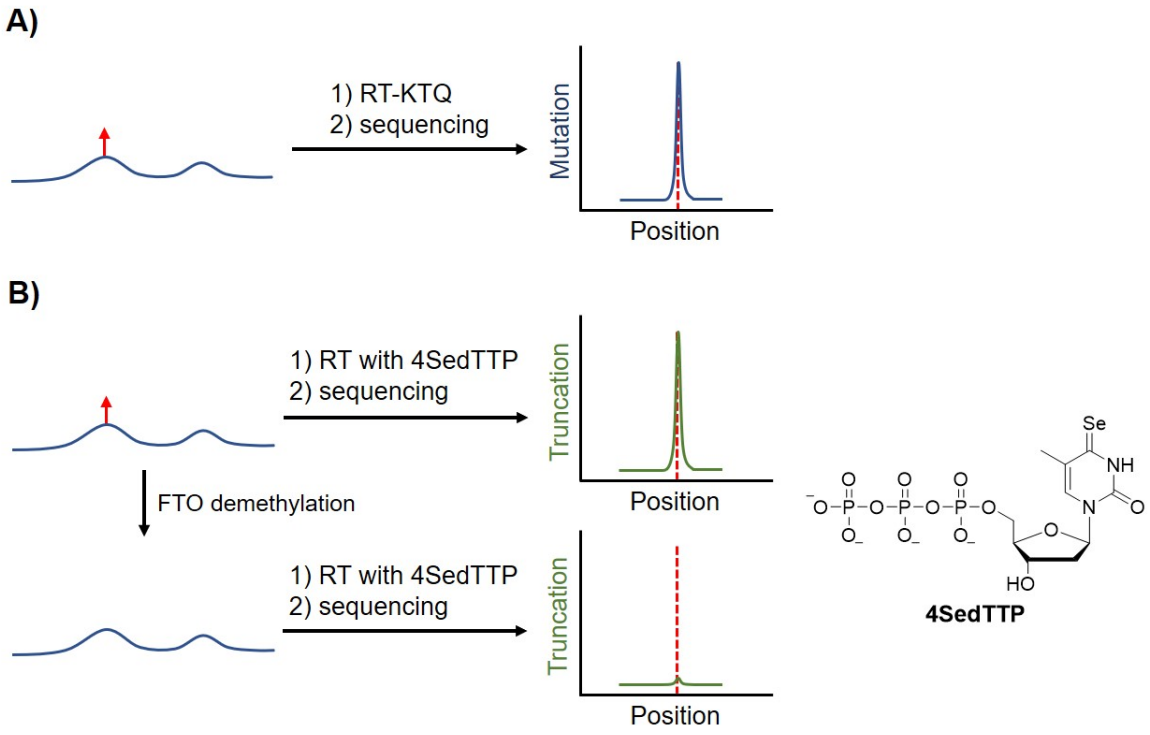

Figure 1.3: Mapping of m^{6}A sites (red arrows) based on modified reverse transcription procedures. A) Detection of methylated sites using the engineered reverse transcriptase RT-KTQ.[64] B) Induction of RT truncation opposite m^{6}A by 4SedTTP.[65] Red dashed lines mark the position of the m^{6}A site.

A different approach aimed at conversion of the usually reverse-transcription (RT)-silent into an RT-active modification. This was achieved by engineering the modified reverse transcriptase RT-KTQ, which displays a higher frequency of misincorporations opposite m^{6}A than opposite A, thereby generating a detectable RT error signature when the substrate is methylated (Figure 1.3A).[64] However, the use of this custom modified enzyme is crucial

to the success of this method and may limit the general applicability of this approach. An alternative method, which allows employment of commercially available reverse transcriptases for m^{6}A detection, centers around the use of the modified nucleoside triphosphate 4SedTTP during reverse transcription (Figure 1.3B).[65] 4SedTTP causes RT truncation opposite m^{6}A sites, but can be efficiently incorporated opposite unmodified A. Subjecting both an untreated sample and a sample treated with the m^{6}A demethylase FTO to reverse transcription in presence of 4SedTTP therefore leads to different RT truncation frequencies of the two samples if the input RNA is methylated. Using this technique, even closely gathered m^{6}A sites can be resolved. Additionally, a linear relationship between the fraction of truncated product and the fraction of A methylation allows for quantification of the methylation level of m^{6}A sites.

Two other individual methods (Figure 1.4) achieved conversion of m^{6}A into RT-active modifications by metabolic labeling. Growing cells expressing the target sequence in a medium containing the *S*-adenosylmethionine (SAM) analogs SeAdoYn or allyl-SeAM leads to the formation of N^6-propargyl- or N^6-allyladenosine at native m^{6}A sites, respectively.

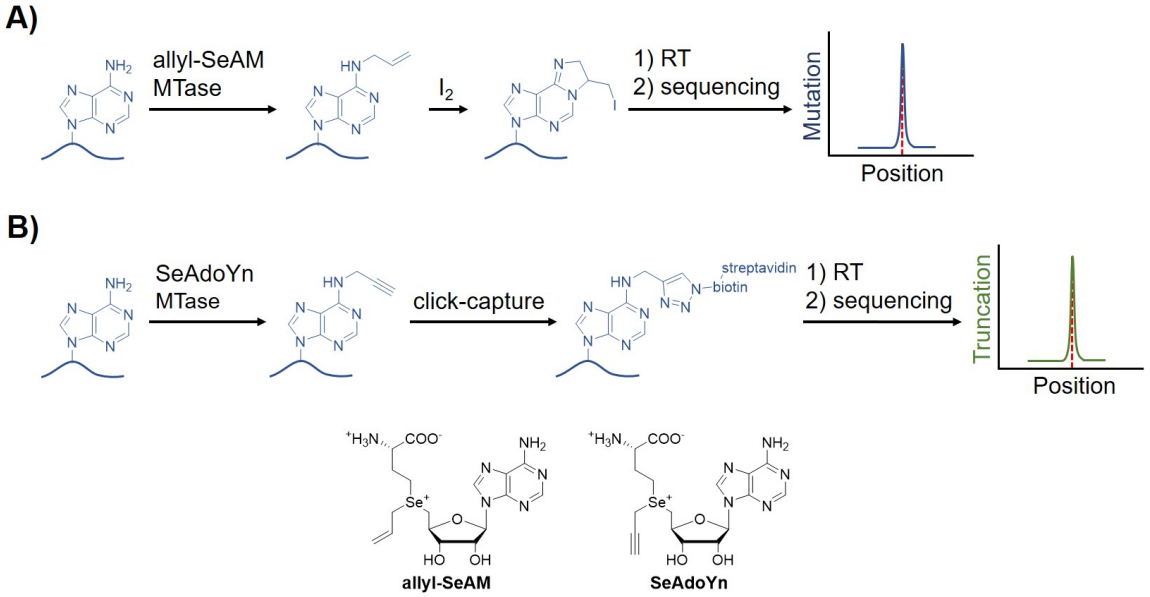

Figure 1.4: Metabolic labeling-based strategies for the detection of m^{6}A sites. A) Iodination of N^6-allyladenosine leads to cyclization and misincorporations during reverse transcription.[66] B) Click-labeling of N^6-propargyladenosine with biotin and capturing with streptavidin-coated magnetic beads causes RT truncation.[67] Red dashed lines mark the position of the m^{6}A site.

The cofactor design counteracts the generally low promiscuity of methyltransferase enzymes for their cofactors: the SAM analogs comprise a selenonium instead of a sulfonium center, which enhances cofactor stability, and β-unsaturated transferable alkyl groups, which

lead to increased acceptance of the substrate by alkyltransferases.[67–70] Thus generated N^6-propargyl-A sites can be labeled with biotin azide using click chemistry followed by immobilization on streptavidin-coated magnetic beads, which causes RT-termination directly downstream of the alkylated site.[67] N^6-Allyladenosine, in contrast, was demonstrated to cyclize upon treatment with iodine.[71] The cyclized species is read as C rather than A, which enables detection of alkylated sites based on a high mutation rate following iodine treatment.[66]

Two recent developments, dubbed MAZTER-seq and m^{6}A-REF-seq (m^{6}A-sensitive RNA-endoribonuclease-facilitated sequencing), make use of the inherent methylation sensitivity of the *E. coli* endoribonuclease MazF, which efficiently cleaves ACA sequence contexts but is inhibited by (m^{6}A)CA.[72–74] Exploiting this selectivity provides a means for detection of methylated A and quantification of the methylation level, but does not enable mapping of m^{6}A sites outside the (m^{6}A)CA context. A broader variety of sequence contexts can be screened by using the RNA-cleaving deoxyribozyme VMC10, which acts on DGACH (D = A, G, U; H = A, C, U) variations of the m^{6}A consensus motif and displays similar m^{6}A sensitivity as MazF.[75] However, VMC10 is not suitable for use in high-throughput methods, since the binding arms of the DNAzyme have to be individually designed for each probed putative methylation site. Nonetheless, VMC10 finds use in validation and quantification of m^{6}A sites detected by other methods.

Finally, two recent advances termed m^{6}A-SEAL and DART (deamination adjacent to RNA modification targets)-seq are able to detect m^{6}A sites at high or single-nucleotide resolution across all variations of the m^{6}A consensus motif DRACH in an antibody-independent method without the need for engineered polymerases or metabolic labeling. DART-seq (Figure 1.5A) instead utilizes the native human m^{6}A reader protein YTHDF2 to detect methylated adenosine sites.[61] Particularly, the m^{6}A binding domain of YTHDF2 is fused to the cytidine deaminase APOBEC1, which catalyzes C-to-U editing events. The m^{6}A-affinity of YTHDF2 guides the fusion protein to methylated RRACH motifs, where APOBEC1 mediates C deamination directly adjacent to the m^{6}A site. The C-to-U mutation generated this way subsequently allows for detection of the neighboring methylation site during high-throughput sequencing. m^{6}A-SEAL (Figure 1.5B), on the other hand, involves the m^{6}A eraser enzyme FTO: the target RNA is first fragmented, followed by FTO-treatment.[76] Here, methylated A-sites are oxidized to N^6-hydroxymethyladenosine (hm^{6}A), which can be converted into the more stable N^6-dithiolthreitolmethyladenosine (dm^{6}A). The presence of the free thiol moiety of this species is then exploited for enrichment of methylated RNA fragments by biotin labeling followed by capture using streptavidin-coated magnetic beads.

m^{6}A sites are finally mapped in high resolution by sequencing of the captured fragments.

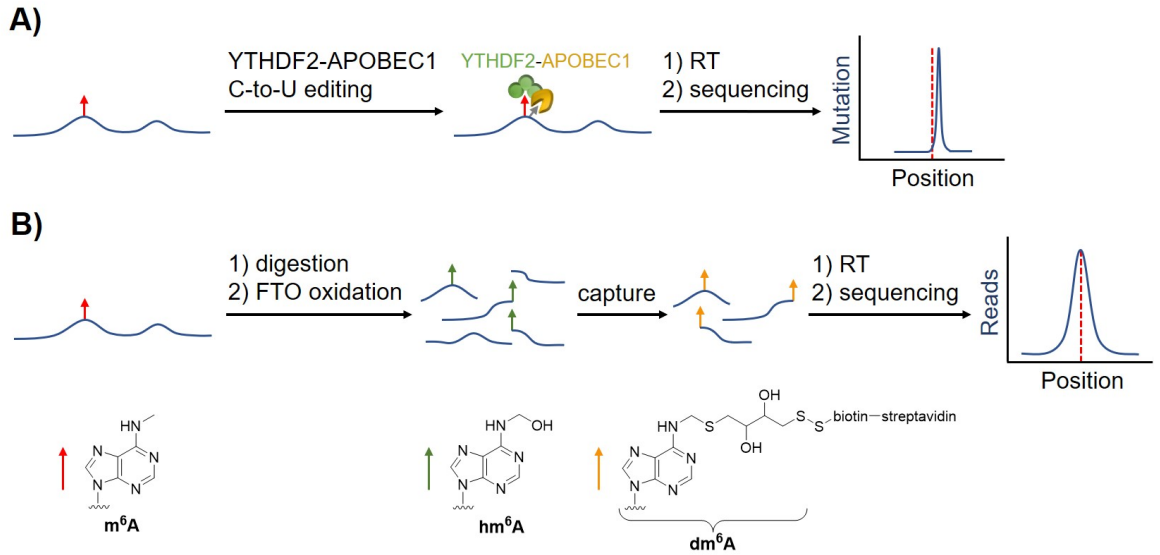

Figure 1.5: Schematic overview of the m^{6}A mapping techniques DART-seq and m^{6}A-SEAL. A) DART-seq uses a YTHDF2-APOBEC1 fusion protein to induce C (grey arrow) deamination adjacent to the m^{6}A site (red arrow).[61] B) m^{6}A-SEAL relies on FTO-mediated oxidation of m^{6}A followed by capture of the oxidized intermediate.[76] Red dashed lines mark the position of the m^{6}A site.

Using individual or combinations of the methods described above, several thousand m^{6}A sites have been mapped across all types of RNA. Analysis of these maps reveals that the vast majority of m^{6}A sites in mRNA are situated in a RRACH sequence context with GGACU as the most frequently detected member.[34,60] The methylation sites are not evenly distributed across the whole transcripts; instead, m^{6}A sites were found to be especially enriched in the 3' UTR and the CDS, where they frequently cluster around stop codons.[34,57,60] This statement was, however, rephrased after further analysis: m^{6}A sites are enriched in the first 150–400 nt of the 3'-terminal exon, which contains $\geq$ 70% of the total m^{6}A sites in mRNA. The apparent clustering around stop codons can be traced back to the fact that most stop codon sites are located within this region. Yet, even mRNAs bearing the stop codon in the second-to-last exon display m^{6}A enrichment in the terminal exon and not around the stop codon.[59] Adenosine methylation inside 3'-terminal exons was shown to be associated with splicing control, reduced transcript stability and destabilization of developmental regulators.[36,57,77] In contrast, the role of m^{6}A in the 5' UTR remained for long elusive; it could eventually be demonstrated to promote cap-independent translation, thereby increasing translation levels of methylated transcripts as a response to cellular stress.[35,78] m^{6}A-dependent regulation of cap-independent translation is achieved by recruitment of the translation initiation factor eIF3 to m^{6}A sites; similarly, the majority of other m^{6}A-

dependent regulatory processes is mediated by m^{6}A-interacting proteins. In general, the fraction of the proteome interacting with m^{6}A can be categorized into writer, reader and eraser proteins.

1.2 The m^{6}A interactome: writer, reader and eraser proteins

1.2.1 m^{6}A writer enzymes

N^6-Methylation of adenosine in mRNA is realized by a multicomponent methyltransferase (MTase) complex. When this complex was first isolated from HeLa cells, only one catalytically active 70 kD subunit, termed MT-A70, could be identified, though it was understood that auxiliary components are necessary for activity.[79] MT-A70, which was later renamed methyltransferase-like protein 3 (METTL3), was found to perform adenosine methylation in a SAM-dependent manner. Genetic deletion of METTL3 leads to (nearly) complete loss of m^{6}A in polyadenylated mRNA, indicating that it is the main methyltransferase responsible for A methylation in mRNA. In contrast, METTL3 deletion has no influence on the methylation levels of rRNA or snRNA, which demonstrates its selectivity for mRNA substrates.[80] The solution structure of METTL3 revealed that a zinc finger domain of METTL3 binds to mRNA containing the sequence motif GGACU, or more general DRACH (D = A, G, U; R = A, G; H = A, C, U), but does not bind to transcripts without this motif; as a result, m^{6}A sites are mainly found inside the DRACH consensus motif.[81]

As additional components of the m^{6}A writer complex, METTL14 and Wilms' tumor 1-associating protein (WTAP) were identified. METTL14 is structurally very similar to METTL3 and forms a METTL3/METTL14 heterodimer *in vivo* as well as *in vitro*. Elucidation of the METTL3/METTL14 crystal structure revealed that solely METTL3 binds SAM and is the catalytically active subunit, whereas METTL14 possesses a degenerate SAM binding pocket and plays a non-catalytic role by stabilizing the active METTL3 conformation.[82–84]

The WTAP component of the MTAse complex was, similar to METTL14, also found to be crucial for methyltransferase activity *in vivo*; *in vitro*, however, absence of WTAP interestingly did not affect activity.[85] *In vivo*, WTAP is responsible for localization of the MTase complex to the nuclear speckles where adenosine methylation as well as alternative splicing events take place, thereby indirectly affecting the methyltransferase activity.[85,86]

Methylation of almost all internal m^6A sites in mRNA but not the first nucleotide adjacent to the 5' m^7G-cap was identified as WTAP-dependent, which suggested the existence of a separate MTase responsible for 5' cap m^6A_m generation.[87]

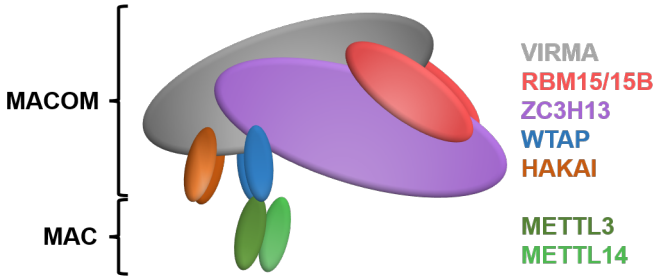

Figure 1.6: Schematic structure of the MAC-MACOM methyltransferase complex.[88] The size of the components was scaled to their molecular weight.

Besides METTL3, METTL14 and WTAP, four additional MTase complex components have been identified: VIRMA, RBM15/15B, ZC3H13 and HAKAI form, alongside WTAP, the m^6A-METTL-associated complex (MACOM), which aids activity of the m^6A-METTL complex (MAC) comprised of METTL3 and METTL14 (Figure 1.6).[89] VIRMA is the largest component of the MACOM and serves as a scaffold for assembly of the other MACOM components, in particular mediating the interaction between WTAP and HAKAI.[88,90] Furthermore, it stabilizes WTAP and effects the selectivity of the MTase for methylation in the 3' UTR. RBM15 and its paralog RBM15B, in turn, are responsible for the site specificity of the complex: while DRACH motifs are distributed uniformly across the mRNA, not all of them are MAC-MACOM targets. Instead, methylation only occurs at DRACH motifs in proximity to RBM15/15B binding sites.[80,91] HAKAI stabilizes WTAP, RBM15/15B and VIRMA and is required for the interaction between the other MACOM components.[88] Lastly, zinc finger CCCH domain-containing protein 13 (ZC3H13) also takes part in stabilization of the MTase complex and serves as an adapter connecting WTAP and RBM15/15B.[89]

Although the MAC-MACOM complex is responsible for the methylation of most mRNA m^6A sites, another METTL enzyme, METTL16, has been found to act on mRNA substrates as well.[92,93] METTL16 was initially identified as a methyltransferase acting on pre-mRNAs and non-coding RNAs such as the U6 snRNA, which is part of the spliceosome. Thus, METTL16 activity likely plays a role in splicing regulation.[94] Additionally, the enzyme methylates the human MAT2A mRNA, which results in subsequent MAT2A degradation mediated by the m^6A binding protein YTHDC1.[92,93] Thus, the expression of MAT2A, which encodes the SAM synthetase, is regulated by METTL16 methylation, thereby generating a regulatory circuit mechanism controlling SAM synthesis. High intra-

cellular SAM levels enable efficient SAM-dependent MAT2A methylation by METTL16. This MAT2A methylation, in turn, impairs expression of the SAM synthetase, ultimately resulting in reduction of intracellular SAM levels.[92,93] Recent studies confirmed MAT2A mRNA as the primary target of endogenous METTL16, but additionally suggested activity on a multitude of other mRNA targets, which implies a larger influence of METTL16 on global m^{6}A levels in mRNA than initially assumed.[95,96]

Independent from the MAC-MACOM MTase, which methylates internal adenosines inside RRACH motifs, synthesis of m^{6}A$_m$ at the 5' cap structure is mediated by the SAM-dependent cap-specific adenosine-*N*^{6}-MTase (CAPAM), also known as PCIF1 (phosphorylated CTD interacting factor 1).[81,97] CAPAM recognizes the m^{7}G cap structure and methylates the adjacent adenosine site; here, it shows preference for m^{7}GpppA$_m$ over m^{7}GpppA structures. As it was found that the *N*-terminal domain of CAPAM interacts with the C-terminal domain of RNA polymerase II, installation of cap m^{6}A$_m$ is assumed to occur cotranscriptionally.

1.2.2 m^{6}A reader proteins

Following the installation of m^{6}A sites in mRNA by methyltransferases, these methylation marks are recognized by reader proteins. Upon binding to their target methylation sites, the readers affect the cellular fate of their bound substrates and therefore mediate a broad variety of m^{6}A-dependent regulatory processes (Figure 1.8). m^{6}A binders acting on mRNA can be categorized in three groups based on their mechanism of m^{6}A recognition.[98] Class I comprises YTH domain proteins, which share a conserved binding domain to bind m^{6}A inside its RRACH consensus motif. Class II readers, in contrast, do not bind directly to the modification site, but instead recognize local structural changes induced by the presence of m^{6}A. Class III includes proteins that display direct, structure-independent recognition of m^{6}A sites without possessing a YTH binding domain.

The YTH (YT-521B homology) domain, first characterized as a domain of splicing factor YT-521B (later renamed YTHDC1), was initially reported as a general RNA binding domain but later identified to be m^{6}A-selective.[36,57,99] In human cells, five members of the YTH-domain protein family are found, namely YTHDC1, YTHDC2, and YTHDF1–3. Crystal structures have shown that these five proteins share a conserved m^{6}A binding pocket (Figure 1.7A+B). The methylated adenine nucleobase is accommodated in a hydrophobic aromatic cage comprising three tryptophane residues in YTHDF1–3 or two tryptophanes and one leucine in YTHDC1 and YTHDC2.

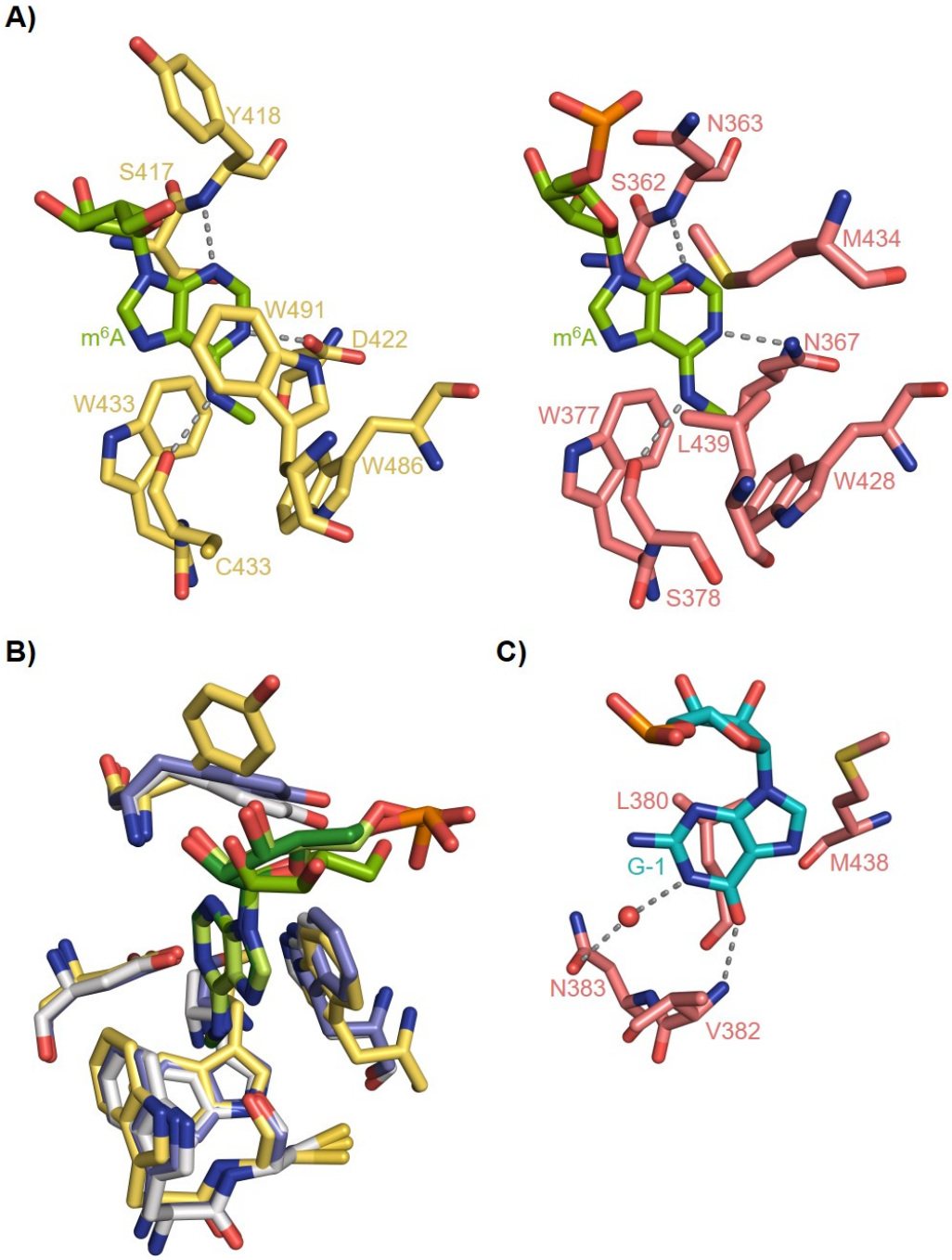

Figure 1.7: Crystal structures of the YTH protein binding sites. A) Structurally similar aromatic cage structures accomodate m^6A (green sticks) in the YTH domains of YTHDF2 (left, yellow sticks) and YTHDC1 (right, salmon sticks). Both complexes are stabilized by hydrogen bonds (grey dashed lines) between the nucleobase nitrogens and nearby polar amino acid residues. B) The aromatic cage structures among the YTHDF subfamily members YTHDF1 (blue sticks), YTHDF2 (yellow sticks) and YTHDF3 (white sticks) are highly conserved and almost perfectly superimposable. C) The G-1 (cyan sticks) binding pocket of YTHDC1 (salmon sticks) features stabilizing hydrogen bonds (grey dashed lines) between nucleobase and protein scaffold. YTHDF1: PDB ID 4RCJ; YTHDF2: PDB ID 4RDN; YTHDF3: PDB ID 6ZOT, YTHDC1: PDB ID 4R3I.

The m^{6}A methyl group is pointed toward one Trp to engage in methyl-π-interactions while the other two residues sandwich the nucleobase heterocycle and provide stabilizing π-π-stacking interactions. In addition to this m^{6}A-specific aromatic cage, hydrogen bonds between YTH domain and RNA substrate, involving N1, N3, N7 and the exocyclic methylamino group of m^{6}A, stabilize the complex structure.[100–103] YTHDC1 features an additional binding pocket for the G-1 nucleoside of the substrate RRACH motif (Figure 1.7C). The guanosine nucleobase engages in hydrogen bonding interactions with Val382 and Asn383 (bridged by a water molecule). As these stabilizing interactions would be lost if adenosine were at position -1, YTHDC1 is the only human YTH domain protein displaying explicit preference for G(m^{6}A)C over A(m^{6}A)C substrates.

Although the five members of the YTH domain protein family are structurally similar, their cellular localization and biological roles differ (Figure 1.8). YTHDC1 is the only YTH domain protein localized in the nucleus; here, it is involved in alternative splicing of pre-mRNAs. YTHDC1 affects the localization of the splicing factors SRSF3 and SRSF10, which promote exon inclusion or exon skipping, respectively.[104] YTHDC1 recruits SRSF3 to the splicing sites in the nuclear speckles while simultaneously repelling SRSF10; therefore, YTHDC1 induces exon inclusion in its bound pre-mRNA targets. Following the splicing events, YTHDC1 mediates the nuclear export of the mature RNA *via* interactions with the export adaptor protein SRSF3 and the nuclear export factor NXF1.[105]

In the cytoplasm, methylated transcripts further interact with YTHDF1–3 and YTHDC2. Here, YTHDF1 acts together with YTHDF3 in a cooperative manner to promote translation of its target transcripts.[106,107] YTHDF1 was shown to increase ribosome occupancy of its mRNA targets *via* interaction with the transcription initiation factor eIF3. YTHDF1 recognition sites, however, are mainly located in the 3' UTR, whereas the translation initiation complex binds at the 5' cap structure. To explain the experimental results, a closed loop structure was proposed (Figure 1.9A).[35] Aided by the poly-A binding protein (PABP), YTHDF1 binding is suggested to recruit the translation initiation complex (eIF3, eIF4E, eIF4G) to the 5' cap structure, which in turn recruits the 40S rRNA to initiate the translation process. Alternatively, eIF3 was also found to bind directly, independent of YTHDF1, to m^{6}A sites in the 5' UTR to promote cap-independent translation (Figure 1.9B).[78]

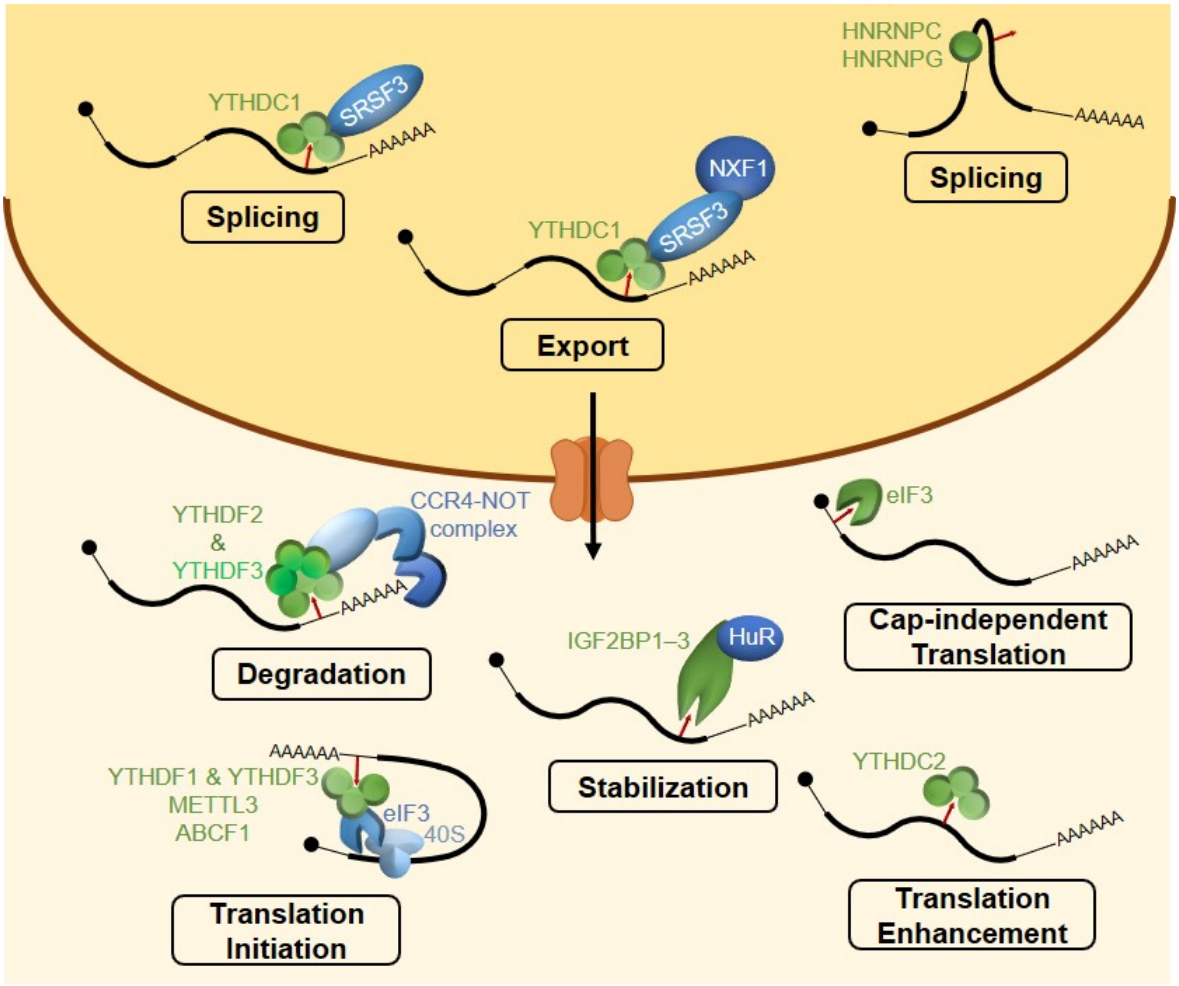

Figure 1.8: Cellular localization and biological roles of m^{6}A reader proteins. Inside the nucleus, YTHDC1, HNRNPC and HNRNPG mediate splicing processes and subsequent nuclear export of the mRNA. In the cytoplasm, binding of m^{6}A by YTHDF1–3, IGF2BP1–3 as well as METTL3, ABCF1 and eIF3 promotes translation, stabilization or degradation of methylated transcripts.[108]

While YTHDF1 promotes translation of its target transcripts, YTHDF2 facilitates RNA degradation; also this function is fulfilled in synergy with YTHDF3.[107] Upon binding to methylated mRNA, YTHDF2 relocalizes the bound targets to processing bodies (P bodies) and recruits the CCR4-NOT deadenylase complex to initiate mRNA degradation by removal of the poly-A tail.[36,109] In contrast to its destabilizing function in the cytoplasm under normal cellular conditions, heat-shock stress induces relocalization of YTHDF2 to the nucleus, where it binds to m^{6}A sites in the 5' UTR to shield them from demethylation by FTO and to promote cap-independent translation.[110] Although several publications reported YTHDF1–3 to affect different cellular processes (translation vs. decay), the role of these three proteins is still debated. Upon HIV-1 infection, all three YTHDF proteins have been demonstrated to bind to m^{6}A sites in the viral RNA to inhibit reverse transcription; therefore, some reports have proposed redundancy of YTHDF1–3.[80,111]

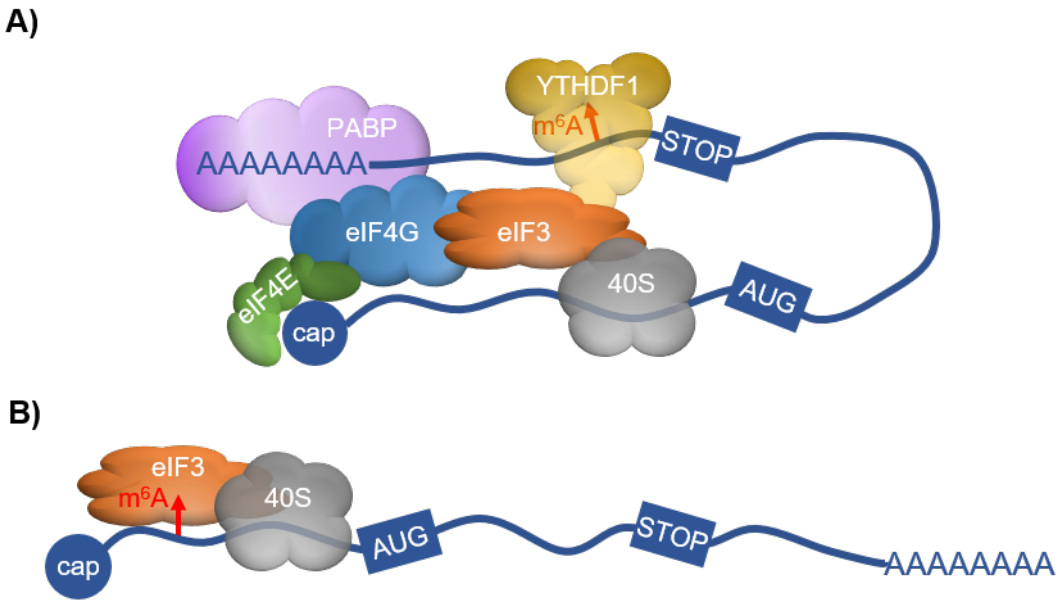

Figure 1.9: Mechanisms of m^{6}A-dependent translation. A) Recruitment of the translation initiation complex by YTHDF1 binding to 5' UTR m^{6}A sites *via* a closed loop structure. B) Direct binding of eIF3 to m^{6}A sites in the 3' UTR to initiate cap-independent translation.[35,78]

YTHDC2 is the largest human YTH domain protein and the only one featuring additional functional domains besides the YTH domain.[112] In case of YTHDC2, both the conserved YTH domain and an additionally present R3H domain contribute to *in vivo* RNA binding. *Via* its two ankyrin repeat domains YTHDC2 associates with the cytoplasmic 5'–3' exoribonuclease XRN1, thereby mediating the degradation of its mRNA targets and decreasing their cellular abundance.[112,113] Furthermore, YTHDC2 interacts with the 40S ribosomal subunit close to mRNA entry and exit site and thus facilitates the association of its methylated mRNA targets with the ribosome to enhance translation.[112,113] This translation enhancement is further supported by a helicase domain of YTHDC2, which, upon binding of the YTHDC2 YTH domain to m^{6}A sites in the CDS, locally unwinds the mRNA secondary sructure. This, in turn, results in lower ribosomal pausing during the translation process.[114]

Unlike YTH domain proteins, class II m^{6}A readers do not possess any domains for direct m^{6}A recognition. Instead, these readers respond to m^{6}A-induced local changes to the mRNA secondary structure. The methyl group at N^6 can adopt two conformations (Figure 1.10A). While the *syn* conformation is favored, the methyl group needs to adopt the sterically disfavored *anti* conformation to enable engagement in Watson-Crick base pairing. As a consequence, N^6-methylation of adenosine destabilizes duplex structures by 0.7–1.5 kcal/mol.[115] Conversely, the methylated base stacks more strongly than unmethylated A in unpaired RNA regions. The resulting overall preference of m^{6}A for unpaired

regions may lead to methylation-induced structural changes in regions of low duplex stability (m^6A switch), which can facilitate binding of proteins to their cognate regions. As an example, the class II binder heterogeneous ribonucleoprotein C (HNRNPC) binds to single-stranded U_5 tracts. In MALAT1 RNA, for example, the U_5 motif is partially hybridized in a stem loop. Introduction of m^6A destabilizes the stem and increases the loop size, thereby making the HNRNPC binding site accessible (Figure 1.10B).[116] Confirmed class II binders are the nuclear HNRNPC and HNRNPG, which regulate pre-mRNA splicing.[116,117]

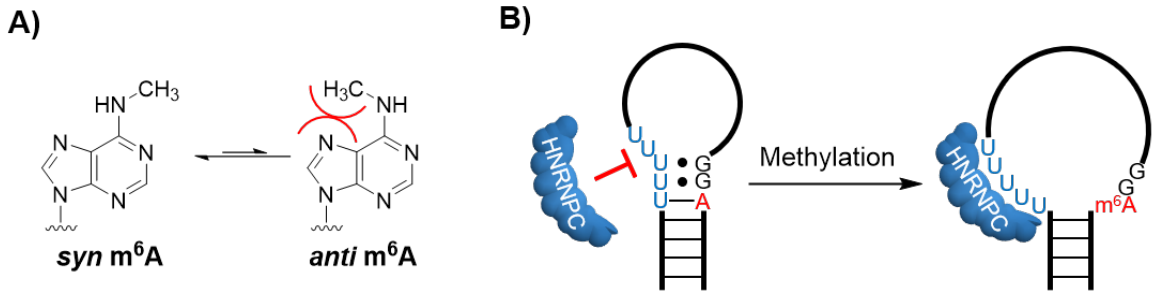

Figure 1.10: Principle of m^6A binding by class II reader proteins. A) *Syn* (favored) and *anti* (disfavored) conformations of the N^6-methyl group of m^6A. B) Local structural change in MALAT1 RNA following duplex destabilization induced by adenosine N^6-methylation. The structural change enables binding by the class II reader protein HNRNPC.[116]

Class III comprises the insuline-like growth factor 2 mRNA-binding proteins 1–3 (IGF2BP1–3), which recognize m^6A inside a UGG(m^6A)C consensus motif *via* their KH domains; the recognition mechanism is not yet fully elucidated.[98,118] IGF2BPs stabilize their mRNA targets by recruitment of stabilizer proteins, e. g. HuR, and promote their expression.[118] Other notable class III members are METTL3 and eIF3. Besides its function in the nuclear MTase complex, METTL3 is also found in the cytosol. Here, it binds to m^6A sites and recruits eIF3 *via* its non-catalytic *N*-terminal domain to promote cap-independent translation.[119] Similar translation-promoting effects are achieved by binding of ATP-binding cassette protein F1 (ABCF1) or direct m^6A binding by eIF3.[78,120]

The involvement of m^6A and its reader proteins in a large variety of regulatory processes, as previously outlined, as well as their role in the development (e. g. colon cancer metastasis) or inhibition (e. g. HIV-1) of diseases sparked the interest in this mRNA modification and made m^6A one of the most extensively studied modified nucleosides in the epitranscriptome.[111,121] This interest was further fueled when FTO was identified as an *in vivo* m^6A eraser enzyme, which suggested a reversible nature of the m^6A modification and highlighted its regulatory relevance.[38]

1.2.3 m^{6}A eraser enzymes

The human *fto* (fat mass and obesity-associated) gene received its name after single nucleotide polymorphisms in its first intron were found to be closely linked to obesity-associated traits.[122–124] Shortly after, the *fto* gene was reported to encode a non-heme Fe(II)- and α-ketoglutarate-dependent dioxygenase enzyme, consequently named FTO.[125] FTO was found to be selective for single-stranded (ss) nucleic acids and to catalyze oxidative demethylation of m^{3}dT, m^{1}dA and m^{3}dC in ssDNA and m^{3}U in ssRNA.[125,126] However, the remarkably low demethylation activity suggested that none of these modifications represent physiologially relevant FTO targets. Instead, m^{6}A in nuclear mRNA was identified as a major substrate of FTO.[38] Owing to the nuclear localization of FTO but high abundance of m^{6}A sites in mature cytoplasmic mRNA, some reports questioned the biological relevance of m^{6}A demethylation by FTO and challenged the concept of m^{6}A reversibility.[80,127] These doubts appeared to be corroborated by the identification of 5' cap m^{6}A$_m$ as an additional FTO substrate, which was demethylated even more effectively than m^{6}A.[24,128] More recent research results, however, strongly support the notion that both internal m^{6}A and cap-m^{6}A$_m$ are relevant *in vivo* substrates of FTO. Despite the primarily nuclear localization of FTO, a shuttle mechanism between nucleus and cytoplasm results in an additional cytoplasmic FTO abundance.[129] Depending on its localization, FTO was found to display differential substrate preferences. While FTO in the nucleus acts on internal m^{6}A sites, but hardly on m^{6}A$_m$, cytoplasmic FTO reflects the activity profile observed *in vitro* and mainly targets the m^{6}A$_m$ modification.[128]

Besides FTO, one additional m^{6}A demethylase is expressed in human cells. AlkB homolog 5 (ALKBH5) belongs to the same Fe(II)- and α-ketoglutarate-dependent dioxygenase family as FTO and also shares its nuclear localization.[39,130] Unlike FTO, however, which requires its full-length structure for catalytic activity, ALKBH5 remains active even upon truncation of its *C*-terminal domain.[86] In addition to m^{6}A in mRNA, ALKBH5 demethylates N^6-dimethyladenosine (m$^6{}_2$A) inside a GUG(m$^6{}_2$A)(m$^6{}_2$A)CUU motif in rRNA.[131]

As members of the same enzyme family, FTO and ALKBH5 share common substrate preferences: both demethylases strongly prefer single-stranded substrates and a minimal substrate length of 5 nt is required for efficient demethylation.[39,132,133] Embedding the target m^{6}A inside its RRACH consensus motif slightly enhances catalytic activity, but is no strict requirement.[39,133] With both enzymes being Fe(II)- and α-ketoglutarate-dependent dioxygenases, the oxidation of the m^{6}A methyl group follows the same mechanism, involving an iron(IV)-oxo complex as catalytically active species (Scheme 1.1).

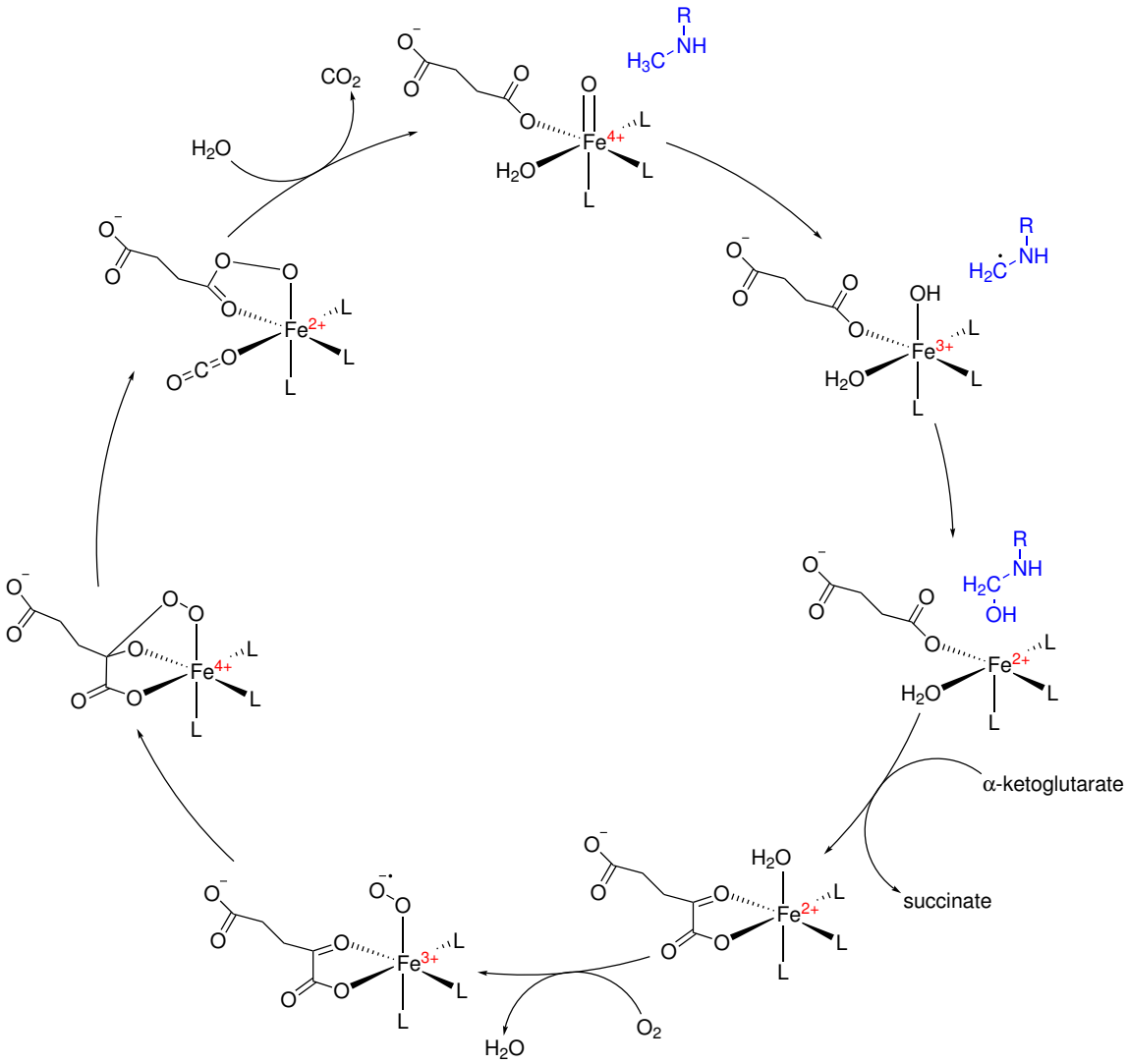

Scheme 1.1: General catalytic mechanism of the oxidation of a methylamino-substrate (blue) by an Fe(II)- and α-ketoglutarate-dependent dioxygenase. For clarity, only the inner coordination sphere of the catalytically active iron center is shown (L = ligand amino acid; typically, the three ligands are two histidines and one aspartate or glutamate side chain).[134]

Yet, m^{6}A demethylation by FTO or ALKBH5 furnishes different product distributions. While ALKBH5 catalyzes direct removal of the N^6-methyl group to yield adenosine, FTO releases the oxidized intermediates N^6-hydroxymethyladenosine (hm^{6}A) and N^6-formyladenosine (f^{6}A).[135,136] The two-step demethylation *via* f^{6}A represents the minor reaction pathway.

The divergent product distributions of FTO and ALKBH5 were not easily explicable given their similar oxidative mechanisms (Scheme 1.1) and the high structural resemblance of their catalytic centers (Figure 1.11).[132,137,138]

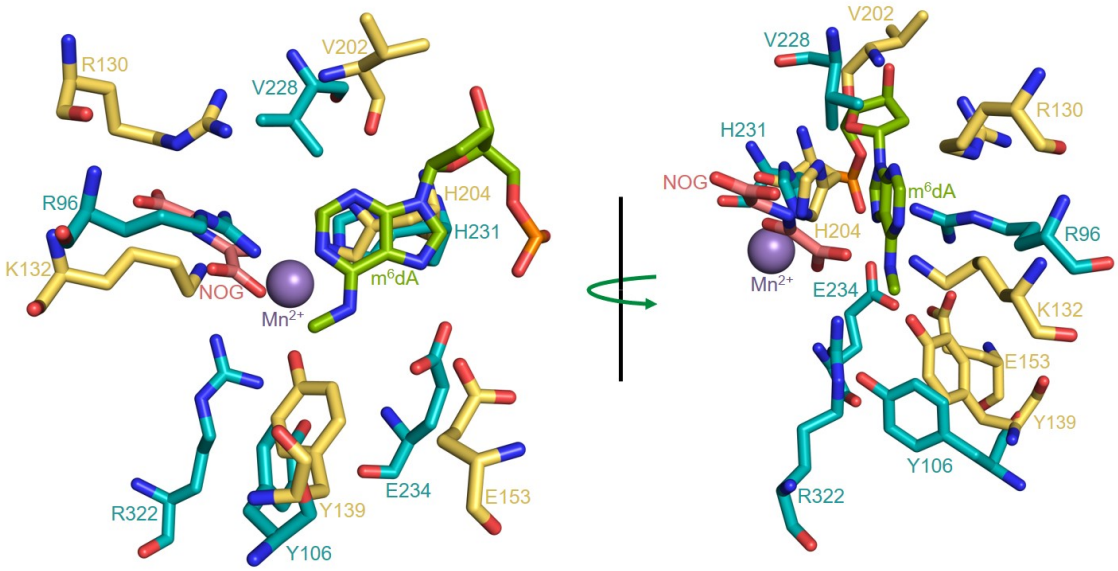

Figure 1.11: Structural comparison of the m^6(d)A (green sticks) binding sites of FTO (cyan sticks) and ALKBH5 (yellow sticks). This figure was generated by superimposition of an FTO-m^{6}dA co-crystal structure (PDB ID 5ZMD) with an ALKBH5 crystal structure (PDB ID 4NRP). Both structures contain the inactive cofactor surrogates Mn^{2+} (purple sphere) and *N*-oxalylglycine (NOG, salmon sticks).[132,137]

As a consequence, many studies recently attempted to elucidate the underlying mechanistic differences between FTO- and ALKBH5-mediated demethylation in order to explain the observed discrepancies. The absence of oxidized intermediates throughout the ALKBH5-mediated pathway was explained by formation of a covalent RNA-enzyme-intermediate generated by nucleophilic attack of the enzyme on an *in situ* generated m^{6}A Schiff base.[139] Hydrolysis of this intermediate would lead to transfer of the methyl group onto the enzyme and immediate release of unmethylated RNA (Scheme 1.2A). In contrast, the hydrogen-bonding pattern of m^{6}A inside the FTO binding pocket was proposed to imbue a partial positive charge on the nucleobase, which in turn would disfavor Schiff base formation. As this would prevent formation of a covalent intermediate, the oxidized substrate would be released from the binding site and decompose in the aqueous environment (Scheme 1.2B).[139] An additional study proposed that the N1 atom could aid this hydrolytic process by acting as an internal base.[140]

Notably, all of the aforementioned assumptions about ALKBH5-mediated demethylation relied on modeling m^{6}A into the ALKBH5 structure. This was done by superimposition of an FTO-m^{6}dA co-crystal structure with an ALKBH5 structure, as shown in Figure 1.11, which appeared reasonable due to their structural similarity. Unexpectedly, the recent publication of the first ALKBH5 crystal structure in complex with an m^{6}A-containing oligonucleotide

revealed an inverted 3'–5' binding direction of the RNA substrate compared to FTO (and every other ALKBH family protein characterized so far).[141] The inverse RNA binding direction also results in an inverted facial orientation of the m^6A nucleobase inside the active site (Figure 1.12).

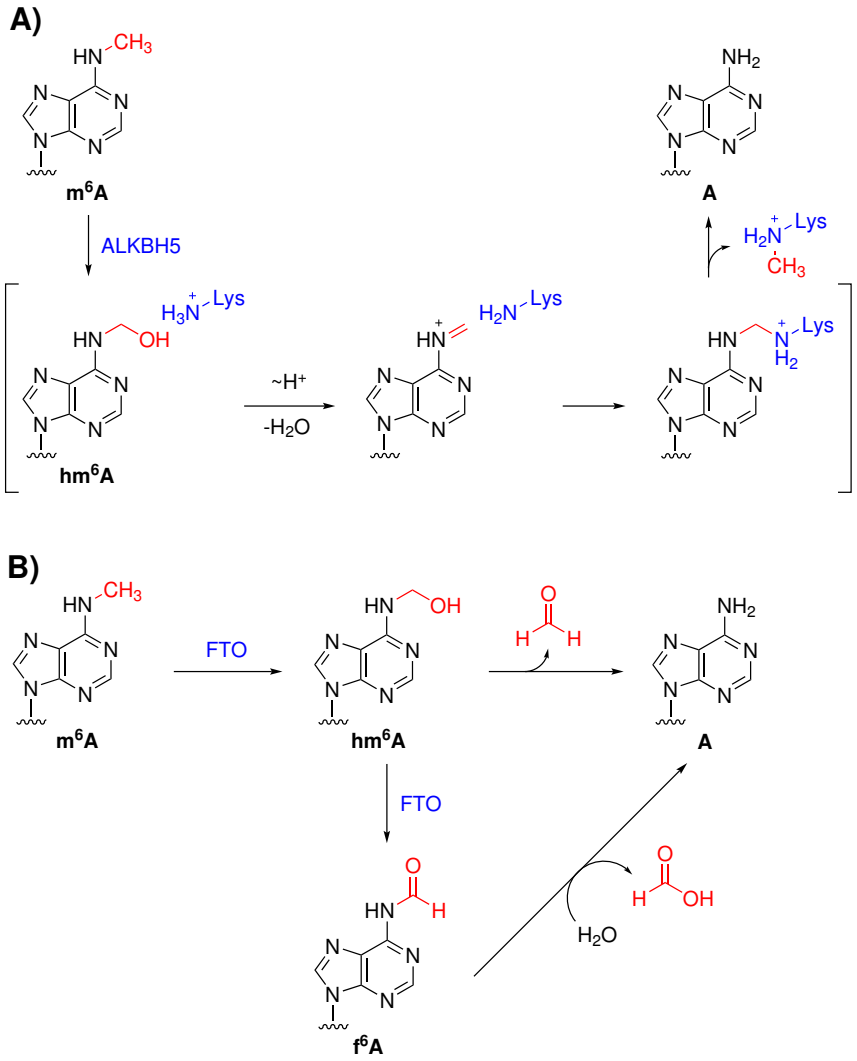

Scheme 1.2: Proposed mechanisms of the m^6A demethylation by ALKBH5 and FTO. A) Suggested ALKBH5-mediated m^6A demethylation pathway involving Schiff base formation from hm^6A and transfer of the methyl group onto ALKBH5 *via* a covalent intermediate. The methyl group is subsequently released as formaldehyde.[139] B) FTO-mediated m^6A demethylation without intermediary Schiff base formation. hm^6A is released, but may be rebound for a second oxidation step yielding f^6A (minor pathway). Decomposition of the oxidized intermediates in aqueous solution yields adenosine.[136]

The distinct nucleobase orientations and the thus different electrostatic interactions with the demethylase binding sites may offer another explanation for the non-identical demethylation pathways of FTO and ALKBH5. As the ALKBH5-m^6A co-crystal structure as well as the

detailed mechanistic investigations of FTO- and ALKBH5-mediated demethylation have been published well after the launch of this project, they will be discussed in further detail in Section 3.4.

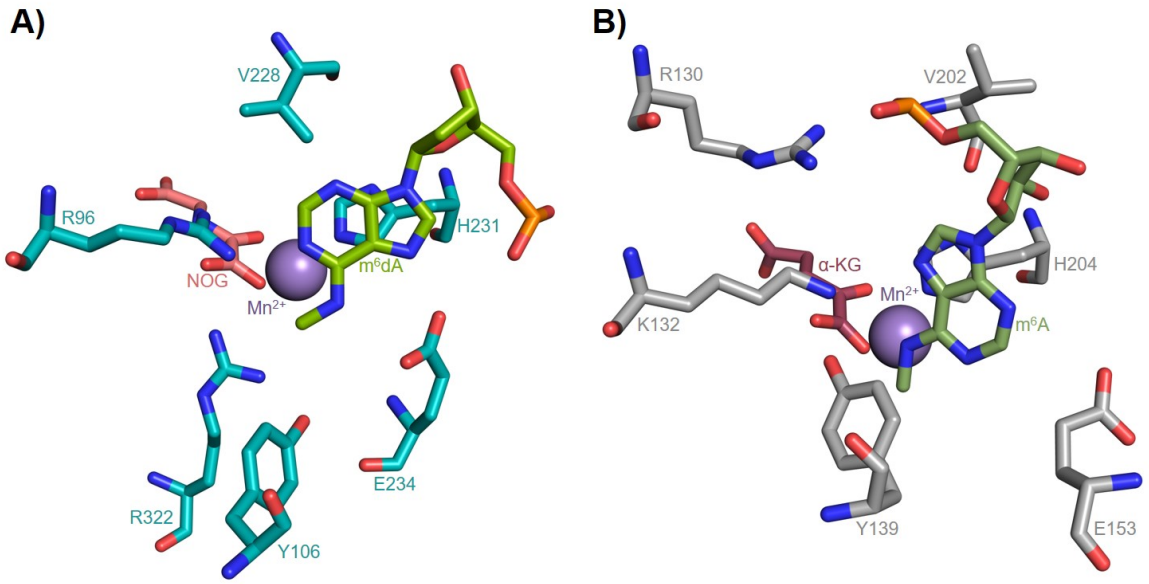

Figure 1.12: Crystal structures of FTO and ALKBH5 bound to m^6(d)A-containing oligonucleotides. A) Co-crystal structure of FTO and an m^{6}dA-containing ssDNA substrate (PDB ID 5ZMD).[137] The crystallized complex contains Mn^{2+} (purple sphere) and NOG (salmon sticks) as inactive cofactor surrogates. B) Co-crystal structure of ALKBH5 and an m^{6}A-containing ssRNA substrate (PDB 7WKV).[141] A reversed substrate binding direction relative to the FTO complex results in an inverted facial orientation of the m^{6}A nucleobase. The crystallized complex contains the cofactor surrogate Mn^{2+} and the native cofactor α-ketoglutarate (α-KG).

2 Research objectives

The previous sections have highlighted the biological relevance of the abundant m^6A modification in mRNA. Not only is m^6A involved in a large variety of regulatory cellular processes, but the modification and its writer, reader and eraser proteins have also been linked to a multitude of diseases, such as obesity, tumorigenesis and cancer metastasis, and Alzheimer's disease.[122–124,142,143] As a consequence, m^6A has become one of the most extensively studied modifications in the epitranscriptome and a multitude of analytical methods for the mapping and validation of m^6A sites, outlined in Section 1.1, has been developed.

An additional focus has been kept on uncovering the mechanisms and interactions which mediate recognition and processing of m^6A by its readers, writers and erasers. A comprehensive understanding of these underlying principles is crucial to enable specific targeting of m^6A-dependent processes for therapeutic purposes. A multitude of studies aimed at elucidating m^6A recognition by reader proteins of the YTH domain protein family. These play important roles in m^6A-mediated regulatory processes as they impact localization, translation efficiency and stability of their methylated mRNA targets.[104–107,112,113] Recent research has been increasingly focused on the two human m^6A demethylases FTO and ALKBH5, as their activity brings about the reversible nature of the m^6A modification. Interestingly, it was found that the two demethylases furnish different reaction products during m^6A demethylation: while ALKBH5 mediates direct demethylation, FTO releases two oxidized intermediates.[135,136] Owing to the structural similarity of the two binding sites and the lack of an ALKBH5-m^6A co-crystal structure, this observation remained long inexplicable.

The goal of the first part of this thesis is to gain a deeper mechanistic understanding of m^6A reader proteins and eraser enzymes beyond the state of knowledge outlined in the previous section. Commonly, protein-substrate interactions are characterized using mutagenesis of the protein. Mutations of mechanistically relevant amino acids affect the possible interactions between substrate and protein; the resulting changes in binding affinity or enzymatic activity are read out by analytical methods and allow conclusions about the role and importance of the mutated amino acid. A major drawback of this method is an additional undesired effect of amino acid mutations on the structure of the binding site. Therefore, in this thesis atomic mutagenesis of the m^6A nucleoside is utilized to probe protein-substrate interactions. Atomic mutagenesis describes the controlled variation of specific atomic sites in the target molecule (here: m^6A) to alter its steric or electronic properties. This approach allows to selectively alter defined interactions between RNA substrate and protein, while

minimizing undesired secondary influences on the complex structure. In particular, seven m^6A atomic mutants are synthesized throughout this work (Figure 2.1); the respective synthetic pathways are described in Section 3.1.

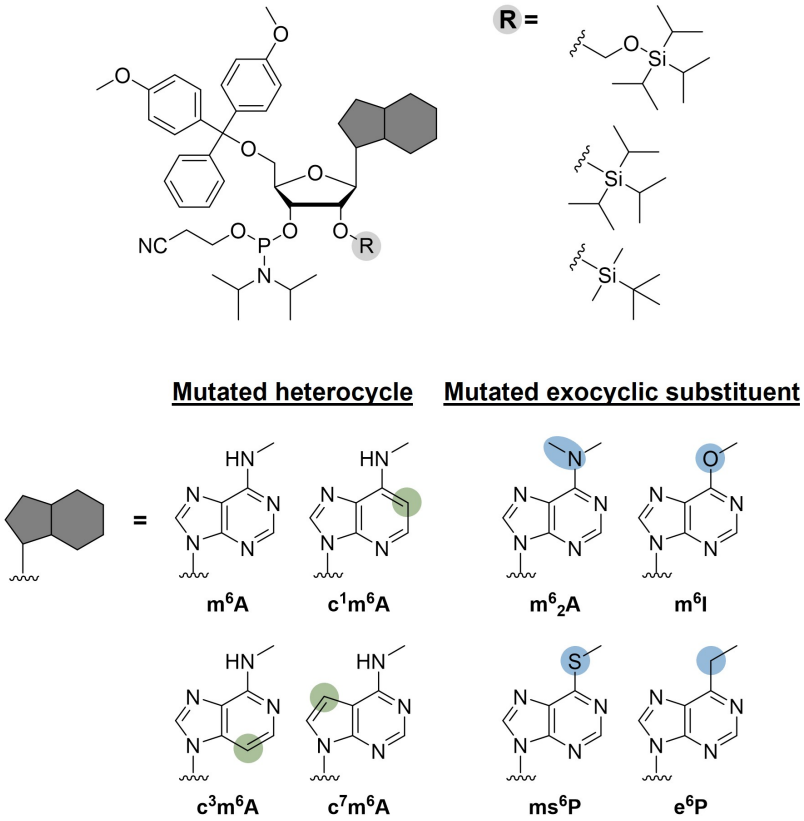

Figure 2.1: Overview of the m^6A phosphoramidite building block and its atomic mutants synthesized in the course of this project.

$m^6{}_2A$ increases the steric demand of the exocyclic substituent while simultaneously preventing its engagement in hydrogen bonding interactions. O^6-Methylinosine (m^6I) and 6-(methylthio)purine (ms^6P) both feature hydrogen bond acceptor instead of donor substituents at C6, but differ in the degree of polarization of the methyl group. 6-Ethylpurine (e^6P), in contrast, contains a completely unpolar substituent at position 6. Finally, the 1-, 3-, and 7-deaza mutants of m^6A (c^1m^6A, c^3m^6A, c^7m^6A) display altered hydrogen bonding patterns of the nucleobase heterocycle. These m^6A atomic mutants are further converted into phosphoramidite building blocks and incorporated into RNA substrates *via* RNA solid-phase synthesis (Section 3.2). Unlike incorporation by *in vitro* transcription, this method enables facile site-specific incorporation of the modified nucleoside.

The synthesized oligonucleotides containing m^6A or its atomic mutants are utilized to determine the structural prerequisites for substrate recognition by the three human m^6A

reader proteins YTHDF2, YTHDC1 and YTHDC2 (Section 3.3). For this, the effects of substrate atomic mutagenesis on the respective protein binding affinities is investigated using fluorescence anisotropy studies.

Finally, in Section 3.4 the influence of the m^6A atomic mutagenesis on the demethylation activity of FTO and ALKBH5 is elucidated. HPLC-MS-based assays are employed to analyze the product profiles obtained upon treatment of the substrate RNAs with FTO or ALKBH5. Systematic evaluation of these product profiles allows to draw conclusions about the structural requirements for substrate recognition and about the influence of steric and electronic substrate properties on demethylase activity and mechanism. These experimentally gained insights are complemented by further analytical methods as well as by quantum-mechanical approaches to uncover interesting new aspects of FTO- and ALKBH5-mediated demethylation.

3 Results and Discussion

3.1 Synthesis and spectroscopic characterization of modified purine nucleosides and phosphoramidites

3.1.1 Synthesis of m^{6}A atomic mutant nucleosides

The incorporation of modified phosphoramidite building blocks into RNA or DNA oligonucleotides by solid-phase synthesis is the common approach to site-specifically introduce non-canonical nucleosides into nucleic acid scaffolds. Although very recently a protocol for the chemical modification on the phosphoramidite stage in a biphasic system using phase transfer catalysis has been reported, this method is solely applicable for the introduction of nucleobase *N*-alkylations.[144] The general strategy toward non-canonical building blocks involves the synthesis of the modified nucleosides followed by conversion into their corresponding phosphoramidite structures.

For the systematic investigation of m^{6}A interactions with reader and eraser proteins, this study centered around eight distinct m^{6}A atomic mutants with different steric and electronic properties, as outlined in Chapter 2. The combination of these eight key compounds along with their respective unmethylated and/or oxidized analogs, which were used as analytical standards, resulted in a required pallette of 16 canonical and non-canonical nucleoside structures (Table 3.1).

The synthetic strategies to access the desired nucleoside structures were designed to minimize synthetic effort while starting from commercially available and affordable starting materials. The retrosynthetic analyses of all nucleosides (apart from the canonical adenosine (**1**) and its deamination product inosine (**6**), which are readily commercially available) are outlined in Scheme 3.1. The routes toward C6-modified purine nucleosides were either based on N^6-modification of adenosine to obtain the oxidized m^{6}A analogs **4** and **5** or proceeded *via* conversion of 6-chloropurine riboside. Similar pathways were chosen for the deazapurine nucleosides **12**–**17**. Unlike 6-chloropurine riboside, its 1-, 3-, and 7-deaza analogs are not readily available and were therefore prepared by glycosylation of the respective nucleobases. In case of 1- and 3-deazapurines, access to the relatively costly nucleobase structures was achieved by conversion of suitable substituted pyridine precursors. In the following, the synthetic procedures will be discussed in further detail.

Table 3.1: Chemical structures and abbreviated names of the modified purine nucleosides used to study m^6A eraser and reader proteins.

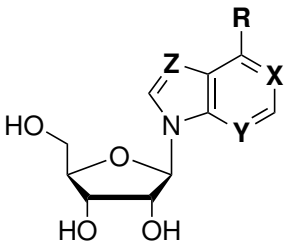

No.	Name	–R	X	Y	Z
1	A	NH_2	N	N	N
2	m^6A	$HN{-}CH_3$	N	N	N
3	$m^6{}_2A$	$H_3C{-}N{-}CH_3$	N	N	N
4	hm^6A	$HN{-}OH$	N	N	N
5	f^6A	$HN{=}O$	N	N	N
6	I	OH	N	N	N
7	m^6I	$O{-}CH_3$	N	N	N
8	s^6P	SH	N	N	N
9	ms^6P	$S{-}CH_3$	N	N	N
10	e^6P	CH_3	N	N	N
11	he^6P	OH	N	N	N
12	c^1A	NH_2	CH	N	N
13	c^1m^6A	$HN{-}CH_3$	CH	N	N
14	c^3A	NH_2	N	CH	N
15	c^3m^6A	$HN{-}CH_3$	N	CH	N
16	c^7A	NH_2	N	N	CH
17	c^7m^6A	$HN{-}CH_3$	N	N	CH

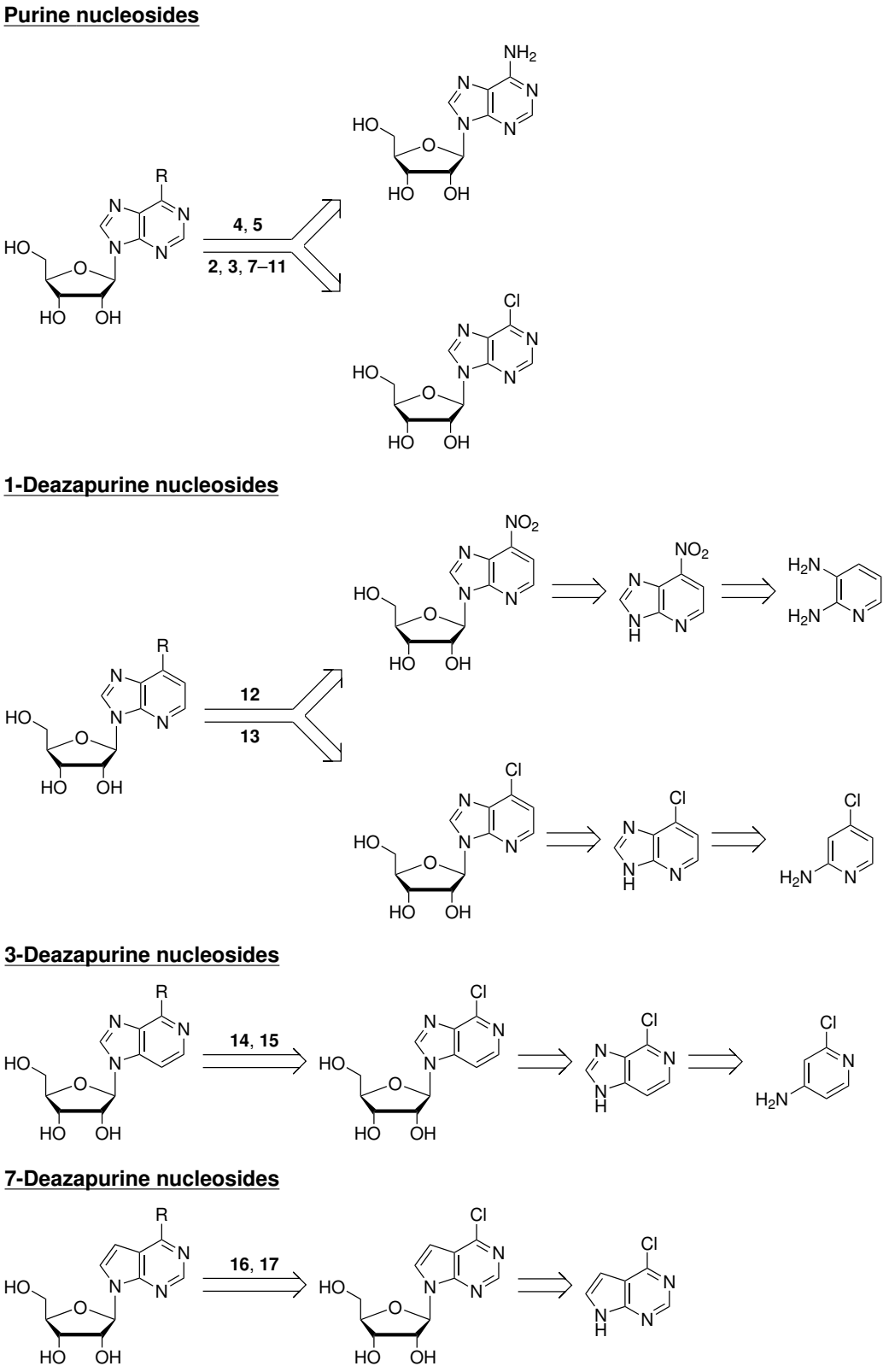

Scheme 3.1: Retrosynthetic strategies for the synthesis of modified purine nucleoside analogs.

3.1.1.1 Variation of the C6-substituent

6-Chloropurine riboside (**18**) presents a suitable starting point to easily introduce a variety of substituents at C6. Featuring chlorine as a good leaving group, **18** readily participates in S_NAr reactions with nucleophilic reagents even under mild conditions. Therefore, treatment with the respective free amines or sodium (thio)methoxide salts resulted in formation of the products **2**, **3**, **7** and **9** in high yields (Scheme 3.2). For the synthesis of thioinosine (**8**), thiourea was chosen as the sulfur-containing nucleophile due to its non-toxic characteristics and convenient handling.[145] Attack of the nucleophilic sulfur center at C6 of the nucleoside results in an intermediary isothiouronium species, which is subsequently hydrolyzed in ethanolic solution to form the thiol product.

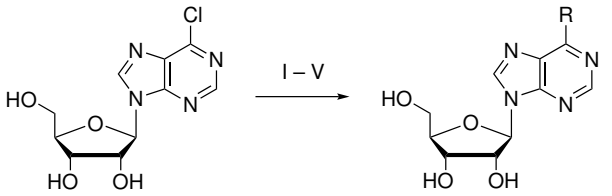

18

2: R = NHMe
3: R = NMe_2
7: R = OMe
8: R = SH
9: R = SMe

Scheme 3.2: Syntheses of the nucleosides **2**, **3** and **7**–**9** *via* nucleophilic aromatic substitution of 6-chloropurine riboside (**18**). I) $MeNH_2$, EtOH, rt, 16 h, 90% (for **2**); II) Me_2NH, EtOH, rt, 16 h, 90% (for **3**); III) NaOMe, MeOH, rt, 3 d, 92% (for **7**); IV) thiourea, EtOH, 50 °C, 24 h, 11% (for **8**); V) NaSMe, DMF, rt, 3 d, 96% (for **9**).

While nucleophilic substituents containing heteroatoms can be easily introduced by S_NAr reactions, the C6-chlorinated compound **18** also allows introduction of alkyl substituents *via* metal-catalyzed cross-coupling reactions. Thus, ribose-protected derivatives of **18** were subjected to Negishi or Reformatsky reactions to achieve conversion into 6-ethylpurine riboside (**10**) and 6-hydroxyethylpurine riboside (**11**), respectively (Scheme 3.3). For Negishi coupling, first ethylmagnesium bromide was generated by treatment of bromoethane with elementary magnesium. Subsequent addition of $ZnBr_2$ resulted in transmetalation and formation of ethylzinc bromide *in situ*.[146] Palladium-catalyzed cross-coupling with the tri-*O*-acetyl-protected nucleoside **19** yielded the alkylated product **20**; the choice of acetyl protecting groups allowed basic deprotection of the ribose under mild conditions to obtain e^6P (**10**) in almost quantitative yield. For the synthesis of he^6P, in contrast, *tert*-butyldimethylsilyl (TBDMS) protecting groups were chosen, as they display a higher stability toward reductive conditions. The protected nucleoside **21** was subjected to palladium-catalyzed cross-coupling with Reformatsky reagent to introduce the ethyl acetate substituent at C6.[147,148]

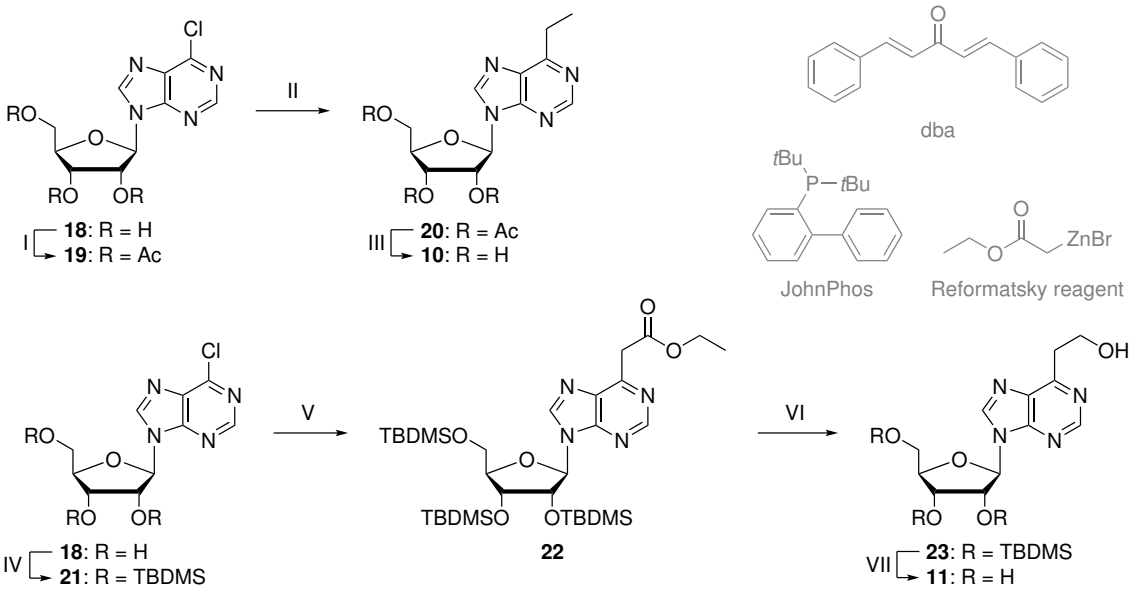

Scheme 3.3: Syntheses of e^{6}P (**10**) and he^{6}P (**11**) *via* Pd-catalyzed cross-coupling reactions. I) Ac_2O, DMAP, NEt_3, MeCN, rt, 21 h, 96%; II) EtZnBr, $Pd(PPh_3)_4$, THF, 55 °C, 90 min, 92%; III) NH_3, MeOH, rt, 16 h, 99%; IV) TBDMSCl, imidazole, DMF, rt, 27 h, 97%; V) Reformatsky reagent, $Pd_2(dba)_3$, JohnPhos, THF, 4 d, 65%; VI) $NaBH_4$, EtOH, rt, 14 h, then MnO_2, rt, 1 h, 50%; VII) HF·NEt_3, THF, rt, 16 h, 65%.

The reaction could not be driven to complete conversion and even long reaction times resulted in mediocre product yield. The poor conversion is presumably attributed to a low concentration of active Reformatsky reagent formed upon treatment of ethyl bromoacetate with zinc powder. This indicates that the formation of an organozinc reagent by direct treatment of alkyl halide with zinc may be inferior to the transmetalation of a pre-formed Grignard reagent as described above. The ester substituent was subsequently reduced to the corresponding alcohol **23**. While ester functions are commonly reduced using $LiAlH_4$, this reagent has been observed to cause reduction of pyrimidine heterocycles as an undesired side reaction.[149] To avoid notable formation of byproducts, $NaBH_4$ was used instead. Despite being generally unreactive toward esters unless additives such as $CaCl_2$ or $AlCl_3$ are used, $NaBH_4$ had previously been efficiently utilized for the reduction of heteroaromatic (pyridine, pyrimidine) esters.[149,150] Even this mild reducing agent, however, has been reported to partly reduce the purine core of compound **23** and thus to yield its 1,6-dihydropurine analog as a byproduct of the ester reduction. To reverse this over-reduction, the crude product mixture was treated with MnO_2 to reoxidize this species.[148] Finally, cleavage of the fluoride-labile TBDMS groups yielded he^{6}P (**11**).

The oxidized m^{6}A analogs hm^{6}A (**4**) and f^{6}A (**5**) were obtained by functionalization of commercially available adenosine (Scheme 3.4). hm^{6}A is formed upon treatment of adeno-

sine with an aqueous solution of formaldehyde. However, hm^{6}A is not stable in aqueous solution and will revert back to adenosine under release of formaldehyde. Thus, an equilibrium between A and hm^{6}A is formed, which makes an isolation of pure hm^{6}A *via* this route impossible. Instead, the reaction yield was determined by HPLC analysis of the crude sample (Figure 3.1).

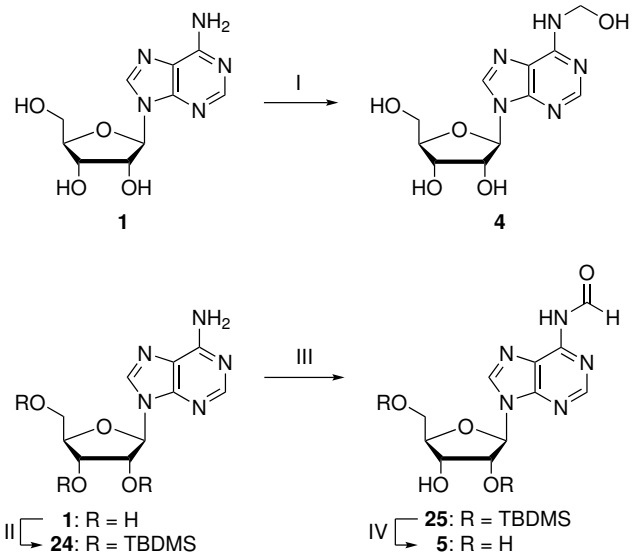

Scheme 3.4: Synthesis of hm^{6}A (**4**) and f^{6}A (**5**) from adenosine (**1**). I) formaldehyde, H_2O, 60 °C, 4 h, 19% (not isolated); II) TBDMSCl, imidazole, DMF, rt, 20 h, 92%; III) HCOOH, Ac_2O, DMAP, DCM, rt, 66 h, 98%; IV) HF·pyridine, THF, rt, 4 h, 29%.

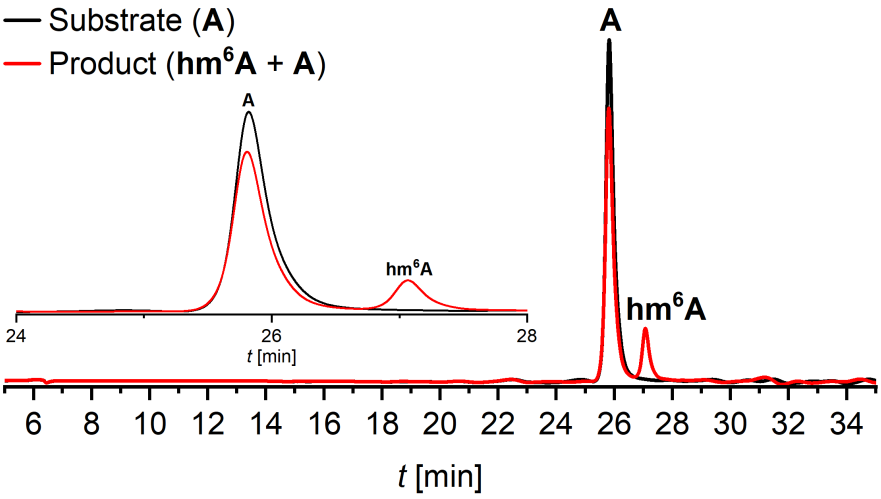

Figure 3.1: Superimposed RP-HPLC chromatograms (260 nm) of adenosine (black line) and a sample of A treated with aqueous formaldehyde solution at 60 °C for 4 h (red line). An enlarged view of the substrate and products peaks is shown as inset. The identity of the assigned species was confirmed by on-line ESI-MS detection. The product (hm^{6}A) yield was calculated based on the peak areas. RP-HPLC conditions: Phenomenex Synergi Fusion 2×250 mm, flow rate 0.2 mL/min, at 20 °C; eluent A: H_2O; eluent B: MeCN; gradient: 0–20 % eluent B in 40 min.

f^{6}A, in contrast, was obtained by N^6-formylation of 2',3',5'-tri-*O*-TBDMS-adenosine (**24**). Here, reaction of formic acid and acetic anhydride catalyzed by 4-dimethylaminopyridine (DMAP) resulted in an *in situ* generation of the mixed anhydride. Nucleophilic attack of the exocyclic amino group of adenosine at the more electrophilic carbonyl center of the anhydride ensures selective transfer of the formyl group onto the nucleobase. Finally, the fluoride-labile TBDMS groups of the *N*-formylated product **25** were cleaved using Olah's reagent (HF·pyridine). During deprotection of the ribose, however, significant deformylation was observed, resulting in a low yield of the desired product **5**. Potentially, cleavage of the TBDMS groups under milder conditions, using a solution of tetrabutylammonium fluoride (TBAF) in THF, might improve the yield of this deprotection step.

3.1.1.2 Atomic mutagenesis of the purine scaffold

While all modified nucleosides featuring a purine nucleobase were synthesized starting from commercially available nucleoside precursors, such suitable starting materials are not readily available for the synthesis of deazapurine nucleosides. Therefore, the route toward 1- and 3-deazanucleosides involved the synthesis of the respective nucleobases starting from 2,4-disubstituted pyridine precursors, followed by glycosylation (Scheme 3.5). First, nitration of the respective 2,4-substituted chloro-amino-pyridine (**26** or **30**) resulted in formation of a mixture of 3- and 5-nitro isomers. The desired 3-nitro isomer was subsequently reduced and cyclized in a Traube purine synthesis-like reaction.

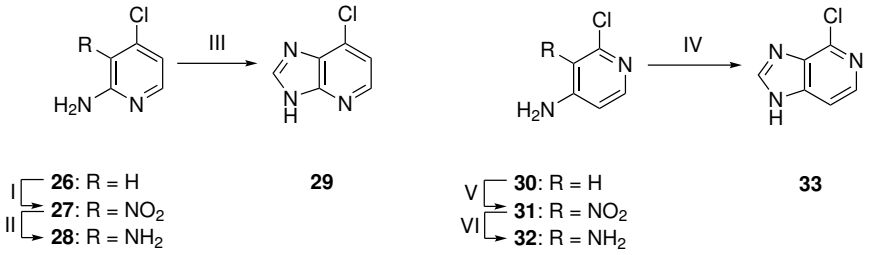

Scheme 3.5: Synthetic routes toward 1- and 3-deaza-6-chloropurine (**29** and **33**.I) H_2SO_4, HNO_3, 0 °C, 30 min, then rt, 19 h, 39% (for **27**), 60% (for 4-amino-2-chloro-3-nitro-pyr); II) NH_4Cl, Zn, MeOH, rt, 30 min, 96% (for **28**), 84% (for **32**); III) $(EtO)_3CH$, 110 °C, 3 h, then HCOOH, 110 °C, 2.5 h, 80%; IV) $(MeO)_3CH$, aq. HCl, rt, 16 h, 81%.

The original purine synthesis described by Traube in 1900 obtained purine nucleobases by condensation of 5,6-diaminopyrimidines with formic acid.[151,152] This method, however, does not guarantee the formation of purine derivatives; in some cases only *N*-formylation without subsequent cyclization occurs.[153] Substitution of formic acid for trialkylorthorformates provides improved leaving groups (alkoxides) and therefore increases the energetic and entropic driving force of the reaction; addition of acids to enable protonation of the

alkoxide leaving groups further facilitates the cyclization step (Scheme 3.6). Here, the choice of reaction conditions was found to play a crucial role for the formation of the correct product. While **28** was smoothly converted to 1-deaza-6-chloropurine (**29**) by refluxing in triethyl orthoformate and formic acid, the corresponding 3-deaza-6-chloropurine proved to be less stable toward acidic conditions. Heating in formic acid caused hydrolysis of the chlorine substituent and thus quantitative conversion to 3-deazahypoxanthine. To avoid hydrolysis, an altered cyclization procedure utilizing milder conditions was employed: treatment of **32** with trimethyl orthoformate and a catalytic amount of aq. HCl at ambient temperature yielded the 6-chlorinated nucleobase **33** without formation of the 3-deazahypoxanthine byproduct.

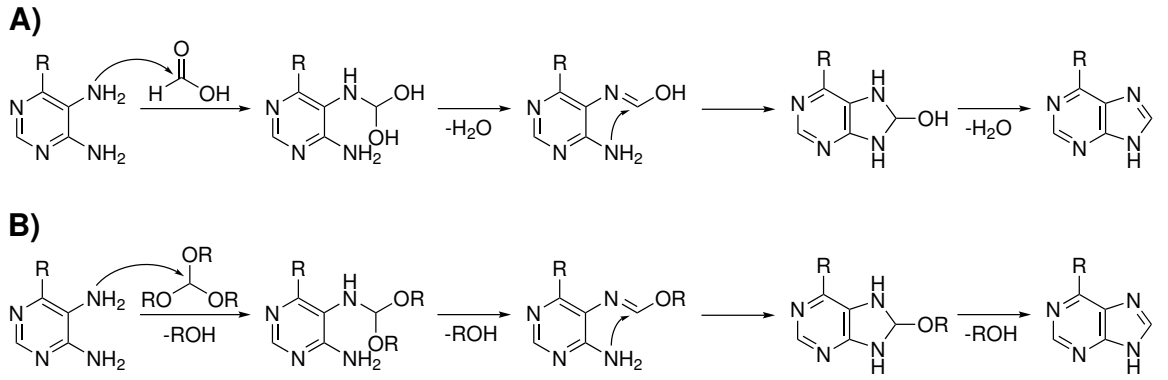

Scheme 3.6: The original Traube purine synthesis (A) and a variation utilizing trialkyl orthoformate (B). In the latter variation, the presence of better leaving groups leads to a facilitated cyclization of the purine scaffold.

The nucleobases **29** and **33** were glycosylated under Vorbrüggen conditions to yield the tri-*O*-benzoyl-protected nucleosides **34** and **35** (Scheme 3.7). The Vorbrüggen method is an advancement of the classical Fischer-Helferich glycosylation. This reaction and modifications thereof achieved glycosylation using a 2',3',5'-tri-*O*-acyl-1'-haloribose and nucleobase heavy metal salts (silver or mercury).[154,155] The Vorbrüggen method avoids these poorly soluble and often toxic metal salts by using a tetraacylated ribose, which is activated by a Lewis acid such as trimethylsilyl triflate (TMSOTf) or $SnCl_4$.[156,157] The resulting positive charge is stabilized by formation of a cyclic oxocarbenium ion, which simultaneously serves as a steric block of the α-face of the sugar (Scheme 3.8).[158] Therefore, attack of the nucleobase takes place from the sterically more accessible side, which leads to selective formation of the β-nucleoside.

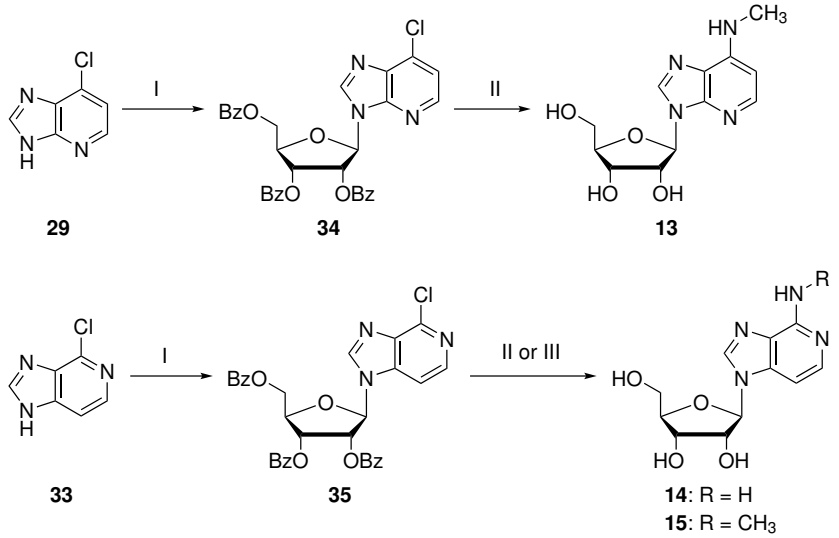

Scheme 3.7: Synthetic routes toward c^1m^6A (**13**), c^3A (**14**) and c^3m^6A (**15**). I) BSA, MeCN, 100 °C, 30 min, then 1-*O*-acetyl-2,3,5-tri-*O*-benzoyl-β-D-ribofuranose, TMSOTf, 100 °C, 16 h, 94% (for **34**), 84% (for **35**); II) $MeNH_2$, EtOH, 125 °C, 24 h, 88% (for **13**), 88% (for **15**); III) NH_3, H_2O, 125 °C, 24 h, 88% (for **14**).

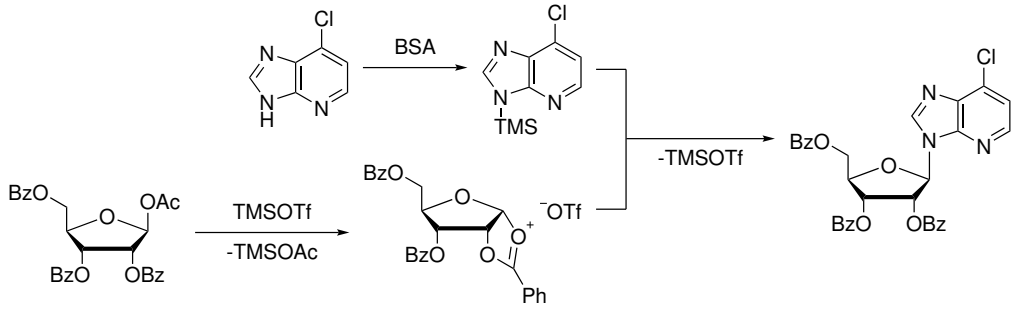

Scheme 3.8: Mechanism of the Vorbrüggen glycosylation. Formation of a cyclic oxocarbenium intermediate shields the α-face from nucleophilic attack and ensures selective formation of the β-anomer. The example utilizes TMSOTf as Lewis acid and *N*,*O*-bis(trimethylsilyl)acetamide (BSA) to silylate the nucleobase.

The final synthetic step combined basic deprotection of the benzoylated ribose with substitution of the chlorine at C6 of the nucleobase. Thus, deprotection of **34** and **35** using methylamine resulted in formation of c^1m^6A (**13**) and c^3m^6A (**15**), respectively, while reaction of **35** with ammonia resulted in formation of c^3A (**14**). Notably, while debenzoylation proceeded smoothly at ambient temperature, no substitution at the nucleobase was observed. Both 1- and 3-deazapurine nucleosides required high temperatures for conversion, whereas nucleophilic substitution at the related 6-chloropurine scaffold (Scheme 3.2) was conveniently achieved at ambient temperature.

Two features contribute to the reduced susceptibility of 1- and 3-deazapurines toward nucleophilic attacks. First, the chlorinated aromatic ring is formally a pyridine, which is more electron-rich and therefore less electrophilic than the pyrimidine ring in the 6-chloropurine scaffold. Second, the pyridine system provides less mesomeric stabilization of the intermediary Meisenheimer adduct, as the negative charge of this intermediate is less efficiently delocalized. The different reactivities of 6-chloropurine and its deaza-analogs in nucleophilic substitution reactions are also mirrored by different calculated local electrophilicities at C6 (Figure 3.2).

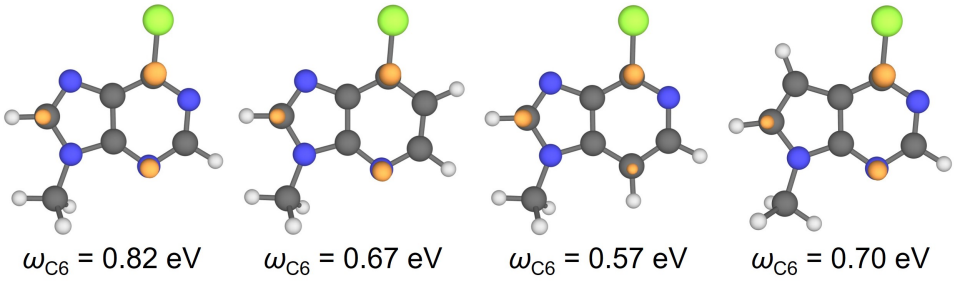

Figure 3.2: Representations of the electrophilic Parr functions P^+ (orange) for 6-chloro-9-methylpurine and its 1-deaza-, 3-deaza-, and 7-deaza-analogs (left to right). The local electrophilicities at C6 (ω_{C6}) are given below the structures. Geometry optimizations and calculations of P^+ and ω_{C6} were performed on the UB3LYP/def2-TZVP level of theory. To simplify calculations, the ribose units of the nucleoside structures used experimentally were substituted for methyl groups at N9.

Figure 3.2 shows that the 1-deaza-6-chloropurine nucleobase has a larger local electrophilicity at C6 than the 3-deaza analog and therefore should be more susceptible toward nucleophilic attacks at this position. At high temperatures, even the relatively weak nucleophile ammonia was able to substitute the chlorine atom of 3-deaza compound **35** to yield c^3A, as shown in Scheme 3.5. Thus, it should be possible to convert the more reactive **34** into c^1A using the same reaction conditions. However, to avoid the poor-yielding nitration step during nucleobase synthesis and to circumvent the harsh conditions required for amination at C6, an alternative route toward c^1A was chosen (Scheme 3.9).[159] Starting from 2,3-diaminopyridine (**36**), cyclization with triethyl orthoformate yielded the nucleobase **37**. Generation of the N3-oxide directed the subsequent electrophilic nitration to the *para*-position (C6). Here, two different reaction conditions were tested according to previous reports; the obtained yields did however not differ significantly.[159,160] The *N*-oxide was reduced under mild conditions, using PCl_3 at 0 °C, to avoid simultaneous reduction of the nitro group. With the nitro group still intact, the nucleobase could be glycosylated without a need to protect the C6-substituent beforehand. Unlike the other glycosylations described so far, this reaction did not result in convenient conversion using BSA and TMSOTf. Using

the stronger Lewis acid $SnCl_4$, in contrast, the nucleoside was formed even at ambient temperature, although the obtained yield was moderate. Finally, basic deprotection of the ribose and Pd-catalyzed reduction of the exocyclic nitro group yielded the c^1A nucleoside (**12**).

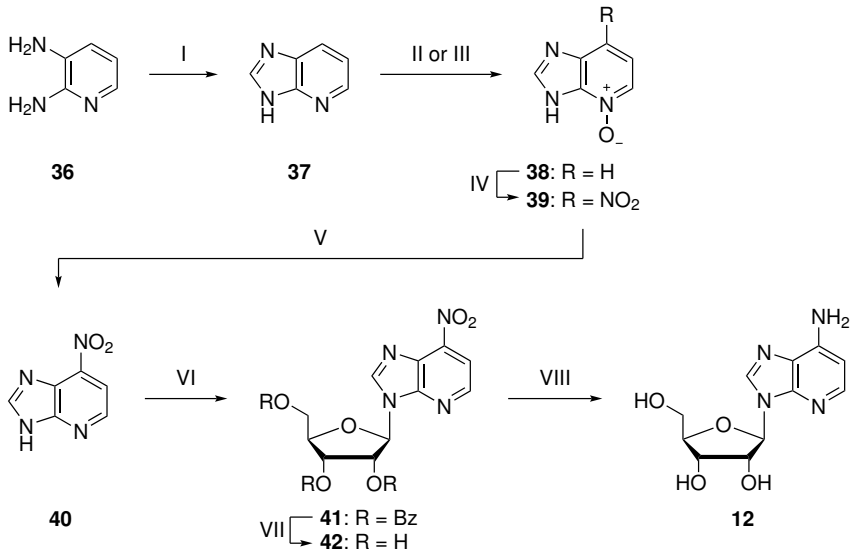

Scheme 3.9: Synthetic route toward c^1A (**12**). I) $(EtO)_3CH$, 145 °C, 3 h, then HCOOH, 110 °C, 2 h, 98%; II) *m*-CPBA, $CHCl_3$, rt, 48 h, 90%; III) *m*-CPBA, AcOH, 50 °C, 16 h, 95%; IV) $HNO_3{\cdot}NO_2$, TFA, 90 °C, 3 h, 80%; V) PCl_3, MeCN, 0 °C, 90 min, 63%; VI) 1-*O*-acetyl-2,3,5-tri-*O*-benzoyl-β-D-ribofuranose, $SnCl_4$, MeCN, rt, 16 h, 66%; VII) NH_3, MeOH, rt, 24 h, 86%, VIII) H_2, Pd/C, MeOH, rt, 72 h, 58%.

In contrast to 1- and 3-deazapurines, 7-deazapurine nucleobases do not possess inherent reactivity under Vorbrüggen glycosylation conditions.[161,162] The absence of N7 renders the five-membered (pyrrole) ring more electron-rich than the imidazole substructure of native purines and their 1-deaza- and 3-deaza-analogs. Therefore, more electron density is located at N9, the acidity of the N9-proton is reduced, and silylation of the nucleobase is hampered. As a consequence, halogenation at C7 is required to reduce the ring electron density and to activate the nucleobase for Vorbrüggen glycosylation. Iodination using *N*-iodosuccinimide (NIS) was chosen, as the iodine could easily be removed after glycosylation by converting it into an organomagnesium compound (Grignard reagent) followed by acidic hydrolysis.[163] In analogy to the 3-deazanucleosides described in Scheme 3.5, treatment of the protected nucleoside with either methylamine or ammonia at elevated temperatures led to simultaneous ribose deprotection and chlorine substitution and yielded c^7A (**16**) and c^7m^6A (**17**), respectively, in single steps (scheme 3.10).

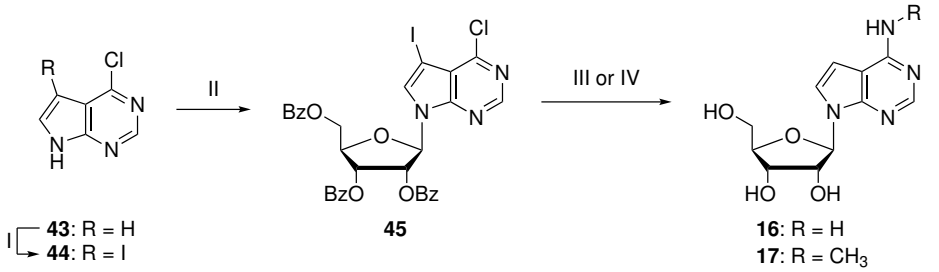

Scheme 3.10: Synthetic route toward c^7A (**16**) and c^7m^6A (**17**). I) NIS, DMF, rt, 30 min, 80%; II) BSA, MeCN, rt, 10 min, then 1-*O*-acetyl-2,3,5-tri-*O*-benzoyl-β-D-ribofuranose, TMSOTf, rt, 10 min, 80 °C, 1 h, 80%; III) *i*-PrMgCl·LiCl, THF, -10 °C, 1 h, then NH_4Cl, H_2O, then NH_3, H_2O, 125 °C, 24 h, 88% (for **16**); IV) *i*-PrMgCl·LiCl, THF, -10 °C, 1 h, then NH_4Cl, H_2O, then $MeNH_2$, EtOH, 125 °C, 18 h, 86% (for **17**).

3.1.1.3 Synthetic attempts toward an oxidation-resistant m^6A analog

While all of the m^6A atomic mutants discussed above are potential demethylase substrates, also a non-oxidizable m^6A analog presents a highly interesting building block. It was envisioned that an RNA oligonucleotide containing a modified nucleoside with high structural similarity to native m^6A but without abstractable protons at the exocyclic substituent might act as an enzyme inhibitor: maintaining all crucial sites for interaction with the demethylase (N1, N3, N7, N^6-H, ribose), the substrate may be recognized and bound, but not oxidized, thereby acting as a (temporary) block in the active site. N^6-(trifluoromethyl)adenosine (m^6A^{F3}, **46**) was regarded a promising target compound, as it combines the m^6A nucleoside structure with a non-oxidizable (due to a lack of protons) exocyclic (trifluoromethyl)amino substituent. While the trifluoromethyl group has gained some popularity in therapeutic compounds, its use in nucleoside chemistry is rather limited. So far, only one case of nucleobase-*N*-trifluoromethylation has been reported, whereas nucleosides featuring *N*-CF_3 substituents are not known.[164]

Most strategies for the introduction of *N*-trifluoromethyl groups either involve hazardous reagents such as HF, SbF_3 or SF_4 or rely on sophisticated fluorination agents which need to be prepared in multi-step syntheses.[165] However, two convenient methods for the preparation of aromatic trifluoromethylamines have been reported. Firstly, the *N*-CF_3 group is accessible by conversion of nitrosoarenes with sodium triflinate in presence of hydroquinone, *tert*-butylhydroperoxide and a copper catalyst (Scheme 3.11A).[166] *Via* a radical fluorination mechanism, the reaction initially furnishes *N*-trifluoromethylated hydroxylamines, which are subsequently reduced to the corresponding trifluoromethylamines.

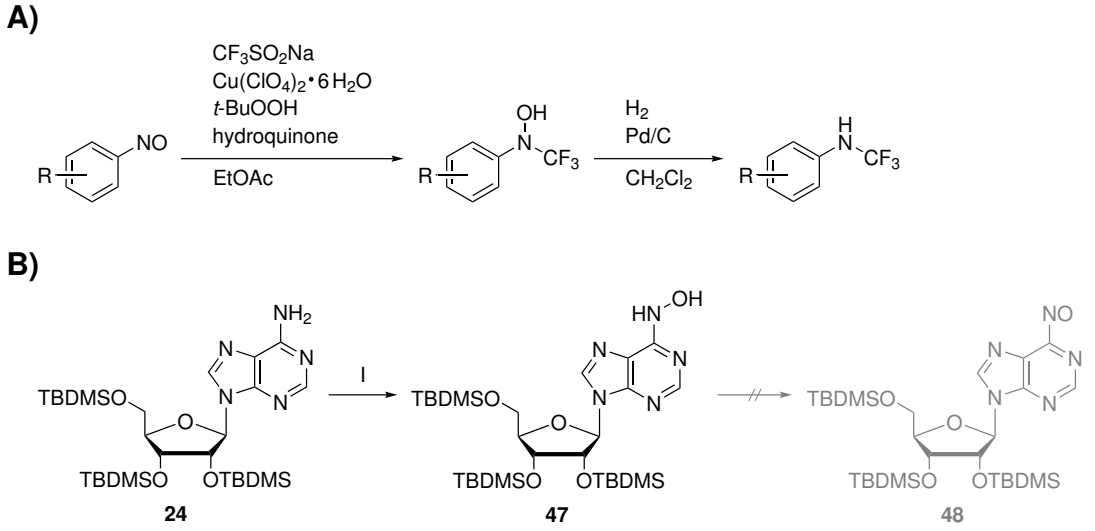

Scheme 3.11: Trifluoromethylation *via* a nitrosoarene intermediate. A) Reported synthesis of *N*-trifluoromethylanilines from nitrosoarenes by radical fluorination.[166] B) Attempted synthesis of a protected 6-nitrosopurine riboside (**48**) by oxidation of the corresponding adenosine (**24**). Oxidation stopped at the hydroxylamino-stage (**47**). I) Oxone, DCM, H_2O, rt, 2 h, 29%.

In an attempt to synthesize the required nitrosopurine substrate, the exocyclic amino group of adenosine was oxidized using Oxone (2 $KHSO_5 \cdot KHSO_4 \cdot K_2SO_4$). This oxidant has previously been utilized for oxidation of various substituted aniline derivatives to the corresponding nitrosobenzenes.[167] For these substrates, performing the reaction in a biphasic mixture of DCM/water reduced the formation of byproducts such as overoxidized nitro compounds and azoxybenzenes. Consequently, the tri-*O*-TBDMS-protected adenosine derivative **24** was used as starting material to provide solubility in the organic layer. Unfortunately, the adenosine amino group was less prone to oxidation than the more electron-rich aniline amino function; the reaction stalled after formation of the hydroxylamine intermediate and could not be driven further to yield the desired nitrosopurine (Scheme 3.11B). In an attempt to increase the oxidation power of Oxone, the reaction was repeated with unprotected adenosine in a monophasic environment. Here, no conversion was achieved at all. Also the exchange of Oxone for hydrogen peroxide in presence of a molybdenum catalyst (ammonium heptamolybdate, which had previously been shown to catalyze oxidation of substituted anilines to nitrosobenzenes) did not lead to adenosine oxidation.[168]

As direct oxidation of adenosine derivatives to nitrosopurine nucleosides was not successful, generation of the nitroso species was attempted by oxidative cleavage of a sulfimide derivative.[169] In the first step, protected adenosine **24** was converted into an *S*-dimethylsulfimide *via* a chloramine intermediate (Scheme 3.12). The reaction proceeded with high conversion, but the product **49** could not be purified due to decomposition of the sulfimide moiety on

silica gel.

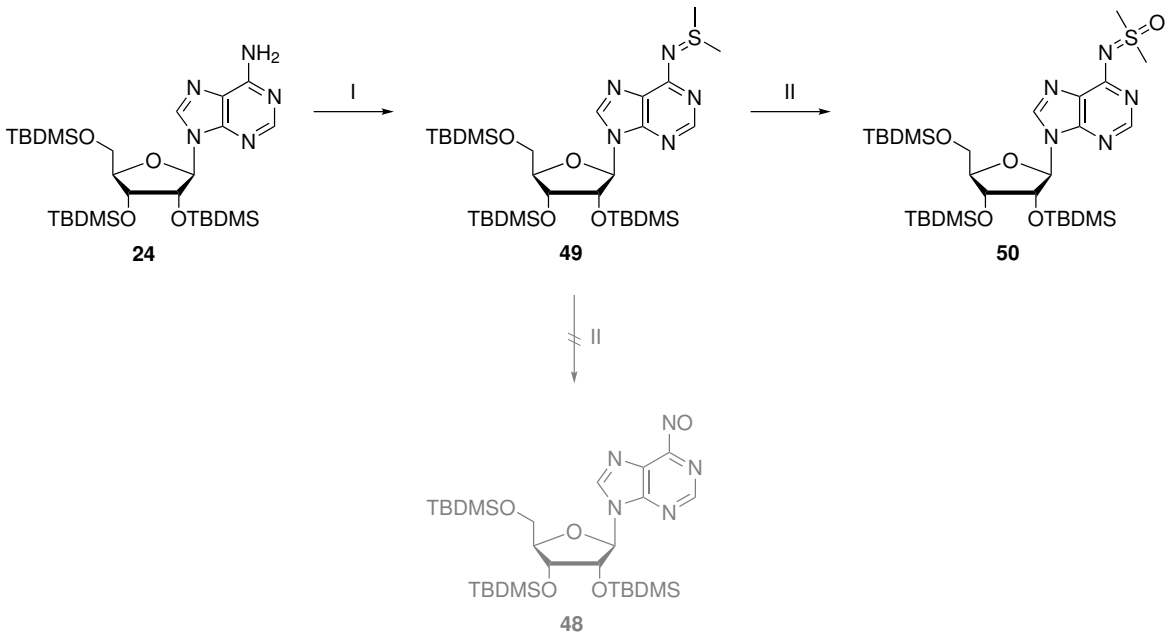

Scheme 3.12: Attempted synthesis of 6-nitrosopurine-derivative **48**. Instead of the desired product, sulfoximide **50** was formed. I) Me_2S, NCS, DCM, 0 °C, 30 min, then rt, 90 min, then NaOMe, MeOH, rt, 10 min, then H_2O, rt, 10 min, 85% (by NMR), product not isolated; II) *m*-CPBA, DCM, 0 °C, 90 min, then rt, 90 min, product not isolated.

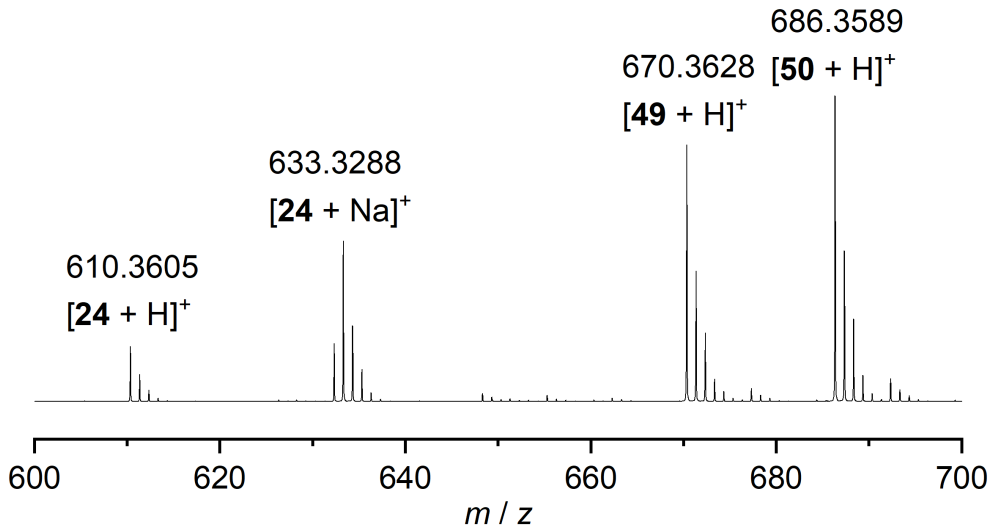

Figure 3.3: ESI-MS spectrum of the crude product obtained from treatment of **49** with *m*-CPBA. The presence of **24**, **49** and the sulfoximide **50**, but not the desired nitroso-product **48** (m/z = 624.34; $[M+H]^+$) is detectable.

According to Taylor *et al.* sulfimides are oxidatively cleaved by *m*-CPBA to yield nitroso products.[169] However, instead of N^6 the adjacent sulfur atom was oxidized, resulting in

formation of the sulfoximide **50** (Figure 3.3) instead of the desired nitrosopurine **48**. Similar to its precursor, isolation of the product was not possible.

As formation of a 6-nitrosopurine species was not successful, a different route toward trifluoromethylation was employed. Kanie *et al.* have reported the conversion of secondary amines into dithiocarbamates, which were further transformed into trifluoromethylamines by oxidative desulfurization-fluorination.[164] Since the synthetic route involves both harsh basic conditions (*n*-butyllithium) and fluoride sources, neither acyl- nor silyl-protected nucleoside building blocks are suitable starting materials. It was therefore envisioned to introduce the trifluoromethyl group on the nucleobase and subject the product to Vorbrüggen glycosylation.

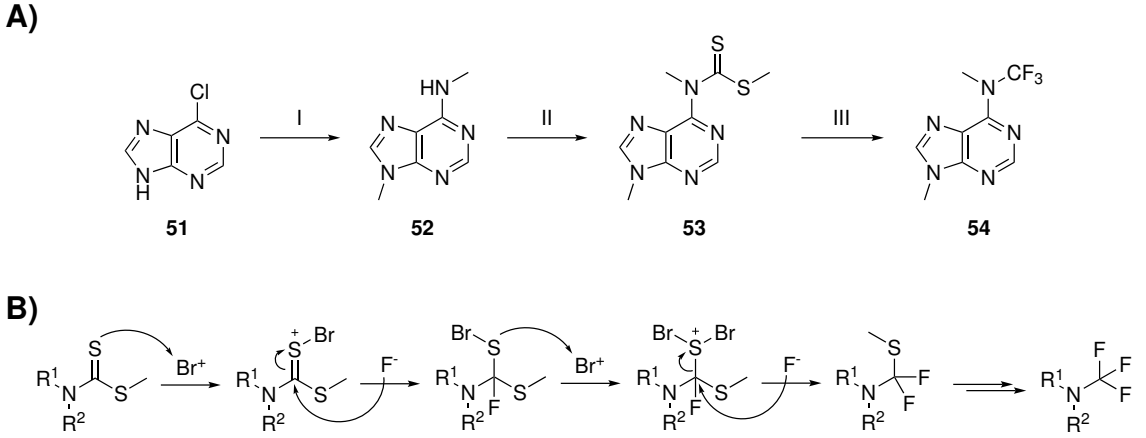

Scheme 3.13: Synthesis of an N^6-trifluoromethylated adenine derivative. A) Reaction scheme. I) MeI, K_2CO_3, DMF, rt, 2 h, then $MeNH_2$, EtOH, rt, 16 h, 41%; II) *n*-BuLi, THF, -40 °C, 2 h, then CS_2, THF, rt, 16 h, then MeI, THF, 0 °C, to rt, 6 h, 59%; III) DBDMH, HF·pyridine, DCM, 50 °C, 4 h, 93%. B) Putative mechanism of the desulfurization-fluorination reaction. A bromonium source activates the dithiocarbamate for fluorination.[164]

Although a removable protecting group at N9 of the nucleobase is required for this approach, a test synthesis was performed with an N9-methylated nucleobase to probe the overall applicability of this approach (Scheme 3.13A). Following treatment of 6-chloropurine (**51**) with methyl iodide to mask N9, a methylamino group was introduced at C6. Generation of a 6-alkylamino nucleobase was required, as the dithiocarbamate moiety can only be installed on secondary amines.[164] Compound **53** was then generated by deprotonation of N^6 followed by consecutive addition of carbon disulfide and methylation with methyl iodide. The dithiocarbamate was subsequently activated by a bromonium ion source for fluorination (Scheme 3.13). In contrast to the report by Kanie *et al.*, desulfurization-fluorination employing tetrabutylammonium dihydrogen trifluoride ($TBAH_2F_3$) as fluoride source did not result in formation of product **54**. Exchaniging the fluoride source for Olah's reagent

(HF·pyridine) and 1,3-dibromo-5,5-dimethylhydantoin (DBDMH) as activator, however, led to smooth trifluoromethylation and the product **54** could be isolated in high yield.

For the purpose of later deprotection of the nucleobase, the introduction of benzyl groups instead of methyl substituents at N^6 and N9 was considered a promising alternative: benzyl groups are stable in presence of both *n*-butyllithium and fluoride, and may be cleaved hydrogenolytically or under strongly acidic conditions. N^6,9-dibenzyladenine (**56**) was synthesized starting from 6-chloropurine, and converted to the dithiocarbamate **57** using the procedure discussed above (Scheme 3.14). Treatment of **57** with DBDMH and Olah's reagent at 50 °C, however, resulted in a mixture of various brominated species instead of a trifluoromethylated product.

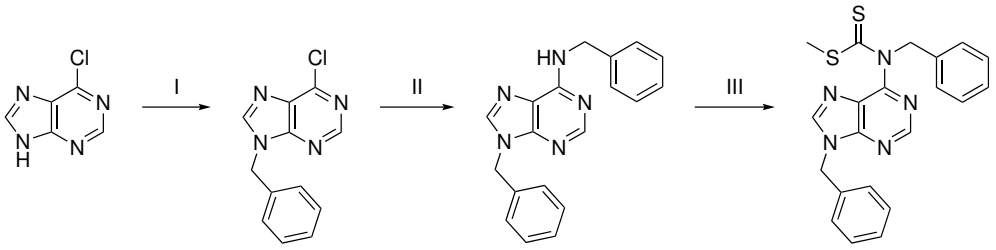

Scheme 3.14: Synthesis of a benzyl-protected adenine derivative. I) BnBr, K_2CO_3, DMF, rt, 16 h, 60%; II) $BnNH_2$, DMF, rt, 16 h, 84%; III) *n*-BuLi, THF, -40 °C, 2 h, then CS_2, THF, rt, 16 h, then MeI, THF, 0 °C, to rt, 6 h, 70%.

Further optimization, especially regarding a suitable protecting group startegy, is required to progress toward an N^6-trifluoromethylated adenosine nucleoside. For temporary masking of N^6 a methyl group might be the substituent of choice, as it can later be photocatalytically removed on the nucleoside stage.[170,171] Yet, as this approach is not suitable for protection of N9, the evaluation of other suitable protecting groups is necessary. However, such further optimization has not been performed in the course of this thesis.

3.1.2 Spectroscopic analysis of m^{6}A atomic mutants

3.1.2.1 UV/Vis spectroscopy

Besides NMR spectroscopy and mass spectrometry for identification and determination of purity, the nucleoside building blocks **1–17** were characterized by UV/Vis spectroscopy to investigate the effects of the introduced structural mutations on absorbance maxima and extinction coefficients (ϵ). For novel nucleoside products, especially ϵ needs to be determined, as this parameter is required to calculate oligonucleotide concentrations and

yields based on UV absorbance. UV/Vis spectra of all samples were recorded in water. Serial dilutions of the samples were measured to obtain ϵ from plotting absorbance (A) *vs.* sample concentration (c) according to Lambert-Beer's law:

$$A = \epsilon \cdot c \cdot d \tag{3.1}$$

with d being the path length of the sample cell. For the hydrolysis-prone hm^{6}A and f^{6}A, aqueous samples inevitably contain traces of adenosine, which influence the absorption pattern. For these samples, the extinction coefficients were determined by HPLC (for further detail see Experimental Section, Chapter 7) and the absorption spectra were recorded on-line using a photodiode array (PDA) detector. The recorded absorption spectra and key spectral data of all compounds are given in Figure 3.4 and Table 3.2.

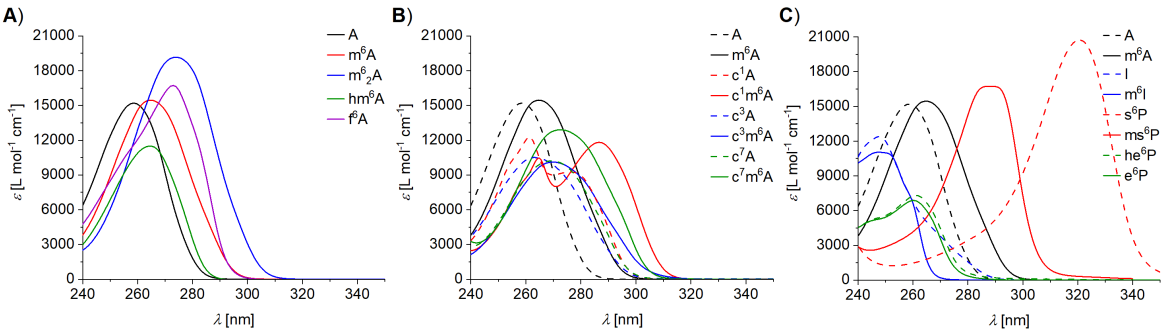

Figure 3.4: UV/Vis absorption spectra of purine nucleosides. A) UV/Vis spectra of adenosine derivatives bearing different substituents at N^6. B) UV/Vis spectra of A, m^{6}A and their 1-, 3-, and 7-deaza variants. C) UV/Vis spectra of purine nucleosides bearing different substituents at C6.

While methylation at N^6 of adenosine does not significantly change absorption maximum or extinction coefficient, oxidation of the methyl group has more pronounced effects on the spectral properties (Figure 3.4). Interestingly, oxidation of m^{6}A does not impact the absorption maximum but decreases the extinction coefficient by ca. 25%, while further oxidation to f^{6}A restores ϵ but leads to red-shifted absorption. The electron-donating influence of a second methyl group (m$^6{}_2$A) increases both ϵ and λ_{max}. Introduction of either deaza modification leads to diminished maximum absorbance, while methylation at N^6 results in slightly red-shifted maxima in all cases (Figure 3.4B). Absence of N1 or N7 affords interesting spectral characteristics: while the 7-deaza modification renders the extinction coefficient more methylation-sensitive (21% difference between c^{7}A and c^{7}m^{6}A), absence of N1 leads to emergence of two absorption maxima; the peak ratio of which is dependent on the N^6 methylation status. Absence of N^6 causes an even larger detrimental effect on the absorbance than deaza-modifications of the purine scaffold: e^{6}P displays less than half of

m^6A absorbance, although the maximum wavelength is not affected (Figure 3.4C). Finally, exchanging the exocyclic nitrogen for oxygen or sulfur (I/m^6I and s^6P/ms^6P) results in blue- or red-shifted absorption, respectively.

Table 3.2: Absorption maxima λ_{max} and molar extinction coefficients at the absorption maximum (ϵ_{max}) and at 260 nm (ϵ_{260}). Values are given as mean ± s.e.m of triplicates.

No.	Nucleoside	λ_{max} [nm]	ϵ_{max} [L·mol^{-1}·cm^{-1}]	ϵ_{260} [L·mol^{-1}·cm^{-1}]
1	A	258	15180 ± 90	15080 ± 80
2	m^6A	265	15450 ± 50	14580 ± 40
3	$m^6{}_2A$	274	19160 ± 570	12900 ± 390
4	hm^6A	264	11530 ± 210	10970 ± 190
5	f^6A	273	15930 ± 370	11740 ± 210
6	I	248	12390 ± 360	6750 ± 220
7	m^6I	249	11020 ± 250	6610 ± 90
8	s^6P	321	20720 ± 580	1530 ± 20
9	ms^6P	288	16730 ± 110	4150 ± 60
10	e^6P	260	6880 ± 70	6880 ± 70
11	he^6P	261	7320 ± 140	7260 ± 140
12	c^1A	261 276	12240 ± 130 9300 ± 110	12030 ± 140
13	c^1m^6A	265 287	10340 ± 200 11810 ± 220	8680 ± 180
14	c^3A	263	10510 ± 250	10320 ± 240
15	c^3m^6A	270	10110 ± 230	8510 ± 240
16	c^7A	269	10220 ± 200	8770 ± 60
17	c^7m^6A	273	12900 ± 120	9470 ± 110

3.1.2.2 Fluorescence spectroscopy

Although canonical nucleosides are inherently non-fluorescent, already minor structural changes to the nucleobase scaffold, e. g. attachment of a vinyl substituent to adenosine to obtain 8-vinyladenosine (v^8A) or changing the attachment point of the exocyclic amino group (2-aminopurine, 2-AP), are able to induce fluorescence activity.[172,173] Fluorescence spectra of the m^6A atomic mutants **12–17** were recorded and compared to native A and m^6A to elucidate if deaza-mutation of m^6A also provides a fluorescence-activating effect. When irradiated at 260 nm, A and c^7A in both unmethylated and methylated state were found to be non-fluorescent, while their 1-deaza and 3-deaza analogs showed fluorescence emission (Figure 3.5A).

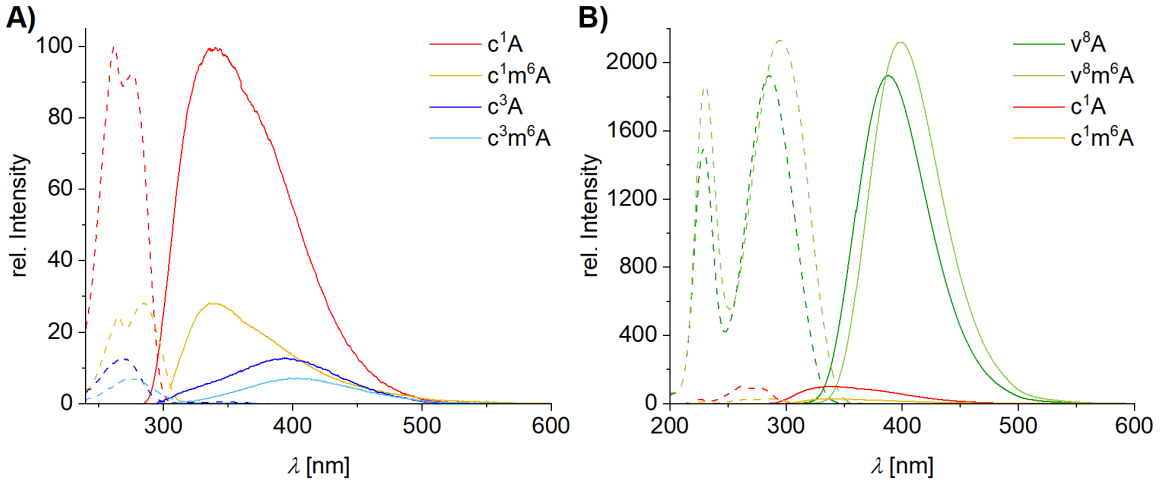

Figure 3.5: Fluorescence spectra of N^6-methylated and unmethylated adenosine analogs. A) Fluorescence emission spectra upon excitation at 260 nm. B) Excitation (dashed lines) and emission (solid lines) spectra of the fluorescent 1-deaza and 3-deaza nucleosides. Spectra were recorded at the respective excitation or emission maxima (c^1A: 261/339 nm; c^1m^6A: 285/339 nm; c^3A: 269/392 nm; c^3m^6A: 275/404 nm). C) Fluorescence excitation (dashed lines) and emission (solid lines) spectra of 1-deazadenosine nucleosides in comparison with the respective 8-vinyladenosines (c^1A: 261/339 nm; c^1m^6A: 285/339 nm; v^8A: 285/389 nm; v^8m^6A: 295/398 nm). In all spectra, excitation and emission intensities are given relative to c^1A intensity (set to 100).

When excited at their respective excitation maxima, c^1A emission intensity was 5-fold higher than c^3A intensity (Figure 3.5B). Notably, for both deaza-modifications fluorescence intensity was strongly dependent on the methylation state of the nucleobase; methylation at N^6 reduced the emission by 70% and 45%, respectively. Being both brighter in the unmethylated state and quenched more strongly upon methylation, c^1A might be an interesting candidate for fluorescent monitoring of adenosine methylation and demethylation events in biologically relevant systems. Nonetheless, c^1A emission intensity is by far outclassed by established fluorescent nucleobases for *in vivo* applications such as v^8A, which emits at a 20-fold higher intensity (Figure 3.5C). v^8A, in contrast, is not suitable for monitoring the methylation state, as v^8A and v^8m^6A differ by only 9% emission intensity. Thus, 8-vinyl-1-deazaadenosine (c^1v^8A), potentially combining the brightness of 8-vinyladenosine and the methylation-sensitivity of 1-deazaadenosine, might be an interesting target structure for future projects.

3.1.3 Synthesis of modified phosphoramidite building blocks

Conversion of nucleosides into phosphoramidite building blocks requires orthogonal protection of the three ribose hydroxy groups compatible with the cyclic mechanism of automated solid-phase synthesis. An acid-labile 4,4'-dimethoxytrityl (DMT) group is the standard

choice for 5'-protection, as it is conveniently cleaved by dichloroacetic acid (DCA) or even acetic acid at ambient temperature. Besides, the released resonance-stabilized DMT cation is brightly orange-colored, which allows photometric monitoring of the deprotection step during solid-phase synthesis.[174] DMT is chosen over trityl or monomethoxytrityl (MMT) due to the higher mesomeric stabilization of the corresponding cation, which enables deprotection under milder conditions. The regioselectivity of the tritylation can be assisted by transient protection of 2'- and 3'-OH (e. g. as dimethylacetal). However, the primary 5'-hydroxy group already possesses a higher inherent reactivity than the two secondary hydroxy groups. Thus, DMT-protection of the free nucleoside was performed for all m^6A analogs (Scheme 3.15); no formation of undesired regioisomers was observed in any case.

The 2'-hydroxy groups of phosphoramidite building blocks are required to be stable in presence of the acid used for DMT cleavage during the solid phase synthesis as well as under basic conditions during nucleobase deprotection. Unintended cleavage of the 2'-protecting groups would render the oligonucleotide susceptible to alkaline hydrolysis: under basic conditions, the free 2'-hydroxy group nucleophilically attacks the neighboring 3'-phosphate to form a 2',3'-cyclic phosphate, thereby causing strand cleavage.[175] Thus, fluoride-labile silyl moieties are chosen as 2'-protecting groups. Because trimethylsilyl (TMS) and triethylsilyl (TES) ethers also display a significant instability under acidic conditions and the large steric demand of the stable *tert*-butyldiphenylsilyl (TBDPS) substituents may impair efficient installation of the phosphoramidite moiety at 3'-OH, three silyl substituents of moderate size and stability have proven to be the optimal choices: TBDMS, TIPS and TOM.[174] The first and still most widely used protecting group TBDMS has over time been partially displaced by [(triisopropylsilyl)oxy]methyl (TOM) groups. TOMCl is a more costly reagent than TBDMSCl and therefore its use is mainly restricted to small-scale syntheses. Yet, TOM provides significant advantages over TBDMS and TIPS. Unlike these classical silyl ethers, which may undergo isomerization/migration from 2'-OH to 3'-OH under basic conditions in protic solvents, TOM does not feature a direct Si-O bond at the ribose and therefore retains isomeric purity after isolation. Besides, the more flexible TOM substituent provides less steric restrictions for reactions at 3'-OH and may therefore result in improved yields both during phosphoramidite synthesis and in the solid-phase synthesis coupling steps. TIPS (triisopropylsilyl), being both sterically demanding and able to migrate, is the least commonly used silyl ether for silyl protection.

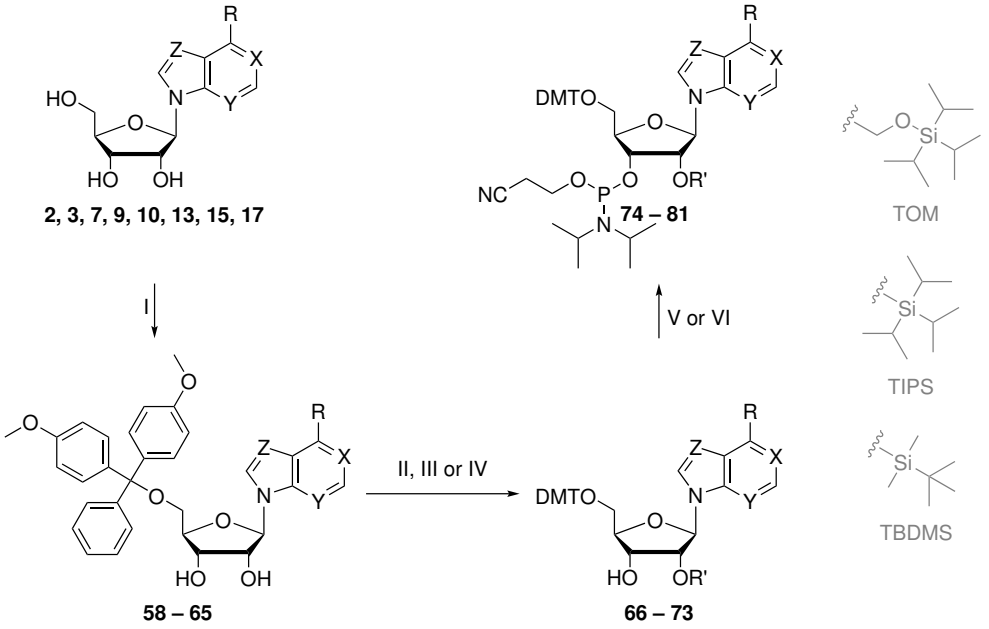

No.	–R	X	Y	Z	R'
2, **58**, **66**, **74**	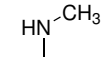	N	N	N	TOM
3, **59**, **67**, **75**	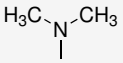	N	N	N	TOM
7, **60**, **68**, **76**		N	N	N	TOM
9, **61**, **69**, **77**		N	N	N	TOM
10, **62**, **70**, **78**		N	N	N	TOM
13, **63**, **71**, **79**		CH	N	N	TIPS
15, **64**, **72**, **80**		N	CH	N	TIPS
17, **65**, **73**, **81**		N	N	CH	TBDMS

Scheme 3.15: Conversion of the m^6A atomic mutant nucleosides into their corresponding phosphoramidite building blocks. I) DMTCl, DMAP, NEt_3, pyridine, rt, 14–23 h, 77% (for **2**), 80% (for **3**), 67% (for **7**), 64% (for **9**), 87% (for **10**), 88% (for **13**), 67% (for **15**); 60% (for **17**); II) $(t\text{-Bu})_2SnCl_2$, DIPEA, DCE, 70 °C, 15 min, then TOMCl, rt, 30 min, 36% (for **58**), 26% (for **59**), 34% (for **60**), 19% (for **61**), 37% (for **62**); III) $AgNO_3$, pyridine, rt, 30 min, then TIPSCl, rt, 22 h, 35% (for **63**), 37% (for **64**); IV) $AgNO_3$, pyridine, rt, 30 min, then TBDMSCl, rt, 15 h, 35% (for **65**); V) CEPCl, Me_2NEt, DCM, rt, 2.5–5 h, 75% (for **66**), 89% (for **67**), 81% (for **68**), 64% (for **69**), 82% (for **70**), 51% (for **71**), 31% (for **73**); VI) CEPCl, $i\text{-Pr}_2NEt$, pyridine, rt, 5 h, 58% (for **72**).

The TOM group, as the silyl protecting group of choice, was introduced by activation of the ribose as cyclic 2'-3'-di-*O*-dibutylstannilydene or di-*tert*-butylstannilydene derivative under basic conditions followed by reaction with TOMCl (Scheme 3.16.[176] Using this strategy, all C6-substituted purine nucleosides were converted into mixtures of 5'-*O*-DMT-2'-*O*-TOM and 5'-*O*-DMT-3'-*O*-TOM isomers. These were separable *via* column chromatography, with the desired 2'-*O*-TOM isomer being the first eluted species in all cases, and unambiguously identified by 2D NMR spectroscopy.

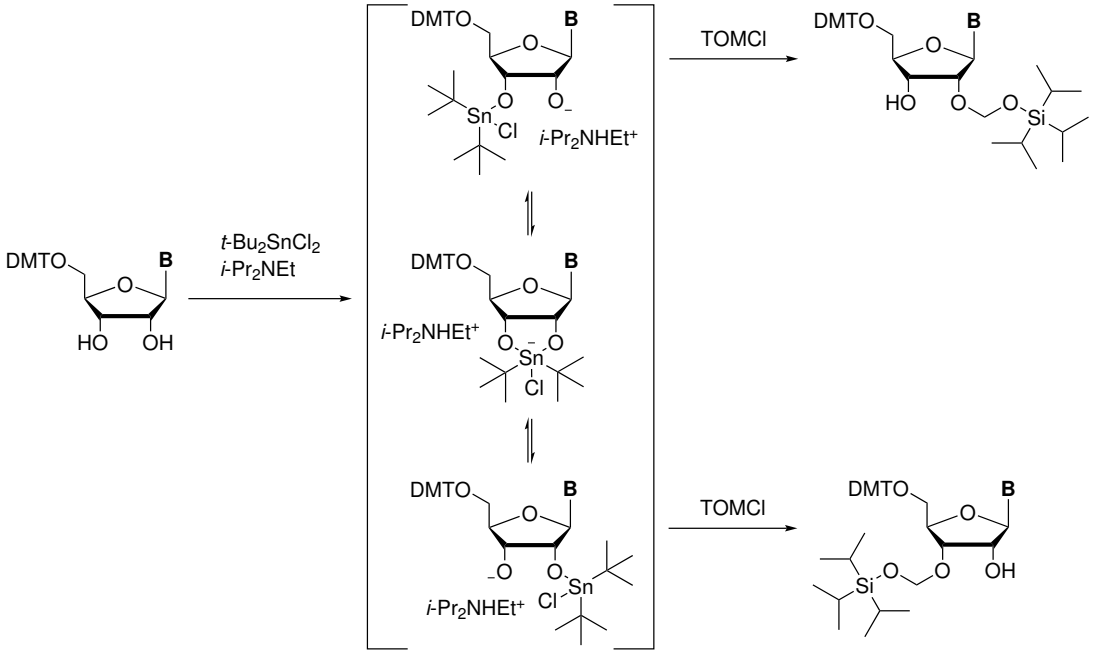

Scheme 3.16: Mechanism of ribose protection with TOM groups. Before addition of TOMCl, the 2'- and 3'-hydroxy groups are activated as a dibutyl- or di-*tert*-butylstannylidene derivative, which are hydrolyzed upon aqueous workup.

Unexpectedly, when heating 5'-*O*-DMT-c^{1}m^{6}A in the presence of *t*-Bu_2SnCl_2, a major fraction of the starting material decomposed due to cleavage of the glycosidic bond. As a consequence, TOM-protection was not feasible for the 1-deaza-nucleoside. A similar issue had also been reported by Mairhofer *et al.* for the synthesis of 3-deazaadenosine phosphoramidite. For this building block, the authors could neither successfully install 2'-TOM nor 2'-TBDMS protecting groups and finally resorted to 2'-TIPS protection.[177] Following this reported approach, the 2'-*O*-TIPS derivatives **71** and **72** along with their respective 3'-*O*-TIPS isomers were obtained in convenient yields. The 7-deaza-building block, on the contrary, was 2'-protected as a TBDMS-ether in analogy to the synthesis of the c^{7}A phosphoramidite, which had been described previously.[178] During TIPS- and TBDMS-protection, silver(I) nitrate was used as an additive to favor formation of the desired 2'-isomer. While it would be obvious to assume that coordination of the silver ion

to the ribose hydroxy groups influences regioselectivity, this theory has been disproven by Hakimelahi *et al.*: direct use of $TBDMSNO_3$ in absence of metal ions resulted in the same 2'-3'-selectivity as a combination of TBDMSCl and $AgNO_3$[179] Thus, the nitrate anion instead of the silver cation appears to be the relevant factor impacting regioselectivity; however, the underlying mechanistic principles have not yet been fully elucidated.

Finally, the 5'-*O*-DMT-2'-*O*-silyl-protected nucleosides were converted into the corresponding phosphoramidite building blocks by reaction with 2-cyanoethyl *N*,*N*-diisopropylchlorophosphoramidite (CEPCl) under basic conditions. The standard procedure for this conversion uses the substrate as a solution in DCM and employed the non-nucleophilic and easily removable (volatile) *N*,*N*-dimethylethylamine as auxiliary base. All purine-based building blocks (**74**–**78**) as well as the c^1m^6A phosphoramidite **79** were obtained in moderate to high yields. For synthesis of the 3-deaza-building block **80**, however, the strategy proved not to be efficient: although TLC showed consumption of the starting material over the course of the reaction, only starting material was isolated after evaporation of the solvent and purification of the crude product by column chromatography. Thus, the product **80** is either unstable at elevated temperatures, as used for removal of the solvent, or decomposed in contact with silica gel during column chromatography. To avoid evaporation to dryness, the synthetic procedure was altered: substrate **72** was reacted with CEPCl in presence of *N*,*N*-diisopropylethylamine (DIPEA) in pyridine, and precipitated from heptane prior to column chromatography. Here, the phosphoramidite product was isolated in moderate yield, which indicates that concentration of the reaction mixture to dryness is detrimental for product stability.

A similar instability of the phosphoramidite was observed in case of the 7-deaza-analog **81**: after initial product formation upon treatment of **73** with CEPCl, the desired phosphoramidite decomposed upon concentration of the reaction mixture. In this case, precipitation of the product was not necessary; instead, decomposition could be avoided by removal of the solvent at ambient temperature.

3.2 Oligonucleotide synthesis, labeling and characterization

3.2.1 Solid-phase synthesis

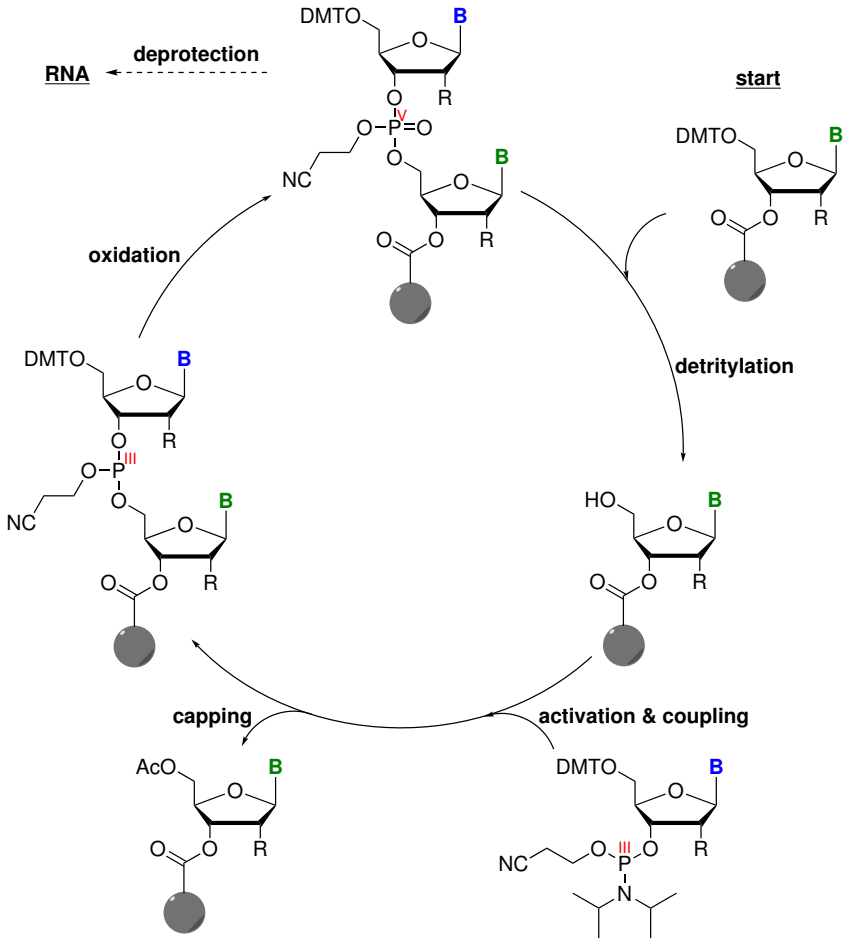

Scheme 3.17: Reaction cycle for the solid-phase synthesis of RNA and DNA oligonucleotides. After acidic deprotection the 5'-OH group is coupled to a (preactivated) phosphoramidite building block. Unreacted 5'-OH groups are capped by acylation before the phosphite triester linkage (P^{III}) is oxidized to a more stable phosphotriester species (P^{V}). After the final cycle, cleavage from the solid support and deprotection yield the product oligonucleotide.

The phosphoramidite building blocks described in Section 3.1.3 were used to incorporate the various m^6A atomic mutants into RNA oligonucleotides *via* automated RNA solid-phase synthesis. In this process, the 3'-terminal nucleoside of the target oligonucleotide sequence is tethered to a solid support (controlled-pore glass, CPG), and the oligomer is synthesized by stepwise coupling of phosphoramidite building blocks. The covalent linkage of the growing product to the solid support allows for removal of reagents and excess phosphoramidites

by simple washing steps without the need for tedious extraction procedures.

Each cycle to extend the oligonucleotide by one monomer unit comprises four steps (Scheme 3.17). First, the 5'-DMT protecting group is cleaved under acidic conditions. Among the two commonly used acids DCA (dichloroacetic acid, pK_a = 1.5) and TCA (trichloroacetic acid, pK_a = 0.7) DCA is preferred, because stronger acidic conditions increase the risk of nucleoside depurination.[180] The cleaved DMT cation is brightly orange colored (λ_{max} = 498 nm) and allows photometric monitoring of the deprotection step.[181] Based on the ratio of the UV peak areas in each reaction cycle, the stepwise and overall coupling yields can be calculated.

The deprotected 5'-OH group is next used for coupling with an incoming phosphoramidite building block. The phosphoramidite is premixed with a tetrazole activator to enhance its reactivity (Scheme 3.18). The tetrazole first protonates and then substitutes the diisopropylamino group by nucleophilic attack on the phosphorous center. The formed activated tetrazolide intermediate is subsequently attacked by the free 5'-OH of the growing oligonucleotide to form a phosphite triester linkage. Especially for RNA synthesis, where the bulky 2'-protecting group leads to less efficient coupling, the simple unsubstituted activator 1*H*-tetrazole is often replaced by 5-(ethylthio)-1*H*-tetrazole (ETT) or 5-(benzylthio)-1*H*-tetrazole (BTT). These can be used in higher concentrations owing to an improved solubility in MeCN, and provide a higher activation potential due to increased acidity (1*H*-tetrazole: pK_a = 4.89; ETT: pK_a = 4.28; BTT: pK_a = 4.08).[182] An alternative to tetrazole activators is 4,5-dicyanoimidazole, which is more less acidic but more nucleophilic than ETT or BTT.[183] The reduced acidity avoids partial detritylation of the oligonucleotide, which occurs during ETT- or BTT-activated coupling and is especially detrimental for the synthesis of long oligonucleotides.[184]

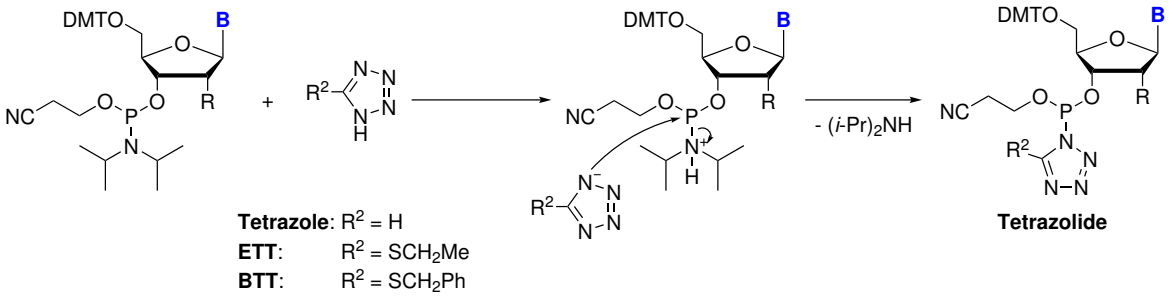

Scheme 3.18: Activation of a phosphoramidite building block by a tetrazole activator. Protonation and nucleophilic substitution of the diisopropylamino group yield an activated tetrazolide intermediate. Especially for RNA synthesis, the more active derivatives ETT and BTT are preferred over unsubstituted 1*H*-tetrazole.[182]

After coupling, unreacted 5'-hydroxy groups are capped by acylation to prevent accumulation of deletion products throughout the synthetic process.[185] The extended oligonucleotide strands are subjected to oxidizing conditions (I_2, water, pyridine) to convert the unstable phosphite triester (P^{III}) linkage into a phosphotriester (P^V) moiety. Afterwards, the cycle is repeated for coupling of the next phosphoramidite building block. Once the final product length is obtained, the oligonucleotides are cleaved from the solid support under basic conditions (typically ammonia and/or methylamine in water/ethanol). This treatment simultaneously cleaves the base-labile nucleobase protecting groups (acyl or amidine groups). For RNA, the 2'-silyl ether groups are removed by treatment with a fluoride source such as $HF{\cdot}NEt_3$ or TBAF. Finally, the samples are desalted and purified *via* denaturing polyacrylamide gel electrophoresis (PAGE) or HPLC.

Using the solid-phase synthesis method described above, the modified phosphoramidite building blocks as well as the unmodified adenosine phosphoramidite were incorporated into 12-mer oligonucleotides of the sequence Hex-AACCGGXCUGUC. As a key feature of this construct, the nucleoside of interest (X) is incorporated inside the core motif GGXCU. Being a variant of the native m^6A consensus motif RRACH, the oligonucleotide design closely resembles the sequence context of m^6A sites in mammalian mRNA. Furthermore, a hexynyl linker (Hex) was installed at the 5'-terminus of the sequence to enable subsequent fluorescent labeling of the oligonucleotides using click chemistry.

Following solid-phase synthesis, cleavage of the oligonucleotides from their solid support as well as deprotection of the nucleobases was achieved using $MeNH_2$ in $EtOH/H_2O$ at 37 °C for 5 h; the 2'-protecting groups were removed by treatment with TBAF in THF at ambient temperature overnight. Nuclease digestion and HPLC-MS analysis of the purified oligonucleotides revealed that the products containing m^6I and ms^6P had suffered from nucleophilic substitution during incubation with methylamine, resulting in partial formation of m^6A-containing sequences. As these product mixtures could neither be separated by PAGE nor by HPLC, the conditions of the basic deprotection step needed to be changed for the oligonucleotides containing m^6I and ms^6P. A mixture of $H_2O/MeOH/NEt_3$ (5:4:1) at 25 °C for 3 d achieved quantitative nucleobase deprotection without undesired conversion of the modified nucleosides. Desalting of the deprotected samples by size exclusion chromatography and purification using denaturing PAGE finally yielded the desired oligonucleotides in high purities.

Table 3.3: Sum formulae, calculated and measured monoisotopic masses of the RNA oligonucleotides **R1** – **R9** (Hex-AACCGGXCUGUC) and the complementary oligonucleotide **R10** (GACAGUCCGGUU).

No.	Modification X	Sum Formula	Mass calculated [Da]	Mass found [Da]
R1	A	$C_{120}H_{152}N_{46}O_{84}P_{12}$	3952.58933	3952.58980
R2	m^6A	$C_{121}H_{154}N_{46}O_{84}P_{12}$	3966.60443	3966.58816
R3	c^1m^6A	$C_{122}H_{155}N_{45}O_{84}P_{12}$	3965.60918	3965.61277
R4	c^3m^6A	$C_{122}H_{155}N_{45}O_{84}P_{12}$	3965.60918	3965.62937
R5	c^7m^6A	$C_{122}H_{155}N_{45}O_{84}P_{12}$	3965.60918	3965.57447
R6	$m^6{}_2A$	$C_{122}H_{156}N_{46}O_{84}P_{12}$	3980.62063	3980.60146
R7	m^6I	$C_{121}H_{153}N_{45}O_{85}P_{12}$	3967.58899	3967.62270
R8	ms^6P	$C_{121}H_{153}N_{45}O_{84}P_{12}S$	3983.56615	3983.59401
R9	e^6P	$C_{122}H_{155}N_{45}O_{84}P_{12}$	3965.60973	3965.62694
R10	–	$C_{114}H_{142}N_{45}O_{83}P_{11}$	3809.53932	3809.53574

3.2.2 UV melting curve measurements

Inside the RNA structure, the m^6A nucleobase is able to adopt two different conformations, as outlined in Section 1.2 (Figure 1.10). Only the energetically disfavored *anti* conformation exposes the Watson-Crick face of the nucleobase and allows base-pairing; thus, m^6A leads to a destabilization of duplex structures by 0.7–1.5 kcal/mol compared to the unmethylated reference.[115] Making use of this phenomenon, UV melting curves may provide hints toward the preferred nucleobase conformation of m^6A atomic mutants: an energetic preference for the *syn* conformation as observed for native m^6A should lead to a similar destabilizing influence on RNA duplex structures.

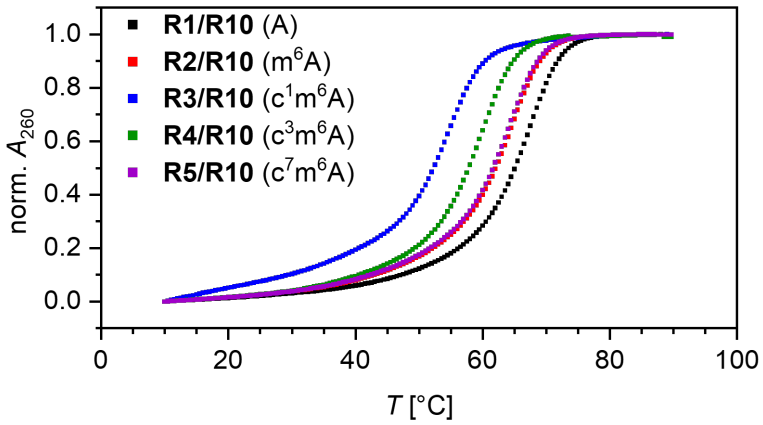

Figure 3.6: UV melting curves of 5 µM RNA duplexes, recorded at 260 nm. Compared to the unmodified duplex **R1/R10**, the introduction of m^6A or one of its deaza-analogs reduces the thermal duplex stability.

Indeed, all duplex constructs containing methylated nucleosides displayed reduced melting temperatures and less negative Gibbs free energies (Figure 3.6, Table 3.4). Whereas the destabilizing effects of m^6A and c^7m^6A were found to be comparable, the incorporation of c^3m^6A had a more detrimental effect on the duplex stability. An analogous trend has been reported for their unmethylated counterparts: while DNA or RNA duplexes containing either (d)A or c^7(d)A showed no significant differences regarding their thermal stabilities, the introduction of c^3A into a 10-mer RNA oligonucleotide reduced the melting temperature by 2.9 °C.[186,187] The destabilizing effect of 3-deazaadenosine in duplex structures was attributed to a distorted local hydration network in the minor groove of c^3A–U base pairs.[187] c^1m^6A has the largest impact on the RNA duplex structure, since neither its *syn* nor its *anti* conformation are able to engage in pase pairing; the absence of N1 presents a lesion on the Watson-Crick face of the nucleobase regardless of the orientation of the methyl group.

Table 3.4: Melting temperatures (for 5 µM duplex) and thermodynamic data of the analyzed duplexes. For the melting temperatures, an error of ±0.5 °C is assumed.

Duplex	$T_{m,\ 5\ \mu M}$ [°C]	$\Delta T_{m,\ 5\ \mu M}$ [°C]	ΔH [kcal mol^{-1}]	ΔS [cal mol^{-1} K^{-1}]	$\Delta G_{37\ °C}$ [kcal mol^{-1}]
R1/R10	66.2	–	-94.6	-253	-16.2
R2/R10	63.4	-2.8	-97.4	-263	-15.8
R3/R10	53.9	-12.3	-93.4	-260	-12.9
R4/R10	58.7	-7.5	-94.7	-260	-14.2
R5/R10	62.9	-3.3	-95.5	-258	-15.5

The results of the thermal denaturation experiments indicate that akin to m^6A also its 1-, 3- and 7-deaza analogs preferentially adopt the *syn* (or *anti* in case of c^1m^6A) conformation. DFT-based calculations predict the same preferences and thus further support this assumption (Figure 3.7). Also for m^6I and ms^6P the *syn* conformation is predicted as energetically favored, whereas DFT-based optimization of the e^6P structure yields a *gauche* conformation as its sole energetic minimum; therefore, e^6P is suggested to display a unique conformational preference among the synthesized m^6A atomic mutants. Nonetheless, all of the prepared atomic mutants of m^6A adopt a conformation with the exocyclic methyl substituent facing toward the Watson-Crick face of the nucleobase. Even though this orientation disrupts RNA base pairing, it is a prerequisite for recognition by m^6A reader and eraser proteins. In the binding pocket of YTH domain reader proteins, the *syn*-oriented methyl group engages in stabilizing methyl–π interactions with the aromatic cage structure of the binding site. Similarly, upon binding of the modified oligonucleotides by the human m^6A demethylases FTO or ALKBH5, this conformation correctly aligns the methyl

group with the Fe(II) ion in the catalytic center of the enzyme for oxidation. The thermal denaturation experiments and DFT-based studies described above confirm similar structural premises for protein recognition in case of all m^6A atomic mutants, which ensures comparability of all compounds in protein binding and enzymatic activity assays.

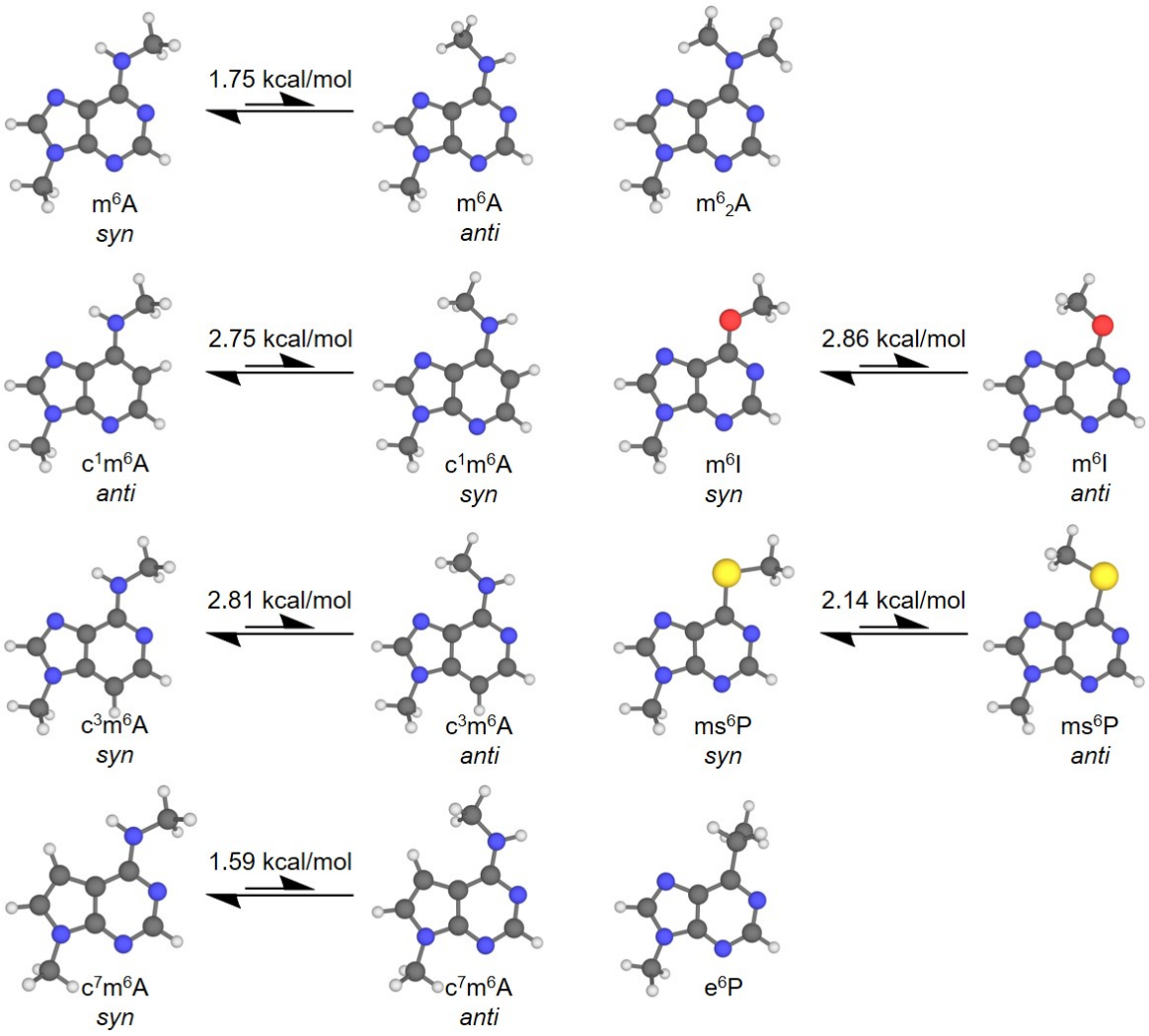

Figure 3.7: Geometry-optimized structures of the m^6A atomic mutants. Geometry optimizations were performed on the B3LYP/def2-TZVPPD level of theory. For structures showing two local energetic minima (i. e. *syn* and *anti* conformation), the energetic differences ΔG^0 (in kcal/mol) between the two conformations are given. To simplify calculations, the ribose units of the nucleoside structures were substituted for methyl groups at N9.

3.2.3 Fluorescent labeling

The 5'-hexynyl-labeled oligonucleotides **R1**–**R9** were fluorescently labeled with 6-carboxyfluorescein (6-FAM) azide *via* Cu(I)-catalyzed azide-alkyne cycloaddition. While uncatalyzed 1,3-dipolar cycloadditions yield mixtures of 1,4- and 1,5-disubstituted triazole prod-

ucts, regioselectivity is achieved by Cu(I) or Ru(I) catalysis. An antioxidant such as tris[(1-benzyl-1*H*-1,2,3-triazol-4-yl)methyl]amine (TBTA) is added as a ligand to stabilize the catalytically active oxidation state (+I) of the metal. The labeled oligonucleotides were obtained in high quality after purification by denaturing PAGE.

Table 3.5: Sum formulae, calculated and measured monoisotopic masses of the fluorescently labeled RNA oligonucleotides **R1-FAM** – **R9-FAM**.

No.	Modification X	Sum Formula	Mass calculated [Da]	Mass found [Da]
R1-FAM	A	$C_{144}H_{170}N_{50}O_{90}P_{12}$	4410.71196	4410.71356
R2-FAM	m^6A	$C_{145}H_{172}N_{50}O_{90}P_{12}$	4424.72706	4424.72774
R3-FAM	c^1m^6A	$C_{146}H_{173}N_{49}O_{90}P_{12}$	4423.73181	4423.73623
R4-FAM	c^3m^6A	$C_{146}H_{173}N_{49}O_{90}P_{12}$	4423.73181	4423.75013
R5-FAM	c^7m^6A	$C_{146}H_{173}N_{49}O_{90}P_{12}$	4423.73181	4423.72953
R6-FAM	$m^6{}_2A$	$C_{146}H_{174}N_{50}O_{90}P_{12}$	4438.74326	4438.72879
R7-FAM	m^6I	$C_{145}H_{171}N_{49}O_{91}P_{12}$	4425.71108	4425.69994
R8-FAM	ms^6P	$C_{145}H_{171}N_{49}O_{90}P_{12}S$	4441.68878	4441.70968
R9-FAM	e^6P	$C_{146}H_{173}N_{49}O_{90}P_{12}$	4423.73236	4423.76219

3.3 Recognition of m^6A atomic mutants by YTH proteins

Different physico-chemical properties may be exploited to assess interactions between biomolecules, such as protein-ligand, protein-RNA or protein-protein interactions. For fluorescent or fluorescently labeled ligands, the dissociation constant K_d of a ligand-receptor (e. g. RNA-protein) complex can be assessed based on the fluorescence anisotropy of the sample. Irradiation of a fluorophore sample with plane polarized light leads to excitation of the population of fluorophore molecules, the absorption transition dipoles of which are parallel to the electric field vectors of the light (Figure 3.8A).[188] In turn, emission will occur parallel to the emission transition dipole of the excited state. Thus, without motion, the fluorescence emission is anisotropic, with the dregree of anisotropy being determined by the angle β between the two dipole moments. In solution, however, this theoretical maximum anisotropy is decreased due to rotational diffusion: during the lifetime of the excited state (ca. 10^{-9}–10^{-8} s), the fluorophores can rotate several times (rotational correlation times: ca. 10^{-12} s), which displaces their emission transition dipoles and leads to depolarization of the emitted light (Figure 3.8B). As a consequence, the anisotropy of fluorophores moving freely in solution is near zero. Compared to free fluorophores, fluorophore-protein complexes

exhibit much longer rotational correlation times: binding of the fluorescent ligand by the protein restricts rotational diffusion of the fluorophore due to the large hydrodynamic radius of the resulting complex. Consequently, less rotational depolarization of the sample occurs during the lifetime of the excited state; the observed anisotropy of emission is increased. As ligand binding correlates with increased anisotropy, the measured anisotropy value can be translated into a 'fraction of ligand bound'; doing so for different protein concentrations allows determination of the K_d value of the protein-ligand complex.

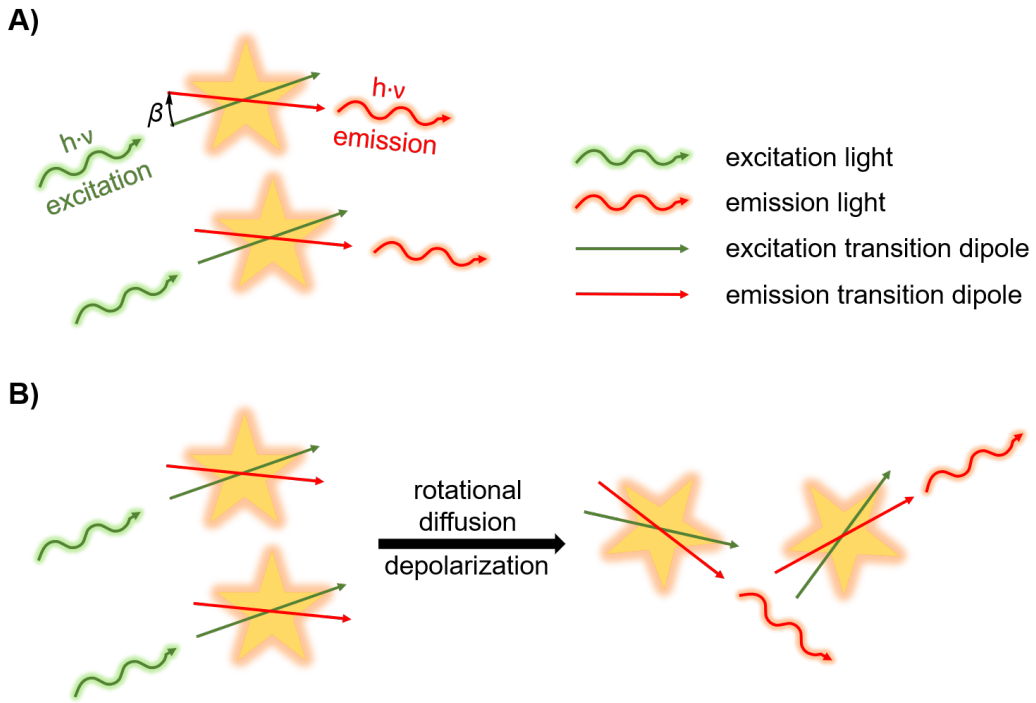

Figure 3.8: Principles of fluorescence anisotropy. A) Fluorophores are excited by planar polarized light, the electric field vector of which is parallel to their excitation transition dipole, and emit light parallel to the emission transition dipole of their excited state. Without molecular motion, the emission is anisotropic; the anisotropy is dependent on the angle β between the two dipoles. B) In solution, rotational diffusion of the fluorophore during the lifetime of the excited state displaces the emission dipoles and leads to depolarization of the emitted light.

Following this principle, the fluorescently labeled oligonucleotides **R1–R9** were used in fluorescence anisotropy studies to determine the influence of m^{6}A atomic mutagenesis on the binding affinity of the human m^{6}A reader proteins YTHDF2, YTHDC1 and YTHDC2. The recombinantly expressed YTH domains of the three reader proteins (YTHDF2$^{380–579}$, YTHDC1$^{344–509}$ and YTHDC2$^{1277–1430}$, in the following referred to as YTHDF2, YTHDC1 and YTHDC2) were provided by Jens Kretschmer in the group of Prof. Dr. Markus Bohnsack, University Medical Center Göttingen. Constant concentrations of oligonucleotide were titrated with increasing protein concentrations and subjected to anisotropy measurements.

The resulting binding isotherms were fitted according to a reversible 1:1 binding model (see Experimental Section, Section 7.2) and the dissociation constant K_d was calculated from

$$r = r_f + (r_b - r_f) \cdot \frac{[L] + K_d + [R] - \sqrt{([L] + K_d + [R])^2 - 4[L][R]}}{2[L]} \tag{3.2}$$

with r being the measured anisotropy of the sample, r_b the anisotropy of the RNA-protein complex, r_f the anisotropy of the free RNA, [L] the total RNA (ligand) concentration in the sample and [R] the total protein (receptor) concentration in the sample. The resulting binding isotherms and K_d values are summarized in Figure 3.9 and Table 3.6.

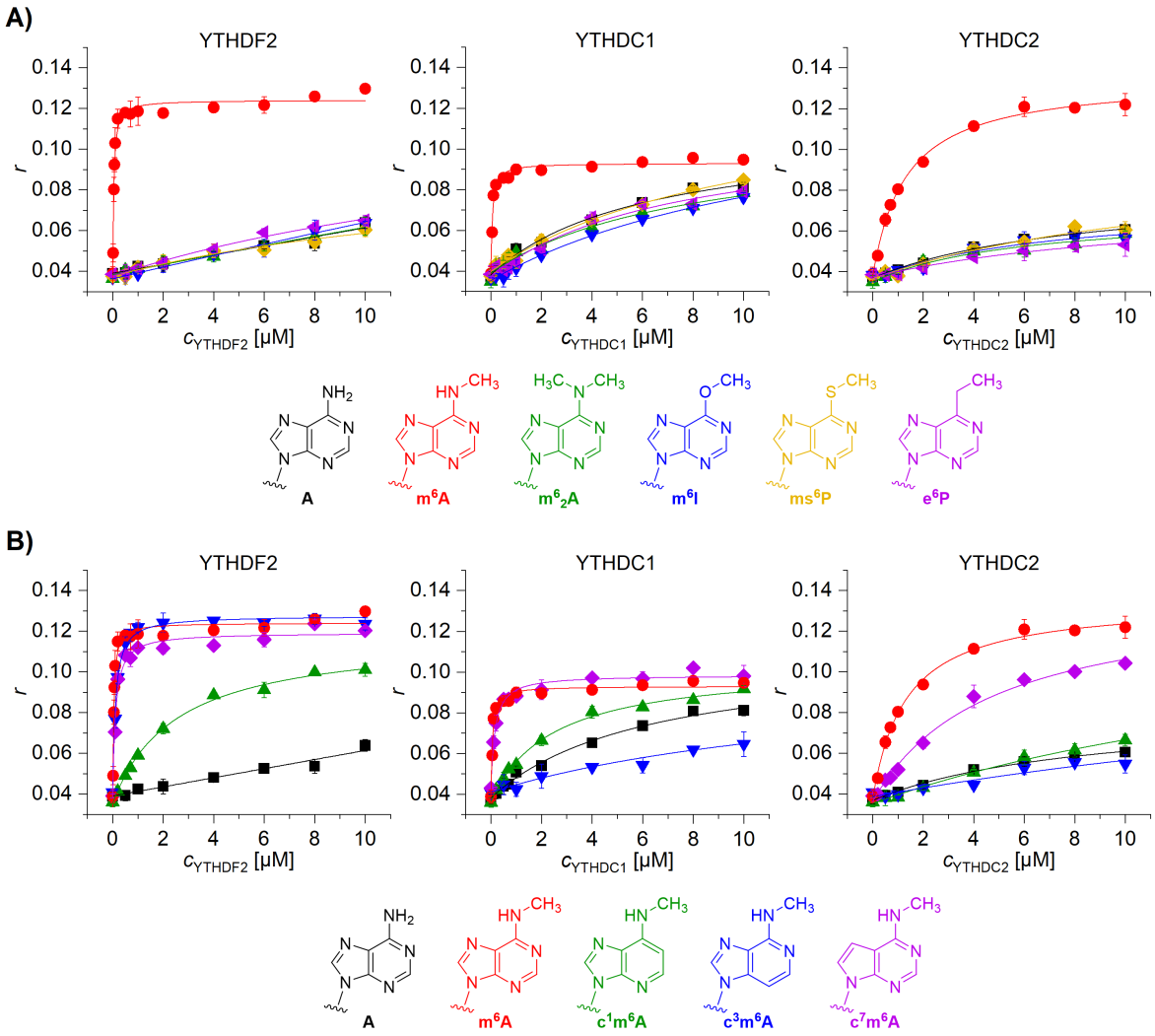

Figure 3.9: Binding isotherms of the m^{6}A reader poteins YTHDF2, YTHDC1 and YTHDC2 in complex with RNA oligonucleotides (FAM–AACCGGXCUGUC) containing different m^{6}A atomic mutants, as determined by fluorescence anisotropy measurements. Binding isotherms were obtained by titration of RNA (20 nM) with increasing concentrations of protein. All data points were collected as triplicates and are presented as mean ± s.e.m.

Table 3.6: Dissociation constants of the m^{6}A reader proteins YTHDF2, YTHDC1 and YTHDC2 in complex with fluorescently labeled RNA oligonucleotides (FAM–AACCGGXCUGUC), as determined by fluorescence anisotropy measurements. K_d values are given as mean ± s.e.m. of triplicates. In case of negligible binding at 10 µM protein, K_d values were not determined (n. d.).

No.	Modification X	K_d [µM]		
		YTHDF2	YTHDC1	YTHDC2
R1-FAM	A	n. d.	6.2 ± 1.5	n. d.
R2-FAM	m^{6}A	0.035 ± 0.007	0.05 ± 0.01	1.3 ± 0.2
R3-FAM	c^{1}m^{6}A	2.5 ± 0.3	2.4 ± 0.3	n. d.
R4-FAM	c^{3}m^{6}A	0.10 ± 0.02	n. d.	n. d.
R5-FAM	c^{7}m^{6}A	0.10 ± 0.02	0.15 ± 0.03	4.6 ± 1.0
R6-FAM	m$^6{}_2$A	n. d.	8.0 ± 3.6	n. d.
R7-FAM	m^{6}I	n. d.	13.4 ± 3.0	n. d.
R8-FAM	ms^{6}P	n. d.	10.6 ± 3.4	n. d.
R9-FAM	e^{6}P	n. d.	7.5 ± 3.2	n. d.

Among the three reader proteins, YTHDF2 displayed the strongest binding affinity toward its m^{6}A substrate. With an aromatic m^{6}A binding cage comprising three tryptophan residues, the YTHDF2 binding pocket provides stabilizing π-stacking interactions on both sides of the purine heterocycle (Figure 3.10A). In YTHDC1 and YTHDC2 (Figure 3.10B+C), however, one Trp is substituted by leucine, which allows more flexibility of the m^{6}A nucleoside inside the binding pocket and hence reduces the stability of the RNA-protein complex. For YTHDC2, this results in a more than 35-fold increased K_d value. For YTHDC1, in contrast, the presence of an additional binding pocket accommodating the G-1 nucleoside is able to rescue the complex stability; ultimately, only a 1.5-fold increased K_d value compared to YTHDF2 was observed. This trend in dissociation constants matches previous results obtained by Kretschmer (YTHDF2: K_d = 0.019 µM, YTHDC1: K_d = 0.043 µM, YTHDC2: K_d = 3.2 µM for a 9-mer RNA substrate with GGXCU core motif).[189] However, note that Xu *et al.* reported YTHDC1 as the strongest m^{6}A binder based on ITC studies (4-fold lower K_d than YTHDF2 for a 9-mer RNA substrate, 6-fold lower K_d than YTHDF2 for a 16-mer RNA substrate with GGXCU core motif); this is in disagreement with the data obtained from fluorescence anisotropy experiments in the course of this thesis.[102] Either of the three proteins strongly selects against unmodified RRACH motifs. Yet, while the unmethylated sequence is not recognized by YTHDF2 and YTHDC2, YTHDC1 still retains (albeit reduced) binding affinity due to its additional G-1 binding pocket.

All three YTH domain proteins share a dependence of substrate binding on the presence of a hydrogen bond interaction between the exocyclic methylamino substituent and a backbone

carbonyl oxygen inside the binding site of the protein. As a consequence, any atomic mutagenesis disrupting this interaction by either steric ($m^6{}_2A$, introduction of a second methyl group) or electronic means (m^6I, ms^6P, e^6P, introduction of a hydrogen bond acceptor or a non-polarized substituent) reduced substrate affinity to the level of an unmethylated RRACH motif.

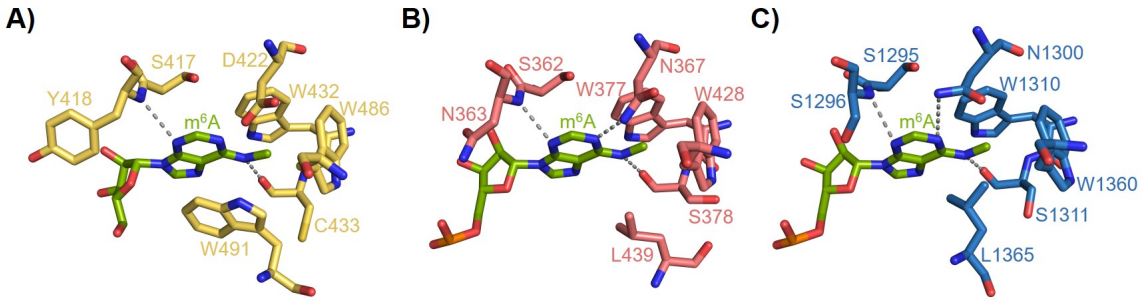

Figure 3.10: Recognition of m^6A by the binding pockets of YTH domain proteins. A) Crystal structure of m^6A (green sticks) inside the binding pocket of YTHDF2 (yellow sticks); PDB ID 4RDN. B) Crystal structure of m^6A inside the binding pocket of YTHDC1 (salmon sticks); PDB ID 4R3I. C) Structure of m^6A (green sticks) inside the binding pocket of YTHDC2 (blue sticks). The structure was generated by superimposition of a YTHDC1-m^6A co-crystal structure (PDB ID 4R3I) with a YTHDC2 crystal structure (PDB ID 6LR2), YTHDC1 was removed for clarity. Possible hydrogen bond interactions between m^6A and the protein binding sites are indicated as grey dashed lines.

While the presence of N^6 is crucial, the N7 ring nitrogen does not engage in any hydrogen bonds with the protein binding site and is therefore expensable: for all three YTH proteins, binding affinity to a c^7m^6A-modified RNA substrate is only reduced by a factor of 3–4. The slight destabilization of the complex may be caused by the electronic influence of the 7-deaza mutation, which might engage less efficiently in π-stacking with the adjacent tryptophane residues.

A much more drastic impact on the RNA–protein complex stability was observed upon introduction of a c^1m^6A nucleoside in the RNA substrate. A 50–60-fold increase in K_d values for YTHDF2 and YTHDC1 and complete disruption of YTHDC2 binding highlight the importance of the purine N1 atom for substrate recognition. In the binding sites of YTHDC1 and YTHDC2 the N1 atom engages in hydrogen bonds with an asparagine residue (Asn367 or Asn1300, respectively), whereas the putative interaction partner is an aspartate residue (Asp422). As a consequence, either Asp422 is protonated even at physiological pH due to a local acidic environment inside the binding pocket or the interaction between the nucleobase N1 and Asp422 is mediated by a bridging water molecule. For future studies this finding suggests the D422N mutant of YTHDF2 as an interesting engineered m^6A reader

with potentially increased substrate binding affinity due to an improved hydrogen bonding interaction with the nucleobase N1.

Incorporation of a c^3m^6A nucleoside into the DRACH motif of the RNA substrate was well tolerated by YTHDF2. Analogous to the 7-deaza modification, binding affinity was only reduced by a factor of three compared to the native m^6A substrate. In stark contrast, YTHDC1 and YTHDC2 displayed no binding affinity toward c^3m^6A-modified RNA. This was especially unanticipated for YTHDC1, which, due to its additional G-1 binding site, was even able to recognize an unmethylated DGACH motif. Thus, the presence of the 3-deaza-modified nucleoside apperas to exert an influence which distorts either the structure of the protein binding site or impacts the structure of the RNA substrate itself, thereby preventing RNA-protein complex formation. A possible, however yet unconfirmed, explanation is the tendency of c^3m^6A to exist (partially) in its cationic, N1-protonated form at physiological pH due to an elevated pK_a value compared to m^6A (see also Section 3.4.3). In this case, the protonation at N1 would disrupt the hydrogen bond between N1 and Asn367 or Asn1300 in YTHDC1 or YTHDC2, respectively. In the binding site of YTHDF2, however, an interaction of the protonated nucleobase with the hydrogen bond acceptor Asp422 could still be realized. While this explanation apperas reasonable based on the published complex crystal structures, further experimental evidence is required to support or reject it. Fluorescence anisotropy measurements at a higher pH would ensure presence of the neutral form of c^3m^6A and may shed light on the impact of the nucleobase protonation state on the protein binding affinity.

3.4 Influence of m^6A atomic mutagenesis on demethylase activity

In contrast to YTH-domain family m^6A reader proteins, which possess highly m^6A-specific binding pockets, the human eraser enzymes FTO and ALKBH5 have been shown to act on a variety of structurally different substrate nucleosides, although the observed activites greatly varied.[38,39,125,126,128,131] To gain further insight into the structural requirements of the substrate for efficient enzymatic recognition and demethylation, the effects of m^6A atomic mutagenesis on FTO- and ALKBH5-mediated demethylation were systematically investigated.

3.4.1 Enzyme expression and purification

The demethylase samples used in this study were prepared by Nicole Kleiber in the group of Prof. Dr. Markus Bohnsack, University Medical Center Göttingen. In brief, *C*-terminally His_6-tagged FTO and *N*-terminally His_{10}-tagged truncated ALKBH5 (residues 66-292) were recombinantly expressed in *E. coli* Rosetta 3 (DE2) cells. FTO-His_6 and His_{10}-ALKBH5$^{66\text{-}292}$ (in the following called FTO and ALKBH5) were purified by affinity chromatography using a nitrilotriacetic acid (NTA)-modified sepharose resin loaded with Ni^{2+}. Alternative constructs were expressed as His_{14}-MBP-FTO and His_{14}-MBP-ALKBH5 fusion proteins. Here, the additional presence of a maltose-binding protein (MBP) purification tag provides binding affinity of the protein construct to amylose resins, from which it can be eluted with maltose. This allowed a dual purification strategy by two subsequent affinity chromatography steps (Ni-NTA and amylose).

3.4.2 Method development and optimization

While (de-)methylation processes altering the charge state of the oligonucleotide (such as A↔m^1A) can directly be monitored by PAGE or ion-exchange HPLC, these options are not available for the uncharged m^6A.[190] Furthermore, the sole addition or removal of a single methyl group is not sufficient to affect the elution an oligonucloetide in RP-HPLC experiments. Thus, an HPLC-MS-based assay was developed to investigate the influence of m^6A atomic mutagenesis on the demethylase activity of FTO and ALKBH5. First, the substrate oligonucleotide was incubated with the demethylase in presence of the cofactors Fe(II) (supplied as $(NH_4)_2Fe(SO_4)_2{\cdot}6H_2O$) and α-ketoglutaric acid (α-KG). The antioxidant ascorbic acid was used as additive to stabilize the catalytically active (+II) oxidation state of the iron cation. The resulting mixture of methylated, oxidized and demethylated species was digested into mononucleosides using a combination of phosphodiesterase and alkaline phosphatase. The composition of the digested sample was analyzed by HPLC-MS. Here, electrospray ionization mass spectrometry (ESI-MS) in positive ion mode enabled identification of the eluted nucleoside species based on their respective mass spectra or extracted ion chromatograms (EICs), while the peak areas of the UV chromatogram were used for quantification.

Initial scouting experiments were performed to optimize the conditions of demethylation, digestion and HPLC-MS analysis. Incubation of **R2** (20 µM) with either FTO or His_{14}-MBP-FTO (4 µM) under the same conditions resulted in significantly different demethylation efficiencies (Figure 3.11).

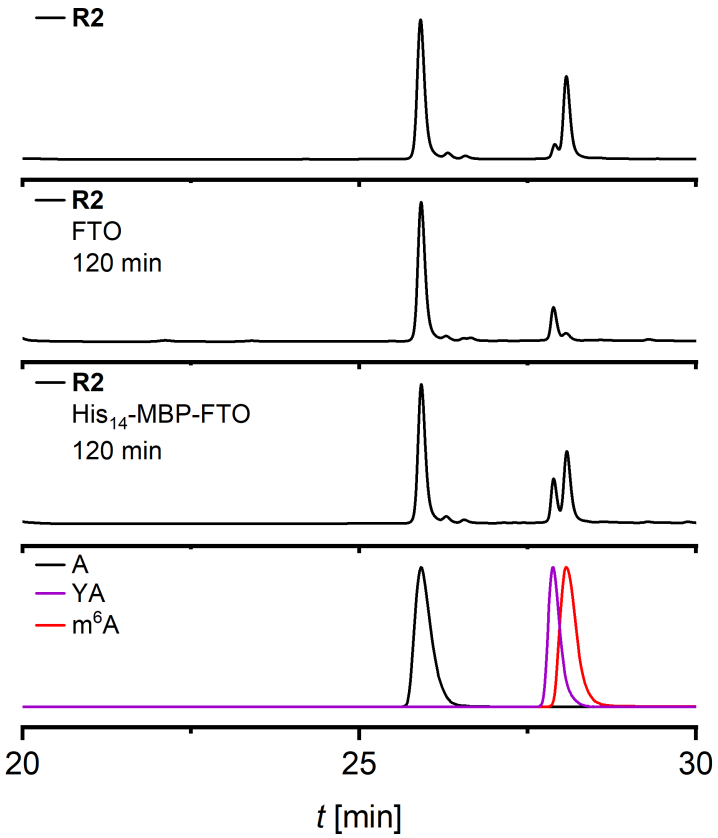

Figure 3.11: HPLC-MS analyses of digested **R2** oligonucleotide samples. The UV (260 nm) chromatograms of **R2** and **R2** treated with FTO or His_{14}-MBP-FTO are shown stacked on top of the nucleoside $[M+H]^+$ extracted ion chromatograms of the His_{14}-MBP-FTO sample. Only the excerpt of the chromatograms including A and its derivatives is shown. Besides A and m^{6}A, residual 5'-hexynyl-labeled adenosine (YA) was observed, because the phosphodiester linkage between nucleoside and hexynyl moiety was not quantitatively digested. Demethylation conditions: 20 µM **R2** (total: 400 pmol), 4 µM enzyme, 100 µM $(NH_4)_2Fe(SO_4)_2$, 100 µM α-KG, 4 mM ascorbic acid, 5 mM $MgCl_2$, 50 mM HEPES pH = 7.0, 22 °C, 2 h. Digestion conditions: 2.6 µM RNA, 2.5 U/mL SVPD, 424 U/mL BAP, 10 µM TRIS pH = 7.5, 37 °C, 24 h. RP-HPLC conditions: Phenomenex Synergi Fusion, 2 × 250 mm, flow rate 0.2 mL/min, at 25 °C; solvent A: 10 mM NH_4OAc in H_2O; solvent B: MeCN; Gradient: 0–5% solvent B in 0–15 min, 5–72.5% solvent B in 15–45 min.

After 2 h incubation at 22 °C, the FTO-treated sample contained only 16% of residual m^{6}A, while in the His_{14}-MBP-FTO sample 59% of the oligonucleotides remained methylated. A similarly reduced activity was observed for His_{14}-MBP-ALKBH5 compared to ALKBH5. These results demonstrate a detrimental effect of the MBP tag on the activity of the fused demethylase. A corresponding observation has been previously described for m^{6}dA demethylation in ssDNA by human ALKBH1.[191] To study the weak inherent m^{6}dA demethylase activity of the native m^{1}A demethylase ALKBH1, the enzyme was expressed as an MBP-tagged fusion protein in human HEK293 cells. The low observed m^{6}A demethy-

lation activity increased 3-fold upon enzymatic cleavage of the MBP tag. Simultaneously, MBP cleavage also increased the abasic site (AP) lyase activity of ALKBH1. Altogether, the results indicate that the presence of MBP purification tags not only impairs oxidative demethylation but generally decreases the enzymatic activity of the respective fusion protein. Thus, all further experiments focused solely on the FTO and ALKBH5 constructs bearing only His-tags.

Buffer conditions for the demethylation reactions were chosen to match physiological ion concentrations (K^+, Mg^{2+}) and neutral pH. RNA substrates were used in 5-fold excess over demethylase to ensure multiple-turnover conditions. The enzymes were supplemented with an excess of Fe^{2+} and α-KG as cofactors as well as ascorbic acid as antioxidant (Table 3.7). Since ALKBH5-mediated demethylation was found to proceed rapidly, enzymatic reactions were performed at 25 °C rather than at physiological temperature (37 °C) to delay the time until complete demethylation.

Table 3.7: Sample composition of FTO- and ALKBH5-mediated demethylation reactions. Reactions were performed in a final volume of 10 µL at 25 °C.

Component	Concentration
RNA	20 µM
FTO / ALKBH5	4 µM
HEPES pH 7.0	50 mM
$(NH_4)_2Fe(SO_4)_2$	300 µM
α-KG	300 µM
ascorbic acid	4 mM
KCl	100 mM
$MgCl_2$	2 mM

Digestion of RNA samples into mononucleosides was achieved by snake venom phosphodiesterase (SVPD) and bacterial alkaline phosphatase (BAP), as shown in Figure 3.11. A major drawback of this exonuclease/phosphatase combination was the slow digestion speed; overnight incubation was necessary to quantitatively yield mononucleoside mixtures. For studying reaction profiles of FTO and ALKBH5, detection of oxidized nucleo-side intermediates was however crucial. As these intermediates have half-lives of ca. 3 h, they would decompose during long incubation times in aqueous solution.[136] Using nuclease P1 and recombinant shrimp alkaline phosphatase (rSAP) instead of SVPD and BAP, complete digestion was achieved in only 20 min at 37 °C, which allowed for detection of unstable oxidized species.

After inactivation by snap-freezing in liquid nitrogen, residual enzymes were removed by extraction with $CHCl_3$ and the samples were analyzed by HPLC-MS. The best HPLC resolution was achieved on the polar-embedded C18 matrix of a Phenomenex Synergi Fusion column, while an eluent system consisting of 10 mM aq. NH_4OAc, pH = 5.3 (solvent A) and MeCN (solvent B) provided the optimal trade-off between pH stability and ESI ionization efficiency/signal intensity.

3.4.3 Influence of the nucleobase heterocycle

3.4.3.1 HPLC-MS-based investigations

Employing the optimized HPLC-MS-based assay outlined above, a first set of experiments focused on the influence of the nucleobase heterocycle structure on the demethylation activities of FTO and ALKBH5. The oligonucleotides **R2**–**R5**, containing m^6A or its deaza-analogs c^1m^6A, c^3m^6A or c^7m^6A, respectively, were incubated with FTO or ALKBH5 in presence of the native cofactors Fe(II) and α-KG at 37 °C for incubations times of 5 min, 30 min and 2 h. Following digestion into nucleosides, the samples were analyzed by HPLC-MS to elucidate their respective nucleoside compositions. The results are summarized in Figure 3.12.

Treatment of oligonucleotide **R2** with FTO resulted in conversion of m^6A into the oxidized intermediate hm^6A and unmethylated A, with 37.6% of residual methylated species remaining after 2 h. Hydrolytic decomposition of hm^6A was rather slow under the given conditions, which led to a notable accumulation of the oxidized intermediate over time (57.9% after 2 h). Despite the steadily increasing concentration of hm^6A no formation of f^6A was observed, which demonstrates that a second oxidation step *via* hm^6A re-binding is indeed only a minor enzymatic pathway. Additionally, f^6A formation was reported to benefit from high FTO concentrations; this is not given under the reaction conditions used in this study.[136] Introduction of a 7-deaza-mutation at the substrate m^6A site (**R5**) markedly impaired FTO-mediated demethylation. After an incubation time of 2 h, 69.9% of the initial c^7m^6A were still methylated. This corresponds to an almost two-fold reduced conversion after 2 h compared with native m^6A. The resulting product species, in contrast, were not affected by the 7-deaza-modification: besides formation of unmethylated c^7A (9.8% after 2 h), an increase of the oxidized intermediate c^7hm^6A (20.3%) was observed, while no second oxidation yielding formylated product was detectable. In comparison with native hm^6A, its 7-deaza mutant appeared to be more susceptible to hydrolysis, as less c^7hm^6A accumulation and a steeper increase of the c^7A concentration were observed (**R2**: hm^6A:A =

13:1 after 2 h; **R5**: c^7hm^6A:c^7A = 2:1 after 2 h). In stark contrast to modifications at N^6 and N7, FTO displayed no tolerance for atomic mutagenesis of N1 and N3, rendering the enzyme essentially inactive on c^1m^6A (**R3**) and c^3m^6A (**R4**).

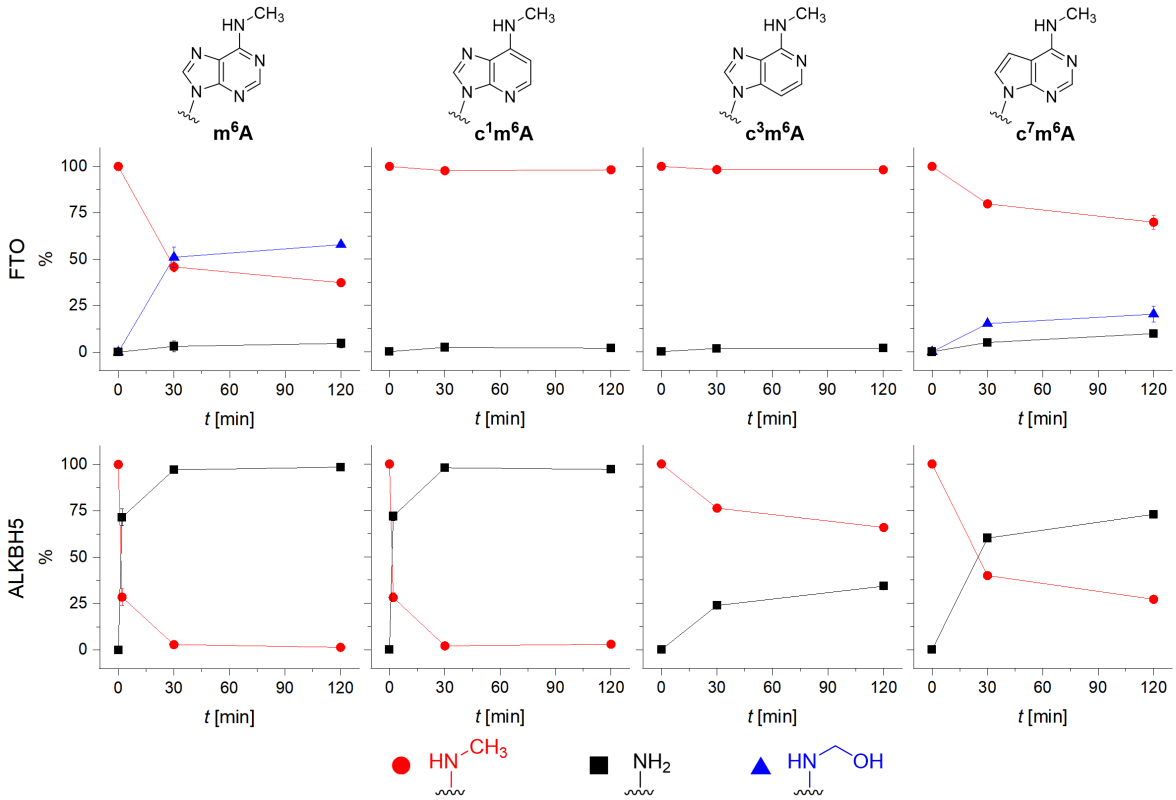

Figure 3.12: Product distributions obtained from oxidative demethylation of m^6A and its 1-, 3- and 7-deaza analogs in ssRNA (**R2**–**R5**) by FTO (top row) or ALKBH5 (bottom row). Product species were identified and quantified by HPLC-MS-based analyses. All data points were collected as duplicates and are represented as mean ± s.e.m.

ALKBH5-mediated demethylation of **R2**–**R5** (Figure 3.12, bottom row) yielded remarkably different results. In agreement with previously reported results, m^6A was directly converted to adenosine without appearance of oxidized intermediate species.[139] Compared to FTO, ALKBH5 displayed a notably higher activity: already after 2 min, 71% of initial m^6A was demethylated and nearly quantitative conversion was achieved within 30 min of incubation. Besides a higher catalytic activity, ALKBH5 also displayed markedly higher tolerance toward atomic mutagenesis of the endocyclic nucleobase nitrogens than FTO. The most striking difference to FTO was observed for c^1m^6A, which was almost as efficiently demethylated as the native m^6A modification. ALKBH5 accepted c^3m^6A and c^7m^6A substrates as well; for both modifications, the demethylated fractions after 2 h (34% and 73%, respectively) exceeded those obtained from FTO-mediated demethylation. Altogether, FTO and ALKBH5

display very distinct structural requirements for efficient substrate demethylation. ALKBH5 tolerates absence of all three purine ring nitrogens, although 3-deaza and 7-deaza mutations reduce enzymatic activity. FTO-mediated demethylation, in contrast, is dependent on the presence of both N1 and N3, while presence of N7 is not strictly required, but highly beneficial.

Introduction of mutations in either the substrate or the active site/binding pocket of the enzyme can result in two different effects on the enzymatic activity. On one hand, the structural changes may influence enzymatic substrate recognition by altering stabilizing substrate–protein interactions. If the catalytic mechanism is unaffected, reduced or increased substrate binding affinity directly translates to increased or decreased enzyme activity. On the other hand, the introduced mutation may directly affect the catalysis itself, e. g. by reducing or increasing reaction barriers or by stabilization of transition states or intermediates.

Most commonly, differentiation between effects on substrate binding affinity *vs.* catalytic activity is achieved by Michaelis-Menten kinetics.[192] The Michaelis-Menten model describes the kinetics of enzymatic reactions between an enzyme E and a substrate S, which form a complex ES that catalyzes conversion of the substrate and releases the enzyme and the product P:

$$\mathrm{E{+}S} \rightleftarrows \mathrm{ES} \rightarrow \mathrm{E{+}P} \tag{3.3}$$

Assuming quasi-steady state conditions (large excess of substrate over enzyme; therefore, the substrate concentration [S] remains effectively constant during the reaction), the model derives the reaction velocity v (the change of the product concentration [P] over time t) as

$$v = \frac{\mathrm{d[P]}}{\mathrm{d}t} = \frac{V_{\mathrm{max}} \cdot [\mathrm{S}]}{K_{\mathrm{M}} + [\mathrm{S}]} \tag{3.4}$$

with

$$V_{\mathrm{max}} = [\mathrm{E}]_0 \cdot k_{\mathrm{cat}} \tag{3.5}$$

Here, V_{max} is the maximal reaction velocity, $[\mathrm{E}]_0$ represents the initial enzyme concentration, the Michaelis-Menten constant K_{M} is the inverse of the substrate binding affinity, and the catalytic rate constant k_{cat} describes the reaction speed of the catalytic conversion. A Michaelis-Menten analysis requires several kinetic measurements of the catalytic reaction. Plotting the product concentration against the reaction time for a fixed enzyme concentration and assuming a linear initial reaction phase, the reaction velocity v is obtained as the slope of a linear curve fit (Figure 3.13A). After collecting values of v at different substrate

concentrations, the resulting Michaelis-Menten plot (Figure 3.13B) allows for determination of both K_M and k_{cat}.

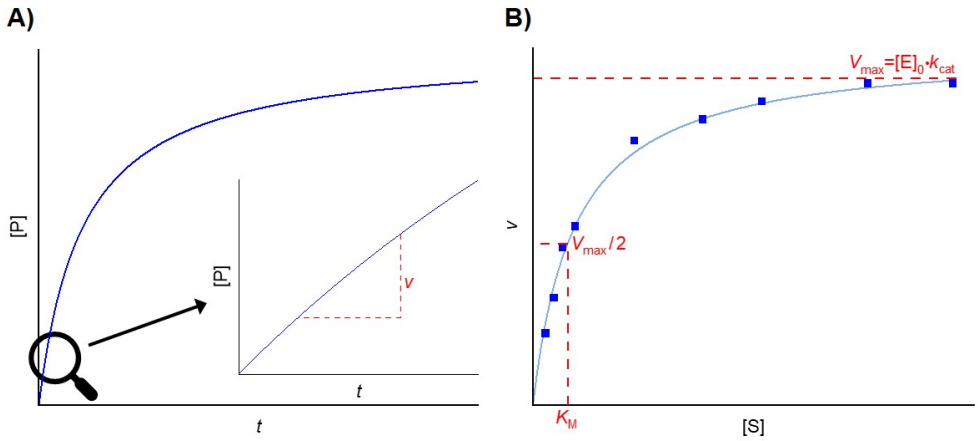

Figure 3.13: Schematic overview of Michaelis-Menten kinetics. A) The time-dependent formation of product at a fixed enzyme concentration is recorded. Assuming a linear initial phase, the slope of the linear fit yields the reaction velocity v (inset). B) Determination of v at different substrate concentrations (blue dots) and fitting the data points (blue line) allows the determination of K_M and k_{cat} according to Equations (3.4) and (3.5).

Since kinetic measurements at typically 6–8 different substrate concentrations are required to yield convenient fit qualities, the Michaelis-Menten method is both substrate- and enzyme-consuming. Due to limited available supplies of FTO and ALKBH5, a competitive binding assay was employed instead to differentiate between effects on binding affinity or catalytic activity. When only one substrate is available for an enzyme, a simple catalytic pathway, as shown in Equation (3.3), results. Addition of a competing substrate S_2 to the system, however, provides an additional possibility for enzymatic binding and activity.

$$P_2{+}E \leftarrow ES_2 \overset{S_2}{\rightleftarrows} E \overset{S}{\rightleftarrows} ES \rightarrow E{+}P \tag{3.6}$$

As part of the enzyme concentration is involved in the complex ES_2, less enzyme is available for binding and conversion of the substrate S. Higher affinity of the enzyme toward the competitor molecule therefore leads to more strongly reduced conversion of the primary substrate. Conversely, addition of a competitor that does not interact with the enzyme does not affect the demethylation rate of the primary substrate. This concept was used to indirectly assess the binding affinities of FTO and ALKBH5 for the three deaza-m^{6}A variants. First, the m^{6}A (**R2**) demethylation efficiencies of FTO and ALKBH5 were measured by HPLC-MS as described above. For comparison, the same demethylase concentrations and reaction times were used to demethylate **R2** in presence of an equimolar concentration of competitor oligonucleotide **R3**–**R5** or the unmethylated **R1** as a reference. The results

are summarized in Figure 3.14.

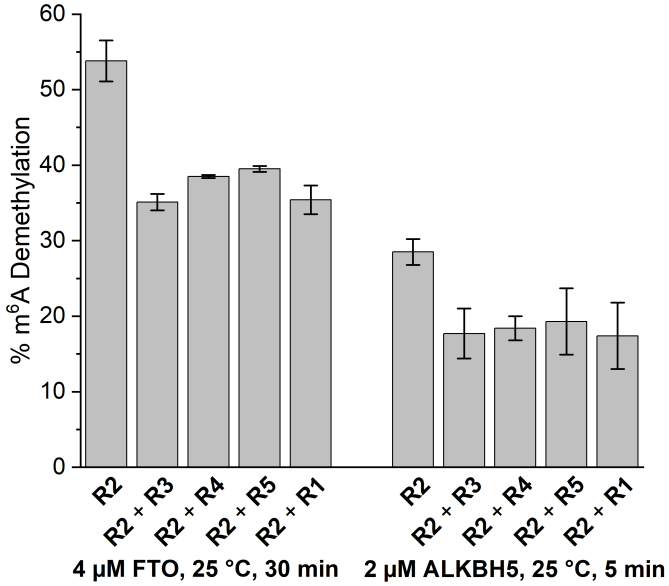

Figure 3.14: Competitive demethylation of m^{6}A in oligonucleotide **R2** by FTO or ALKBH5. **R2** (20 µM) was incubated with FTO (4 µM, 25 °C, 30 min) or ALKBH5 (2 µM, 25 °C, 5 min) in demethylation buffer (300 µM $(NH_4)_2Fe(SO_4)_2$, 300 µM α-KG, 4 mM ascorbic acid, 2 mM $MgCl_2$, 100 mM KCl, 50 mM HEPES pH = 7.0) alone or in presence of a competitor oligonucleotide (**R1**, **R3**–**R5**, 20 µM). The samples were digested into mononucleosides by nuclease P1 and rSAP, and the fraction of demethylated m^{6}A was quantified by HPLC-MS analyses (for details see Experimental Section). All data points were collected as duplicates and are represented as mean $\pm$ s.e.m.

m^{6}A demethylation of **R2** by either demethylase enzyme was inhibited in presence of competitor oligonucleotide in comparison to the reference sample containing only **R2**. The concentration of **R2** was kept constant throughout all samples, which rules out a role of dilution effects; therefore, the reduced m^{6}A demethylation can unequivocally be attributed to interactions between demethylase and competitor oligonucleotide. The extent of enzyme inhibition was independent of the m^{6}A atomic mutant incorporated in the competitor RNA: **R3**–**R5** and surprisingly also the completely unmethylated **R1** reduced m^{6}A demethylation to similar levels, which translates to similar binding affinities of the demethylases toward all four substrates. This, in turn, implies that FTO and ALKBH5 binding is not dependent on the methylation or modification state of their substrate RNA, which presents a major difference to YTH domain m^{6}A reader proteins. Instead of highly specific binding to their methylated substrate RNA, FTO and ALKBH5 rather appear to recognize their substrate RNAs by their sequence contexts or structural features. Given that m^{6}A sites in mRNA are rarely 100% methylated, this novel insight raises the question how demethylases find the methylated members of their target sequences *in vivo*.

Furthermore, the results of the competitive demethylation assay corroborate that the partially detrimental effects of deaza-nucleobase structures on N^6 demethylation (Figure 3.12) do not originate from differences in substrate binding. Consequently, the endocyclic nitrogens appear to influence the demethylation activity itself. Here, they may either engage in electrostatic interactions with the binding pocket, which help with an ideal alignment of the methyl group with the active site metal ion for oxidation, or emit an inherent electronic influence that facilitates oxidation. To address this question, the results from enzymatic demethylation were compared to photocatalytic oxidative demethylation of the m^6A mutants: if the different efficiencies of FTO- and ALKBH5-mediated demethylation resulted from inherent reactivity differences of the m^6A mutants, a comparable order of reactivities should be observed regardless of the catalyst (enzyme *vs.* photocatalyst).

3.4.3.2 Photocatalytic demethylation

Xie *et al.* have identified flavine mononucleotide (FMN) as a photosensitizer capable of catalyzing oxidative demethylation of m^6A upon irradiation with blue light.[170,171] Similar to FTO- or ALKBH5-mediated demethylation, the reaction proceeds *via* a radical mechanism, which leads to formation of hm^6A and/or f^6A (Scheme 3.19).[171] These intermediates then decompose in aqueous environment.

Samples of m^6A nucleoside (**2**) or its deaza-mutants (**13**, **15**, **17**) were treated with FMN under an O_2 atmosphere and irradiated with blue LED light (λ_{max} = 465 nm) for 2 h, before they were analyzed using HPLC-MS (Figure 3.15). The UV chromatograms of these analyses showed product distributions distinct from those which were obtained from enzymatically demethylated samples. While enzymatic generation of N^6-formylated nucleosides is only a very minor pathway due to necessary rebinding of the hydroxymethyl species, FMN-mediated demethylation more readily involves a second oxidation step. Whereas m^6A still yielded mainly hm^6A as oxidized intermediate (Figure 3.15A), c^1m^6A and c^3m^6A efficiently underwent further oxidation to the formyl-intermediates (Figure 3.15B–C). FMN-catalyzed demethylation did not only yield different product distributions, but also the relative reactivity order of the nucleoside substrates did not match the results from either FTO- or ALKBH5-mediated demethylation. After 2 h of irradiation, ca. 68% of c^1m^6A was either oxidized or already fully demethylated. m^6A (ca. 31% conversion) and c^3m^6A (ca. 20%) showed a much lower reactivity, while c^7m^6A was almost unresponsive to the reaction conditions utilized (ca. 8% conversion after 2 h).

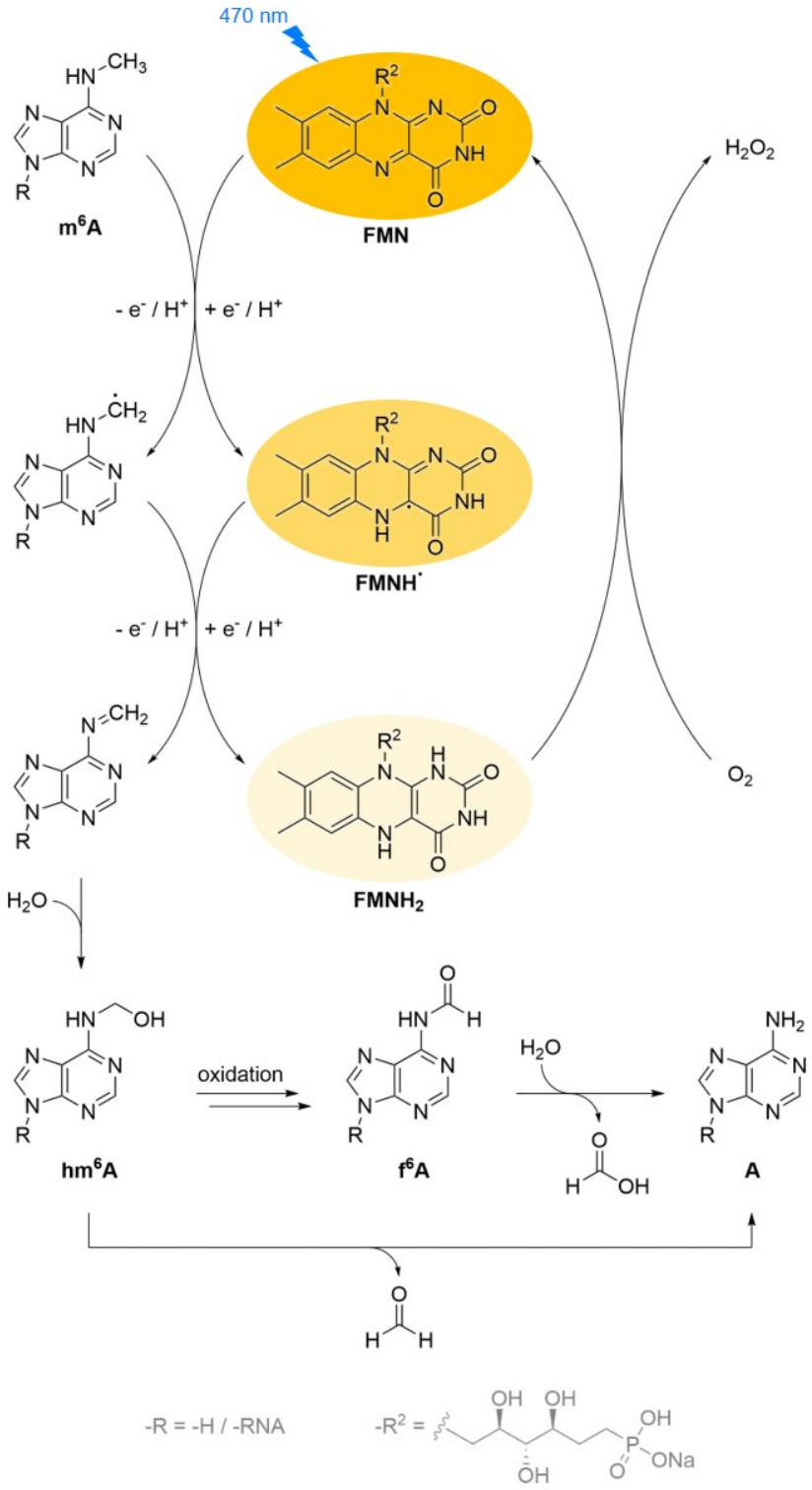

Scheme 3.19: Mechanism of photocatalytic m^{6}A demethylation under blue light irradiation using FMN as photosensitizer.[171]

Samples of m^{6}A nucleoside (**2**) or its deaza-mutants (**13**, **15**, **17**) were treated with FMN under an O_2 atmosphere and irradiated with blue LED light (λ_{max} = 465 nm) for 2 h,

before they were analyzed using HPLC-MS (Figure 3.15). The UV chromatograms of these analyses showed product distributions distinct from those which were obtained from enzymatically demethylated samples. While enzymatic generation of N^6-formylated nucleosides is only a very minor pathway due to necessary rebinding of the hydroxymethyl species, FMN-mediated demethylation more readily involves a second oxidation step. Whereas m^6A still yielded mainly hm^6A as oxidized intermediate (Figure 3.15A), c^1m^6A and c^3m^6A efficiently underwent further oxidation to the formyl-intermediates (Figure 3.15B–C). FMN-catalyzed demethylation did not only yield different product distributions, but also the relative reactivity order of the nucleoside substrates did not match the results from either FTO- or ALKBH5-mediated demethylation. After 2 h of irradiation, ca. 68% of c^1m^6A was either oxidized or already fully demethylated. m^6A (ca. 31% conversion) and c^3m^6A (ca. 20%) showed a much lower reactivity, while c^7m^6A was almost unresponsive to the reaction conditions utilized (ca. 8% conversion after 2 h).

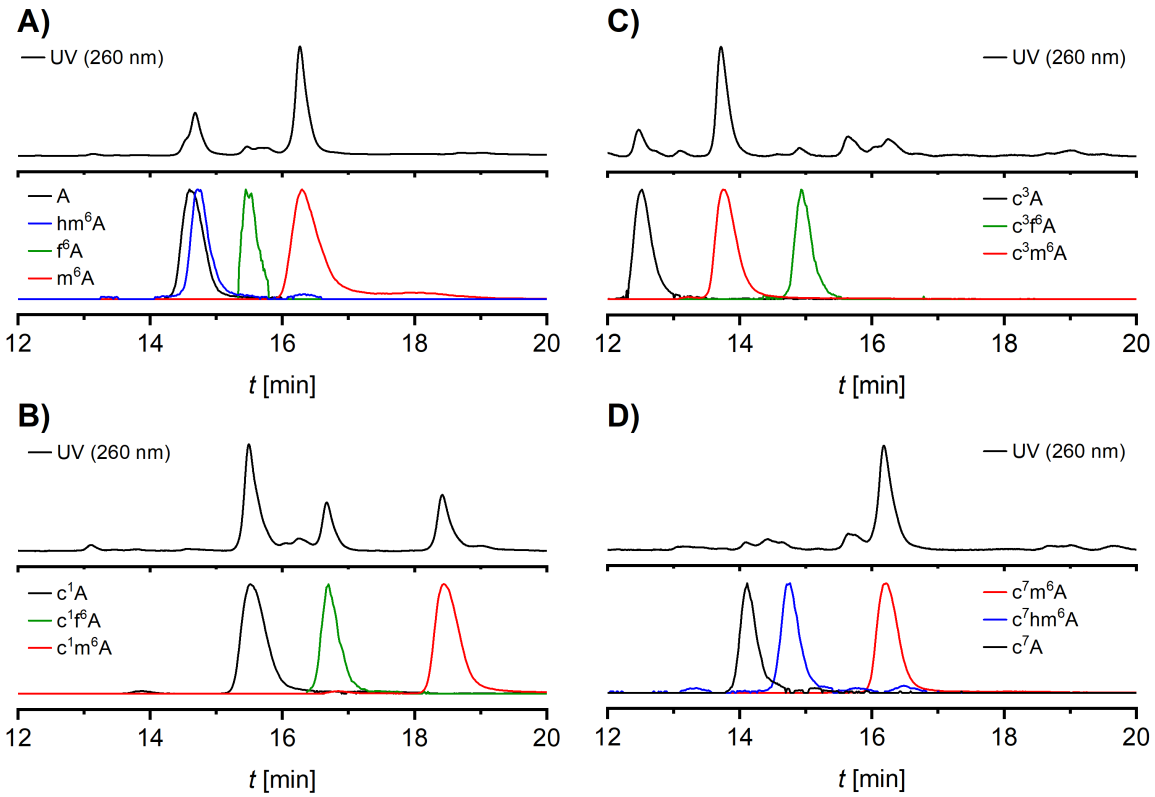

Figure 3.15: HPLC-MS analyses of photocatalytic demethylation reactions. The UV (260 nm) chromatograms are shown stacked on top of the nucleoside $[M+H]^+$ extracted ion chromatograms. A) Photocatalytic demethylation of m^6A. B) Photocatalytic demethylation of c^1m^6A. C) Photocatalytic demethylation of c^3m^6A. D) Photocatalytic demethylation of c^7m^6A. Reaction conditions: 200 µM nucleoside, 100 µM FMN, 100 mM NaH_2PO_4/Na_2HPO_4 pH 7.0, 1 atm O_2, blue LED light (λ_{max} = 465 nm), 25 °C, 2 h. Single experiments were performed and need to be replicated to improve the quality of product quantification.

These results suggest a notable influence of the endocyclic nitrogen substitution pattern of the purine heterocycle on the C-H bond strength of the exocyclic N^6-methyl group: while removal of N1 appears to facilitate homolytic C-H bond cleavage, the 7-deaza modification renders the exocyclic methyl group less susceptible toward radical oxidation. The trend in reactivity of the m^{6}A mutant nucleosides deduced from this experiment, however, do not agree with the results obtained from enzymatic demethylation reactions. The great discrepancy between FTO/ALKBH-mediated and photocatalytic demethylation indicates that inherent reactivity differences of the m^{6}A mutants are most likely not the central reason for their different demethylation efficiencies by FTO and ALKBH5. Instead, it appeared reasonable that the introduced deaza-mutations disrupt the network of stabilizing interactions between substrate nucleoside and enzymatic binding pocket and thus interfere with correct alignment of the N^6-methyl group for oxidation. To further investigate this hypothesis, DFT-based geometry optimizations of the enzymatic active sites accomodating the different m^{6}A atomic mutants were performed.

3.4.3.3 DFT-based structural investigations

In the FTO binding site, N1 of the nucleobase is located in proximity (3 Å) of Arg96, which is protonated under physiological conditions, and may therefore engage in hydrogen-bonding interactions (Figure 3.16A).[73] Simultaneously, the exocyclic methylamino group of the nucleobase can serve as a hydrogen bond donor for Glu234. If m^{6}A adopted a similar binding mode inside the ALKBH5 binding pocket, analogous interactions with the protonated Lys132 and with Glu153 would be possible (Figure 3.16B). However, the crystal structure of an ssRNA-ALKBH5 complex clearly shows a reversed RNA binding direction compared to FTO, which also results in an inverted facial orientation of the m^{6}A nucleobase in the binding pocket (Figure 3.16C).[141] In this substrate orientation, no polar amino acid residue is present in proximity to N1 to engage in electrostatic or hydrogen bonding interactions. Instead, the inverted substrate orientation enables interaction of N7 with a protonated Lys132. An interaction between Tyr139 and the methylamino group is possible, though questionable: while the distance between the N^6-H of m^{6}A and the Tyr139 side chain oxygen would allow for hydrogen bonding, the almost parallel alignment of the two residues argues against an interaction.

Based on the crystal structure (PDB ID 5ZMD) shown in Figure 3.16, the key residues for FTO-mediated m^{6}A oxidation were identified and used to construct a minimized catalytic core structure (Figure 3.17A).

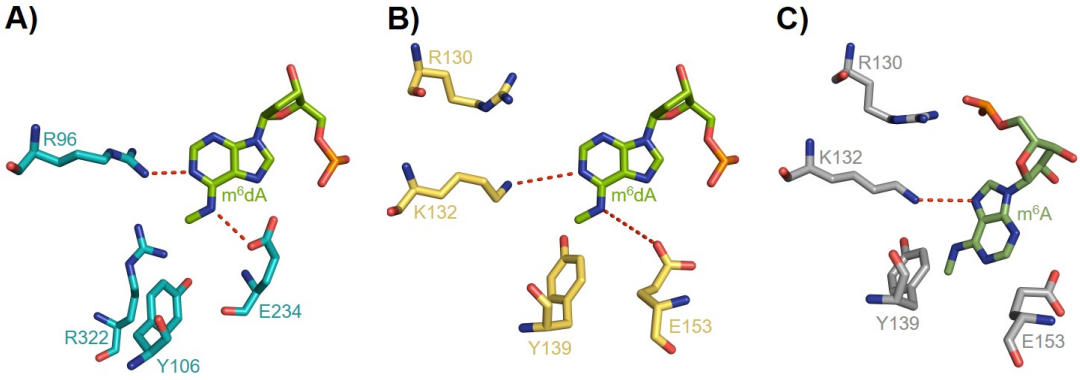

Figure 3.16: Possible interactions (red dashed lines) of the m^6(d)A nucleoside with the surrounding polar amino acid side chains of the FTO or ALKBH5 binding pockets. A) The crystal structure of an ssDNA-FTO complex (PDB ID 5ZMD) suggests hydrogen bonds involving N1 and the exocyclic methylamino group.[73] B) Similar interactions would be possible for an m^6A-ALKBH5 complex in the same binding mode. This structure was generated by modeling of m^6dA into the ALKBH5 active site: an m^6dA-FTO co-crystal structure (PDB ID 5ZMD) was superimposed with an ALKBH5 crystal structure (PDB ID 4NRP), FTO was removed for improved clarity. This binding mode of m^6A is not adopted *in vivo* or *in vitro*.[141] C) The m^6A-ALKBH5 co-crystal structure (PDB ID 7WKV) shows an inverted facial orientation of the nucleobase, which results in different possible interactions with the active site.[141]

The construct contained the metal ion as well as its four ligands (His231, Asp233, His307, NOG), the nucleoside and its two putative interaction partners (Arg96, Glu234). Based on this structure, an initial model of the catalytically active state was modeled for further geometry optimization. The catalytically inactive Mn(II) was substituted for the active Fe(IV)-oxo moiety, while the inactive cofactor surrogate *N*-oxalylglycine (NOG) was substituted for succinate (SUC). A water molecule, which was not present in the m^6A-bound crystal structure (PDB ID 5ZMD) but in a crystal structure without RNA ligand (PDB ID 4IDZ), was added as an additional ligand of the active site metal to restore octahedral coordination geometry.[140] Afterwards, all moieties were truncated adjacent to their functionally relevant domains to yield a minimal catalytically active FTO structure (Figure 3.17B). This structure was subjected to DFT-based geometry optimization on the UB3LYP level of theory, using a combination of the LANL2DZ basis set for iron and the 6-31G(d) basis set for all other atoms, collectively labeled as B1.[140] All optimizations focused on the catalytically active quintet spin state of Fe(IV).[140]

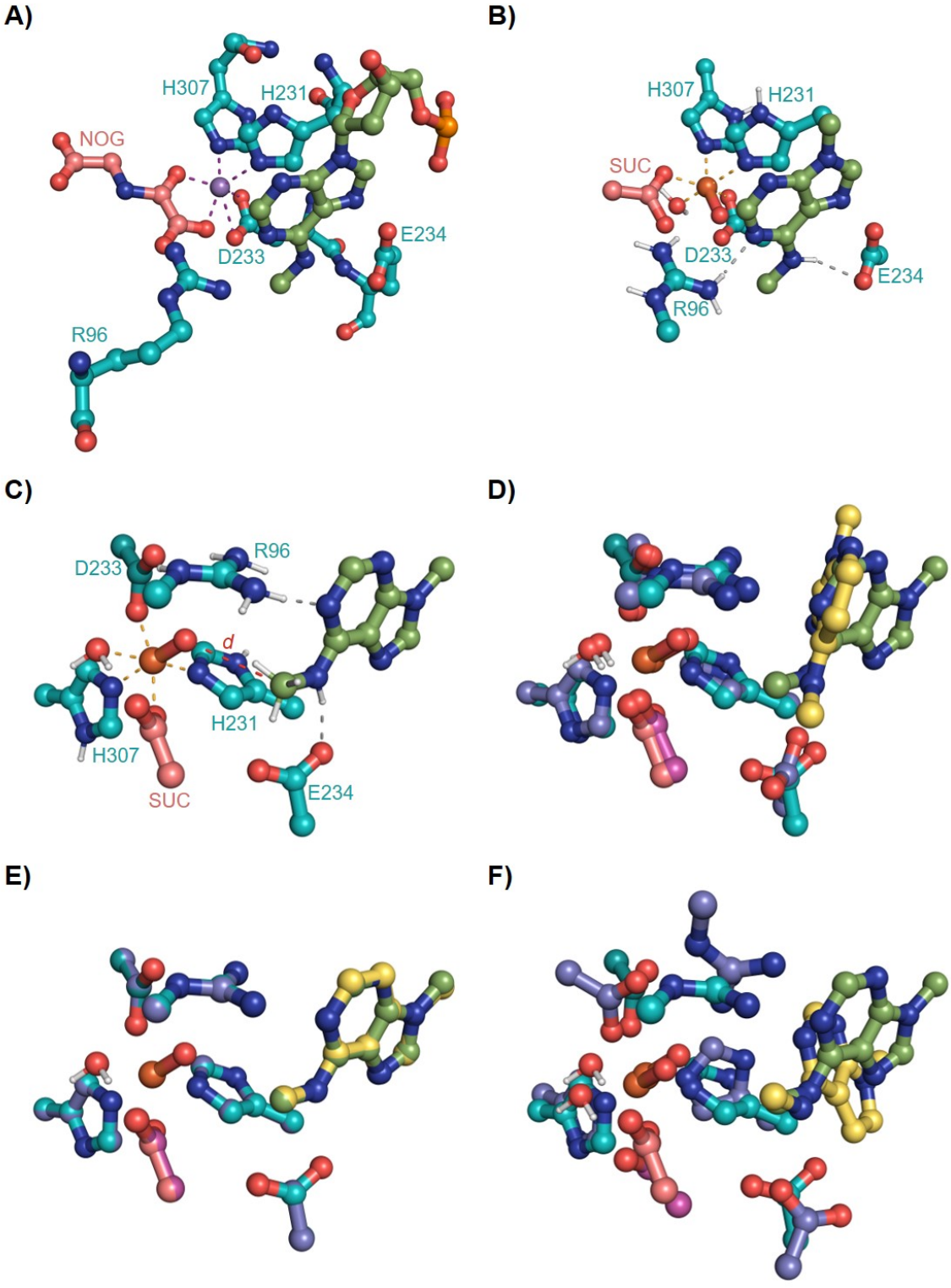

Figure 3.17: Geometry optimizations of m^{6}A atomic mutants inside the FTO active site. A) FTO catalytic core structure containing the active site metal (Mn^{2+}, purple sphere), its ligands, the nucleoside and its putative interaction partners. Extracted from PDB ID 5ZMD. B) Minimized catalytically active FTO/m^{6}A model containing the decarboxylated cofactor succinate (SUC) and the catalytically active Fe(IV)-oxo species. A water molecule completing the coordination sphere

was adopted from PDB ID 4IDZ. All residues were truncated adjacent to their functional moieties to reduce computational cost. C) Geometry-optimized (UB3LYP/B1) catalytically active FTO/m^{6}A construct. The distance d between N^6-CH_3 and FeO is marked in red. D) Superimposition of the geometry-optimized structures of FTO/m^{6}A and FTO/c^{1}m^{6}A (blue/yellow/pink sticks). E) Superimposition of the geometry-optimized structures of FTO/m^{6}A and FTO/c^{3}m^{6}A (blue/yellow/pink sticks). F) Superimposition of the geometry-optimized structures of FTO/m^{6}A and FTO/c^{7}m^{6}A (blue/yellow/pink sticks).

The optimized geometry of the active site (Figure 3.17C) shows the m^{6}A nucleobase engaged in stabilizing hydrogen bonds with Arg96 and Glu234, as already deduced from the crystal structure. The N^6-methyl group points toward the catalytic Fe(IV)-oxo moiety, with a C–O distance d = 3.5 Å. Analogous geometry optimizations with c^{1}m^{6}A, c^{3}m^{6}A and c^{7}m^{6}A (Figure 3.17C–E) revealed an important role of N1 and N7 in correct positioning of the nucleobase inside the active center. While absence of N3 has no structural impact (d = 3.6 Å), the 7-deaza nucleobasecauses minor distortion of the active site structure, leading to a slightly increased C–O distance (d = 3.8 Å). Introduction of the 1-deaza nucleobase has an even greater influence on the nucleobase positioning: while the protein scaffold is mostly undisturbed, the c^{1}m^{6}A nucleobase is tilted by 46° with respect to m^{6}A. The N^6-methyl group faces away from the catalytic Fe(IV)-oxo moiety (d = 5.1 Å), which significantly interferes with the oxidation process.

In analogy to the procedure described above, geometry optimization of the ALKBH5 catalytic center in complex with each of the four (deaza-)m^{6}A nucleosides was performed. Starting from the reported cystal structure (PDB ID 7WKV), a minimal catalytic core structure was identified (Figure 3.18A). This construct comprised the active site metal and its ligands as well as the m^{6}A nucleoside and Lys132, which may serve as a hydrogen bond donor for the nucleobase N7. Furthermore, Tyr139 was included in the minimal catalytic core structure, as it has been shown to be highly beneficial for catalytic activity.[139] Substitution of the catalytically inactive Mn^2+ for an Fe(IV)-oxo moiety and α-ketoglutarate for succinate followed by truncation of the residues led to a minimized catalytically active construct (Figure 3.18B). Geometry optimization on the UB3LYP/B1 level of theory finally resulted in the structure shown in Figure 3.18C. Here, N7 of the nucleobase is engaged in a hydrogen bond with the protonated Lys132, while Tyr139 does not form any interactions with the substrate. While, unlike in the FTO active site, the N^6-methyl group is not facing directly toward the Fe(IV)-oxo center, the C–O distance is comparable to the FTO/m^{6}A complex (d = 3.4 Å).

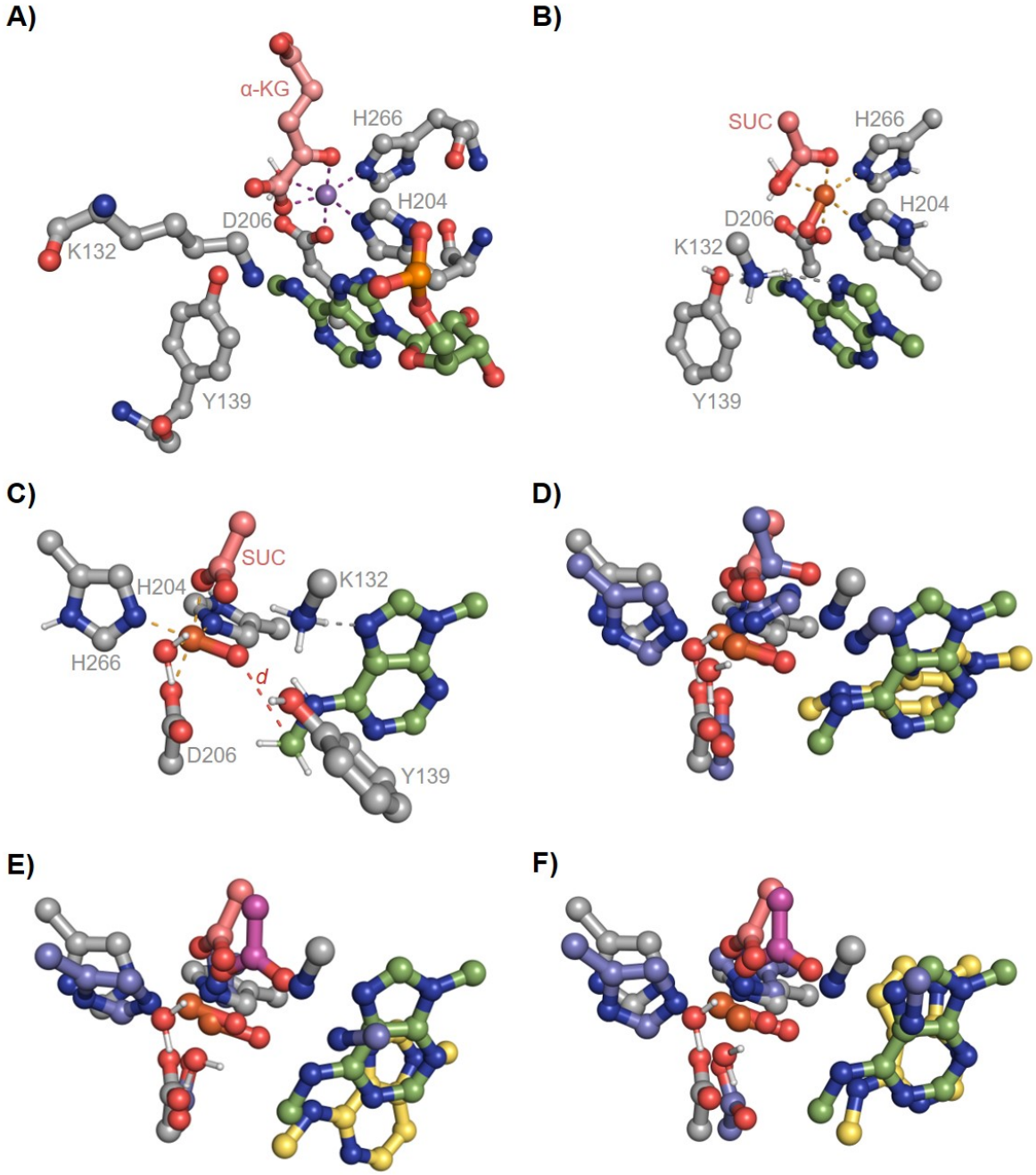

Figure 3.18: Geometry optimizations of m^{6}A atomic mutants inside the ALKBH5 active site. A) ALKBH5 catalytic core structure containing the active site metal (Mn^{2+}, purple sphere), its ligands, the nucleoside and its putative interaction partners. Extracted from PDB ID 7WKV. B) Minimized catalytically active ALKBH5/m^{6}A model containing the decarboxylated cofactor succinate (SUC) and the catalytically active Fe(IV)-oxo species. All residues were truncated adjacent to their functional moieties to reduce computational cost. C) Geometry-optimized (UB3LYP/B1) catalytically active ALKBH5/m^{6}A construct. The distance *d* between N^6-CH_3 and FeO is marked in red. D) Superimposition of the geometry-optimized structures of ALKBH5/m^{6}A and ALKBH5/c^{1}m^{6}A (blue/yellow/pink sticks). E) Superimposition of the geometry-optimized structures of ALKBH5/m^{6}A and ALKBH5/c^{3}m^{6}A (blue/yellow/pink sticks). F) Superimposition

of the geometry-optimized structures of ALKBH5/m^{6}A and ALKBH5/c^{7}m^{6}A (blue/yellow/pink sticks). In panels D–F, Tyr139 was removed for improved clarity.

While the overall distortions of the active site structure upon introduction of 1-deaza-, 3-deaza- or 7-deaza-mutations are larger than for FTO, the C–O distance between Fe(IV)-oxo moiety and N^6-methyl group is not subject to significant changes (d = 3.7 Å/3.7 Å/3.9 Å). Notably, especially the structures containing m^{6}A and c^{1}m^{6}A show a high similarity, which agrees with the experimentally observed similar demethylation efficiencies.

Combined with the results from the photocatalytic demethylation experiments (Figure 3.15), the geometry optimized structures help explain the trends in demethylation efficiencies of m^{6}A, c^{1}m^{6}A and c^{7}m^{6}A observed experimentally. Inside the FTO active site, the 1-deaza nucleobase is tilted by 46° relative to m^{6}A, which results in the N^6-methyl group facing away from the catalytic Fe(IV)-oxo moiety; thus, c^{1}m^{6}A is not correctly oriented for oxidation by FTO. In contrast, the ALKBH5 complexes of m^{6}A and its 1-deaza mutant are structurally highly similar and therefore display comparable demethylation efficiencies.

The c^{7}m^{6}A nucleoside causes distortions of the active site structures when bound by either FTO or ALKBH5; yet, positioning of the nucleobase and alignment of the exocyclic methylamino substituent are not significantly altered. However, the 7-deaza modification appears to induce an inherently lower susceptibility toward oxidative demethylation. As a consequence, c^{7}m^{6}A is demethylated by either enzyme, but displays lower demethylation efficiencies than m^{6}A.

The studies described so far failed to explain the behaviour of c^{3}m^{6}A in FTO- and ALKBH5-mediated demethylation reactions. Although m^{6}A and c^{3}m^{6}A displayed similar demethylation efficiencies upon photocatalytic demethylation (Section 3.4.3.2) and DFT-based studies predict similar accomodation of the nucleobases in the active sites (Figure 3.17, Figure 3.18), c^{3}m^{6}A was found to be a significantly worse substrate regarding enzymatic demethylation by both FTO and ALKBH5 (Section 3.4.3.1). An explanation can be found in different protonation states of the m^{6}A analogs. The unmethylated 3-deazaadenosine (c^{3}A) is known to display an increased pK_a value for protonation at N1 (6.80) compared to A (3.62), c^{7}A (5.25) and c^{1}A (4.70, protonation at N3).[193] In agreement with the difference of about three pK_a units between A and c^{3}A, the pK_a value of c^{3}m^{6}A was determined as 7.14 (Figure 3.19A), which is about three pK_a units higher than for m^{6}A (4.01).[194] Accordingly, c^{3}m^{6}A was found to be protonated under the conditions used for enzymatic demethylation (Figure 3.19B).

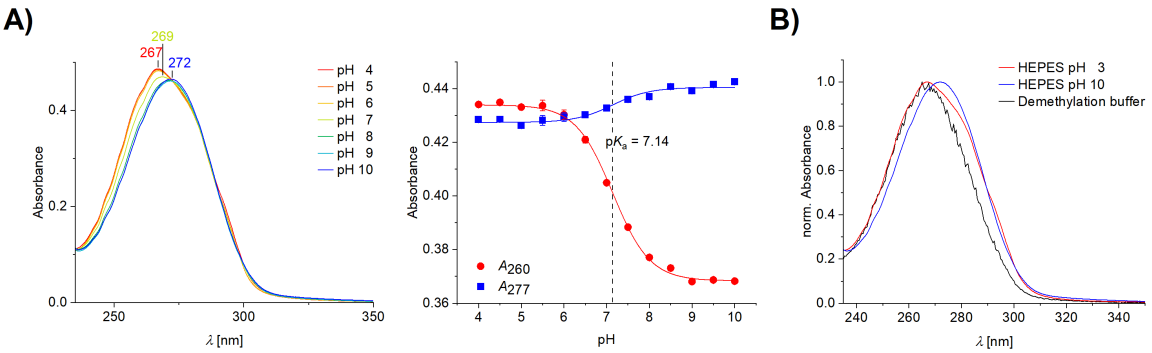

Figure 3.19: Determination of pK_a and protonation state of c^{3}m^{6}A. A) Left: UV/Vis absorption spectra of c^{3}m^{6}A at different pH values. Sample conditions: 50 µM c^{3}m^{6}A in 30 mM Britton-Robinson buffer of respective pH. For improved clarity, only every second spectrum is shown. All spectra were measured as triplicates and averaged for pK_a determination. Right: Plot of absorbance vs. pH value for two wavelengths for pK_a determination according to the Henderson-Hasselbalch equation. A pK_a value of 7.14±0.02 was obtained, corresponding to the inflection point of the fit curves. B) Superimposed normalized UV/Vis absorption spectra of c^{3}m^{6}A in Britton-Robinson buffer at pH = 3 and pH = 10 (cationic and neutral form of c^{3}m^{6}A, respectively) and in Fe(II)/α-ketoglutarate-containing demethylation buffer. The spectrum of c^{3}m^{6}A under demethylation conditions (in absence of demethylase) corresponds to the protonated, cationic form of the nucleoside.

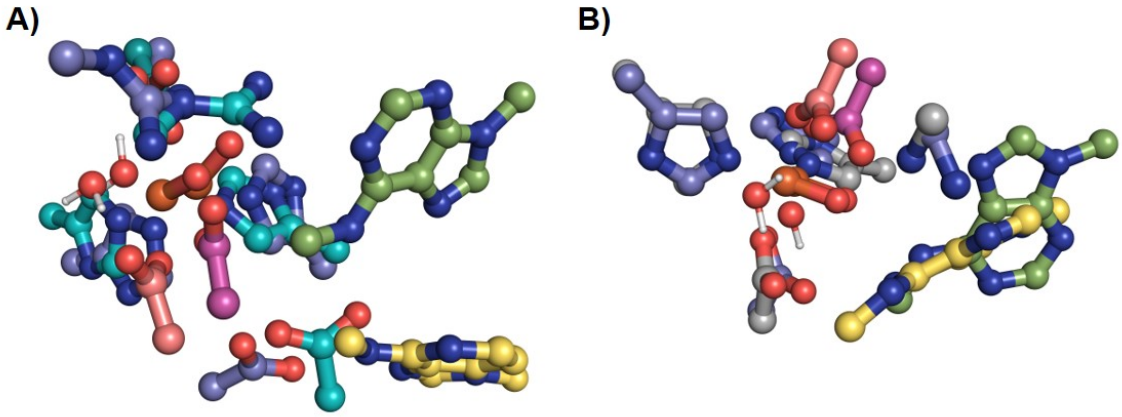

Figure 3.20: Geometry-optimized (UB3LYP/B1) structures of the cationic c^{3}m^{6}AH$^+$ inside the active sites of FTO and ALKBH5. A) Superimposition of the geometry-optimized structures of FTO/m^{6}A (green/cyan/salmon sticks) and FTO/c^{3}m^{6}AH$^+$ (yellow/blue/magenta sticks). B) Superimposition of the geometry-optimized structures of ALKBH5/m^{6}A (green/grey/salmon sticks) and ALKBH5/c^{3}m^{6}AH$^+$ (yellow/blue/magenta sticks). Tyr139 was removed for improved clarity.

The altered protonation state at N1 of the nucleobase has a major impact on its positioning inside the active sites of FTO and ALKBH5 (Figure 3.20). The FTO active site is significantly distorted due to electronic repulsion of the N1-protonated nucleoside (c^{3}m^{6}AH$^+$)

and the cationic side chain of Arg96. As a consequence, the nucleoside is translocated to the edge of the binding pocket, which leads to an increased C–O distance d = 6.2 Å between N^6-methyl group and the Fe(IV)-oxo moiety and prevents the oxidation event. For ALKBH5, the decreased demethylation activity for $c^3m^6AH^+$ results from an increased C–O distance (d = 5.0 Å) due to a tilted orientation of the cationic nucleobase with respect to native m^6A.

3.4.3.4 ALKBH5 mechanism: Covalent intermediate or proton shuttle?

Although both FTO and ALKBH5 remove the N^6-methyl group of m^6A *via* an oxidative pathway, ALKBH5 does not furnish any detectable oxidized intermediate species. Instead, the oxidized methyl group is directly released as formaldehyde, yielding demethylated adenosine.[139] Previous publications have suggested two possible explanations for this observation. Toh *et al.* proposed the involvement of an intermediate covalent adduct of oxidized RNA and ALKBH5 (Scheme 3.20).

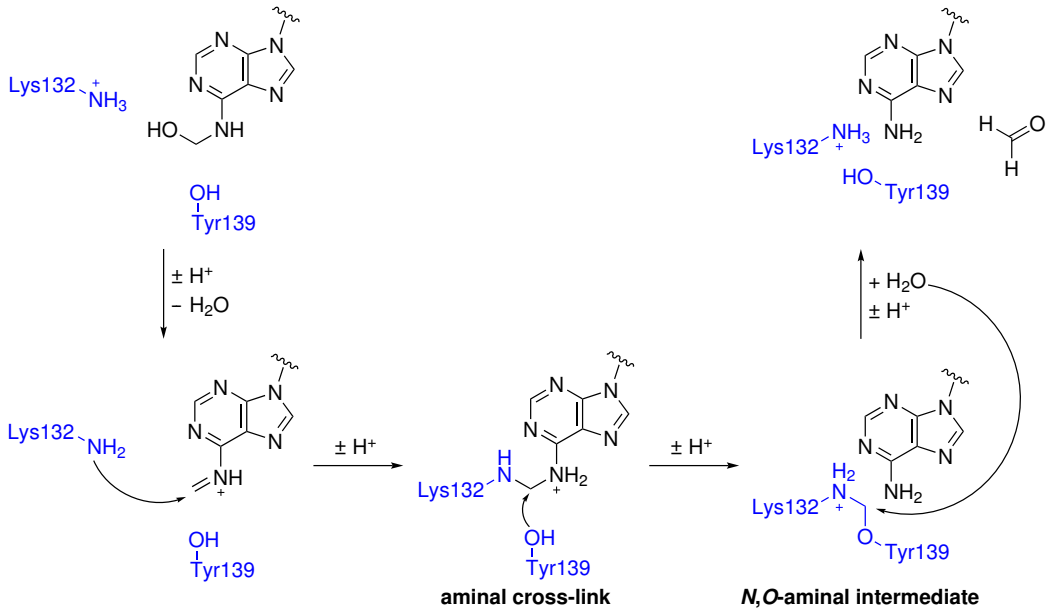

Scheme 3.20: Mechanism of ALKBH5-mediated demethylation of m^6A, as proposed by Toh *et al.*[139] Following oxidation of the methyl group to the corresponding alcohol, a covalent intermediate is formed *via* a Schiff base intermediate. The methyl group is transferred onto the protein and subsequently realeased as formaldehyde upon aqueous hydrolysis. Notably, the order of the two subsequent nucleophilic attacks by Lys132 and Tyr139 is unknown; due to the higher nucleophilicity of lysine, however, the drawn mechanism appears reasonable.

The authors suggested that after oxidation of the bound m^6A to hm^6A the alcohol is protonated by the nearby Lys132. This protonation facilitates formation of an intermediate m^6A Schiff base, which is susceptible to nucleophilic attack by Lys132 to form a covalent adduct

of substrate RNA and enzyme. A subsequent nucleophilic attack by Tyr139 releases adenosine and transfers the methylene unit onto the active site. The resulting aminal structure is finally hydrolyzed, releasing the C_1 unit as formaldehyde. In agreement with this proposed mechanism, mutation of Lys132 to glutamine, which removes the acidic ammonium proton in proximity to the substrate methylamino group, changed the product profile of ALKBH5 to resemble FTO-mediated oxidation (notable accumulation of hm^{6}A).[139]

Toh *et al.* based their proposed mechanism on the assumption that ALKBH5 binds its substrate in a similar conformation as FTO (Figure 3.16B). In view of the (later elucidated) opposite binding direction of ALKBH5 (Figure 3.16C), however, Lys132 and Tyr139 are not ideally aligned with the N^6-methyl group for nucleophilic attack on a putative Schiff base intermediate. Therefore, Kaur *et al.* postulated a different mechanistic pathway considering the novel structural insights.[141] Instead of demethylation *via* a covalent intermediate, the authors proposed a proton shutteling mechanism of ALKBH5 (Scheme 3.21). Following m^{6}A oxidation, cyclic proton transfer between Lys132, Tyr139 and hm^{6}A would lead to a direct release of the methyl group as formaldehyde and generate unmethylated adenosine. Notably, the authors proposed the involvement of an uncharged Lys132 side chain in this mechanism; under physiological conditions, however, lysine ($pK_{a,\epsilon\text{-}NH_3}$ = 10.2) is usually present as a monocationic species.[195]

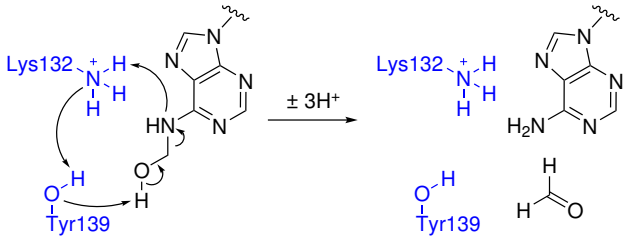

Scheme 3.21: Mechanism of ALKBH5-mediated m^{6}A demethylation *via* a cyclic proton shutteling mechanism, as proposed by Kaur *et al.*[141] In the publication the authors assumed an uncharged state of Lys132; under physiological conditions, however, lysine is present as a monocationic species (protonated ϵ-NH_2).[195]

In order to find experimental support for one or the other of the two proposed mechanisms, the interaction between RNA and ALKBH5 was investigated using an electrophoretic mobility shift essay (EMSA). This experiment, previously reported by Toh *et al.*, is based on stabilization of the putative covalent intermediate to enable visualization on a polyacrylamide gel.[139] As already outlined in Scheme 3.20, oxidation of m^{6}A by FTO yields hm^{6}A, which may further undergo conversion into a Schiff base. The covalent aminal intermediate formed by attack of Lys132 is rather unstable and readily releases adenosine upon nucleophilic attack by Tyr139. Using a pre-oxidized RNA substrate, it is however possible

to stabilize the covalent intermediate (Scheme 3.22). In a first step, the substrate RNA containing m^6A is oxidized by FTO. The resulting hm^6A species is subsequently incubated with ALKBH5, which oxidizes hm^6A to f^6A. Like the m^6A Schiff base intermediate, f^6A contains an electrophilic (carbonyl) carbon center, which is susceptible to nucleophilic attack by Lys132. The resulting amidine cross-link is more stable than the native aminal linkage shown in Scheme 3.20: nucleophilic attack of Tyr139 does not result in release of adenosine, but converts the cross-link into an aminal ester; the covalent linkage remains intact.

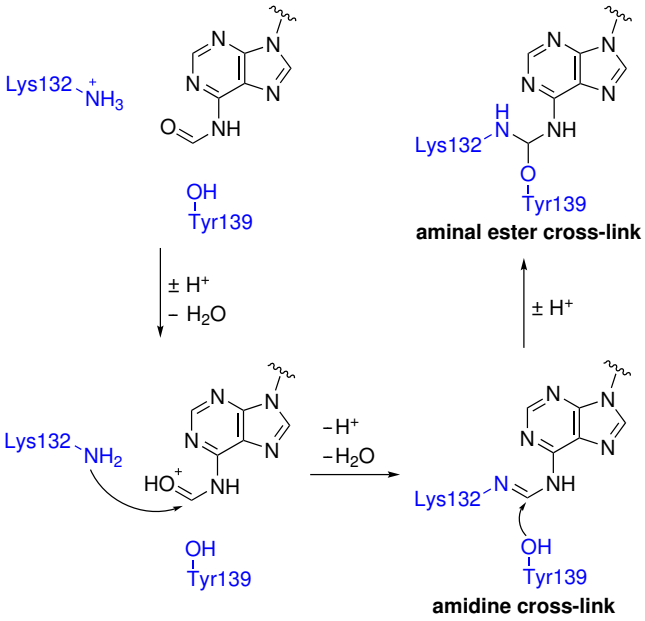

Scheme 3.22: Formation of a stabilized cross-link between RNA and ALKBH5, as proposed by Toh *et al.*[139] Following oxidation of hm^6A to f^6A by ALKBH5, nucleophilic attack of Lys132 yields a covalent amidine intermediate. Unlike an aminal linkage, this species does not release adenosine when nucleophilically attacked by Tyr139, but instead is converted into an aminal ester cross-link.

As Toh *et al.* were able to visualize the stabilized cross-linked species as a supershifted band appearing during gel electrophoresis, the experimental approach was adopted for the analysis of ALKBH5-mediated demethylation of deaza-m^6A analogs.[139] The fluorescently labeled oligonucleotides **R2-FAM** – **R5-FAM** were either directly incubated with ALKBH5 or pre-oxidized by FTO treatment. Incubation with ALKBH5 was done either in presence of the native ALKBH5 cofactors Fe^{2+} and α-KG or their inactive surrogates Mn^{2+} and NOG. Reference samples were generated by exposure of the oligonucleotides to analogous reaction conditions without addition of ALKBH5. The samples were analyzed by native PAGE, utilizing the fluorescent label for band detection (Figure 3.21).

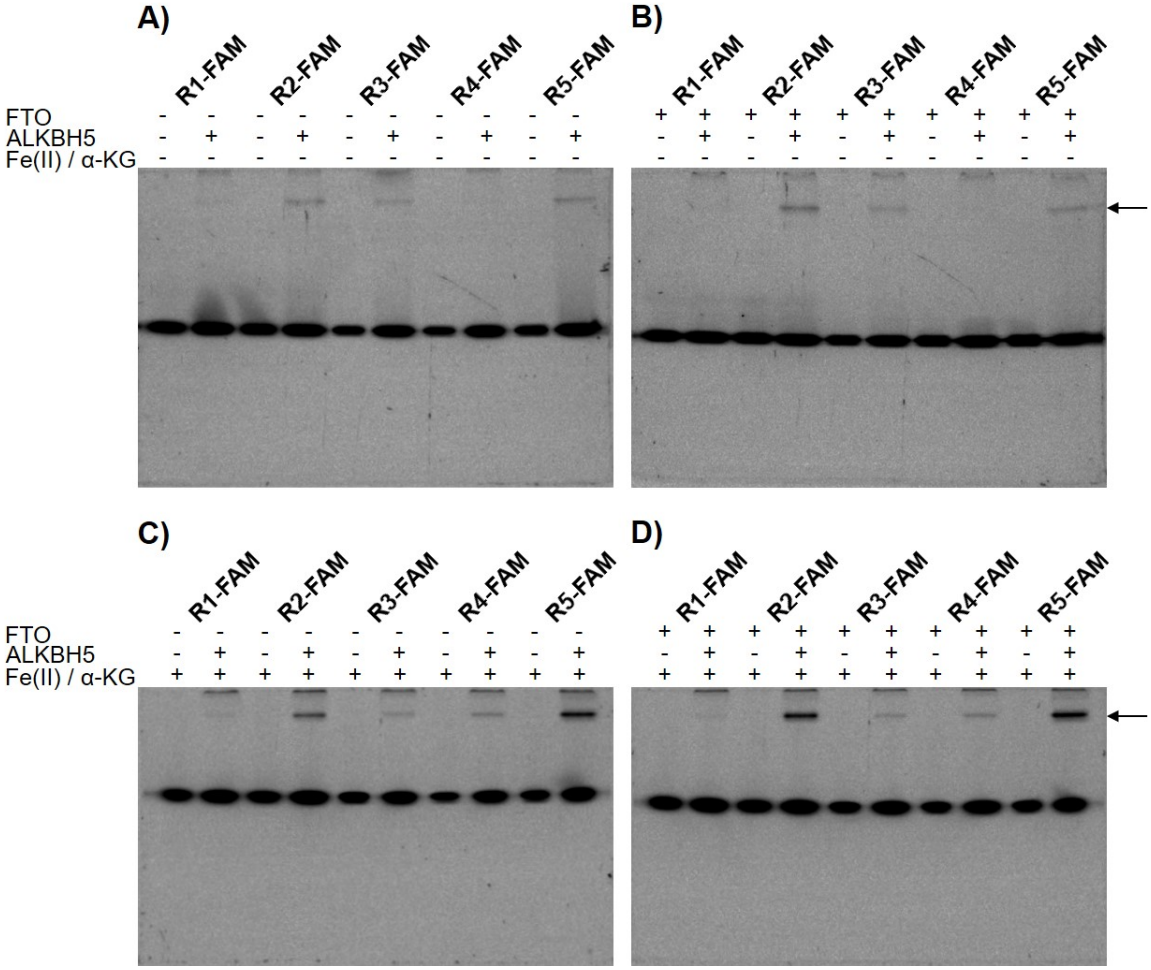

Figure 3.21: Electrophoretic mobility shift assays. A) **R1**–**R5** were incubated with ALKBH5 and its cofactors Fe^{2+} and α-KG. B) **R1**–**R5** were pre-oxidized by treatment with FTO and then incubated with ALKBH5 and its cofactors Fe^{2+} and α-KG. C) **R1**–**R5** were incubated with ALKBH5 and the inactive cofactor surrogates Mn^{2+} and NOG. D) **R1**–**R5** were pre-oxidized by treatment with FTO and then incubated with ALKBH5 and the inactive cofactor surrogates Mn^{2+} and NOG. As control samples, each reaction condition was replicated in absence of ALKBH5. The samples were analyzed by native PAGE; bands were detected based on their fluorescence upon blue light irradiation. Bands corresponding to RNA-ALKBH5 adducts are marked with arrows, the bottom band comprises free RNA.

Incubation of the oligonucleotides with ALKBH5 in presence of catalytically inactive cofactor surrogates (Figure 3.21A) only allowed for the formation of unstable non-covalent RNA-ALKBH5 adducts; thus, only faint supershifted adduct bands were visible on gel. Pre-oxidation with FTO resulted in a slightly more pronounced **R2-FAM** adduct band, whereas the other oligonucleotide samples appeared rather unaffacted (Figure 3.21B). Although pre-oxidized nucleosides should be able to form (aminal) cross-links with the active site of ALKBH5, this process seemed to be rather inefficient in absence of active cofactors. The same type of aminal cross-link was achieved by treatment of the oligonucleotides

with ALKBH5 in presence of active cofactors (Figure 3.21C). Since ALKBH5-mediated oxidation was more efficient than FTO-mediated oxidation, the adduct bands were more intense than in Figure 3.21B. In case of **R2-FAM** (m^6A) and **R5-FAM** (c^7m^6A), intensity of the adduct bands was even further increased by pre-oxidation with FTO, as now the more stable amidine and orthoaminal cross-links could be formed (Figure 3.21D). The adduct band intensities of **R1-FAM**, **R3-FAM** and **R4-FAM**, which are not oxidized by FTO, were however not affected. Overall, the appearance of intense RNA-ALKBH5 adduct bands is a strong argument for the formation of covalent intermediates during ALKBH5-mediated demethylation, while the possibility to stabilize these adducts by FTO pre-oxidation supports the catalytic mechanism proposed by Toh *et al.*[139] In addition, the similar behavior of m^6A- and c^7m^6A-containing oligonucleotides shows that chemical modifications of the nucleobase scaffold only affect demethylation efficiency but do not alter the catalytic mechanism.

3.4.4 Influence of the C6-substituent

Besides the effects of structural modifications to the m^6A heterocycle on demethylase activity and mechanism, as discussed in the previous section, it was also of interest to investigate the tolerance of FTO and ALKBH5 toward m^6A analogs bearing different exocyclic C6 substituents. Thus, oligonucleotides containing $m^6{}_2A$ (**R6**), m^6I (**R7**), ms^6P (**R8**) or e^6P (**R9**) were subjected to demethylase treatment, nuclease digestion and HPLC-MS-based analysis as outlined in Section 3.4.3. The results are presented in Figure 3.22.

Using **R6** as substrate for FTO, stepwise removal of the two N^6-methyl groups of $m^6{}_2A$ was observed. The reaction proceeded slower than for monomethylated adenosine, with 63.4% of $m^6{}_2A$ still remaining after 2 h. In contrast to the stabilizing hydrogen bond between the m^6A methylamino group and Glu234, which aids positioning of native m^6A, the second, *anti*-oriented, N^6-methyl group invokes a steric clash with Glu234 (Figure 3.23). This likely results in partial structural rearrangement of the binding site, which leaves the nucleobase in a slightly disfavorable orientation and is responsible for the less efficient demethylation compared to m^6A. According to the experimental results, both demethylation steps proceed *via* the respective hydroxymethyl intermediates (hm^6m^6A and hm^6A). Intermediates with both methyl groups oxidized simultaneously, such as $hm^6{}_2A$, were however not detected. This is reasonable, as generation of a double-oxidized species would require re-binding of the hm^6m^6A intermediate. The presence of the hydroxymethyl group would however further increase the steric clash with the protein scaffold, leading to a highly unfavorable binding situation and thus making hm^6m^6A an unsuitable substrate for further oxidation. Interestingly, **R6** treatment with ALKBH5 yielded a very similar product pattern. Also here, a

stepwise removal of the two methyl groups was observed, with hm^{6}m^{6}A and even f^{6}m^{6}A emerging as oxidized intermediates of the first demethylation step. Thus, removal of the first methyl group resembled an FTO-like mechanism, while the second demethylation occurred in a direct fashion as observed for m^{6}A. Carrying a tertiary amino substituent, m$^6{}_2$A is unable to form a Schiff base after being oxidized by ALKBH5; thus, the native demethylation mechanism *via* a covalent intermediate cannot proceed and decomposition of the hydroxy-methylated species occurs in solution. The resulting m^{6}A is then further processed as illustrated in Scheme 3.20.

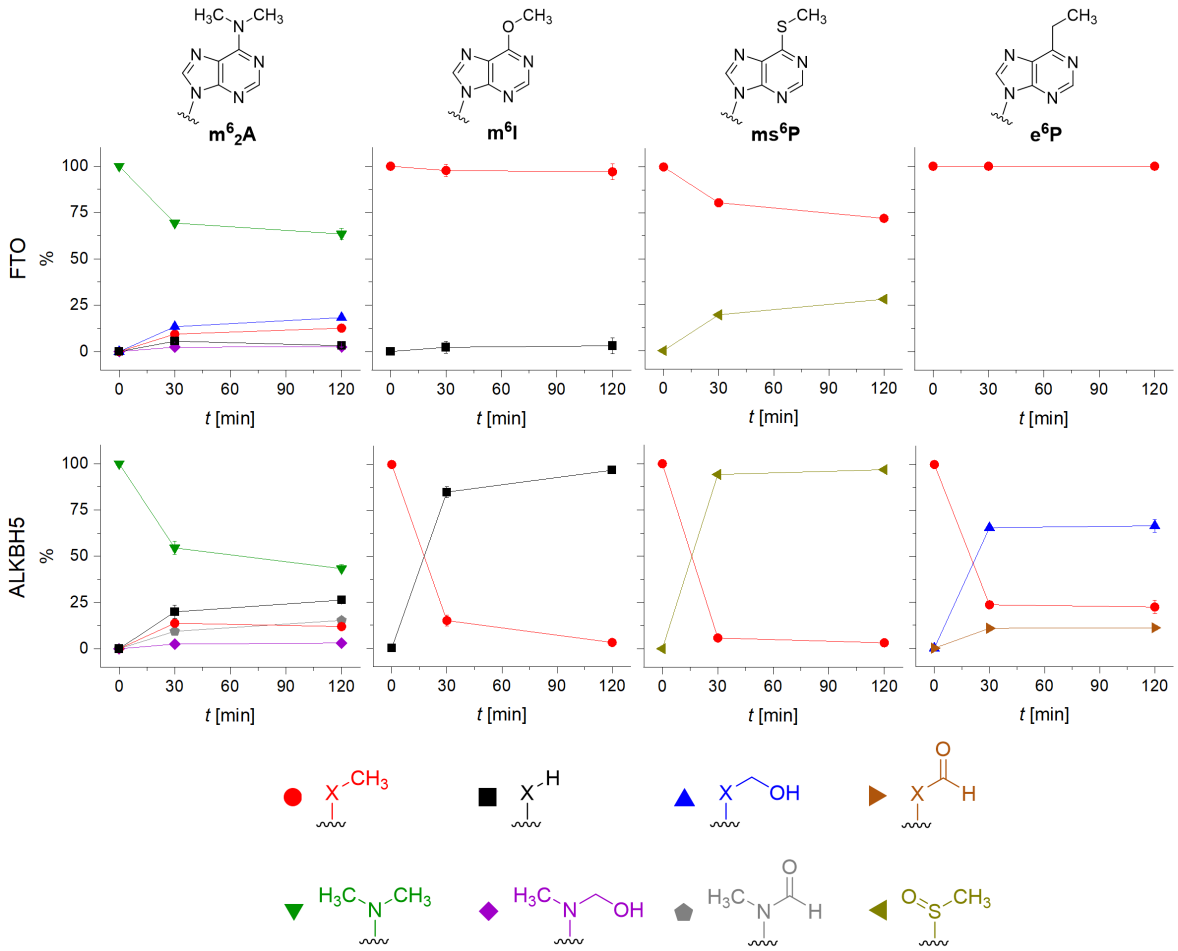

Figure 3.22: Product distributions obtained from oxidative demethylation of m^{6}A analogs bearing different exocyclic substituents at C6 in ssRNA (**R6**–**R9**) by FTO (top row) or ALKBH5 (bottom row). Product species were identified and quantified by HPLC-MS-based analyses. All data points were collected as duplicates and are represented as mean ± s.e.m.

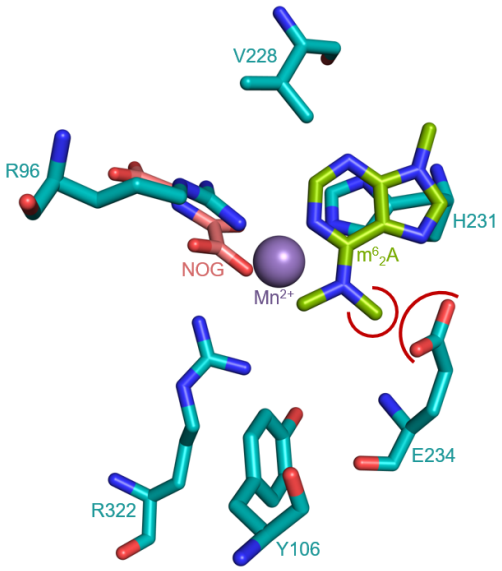

Figure 3.23: Model of the m$^6_2$A nucleobase inside the FTO active site. This figure was generated by superimposition of the geometry-optimized structure of N^6-dimethyl-9-methyladenine (see Section 3.2.2) with an FTO-m^{6}dA co-crystal structure (PDB ID 5ZMD). The m^{6}dA nucleoside was removed for clarity. The *anti*-oriented N^6-methyl group clashes with the side chain oxygen of Glu234 (d_{C-O} = 1.9 Å), as indicated in red.

While the steric clash of the m$^6_2$A dimethylamino group with Glu234 did sigificantly hinder but not completely abolish demethylation activity of FTO, induction of an electronic repulsion was interestingly even more detrimental. **R7**, bearing an m^{6}I modification, was hardly converted at all. In stark contrast, this oligonucleotide was very efficiently demethylated by ALKBH5 (96.7% demethylation after 2 h). The distinct tolerances of FTO and ALKBH5 toward this modification resemble the results for c^{1}m^{6}A described in Section 3.4.3; thus, the hydrogen bond between Glu134 and the exocyclic amino group appears to be equally important for positioning of the nucleobase inside the FTO binding pocket as the interaction between Arg96 and the N1 atom. In the ALKBH5 active center, neither of these two nucleobase sites is involved in interactions with the protein scaffold.

Despite bearing a hydrogen bond acceptor substituent at C6 as well, enzymatic treatment of **R8** unexpectedly led to consumption of ms^{6}P by both ALKBH5 and FTO while four new peaks emerged in the HPLC chromatograms (Figure 3.24B). In both cases, one product species was an oxidized derivative of ms^{6}P (ms^{6}P^{ox}, $\Delta m/z$ = +16). Furthermore, the nucleobases of both ms^{6}P and ms^{6}P^{ox} were detected. As they coeluted with the respective nucleosides, they most likely originated from cleavage of the glycosidic bond under ESI-MS conditions. Finally, ms^{6}P^{ox} appears to interfere with RNA digestion by nuclease P1, as an ms^{6}P^{ox}–C dinucleotide was observed as an additional digestion product.

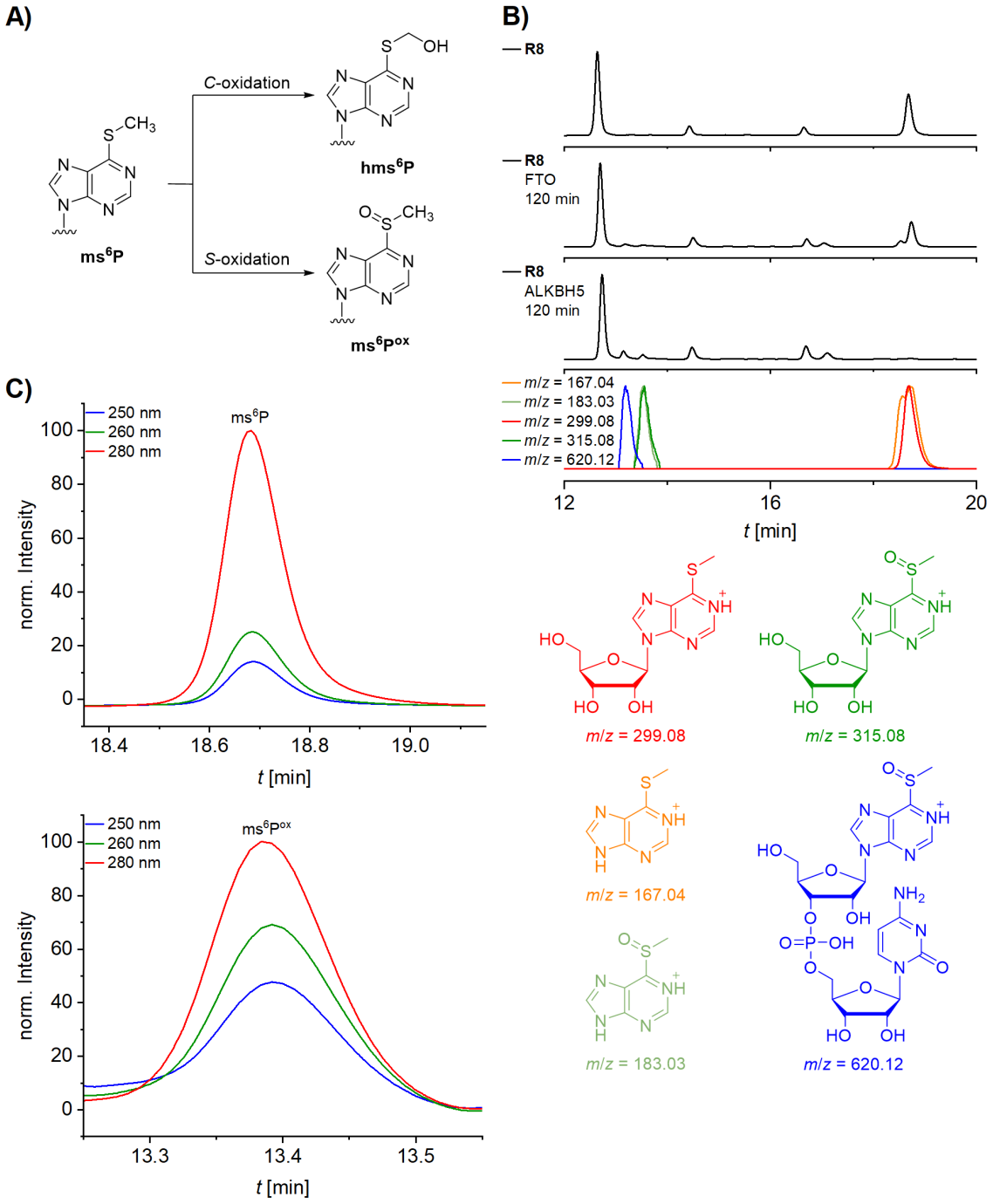

Figure 3.24: Identification of ms^{6}P derivatives formed upon enzymatic oxidation of **R8**. A) Possible oxidation products of ms^{6}P, formed by either *C*- or *S*-oxidation. B) HPLC-MS analyses of demethylase-treated **R8** samples. Top: The UV (280 nm) chromatograms are shown stacked on top of the nucleoside $[M+H]^+$ extracted ion chromatograms (EICs). Bottom: Color-coded structures corresponding to the EICs above. C) Superimposed UV chromatogram traces at 250, 260 and 280 nm showing the ms^{6}P (top) and ms^{6}P^{ox} (bottom) UV peaks. The smaller A_{250}/A_{280} and A_{260}/A_{280} ratios indicate a blue-shifted absorption band of ms^{6}P^{ox} compared to ms^{6}P.

Unlike for m^6A, two different oxidation products of ms^6P are imaginable (Figure 3.24A): oxidation of the exocyclic methyl group would yield a hemithioacetal (hms^6P), while the sulfur center itself may be oxidized to a sulfoxide (ms^6P^{ox}). Two features helped identify the product as the sulfoxide instead of the hemithioacetal derivative: firstly, even after 2 h, no formation of demethylated s^6P was detected; hemithioacetals, however, are usually unstable and exist in equilibrium with thiol and aldehyde.[196] Secondly, compared to ms^6P UV absorption of the oxidized product was markedly blue-shifted (Figure 3.24C). However, *C*-oxidation of methylated nucleosides mostly has no influence on the absorption maximum, as experimentally observed for m^6A/hm^6A and e^6P/he^6P (Section 3.1.2, Figure 3.4). On the other hand, *S*-oxidation of sulfides to sulfoxides is known to give rise to blue-shifted absorption spectra.[197] Hence, all analytical data gathered disagree with ms^6P being oxidized to its hydroxymethyl derivative hm^6P; instead, S-oxidation takes place. This oxidative pathway renders ms^6P unique among all m^6A atomic mutants investigated in this study.

Lastly, the enzymatic oxidation of the e^6P-containing oligonucleotide **R9** was investigated (Figure 3.22). This substrate was expected to be less susceptible to radical oxidation, as initial homolytic H-abstraction requires more energy than for m^6A mutants bearing polarized substituents at C6 (compare the difference between the bond dissociation energies of H–CH_2CH_3 = 421.8 kJ/mol vs. H–CH_2OH = 402.1 kJ/mol at 25 °C).[198] Surprisingly, however, ALKBH5 efficiently oxidized e^6P, forming the hydroxyethyl derivative (66.6% after 2 h) as the main product accompanied by further oxidation to the corresponding aldehyde (11.1% after 2 h). A third oxidation step to form a carboxylic acid was not observed; neither was cleavage of the exocyclic C-C bond, since the primary alcohol formed upon e^6P oxidation is not susceptible toward hydrolysis (as opposed to the hemiaminal or hemiacetal species resulting from oxidation of m^6A or m^6I). In contrast to the convenient oxidation of e^6P achieved by ALKBH5, treatment of oligonucleotide **R9** with FTO did not result in any conversion of the modified nucleoside. This outcome mirrors the result described above for m^6I and again highlights the importance of a hydrogen bond donor substituent at C6 for correct substrate positioning inside the catalytic center and hence for enzymatic activity of FTO.

4 Summary and Outlook

In the first part of this thesis, atomic mutagenesis of N^6-methyladenosine was employed to systematically study the structural basis of m^6A recognition by human YTH domain reader proteins as well as the oxidative demethylation by the human demethylases FTO and ALKBH5. Seven analogs of m^6A featuring modifications of either the exocyclic substituents at C6 or the heterocyclic purine core were synthesized and incorporated into RNA oligonucleotides by solid-phase synthesis. Here, the modifications were placed inside a DRACH motif to mirror the native consensus motif of m^6A sites in human mRNA. All atomic mutants were designed to display different steric and electronic properties and hence engage in electrostatic interactions with protein binding sites distinct from the parent m^6A substrate.

The spectroscopic properties of all synthesized nucleosides as well as their conformation adopted inside an RNA oligonucleotide were elucidated using UV/Vis and fluorescence spectroscopy supported by DFT-based calculations. For almost all m^6A atomic mutants, the C6 substituent preferably adopts the *syn* conformation with the methyl group pointed toward the Watson-Crick face of the nucleobase; only the unpolarized C6-ethyl substituent of 6-ethylpurine riboside (e^6P) favors a *gauche* conformation. In contrast to native adenosine, its 1-deaza and 3-deaza analogs were found to be fluorescent. Although their brightness is far exceeded by established fluorescent adenosine analogs such as 8-vinyladenosine (v^8A), they still hold potential for future applications: c^1A and c^3A fluorescence brightness strongly depends on the methylation state at N^6 and may therefore be used as a spectroscopic readout for MTase and demethylase activities. Potentially, the methylation-sensitivity of the 1-deazapurine core and the fluorescence-enhancing effect of an 8-vinyl substituent may be combined to furnish an improved fluorescent adenosine analog.

The oligonucleotides containing m^6A or its atomic mutants were used as ligands of the human m^6A readers YTHDF2, YTHDC1 and YTHDC2. The dissociation constants of RNA–protein complexes were determined using fluorescence anisotropy measurements and used to assess the effects of the introduced atomic mutations on the protein binding affinities. YTHDF2 was identified as the strongest m^6A binder, which agrees with previous reports. Whereas YTHDF2 and YTHDC2 strongly select against unmethylated RRACH motifs, YTHDC1 is less specific due to an additional binding pocket accommodating the G-1 nucleoside. Upon substitution of m^6A by its atomic mutants, it was found that mutations of the exocyclic methylamino substituent are not tolerated, as any modification at

this position reduced protein binding to the level of the unmethylated control sequence. Hence, hydrogen bonding between the methylamino group and the protein binding site was identified as a crucial prerequisite for substrate recognition by the investigated YTH domain proteins. Deaza mutations of the heterocyclic purine scaffold were tolerated to different degrees. For all three YTH proteins investigated, introduction of a 7-deaza mutation of m^6A in the substrate RNA reduced the binding affinity by ca. threefold. Thus, the presence of N7 stabilizes the RNA-protein complex, but is not crucial for substrate recognition. Based on previously published crystal structures, N7 does not appear to engage directly in interactions between nucleobase and protein binding pocket; instead, the altered electronic properties of a 7-deazapurine heterocycle probably result in weaker π-stacking interactions of the nucleobase with adjacent tryptophane residues. Replacing N1 of the nucleobase by a CH unit showed to have a more detrimental effect: the binding affinities of YTHDF2 and YTHDC1 were reduced by a factor of ca. 50, while YTHDC2 did not recognize this mutant substrate. Therefore, the hydrogen bonding interactions between N1 and the respective protein binding pockets were identified as important contributors to substrate recognition. While 1-deaza and 7-deaza mutations of the substrate m^6A each showed similar effects on all three YTH proteins, introduction of c^3m^6A was tolerated to very different degrees: whereas YTHDF2 affinity was only reduced by a factor of three, recognition by YTHDC1 and YTHDC2 was completely abolished. It is reasonable to assume that binding by YTHDC1 and YTHDC2 is disrupted because of (partial) protonation of the c^3m^6A nucleobase at N1 under physiological conditions; however, this assumption does yet require experimental evidence. All in all, the obtained results provide novel insight into the structural prerequisites of substrate recognition by YTH domain m^6A reader proteins. The observed distinct tolerances toward substrate atomic mutagenesis suggest c^3m^6A-modified oligonucleotides as a possible selective competitive inhibitor of YTHDF2 without off-target effects on YTHDC1 or YTHDC2.

The m^6A atomic mutants described above were furthermore applied as substrates of the human m^6A eraser enzymes FTO and ALKBH5. Here, a combination of HPLC-MS- and gel electrophoresis-based demethylation assays and DFT-based calculations was utilized to monitor the effects of m^6A atomic mutagenesis on the enzymatic demethylation efficiency as well as the product distribution. Although both demethylases belong to the same enzyme class, their catalytic pathways differ: while FTO furnishes oxidized m^6A intermediates, which decompose in solution, ALKBH5 directly releases demethylated adenosine products. The ALKBH5-mediated reaction was found to proceed *via* a covalent RNA-ALKBH5 intermediate, which matches a previous report. This mechanism is consistent across all atomic mutants investigated.

In stark contrast to YTH domain family readers, which bind their substrates *via* a conserved m^6A binding pocket, FTO and ALKBH5 appear to recognize general structural features of the m^6A consensus motif, as oligonucleotides containing an unmethylated RRACH motif or m^6A atomic mutants were bound with comparable affinities as the native substrate. However, although all investigated m^6A mutants were effectively bound, they were oxidized/demethylated with significantly different efficiencies. FTO activity depends on hydrogen bonds involving N1 and N^6, which are essential to correctly align the methyl group with the catalytic center for oxidation. Hence, the enzyme was inactive on substrates bearing ethyl or methoxy substituents at C6 or a 1-deaza mutation of the purine scaffold. Notably, the ms^6P mutant was efficiently oxidized; yet, the process was identified as an *S*- instead of a *C*-oxidation. Presence of N7 further aids FTO activity, although it is not strictly required. N3 does not engage in any electrostatic interactions with the binding site; nonetheless, its presence was identified as an additional prerequisite for demethylase activity. This unexpected result was attributed to a significantly increased pK_a value of the 3-deaza nucleoside; this causes the substrate to be cationic under physiological conditions, which leads to electrostatic repulsions and thus interferes with correct positioning of the nucleoside inside the enzyme binding pocket.

ALKBH5 binds its RNA substrates in an inverse 5'-3' direction compared to all other ALKBH family enzymes. As a consequence, also the facial orientation of the m^6A nucleoside inside the active center is reversed. Therefore, despite a large structural similarity of the FTO and ALKBH5 binding sites, the interactions between substrate nucleobase and protein scaffold are highly different. Introduction of a 1-deaza modification of the m^6A nucleobase thus does not impact ALKBH5-mediated demethylation efficiency. c^3A and c^7A, in contrast, are demethylated less efficiently; however, unlike for FTO, these mutations do not completely abolish the enzymatic activity. Furthermore, ALKBH5 was found to even oxidize the non-polarized exocyclic substituent of the e^6P atomic mutant. In case of ms^6P, ALKBH5 furnished *S*-oxidized products, as also found for FTO-mediated oxidation.

Overall, the experimental results described in the course of this thesis provide an in-depth insight into the structural basis for substrate recognition by m^6A eraser enzymes as well as reader proteins. Being involved in not only various cellular regulatory processes but also in a multitude of diseases, especially m^6A erasers have been regarded as potential drug targets. A deeper understanding of substrate-protein interactions crucial for substrate recognition, as provided by the presented results, may help in rational design of future small molecule inhibitors or modulators of m^6A-interacting proteins and enzymes.

Part II

Derivatives of remdesivir as antiviral nucleoside analogs against SARS-CoV-2

1 Background

1.1 Antiviral strategies against SARS-CoV-2

In 2019, a novel coronavirus emerged in the chinese city of Wuhan and the local outbreak rapidly evolved into a global pandemic.[199,200] The new pathogen was named severe acute respiratory syndrome coronavirus 2 (SARS-CoV-2) because it shares 82% genetic identity with SARS-CoV, which emerged in 2012.[201] Accordingly, the emerging pandemic was termed coronavirus disease 2019 (COVID-19).[202] Due to the rapid increase in infections and fatalities, the development of an antiviral treatment was urgently needed. Extensive screenings of antiviral compound libraries were conducted to identify drug candidates that may be repurposed as anti-SARS-CoV-2 agents.

1.1.1 Inhibitors of the viral main protease

SARS-CoV-2 is a member of the class of betacoronaviruses, which are enveloped (+)ssRNA (positive-sense single-stranded RNA) viruses.[203] Their genetic information is encoded as single-stranded RNA of ca. 30 kb size, which represents the largest genome among all known RNA viruses. The genome is organized in 14 open reading frames (ORFs), which encode 27 proteins.[204] The 5'-terminal two thirds of the genome are occupied by the two overlapping open reading frames ORF1a and ORF1b (Figure 1.1).[205] These encode the 16 viral non-structural proteins (nsps), which include the viral replication machinery, in the form of two large polyproteins (pp1a and pp1ab).

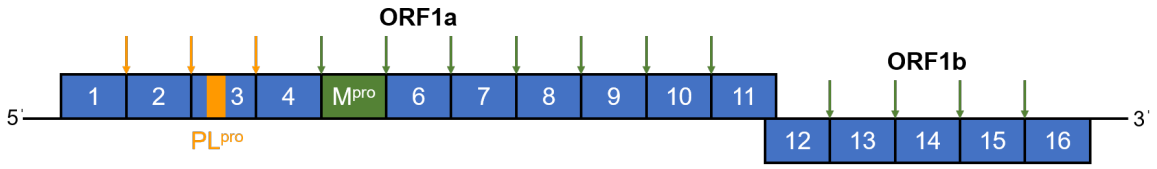

Figure 1.1: Structure of SARS-CoV-2 ORF1, containing the partially overlapping ORF1a and ORF1b.[205] The two viral proteases, M^{pro} and PL^{pro}, are colored in green and orange, respectively. Green and orange arrows indicate the sites which are processed by M^{pro} and PL^{pro}, respectively, during cleavage of the polyproteins pp1a and pp1ab into the 16 individual non-structural proteins (nsps, blue).

Pp1a is encoded in ORF1a, while ORF1a and ORF1b together encode the larger polyprotein pp1ab. Translation of the ORF1b-encoded part requires a -1 frameshift of the polymerase near the stop codon of ORF1a.[206] After expression, the two polyproteins are cleaved by

the viral main protease (M^{pro}) and the papain-like protease (PL^{pro}) to release the 16 SARS-CoV-2 non-structural proteins (nsps), including the viral RNA-dependent RNA polymerase (nsp12) and its accessory proteins nsp7 and nsp8.[205] The main protease is the major enzyme responsible for this polyprotein processing and consequently one of the main targets for the development of antiviral agents. Several peptide-based M^{pro}-inhibitors, among them being GC-376 and the FDA-approved anti-HCV agent boceprevir have been identified (Figure 1.2).[207,208] All of these inhibitors show broadband-activity against several coronaviruses including the novel SARS-CoV-2 strain, against which low micromolar EC_{50} values have been measured.

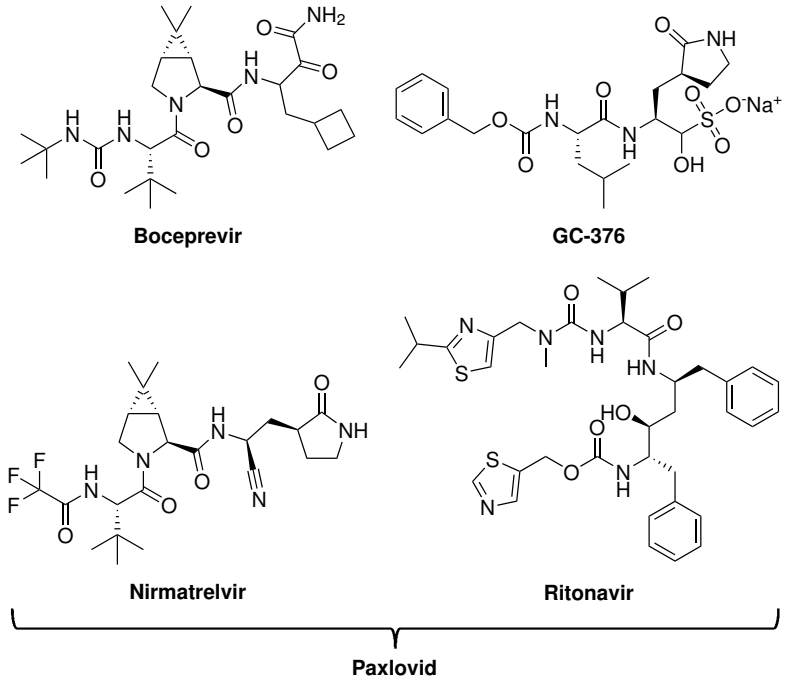

Figure 1.2: Chemical structures of the M^{pro}-inhibitors boceprevir, GC-376 and nirmatrelvir.[207,209] A combination of nirmatrelvir and ritonavir, which slows down metabolism of nirmatrelvir, is used against SARS-CoV-2 under the name Paxlovid.[210]

M^{pro} inhibitors are mainly chemically modified tetra- or pentapeptides. As such, they bear structural resemblance to the Leu-Gln↓(Ser, Ala, Gly) recognition sequence found at M^{pro} cleavage sites in the large polyprotein pp1ab (↓ marks the cleavage site).[202] Therefore, the inhibitors are able to bind to the enzymatic active site and prevent binding of the native substrates.[202,207] The EMA-approved anti-SARS-CoV-2 drug Paxlovid combines the M^{pro} inhibitor nirmatrelvir with the protease inhibitor ritonavir, which slows down nirmatrelvir metabolism *via* inhibition of cellular proteases and thus leads to increased active cellular nirmatrelvir levels.[210] As a consequence, Paxlovid displays higher antiviral activity than nirmatrelvir alone and is therefore regarded a promising drug for COVID-19 treatment.

1.1.2 Antiviral agents targeting the viral RdRp

Besides the main protease, the second promising target for drug development is the RdRp as the central component of the SARS-CoV-2 replication machinery. The viral replicase complex of SARS-CoV-2 comprises the RdRp itself (nsp12) along with the auxiliary components nsp7 and two copies of nsp8, which significantly enhance nsp12 activity.[211] The viral exonuclease (ExoN) nsp14 can associate with this complex to add a proofreading functionality to the viral replicase. Nsp12 contains an *N*-terminal nidovirus RdRp-associated nucleotidyltransferase (NiRAN) domain, which is assumed to possess kinase activity, an interface domain and a *C*-terminal RdRp domain (Figure 1.3).[212–214]

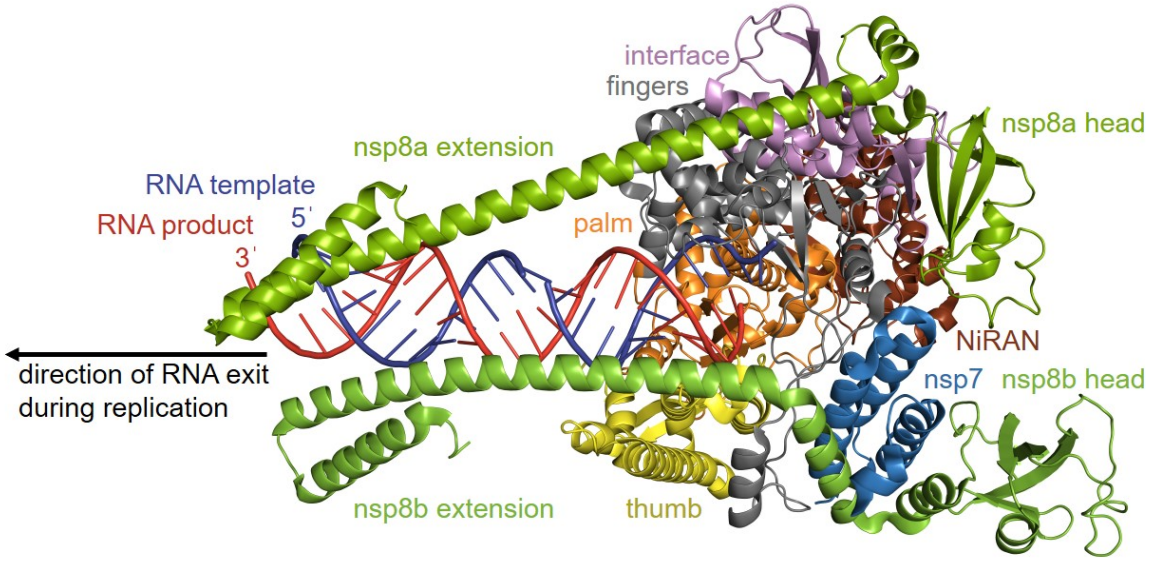

Figure 1.3: Cryo-EM structure of the SARS-CoV-2 replicase complex comprising nsp12, nsp7 (blue) and two nsp8 (green) subunits (PDB ID 6YYT).[213] The central nsp12 subunit contains an *N*-terminal NiRAN domain (brown), an interface domain (purple) and a *C*-terminal RdRp domain comprising palm (orange), thumb (yellow) and fingers (grey) subdomains.

The RdRp domain resembles a right hand with fingers, palm and thumb subdomains.[213] The auxiliary replicase subunits nsp7 and nsp8 bind to the RdRp thumb domain, one additional nsp8 binds to the fingers. Fingers and thumb domain bind the first turn of the double-stranded RNA product; the interaction is stabilized by contacts between the exiting RNA and long α-helical extensions of the two nsp8 subunits up to 28 bp away from the active site. The contacts of nsp12 and nsp8 with the RNA are mainly polar interactions with the phosphoribosyl backbone and therefore provide discrimination between RNA and DNA.[215] No interactions of the replicase complex with the nucleobase pairs are observed; as a consequence, substrate recognition by the RdRp is not sequence-dependent. The active site itself is formed by seven polymerase motifs conserved among coronaviruses, which

are located in the palm (motifs A–E) and fingers (motifs F–G) domains.[215,216]

The structural similarity of the SARS-CoV-2 RdRp to other (+)ssRNA viruses allowed repurposing of already established antiviral agents to combat the novel strain.[216] Yet, the ExoN activity of nsp14 rendered some of the most common broadband antiviral nucleosides such as 5-fluorouracil and ribavirin ineffective.[42] Screening experiments ultimately led to three main promising drug candidates: favipiravir, molnupiravir and remdesivir (Figure 1.4).

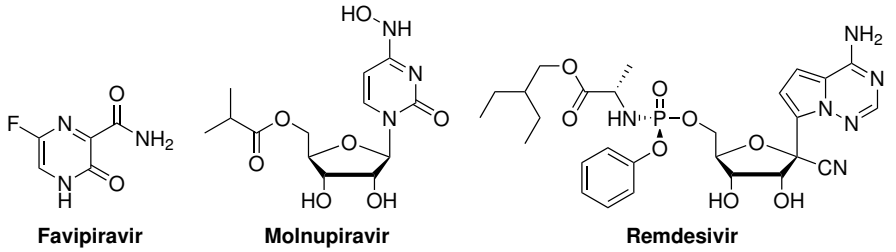

Figure 1.4: Chemical structures of favipiravir, molnupiravir and remdesivir. The respective prodrug forms are shown, which are metabolized to the active triphosphate forms *in cellulo*.

1.1.2.1 Favipiravir

Favipiravir was first developed as a drug against the influenza A virus. Several studies unanimously reported activity of favipiravir against this virus and agreed on the *in vivo* activation of the prodrug: following cellular uptake, the nucleobase prodrug is glycosylated, converted into its nucleoside triphosphate form (FTP) and incorporated into the viral RNA as a purine surrogate opposite C or U.[53,217,218] The antiviral activity, however, was attributed to different modes of action (MOA). While one study observed immediate chain termination after FTP incorporation by the viral polymerase, a contradicting report found no efficient chain termination activity of one single triphosphate moiety; yet, a high chain termination efficiency was observed following two consecutive incorporations.[217,218] A third study was not able to connect favipiravir treatment to polymerase termination, but instead found the viral RNA to be enriched in G-to-A and C-to-U transversion mutations.[53] Thus, the authors postulated lethal mutagenesis as the predominant MOA. A recent publication investigating antiviral activity against SARS-CoV-2 partly agreed with the previous results.[50] The both high NTP incorporation and error rates of the SARS-CoV-2 RdRp allowed for a facile incorporation of FTP into the viral RNA. Here, favipiravir was predominantly acting as a guanosine analog. FTP incorporation gave rise to 12-fold increased transition mutation rates, which supported the suspected action as a mutagen. Additionally, the incorporation affected further RNA extension; yet, the effect varied for incorporation in place of A or G. Opposite U, FTP was efficiently incorporated, but further RNA extension was decelerated.

Supposedly, favipiravir-U base pairs destabilize the RNA-replicase complex and promote template dissociation. In contrast, when favipiravir acted as a G-analog, the RdRp stalled before each FTP incorporation opposite a template C, but more full-length product was observed. Efficient chain termination could only be observed after multiple consecutive incorporations. Due to comparably low favipiravir concentrations *in vivo*, such an event was however deemed unlikely and lethal mutagenesis was proposed as the primary mechanism of action.

Favipiravir showed promising results in the treatment of COVID-19 patients in preliminary clinical studies.[219] It advanced to phase III clinical trials, where it was found to reduce time of clinical improvements well as time of viral clearance in hospitalized patients while not causing significant levels of adverse effects.[220] Yet, as of 2022 favipiravir has not been approved as anti-SARS-CoV-2 drug by either FDA or EMA.

1.1.2.2 Molnupiravir

An antiviral mechanism similar to favipiravir is exerted by the nucleoside analog molnupiravir. Molnupiravir is the 5'-*O*-isopropyl ester prodrug of the antiviral nucleoside N^4-hydroxycytidine (NHC). NHC had previously displayed activity against murine hepatitis virus (MHV) and Middle East respiratory syndrome-related coronavirus (MERS-CoV) while showing minimal cytotoxicity.[221,222] The isopropyl ester moiety introduced in the anti-SARS-CoV-2 drug molnupiravir improves the bioavailability of NHC and allows oral administration of the prodrug.[222] Inside the cell, the prodrug is hydrolyzed to the free nucleoside (NHC/M), which is further triphosphorylated by host kinases to yield MTP as the active drug species (Figure 1.5A).[223] During viral replication, the SARS-CoV-2 RdRp efficiently incorporates MTP into the viral RNA opposite template G or A nucleosides (Figure 1.5B); no RdRp stalling after MTP incorporation was observed.[52] Once incorporated into the (-)gRNA (negative-sense genomic RNA) strand, NHC induces transition mutations during the following (+)gRNA synthesis because it can serve as a template for both ATP and GTP incorporations. Over several replication cycles, the molnupiravir-induced mutations accumulate and finally lead to lethal mutagenesis of the viral gRNA. The ability to form base pairs with both A and G results from amino-imino tautomerism of the NHC nucleobase, with *amino*-NHC and *imino*-NHC tautomer resembling the Watson-Crick faces of C and U, respectively (Figure 1.5C). Potentially due to its formation of stable base pairs, NHC largely escapes viral ExoN proofreading and only slightly enhanced antiviral activity of molnupiravir is observed in absence of ExoN.[52,221] The largely retained antiviral activity despite ExoN proofreading presents a major advantage of molnupiravir over many other

antiviral nucleoside analogs such as ribavirin, which ExoN renders almost inactive.[42]

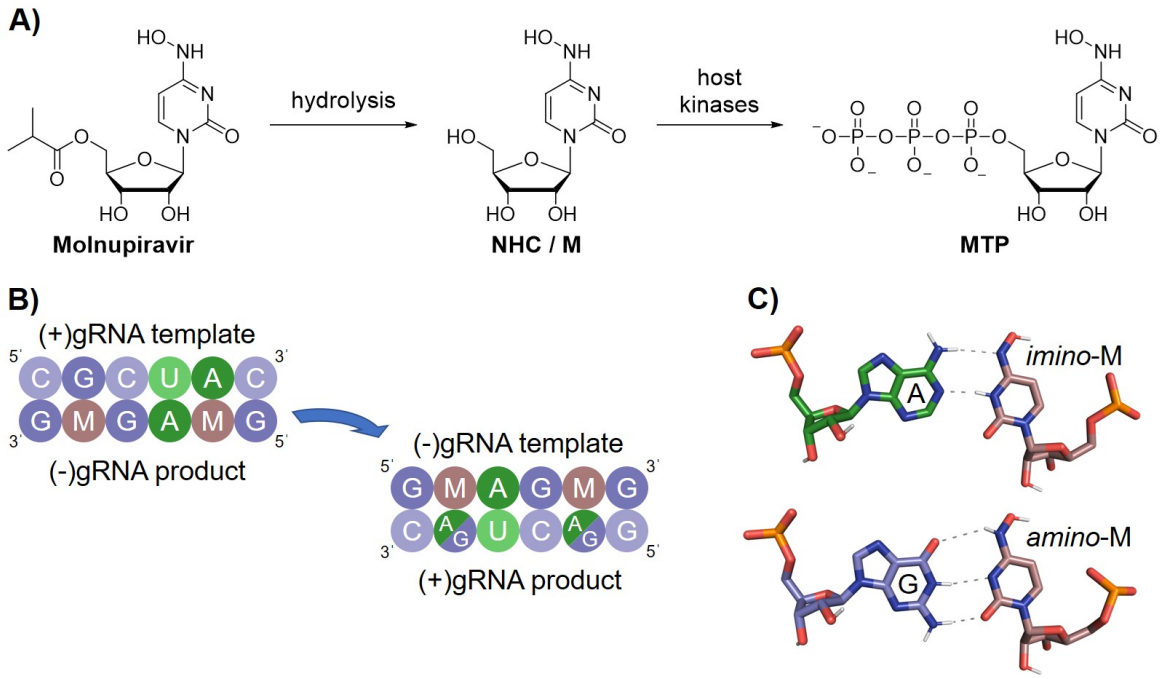

Figure 1.5: Overview of the antiviral mechanism of molnupiravir. A) Schematic representation of the intracellular metabolism of the prodrug molnupiravir to the active drug species MTP. B) The mutagenic effect of viral MTP incorporation. In the first step of viral replication, MTP is incorporated opposite A or G in the (-)gRNA product. During the second replication step, the NHC-containing (-)gRNA serves as a template for (+)gRNA synthesis; incorporation of both ATP or GTP opposite NHC leads to mutations.[223] C) Base pairing of NHC (brown sticks) in the template strand with either A (top, green sticks, PDB ID 7OZU) or G (bottom, purple sticks, PDB ID 7OZV). Due to amino-imino tautomerism, NHC forms stable Watson-Crick base pairs with both G and A.[52]

Following an emergency use authorization issued by the FDA, molnupiravir has been used for the clinical treatment of COVID-19 patients in several european countries and the USA.[224]

1.1.2.3 Remdesivir

The first FDA-approved drug for the treatment of COVID-19 was the nucleoside-based antiviral agent remdesivir. The core structure of remdesivir is formed by the adenosine analog 4-aza-7,9-dideazaadenosine. This nucleoside was first synthesized in 1994 as a potential biomedically interesting nucleoside owing to the structural similarity to the cytotoxic nucleosides tubercidin (7-deazaadenosine, c^7A) and 9-deazaadenosine (c^9A) and a high similarity of its calculated molecular electrostatic potential (MEP) to that of the canonical nucleoside adenosine.[225] Indeed, similar to tubercidin triphosphate, 4-aza-7,9-dideazaadenosine triphosphate was efficiently incorporated into RNA by human polymerases and exhibited a

potent cytotoxic effect against cancer cells.[55,225] In 2012, a series of 1'-substituted derivatives of 4-aza-7,9-dideazaadenosine (R = CN, Me, vinyl, ethynyl) was synthesized in an attempt to reduce cytotoxicity of the nucleoside and to achieve antiviral selectivity.[55] Among the four candidates, 1'-cyano-4-aza-7,9-dideazaadenosine (Rem) was the most promising candidate, combining the lowest cytotoxicity with antiviral activity against HCV, SARS-CoV and other viruses.

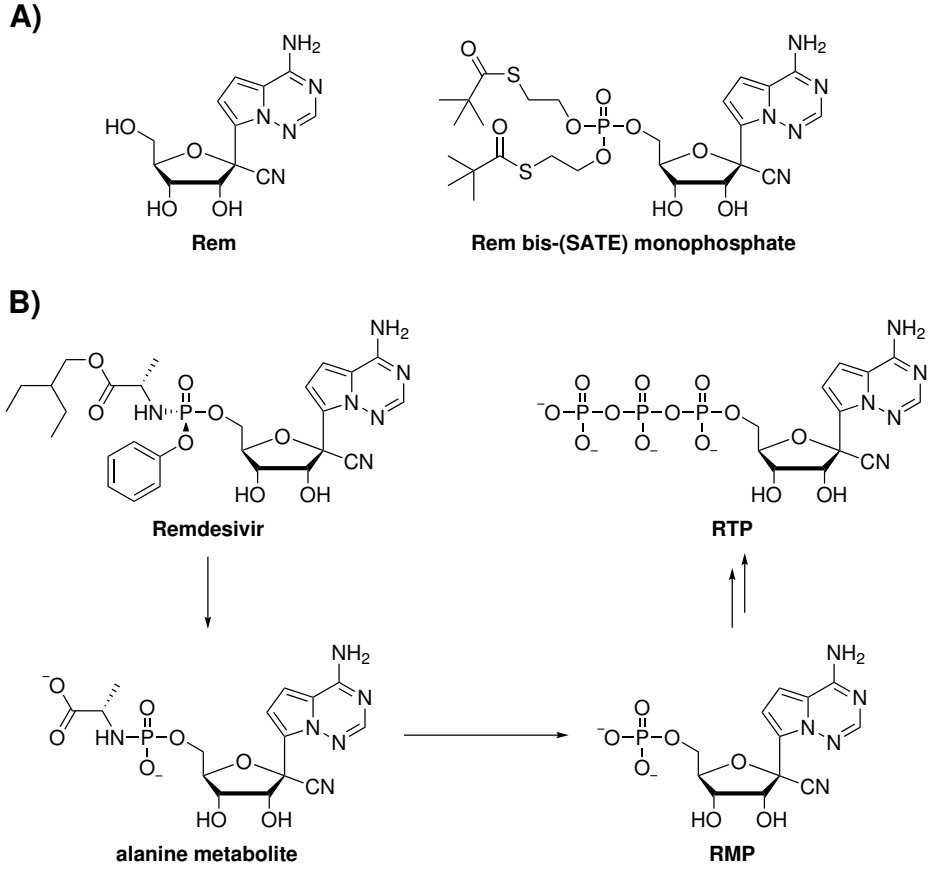

Figure 1.6: The antiviral nucleoside Rem and its prodrugs. A) Chemical structures of Rem and its bis-(SATE) monophosphate prodrug.[55] B) Metabolism of the prodrug remdesivir to the active species RTP.[226]

The antiviral activity was strongly enhanced when the bis-(*S*-acyl-2-thioethyl) (bis-(SATE)) monophosphate prodrug of Rem (Figure 1.6A) instead of the free nucleoside was used, as application of the prodrug circumvented the rate limiting first phosphorylation step during the conversion of the nucleoside into its active triphosphate form and therefore led to higher intracellular Rem triphosphate (RTP) levels. However, upon use of the bis-(SATE) monophosphate prodrug also an increased cytotoxicity was observed. Therefore, the prodrug design was refined, resulting in the development of GS-5734, later renamed remdesivir, which is the *S*p isomer of the phenyl 2-ethylbutyloxy-L-alaninyl phosphoramidate prodrug

of Rem.[226] The concept of using phosphoramidate prodrugs (ProTides) originates from research on anti-HIV drugs, as the phosphoramidate moiety comprising an oligopeptide substituent was thought to be cleavable by HIV proteases.[227] Screening experiments revealed that already use of single amino acids results in potent activity, with alanine being the preferred amino acid.[227,228] In particular, the phenyl alkyloxy-L-alaninyl prodrug design afforded highly increased antiviral potency.[227] Here, acylation of the amino acid with small linear or branched alkyl groups resulted in higher antiviral activity than the use of phenyl or halogenated alkyl esters, which did not yield sufficiently low effective concentrations.[229] Prior to its adaption for the synthesis of remdesivir, the phenyl alkyloxy-alaninyl ProTide was already successfully implemented for the syntheses of the HCV inhibitor sofosbuvir and the anti-HIV drug tenofovir alafenamide.[229,230]

Like the formerly reported bis-(SATE) monophosphate prodrug, remdesivir provides improved bioavailability of the nucleoside and bypasses the first phosphorylation step (Figure 1.6B). Follow-up studies found remdesivir to be active against a variety of human endemic as well as zoonotic coronaviruses, while its active metabolite RTP displayed excellent antiviral selectivity and no incorporation by human polymerases.[226,231]

Mechanistically, remdesivir can be assigned to the class of delayed chain terminators. First, RTP is incorporated opposite U into the (-)gRNA product strand during replication (Figure 1.7A). In coronaviruses, this incorporation occurs with ATP:RTP selectivities of 0.35 (MERS-CoV) to 0.26 (SARS-CoV-2), which means that the viral RdRp incorporates RTP ca. 3–4 times more efficiently than ATP.[232,233] The high efficiency of RTP incorporation can be traced back to RTP being well accommodated in the active site of the enzyme. As shown in Figure 1.7B, the 1'-cyano group is accommodated in a pocket formed by Thr687 and Ala688, while the 2'-OH group of RTP interacts with a set of polar amino acids. Accordingly, maintaining the 2'-OH functionality is a crucial aspect in drug design, and incorporation efficiency of RTP analogs decreases within the series RTP $>$ 2'-deoxy-2'-fluoro-RTP $>>$ 2'-deoxy-RTP.[233]

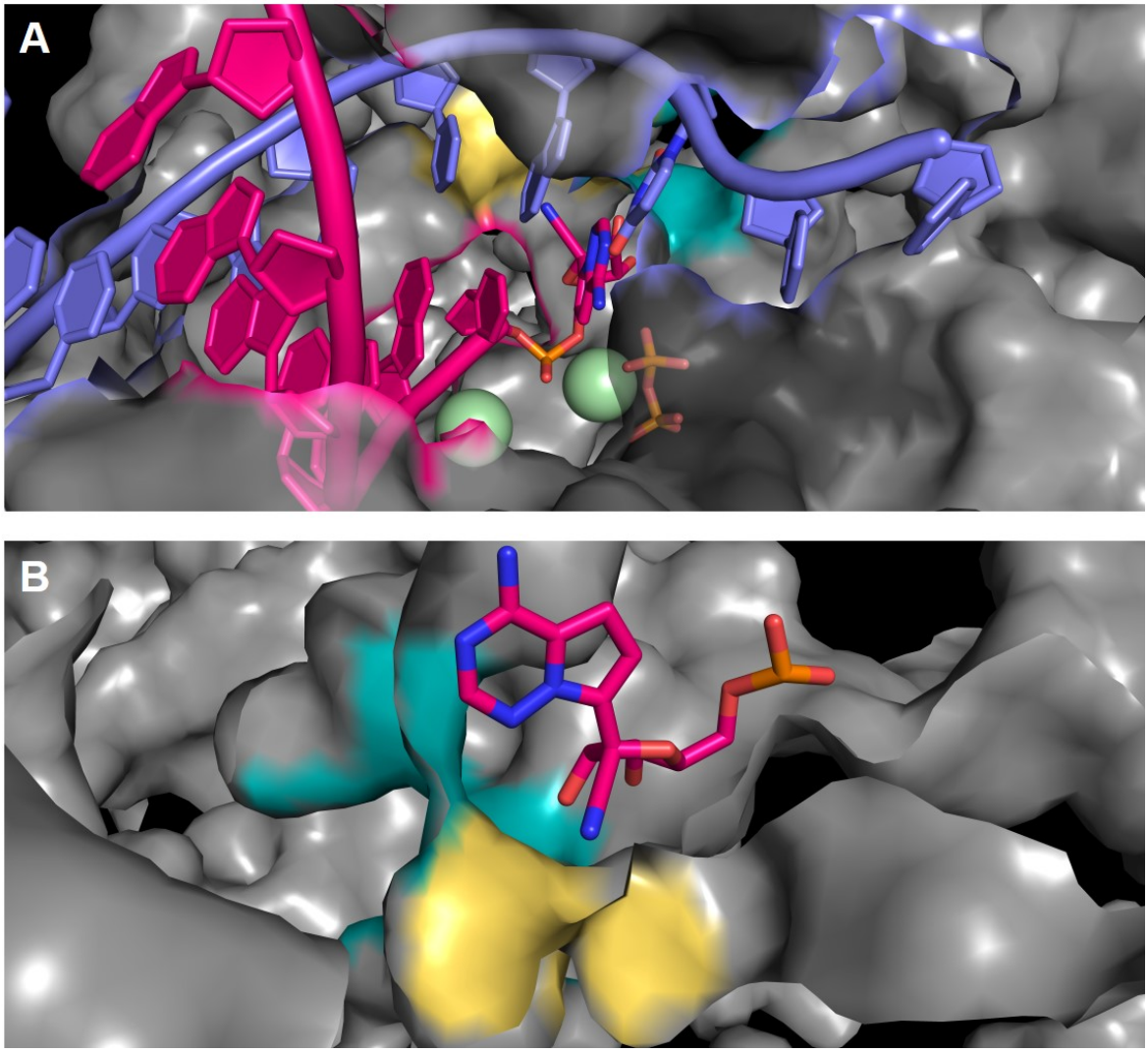

Figure 1.7: Incorporation of RTP into viral RNA by the SARS-CoV-2 replicase complex. A) Cryo-EM structure of the replicase complex (grey surface) with bound RNA template (blue cartoon), primer (magenta cartoon) and RMP (magenta sticks), post-incorporation state (PDB ID 7BV2). RTP was incorporated opposite a template U (blue sticks). Further ligands are two Mg^{2+} ions (green spheres) and the cleaved pyrophosphate group of RTP (orange sticks).[215] B) Enlarged view of the incorporated RMP and the two protein pockets accommodating the 1'-cyano group (yellow surface) and the 2'-OH group (cyan surface). Other ligands (primer, template, active site metals, pyrophosphate) are hidden for improved clarity.

Following RTP incorporation, the RNA product is efficiently extended by three nucleotides before polymerase arrest is observed (Figure 1.8).[232] The position at which delayed chain termination occurs depends on the virus species: while SARS-CoV, SARS-CoV-2 and MERS-CoV RdRps add three additional nucleotides, ebola virus (EBOV) RdRp stalls after five incorporations following RTP. The 3 nt extension might protect Rem from excision by nsp14 and therefore be the reason for the high potency of remdesivir in cell-based assays despite viral ExoN activity.[232] The remdesivir-induced delayed RdRp stalling was shown to

be efficiently overcome at high NTP concentrations, which led to high yields of full-length RNA product despite RTP incorporation.[233,234] Although remdesivir was reported to act through an additional secondary mechanism of action, hampering the opposite incorporation of UTP when present in the template strand, the low efficiency of RdRp stalling at high NTP concentrations presents a major drawback of remdesivir and limits its usefulness as an anti-SARS-CoV-2 drug.[234]

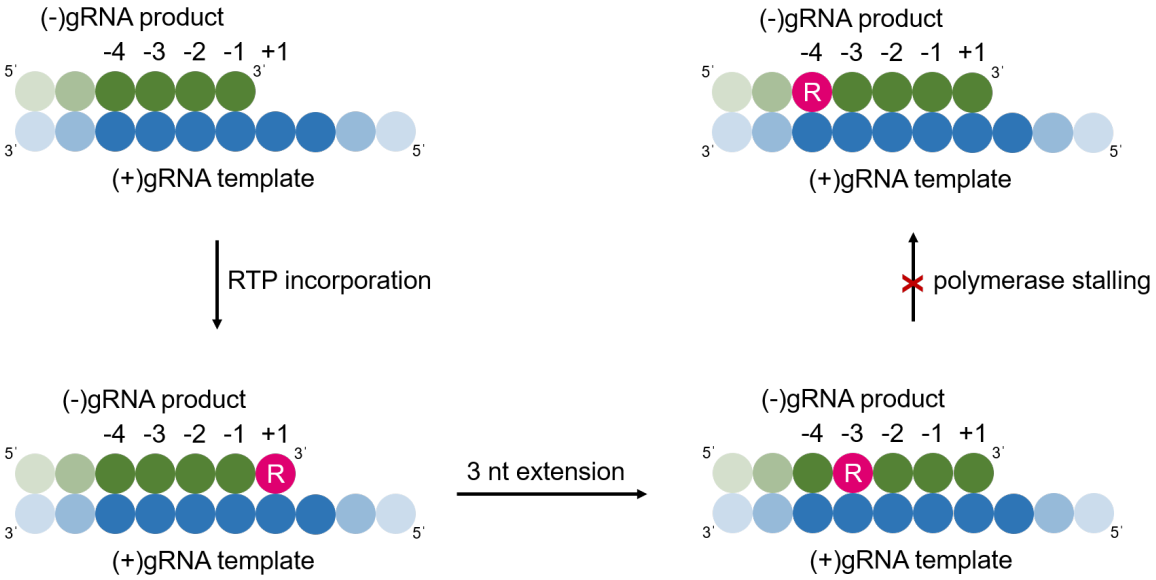

Figure 1.8: Remdesivir-induced polymerase stalling mechanism. After incorporation of RTP, the growing strand is extended by three further nucleotides. RMP at position -3 then causes polymerase stalling.[232]

2 Research Objectives

As pointed out in Section 1.1, the discovery and improvement of anti-SARS-CoV-2 agents is urgently needed to respond to the COVID-19 pandemic. The first FDA-approved drug remdesivir presents a valuable first step towards an effective treatment of the viral infection. However, the mechanism of action of remdesivir showed not to be ultimate chain termination but rather viral polymerase stalling, which was overcome at elevated NTP concentrations.[233,234] To further improve the antiviral efficacy of next generation remdesivir derivatives, the mechanistic background of the stalling process needs to be understood. Several studies found that S861A or S861G mutations of nsp12 reduce the frequency of chain termination events following RTP incorporation and therefore speculated that a steric clash between the 1'-CN group of Rem and the Ser861 side chain might cause the stalling event, possibly by inhibition of the RdRp translocation step.[212,233,234] However, this hypothesis had, at the time this project was launched, not been experimentally proven. The main techniclal limitation was the lack of suitable RdRp-RNA constructs containing Rem at internal and well-defined positions. Primer extension using RTP would lead to inhomogeneous mixtures of RNA comprising oligonucleotides of different lengths; such inhomogeneous samples, in turn, would not allow structural elucidation of the RdRp-RNA complexes by X-ray spectroscopy or cryo-EM. Thus, the generation of structurally uniform samples with Rem at a defined position required site-specific installation of Rem by solid-phase synthesis; for this, in turn, a suitable Rem phosphoramidite building block needed to be generated.

The second part of this thesis therefore focuses on the synthesis of Rem-containing RNA constructs for structural investigations of the replicase-primer-template complex. Section 3.1.1 describes the chemical synthesis of the Rem phosphoramidite building block (Rem-PA), which was subsequently incorporated at different positions into RNA oligonucleotides, as outlined in Section 3.1.2. In collaboration with the group of Prof. Dr. Patrick Cramer, Max Planck Institute for Multidisciplinary Sciences Göttingen, these RNA constructs were used to obtain cryo-EM structures of the replicase-RNA complex and thus draw conclusions about the stalling mechanism. Making use of the insights gained from this study, Section 3.2 describes the synthesis of novel Rem derivatives and their respective nucleoside triphosphates as potential anti-SARS-CoV-2 agents with improved RdRp stalling efficacies. Finally, in Section 3.3 the spectroscopic properties of the Rem nucleoside along with potential applications as a fluorescent probe are discussed.

3 Results and Discussion

3.1 Remdesivir-induced SARS-CoV2 RdRp stalling

3.1.1 Synthesis of Rem phosphoramidite building blocks

The Rem phosphoramidite building block (Rem-PA, **86**) was synthesized starting from commercially available Rem nucleoside (**82**). Reaction of the nucleoside with *N*,*N*-dimethylformamide dimethylacetal (DMFDMA) resulted in simultaneous protection of the exocyclic amino group at C6 as a dimethylformamidine and of the 2'- and 3'-hydroxy groups of the ribose as an acetal moiety, which allowed for selective installation of a DMT group on the 5'-OH. Afterwards, the acetal was cleaved by addition of methanol to yield nucleoside **83** (Scheme 3.1).

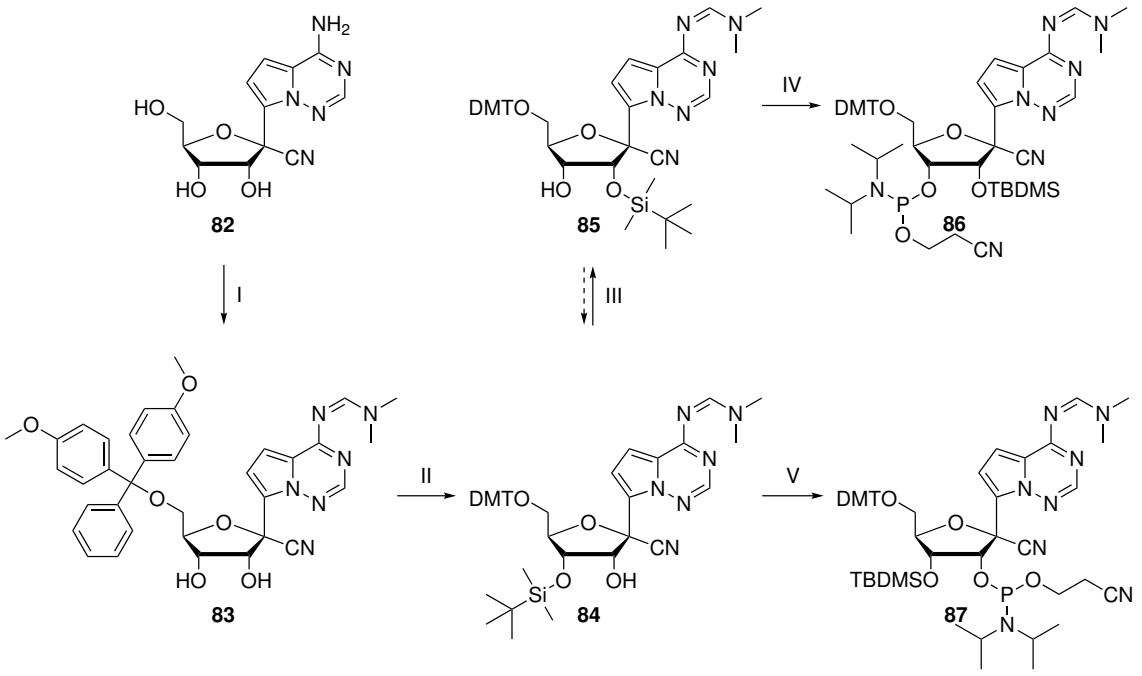

Scheme 3.1: Synthesis of Rem phosphoramidite building blocks. I) DMFDMA, pyridine, rt, 18 h, then DMTCl, pyridine, rt, 3.5 h, then MeOH, rt, 30 min, 93%; II) TBDMSCl, $AgNO_3$, pyridine, rt, 22 h, 72%; III) MeOH, NEt_3, rt, 30 min, 30%; IV) CEPCl, Me_2NEt, DCM, rt, 5 h, 75% (for **86**), 85% (for **87**).

The negative inductive effect of the 1'-cyano substituent of Rem markedly affects the electronic structure of the ribose unit, strongly reducing the electron density at the adjacent 2'-OH group. Therefore, also the nucleophilicity of 2'-O is notably lower than that of 3'-O, which is in stark contrast to nucleosides featuring an unmodified ribose (e. g. adenosine),

where both oxygens are similarly nucleophilic (Figure 3.1). As a consequence, treatment of **83** with TBDMSCl in presence of $AgNO_3$ did not result in the usually observed mixture of 2'-*O*- and 3'-*O*-protected regioisomers, but led to exclusive formation of the 3'-*O*-silylated isomer **84**.

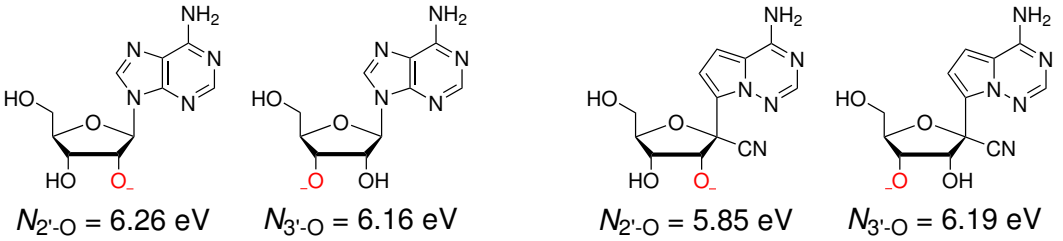

Figure 3.1: Local nucleophilicity parameters *N* of the 2'- and 3'-hydroxy groups of adenosine (left) and Rem (right). As silyl protecting groups are introduced under basic conditions, the reactivities of the 2'- and 3'-hydroxy groups are best represented by the nucleophilicities of the respective deprotonated species. Geometry optimizations and calculations of *N* were performed on the UB3LYP/def2-TZVP level of theory.

Nonetheless, 2'- and 3'-TBDMS groups are known to interconvert in solution; the isomerization rate is particularly large in methanol in presence of base.[235] As a consequence, intramolecular isomerization of the 3'-silyl ether in MeOH/NEt_3 was possible; the reaction led to a 1:1 equilibrium of regioisomers, from which the 2'-*O*-protected nucleoside **85** was isolated by column chromatography. The identities of both regioisomers were unambiguously assigned by 2D-NMR spectroscopy: the ^{1}H-^{1}H-COSY spectra (Figure 3.1) show correlations between the respective unprotected OH group proton and the adjacent CH proton. Finally, the two regioisomers were independently phosphitylated to yield the 3'-phosphoramidite (**86**) and 2'-phosphoramidite (**87**) building blocks of Rem, respectively.

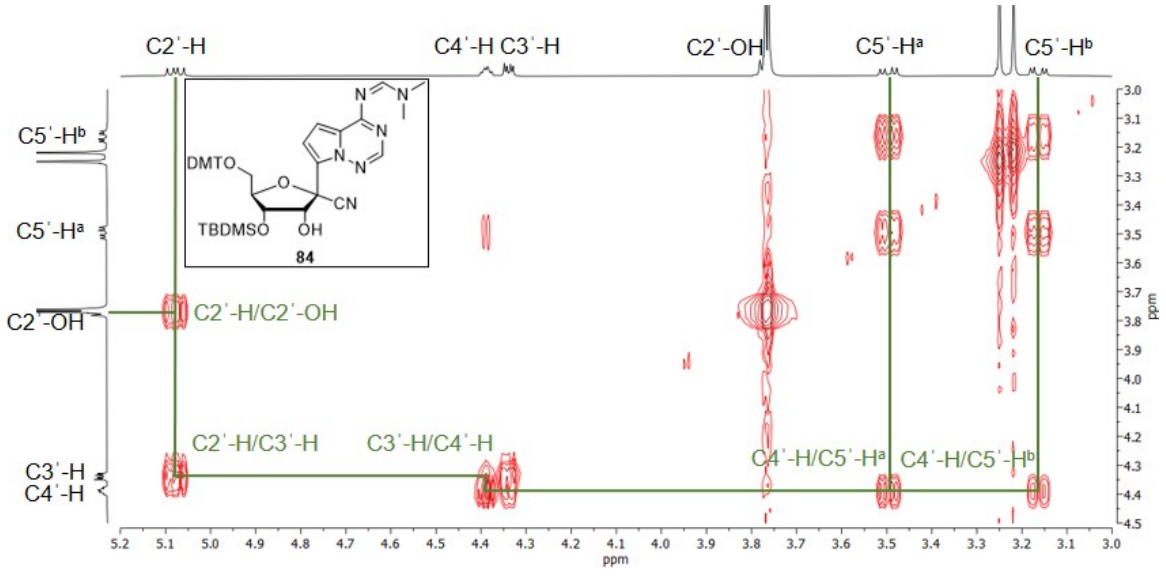

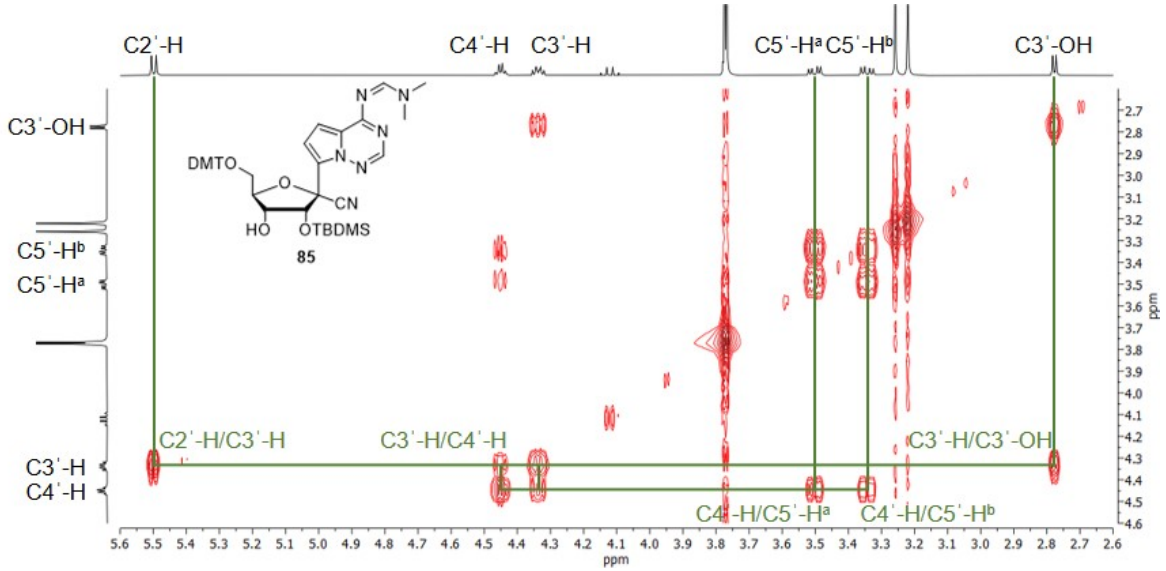

Figure 3.1: ^{1}H-^{1}H-COSY spectra of the 3'-*O*-silylated nucleoside **84** and its 2'-*O*-protected isomer **85**, recorded in $CDCl_3$. The relevant cross-peaks displaying the connectivity of the ribose atoms are highlighted. For the 3'-*O*-silylated **84**, correlations between C2'-H and the unprotected C2'-OH are detectable, while the spectrum of **85** shows correlations between C3'-H and the free C3'-OH.

The identities of both regioisomers were unambiguously assigned by 2D-NMR spectroscopy: the ^{1}H-^{1}H-COSY spectra (Figure 3.1) show correlations between the respective unprotected OH group proton and the adjacent CH proton. Finally, the two regioisomers were independently phosphitylated to yield the 3'-phosphoramidite (**86**) and 2'-phosphoramidite (**87**) building blocks of Rem, respectively.

3.1.2 Synthesis and characterization of Rem-containing RNA

The phosphoramidite building blocks were subsequently incorporated into RNA oligonucleotides using solid-phase synthesis. While building block **86** was incorporated at internal positions, the 2'-phosphoramidite **87** was used to install Rem at the 3'-end. The latter incorporation was performed on an in-house made phosphate CPG, which yielded **R11** as a 2'phosphorylated oligonucleotide after synthesis, cleavage and deprotection. Due to poor solubility in MeCN, both phosphoramidite building blocks were used as solutions in DCE. To compensate rather low coupling efficiencies, coupling times were prolonged to 24 min. Standard basic deprotection of a Rem-containing oligonucleotide ($MeNH_2$ in H_2O/EtOH, 37 °C, 5 h) led to formation of two species: besides the product oligonucleotide a byproduct with a mass difference of ΔM = +31 g/mol was formed, which coeluted during anion exchange HPLC and could not be separated from the product by PAGE. The formation of

these byproducts was caused addition of $MeNH_2$ to the Rem 1'-cyano group, forming an amidine structure. To avoid this undesired reaction, the oligonucleotides were deprotected under mild conditions (25% aq. NH_3, 25 °C, 30 h, followed by TBAF in THF for 12 h). A significantly prolonged time for basic deprotection (30 h vs. 5 h for standard $MeNH_2$ deprotection) was required to ensure efficient cleavage of the nucleobase acetyl protecting groups despite the milder conditions. The deprotected oligonucleotides were purified by denaturing polyacrylamide gel electrophoresis and analyzed by anion exchange HPLC and ESI-MS. Besides three modified oligonucleotides containing Rem at the 3'-terminus (**R11**), at position -3 (**R12**) and -4 (**R13**), the unmodified analog (**R14**) and the complementary sequence (**R15**) of **R13** were synthesized (Table 3.1).

Table 3.1: Sum formulae, calculated and measured monoisotopic masses of the RNA oligonucleotides **R11** – **R15**. R denotes the Rem nucleoside.

No.	Sequence	Sum Formula	Mass calculated [Da]	Mass found [Da]
R11	UGAGCCUACGCGR	$C_{126}H_{156}N_{51}O_{91}P_{13}$	4241.57361	4241.57032
R12	UGAGCCUACGCGRUG	$C_{145}H_{178}N_{58}O_{103}P_{14}$	4812.68057	4812.70243
R13	UGAGCCUACGCRGUG	$C_{145}H_{178}N_{58}O_{103}P_{14}$	4812.68057	4812.67966
R14	UGAGCCUACGCAGUG	$C_{143}H_{178}N_{58}O_{103}P_{14}$	4788.68002	4788.70244
R15	CACUGCGUAGGCUCA	$C_{142}H_{178}N_{56}O_{103}P_{14}$	4748.67387	4748.67166

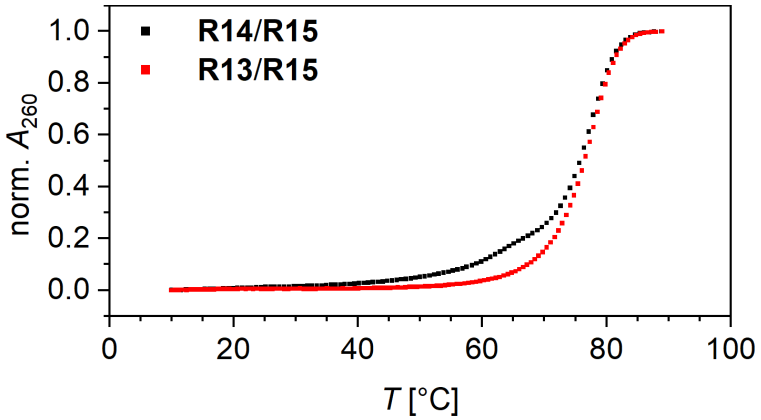

Figure 3.2: UV melting curves of 5 µM RNA duplexes in PBS (10 mM Na_2HPO_4/NaH_2PO_4 pH 7.4, 150 mM NaCl), recorded at 260 nm. The unmodified duplex **R14/R15** (black) and the duplex **R13/R15** containing Rem (red) display similar thermal stabilities.

UV melting curves of the duplexes **R13/R15** and **R14/R15** in PBS (phosphate-buffered saline) were recorded to investigate the influence of the Rem nucleoside on duplex stability. Although the melting curve of the unmodified duplex was not perfectly sigmoidal (Figure 3.2), it was evident that the presence of Rem does not cause a strong duplex

destabilization (Table 3.2). Evaluation of the thermodynamic parameters shows that the incorporation of Rem leads to an enthalpic stabilization of the duplex structure, which compensates the large entropic destabilizing effect due to the rigid 1'-cyano substituent.

Table 3.2: Melting temperatures (for 5 µM duplex) and thermodynamic data of the analyzed duplexes. For the melting temperatures, an error of ±0.5 °C is assumed. ΔT_m is given relative to the unmodified duplex.

Duplex	T_m [°C]	ΔT_m [°C]	ΔH [kcal mol^{-1}]	ΔS [cal mol^{-1} K^{-1}]	$\Delta G_{37°C}$ [kcal mol^{-1}]
R14/R15	78.2	–	-90.3	-231	-18.6
R13/R15	77.2	-1.0	-130	-345	-22.7

3.1.3 Elucidation of Rem-induced RdRp stalling

As noted in Section 1.1.2.3, incorporation of RTP by the viral RdRp complex is followed by addition of three nucleotides. The polymerase stalls once Rem is located at position -4 in the growing primer strand. The oligonucleotides **R12** and **R13**, which represent model primers with Rem at position -3 and -4, respectively, were used for structural investigations to elucidate the underlying stalling mechanism. Generation of RNA scaffolds and subsequent structural elucidation were performed by the group of Prof. Dr. Patrick Cramer, Max Planck Institute for Multidisciplinary Sciences Göttingen.

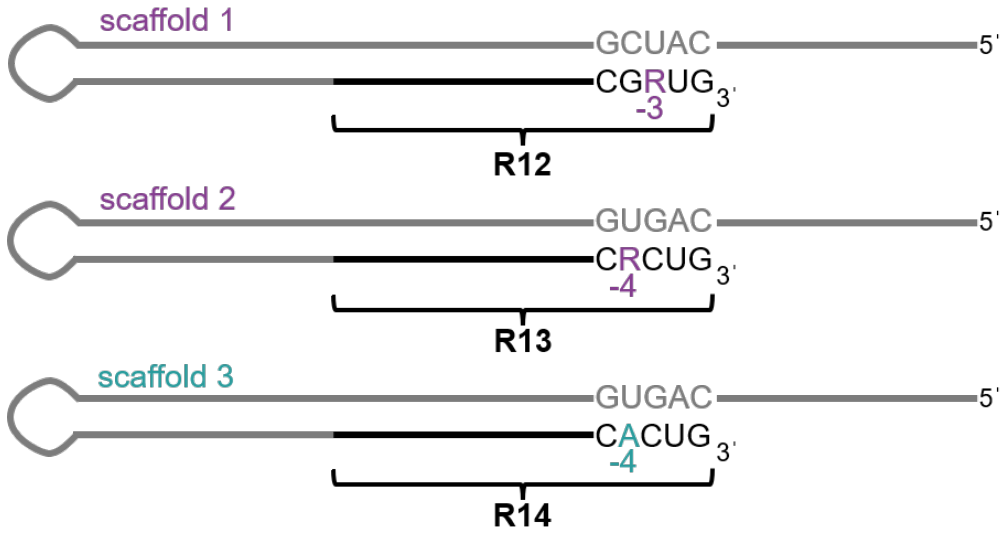

Figure 3.3: Design of RNA scaffolds for cryo-EM analysis. Model template-primer duplex constructs with Rem at position -3 or -4 or with A at position -4 were obtained by annealing oligonucleotides **R12**–**R14** (black) to long, loop-forming oligonucleotides (gray).

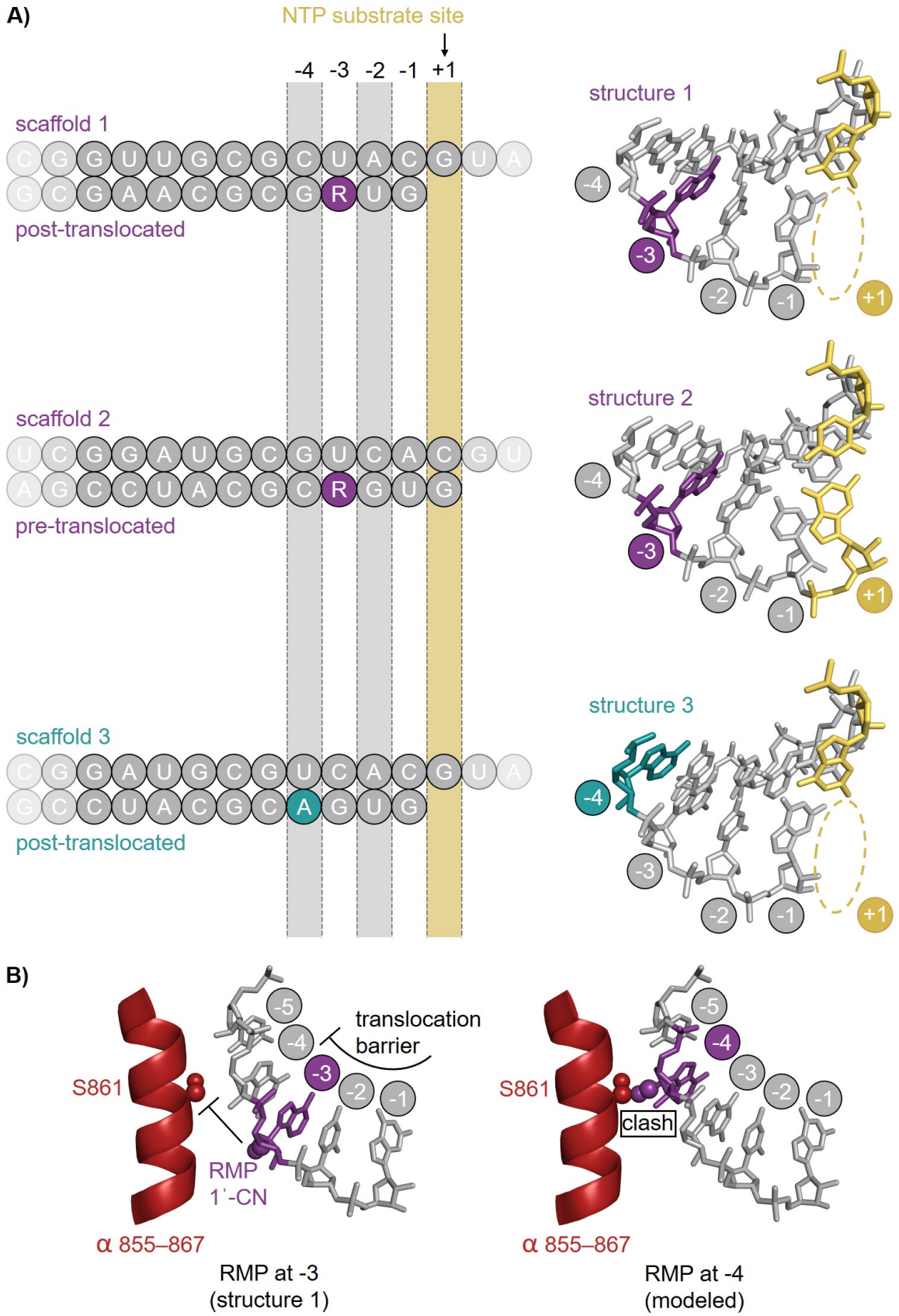

Figure 3.4: Structural analysis of Rem-induced RdRp stalling by cryo-EM. A) Positions of the

RNA scaffolds 1–3 (left), as observed in the complex structures 1–3 (right) by cryo-EM. While scaffold 1 and 3 were observed in the post-translocated state, Rem at position -4 (scaffold 2) led to adoption of the pre-translocated state. B) A steric translocation barrier is responsible for RdRp stalling. Translocation of Rem from position -3 (left) to -4 (right) would cause a steric clash between the Rem 1'-CN group (purple spheres) and the side chain of Ser861 (red spheres). Figure reproduced from [236].

RNA scaffolds with Rem at position -3 or -4 were obtained by annealing **R12** or **R13** to complementary long, loop-forming oligonucleotides, thereby yielding stable, physically linked template-primer duplexes (Figure 3.3). A reference scaffold containing an A-4 nucleoside was obtained using **R14**.

Incubation of the respective RNA scaffolds with equimolar recombinantly expressed nsp12 and threefold molar excess of each recombinant nsp7 and nsp8 yielded RdRp-RNA complexes, which were subjected to cryogenic electron microscopy (cryo-EM) analysis. The complex structures 1 (PDB ID 7B3B), 2 (PDB ID 7B3C) and 3 (PDB ID 7B3D) were resolved at 3.1 Å, 3.4 Å and 2.8 Å resolution, respectively.

Structure 1 (Figure 3.4A) showed the post-translocated state of the RdRp-RNA complex: Rem was located at position -3, as intended upon scaffold design, and the active site (position +1) was free to accommodate a new NTP substrate. Structure 2, in contrast, did not show Rem at position -4, as would be expected from the design of the scaffold. Instead, the complex adopted a pre-translocated state with Rem at position -3 and the +1 site blocked by the 3'-terminal nucleoside. Exchange of Rem for a canonical A at position -4 (structure 3), on the contrary, resulted in formation of the post-translocated complex state. In conclusion, these results showed that the Rem nucleo-side is not well tolerated at position -4 of the RdRp-RNA complex and therefore hinders further translocation of the RNA after Rem has reached position -3. Thus, RTP-induced RdRp stalling is due to Rem providing a translocation barrier. The nature of this barrier was further elucidated by modeling the Rem nucleoside at position -4 of structure 3 (Figure 3.4B), thereby simulating the experimentally not observed post-translocated state of the complex. The model shows that in the post-translocated state the 1'-cyano group of Rem would clash with the side chain of Ser861, which indicates that the translocation barrier is a steric barrier caused by the presence of the Rem 1'-CN substituent. This conclusion agrees with previous observations that mutation of Ser861 to sterically less demanding alanine or glycine residues results in reduced inhibitory efficiency of remdesivir.[212,234]

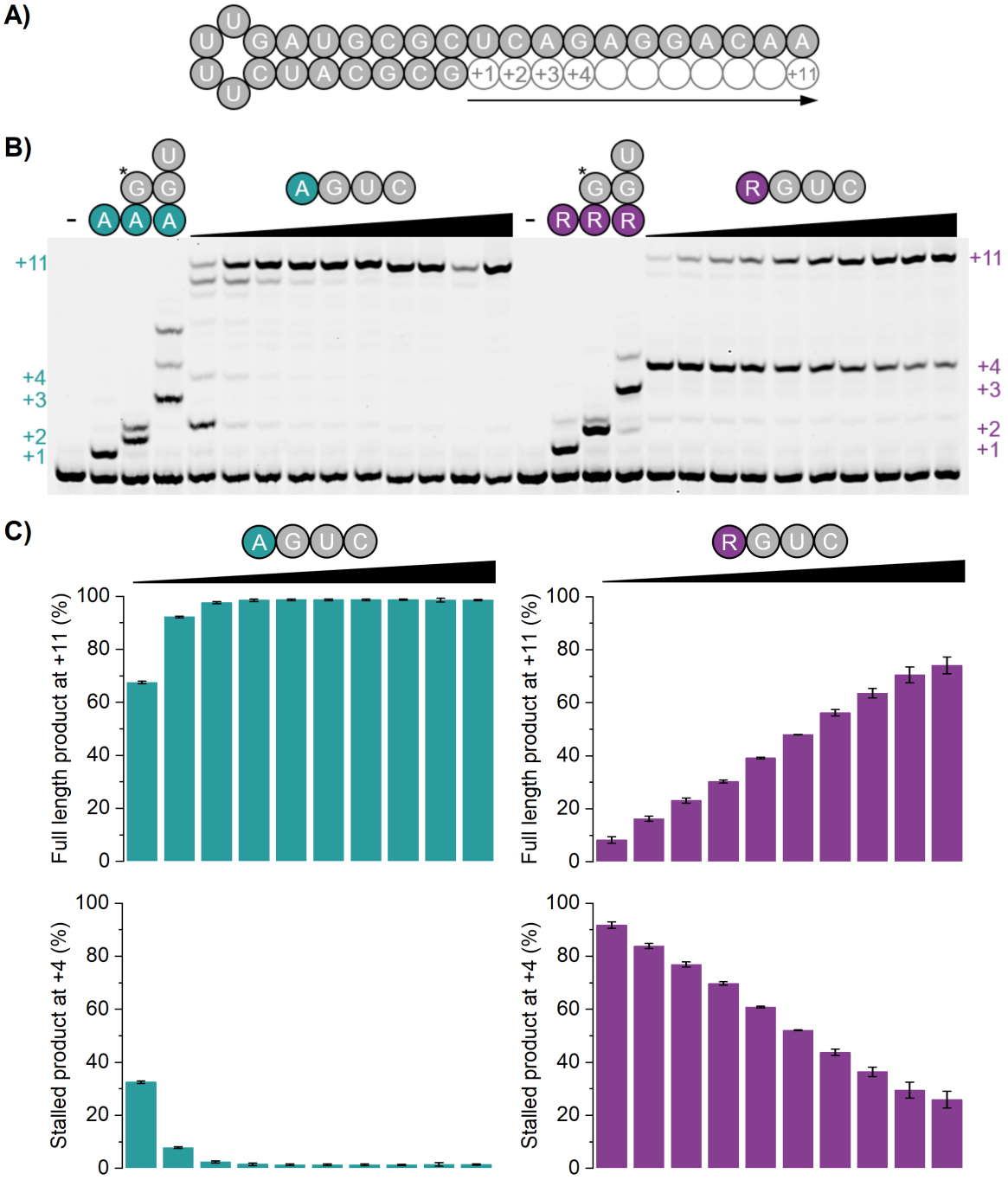

Figure 3.5: Primer extension assay for quantification of RTP-induced RdRp stalling. A) Primer-template construct used for primer extension experiments. The direction of extension is indicated by an arrow. B) PAGE analysis of primer extension experiments. RdRp complex (3 µM nsp12, 9 µM nsp7, 9 µM nsp8) and RNA scaffold (2 µM) were incubated with increasing concentrations of NTPs (1–500 µM). Replacing ATP (left) by RTP (right) led to increased +4 nt stalled product bands at the expense of full length product. At elevated NTP concentrations, the barrier was largely overcome. G* denotes 3'-deoxy-GTP, which causes chain termination after incorporation. C) Quantification of the +4 nt and +11 nt bands at different NTP concentrations, as shown in the gel image in panel B. Values are given as mean ± s.e.m. of triplicates.[236]

While incorporation of RTP by the viral RdRp does lead to a pronounced stalling band after 3 additional NTP incorporations (Figure 3.5B), the inhibitory effect of Rem is largely overcome at elevated NTP concentrations (Figure 3.5C). This severely limits the antiviral efficacy of remdesivir in clinical use and raises the need for improved next-generation drug candidates, which will be discussed in the following chapter.

3.2 Synthesis of novel Rem derivatives

As a steric translocation barrier induced by the presence of the 1'-cyano group is responsible for Rem-induced RdRp stalling, two strategies for Rem derivatization might lead to improved antiviral efficacy. Firstly, the introduction of sterically more demanding 1'-substituents in place of CN should provide a more efficient translocation block, which is only overcome at higher NTP concentrations. Thus, a sufficiently large 1'-substituent may provide a stable barrier under physiological NTP concentrations. On the opposite, introduction of a sterically very demanding substituent may prevent accommodation of the RTP derivative in the RdRp binding pocket and its incorporation into the primer strand. As an alternative strategy, 1'-CN-substituted analogs of the other three canonical nucleosides may be synthesized. While in this case the stalling efficiency of each individual nucleoside would be unchanged, application of a combination preparation of remdesivir and, e. g., a guanosine analog would increase the number of possible sites in the primer, at which an RTP derivative can be incorporated. The resulting higher number of translocation barrier sites should more efficiently inhibit formation of full-length RNA product.

3.2.1 Rem derivatives bearing altered C1'-substituents

3.2.1.1 1'-Methylamidine substitution

A simple route toward sterically more demanding 1'-substituents is provided by nucleophilic addition of amines or alkoxides to the nitrile moiety of the Rem nucleoside. Following this approach, Rem (**82**) was incubated in an aqueous solution of $MeNH_2$, which resulted in quantitative conversion to the 1'-methylamidine derivative **88** (Scheme 3.2). The nucleoside was further converted into the respective triphosphate **89**. Reaction of **88** with $POCl_3$ in presence of proton sponge to activate the 5'-OH resulted in *in situ* formation of a phosphorodichloridate intermediate.[237] Upon addition of $(NH_4)_2PP_i$ (bis(tetrabutylammonium) pyrophosphate), which was generated by protonation of tetrasodium pyrophosphate followed by titration with tetrabutylammonium hydroxide, the cyclic nucleoside triphosphate was formed, which opened upon aqueous workup to yield the product **89** as triethylammo-

nium salt. The product was separated from unreacted nucleoside **88** and monophosphate byproduct by anion exchange chromatography and further purified by reversed-phase HPLC. While negligible amounts of nucleoside monophosphate were detected, a large fraction of unreacted nucleoside was separated, which accounts for the overall low yield of the synthesis. The unsatisfactory conversion of nucleoside to phosphorodichloridate thus indicates non-optimal reaction conditions for the first reaction step; most probably the low temperature was insufficient for conversion of the present substrate.

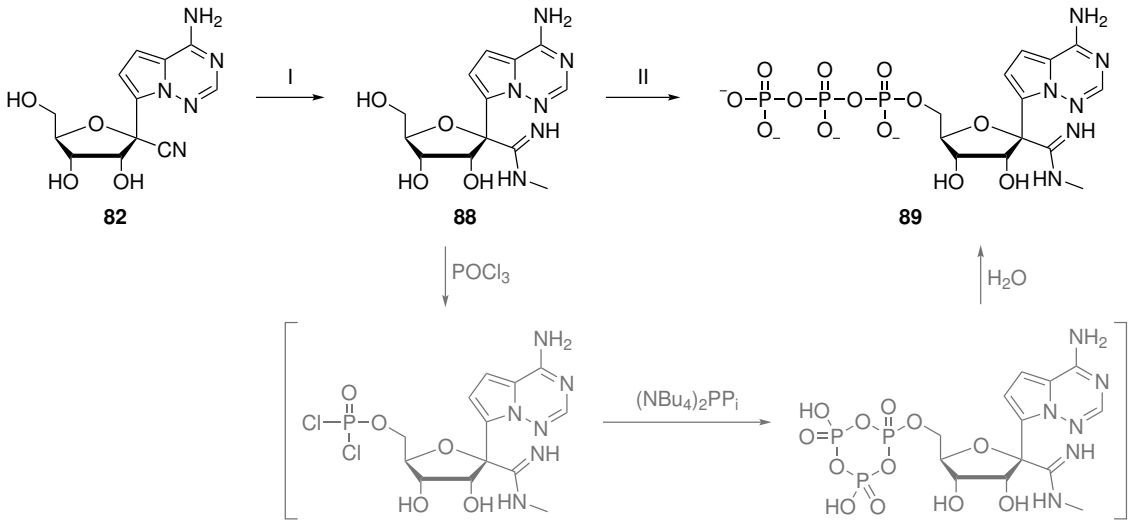

Scheme 3.2: Synthesis of the RTP derivative **89** bearing a C1'-methylamidine substituent. Relevant intermediates of the triphosphate synthesis are shown in gray. I) $MeNH_2$, H_2O, 37 °C, 15 h, quant.; II) $POCl_3$, proton sponge, $(MeO)_3PO$, -20 °C, 3 h, then $(NBu_4)_2PP_i$, NBu_3, DMF, 0 °C, 2 h, then aq. TEAB pH = 7.7, 4%. The product **89** was obtained as triethylammonium salt.

RdRp inhibition by the novel triphosphate was tested by Florian Kabinger in the group of Prof. Dr. Patrick Cramer, Max Planck Institute for Multidisciplinary Sciences Göttingen. In agreement with previous results, RTP incorporation led to formation of a +4 nt stalling product; the translocation barrier was overcome at elevated NTP concentrations (Figure 3.6). When RTP was substituted for triphosphate **89**, no extension of the primer was observed; addition of ATP resulted in extension to the full-length product. These results indicate that the C1'-methylamidine substituent is sterically too demanding to allow for NTP incorporation by the viral RdRp.

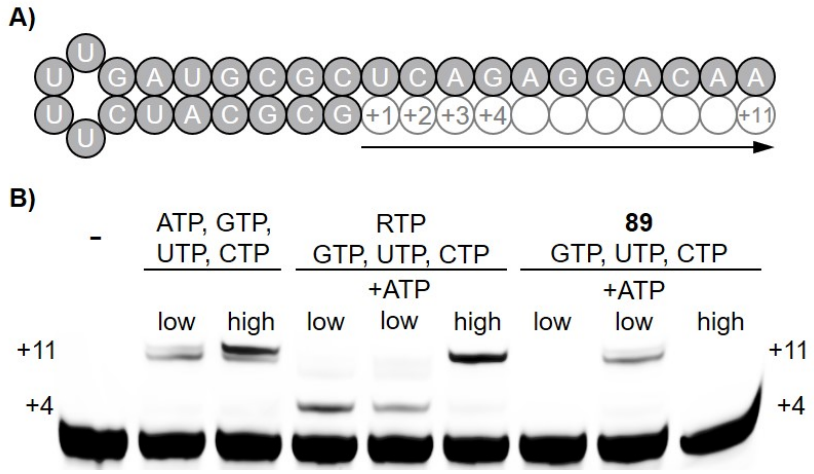

Figure 3.6: Test for RdRp inhibition by the novel triphosphate **89**. A) Primer-template construct used for primer extension experiments. The direction of extension is indicated by an arrow. B) PAGE analysis of primer extension experiments. RdRp complex (3 µM nsp12, 9 µM nsp7, 9 µM nsp8) and RNA scaffold (2 µM) were incubated with low (4 µM) or high (250 µM) NTPs. While RTP induced RdRp stalling at position +4, which was overcome at high NTP concentrations, **89** was not incorporated by the polymerase.

3.2.1.2 1'-Propynyl substitution

Due to the methylamidine substituent being sterically too demanding to be incorporated by the viral RdRp, a linearly extended substituent was considered a promising alternative. Here, compared to the diatomic cyano-substituent of Rem, either an azido- or a propynyl substituent (both being linear 3-atom moieties) were obvious candidates. Since successful installation of the structurally similar ethynyl moiety had already been previously reported, the 1'-propynyl-substituted nucleoside ^{Pro}Rem (**90**) was chosen as the target compound in this work.[55]

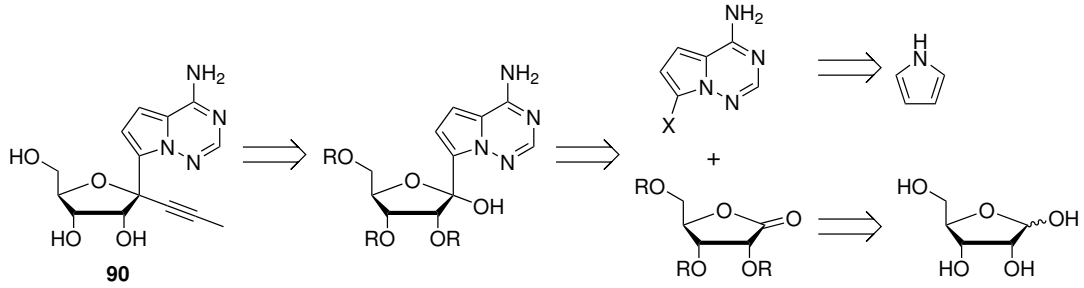

Scheme 3.3: Retrosynthetic strategy for the synthesis of the C1'-propynyl-substituted Rem derivative ^{Pro}Rem (**90**).

The synthetic route toward the target product **90** was designed to introduce the 1'-propynyl group by substitution of a protected 1'-hydroxy precursor (Scheme 3.3). This precursor was

accessible by *C*-glycosylation of a 9-halo-substituted nucleobase with a protected ribonolactone by organometallic coupling. Finally, the ribonolactone was obtainable by conversion of D-ribose, while the nucleobase could be generated in a multistep reaction starting from pyrrole.

Ribonolactone building blocks carrying either benzyl (Bn) or TBDMS protecting groups were synthesized starting from commercially available D-ribose (Scheme 3.4). The benzyl-protected ribonolactone **92** was generated by modification of a procedure reported by Bouton *et al.*[238] First, the anomeric hydroxy group was acetylated, followed by benzylation of the three remaining free hydroxy functions in presence of a catalytic amount of tetrabutylammonium iodide (TBAI). After acidic hydrolysis of the ester moiety at C1', the resulting hemiacetal was converted to the lactone **92** by Albright-Goldman oxidation, using a combination of dimethyl sulfoxide (DMSO) and acetic anhydride as oxidant. By careful control of the reaction conditions, chromatographic purification of intermediates, as described in literature, could be omitted and substituted by washing or extraction procedures. This refined workflow gave rise to an improved product yield (55% vs. 43% reported). The acetyl chloride used for protection of the anomeric OH was used in deficit, according to the reported procedure. Thus, the yield might be further improved by increasing the amount of AcCl to an equimolar amount to ensure complete protection and to reduce formation of byproducts in the following reaction steps.

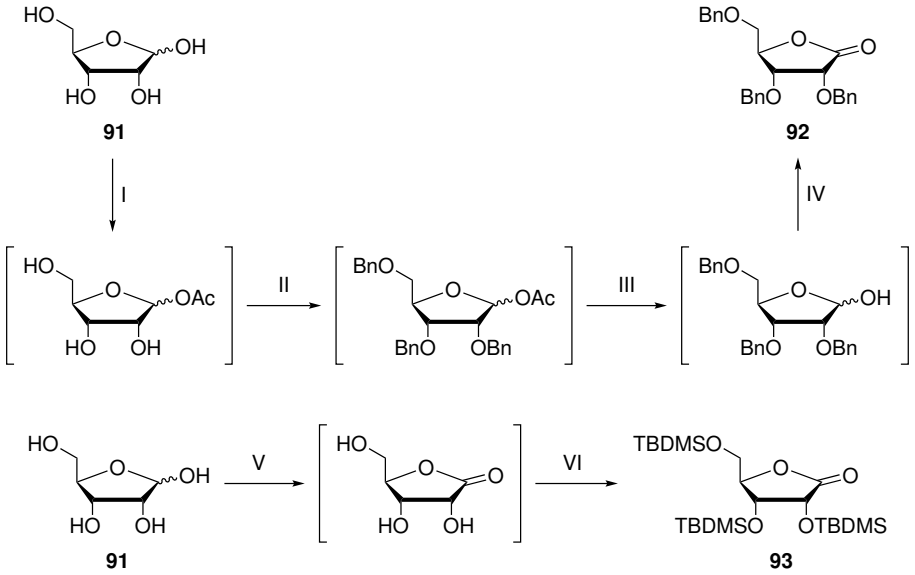

Scheme 3.4: Synthetic routes toward the protected ribonolactone products **92** and **93**. I) AcCl, MeOH, rt, 16 h; II) BnBr, NaH, TBAI, DMF, 0 °C to rt, then rt, 16 h; III) AcOH, H_2O, 110 °C, 16 h; IV) DMSO, Ac_2O, rt, 16 h, 55% over 4 steps; V) Br_2, $NaHCO_3$, H_2O, 0 °C to rt, then rt, 3 d; VI) TBDMSCl, imidazole, DMF, rt, 16 h, 27% over 2 steps.

For generation of the TBDMS-protected ribonolactone **93**, D-ribose was first oxidized to the corresponding lactone using a basic aqueous solution of bromine, followed by silylation of the three hydroxy groups.[239] Due to quenching of the bromine-mediated oxidation by addition of aqueous $Na_2S_2O_3$ solution, a considerable amount of salts was carried over into the second reaction step, as the intermediary unprotected ribonolactone is well water-soluble and could not be conveniently extracted from the aqueous solution. This impurity of the intermediate may contribute heavily to the low overall yield of the reaction.

Several different synthetic strategies to access the Rem nucleobase pyrrolo[2,1-*f*][1,2,4]triazin-4-amine (**101**) have been previously reported. While all of them obtain the nucleobase by condensation of *N*-amino-2-cyanopyrrole (**96**) and formamidine acetate, the routes toward **96** strongly differ. The original synthesis, published by Patil *et al.* (Scheme 3.5A), relied on treatment of pyrrole-2-carboxaldehyde (**94**) with hydroxylamine-*O*-sulfonic acid, which resulted in formation of *N*-aminated cyanopyrrole (**96**) alongside unsubstituted cyanopyrrole (**95**).[240]

In an alternative route, as patented by Bayer Healthcare (Scheme 3.5B), reaction of 2,5-dimethoxytetrahydrofuran (**97**) with *tert*-butyl carbazate yielded a protected *N*-aminopyrrole derivative (**98**). Following introduction of the cyano group using chlorosulfonyl isothiocyanate, acidic deprotection yielded product **96**.

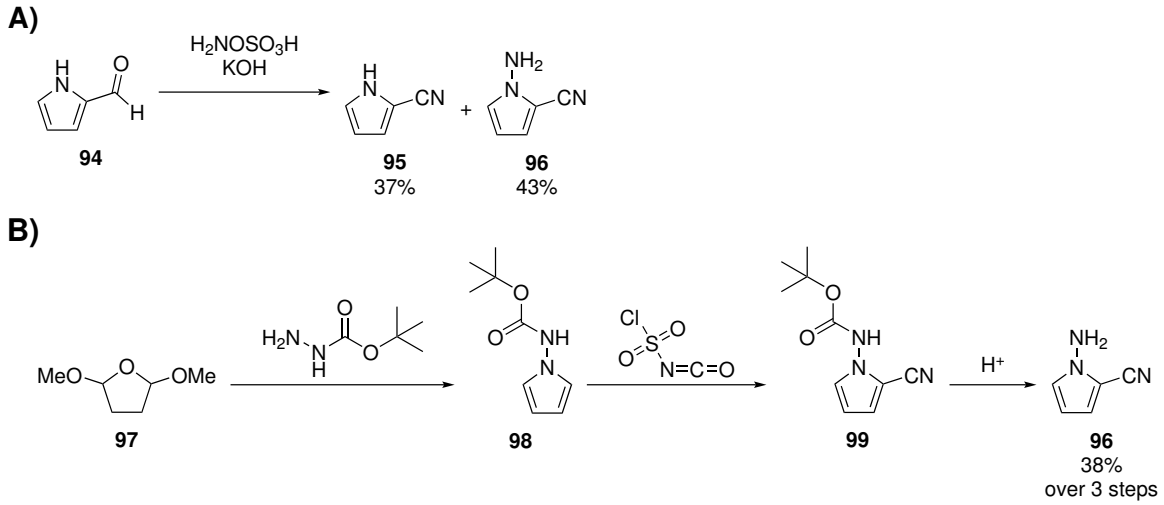

Scheme 3.5: Previously published synthetic routes toward *N*-amino-2-cyanopyrrole (**96**). A) Original route, starting from pyrrole-2-carboxaldehyde (**94**).[240] B) Synthesis using 2,5-dimethoxytetrahydrofurane (**97**) as starting material.[241]

Besides being rather low-yielding, both routes rely on sophisticated, costly reagents. Therefore, for this project a recently developed, improved procedure was adopted.[242] Starting

from commercially available, inexpensive pyrrole, a one-pot oxidative Vilsmeyer-Haack cascade (Scheme 3.6) was used to install the cyano group at C2. Treatment of pyrrole with Vilsmeyer reagent, generated from DMF and $POCl_3$, followed by hydrolysis yielded aldehyde **94** *in situ*. Subsequent addition of hydroxylamine and acetic anhydride resulted in formation of an acetylated aldoxime, which yielded the nitrile product **95** upon release of acetate under basic conditions. Further *N*-amination of 2-cyanopyrrole (**95**) with NaH and a solution of *in situ* generated chloramine yielded intermediate **96** *in situ*, which was directly condensed with formamidine acetate to obtain the pyrrolotriazine nucleobase.[242] The required chlor-amine was obtained by reaction of NH_4Cl and NaOCl in aqueous ammonia and the NH_2Cl gas was extracted into methyl *tert*-butyl ether (MTBE) to obtain an ethereal solution, the concentration of which had been reported to be on average ca. 0.74 M.[242] Due to the relatively low concentration, a large volume of ethereal chloramine solution would be required to provide the optimal 4-fold excess of chloramine over the pre-formed sodium cyanopyrrolide salt; however, the reaction yield was shown to drop with decreasing reactant concentration.[242] Thus, the NH_2Cl solution was added in four batches: after addition of 1 eq. of chloramine solution and reaction for 30 min, the ether was removed by distillation before another chloramine batch was added. This procedure allowed the use of excess chloramine without major dilution of the reaction mixture with MTBE. Providing the product nucleobase **101** in a combined yield of 44% over three steps (starting from pyrrole), the chosen synthetic route presents a major improvement over the two classical synthetic pathways outlined in Scheme 3.5.

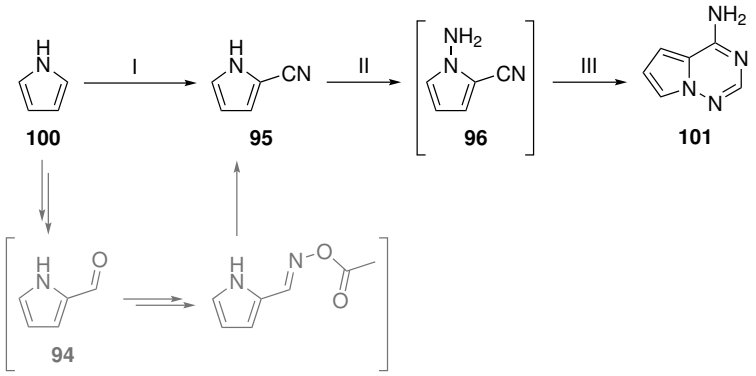

Scheme 3.6: Synthesis of the Rem nucleobase (**101**). I) DMF, $POCl_3$, 0 °C to rt, then rt, 1 h, then H_2O, 0 °C, 1 h, then $H_2NOH{\cdot}HCl$, Ac_2O, pyridine, 90 °C, 3 d, then H_2O, rt, 15 min, 75%; II) NaH, MTBE, 0 °C to rt, then rt, 30 min, then DMF, NH_2Cl, MTBE, 3 × 30 min; III) formamidine acetate, DMF, 120 °C, 48 h, 58% over 2 steps. Key intermediates of the oxidative Vilsmeyer-Haack cascade are included in grey.

Methods for *C*-glycosylation of Rem nucleobase **101** and ribonolactone **92** have been first reported in 2010; three generations of improved synthetic routes have been developed since

(Scheme 3.7). The first generation utilized the 9-bromo nucleobase **102**, which was *in situ* TMS-protected and coupled to the ribose *via* an organolithium intermediate to yield the nucleoside **103** in a low yield of 25%.[243] Substituting the TMS groups for the more stable cyclic 1,2-bis(chlorodimethylsilyl)ethane (BCDSE) protecting group resulted in a greatly improved yield due to reduced quenching of the organolithium species by unprotected amino groups.[55,244]

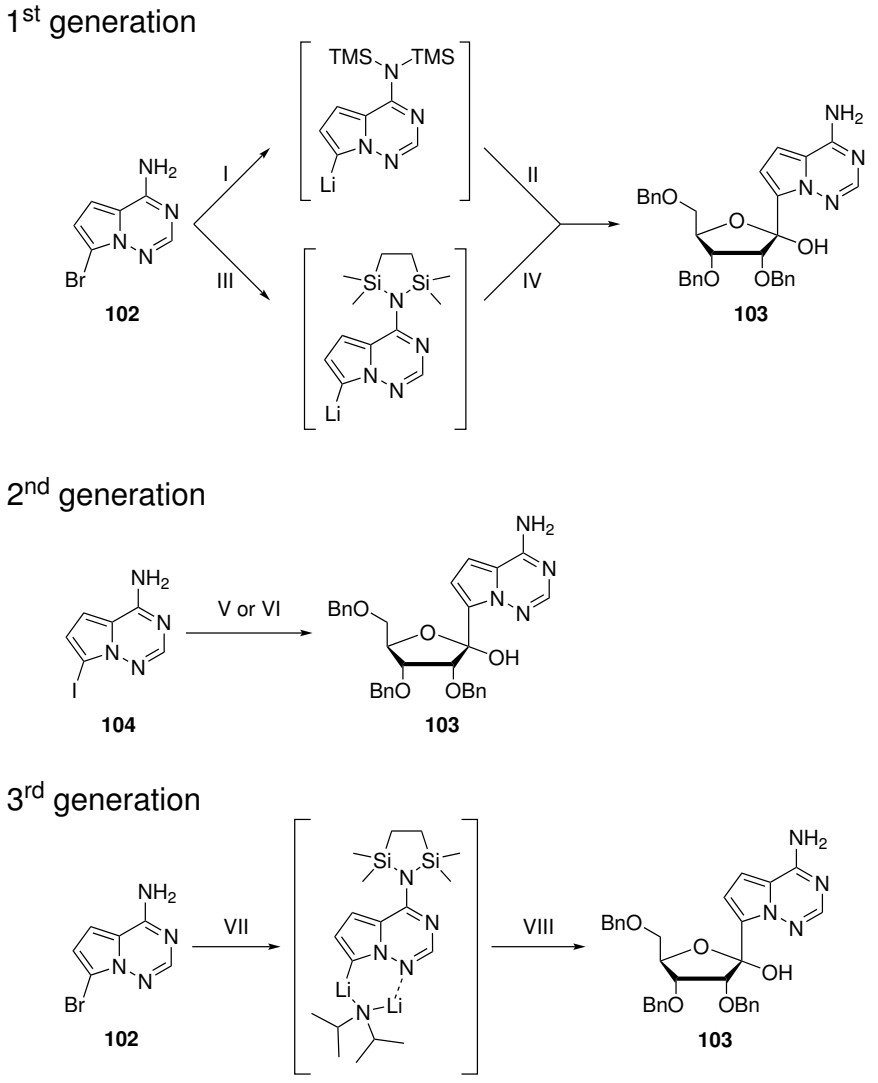

Scheme 3.7: Three generations of reported *C*-glycosylation procedures for the synthesis of Rem nucleoside.[55,226,243–247] I) TMSCl, THF, rt, 20 min, then *n*-BuLi, *n*-hexane, -78 °C, 10 min; II) **92**, THF, 25 % over 2 steps; III) BCDSE, NaH, *n*-BuLi, THF, -78 °C, IV) **92**, -78 °C, 1 h, 60 % over 2 steps; V) TMSCl, THF, rt, 10 min, then PhMgCl, THF, 0 °C, 20 min, then *i*-PrMgCl, THF, 0 °C, 15 min, then **92**, THF, -20 °C, 1 h, 41%; VI) TMSCl, THF, 0 °C, 30 min, then PhMgCl, THF, -10 °C, 30 min, then *i*-PrMgCl, THF, -20 °C, 2 h, then **92**, $NdCl_3$, NBu_4Cl, THF, -20 °C, 8 h, 69%; VII) BCDSE, THF, rt, 10 min, then *i*-Pr_2NH, rt, 5 min, then 0 to -78 °C, 20 min, then *n*-BuLi, *n*-hexane, -78 °C, 45 min; VIII) **92**, THF, -78 °C, 2 h, 74% over 2 steps.

The second generation synthesis utilized an iodinated nucleobase derivative (**104**) to facilitate metal-halogen exchange and converted the nucleobase into a Grignard reagent for glycosylation, thus avoiding the requirement for cryogenic temperatures encountered in organolithium-mediated glycosylation.[226] In this procedure, the product yield could be enhanced by addition of $NdCl_3$ and NBu_4Cl, which agreed with previous reports about lanthanide trichlorides activating carbonyl functions to facilitate addition of organometallic reagents.[245,248]

Finally, the third generation achieved high glycosylation yields *via* organolithium-mediated coupling while employing bulky secondary amines, such as diisopropylamine, as additives to stabilize the organolithium species.[246] As an alternative route, also the synthesis of **103** *via* Grignard addition has recently been revised and improved. Conversion of ribonolactone **92** into a Weinreb amide prior to coupling of the C9-iodinated nucleobase reduced side reactions, such as the deiodination of the nucleobase and overaddition of two nucleobase moieties to one ribonolactone; an improvement in yield compared to the third generation synthesis was, however, not achieved.[247]

In order to directly compare the performances of the reported second and third generation procedures, both the C9-brominated and iodinated nucleobase derivatives were synthesized by treatment of Rem nucleobase **101** with the respective *N*-halosuccinimide (Scheme 3.8). At 0 °C, high yields of C9-substituted product were obtained, while higher temperatures led to increasing formation of dihalogenated byproducts.

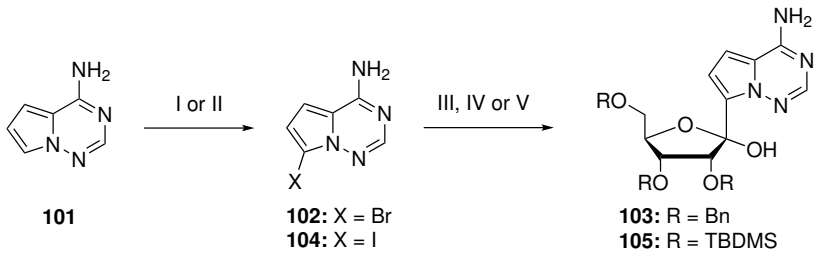

Scheme 3.8: Halogenation and *C*-glycosylation of the Rem nucleobase **101**. I) NBS, DMF, 0 °C, 3 h, 93% (for **102**); II) NIS, DMF, 0 °C, 3 h, 90% (for **104**); III) BCDSE, THF, rt, 10 min, then *i*-Pr_2NH, rt, 10 min, then *n*-BuLi, *n*-hexane, -78 °C, 45 min, then **92**, -78 °C, 2 h, 59% (for **103** from **102**); IV) TMSCl, THF, rt, 10 min, then PhMgCl, THF, 0 °C, 20 min, then *i*-PrMgCl·LiCl, THF, 0 °C, 15 min, then **92**, THF, -20 °C, 2 h, 23% (for **103** from **104**); V) BCDSE, THF, rt, 10 min, then *i*-Pr_2NH, rt, 10 min, then *n*-BuLi, *n*-hexane, -78 °C, 45 min, then **93**, -78 °C, 2 h, 60% (for **105** from **102**).

C-Glycosylation reactions using these two nucleobases confirmed the superiority of the organolithium-mediated coupling reported by Xue *et al.* over the second generation Grig-

nard approach.[226,246] While the Grignard reaction yielded only 23% of nucleoside **103**, coupling of the BCDSE-protected 9-bromo nucleobase in presence of diisopropylamine resulted in more than doubled product yield (Scheme 3.8). Comparable yield was obtained for organolithium-mediated glycosylation using the tri-*O*-TBDMS-protected ribonolactone **93**. The fluoride-lability of TBDMS-groups was envisioned to provide a more facile and convenient means of nucleoside deprotection after introduction of the 1'-propynyl group, as compared to the relatively stable benzyl groups employed in the original remdesivir synthesis.

In the reported procedures for the preparation of remdesivir, the 1'-cyano substituent was introduced by an S_N1-type substitution of the 1'-hydroxy group of nucleoside **103** using TMSCN as cyanide source. Several Lewis and Brønstedt acids were tested for activation of the substrate, with a mixture of TMSOTf and TfOH providing the highest product yield and anomeric selectivity.[244,245] In general, lower reaction temperatures and (for Brønstedt acids) increasing acid strength led to higher yields and increased β-selectivity.

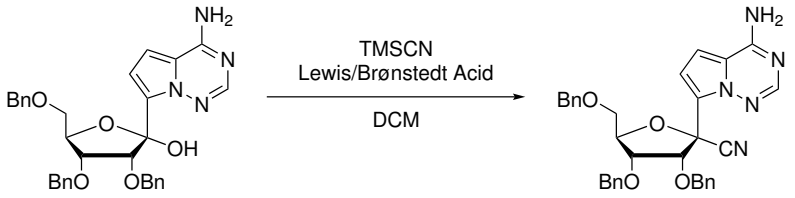

103 **106**

Lewis/Brønstedt Acid	Temperature [°C]	Yield [%]	Anomeric Ratio (β:α)
$BF_3{\cdot}Et_2O$	-78	58	85:15
TMSOTf, HCOOH	-15	17	66:34
TMSOTf, TFA	-15	63	85:15
TMSOTf, TFA	-30	95	93: 7
TMSOTf, TfOH	-15	45	71:29
TMSOTf, TfOH	-78	94	96: 4

Scheme 3.9: Reported reaction yields and anomeric selectivities for 1'-cyanation reactions mediated by different Lewis or Brønstedt acid systems.[244,245]

Using these described conditions, however, introduction of a propynyl group at C1' using TMS-propyne showed not to be possible. While at -78 °C in presence of TMSOTf and TfOH the propynyl moiety was not nucleophilic enough to achieve substitution, higher temperature (-20 °C) led to gradual decomposition of the starting material due to acidic deprotection of the benzyl groups. Likewise, reaction of **103** with TMS-propyne and BF_3-diethyletherate at 0 °C solely led to substrate decomposition instead of propynylation. Changing the Lewis acid to AgOTf minimized substrate decomposition; yet, no propynylation was observed even

at ambient temperature.

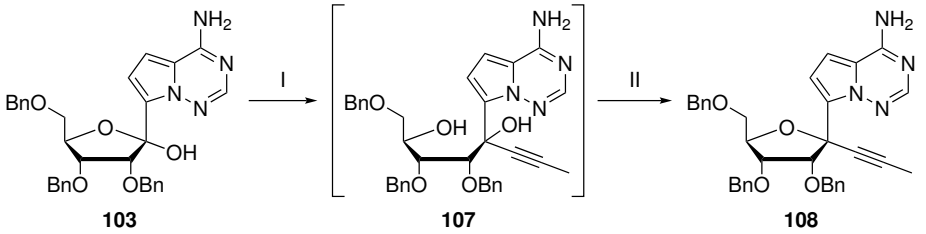

Scheme 3.10: Synthetic route toward nucleoside **108**, introducing the propynyl substituent by nucleophilic addition of an organolithium species. I) 1,2-dibromopropane, LDA, THF, -78 °C to rt, then rt, 16 h; II) MsOH, DCM, rt, 15 min, 42 % over 2 steps.

As introduction of the propynyl substituent *via* S_N1 reaction was not successful, it was introduced by addition of an organometallic reagent at C1' (Scheme 3.10). Reaction of 1-propynyllithium, which was generated *in situ* from 1,2-dibromopropane and lithium diisopropylamide (LDA) *via* two consecutive eliminations of HBr, with nucleoside **103** resulted in formation of intermediate **107**, bearing a ring-opened ribose moiety. Without further purification, the ribose was subsequently re-cyclized upon dehydration in presence of a strong acid. Here, the reaction conditions had to be chosen carefully: while weaker acids, such as TFA and AcOH, were not suitable to induce dehydration, prolonged exposure to methanesulfonic acid (MsOH) led to product decomposition. As cyclization and decomposition were competing reaction pathways, only moderate yields of propynylated product **108** were obtained.

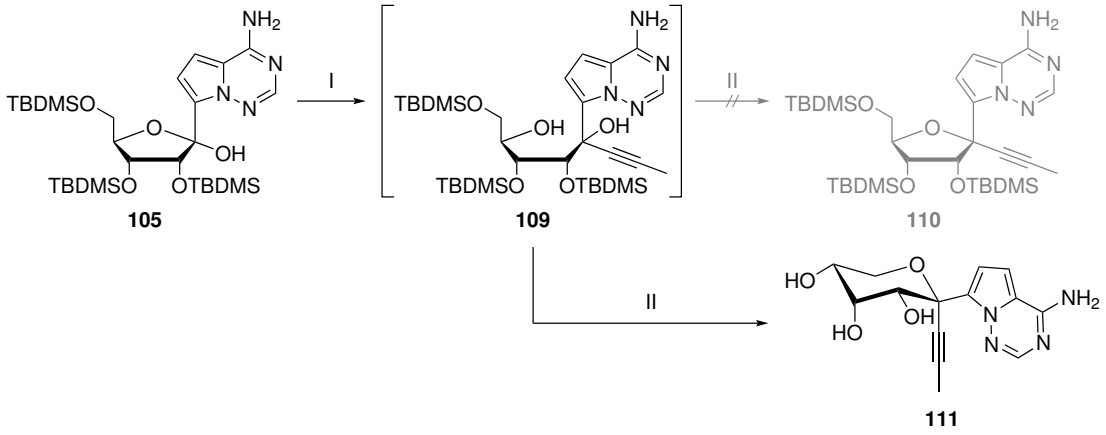

Scheme 3.11: 1'-Alkynylation of the tri-*O*-TBDMS-protected nucleoside **105** with 1-propynyllithium. Acidic ring closure did not yield the desired product **110** but the deprotected ribopyranoside **111**. I) I) 1,2-dibromopropane, LDA, THF, -78 °C to rt, then rt, 16 h; II) MsOH, DCM, rt, 15 min.

Adaption of the same strategy for propynylation of the tri-*O*-TBDMS-protected nucleoside **105**, in contrast, was not successful. While treatment of **105** with *in situ* generated

1-propynyllithium resulted in formation of the ring-opened intermediate **109**, this species could not be cyclized under acidic conditions to yield nucleoside **110** (Scheme 3.11). Instead, treatment with MsOH led to rapid cleavage of the TBDMS protecting groups. As a consequence, not the 4'-OH but the, now deprotected, more nucleophilic 5'-hydroxy group attacked at C1', which resulted in formation of the ribopyranoside product **111**. The six-membered ribopyranose ring could be unambiguously identified by the ^{1}H-^{1}H-COSY correlation between C4'-H and the adjacent C4'-OH, while the two protons at C5' did not show any correlation with a neighboring hydroxy group (Figure 3.7).

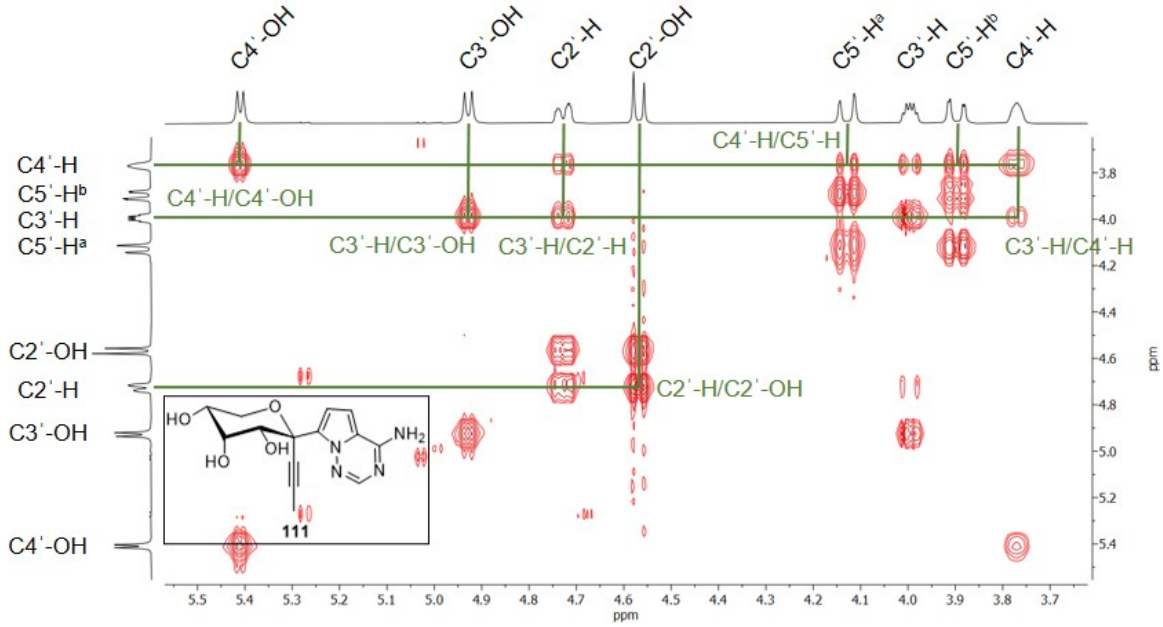

Figure 3.7: ^{1}H-^{1}H-COSY spectrum of the ribopyranoside **111**, recorded in DMSO-d_6. The relevant cross-peaks displaying the connectivity of the ribose atoms are highlighted. The presence of a 4'-OH group, showing a cross-peak with the adjacent C4'-H, and the absence of a 5'-OH identify the pyranose form of the ribose ring.

While removal of benzyl protecting groups is most commonly achieved by hydrogenolysis, this strategy was not applicable for deprotection of nucleoside **108** due to the presence of the reducible 1'-propynyl substituent. Therefore, debenzylation using BCl_3 was attempted, as previously described for Rem and Rem derivatives.[226,241,243,249] Reactions at -78 °C or -20 °C did not lead to any deprotection of the substrate. At higher temperatures conversion was observed; yet, reactions at 0 °C or even ambient temperature using between 4 eq. and up to 10 eq. BCl_3 did not yield fully deprotected nucleoside. Instead, in each case the mass of the resulting product matched a monobenzylated species.

Unexpectedly, NMR spectroscopy of the product showed the presence of hydroxy groups at C3', C4' and C5', which corresponds to a ring-opened isomer of the ribose. Additionally, the benzyl moiety protecting the 2'-oxygen possessed only 4 instead of the expected 5 aromatic protons, all of them being chemically inequivalent. Further analysis based on 2D-NMR spectroscopy led to identification of the product species as nucleoside **112** (Scheme 3.12). Evidently, treatment with BCl_3 at ambient temperature led to C-H activation at the *ortho*-position of the phenyl ring followed by C-C bond formation with C1' concomitant with opening of the ribose ring structure. No similar reactions have been described in literature before, and the structural prerequisites as well as the reaction mechanism are not yet understood.

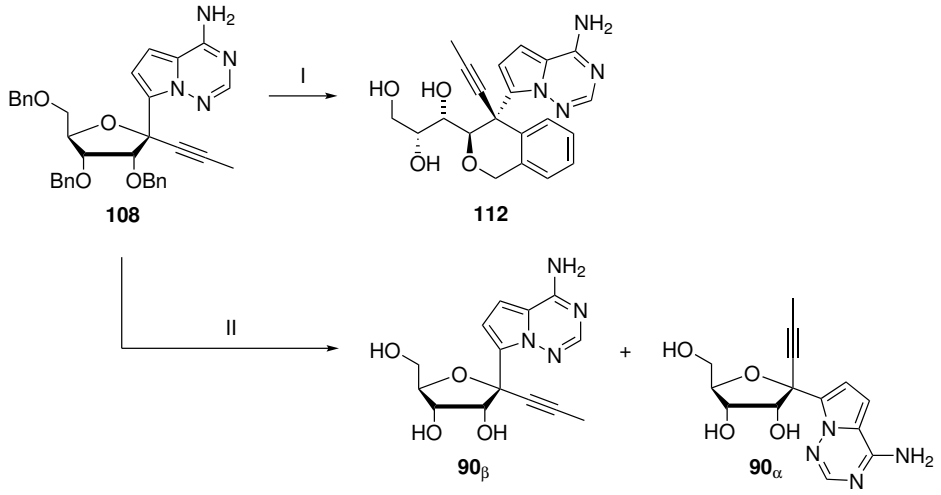

Scheme 3.12: Deprotection of the 1'-propynylated nucleoside **108**. With BCl_3, temperatures $\geq$0 °C were required, which led to formation of compound **112**. Using BBr_3, deprotection at -78 °C without side reactions was possible. I) BCl_3, 0 °C – rt, 2–16 h; II) BBr_3, -78 °C, 2 h.

Exchanging BCl_3 for the more reactive BBr_3 allowed for debenzylation at -78 °C, which prevented CH activation as a side reaction. HPLC-MS analysis of the crude product showed the presence of ^{Pro}Rem (**90**) as a mixture of α- and β-anomer (Figure 3.8) with only minor traces of byproducts (addition products of HBr to the triple bond of **90**). A preparative chromatographic separation of these anomers was, however, so far not achieved. While the analytical RP-HPLC chromatogram showed a convenient separation of the two anomers, the large content of pyridinium salts present in the sample after quenching of the reaction with pyridine/MeOH significantly hampered separation during preparative RP-HPLC; severe peak-broadening and a reduced difference in retention times were observed, which caused the two anomers to coelute. Further optimization of chromatographic conditions or a refined workup strategy to reduce the pyridinium salt content in the sample are required to purify the desired β-anomer for subsequent triphosphorylation and activity tests.

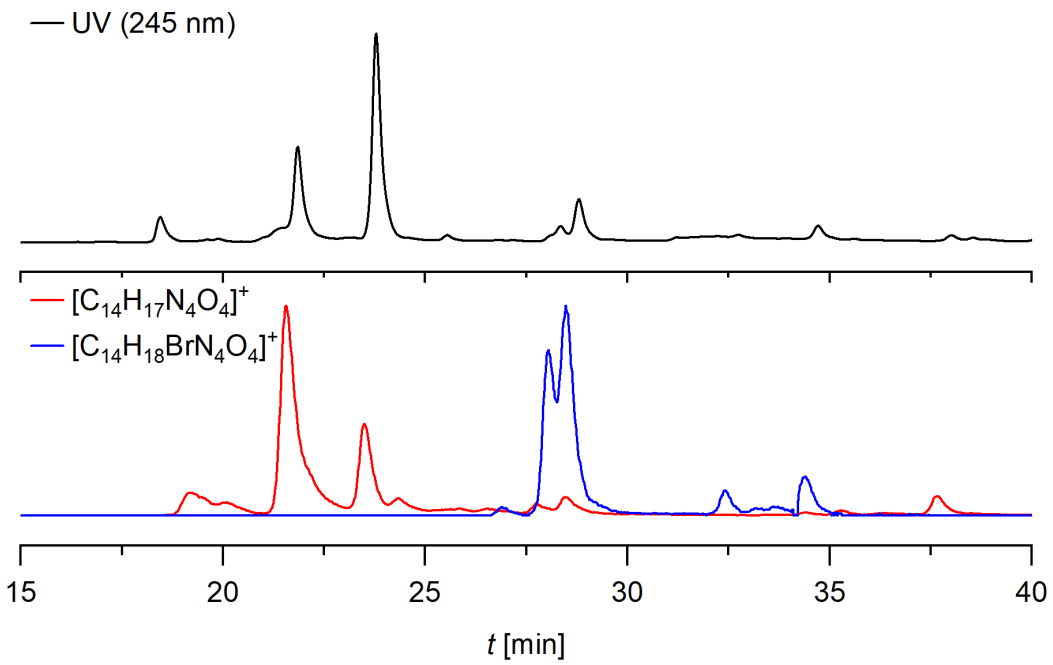

Figure 3.8: HPLC-MS analysis of the crude product obtained from debenzylation of nucleoside **108** with BBr_3 at -78 °C for 2 h. The UV (245 nm) chromatogram (black) is shown stacked on top of the nucleoside $[M+H]^+$ extracted ion chromatograms. Besides the two anomers of the debenzylated product ^{Pro}Rem (**90**, red), addition products of HBr to the triple bond of **90** (blue) are detectable.

3.2.2 Rem derivatives with altered nucleobase structures

The Rem nucleoside as an adenosine analog may be administered as a combination preparation with a derivative resembling the Watson-Crick face of G, C, or U. This way, the possible incorporation sites of NTPs bearing a 1'-cyano group as steric block would be increased, which should lead to more efficient inhibition of the viral RdRp. It was envisioned to adapt the strategy used for the synthesis of the Rem nucleobase (Scheme 3.6) to generate a 2,6-diamino derivative (**113**); subsequent glycosylation and deamination at C6 would yield a Rem analog resembling guanosine (Rem^G, **116**, Scheme 3.13).

As previously described, 2-cyanopyrrole (**95**) was *N*-aminated *in situ* using NaH and chloramine. Reaction of the resulting intermediate **96** with guanidine carbonate under basic conditions at high temperature yielded the 2,6-diamino nucleobase **113**, which was in turn smoothly converted into its 9-iodinated derivative **114**.[240] *C*-Glycosylation of **114** *via* a Grignard reaction, as described for the synthesis of the Rem nucleoside (Scheme 3.8), however, was not successful. In a parallel project in the working group, transformation of **113** into its 9-bromo derivative followed by organolithium-mediated glycosylation succeeded in

low yields; yet, the reaction product was identified as the N3-glycoside instead of the desired C9-glycosylated product.[250]

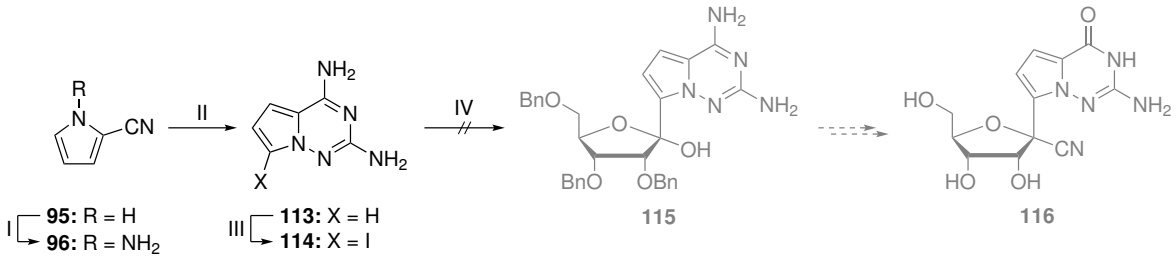

Scheme 3.13: Synthetic route toward a Rem analog resembling guanosine (**116**). Glycosylation of nucleobase **114**, and thus also subsequent deamination and C1'-cyanation, was not successful. I) NaH, MTBE, 0 °C to rt, then rt, 30 min, then DMF, NH_2Cl, MTBE, 3 h, then NH_2Cl, MTBE, 3 × 30 min; II) guanidine carbonate, NEt_3, EtOH, 125 °C, 65 h, 47% over 2 steps; III) NIS, DMF, 0 °C, 3 h, 72%; IV) TMSCl, THF, rt, 10 min, then PhMgCl, THF, 0 °C, 20 min, then *i*-PrMgCl·LiCl, THF, 0 °C, 15 min, then **92**, THF, -20 °C, 20 h.

As an alternative to the unsuccessful route *via* 2,6-diamino nucleoside **115**, the guanosine analog of Rem (**116**) may be accessible by synthesis of the nucleobase (**118**) according to a published procedure followed by *C*-glycosylation (Scheme 3.14).[240]

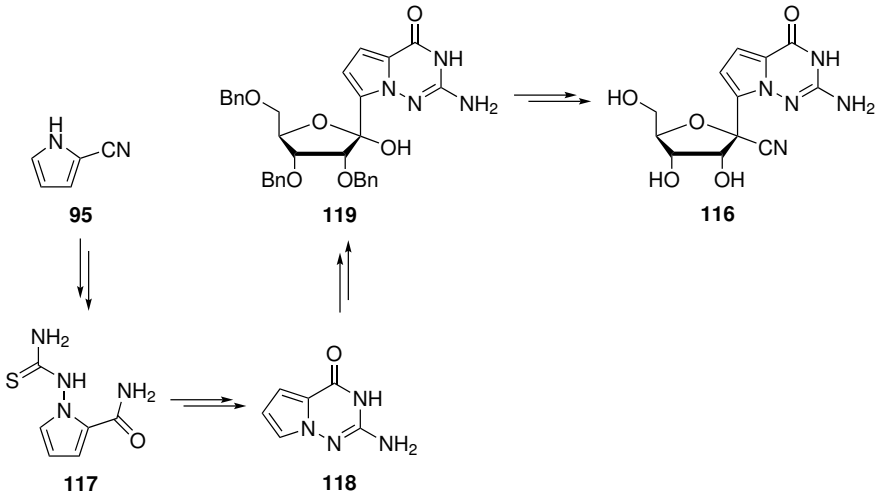

Scheme 3.14: Potential alternative route toward a guanosine analog of Rem (**116**) involving synthesis of the nucleobase **118** according to a reported procedure followed by Grignard- or organolithium-mediated *C*-glycosylation and 1'-cyanation.[240]

Yet, since this route would involve more than 10 steps starting from 2-cyanopyrrole, the focus was instead shifted to an inosine analog of Rem (Rem^I, **120**) as a derivative able to base-pair with template cytidine. Rem nucleoside **82** was deaminated in analogy to a procedure previously reported for chemical A-to-I editing: diethylene glycol dinitrite (DEGDN,

123) was used to convert **82** into a diazonium salt, which was hydrolyzed to **120** upon release of molecular nitrogen (Scheme 3.15).[251]

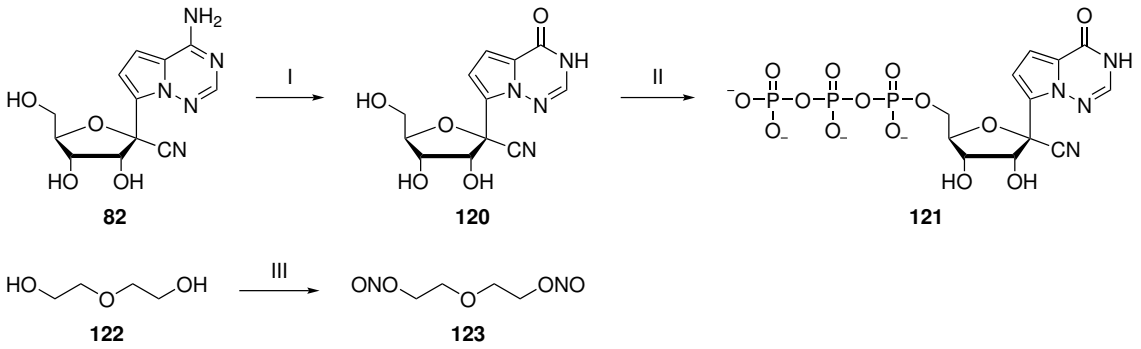

Scheme 3.15: Synthetic route toward the nucleoside triphosphate **121** and synthesis of the required deaminating reagent DEGDN (**123**). I) DEGDN, KSCN, pyridine, H_2O, 37 °C, 4 h, 99%; II) $POCl_3$, $(MeO)_3PO$, 0 °C, 3 h, then $(NBu_4)_2PP_i$, NBu_3, MeCN, 0 °C, 3 h, then aq. TEAB pH = 7.5, 20%. The product **121** was obtained as triethylammonium salt and further converted into lithium salt by precipitation from MeOH with $LiClO_4$ in acetone. III) $NaNO_2$, HCl, H_2O, 5 °C, 5 min, 44%.

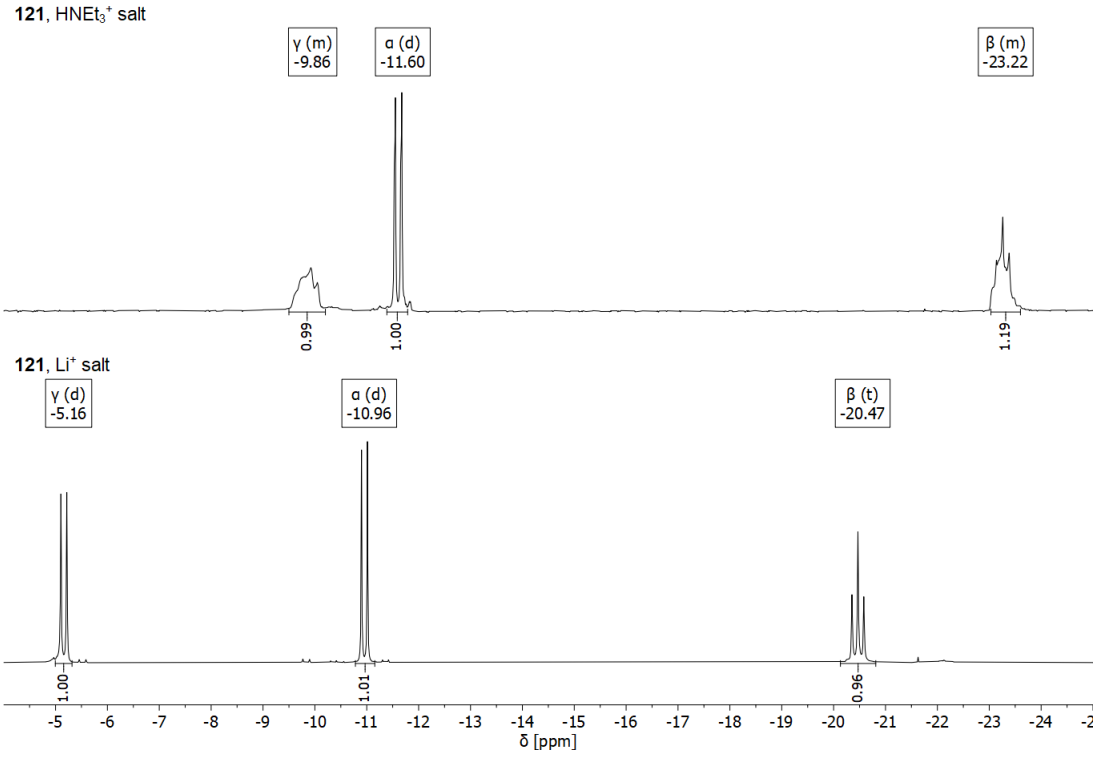

Figure 3.9: $^{31}P\{^1H\}$ NMR spectra (162 MHz, D_2O) of Rem^I triphosphate **121** as triethylammonium salt (top) and lithium salt (bottom). The successful cation exchange is evident by changes in the chemical shifts of the signals. While the signals in the top spectrum are not well resolved, the bottom spectrum clearly shows the typical signal multiplicities (d, d, t for γ-, α- and β-phosphate, respectively) of nucleoside triphosphates.

3.3 Spectroscopic properties of Rem and its derivatives

Besides being a valuable pharmacochemical tool due to its antiviral properties, the Rem nucleoside also features interesting spectroscopic characteristics. The pyrrolotriazine nucleobase provides a greatly increased molar extinction coefficient as well as a blue-shifted absorption maximum compared to the structuraly similar canonical adenosine (Figure 3.10, Table 3.3). Deamination of Rem leads to a 25% decrease of the extinction coefficient and a blue-shift of 13 nm, which is similar to the spectral changes observed upon A-to-I conversion ($\Delta\epsilon_{max}$ = -18%, $\Delta\lambda_{max}$ = -11 nm).

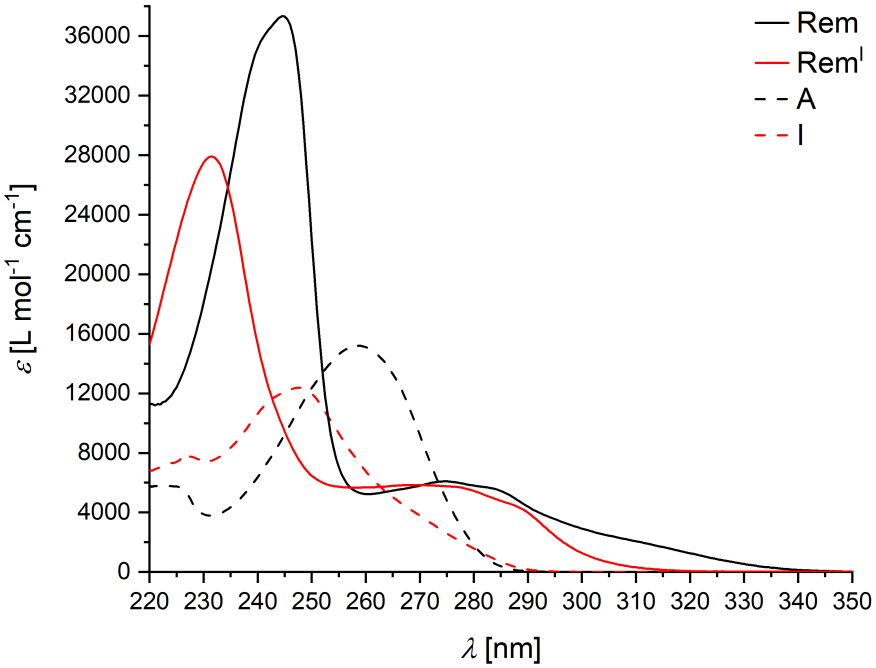

Figure 3.10: UV/Vis absorption spectra of Rem and its deaminated derivative Rem^{I} (solid lines), recorded in water. Spectra of their naturally occuring purine nucleoside analogs A and I (dashed lines) are included for comparison.

Table 3.3: Absorption maxima λ_{max} and molar extinction coefficients at the absorption maximum (ϵ_{max}) and at 260 nm (ϵ_{260}). Values are given as mean ± s.e.m of triplicates.

No.	Nucleoside	λ_{max} [nm]	ϵ_{max} [L·mol^{-1}·cm^{-1}]	ϵ_{260} [L·mol^{-1}·cm^{-1}]
82	Rem	245	37320 ±800	5210 ±120
120	Rem^{I}	231	27880 ±880	5670 ±180

Unlike canonical adenosine, the Rem nucleoside is fluorescent, with its excitation maximum laying at 245 nm and its emission maximum at 418 nm (Figure 3.11A).

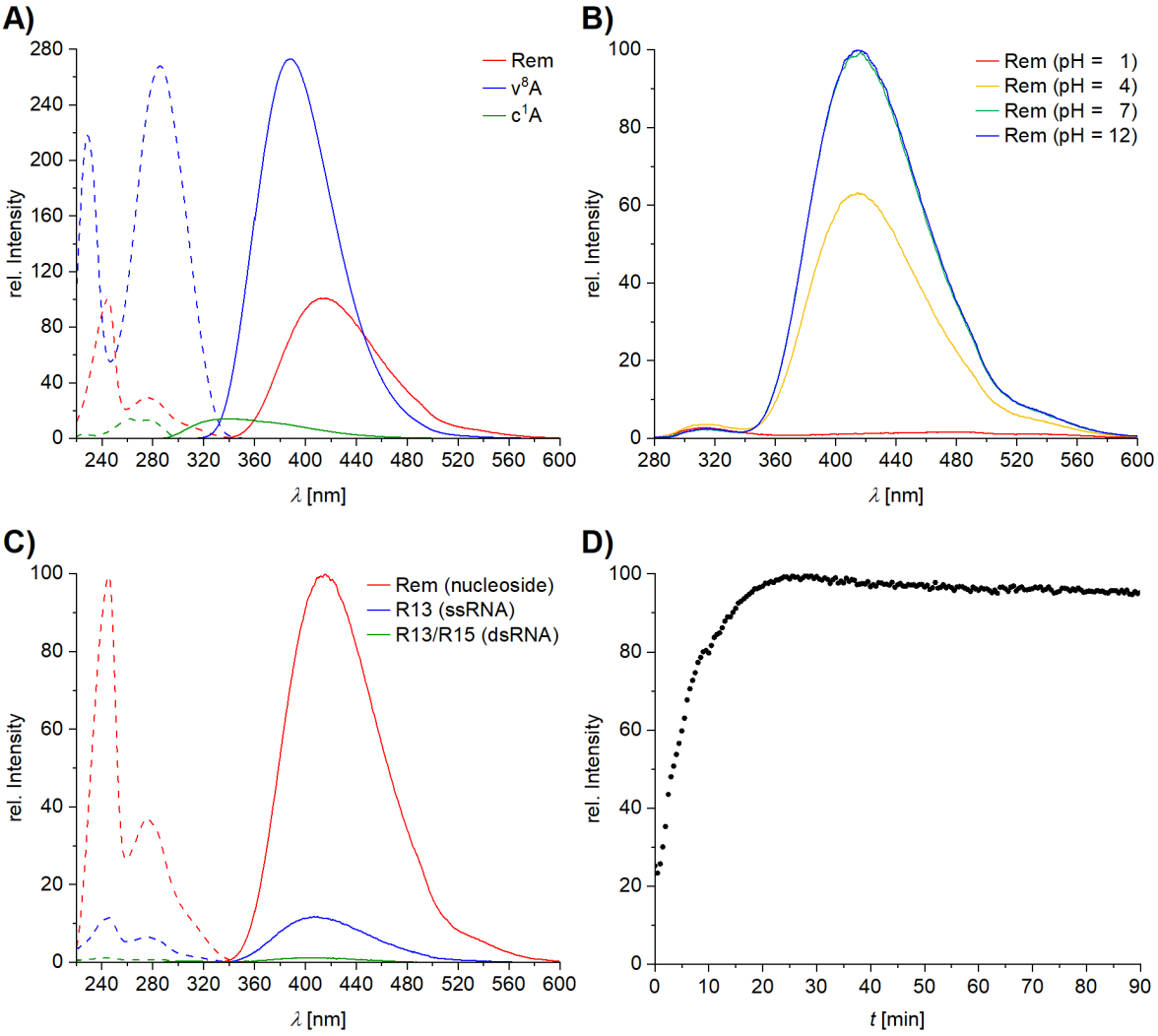

Figure 3.11: Fluorescent properties of Rem. A) Excitation (dashed lines) and fluorescence emission (solid lines) spectra of Rem, v^8A and c^1A. Spectra were recorded at the respective excitation or emission maxima (Rem: 245/418 nm; v^8A: 285/388 nm; c^1A: 261/339 nm). Intensities are given relative to Rem intensity (set to 100). B) Fluorescence emission spectra (λ_{ex} = 245 nm) of Rem in Britton-Robinson buffer at different pH values. Intensities are given relative to neutral pH (set to 100). C) Excitation (dashed lines) and emission (solid lines) spectra of Rem as free nucleoside as well as incorporated inside a 15-mer ssRNA oligonucleotide (**R13**) or RNA duplex (**R13/R15**). Spectra were recorded at the respective excitation or emission maximum (245/418 nm). Intensities are given relative to the intensities of free Rem nucleoside (set to 100). D) Time-course measurement of the fluorescence emission intensity (λ_{ex} = 245 nm; λ_{em} = 418 nm) during digestion of **R13** (2 µM) with SVPD (2 U/mL) in presence of $MgCl_2$ (6 mM). The maximum observed intensity was normalized to 100.

The fluorescence intensity of Rem is 14-fold higher than that of the fluorescent adenosine analog c^1A discussed in Part I, Section 3.1.2. As the established fluorescent nucleoside v^8A exceeds the emission intensity of Rem only by a factor of 2.6, Rem may be an interesting candidate to be evaluated regarding *in vitro* and *in vivo* applications. A notable feature in

this regard is a high environmental sensitivity of Rem fluorescence. Firstly, Rem is solely fluorescent in its neutral state and loses its emissive character upon protonation. Thus, emission intensity decreases with pH when below its pK_a value (Figure 3.11B), which might offer applications as fluorescent sensor of local acidities. Secondly, fluorescence is lost completely upon deamination yielding Rem^I. Therefore, Rem or derivatives featuring the same nucleobase structure may be used for monitoring activity and reaction kinetics of adenosine deaminase enzymes acting on the adenosine nucleoside (ADA), adenosine in RNA (ADAR) or adenosine in tRNA (ADAT), which are key enzymes in cellular purine metabolism and RNA editing.[252–254] Furthermore, the fluorescence of Rem is quenched by a factor of 10 upon incorporation into ssRNA and by a further factor of 10 upon duplex formation (Figure 3.11C). This sensitivity makes Rem and derivatives thereof interesting candidates for reporters of helicase or nuclease activities. As proof of principle, digestion of a Rem-containing ssRNA oligonucleotide (**R13**) by the 3^I-to-5^I-exonuclease SVPD was monitored by fluorescence spectroscopy (Figure 3.11). Emission intensity at 418 nm increased with progressing release of RMP from the oligonucleotides and reached a plateau upon complete digestion of the sample. This demonstrates the correlation between Rem fluorescence and oligonucleotide digestion and shows that Rem may be used as a fluorescent probe to monitor exonuclease activity.

4 Summary and Outlook

In the second part of this thesis, the antiviral mechanism of the nucleoside-based drug remdesivir was investigated, which acts as an inhibitor of the RNA-dependent RNA polymerase (RdRp) of SARS-CoV-2. The central nucleoside moiety of remdesivir, termed Rem, was converted into phosphoramidite building blocks, which were site-specifically incorporated into RNA oligonucleotides. This strategy allowed for the generation of homogenous and structurally well-defined RNA oligonucleotides bearing the Rem nucleoside at defined positions. The synthesis of RNA with a single internal Rem cannot be accomplished by *in vitro* transcription using Rem triphosphate (RTP). The synthetic RNAs were used by collaborators for the elucidation of RNA-RdRp complex structures *via* cryogenic electron microscopy (Cryo-EM). While scaffolds bearing Rem at position -3 or A at position -4 in the primer strand were observed in the post-translocated state, Rem at position -4 resulted in a structure representing the pre-translocated state. Thus, Rem-induced RdRp stalling is caused by inhibition of the polymerase translocation process. A steric clash between the 1'-cyano substituent of Rem and the side chain of Ser861 in the polymerase was identified as the underlying molecular mechanism.

As the steric translocation barrier was found to be overcome at elevated NTP concentrations, further focus was placed on the development of novel derivatives of Rem with potentially improved antviral properties. The two strategies employed here centered around the variation of either the nucleobase structure or the 1'-substituent. In the course of this thesis, three Rem analogs were generated. Firstly, a Rem derivative comprising a 1'-methylamidine substituent was synthesized, converted into a nucleoside triphosphate and subjected to *in vitro* activity tests by collaborators. In initial experiments, this triphosphate was not accepted as a substrate by the viral RdRp. Secondly, an RTP analog resembling inosine was generated, which will be tested for incorporation by the RdRp as a guanosine analog. Finally, a Rem derivative bearing a 1'-propynyl substituent was synthesized. Here, the product was obtained as a mixture of α- and β anomers, which need to be separated for further investigation.

Future directions of research may focus on the refinement of the procedures for synthesis and purification of Rem and RTP derivatives established so far, thereby facilitating synthetic access to further potential antiviral nucleoside candidates. *In vitro* activity screening will reveal their utility as therapeutic agents to combat SARS-CoV-2 and related viruses. Overall, the novel insights gained from this work may aid the development of second gen-

eration remdesivir derivatives with improved antiviral properties.

Additionally, the spectroscopic properties of the Rem nucleoside were investigated. Rem was found to fluoresce with an intensity similar to the established fluorescent nucleoside 8-vinyladenosine (v^8A). The fluorescent emission is highly environment-sensitive, decreasing significantly at acidic pH, upon nucleobase deamination as well as upon incorporation of the nucleoside into oligonucleotides or RNA duplex structures. Rem is therefore a promising lead structure for fluorescent probes, which deserves further detailed investigation. Possible applications include pH sensoring as well as probing enzymatic activities of helicases, adenosine deaminases and nucleases.

Experimental Section

5 Chemical Synthesis

5.1 General methods

Reagents used for synthesis were purchased in 'pro analysis' or 'pro synthesis' quality and used without further purification. Solvents used for synthesis were purchased in 'puriss. over molecular sieves', 'pro analysis' or 'pro synthesis' quality and used without further purification. For column chromatography, solvents in technical quality were purchased and purified by distillation. For solid-phase synthesis, acetonitrile and dichloroethane were dried over molecular sieves. Thin layer chromatography (TLC) was performed on aluminum plates precoated with silica gel 60 F254 (Merck). Substances were detected based on fluorescence quenching at 254 nm. For column chromatography, silica gel 60 (Merck) with a particle size of 40–63 µm was used. NMR spectra were recorded using Bruker Avance III (300 MHz), Bruker Avance III (400 MHz), Bruker Avance III HD (400 MHz), Bruker Avance III HD (500 MHz), and Varian Inova (600 MHz) spectrometers. Chemical shifts (δ) are given in ppm and were referenced using the deuterated solvent as internal standard. Data are reported as: s = singlet, d = doublet, t = triplet, q = quartet, m = multiplet, br = broad. Coupling constants (J) are given in Hz. Peaks were assigned based on 2D-spectroscopy (COSY, HSQC, HMBC). High resolution (HR) electrospray ionization (ESI) mass spectra (MS) were recorded on Bruker micrOTOF-Q III and Bruker micrOTOF spectrometers. The detected mass-to-charge ratio (m/z) is given, as well as the calculated monoisotopic mass.

5.2 Compounds described in Part I

N^6-Methyladenosine (2)

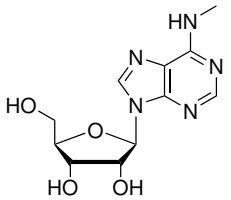

2

$C_{11}H_{15}N_5O_4$

281.27 g·mol^{-1}

6-Chloropurine-9-riboside (**18**, 200 mg, 698 µmol, 1.00 eq.) was treated with methylamine (33% in ethanol, 5 mL) and stirred at ambient temperature for 16 h. The solvent was removed under reduced pressure and the residue was purified by column chromatography (silica gel, CH_2Cl_2:MeOH = 9:1) to yield the product **2** as an off-white solid (178 mg, 633 µmol, 90%). Analytical data agreed with reported values.[255]

^{1}H NMR (400 MHz, DMSO-d_6): δ (ppm) = 8.34 (s, 1H, C8-H), 8.23 (s, 1H, C2-H), 7.84 (s, 1H, N<u>H</u>CH$_3$), 5.88 (d, *J* = 6.2 Hz, 1H, C1'-H), 5.45 (dd, *J* = 6.9, 4.8 Hz, 2H, C2'-OH, C5'-OH), 5.20 (d, *J* = 4.6 Hz, 1H, C3'-OH), 4.61 (td, *J* = 6.2, 4.8 Hz, 1H, C2'-H), 4.14 (td, *J* = 4.8, 2.9 Hz, 1H, C3'-H), 3.97 (q, *J* = 3.4 Hz, 1H, C4'-H), 3.72–3.63 (m, 1H, C5'-H^a), 3.60–3.50 (m, 1H, C5'-H^b), 2.95 (s, 3H, NHC<u>H</u>$_3$).

^{13}C{^{1}H} NMR (100 MHz, DMSO-d_6): δ (ppm) = 155.11 (1C, C6), 152.47 (1C, C2), 148.07 (1C, C4), 139.72 (1C, C8), 119.94 (1C, C5), 87.96 (1C, C1'), 85.96 (1C, C4'), 73.51 (1C, C2'), 70.72 (1C, C3'), 61.72 (1C, C5'), 27.03 (1C, NHCH$_3$).

HR-ESI-MS: *m/z* calc. ($C_{11}H_{15}N_5NaO_4$ [M+Na]$^+$): 304.1016, found: 304.1015.

N^6-Dimethyladenosine (3)

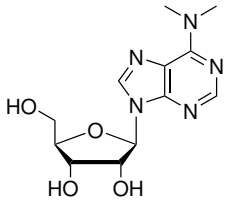

3
$C_{12}H_{17}N_5O_4$
295.30 g·mol^{-1}

6-Chloropurine-9-riboside (**18**, 200 mg, 698 µmol, 1.00 eq.) was treated with dimethylamine (33% in ethanol, 5 mL) and stirred at ambient temperature for 16 h. The solvent was removed under reduced pressure and the residue was purified by column chromatography (silica gel, CH_2Cl_2:MeOH = 9:1) to yield the product **3** as a colorless solid (187 mg, 633 µmol, 90%). Analytical data agreed with reported values.[256]

^{1}H NMR (400 MHz, DMSO-d_6): δ (ppm) = 8.37 (s, 1H, C8-H), 8.21 (s, 1H, C2-H), 5.91 (d, *J* = 6.0 Hz, 1H, C1'-H), 5.45 (d, *J* = 6.1 Hz, 1H, C2'-OH), 5.38 (dd, *J* = 7.0, 4.6 Hz, 1H, C5'-OH), 5.19 (d, *J* = 4.8 Hz, 1H, C3'-OH), 4.57 (td, *J* = 6.1, 4.8 Hz, 1H, C2'-H), 4.14 (td, *J* = 4.8, 3.2 Hz, 1H, C3'-H), 3.96 (q, *J* = 3.5 Hz, 1H, C4'-H), 3.67 (ddd, *J* = 12.1, 4.6, 3.7 Hz, 1H, C5'-H^a), 3.55 (ddd, *J* = 12.1, 7.0, 3.6 Hz, 1H, C5'-H^b), 3.45 (s_{br}, 6H, N(CH$_3$)$_2$).

^{13}C{^{1}H} NMR (100 MHz, DMSO-d_6): δ (ppm) = 154.32 (1C, C6), 151.73 (1C, C2), 149.92 (1C, C4), 138.64 (1C, C8), 119.82 (1C, C5), 87.80 (1C, C1'), 85.78 (1C, C4'), 73.50 (1C, C2'), 70.55 (1C, C3'), 61.57 (1C, C5'), 37.99 (2C, N(CH$_3$)$_2$).

HR-ESI-MS: *m/z* calc. ($C_{12}H_{18}N_5O_4$ [M+H]$^+$): 296.1353, found: 296.1351.

N^6-Hydroxymethyladenosine (4)

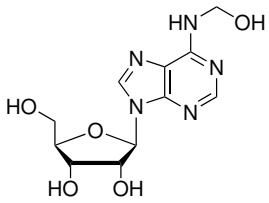

4
$C_{11}H_{15}N_5O_5$
297.27 g·mol^{-1}

An aqueous solution of adenosine (**1**, 100 µM,1.00 eq.) and formaldehyde (30 mM, 300 eq.) was incubated at 60 °C for 4 h. The reaction mixture was analyzed by reversed-phase HPLC (Phenomenex Synergi Fusion 2×250 mm, flow rate 0.2 mL/min, at 20 °C. Eluent A: H_2O. Eluent B: MeCN. Gradient: 0–20 % eluent B in 40 min). A conversion of 19 % was determined (calculated from the peak areas of substrate and product peak at 260 nm). The product was not isolated due to a dynamic equilibrium between substrate and product.

N^6-Formyladenosine (5)

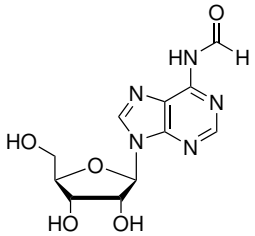

5
$C_{11}H_{13}N_5O_5$
295.26 g·mol^{-1}

A solution of compound **25** (120 mg, 188 µmol, 1.00 eq.) and pyridine (150 µL) in tetrahydrofurane (2 mL) was treated with HF·pyridine (170 µL) and stirred at ambient temperature for 4 h. The reaction was quenched by addition of sat. aq. $NaHCO_3$ solution (4.2 mL). The solvent was removed under reduced pressure and the residue was purified by column chromatography (silica gel, CH_2Cl_2:MeOH = 9:1 to 8:2) to yield the product **5** as a colorless solid (16.2 mg, 54.9 µmol, 29%). Analytical data agreed with reported values.[136]

^{1}H NMR (400 MHz, DMSO-d_6): δ (ppm) = 11.36 (s_{br}, 1H, NH), 9.95 (s, 1H, COH), 8.76 (s, 1H, C8-H), 8.61 (s, 1H, C2-H), 6.02 (d, J = 5.6 Hz, 1H, C1'-H), 5.58 (s_{br}, 1H, C2'-OH), 5.28 (s_{br}, 1H, C3'-OH), 5.16 (s_{br}, 1H, C5'-OH), 4.60 (t, J = 5.3 Hz, 1H, C2'-H), 4.18 (dd, J = 5.0, 3.7 Hz, 1H, C3'-H), 3.98 (q, J = 3.8 Hz, 1H, C4'-H), 3.69 (dd, J = 12.0, 3.9 Hz, 1H, C5'-H^a), 3.63–3.54 (m, 1H, C5'-H^b).

O^6-Methylinosine (7)

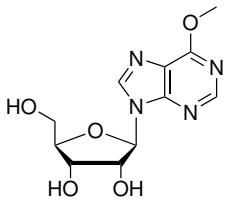

7
$C_{11}H_{14}N_4O_5$
282.26 g·mol^{-1}

6-Chloropurine-9-riboside (**18**, 600 mg, 2.09 mmol, 1.00 eq.) was treated with a solution of sodium methoxide (905 mg, 16.8 mmol, 8.01 eq.) in methanol (20 mL) and stirred at ambient temperature for 3 d. The solution was neutralized by addition of acetic acid and the solvent was removed under reduced pressure. The residue was purified by column chromatography (silica gel, CH_2Cl_2:acetone = 3:7) to yield the product **7** as a colorless solid (541 mg, 1.92 mmol, 92%).

^{1}H NMR (300 MHz, DMSO-d_6): δ (ppm) = 8.61 (s, 1H, C8-H), 8.55 (s, 1H, C2-H), 5.99 (d, J = 5.7 Hz, 1H, C1'-H), 5.44 (d, J = 6.0 Hz, 1H, C2'-OH), 5.16 (d, J = 4.9 Hz, 1H, C3'-OH), 5.08 (dd, J = 6.1, 5.1 Hz, 1H, 5'-OH), 4.60 (q, J = 5.7 Hz, 1H, C2'-H), 4.18 (td, J = 4.9, 3.6 Hz, 1H, C3'-H), 4.11 (s, 3H, OCH_3), 3.98 (q, J = 3.8 Hz, 1H, C4'-H), 3.69 (ddd, J = 12.0, 5.1, 4.0 Hz, 1H, C5'-H^a), 3.57 (ddd, J = 12.0, 6.1, 4.0 Hz, 1H, C5'-H^b).

^{13}C{^{1}H} NMR (125 MHz, DMSO-d_6): δ (ppm) = 160.14 (1C, C6), 151.52 (1C, C4), 151.36 (1C, C2), 142.11 (1C, C8), 120.95 (1C, C5), 87.68 (1C, C1'), 85.57 (1C, C4'), 73.65 (1C, C2'), 70.21 (1C, C3'), 61.23 (1C, C5'), 53.84 (1C, OCH_3).

HR-ESI-MS: m/z calc. ($C_{11}H_{14}N_4NaO_5$ [M+Na]$^+$): 305.0856, found: 305.0853.

6-Mercaptopurine-9-riboside (8)

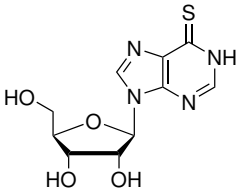

8
$C_{10}H_{12}N_4O_4S$
284.29 g·mol^{-1}

This compound was prepared according to a reported procedure.[145] 6-Chloropurine-9-riboside (**18**, 200 mg, 698 µmol, 1.00 eq.) was dissolved in ethanol (10 mL) and treated with thiourea (79.7 mg, 1.05 mmol, 1.5 eq.). The reaction mixture was stirred at 50 °C for 24 h. The solvent was removed under reduced pressure and the residue was purified by column chromatography (silica gel, CH_2Cl_2:acetone = 3:7) to yield the product **8** as a colorless solid (21.8 mg, 76.7 µmol, 11%). Analytical data agreed with reported values.[145]

6-(Methylthio)purine-9-β-D-ribofuranoside (9)

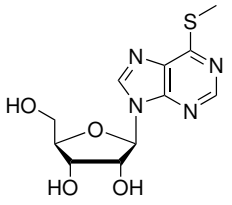

9
$C_{11}H_{14}N_4O_4S$
298.32 g·mol^{-1}

6-Chloropurine-9-riboside (**18**, 200 mg, 2.09 mmol, 1.00 eq.) was treated with a solution of sodium thiomethoxide (1.17 g, 16.7 mmol, 7.99 eq.) in dimethylformamide (20 mL) and stirred at ambient temperature for 3 d. The solution was neutralized by addition of acetic acid and the solvent was removed under reduced pressure. The residue was purified by column chromatography (silica gel, CH_2Cl_2:acetone = 3:7) to yield the product **9** as a colorless solid (592 mg, 2.00 mmol, 96%). Analytical data agreed with reported values.[257]

^{1}H NMR (300 MHz, DMSO-d_6): δ (ppm) = 8.74 (s, 1H, C2-H), 8.68 (s, 1H, C8-H), 6.00 (d, J = 5.6 Hz, 1H, C1'-H), 5.46 (d, J = 5.9 Hz, 1H, C2'-OH), 5.17 (d, J = 5.0 Hz, 1H, C3'-OH), 5.07 (t, J = 5.6 Hz, 1H, 5'-OH), 4.60 (q, J = 5.4 Hz, 1H, C2'-H), 4.19 (q, J = 4.5 Hz, 1H, C3'-H), 3.98 (q, J = 3.9 Hz, 1H, C4'-H), 3.69 (ddd, J = 12.0, 5.0, 3.9 Hz, 1H, C5'-H^a), 3.58 (ddd, J = 12.0, 6.0, 4.0 Hz, 1H, C5'-H^b), 2.68 (s, 3H, SCH_3).

^{13}C{^{1}H} NMR (125 MHz, DMSO-d_6): δ (ppm) = 160.09 (1C, C6), 151.27 (1C, C4), 147.72 (1C, C2), 142.82 (1C, C8), 131.03 (1C, C5), 87.68 (1C, C1'), 85.58 (1C, C4'), 73.67 (1C, C2'), 70.16 (1C, C3'), 61.17 (1C, C5'), 11.15 (1C, SCH_3).

HR-ESI-MS: m/z calc. ($C_{11}H_{14}N_4NaO_4S$ $[M+Na]^+$): 321.06280, found: 321.06216.

6-Ethylpurine-9-β-D-ribofuranoside (10)

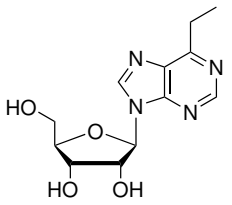

10
$C_{12}H_{16}N_4O_4$
280.28 g·mol^{-1}

A solution of compound **20** (1.97 g, 4.85 mmol, 1.00 eq.) in methanolic ammonia (7 M, 30 mL) was stirred at ambient temperature for 16 h. The solvent was removed under reduced pressure and the residue was purified by column chromatography (silica gel, CH_2Cl_2:acetone 3:7) to yield the product **10** as a colorless solid (1.36 g, 4.85 mmol, 99%).

^{1}H NMR (400 MHz, DMSO-d_6): δ (ppm) = 8.83 (s, 1H, C2-H), 8.76 (s, 1H, C8-H), 6.02 (d, J = 5.8 Hz, 1H, C1'-H), 5.53 (d, J = 6.0 Hz, 1H, C2'-OH), 5.25 (d, J = 4.9 Hz,

1H, C3'-OH), 5.13 (dd, *J* = 6.0, 5.1 Hz, 1H, C5'-OH), 4.64 (td, *J* = 5.9, 4.8 Hz, 1H, C2'-H), 4.18 (td, *J* = 5.0, 3.5 Hz, 1H, C3'-H), 3.97 (q, *J* = 3.9 Hz, 1H, C4'-H), 3.69 (ddd, *J* = 12.0, 5.1, 4.0 Hz, 1H, C5'-H^a), 3.57 (ddd, *J* = 12.0, 6.1, 4.0 Hz, 1H, C5'-H^b), 3.11 (q, *J* = 7.6 Hz, 2H, C$\underline{H}_2$CH$_3$), 1.34 (t, *J* = 7.6 Hz, 3H, CH2C$\underline{H}_3$).

^{13}C{^{1}H} NMR (100 MHz, DMSO-d$_6$): δ (ppm) = 162.71 (1C, C6), 151.87 (1C, C2), 150.28 (1C, C4), 144.07 (1C, C8), 132.25 (1C, C5), 87.60 (1C, C1'), 85.73 (1C, C4'), 73.62 (1C, C2'), 70.39 (1C, C3 '), 61.34 (1C, C5'), 25.76 (1C, $\underline{C}$H$_2$CH$_3$), 12.29 (1C, CH$_2\underline{C}$H$_3$).

HR-ESI-MS: *m/z* calc. (C$_{12}$H$_{17}$N$_4$O$_4$S [M+H]$^+$): 281.12443, found: 281.12497.

1-Deazaadenosine (12)

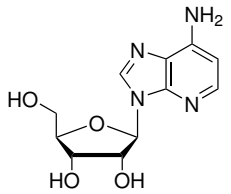

12
C$_{11}$H$_{14}$N$_4$O$_4$
266.26 g·mol^{-1}

This compound was prepared by modification of a reported procedure.[258] A solution of compound **42** (250 mg, 844 µmol, 1.00 eq.) in methanol (40 mL) was treated with 10% Pd/C (125 mg) and stirred under H$_2$ atmosphere at ambient temperature for 3 d. The suspension was filtered through a pad of Celite and the filtrate was evaporated to dryness. The residue was purified by column chromatography (CH$_2$Cl$_2$:MeOH = 9:1) to yield the product **12** as an off-white solid (131 mg, 492 µmol, 58%). Analytical data agreed with reported values.[259]

^{1}H NMR (400 MHz, DMSO-d$_6$): δ (ppm) = 8.25 (s, 1H, C8-H), 7.77 (d, *J*= 5.6 Hz, 1H, C2-H), 6.50 (s, 2H, NH$_2$), 6.39 (d, *J*= 5.6 Hz, 1H, C1-H), 6.09 (s$_{br}$, 1H, C5'-OH), 5.87 (d, *J*= 6.7 Hz, 1H, C1'), 5.39 (d, *J*= 6.5 Hz, 1H, C2'-OH), 5.15 (d, *J*= 4.2 Hz, 1H, C3'-OH), 4.71 (td, *J*= 6.5, 4.9 Hz, 1H, C2'-H), 4.13 (td, *J*= 4.5, 2.3 Hz, 1H, C3'-H), 3.98 (q, *J*= 2.8 Hz, 1H, C4'-H), 3.66 (dd, *J*= 12.3, 3.0 Hz, 1H, C5'-H^a), 3.54 (dd, *J*= 12.3, 3.0 Hz, 1H, 5'-H^b).

^{13}C{^{1}H} NMR (100 MHz, DMSO-d$_6$): δ (ppm) = 147.46 (1C, C6), 146.44 (1C, C4), 144.14 (1C, C2), 140.10 (1C, C8), 123.81 (1C, C5), 102.36 (1C, C1), 88.63 (1C, C1'), 86.27 (1C, C4'), 72.87 (1C, C2'), 71.14 (1C, C3'), 62.11 (1C, C5').

HR-ESI-MS: *m/z* calc. (C$_{11}$H$_{15}$N$_4$O$_4$ [M+H]$^+$): 267.1088, found: 267.1082.

N^6-Methyl-1-deazaadenosine (13)

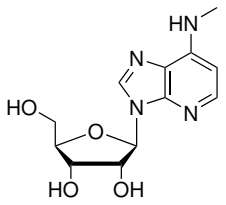

13
$C_{12}H_{16}N_4O_4$
280.28 g·mol^{-1}

In a sealed pressure tube, a solution of compound **34** (1.05 g, 1.75 mmol, 1.00 eq.) in methylamine (33% in ethanol, 50 mL) was stirred at 125 °C for 24 h. The solvent was removed under reduced pressure and the residue was purified by column chromatography (silica gel, EtOAc:MeOH = 8:1) to yield the product **13** as a light yellow solid (433 mg, 1.55 mmol, 88%).

^{1}H NMR (400 MHz, DMSO-d$_6$): δ (ppm) = 8.25 (s, 1H, C8-H), 7.88 (d, J = 5.7 Hz, 1H, C2-H), 6.94 (q, J = 4.9 Hz, 1H, N$\underline{H}$CH$_3$), 6.31 (d, J = 5.7 Hz, 1H, C1-H), 6.02 (dd, J = 8.7, 3.6 Hz, 1H, C5'-OH), 5.88 (d, J = 6.6 Hz, 1H, C1'-H), 5.38 (d, J = 6.4 Hz, 1H, C2'-OH), 5.15 (d, J = 4.2 Hz, 1H, C3'-OH), 4.70 (td, J = 6.4, 4.9 Hz, 1H, C2'-H), 4.13 (td, J = 4.5, 2.4 Hz, 1H, C3'-H), 3.98 (q, J = 2.9 Hz, 1H, C4'-H), 3.67 (dt, J = 12.2, 3.1 Hz, 1H, C5'-H^a), 3.54 (ddd, J = 11.9, 8.3, 3.1 Hz, 1H, C5'-H^b), 2.89 (d, J = 4.9 Hz, 3H, NHC$\underline{H}_3$).

^{13}C{^{1}H} NMR (100 MHz, DMSO-d$_6$): δ (ppm) = 147.58 (1C, C6), 145.75 (1C, C4), 144.74 (1C, C2), 139.77 (1C, C8), 123.76 (1C, C5), 98.52 (1C, C1), 88.54 (1C, C1'), 86.21 (1C, C4'), 72.96 (1C, C2'), 71.08 (1C, C3'), 62.05 (1C, C5'), 29.06 (NHCH$_3$).

HR-ESI-MS: m/z calc. ($C_{12}H_{17}N_4O_4$ [M+H]$^+$): 281.1244, found: 281.1248.

3-Deazaadenosine (14)

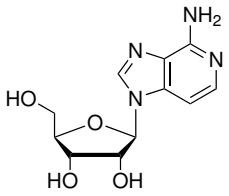

14
$C_{11}H_{14}N_4O_4$
266.26 g·mol^{-1}

In a sealed pressure tube, a solution of compound **35** (500 mg, 836 µmol, 1.00 eq.) in 25% aq. ammonia (50 mL) was stirred at 125 °C for 24 h. The solvent was removed under reduced pressure and the residue was purified by column chromatography (silica gel, EtOAc:MeOH = 8:2) to yield the product **14** as an off-white solid (197 mg, 740 µmol, 88%).

^{1}H NMR (400 MHz, DMSO-d$_6$): δ (ppm) = 8.29 (s, 1H, C8-H), 7.66 (d, J = 5.8 Hz,

1H, C2-H), 6.91 (d, *J* = 5.8 Hz, 1H, C3-H), 6.18 (s, 2H, NH_2), 5.75 (d, *J* = 6.2 Hz, 1H, C1'-H), 5.49 (d, *J* = 6.4 Hz, 1H, C2'-OH), 5.24 (d, *J* = 4.7 Hz, 1H, C3'-OH), 5.10 (t, *J* = 5.2 Hz, 1H, C5'-OH), 4.32 (q, *J* = 5.8 Hz, 1H, C2'-H), 4.09 (q, *J* = 4.1 Hz, 1H, C3'-H), 3.95 (q, *J* = 3.6 Hz, 1H, C4'-H), 3.70-–3.55 (m, 2H, C5'-H).

$^{13}C\{^1H\}$ NMR (100 MHz, DMSO-d_6): δ (ppm) = 152.45 (1C, C6), 140.61 (1C, C2), 139.97 (1C, C8), 137.59 (1C, C4), 126.92 (1C, C5), 97.38 (1C, C3), 88.65 (1C, C1'), 85.55 (1C, C4'), 73.86 (1C, C2'), 70.12 (1C, C3'), 61.25 (1C, C5').

HR-ESI-MS: *m/z* calc. ($C_{11}H_{14}NaN_4O_4$ $[M+Na]^+$): 289.0907, found: 289.0905.

N^6-Methyl-3-deazaadenosine (15)

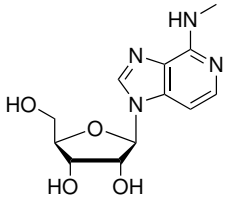

15
$C_{12}H_{16}N_4O_4$
280.28 g·mol^{-1}

In a sealed pressure tube, a solution of compound **35** (1.05 g, 1.75 mmol, 1.00 eq.) in methylamine (33% in ethanol, 50 mL) was stirred at 125 °C for 20 h. The solvent was removed under reduced pressure and the residue was purified by column chromatography (silica gel, EtOAc:MeOH = 1:0 to 6:4) to yield the product **15** as a light yellow solid (433 mg, 1.55 mmol, 88%).

^1H NMR (400 MHz, DMSO-d_6): δ (ppm) = 8.29 (s, 1H, C8-H), 7.73 (d, *J* = 5.9 Hz, 1H, C2-H), 6.92 (d, *J* = 5.9 Hz, 1H, C3-H), 6.78 (s_{br}, 1H, N$\underline{H}$$CH_3$), 5.76 (d, *J* = 6.2 Hz, 1H, C1'-H), 5.50 (d, *J* = 6.5 Hz, 1H, C2'-OH), 5.25 (d, *J* = 4.8 Hz, 1H, C3'-OH), 5.13 (t, *J* = 5.2 Hz, 1H, C3'-OH), 4.30 (q, *J* = 6.0 Hz, 1H, C2'-H), 4.09 (td, *J* = 4.8, 3.1 Hz, 1H, C3'-H), 3.95 (q, *J* = 3.6 Hz, 1H, C4'-H), 3.62 (qdd, *J* = 11.9, 5.2, 3.7 Hz, 2H, C5'-H), 2.93 (d, *J* = 4.8 Hz, 3H, NHC$\underline{H}_3$).

$^{13}C\{^1H\}$ NMR (100 MHz, DMSO-d_6): δ (ppm) = 151.92 (1C, C6), 140.15 (1C, C2), 139.76 (1C, C8), 136.90 (1C, C4), 127.26 (1C, C5), 96.94 (1C, C3), 88.68 (1C, C1'), 85.61 (1C, C4'), 74.01 (1C, C2'), 70.12 (1C, C3'), 61.22 (1C, C5'), 27.67 (1C, $NHCH_3$).

HR-ESI-MS: *m/z* calc. ($C_{12}H_{17}N_4O_4$ $[M+H]^+$): 281.1244, found: 281.1250.

7-Deazaadenosine (16)

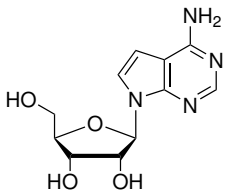

16
$C_{11}H_{14}N_4O_4$
280.26 g·mol^{-1}

This compound was synthesized by modification of a reported procedure.[163] Compound **45** (750 mg, 1.04 mmol, 1.00 eq.) was dissolved in dry tetrahydrofuran (4 mL) under an inert gas atmosphere. The reaction mixture was cooled to -10 °C and *i*-PrMgCl·LiCl (1.30 M in tetrahydrofuran, 930 µL, 1.21 mmol, 1.10 eq.) was added dropwise. The solution was stirred at this temperature for 1 h and then poured onto a mixture of ice (10 g) and sat. aq. NH_4Cl solution (10 mL). This mixture was extracted with dichloromethane (3 × 20 mL), the combined organic layers were dried over $MgSO_4$ and the solvent was removed under reduced pressure. The residue was redissolved 25% aq. ammonia (50 mL), transferred to a sealed pressure tube and stirred at 125 °C for 24 h. The solvent was removed under reduced pressure and the residue was purified by column chromatography (silica gel, EtOAc:MeOH = 8:1) to yield the product **16** as a colorless foam (244 mg, 916 µmol, 88%).

^{1}H NMR (400 MHz, DMSO-d_6): δ (ppm) = 8.04 (s, 1H, C2-H), 7.34 (d, J = 3.7 Hz, 1H, C8-H), 7.05 (s, 2H, NH_2), 6.58 (d, J = 3.7 Hz, 1H, C7-H), 5.98 (d, J = 6.3 Hz, 1H, C1'-H), 5.34 (dd, J = 6.6, 4.7 Hz, 1H, C5'-OH), 5.27 (d, J = 6.5 Hz, 1H, C2'-OH), 5.11 (d, J = 4.7 Hz, 1H, C3'-OH), 4.42 (q, J = 6.1 Hz, 1H, C2'-H), 4.07 (td, J = 4.7, 3.0 Hz, 1H, C3'-H), 3.89 (q, J = 3.6 Hz, 1H, C4'-H), 3.62 (dt, J = 12.0, 4.3 Hz, 1H, C5'-H^a), 3.52 (ddd, J = 12.0, 6.6, 3.8 Hz, 1H, C5'-H^b).

^{1}H NMR (400 MHz, DMSO-d_6): δ (ppm) = 157.59 (1C, C6), 151.58 (1C, C2), 149.93 (1C, C4), 122.35 (1C, C8), 103.13 (1C, C5), 99.55 (1C, C7), 87.61 (1C, C1'), 85.11 (1C, C4'), 73.68 (1C, C2'), 70.77 (1C, C3'), 61.89 (1C, C5').

HR-ESI-MS: m/z calc. ($C_{11}H_{15}N_4O_4$ $[M+H]^+$): 267.1088, found: 267.1085.

N^6-Methyl-7-deazaadenosine (17)

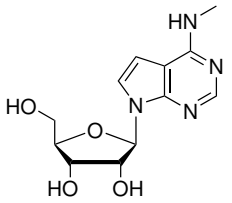

17
$C_{12}H_{16}N_4O_4$
280.28 g·mol^{-1}

This compound was synthesized by modification of a reported procedure.[163] Compound **45** (1.90 g, 2.62 mmol, 1.00 eq.) was dissolved in dry tetrahydrofuran (10.5 mL) under an inert gas atmosphere. The reaction mixture was cooled to -10 °C and *i*-PrMgCl·LiCl (1.30 M in tetrahydrofuran, 2.10 mL, 2.73 mmol, 1.04 eq.) was added dropwise. The solution was stirred at this temperature for 1 h and then poured onto a mixture of ice (30 g) and sat. aq. NH_4Cl solution (20 mL). This mixture was extracted with dichloromethane (1 × 50 mL, 3 × 5 mL), the combined organic layers were dried over $MgSO_4$ and the solvent was removed under reduced pressure. The residue was redissolved in methylamine (33% in ethanol, 100 mL), transferred to a sealed pressure tube and stirred at 125 °C for 18 h. The solvent was removed under reduced pressure and the residue was purified by column chromatography (silica gel, EtOAc:MeOH = 8:1) to yield the product **17** as a colorless foam (629 mg, 2.24 mmol, 86%). Analytical data agreed with reported values.[163]

^{1}H NMR (400 MHz, DMSO-d_6): δ (ppm) = 8.13 (s, 1H, C2-H), 7.53 (q, *J* = 4.6 Hz, 1H, N<u>H</u>CH$_3$), 7.34 (d, *J* = 3.6 Hz, 1H, C8-H), 6.57 (d, *J* = 3.6 Hz, 1H, C7-H), 5.99 (d, *J* = 6.3 Hz, 1H, C1'-H), 5.33 (dd, *J* = 6.7, 4.7 Hz, 1H, C5'-OH), 5.27 (d, *J* = 6.3 Hz, 1H, C2'-OH), 5.11 (d, *J* = 4.7 Hz, 1H, C3'-OH), 4.42 (q, *J* = 5.9 Hz, 1H, C2'-H), 4.08 (td, *J* = 4.7, 3.0 Hz, 1H, C3'-H), 3.89 (q, *J* = 3.7 Hz, 1H, C4'-H), 3.62 (ddd, *J* = 11.9, 4.7, 3.7 Hz, 1H, C5'-H^a), 3.52 (ddd, *J* = 11.9, 6.7, 3.7 Hz, 1H, C5'-H^b), 2.95 (d, *J* = 4.7 Hz, 3H, NHC<u>H</u>3).

^{13}C{^{1}H} NMR (100 MHz, DMSO-d_6): δ (ppm) = 156.71 (1C, C6), 151.50 (1C, C2), 149.15 (1C, C4), 122.18 (1C, C8), 103.50 (1C, C5), 99.12 (1C, C7), 87.61 (1C, C1'), 85.10 (1C, C4'), 73.72 (1C, C2'), 70.75 (1C, C3'), 61.87 (1C, C5'), 27.11 (1C, $NHCH_3$).

HR-ESI-MS: *m/z* calc. ($C_{12}H_{17}N_4O_4$ $[M+H]^+$): 281.1244, found: 281.1253.

2',3',5'-Tri-*O*-acetyl-6-chloropurine-9-β-D-ribofuranoside (19)

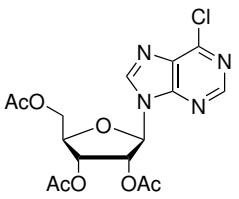

19
$C_{16}H_{17}ClN_4O_7$
412.78 g·mol^{-1}

This compound was synthesized according to a reported procedure.[260] A solution of 6-chloropurine-9-riboside (**18**, 2.50 g, 8.72 mmol, 1.00 eq.) in dry acetonitrile (125 mL) under an inert gas atmosphere was treated with triethylamine (6.10 mL, 43.8 mmol, 5.02 eq.), 4-dimethylaminopyridine (107 mg, 876 µmol, 0.10 eq.) and acetic anhydride (4.20 mL, 44.5 mmol, 5.10 eq.) and stirred at ambient temperature for 24 h. Methanol (17.5 mL) was added and stirring was continued for 1 h. The solvent was removed under reduced pressure and the residue was purified by column chromatography (silica gel, *n*-hexane:EtOAc = 1:4) to yield the product **19** as a colorless amorphous solid (3.46 g, 8.38 mmol, 96%). Analytical data agreed with reported values.[261]

^{1}H NMR (400 MHz, $CDCl_3$): δ (ppm) = 8.77 (s, 1H, C2-H), 8.29 (s, 1H, C8-H), 6.23 (d, J = 5.2 Hz, 1H, C1'-H), 5.94 (t, J = 5.2 Hz, 1H, C2'-H), 5.66–5.62 (m, 1H, C3'-H), 4.51–4.46 (m, 1H, C4'-H), 4.45–4.38 (m, 2H, C5'-H), 2.16 (s, 3H, $C(O)CH_3$), 2.12 (s, 3H, $C(O)CH_3$), 2.09 (s, 3H, $C(O)CH_3$).

^{13}C{^{1}H} NMR (125 MHz, $CDCl_3$): δ (ppm) = 170.20 (1C, $\underline{C}(O)CH_3$), 169.50 (1C, $\underline{C}(O)CH_3$), 169.28 (1C, (1C, $\underline{C}(O)CH_3$), 152.36 (1C, C2), 151.73 (1C, C6), 151.29 (1C, C4), 143.56 (1C, C8), 132.43 (1C, C5), 87.03 (1C, C1'), 80.73 (1C, C2'), 73.29 (1C, C3'), 70.66 (1C, C4'), 63.05 (1C, C5'), 20.95 (1C, $C(O)\underline{C}H_3$), 20.73 (1C, $C(O)\underline{C}H_3$), 20.57 (1C, $C(O)\underline{C}H_3$).

HR-ESI-MS: m/z calc. ($C_{16}H_{18}ClN_4O_7$ $[M+H]^+$): 413.0859, found: 413.0859.

2',3',5'-Tri-*O*-acetyl-6-ethylpurine-9-β-D-ribofuranoside (20)

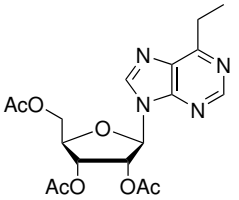

20
$C_{18}H_{22}N_4O_7$
406.15 g·mol^{-1}

This compound was synthesized by modification of a reported procedure.[146] A suspension of magnesium shavings (315 mg, 13.0 mmol, 2.39 eq.) in dry tetrahydrofuran under an inert gas atmosphere was treated dropwise with a solution of bromoethane (1.50 mL, 20.1 mmol, 3.70 eq.) in tetrahydrofuran (3.2 mL). The reaction mixture was stirred at 70 °C for 30 min, then cooled to ambient tempera-

ture and diluted with tetrahydrofuran (900 µL). The solution was cooled to -78 °C and a solution of $ZnBr_2$ (2.89 g, 12.8 mmol, 2.36 eq.) in tetrahydrofuran (11.4 mL) was added dropwise over 1 h. The reaction mixture was warmed to 55 °C and stirred for 15 min before it was cooled to ambient temperature. A solution of $Pd(PPh_3)_4$ (247 mg, 214 µmol, 0.04 eq.) in tetrahydrofuran (21.4 mL) and a solution of compound **19** (2.24 g, 5.43 mmol, 1.00 eq.) in tetrahydrofuran (43.0 mL) were subsequently added. The reaction mixture was stirred at 55 °C for 90 min before it was cooled to ambient temperature and quenched by addition of sat. aq. NH_4Cl solution (100 mL). The reaction mixture was concentrated under reduced pressure and partitioned between chloroform (150 mL) and water (150 mL). The organic layer was separated, dried over Na_2SO_4 and the solvent was removed *in vacuo*. The residue was purified by column chromatography (silica gel, *n*-hexane:EtOAc = 1:4). The product coeluted with $Pd(PPh_3)_4$, which was removed by precipitation from ethyl acetate. The supernatant solution was evaporated to dryness to yield the product **20** as a light yellow oil (2.03 g, 5.00 mmol, 92%).

^{1}H NMR (300 MHz, $CDCl_3$): δ (ppm) = 8.89 (s, 1H, C2-H), 8.17 (s, 1H, C8-H), 6.23 (d, J = 5.2 Hz, 1H, C1'-H), 5.98 (t, J = 5.3 Hz, 1H, C2'-H), 5.69 (dd, J = 5.41, 4.76 Hz, 1H, C3'-H), 4.49–4.43 (m, 2H, C4'-H, C5'-H^a), 4.37 (dd, J = 12.8, 5.2 Hz, 1H, C5'-H^b), 3.23 (q, J = 7.6 Hz, 2H, C$\underline{H}_2$CH$_3$), 2.15 (s, 3H, C(O)CH$_3$), 2.12 (s, 3H, C(O)CH$_3$), 2.08 (s, 3H, C(O)CH$_3$), 1.44 (t, J = 7.6 Hz, 3H, CH$_2$C$\underline{H}_3$).

^{13}C{^{1}H} NMR (100 MHz, $CDCl_3$): δ (ppm) = 170.46 (1C, $\underline{C}$(O)CH$_3$), 169.73 (1C, $\underline{C}$(O)CH$_3$), 169.52 (1C, $\underline{C}$(O)CH$_3$), 164.68 (1C, C6), 152.90 (1C, C2), 150.36 (1C, C4), 142.08 (1C, C8), 133.10 (1C, C5) 86.57 (1C, C1'), 80.43 (1C, C2'), 73.19 (1C, C3'), 70.72 (1C, C4'), 63.15 (1C, C5'), 26.66 (1C, $\underline{C}$H$_2$CH$_3$), 20.91 (1C, C(O)$\underline{C}$H$_3$), 20.69 (1C, C(O)$\underline{C}$H$_3$), 20.56 (1C, C(O)$\underline{C}$H$_3$), 12.65 (1C, CH$_2\underline{C}$H$_3$).

HR-ESI-MS: *m/z* calc. ($C_{18}H_{23}N_4O_7$ [M+H]$^+$): 407.15613, found: 407.15606.

2',3',5'-Tri-*O*-(*tert*-butyldimethylsilyl)-6-chloropurine-9-β-D-ribofuranoside (21)

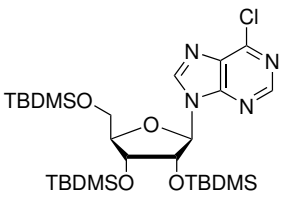

21
$C_{28}H_{53}ClN_4O_4Si_3$
629.46 g·mol^{-1}

A solution of 6-chloropurine-9-riboside (**18**, 1.00 g, 3.49 mmol, 1.00 eq.) in *N*,*N*-dimethylformamide (15 mL) under an inert gas atmosphere was treated with *tert*-butyldimethylsilyl chloride (2.10 g, 14.0 mmol, 4.01 eq.) and imidazole (1.43 g, 20.9 mmol, 5.99 eq.) and the mixture was stirred at ambient temperature for 27 h. The solvent was removed under reduced pressure and the residue was redissolved in CH_2Cl_2 (50 mL) and washed with water (50 mL). The aqueous layer was diluted with sat. aq. $NaHCO_3$ solution (50 mL) and extracted with dichloromethane (3 × 50 mL). The combined organic layers were dried over Na_2SO_4 and the solvent was removed *in vacuo*. The residue was purified by column chromatography (silica gel, *n*-hexane:EtOAc = 6:1) to yield the product **21** as a colorless solid (2.13 g, 3.39 mmol, 97%).

^{1}H NMR (400 MHz, $CDCl_3$): δ (ppm) = 8.75 (s, 1H, C2-H), 8.56 (s, 1H, C8-H), 6.13 (d, J = 5.0 Hz, 1H, C1'-H), 4.58 (t, J = 4.7 Hz, 1H, C2'-H), 4.30 (t, J = 4.0 Hz, 1H, C3'-H), 4.16 (td, J = 3.6, 2.4 Hz, 1H, C4'-H), 4.02 (dd, J = 11.5, 3.5 Hz, 1H, C5'-H^a), 3.80 (dd, J = 11.5, 2.4 Hz, 1H, C5'-H^b), 0.96 (s, 9H, SiC($C\underline{H}_3$)$_3$), 0.93 (s, 9H, SiC($C\underline{H}_3$)$_3$), 0.79 (s, 9H, SiC($C\underline{H}_3$)$_3$), 0.16 (s, 3H, $SiCH_3$), 0.15 (s, 3H, $SiCH_3$), 0.10 (2s, 6H, 2 $SiCH_3$), -0.03 (s, 3H, $SiCH_3$), -0.25 (s, 3H, $SiCH_3$).

^{13}C{^{1}H} NMR (100 MHz, $CDCl_3$): δ (ppm) = 152.10 (1C, C2), 151.65 (1C, C4), 151.14 (1C, C6), 144.22 (1C, C8), 132.23 (1C, C5), 88.71 (1C, C1'), 85.87 (1C, C4'), 76.55 (1C, C2'), 71.95 (1C, C3'), 62.53 (1C, C5'), 26.26 (3C, SiC($\underline{C}H_3$)$_3$), 25.96 (3C, SiC($\underline{C}H_3$)$_3$), 25.76 (3C, SiC($\underline{C}H_3$)$_3$), 18.72 (1C, Si$\underline{C}$(CH_3)$_3$), 18.22 (1C, Si$\underline{C}$(CH_3)$_3$), 17.97 (1C, Si$\underline{C}$(CH_3)$_3$), -4.25 (1C, $SiCH_3$), -4.51 (1C, $SiCH_3$), -4.58 (1C, $SiCH_3$), -4.91 (1C, $SiCH_3$), -5.17 (1C, $SiCH_3$), -5.21 (1C, $SiCH_3$).

HR-ESI-MS: *m*/*z* calc. ($C_{28}H_{53}ClN_4NaO_4Si_3$ [M+Na]$^+$): 651.29553, found: 651.29776.

2',3',5'-Tri-*O*-(*tert*-butyldimethylsilyl)-6-[(2-ethoxycarbonyl)methyl]-9-β-D-ribofuranoside (124)

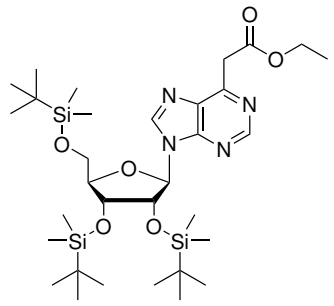

22
$C_{32}H_{60}N_4O_6Si_3$
681.11 g·mol^{-1}

This compound was prepared according to a reported procedure.[148] Under an inert gas atmosphere, zinc powder (519 mg, 7.94 mmol, 10.0 eq.) in tetrahydrofuran (3.2 mL) preactivated with trimethylsilyl chloride (20.7 mg, 191 µmol, 0.24 eq.) was treated with a solution of ethyl bromoacetate (664 mg, 3.97 mmol, 5.00 eq.) in tetrahydrofurane (4.8 mL) and the suspension was stirred at ambient temperature for 1 h to form the Reformatzky reagent (ethyl bromozincacetate). The supernatant was added to a solution of compound **21** (500 mg, 794 µmol, 1.00 eq.), tris(dibenzylideneacetone)palladium (Pd_2dba_3, 14.6 mg, 15.9 µmol, 0.02 eq.) and JohnPhos (19.0 mg, 63.6 µmol, 0.08 eq.) in tetrahydrofuran (1.6 mL). The reaction mixture was stirred at room temperature for four days. It was quenched by addition of sat. aq. NH_4Cl solution (65 mL) and extracted with dichloromethane (3 × 50 mL). The organic layers were combined and the solvent was removed under reduced pressure. The residue was purified by column chromatography (silica gel, *n*-hexane/EtOAc = 7:1) to yield the product **124** as a yellow solid (355 mg, 521 µmol, 65%). Analytical data agreed with reported values.[148]

^{1}H NMR (400 MHz, $CDCl_3$): δ (ppm) = 8.92 (s, 1H, C2-H), 8.46 (s, C8-H), 6.12 (d, J = 5.0 Hz, 1H, C1'-H), 4.65 (t, J = 4.7 Hz, 1H, C2'-H), 4.32 (t, J = 4.0 Hz, 1H, C3'-H), 4.30–4.28 (m, 2H, C6-CH_2), 4.21 (q, J = 7.1 Hz, 2H, C$\underline{H}_2$CH_3), 4.16 (td, J = 3.7, 2.5 Hz, 1H, C4'-H), 4.03 (dd, J = 11.4, 3.8 Hz, 1H, C5'-H^a), 3.80 (dd, J = 11.4, 2.6 Hz, 1H , C5'-H^b), 1.24 (t, J = 7.2 Hz, 3H, CH_2C$\underline{H}_3$), 0.95 (s, 9H, SiC$(CH_3)_3$), 0.94 (s, 9H, SiC$(CH_3)_3$), 0.78 (s, 9H, SiC$(CH_3)_3$), 0.15 (s, 3H, SiCH_3), 0.14 (s, 3H, SiCH_3), 0.11 (s, 3H, SiCH_3), 0.10 (s, 3H, SiCH_3), -0.04 (s, 3H, SiCH_3), -0.26 (s, 3H, SiCH_3).

2',3',5'-Tri-*O*-(*tert*-butyldimethylsilyl)-6-(2-hydroxyethyl)-9-β-D-ribofuranoside (23)

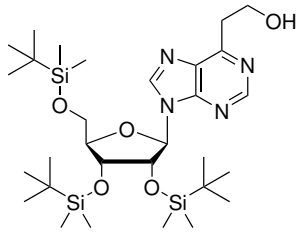

23
$C_{30}H_{58}N_4O_5Si_3$
639.07 g·mol^{-1}

This compound was prepared according to a reported procedure.[148] Under an inert gas atmosphere, a solution of compound **124** (355 mg, 522 µmol, 1.00 eq.) in ethanol (4 mL) was treated with sodium borohydride (197 mg, 5.22 mmol, 10.0 eq.). The reaction was stirred at ambient temperature for 14 h before it was quenched by addition of methanol (4 mL) and 1 M aq. NH_4Cl solution (5 mL). The solvent was evaporated and the residue was extracted with chloroform (3 × 15 mL). The combined organic layers were dried over Na_2SO_4 and the solvent was removed under reduced pressure. The residue was redissolved in dichloromethane (5 mL) and manganese dioxide (90.7 mg, 1.04 mmol, 2.00 eq.) was added. The mixture was sonicated at ambient temperature for 1 h, filtered through a pad of Celite and the solvent was evaporated. The residue was purified by column chromatography (silica gel, EtOAc:MeOH = 9:1) to yield the product **23** as an amber resin (166 mg, 260 µmol, 56%). Analytical data agreed with reported values.[148]

^{1}H NMR (400 MHz, $CDCl_3$): δ (ppm) = 8.85 (s, 1H, C2-H), 8.47 (s, 1H, C8-H), 6.12 (d, J = 4.9 Hz, 1H, C1'-H), 4.64 (t, J = 4.6 Hz, 1H, C2'-H), 4.32 (t, J = 4.1 Hz, 1H, C3'-H), 4.19–4.11 (m, 3H, C4'-H, C$\underline{H}_2$OH), 4.03 (dd, J = 11.5, 3.7 Hz, 1H, C5'-H^a), 3.80 (dd, J = 11.5, 2.6 Hz, 1H, C5'-H^b), 3.45 (dd, J = 5.9, 4.7, 2H, C6-CH_2), 0.95 (s, 9H, SiC(CH_3)$_3$), 0.93 (s, 9H, SiC(CH_3)$_3$), 0.79 (s, 9H, SiC(CH_3)$_3$), 0.15 (s, 3H, SiCH_3), 0.10 (s, 3H, SiCH_3), 0.10 (s, 3H, SiCH_3), 0.03 (s, 3H, SiCH_3), -0.23 (s, 3H, SiCH_3).

^{13}C{^{1}H} NMR (100 MHz, $CDCl_3$): δ (ppm) = 161.46 (1C, C6), 152.17 (1C, C2), 150.66 (1C, C4), 143.09 (1C, C8), 132.88 (1C, C5), 88.49 (1C, C1'), 85.63 (1C, C4'), 76.22 (1C, C2'), 71.87 (1C, C3'), 62.49 (1C, C5'), 60.46 (1C, CH_2OH), 36.21 (1C, C6-$\underline{C}H_2$), 26.23 (3C, SiC($\underline{C}H_3$)$_3$), 25.97 (3C, SiC($\underline{C}H_3$)$_3$), 25.77 (3C, SiC($\underline{C}H_3$)$_3$), 18.68 (1C, Si$\underline{C}$(CH_3)$_3$), 18.22 (1C, Si$\underline{C}$(CH_3)$_3$), 17.99 (1C, Si$\underline{C}$(CH_3)$_3$), -4.24 (1C, SiCH_3), -4.54 (1C, SiCH_3), -4.58 (1C, SiCH_3), -4.91 (1C, SiCH_3), -5.21 (1C, SiCH_3), -5.24 (1C, SiCH_3).

HR-ESI-MS: m/z calc. ($C_{30}H_{59}N_4O_5Si_3$ [M+H]$^+$): 639.37878, found: 639.37995.

2',3',5'-Tri-*O*-(*tert*-butyldimethylsilyl)adenosine (24)

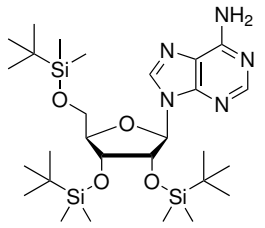

24
$C_{28}H_{55}N_5O_4Si_3$
610.03 g·mol^{-1}

Under an inert gas atmosphere, a solution of adenosine (**1**, 2.00 g, 7.48 mmol, 1.00 eq.) in dry *N*,*N*-dimethylformamide (30 mL) was treated with imidazole (3.06 g, 44.9 mmol, 6.00 eq.) and *tert*-butyldimethylsilyl chloride (4.51 g, 29.9 mmol, 4.00 eq.) and stirred at ambient temperature for 20 h. The solvent was removed under reduced pressure and the residue was redissolved in dichloromethane (70 mL) and washed with water (70 mL). The organic layer was separated, dried over Na_2SO_4 and the solvent was removed *in vacuo*. The residue was purified by column chromatography (silica gel, *n*-hexane:EtOAc = 2:1 to 1:1) to yield the product **24** as a colorless solid (4.23 g, 6.93 mmol, 92%). Analytical data agreed with reported values.[262]

^{1}H NMR (400 MHz, $CDCl_3$): δ (ppm) = 8.34 (s, 1H, C2-H), 8.16 (s, 1H, C8-H), 6.03 (d, J = 5.2 Hz, 1H, C1'-H), 5.71 (s, 2H, NH_2), 4.68 (dd, J = 5.2, 4.3 Hz, 1H, C2'-H), 4.31 (dd, J = 4.3, 3.5 Hz, 1H, C3'-H), 4.16–4.09 (m, 1H, C4'-H), 4.03 (dd, J = 11.3, 4.2 Hz, 1H, C5'-H^a), 3.78 (dd, J = 11.4, 2.9 Hz, 1H, C5'-H^b), 0.95 (s, 9H, $SiC(CH_3)_3$), 0.93 (s, 9H, $SiC(CH_3)_3$), 0.79 (s, 9H, $SiC(CH_3)_3$), 0.14 (s, 9H, $SiC(CH_3)_3$), 0.13 (s, 3H, $SiCH_3$), 0.10 (s, 3H, $SiCH_3$), 0.10 (s, 3H, $SiCH_3$), -0.05 (s, 3H, $SiCH_3$), -0.23 (s, 3H, $SiCH_3$).

^{13}C{^{1}H} NMR (100 MHz, $CDCl_3$): δ (ppm) = 155.47 (1C, C6), 153.08 (1C, C2), 150.11 (1C, C4), 139.81 (1C, C8), 120.23 (1C, C5), 88.42 (1C, C1'), 85.62 (1C, C4'), 75.92 (1C, C2'), 72.13 (1C, C3'), 62.68 (1C, C5'), 26.22 (3C, $SiC(\underline{C}H_3)_3$), 26.00 (3C, $SiC(\underline{C}H_3)_3$), 25.82 (3C, $SiC(\underline{C}H_3)_3$), 18.67 (1C, $Si\underline{C}(CH_3)_3$), 18.24 (1C, $Si\underline{C}(CH_3)_3$), 18.01 (1C, $Si\underline{C}(CH_3)_3$), -4.26 (1C, $SiCH_3$), -4.55 (1C, $SiCH_3$), -4.57 (1C, $SiCH_3$), -4.95 (1C, $SiCH_3$), -5.22 (2C, $SiCH_3$).

HR-ESI-MS: *m/z* calc. ($C_{28}H_{56}N_5O_4Si_3$ [M+H]$^+$): 610.36346, found: 610.36367.

2',3',5'-Tri-*O*-(*tert*-butyldimethylsilyl)-N^6-formyladenosine (25)

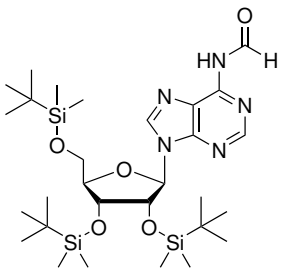

25
$C_{29}H_{55}N_5O_5Si_3$
638.04 g·mol^{-1}

Under an inert gas atmosphere, a solution of formic acid (1.33 mL, 35.2 mmol, 21.5 eq.) and acetic anhydride (2.67 mL, 28.2 mmol, 17.2 eq.) in dry dichloromethane (13.3 mL) was cooled to 0 °C and 4-dimethylaminopyridine (200 mg, 1.64 mmol, 1.00 eq.) was added in portions. The reaction mixture was allowed to warm to ambient temperature and treated with compound **24** (1.00 g, 1.64 mmol, 1.00 eq.). The reaction was stirred for 66 h. The mixture was diluted with dichloromethane (100 mL) and washed with water (20 mL), sat. aq. $NaHCO_3$ solution (20 mL) and water (20 mL). The organic layer was dried over Na_2SO_4 and the solvent was removed under reduced pressure. The residue was purified by column chromatography (silica gel, *n*-hexane:EtOAc = 2:1) to yield the product **25** as a colorless foam (1.03 g, 1.61 mmol, 98%).

^{1}H NMR (400 MHz, $CDCl_3$): δ (ppm) = 10.01 (d, J = 10.4 Hz, 1H, CHO), 9.55 (d, J = 10.4 Hz, 1H, NH), 8.66 (s, 1H, C2-H), 8.48 (s, 1H, C8-H), 6.10 (d, J = 4.9 Hz, 1H, C1'-H), 4.67 (t, J = 4.6 Hz, 1H, C2'-H), 4.33 (t, J = 4.0 Hz, 1H, C3'-H), 4.16 (td, J = 3.9, 2.8 Hz, 1H, C4'-H), 4.04 (dd, J = 11.4, 4.1 Hz, 1H, C5'-H^a), 3.80 (dd, J = 11.4, 2.8 Hz, 1H, C5'-Hb), 0.95 (s, 9H, $SiC(CH_3)_3$), 0.94 (s, 9H, $SiC(CH_3)_3$), 0.80 (s, 9H, $SiC(CH_3)_3$), 0.14 (s, 3H, $SiCH_3$), 0.14 (s, 3H, $SiCH_3$), 0.11 (s, 3H, $SiCH_3$), 0.10 (s, 3H, $SiCH_3$), -0.02 (s, 3H, $SiCH_3$), -0.22 (s, 3H, $SiCH_3$).

^{13}C{^{1}H} NMR (100 MHz, $CDCl_3$): δ (ppm) = 163.15 (1C, CHO), 152.51 (1C, C2), 151.93 (1C, C6), 149.06 (1C, C4), 142.85 (1C, C8), 121.40 (1C, C5), 88.67 (1C, C1'), 85.69 (1C, C4'), 76.04 (1C, C2'), 71.91 (1C, C3'), 62.52 (1C, C5'), 26.22 (3C, $SiC(\underline{C}H_3)_3$), 25.99 (3C, $SiC(\underline{C}H_3)_3$), 25.80 (3C, $SiC(\underline{C}H_3)_3$), 18.68 (1C, $Si\underline{C}(CH_3)_3$), 18.23 (1C, $Si\underline{C}(CH_3)_3$), 18.01 (1C, $Si\underline{C}(CH_3)_3$), -4.24 (1C, $SiCH_3$), -4.52 (1C, $SiCH_3$), -4.56 (1C, $SiCH_3$), -4.87 (1C, $SiCH_3$), -5.21 (1C, $SiCH_3$), -5.25 (1C, $SiCH_3$).

HR-ESI-MS: m/z calc. ($C_{29}H_{56}N_5O_5Si_3$ $[M+H]^+$): 638.35838, found: 638.35924.

2-Amino-4-chloro-3-nitropyridine (27)

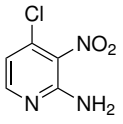

27
$C_5H_4ClN_3O_2$
173.56 g·mol^{-1}

2-Amino-4-chloropyridine (**26**, 5.00 g, 38.9 mmol, 1.00 eq.) was dissolved in conc. sulfuric acid (70 mL) at 0 °C. Conc. nitric acid (2.60 mL, 62.3 mmol, 1.61 eq.) was added dropwise. The reaction mixture was stirred at 0 °C for 30 min, then allowed to warm to ambient temperature and stirred for 19 h. The mixture was poured onto crushed ice (200 g) and adjusted to pH = 9 with 25% aq. ammonia. The resulting suspension was extracted with ethyl acetate (6 × 200 mL). The combined organic layers were dried over Na_2SO_4 and the solvent was removed under reduced pressure. The residue was purified by column chromatography (silica gel, *n*-hexane:EtOAc = 3:1) to yield the product **27** as a yellow solid (2.51 g, 14.5 mmol, 39%). Analytical data agreed with reported values.[263]

^{1}H NMR (400 MHz, DMSO-d_6): δ (ppm) = 8.12 (d, J = 5.3 Hz, 1H, C6-H), 7.25 (s, 2H, NH_2), 6.86 (d, J = 5.3 Hz, 1H, C5-H).

^{13}C{^{1}H} NMR (100 MHz, DMSO-d_6): δ (ppm) = 152.69 (C2), 152.03 (C6), 135.89 (C4), 129.40 (C3), 113.00 (C5).

HR-ESI-MS: *m/z* calc. ($C_5H_5ClN_3O_2$ $[M+H]^+$): 174.0065, found: 174.0069.

2,3-Diamino-4-chloropyridine (28)

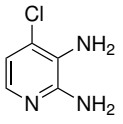

28
$C_5H_6ClN_3$
143.57 g·mol^{-1}

Compound **27** (2.31 g, 13.3 mmol, 1.00 eq.) and ammonium chloride (7.12 g, 133 mmol, 10.0 eq.) were dissolved in methanol (270 mL) under an inert gas atmosphere and stirred at ambient temperature for 5 min. The mixture was cooled to 0 °C and zinc powder (17.4 g, 266 mmol, 20.0 eq.) was added in portions. The reaction mixture was allowed to warm to ambient temperature and stirred for 30 min. Solids were removed by filtration through a pad of Celite and the filtrate was evaporated to dryness. The residue was taken up in ethyl acetate (200 mL) and water (200 mL) and the aqueous layer was adjusted to pH = 9 by addition of 25% aq. ammonia. The layers were separated, and the aqueous layer was extracted with ethyl acetate (4 × 200 mL). The combined organic layers were dried over Na_2SO_4 and the solvent was removed under reduced pressure to yield the product **28** as a light brown solid (1.82 g,

12.7 mmol, 96%). Analytical data agreed with reported values.[264]

^{1}H NMR (400 MHz, DMSO-d_6): δ (ppm) = 7.20 (d, J = 5.5 Hz, 1H, C6-H), 6.49 (d, J = 5.5 Hz, 1H, C5-H), 5.78 (s, 2H, C2-NH_2), 4.90 (s, 2H, C3-NH_2).

^{13}C{^{1}H} NMR (100 MHz, DMSO-d_6): δ (ppm) = 149.22 (1C, C2), 134.85 (1C, C6), 126.31 (1C, C3), 122.24 (1C, C4), 113.20 (1C, C5).

HR-ESI-MS: m/z calc. ($C_5H_7ClN_3$ [M+H]$^+$): 144.0323, found: 144.0326.

6-Chloro-1-deazapurine (29)

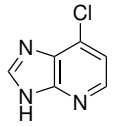

29
$C_6H_4ClN_3$
153.57 g·mol^{-1}

Compound **28** (1.72 g, 12.0 mmol, 1.00 eq.) was suspended in triethyl orthoformate (25.8 mL, 156 mmol, 13.0 eq.) under an inert gas atmosphere. The reaction was stirred at 110 °C for 1 h. The solvent was removed under reduced pressure, and the residue was dissolved in formic acid (38.6 mL, 234 mmol, 19.5 eq.) and stirred at 110 °C for 3 h. The solution was adjusted to pH = 7 by addition of 25% aq. ammonia and extracted with ethyl acetate (5 × 20 mL). The combined organic layers were dried over Na_2SO_4 and the solvent was removed under reduced pressure to yield the product **29** as a light brown solid (1.57 g, 10.3 mmol, 86%).

^{1}H NMR (400 MHz, DMSO-d_6): δ (ppm) = 13.45 (s, 1H, NH), 8.53 (s, 1H, C8-H), 8.30 (d, J = 5.3 Hz, 1H, C2-H), 7.39 (d, J = 5.3 Hz, 1H, C1-H).

^{13}C{^{1}H} NMR (100 MHz, DMSO-d_6): δ (ppm) = 144.49 (2C, C2, C8), 117.93 (1C, C1).

HR-ESI-MS: m/z calc. ($C_6H_5ClN_3$ [M+H]$^+$): 154.0167, found: 154.0171.

4-Amino-2-chloro-3-nitropyridine (31)

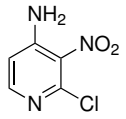

31
$C_5H_4ClN_3O_2$
173.56 g·mol^{-1}

4-Amino-2-chloropyridine (**30**, 5.00 g, 38.9 mmol, 1.00 eq.) was dissolved in conc. sulfuric acid (70 mL) at 0 °C. Conc. nitric acid (2.60 mL, 62.3 mmol, 1.61 eq.) was added dropwise. The reaction mixture was stirred at 0 °C for 30 min, then allowed to warm to ambient temperature and stirred for 19 h. The mixture was poured onto crushed ice (200 g) and adjusted to pH = 9 with 25% aq. ammonia. The resulting suspension was extracted with ethyl acetate (6 × 200 mL). The combined organic layers were dried over Na_2SO_4 and the solvent was removed under reduced pressure. The residue was purified by column chromatography (silica gel, *n*-hexane:EtOAc = 1:1) to yield the product **31** as a yellow solid (4.05 g, 23.3 mmol, 60%). Analytical data agreed with reported values.[265]

^{1}H NMR (400 MHz, DMSO-d_6): δ (ppm) = 7.89 (d, J = 5.9 Hz, 1H, C6-H), 7.35 (s, 2H, NH_2), 6.81 (d, J = 5.9 Hz, 1H, C5-H).

^{13}C{^{1}H} NMR (100 MHz, DMSO-d_6): δ (ppm) = 149.09 (1C, C4), 148.79 (1C, C6), 142.23 (1C, C2), 130.64 (1C, C3), 112.00 (1C, C5).

HR-ESI-MS: *m/z* calc. ($C_5H_5ClN_3O_2$ [M+H]$^+$): 174.0065, found: 174.0066.

3,4-Diamino-2-chloropyridine (32)

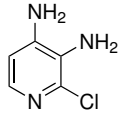

32
$C_5H_6ClN_3$
143.57 g·mol^{-1}

Compound **31** (3.34 g, 19.2 mmol, 1.00 eq.) and ammonium chloride (10.3 g, 192 mmol, 10.0 eq.) were dissolved in methanol (390 mL) under an inert gas atmosphere and stirred at ambient temperature for 5 min. The mixture was cooled to 0 °C and zinc powder (25.2 g, 384 mmol, 20.0 eq.) was added in portions. The reaction mixture was allowed to warm to ambient temperature and stirred for 30 min. Solids were removed by filtration through a pad of Celite and the filtrate was evaporated to dryness. The residue was taken up in ethyl acetate (300 mL) and water (300 mL) and the aqueous layer was adjusted to pH = 9 by addition of 25% aq. ammonia. The layers were separated, and the aqueous layer was extracted with ethyl acetate (4 × 300 mL). The combined organic layers were dried over Na_2SO_4 and the solvent was removed under reduced pressure. The residue was purified by column chromatography (sil-

ica gel, EtOAc) to yield the product **32** as a light brown solid (2.42 g, 16.8 mmol, 84%).

^{1}H NMR (400 MHz, DMSO-d_6): δ (ppm) = 7.28 (d, J = 5.1 Hz, 1H, C6-H), 6.43 (d, J = 5.1 Hz, 1H, C5-H), 5.76 (s, 2H, C4-NH_2), 4.65 (s, 2H, C3-NH_2).

^{13}C{^{1}H} NMR (100 MHz, DMSO-d_6): δ (ppm) = 142.94 (1C, C4), 137.56 (1C, C6), 135.14 (1C, C2), 126.20 (1C, C3), 108.26 (1C, C5).

HR-ESI-MS: m/z calc. ($C_5H_7ClN_3$ $[M+H]^+$): 144.0323, found: 144.0324.

6-Chloro-3-deazapurine (33)

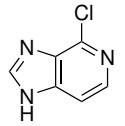

33
$C_6H_4ClN_3$
153.57 g·mol^{-1}

Compound **32** (245 mg, 1.72 mmol, 1.00 eq.) was suspended in trimethyl orthoformate (4.00 mL, 36.5 mmol, 21.2 eq.) and treated with hydrochloric acid (37%, 300 µL, 3.62 mmol, 2.10 eq.). The reaction was stirred at ambient temperature for 16 h. The precipitate was collected by filtration, washed with *n*-hexane and dried to yield the product **33** as a light brown solid (214 mg, 1.39 mmol, 81%).

^{1}H NMR (400 MHz, DMSO-d_6): δ (ppm) = 8.75 (s, 1H, C8-H), 8.18 (d, J = 5.5 Hz, 1H, C2-H), 7.69 (d, J = 5.6 Hz, 1H, C3-H).

^{13}C{^{1}H} NMR (100 MHz, DMSO-d_6): δ (ppm) = 144.69 (1C, C8), 141.19 (1C, C2), 140.65 (1C, C4), 138.94 (1C, C6), 134.08 (1C, C5), 109.00 (1C, C1).

HR-ESI-MS: m/z calc. ($C_6H_5ClN_3$ $[M+H]^+$): 154.01665, found: 154.01768.

2',3',5'-Tri-*O*-benzoyl-6-chloro-1-deazapurine-9-β-D-ribofuranoside (34)

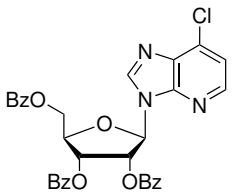

34
$C_{32}H_{24}ClN_3O_7$
598.01 g·mol^{-1}

A solution of compound **29** (1.63 g, 10.6 mmol, 1.00 eq.) and *N*,*O*-bis(trimethylsilyl)acetamide (BSA, 6.25 mL, 21.2 mmol, 2.00 eq.) in acetonitrile (70 mL) under an inert gas atmosphere was stirred at 100 °C for 30 min. After cooling to ambient temperature, 1-*O*-acetyl-2,3,5-tri-*O*-benzoyl-β-D-ribofuranose (5.35 g, 10.6 mmol, 1.00 eq.) and trimethylsilyl trifluoromethanesulfonate (TMSOTf, 3.84 mL, 21.2 mmol, 2.00 eq.) were added. The reaction mixture was stirred at 100 °C for 16 h. It was diluted with ethyl acetate (70 mL) and washed with sat. aq. NH_4Cl solution (4 × 30 mL). The organic layer was dried over Na_2SO_4 and the solvent was removed under reduced pressure. The residue was purified by column chromatography (siliga gel, EtOAc) to yield the product **34** as a light brown solid (5.96 g, 9.97 mmol, 94%).

^{1}H NMR (400 MHz, DMSO-d$_6$): δ (ppm) = 8.83 (s, 1H, C8-H), 8.23 (d, J = 5.3 Hz, 1H, C2-H), 8.00-–7.93 (m, 4H, benzoyl-H), 7.90—7.86 (m, 2H, benzoyl-H), 7.70—7.62 (m, 4H, benzoyl-H), 7.51 (d, J = 5.3 Hz, 1H, C1-H), 7.53—7.42 (m, 5H, benzoyl-H), 6.70 (d, J = 4.6 Hz, 1H, C1'-H), 6.57 (dd, J = 6.0, 4.6 Hz, 1H, C2'-H), 6.28 (t, J = 6.0 Hz, 1H, C3'-H), 4.91—4.86 (m, 1H, 4'-H), 4.79 (dd, J = 12.2, 3.5 Hz, 1H, C5'-H^a), 4.66 (dd, J = 12.2, 4.7 Hz, 1H, C5'-H^b).

^{13}C{^{1}H} NMR (100 MHz, DMSO-d$_6$): δ (ppm) = 165.44 (1C, benzoyl-CO), 164.72 (1C, benzoyl-CO), 164.53 (1C, benzoyl-CO), 146.82 (1C, C4), 145.85 (1C, C8), 144.98 (1C, C2), 134.04 (1C, benzoyl-C), 133.95 (1C, benzoyl-C), 133.73 (1C, benzoyl-C), 133.55 (1C, C6), 133.33 (1C, C5), 129.40 (4C, benzoyl-C), 129.31 (2C, benzoyl-C), 129.26 (1C, benzoyl-C), 128.80 (4C, benzoyl-C), 128.74 (2C, benzoyl-C), 128.62 (1C, benzoyl-C), 128.34 (1C, benzoyl-C), 119.29 (1C, C1), 86.84 (1C, C1'), 79.17 (1C, C4'), 72.87 (1C, C2'), 70.68 (1C, C3'), 63.19 (1C, C5').

HR-ESI-MS: *m/z* calc. ($C_{32}H_{25}ClN_3O_7$ [M+H]$^+$): 598.1376, found: 598.1355.

2',3',5'-Tri-*O*-benzoyl-6-chloro-3-deazapurine-9-β-D-ribofuranoside (35)

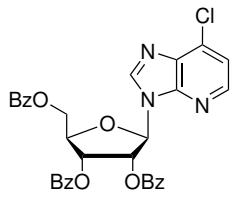

34
$C_{32}H_{24}ClN_3O_7$
598.01 g·mol^{-1}

A solution of compound **33** (1.50 g, 9.77 mmol, 1.00 eq.) and *N*,*O*-bis(trimethylsilyl)acetamide (BSA, 5.75 mL, 19.5 mmol, 2.00 eq.) in acetonitrile (64 mL) under an inert gas atmosphere was stirred at 100 °C for 30 min. After cooling to ambient temperature, 1-*O*-acetyl-2,3,5-tri-*O*-benzoyl-β-D-ribofuranose (4.92 g, 9.75 mmol, 1.00 eq.) and trimethylsilyl trifluoromethanesulfonate (TMSOTf, 3.53 mL, 19.5 mmol, 2.00 eq.) were added. The reaction mixture was stirred at 100 °C for 16 h. It was diluted with ethyl acetate (64 mL) and washed with sat. aq. NH_4Cl solution (4 × 30 mL). The organic layer was dried over Na_2SO_4 and the solvent was removed under reduced pressure. The residue was purified by column chromatography (siliga gel, *n*-hexane:EtOAc = 1:1) to yield the product **35** as a light brown solid (4.92 g, 8.24 mmol, 84%).

^{1}H NMR (400 MHz, $CDCl_3$): δ (ppm) = 8.26 (s, 1H, C8-H), 8.10—8.06 (m, 2H, benzoyl-H), 8.03 (d, *J* = 5.7 Hz, 1H, C2-H), 8.01—7.97 (m, 2H, benzoyl-H), 7.95—7.91 (m, 2H, benzoyl-H), 7.68—7.52 (m, 4H, benzoyl-H, C3-H), 7.54—7.44 (m, 2H, benzoyl-H), 7.48—7.34 (m, 4H, benzoyl-H), 6.35 (d, *J* = 5.6 Hz, 1H, C1'-H), 5.99 (t, *J* = 5.6 Hz, 1H, C2'-H), 5.94 (dd, *J* = 5.6, 4.5 Hz, 1H, C3'-H), 4.94 (dd, *J* = 12.5, 2.6 Hz, 1H, C5'-H^a), 4.89 (dt, *J* = 4.5, 2.9 Hz, 1H, C4'-H), 4.76 (dd, *J* = 12.5, 3.2 Hz, 1H, C5'-H^b).

^{13}C{^{1}H} NMR (100 MHz, $CDCl_3$): δ (ppm) = 166.21 (1C, benzoyl-CO), 165.43 (1C, benzoyl-CO), 165.14 (1C, benzoyl-CO), 143.58 (1C, C6), 142.32 (1C, C8), 142.17 (1C, C2), 138.78 (1C, C5), 138.50 (1C, C4), 134.29 (1C, benzoyl-C), 134.16 (1C, benzoyl-C), 134.00 (1C, benzoyl-C), 129.95 (4C, benzoyl-C), 129.77 (2C, benzoyl-C), 129.07 (1C, benzoyl-C), 129.03 (2C, benzoyl-C), 128.82 (4C, benzoyl-C), 128.53 (1C, benzoyl-C), 128.10 (1C, benzoyl-C), 106.37 (1C, C3), 88.08 (1C, C1'), 81.23 (1C, C4'), 74.11 (1C, C2'), 71.00 (1C, C3'), 63.33 (1C, C5').

HR-ESI-MS: *m*/*z* calc. ($C_{32}H_{24}ClN_3NaO_7$ [M+Na]$^+$): 620.1195, found: 620.1210.

1-Deazapurine (37)

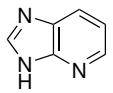

37
$C_6H_5N_3$
119.13 g·mol^{-1}

This compound was prepared according to a reported procedure.[159] 2,3-Diaminopyridine (**36**, 3.00 g, 27.5 mmol, 1.00 eq.) was suspended in triethyl orthoformate (59.0 mL, 360 mmol, 13.1 eq.) and stirred at 145 °C for 3 h. The solvent was removed under reduced pressure and the residue was redissolved in formic acid (300 mL) and stirred at 110 °C for 2 h. The solvent was removed under reduced pressure, the residue was redissolved in methanol (90 mL), treated with decolorizing carbon and stirred at ambient temperature for 12 h. The suspension was filtered through a pad of Celite, the filtrate was evaporated, and the residue was coevaporated with water (3×) and *n*-hexane (3×) to yield the product **37** as a brown solid (3.21 g, 26.9 mmol, 98%). Analytical data agreed with reported values.[159]

^{1}H NMR (400 MHz, DMSO-d_6): δ (ppm) = 12.92 (s_{br}, 1H, NH), 8.43 (s, 1H, C8-H), 8.35 (dd, J = 4.8, 1.5 Hz, 1H, C2-H), 8.01 (dd, J = 8.0, 1.5 Hz, 1H, C6-H), 7.23 (dd, J = 8.0, 4.8 Hz, 1H, C1-H).

^{13}C{^{1}H} NMR (100 MHz, DMSO-d_6): δ (ppm) = 143.95 (1C, C8), 143.73 (1C, C2), 117.76 (1C, C1).

HR-ESI-MS: *m/z* calc. ($C_6H_6N_3$ $[M+H]^+$): 120.05562, found: 120.05663.

1-Deazapurine-3-oxide (38)

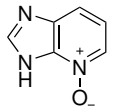

38
$C_6H_5N_3O$
135.13 g·mol^{-1}

Method A (according to a reported procedure):[159] Compound **37** (3.21 g, 26.9 mmol, 1.00 eq.) was suspended in chloroform (27.4 mL), treated with 4-chloroperbenzoic acid (75%, 13.7 g, 59.5 mmol, 2.21 eq.) and stirred at ambient temperature for 48 h. The precipitate was collected by filtration and purified by column chromatography (silica gel, CH_2Cl_2:MeOH = 9:1 to 7:3) to yield the product **38** as an off-white solid (3.28 g, 24.3 mmol, 90%).

Method B (according to a reported procedure):[160] A solution of compound **37** (2.28 g, 19.1 mmol, 1.00 eq.) in acetic acid (100 mL) was treated with 4-chloroperbenzoic acid

(75%, 8.19 g, 35.6 mmol, 1.86 eq.) and stirred at 50 °C for 16 h. The solvent was removed under reduced pressure and the residue was purified by column chromatography (silica gel, CH_2Cl_2:MeOH 9:1 to 7:3) to yield the product **38** as an off-white solid (2.46 g, 18.2 mmol, 95%).

Analytical data agreed with reported values.[159]

^{1}H NMR (400 MHz, DMSO-d_6): δ (ppm) = 13.33 (s_{br}, 1H, NH), 8.43 (s, 1H, C8-H), 8.20 (dd, J = 6.3, 0.8 Hz, 1H, C2-H), 7.61 (d, J = 8.2 Hz, 1H, C6-H), 7.21 (dd, J = 8.1, 6.3 Hz, 1H, C1-H).

^{13}C{^{1}H} NMR (100 MHz, DMSO-d_6): δ (ppm) = 143.45 (1C, C8), 132.88 (1C, C2), 118.98 (1C, C1), 112.03 (1C, C6).

HR-ESI-MS: m/z calc. ($C_6H_5N_3NaO$ $[M+Na]^+$): 158.03248, found: 158.03327.

6-Nitro-1-deazapurine-3-oxide (39)

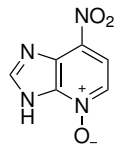

39
$C_6H_5N_4O_3$
135.13 g·mol^{-1}

This compound was prepared according to a reported procedure.[159] Compound **38** (3.27 g, 24.4 mmol, 1.00 eq.) was dissolved in trifluoroacetic acid (25 mL) at 0 °C. Fuming nitric acid (15.3 mL, 366 mmol, 15.0 eq.) was added and the solution was stirred at 90 °C for 3 h. After cooling to ambient temperature, the solution was adjusted to pH = 7 with 25% aq. ammonia. The resulting precipitate was collected by filtration and dried *in vacuo* to yield the product **39** as a yellow solid (3.52 g, 19.7 mmol, 80%). Analytical data agreed with reported values.[266]

^{1}H NMR (400 MHz, DMSO-d_6): δ (ppm) = 14.01 (s_{br}, 1H, NH), 8.61 (s, 1H, C8-H), 8.33 (d, J = 7.2 Hz, 1H, C2-H), 8.09 (d, J = 7.2 Hz, 1H, C1-H).

^{13}C{^{1}H} NMR (100 MHz, DMSO-d_6): δ (ppm) = 145.82 (1C, C8), 133.45 (1C, C2), 115.19 (1C, C1).

HR-ESI-MS: m/z calc. ($C_6H_4N_4NaO_3$ $[M+Na]^+$): 158.03248, found: 158.03327.

6-Nitro-1-deazapurine (40)

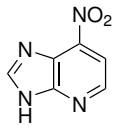

40
$C_6H_4N_4O_2$
164.12 g·mol^{-1}

This compound was prepared according to a reported procedure.[266] A solution of compound **39** (1.20 g, 6.66 mmol, 1.00 eq.) in acetonitrile (25 mL) under an inert gas atmosphere was cooled to 0 °C, treated with phosphorus trichloride (5.28 mL, 60.5 mmol, 9.08 eq.) and stirred at 0 °C for 90 min. The solution was poured onto crushed ice and neutralized by addition of solid Na_2CO_3. The resulting precipitate was collected by filtration and purified by column chromatography (silica gel, CH_2Cl_2:MeOH = 9:1) to yield the product **40** as a reddish yellow solid (695 mg, 4.23 mmol, 63%).

^{1}H NMR (400 MHz, DMSO-d_6): δ (ppm) = 13.74 (s, 1H, NH), 8.78 (s, 1H, C8-H), 8.68 (d, J = 5.4 Hz, 1H, C2-H), 8.00 (d, J = 5.4 Hz, 1H, C1-H).

^{13}C{^{1}H} NMR (100 MHz, DMSO-d_6): δ (ppm) = 148.38 (1C, C8), 144.14 (1C, C2), 110.90 (1C, C1).

HR-ESI-MS: m/z calc. ($C_6H_4N_4NaO_2$ [M+Na]$^+$): 187.02265, found: 187.02189.

2',3',5'-Tri-*O*-benzoyl-6-nitro-1-deazapurine-9-β-D-ribofuranoside (41)

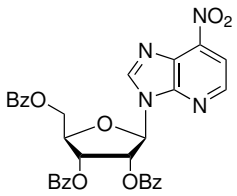

41
$C_{32}H_{24}N_4O_9$
608.56 g·mol^{-1}

A suspension of compound **40** (600 mg, 3.66 mmol, 1.00 eq.) and 1-*O*-acetyl-2,3,5-tri-*O*-benzoyl-β-D-ribofuranose (1.85 g, 3.66 mmol, 1.00 eq.) in acetonitrile (20 mL) under an inert gas atmosphere was treated dropwise with tin tetrachloride (860 µL, 7.32 mmol, 2.00 eq.). The resulting solution was stirred at ambient temperature for 16 h, cooled to 0 °C and neutralized by addition of sat. aq. $NaHCO_3$ solution. The layers were separated and the aqueous layer was extracted with chloroform (4 × 20 mL). The combined organic layers were dried over Na_2SO_4, the solvent was removed under reduced pressure, and the residue was purified by column chromatography (silica gel, CH_2Cl_2:MeOH = 9:1) to yield the product **41** as a yellow foam (1.48 g, 2.43 mmol, 66%).

^{1}H NMR (400 MHz, $CDCl_3$): δ (ppm) = 8.49 (s, 1H, C8-H), 8.47 (d, J = 5.3 Hz, 1H, C2-H), 8.10–8.05 (m, 2H, benzoyl-H), 8.04–8.00 (m, 2H, benzoyl-H), 7.95–7.89 (m, 3H,

C1-H, benzoyl-H), 7.63–7.52 (m, 3H, benzoyl-H), 7.48–7.40 (m, 4H, benzoyl-H), 7.40–7.33 (m, 2H, benzoyl-H), 6.54 (d, *J* = 5.0 Hz, 1H, C1'-H), 6.50 (t, *J* = 5.4 Hz, 1H, C2'-H), 6.26 (dd, *J* = 5.7, 5.0 Hz, 1H, C3'-H), 4.93 (dd, *J* = 12.1, 3.3 Hz, 1H, C5'-H^a), 4.90–4.85 (m, 1H, C4'-H), 4.70 (dd, *J* = 12.1, 4.3 Hz, 1H, C5'-H^b).

^{13}C{^{1}H} NMR (100 MHz, $CDCl_3$): δ (ppm) = 166.23 (1C, benzoyl-C), 165.47 (1C, benzoyl-C), 165.26 (1C, benzoyl-C), 150.06 (1C, C4), 147.12 (1C, C8), 145.41 (1C, C2), 144.52 (1C, C6), 134.05 (1C, benzoyl-C), 133.97 (1C, benzoyl-C), 133.66 (1C, benzoyl-C), 129.98 (2C, benzoyl-C), 129.97 (2C, benzoyl-C), 129.88 (2C, benzoyl-C), 129.40 (1C, benzoyl-C), 128.78 (1C, benzoyl-C), 128.77 (2C, benzoyl-C), 128.75 (2C, benzoyl-C), 128.70 (2C, benzoyl-C), 128.40 (1C, benzoyl-C), 128.38 (1C, C5), 113.03 (1C, C1), 87.81 (1C, C1'), 81.06 (1C, C4'), 73.83 (1C, C2'), 71.59 (1C, C3'), 63.55 (1C, C5').

HR-ESI-MS: *m/z* calc. ($C_{32}H_{24}N_4NaO_9$ [M+Na]$^+$): 631.14355, found: 631.14125.

6-Nitro-1-deazapurine-9-β-D-ribofuranoside (42)

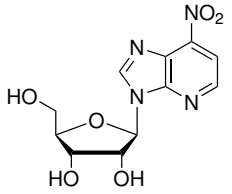

42

$C_{11}H_{12}N_4O_6$

296.24 g·mol^{-1}

A suspension of compound **41** (750 mg, 1.23 mmol, 1.00 eq.) in methanol (12.4 mL) was treated with methanolic ammonia (7 M, 1.80 mL, 12.6 mmol, 10.2 eq.) and stirred at ambient temperature for 24 h. The solvent was removed under reduced pressure and the residue was purified by column chromatography (silica gel, EtOAc:MeOH = 8:2) to yield the product **42** as a light brown solid (314 mg, 1.06 mmol, 86%).

^{1}H NMR (400 MHz, DMSO-d_6): δ (ppm) = 9.08 (s, 1H, C8-H), 8.69 (d, *J*= 5.3 Hz, 1H, C2-H), 8.04 (d, *J*= 5.3 Hz, 1H, C1-H), 6.15 (d, *J*= 5.2 Hz, 1H (C1'-H), 5.59 (d, *J*= 5.8 Hz, 1H, C2'-OH), 5.26 (d, *J*= 5.2 Hz, 1H, C3'-OH), 5.12 (t, *J*= 5.5 Hz, 1H, C5'-OH), 4.61 (q, *J*= 5.3 Hz, 1H, C2'-H), 4.20 (q, *J*= 4.9 Hz, 1H, C3'-H), 4.00 (q, *J*= 3.9 Hz, 1H, C4'-H), 3.72 (ddd, *J*= 12.0, 5.2, 4.0 Hz, 1H, C5'-H^a), 3.59 (ddd, *J*= 12.1, 5.8, 3.9 Hz, 1H, C5'-H^b).

^{13}C{^{1}H} NMR (100 MHz, DMSO-d_6): δ (ppm) = 150.21 (1C, C4), 147.92 (1C, C8), 144.87 (1C, C2), 143.80 (1C, C6), 127.13 (1C, C5), 112.26 (1C, C1), 87.98 (1C, C1'), 85.56 (1C, C4'), 73.94 (1C, C2'), 70.08 (1C, C3'), 61.03 (1C, C5').

HR-ESI-MS: *m/z* calc. ($C_{11}H_{12}N_4NaO_6$ [M+Na]$^+$): 319.0649, found: 319.0652.

6-Chloro-7-iodo-7-deazapurine (44)

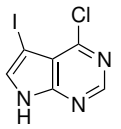

44
$C_6H_3ClIN_3$
279.47 g·mol^{-1}

This compound was prepared according to a reported procedure.[267] A solution of 6-chloro-7-deazapurine (**43**, 1.00 g, 6.52 mmol, 1.00 eq.) in dimethylformamide (2.5 mL) under an inert gas atmosphere was treated with *N*-iodosuccinimide (1.61 g, 7.17 mmol, 1.10 eq.). The reaction mixture was stirred at ambient temperature for 30 min before water (1 mL) was added dropwise to the reaction mixture. The precipitate was collected by filtration, washed with water, and dried to yield the product **44** as a light brown solid (1.46 g, 5.24 mmol, 80%). Analytical data agreed with reported values.[267]

^{1}H NMR (400 MHz, DMSO-d_6): δ (ppm) = 12.95 (s, 1H, NH), 8.59 (s, 1H, C2-H), 7.94 (d, J = 2.5 Hz, 1H, C8-H).

^{13}C{^{1}H} NMR (100 MHz, DMSO-d_6): δ (ppm) = 151.53 (1C, C4), 150.74 (1C, C6), 150.51 (1C, C2), 133.90 (1C, C8), 115.79 (1C, C5), 51.75 (1C, C9).

HR-ESI-MS: m/z calc. ($C_6H_2ClIN_3$ [M−H]$^-$): 277.89875, found: 277.89934.

2',3',5'-Tri-*O*-benzoyl-6-chloro-7-iodo-7-deazapurine-9-β-D-ribofuranoside (45)

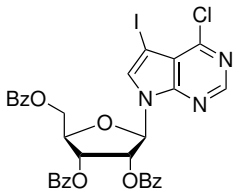

45
$C_{32}H_{23}ClIN_3O_7$
723.90 g·mol^{-1}

This compound was prepared according to a reported procedure.[268] Compound **44** (112 mg, 401 µmol, 1.00 eq.) was suspended in dry acetonitrile (5 mL) under an inert gas atmosphere. *N*,*O*-bis(trimethylsilyl)acetamide (BSA, 110 µL, 450 µmol, 1.12 eq.) was added and the mixture was stirred at ambient temperature for 10 min. 1-*O*-acetyl-2,3,5-tri-*O*-benzoyl-β-D-ribofuranose (223 mg, 442 µmol, 1.10 eq.) was added, followed by trimethylsilyl trifluoromethanesulfonate (TMSOTf, 80.0 µL, 442 µmol, 1.10 eq.). The reaction mixture was stirred at ambient temperature for 15 min, then at 80 °C for 1 h. The solution was diluted with ethyl acetate (20 mL) and washed with sat. aq. $NaHCO_3$ solution (10 mL) and brine (10 mL). The organic layer was separated, dried over Na_2SO_4 and the solvent was removed under reduced pressure. The residue was purified by column chromatography (silica gel, *n*-hexane:EtOAc = 3:1) to yield the product **45** as a colorless foam (232 mg, 320 µmol, 80%).

^{1}H NMR (400 MHz, $CDCl_3$): δ (ppm) = 8.58 (s, 1H, C2-H), 8.14—8.08 (m, 2H, benzoyl-H), 8.02—7.97 (m, 2H, benzoyl-H), 7.95—7.90 (m, 2H, benzoyl-H), 7.65—7.45 (m, 6H, C8-H, benzoyl-H), 7.45—7.32 (m, 4H, benzoyl-H), 6.67 (d, *J* = 5.4 Hz, 1H, C1'-H), 6.17—6.07 (m, 2H, C2'-H, C3'-H), 4.90 (dd, *J* = 12.3, 3.2 Hz, 1H, C5'-H^a), 4.80 (dt, *J* = 4.4, 3.2 Hz, 1H, C4'-H), 4.68 (dd, *J* = 12.3, 3.6 Hz, 1H, C5'-H^b).

^{13}C{^{1}H} NMR (100 MHz, $CDCl_3$): δ (ppm) = 166.26 (1C, benzoyl-CO), 165.51 (1C, benzoyl-CO), 165.21 (1C, benzoyl-CO), 153.27 (1C, C6), 151.39 (1C, C2), 151.13 (1C, C4), 133.97 (1C, benzoyl-C), 133.93 (1C, benzoyl-C), 133.75 (1C, benzoyl-C), 132.14 (1C, C8), 129.99 (2C, benzoyl-C), 129.97 (2C, benzoyl-C), 129.84 (2C, benzoyl-C), 129.38 (1C, benzoyl-C), 128.98 (2C, benzoyl-C), 128.78 (1C, benzoyl-C), 128.72 (2C, benzoyl-C), 128.67 (2C, benzoyl-C), 128.48 (1C, benzoyl-C), 117.93 (1C, C5), 86.90 (1C, C1'), 80.80 (1C, C4'), 74.28 (1C, C2'), 71.56 (1C, C3'), 63.61 (1C, C5'), 53.83 (1C, C7).

HR-ESI-MS: *m/z* calc. ($C_{32}H_{23}ClIN_3NaO_7$ [M+Na]$^+$): 746.01615, found: 746.01704.

2',3',5'-Tri-*O*-(*tert*-butyldimethylsilyl)-N^6-hydroxyadenosine (47)

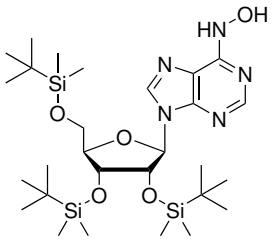

47
$C_{28}H_{55}N_5O_5Si_3$
626.03 g·mol^{-1}

A solution of compound **24** (300 mg, 492 µmol, 1.00 eq.) in dichloromethane (1.5 mL) was treated with a solution of oxone (74.8 mg, 492 µmol, 1.00 eq.) in water (1.5 mL). The reaction was stirred at ambient temperature for 2 h. The organic layer was separated and the solvent was removed under reduced pressure. The residue was purified by column chromatogaphy (silica gel, *n*-hexane:EtOAc = 1:1 to EtOAc:MeOH = 6:4) to yield the product **47** as a red foam (91.3 mg, 146 µmol, 29%).

^{1}H NMR (400 MHz, $CDCl_3$): δ (ppm) = 8.67 (s, 1H, C2-H), 8.32 (s, 1H, C8-H), 5.99 (d, *J* = 5.0 Hz, 1H, C1'-H), 4.56 (t, *J* = 4.6 Hz, 1H, C2'-H), 4.28 (t, *J* = 4.0 Hz, 1H, C3'-H), 4.13 (dt, *J* = 5.1, 2.5 Hz, 1H, C4'-H), 4.01 (dd, *J* = 11.4, 3.9 Hz, 1H, C5'-H^a), 3.79 (dd, *J* = 11.5, 2.6 Hz, 1H, C5'-H^b), 0.96 (s, 9H, $SiC(CH_3)_3$), 0.92 (s, 9H, $SiC(CH_3)_3$), 0.80 (s, 9H, $SiC(CH_3)_3$), 0.15 (s, 3H, $SiCH_3$), 0.14 (s, 3H, $SiCH_3$), 0.10 (s, 3H, $SiCH_3$), 0.09 (s, 3H, $SiCH_3$), -0.03 (s, 3H, $SiCH_3$), -0.22 (s, 3H, $SiCH_3$).

^{13}C{^{1}H} NMR (100 MHz, $CDCl_3$): δ (ppm) = 148.24 (1C, C6), 144.13 (1C, C2), 142.66 (1C, C4), 142.40 (1C, C8), 119.50 (1C, C5), 88.58 (1C, C1'), 85.75 (1C, C4'),

76.33 (1C, C2'), 71.87 (1C, C3'), 62.48 (1C, C5'), 26.20 (3C, SiC($\underline{C}H_3)_3$), 25.94 (3C, SiC($\underline{C}H_3)_3$), 25.78 (3C, SiC($\underline{C}H_3)_3$), 18.66 (3C, Si$\underline{C}(CH_3)_3$), 18.19 (3C, Si$\underline{C}(CH_3)_3$), 17.97 (3C, Si$\underline{C}(CH_3)_3$), -4.26 (1C, $SiCH_3$), -4.56 (1C, $SiCH_3$), -4.60 (1C, $SiCH_3$), -4.91 (1C, $SiCH_3$), -5.22 (1C, $SiCH_3$), -5.28 (1C, $SiCH_3$).

HR-ESI-MS: *m/z* calc. ($C_{58}H_{56}N_5O_5Si_3$ $[M+H]^+$): 626.3584, found: 626.3585.

2',3',5'-Tri-*O*-(*tert*-butyldimethylsilyl)adenosine-N^6-sulfimide (49)

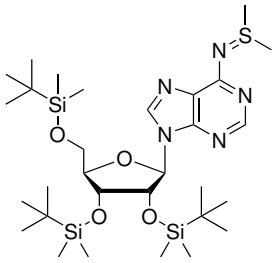

49
$C_{30}H_{59}N_5O_4SSi_3$
670.15 g·mol^{-1}

A solution of compound **24** (200 mg, 328 µmol, 1.00 eq.) in dichloromethane (650 µL) at 0 °C was treated with dimethylsulfide (26.5 µL, 361 µmol, 1.10 eq.) and *N*-chlorosuccinimide (43.8 mg, 328 µmol, 1.00 eq.). The reaction mixture was stirred at 0 °C for 30 min before it was allowed to warm to ambient temperature and stirring was continued for 90 min. A solution of sodium methoxide (30.1 mg, 557 µmol, 1.70 eq.) in methanol (260 µL) was added and the reaction was stirred at ambient temperature for 10 min. Water (500 µL) was added and stirring was continued for 30 min. The organic layer was separated and washed with water (2 × 500 µL). The solvent was removed under reduced pressure. NMR of the crude product showed a ratio of substrate **24** to product **49** = 15:85, corresponding to 85% conversion. The Product could not be purified and was used directly for the following reaction.

N^6,9-Dimethyladenine (52)

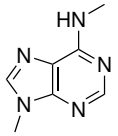

52
$C_7H_9N_5$
163.18 g·mol^{-1}

Under an inert gas atmosphere, a suspension of 6-chloropurine (**51**, 600 mg, 3.88 mmol, 1.00 eq.) and potassium carbonate (776 mg, 5.61 mmol, 1.45 eq.) in *N*,*N*-dimethylformamide (15.5 mL) was treated with iodomethane (290 µL, 4.66 mmol, 1.20 eq.) and stirred at ambient temperature for 2 h. The suspension was filtered and the filtrate was evaporated to dryness. The residue was treated with methylamine (33% in ethanol, 10 mL) and the mixture was stirred at ambient temperature for 16 h. The solvent was removed under reduced pressure and the residue was purified by column chromatography (silica gel, CH_2Cl_2:MeOH = 95:5) to yield the product **52** as a colorless solid (262 mg, 1.61 mmol, 41%).

^{1}H NMR (400 MHz, DMSO-d_6): δ (ppm) = 8.23 (s, 1H, C2-H), 8.07 (s, 1H, C8-H), 7.65 (s_{br}, 1H, N<u>H</u>CH_3), 3.72 (s, 3H, N9-CH_3), 2.95 (s_{br}, 3H, NHC<u>H</u>$_3$).

^{13}C{^{1}H} NMR (100 MHz, DMSO-d_6): δ (ppm) = 154.92 (1C, C6), 152.43 (1C, C2), 148.82 (1C, C4), 141.05 (1C, C8), 119.17 (1C, C5), 29.35 (1C, N9-CH_3, 26.98 (1C, $NHCH_3$).

HR-ESI-MS: *m/z* calc. ($C_7H_{10}N_5$ $[M+H]^+$): 164.0931, found: 164.0938.

Methyl (*N*^{6},9-dimethyladenine)-6-dithiocarbamate (53)

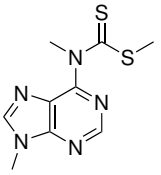

53
$C_9H_{11}N_5S_2$
253.34 g·mol^{-1}

Under an inert gas atmosphere, a solution of compound **52** (100 mg, 613 µmol, 1.00 eq.) in tetrahydrofuran (8 mL) was cooled to -40 °C. *n*-Butyllithium (1.6 M in *n*-hexane, 460 µL, 736 µmol, 1.20 eq.) was added and the reaction was stirred at -40 °C for 2 h. Carbon disulfide (50.0 µL, 828 µmol, 1.35 eq.) was added. The reaction mixture was allowed to warm to ambient temperature and stirred for 16 h. The mixture was cooled to 0 °C and iodomethane (80.0 µL, 1.29 mmol, 2.10 eq.) was added dropwise. The reaction mixture was allowed to warm to ambient temperature and stirred for 6 h before it was diluted with dichloromethane (5 mL) and quenched by addition of sat. aq. $NaHCO_3$ solution (5 mL). The layers were separated and the aqueous layer was extracted with dichloromethane (3 × 5 mL). The combined organic layers were dried over Na_2SO_4 and the solvent was removed *in vacuo*. The residue was purified by column chromatography (silica gel, CH_2Cl_2:MeOH = 95:5) to yield the product **53** as a red oil (92.0 mg, 363 µmol, 59%).

^{1}H NMR (400 MHz, $CDCl_3$): δ (ppm) = 8.92 (s, 1H, C2-H), 8.11 (s, 1H, C8-H), 3.98 (s, 3H, C6-NCH_3), 3.95 (s, 3H, N9-CH_3), 2.63 (s, 3H, SCH_3).

^{13}C{^{1}H} NMR (100 MHz, $CDCl_3$): δ (ppm) = 202.15 (1C, <u>C</u>SSCH_3), 154.46 (1C, C4), 154.03 (1C, C6), 152.34 (1C, C2), 145.61 (1C, C8), 127.94 (1C, C5), 44.62 (1C, C6-N<u>C</u>H_3, 31.41 (1C, N9-CH_3, 21.44 (1C, SCH_3).

HR-ESI-MS: *m/z* calc. ($C_9H_{11}N_5NaS_2$ $[M+Na]^+$): 276.0348, found: 276.0341.

N^6,9-dimethyl,N^6-(trifluoromethyl)adenine (54)

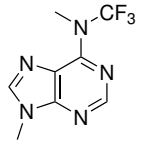

54
$C_8H_8F_3N_5$
231.18 g·mol^{-1}

A suspension of compound **53** (48.0 mg, 189 µmol, 1.00 eq.) and 1,3-dibromo- 5,5-dimethylhydantoin (216 mg, 756 µmol, 4.00 eq.) in dichloromethane (700 µL) was treated with pyridine hydrofluoride (400 µL)and stirred at 50 °C for 4 h. It was quenched by addition of sat. aq. $NaHCO_3$ solution (10 mL). Dichloromethane (10 mL) was added and the layers were separated. The organic layer was evaporated to dryness and the residue was purified by preparative TLC (2 20×20×2 mm silica gel-coated plates, CH_2Cl_2:MeOH = 98:2) to yield the product **54** as a light brown solid (41.0 mg, 177 µmol, 93%).

^{1}H NMR (400 MHz, $CDCl_3$): δ (ppm) = 8.65 (s, 1H, C2-H), 7.95 (s, 1H, C8-H), 3.88 (s, 3H, N9-CH_3), 3.72 (q, J = 2.2 Hz, 3H, C6-NCH_3).

^{19}F$\{^1$H$\}$ NMR (376 MHz, $CDCl_3$): δ (ppm) = -75.12 (s, 3F, NCF_3).

HR-ESI-MS: *m/z* calc. ($C_8H_9F_3N_5$ $[M+H]^+$): 232.0805, found: 232.0810.

9-Benzyl-6-chloropurine (55)

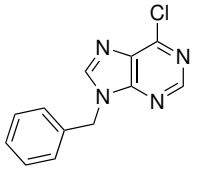

55
$C_{12}H_9ClN_4$
244.68 g·mol^{-1}

Under an inert gas atmosphere, a suspension of 6-chloropurine (**51**, 1.00 g, 6.47 mmol, 1.00 eq.) and potassium carbonate (3.58 g, 25.9 mmol, 4.00 eq.) in *N*,*N*-dimethylformamide (26 mL) was treated with benzyl bromide (4.62 mL, 38.8 mmol, 6.00 eq.) and stirred at ambient temperature for 16 h. The suspension was filtered and the filtrate was evaporated to dryness. The residue was dissolved in dichloromethane (100 mL) and washed with water (3 × 50 mL). The organic layer was dried over Na_2SO_4 and the solvent was removed under reduced pressure. The residue was purified by column chromatography (silica gel, EtOAc) to yield the product **55** as a colorless solid (952 mg, 3.89 mmol, 60%).

HR-ESI-MS: *m/z* calc. ($C_{12}H_9ClN_4Na$ $[M+Na]^+$): 267.0408, found: 267.0405.

N^6,9-Dibenzyladenine (56)

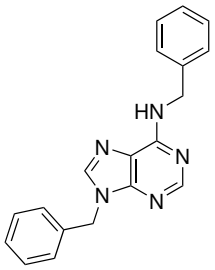

56
$C_{19}H_{17}N_5$
315.38 g·mol^{-1}

A solution of compound **55** (952 mg, 3.89 mmol, 1.00 eq.) in *N*,*N*-dimethylformamide (15.5 mL) was treated with benzylamine (4.26 mL, 39.0 mmol, 10.0 eq.) and stirred at ambient temperature for 16 h. The solvent was removed under reduced pressure. The residue was dissolved in dichloromethane (100 mL) and washed with water (3 × 50 mL). The organic layer was dried over Na_2SO_4 and the solvent was removed *in vacuo*. The residue was purified by column chromatography (silica gel, CH_2Cl_2:EtOAc = 1:0 to 1:1) to yield the product **56** as a colorless solid (1.03 g, 3.27 mmol, 84%).

^{1}H NMR (400 MHz, $CDCl_3$): δ (ppm) = 8.46 (s, 1H, C2-H), 7.64 (s, 1H, C8-H), 7.42–7.23 (m, 10H, benzyl-H), 6.20 (s_{br}, 1H, C6-NH), 5.35 (s, 2H, N9-CH_2), 4.88 (s_{br}, 2H, C6-NHC$\underline{H}_2$).

HR-ESI-MS: *m*/*z* calc. ($C_{19}H_{18}N_5$ $[M+H]^+$): 316.1557, found: 316.1552.

Methyl (N^6,9-dibenzyladenine)-6-dithiocarbamate (57)

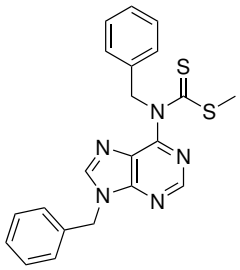

57
$C_{21}H_{19}N_5S_2$
405.54 g·mol^{-1}

Under an inert gas atmosphere, a solution of compound **56** (400 mg, 1.27 mmol, 1.00 eq.) in tetrahydrofuran (16.5 mL) was cooled to -40 °C. *n*-Butyllithium (1.6 M in *n*-hexane, 951 µL, 1.52 mmol, 1.20 eq.) was added and the reaction was stirred at -40 °C for 2 h. Carbon disulfide (103 µL, 1.71 mmol, 1.35 eq.) was added. The reaction mixture was allowed to warm to ambient temperature and stirred for 16 h. The mixture was cooled to 0 °C and iodomethane (167 µL, 2.66 mmol, 2.10 eq.) was added dropwise. The reaction mixture was allowed to warm to ambient temperature and stirred for 6 h before it was diluted with dichloromethane (10 mL) and quenched by addition of sat. aq. $NaHCO_3$ solution (10 mL). The layers were separated and the aqueous layer was extracted with dichloromethane (3 × 10 mL). The combined organic layers were dried over Na_2SO_4 and the solvent was removed *in vacuo*. The residue was purified by column chromatography (silica gel, CH_2Cl_2) to yield the product **57** as a yellow solid (361 mg, 890 µmol, 70%), which could not be completely purified.

HR-ESI-MS: *m/z* calc. ($C_{21}H_{19}N_5NaS_2$ $[M+Na]^+$): 428.0974, found: 428.0968.

General procedure A: 5'-DMT protection

A solution of compound **2** (989 mg, 3.52 mmol, 1.00 eq.) in dry pyridine (25 mL) under an inert gas atmosphere was treated with triethylamine (690 µL, 4.93 mmol, 1.40 eq.) and 4-(dimethylamino)pyridine (DMAP, 21.2 mg, 174 µmol, 0.05 eq.). The solution was cooled to 0 °C and 4,4'-dimethoxytrityl chloride (DMTCl, 1.44 g, 4.27 mmol, 1.20 eq.) was added in four portions over 1 h. The reaction mixture was allowed to warm to ambient temperature and stirred for 16 h. The solvent was removed under reduced pressure and the residue was redissolved in dichloromethane (100 mL) and washed with sat. aq. $NaHCO_3$ solution (3 × 50 mL). The organic layer was separated, dried over Na_2SO_4 and the solvent was removed *in vacuo*. The residue was purified by column chromatography.

5'-*O*-(4,4'-Dimethoxytrityl)-N^6-methyladenosine (58)

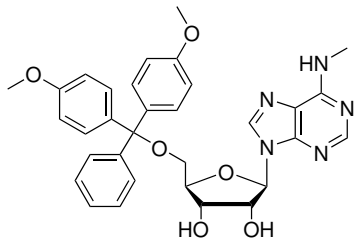

58
$C_{32}H_{33}N_5O_6$
583.65 g·mol^{-1}

Compound **2** (989 mg, 3.52 mmol, 1.00 eq.) was converted according to general procedure A and the crude product was purified by column chromatography (silica gel, CH_2Cl_2:MeOH = 95:5 + 1% NEt_3) to yield the product **58** as a light yellow foam (1.58 g, 2.71 mmol, 77%). Analytical data agreed with reported values.[261]

^{1}H NMR (400 MHz, $CDCl_3$): δ (ppm) = 8.34 (s, 1H, C2-H), 8.03 (s, 1H, C8-H), 7.29—7.24 (m, 2H, trityl-H), 7.20—7.13 (m, 7H, trityl-H), 6.76-–6.69 (m, 4H, trityl-H), 6.04 (s_{br}, 1H, N<u>H</u>CH_3), 5.95 (d, *J* = 6.1 Hz, 1H, C1'-H), 4.77 (t, *J* = 5.6 Hz, 1H, C2'-H), 4.44 (td, *J* = 3.4, 1.7 Hz, 1H, C4'-H), 4.38 (dd, *J* = 5.1, 1.7 Hz, 1H, C3'-H), 3.76 (s, 3H, trityl-OCH_3), 3.75 (s, 3H, trityl-OCH_3), 3.43 (dd, *J* = 10.6, 3.4 Hz, 1H, C5'-H^a), 3.28-–3.12 (m, 4H, C5'-H^b, NHC<u>H</u>$_3$).

^{13}C{^{1}H} NMR (125 MHz, $CDCl_3$): δ (ppm) = 158.62 (2C, trityl-C), 155.67 (1C, C6), 152.69 (1C, C2), 147.86 (1C, C4), 144.39 (1C, trityl-C), 138.00 (1C, C8), 135.69 (1C, trityl-C), 135.52 (1C, trityl-C), 130.07 (2C, trityl-C), 130.04 (2C, trityl-C), 128.12 (2C, trityl-C), 127.95 (2C, trityl-C), 127.00 (1C, trityl-C), 120.36 (1C, C5), 113.23 (4C, trityl-C), 91.07 (1C, C1'), 86.63 (1C, trityl-C), 86.61 (1C, C4'), 76.41 (1C, C2'), 73.08 (1C, C3'), 63.73 (1C, C5'), 55.32 (2C, trityl-OCH_3), 27.61 (1C, $NHCH_3$).

HR-ESI-MS: *m/z* calc. ($C_{32}H_{33}N_5NaO_6$ [M+Na]$^+$): 606.23230, found: 606.23343.

5'-*O*-(4,4'-Dimethoxytrityl)-N^6-dimethyladenosine (59)

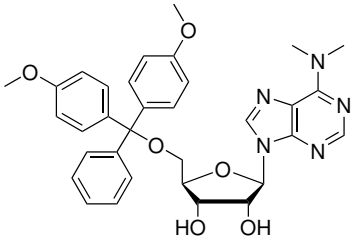

59
$C_{33}H_{35}N_5O_6$
597.67 g·mol^{-1}

Compound **3** (450 mg, 1.52 mmol, 1.00 eq.) was converted according to general procedure A and the crude product was purified by column chromatography (silica gel, CH_2Cl_2:MeOH = 95:5 + 1% NEt_3) to yield the product **59** as a colorless foam (730 mg, 1.22 mmol, 80%). Analytical data agreed with reported values.[261]

^{1}H NMR (300 MHz, $CDCl_3$): δ (ppm) = 8.27 (s, 1H, C2-H), 8.01 (s, 1H, C8-H), 7.30—7.24 (m, 2H, trityl-H), 7.22—7.14 (m, 7H, trityl-H), 6.77—6.70 (m, 4H, trityl-H), 5.92 (d, *J* = 6.2 Hz, 1H, C1'-H), 4.71 (dd, *J* = 6.2, 5.1 Hz, 1H, C2'-H), 4.45 (td, *J* = 3.4, 1.5 Hz, 1H, C4'-H), 4.35 (dd, *J* = 5.1, 1.5 Hz, 1H, C3'-H), 3.77 (s, 3H, trityl-OCH_3), 3.76 (s, 3H, trityl-OCH_3), 3.54 (s_br, 6H, $N(CH_3)_2$), 3.44 (dd, *J* = 10.5, 3.4 Hz, 1H, C5'-H^a), 3.21 (dd, *J* = 10.5, 3.4 Hz, 1H, C5'-H^b).

^{13}C{^{1}H} NMR (125 MHz, $CDCl_3$): δ (ppm) = 158.53 (2C, trityl-C), 155.01 (1C, C6), 151.62 (1C, C2), 149.47 (1C, C4), 144.37 (1C, trityl-C), 136.23 (1C, C8), 135.72 (1C, trityl-C), 135.54 (1C, trityl-C), 130.02 (2C, trityl-C), 130.00 (2C, trityl-C), 128.10 (2C, trityl-C), 127.89 (2C, trityl-C), 126.91 (1C, trityl-C), 120.64 (1C, C5), 113.23 (4C, trityl-C), 91.27 (1C, C1'), 86.74 (1C, C4'), 86.6 (1C, trityl-C), 76.56 (1C, C2'), 73.23 (1C, C3'), 63.84 (1C, C5'), 55.36 (2C, trityl-OCH_3), 38.83 (2C, $N(CH_3)_2$).

HR-ESI-MS: *m/z* calc. ($C_{33}H_{35}N_5NaO_6$ [M+Na]$^+$): 620.2480, found: 620.2482.

5'-*O*-(4,4'-Dimethoxytrityl)-O^6-methylinosine (60)

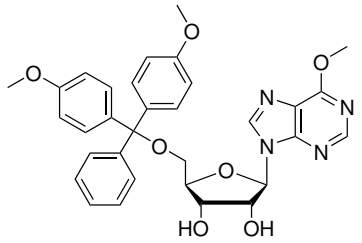

60
$C_{32}H_{32}N_4O_7$
584.63 g·mol^{-1}

Compound **7** (530 mg, 1.88 mmol, 1.00 eq.) was converted according to general procedure A and the crude product was purified by column chromatography (silica gel, CH_2Cl_2:MeOH = 95:5 + 1% NEt_3) to yield the product **60** as a colorless foam (742 mg, 1.27 mmol, 67%).

^{1}H NMR (300 MHz, $CDCl_3$): δ (ppm) = 8.50 (s, 1H, C2-H), 8.17 (s, 1H, C8-H), 7.31–7.25 (m, 2H, trityl-H), 7.22–7.15 (m, 7-H, trityl-H), 6.77–6.70 (m, 4H, trityl-H), 6.00 (d, J = 5.8 Hz, 1H, C1'-H), 4.81 (dd, J = 5.8, 4.8 Hz, 1H, C2'-H), 4.46–4.40 (m, 2H, C3'-H, C4'-H), 4.21 (s, 3H, OCH_3), 3.76 (s, 6H, trityl-OCH_3), 3.43 (dd, J = 10.5, 3.4 Hz, 1H, C5'-H^a), 3.29 (dd, J = 10.5, 3.4 Hz, 1H, C5'-H^b).

^{13}C{^{1}H} NMR (125 MHz, $CDCl_3$): δ (ppm) = 161.30 (1C, C6), 158.57 (2C, trityl-C), 151.76 (1C, C2), 151.09 (1C, C4), 144.31 (1C, trityl-C), 140.63 (1C, C8), 135.54 (1C, trityl-C), 135.48 (1C, trityl-C), 130.03 (2C, trityl-C), 130.00 (2C, trityl-C), 128.07 (2C, trityl-C), 127.90 (2C, trityl-C), 126.97 (1C, trityl-C), 122.23 (1C, C5), 113.24 (4C, trityl-C), 90.93 (1C, C1'), 86.75 (1C, trityl-C), 86.21 (1C, C4'), 76.10 (1C, C2'), 72.78 (1C, C3'), 63.77 (1C, C5'), 55.38 (2C, trityl-OCH_3), 54.61 (1C, OCH_3).

HR-ESI-MS: m/z calc. ($C_{32}H_{32}N_4NaO_7$ [M+Na]$^+$): 607.2163, found: 607.2158.

5'-*O*-(4,4'-Dimethoxytrityl)-6-(methylthio)purine-9-riboside (61)

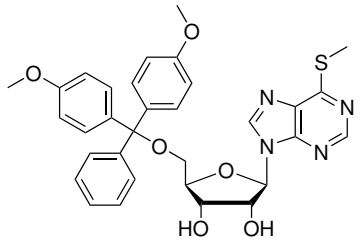

61
$C_{32}H_{32}N_4O_6S$
600.69 g·mol^{-1}

Compound **9** (587 mg, 1.97 mmol, 1.00 eq.) was converted according to general procedure A and the crude product was purified by column chromatography (silica gel, CH_2Cl_2:MeOH = 95:5 + 1% NEt_3) to yield the product **61** as a colorless foam (763 mg, 1.27 mmol, 64%).

^{1}H NMR (300 MHz, $CDCl_3$): δ (ppm) = 8.66 (s, 1H, C2-H), 8.22 (s, 1H, C8-H), 7.31–7.25 (m, 2H, trityl-H), 7.22–7.14 (m, 7H, trityl-H), 6.76–6.70 (m, 4H, trityl-H), 6.02 (d, J = 5.5 Hz, 1H, C1'-H), 4.80 (dd, J = 5.5, 4.8 Hz, 1H, C2'-H), 4.44–4.37 (m, 2H, C3'-H, C4'-H), 3.76 (s, 6H, trityl-OCH_3), 3.45 (dd, J = 11.0, 3.7 Hz, 1H, C5'-H^a), 3.30 (dd, J = 10.6, 3.4 Hz, 1H, C5'-H^b), 2.73 (s, 3H, SCH_3).

^{13}C{^{1}H} NMR (125 MHz, $CDCl_3$): δ (ppm) = 162.63 (1C, C6), 158.56 (2C, trityl-C), 151.35 (1C, C2), 147.07 (1C, C4), 144.28 (1C, trityl-C), 141.02 (1C, C8), 135.56 (1C, trityl-C), 135.49 (1C, trityl-C), 132.07 (1C, C5), 129.98 (4C, trityl-C), 128.08 (2C, trityl-C), 127.91 (2C, trityl-C), 126.99 (1C, trityl-C), 113.24 (4C, trityl-C), 90.77 (1C, C1'), 86.75 (1C, trityl-C), 85.99 (1C, C4'), 75.94 (1C, C2'), 72.53 (1C, C3'), 63.63 (1C, C5'), 56.37 (2C, trityl-OCH_3), 12.07 (1C, SCH_3).

HR-ESI-MS: m/z calc. ($C_{32}H_{33}N_4O_6S$ $[M+H]^+$): 601.2115, found: 601.2107.

5'-*O*-(4,4'-Dimethoxytrityl)-6-ethylpurine-9-riboside (62)

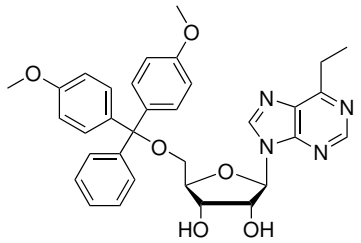

62
$C_{33}H_{34}N_4O_6$
582.66 g·mol^{-1}

Compound **10** (1.20 g, 4.28 mmol, 1.00 eq.) was converted according to general procedure A and the crude product was purified by column chromatography (silica gel, CH_2Cl_2:MeOH = 95:5 + 1% NEt_3) to yield the product **62** as a colorless foam (2.17 g, 3.72 mmol, 87%).

^{1}H NMR (400 MHz, $CDCl_3$): δ (ppm) = 8.84 (s, 1H, C2-H), 8.30 (s, 1H, C8-H), 7.29—7.19 (m, 2H, trityl-H), 7.20—7.11 (m, 7H, trityl-H), 6.76-–6.68 (m, 4H, trityl-H), 6.02 (d, J = 5.9 Hz, 1H, C1'-H), 4.87 (dd, J = 6.0, 4.8 Hz, 1H, C2'-H), 4.48—4.40 (m, 2H, C3'-H, C4'-H)), 3.76 (2 s, 6H, trityl-OCH_3), 3.45 (dd, J = 10.6, 3.5 Hz, 1H, C5'-H^a), 3.31-–3.20 (m, 3H, C5'-H^b, $C\underline{H}_2CH_3$), 1.46 (t, J = 7.6 Hz, 3H, $CH_2C\underline{H}_3$).

5'-*O*-(4,4'-Dimethoxytrityl)-N^6-methyl-1-deazaadenosine (63)

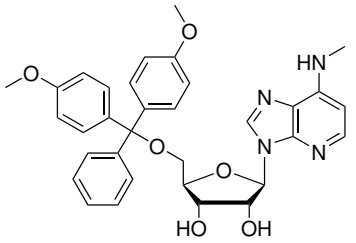

63
$C_{33}H_{34}N_4O_6$
582.66 g·mol^{-1}

Compound **13** (584 mg, 1.96 mmol, 1.00 eq.) was converted according to general procedure A and the crude product was purified by column chromatography (silica gel, CH_2Cl_2:MeOH = 98:2 + 2% NEt_3) to yield the product **63** as an off-white foam (1.00 g, 1.72 mmol, 88%).

^{1}H NMR (400 MHz, $CDCl_3$): δ (ppm) = 8.06 (s, 1H, C8-H), 8.01 (d, J = 5.7 Hz, 1H, C2-H), 7.32-–7.22 (m, 2H, trityl-H), 7.21-–7.14 (m, 7H, trityl-H), 6.75—6.68 (m, 4H, trityl-H), 6.35 (d, J = 5.7 Hz, 1H, C1-H), 5.97 (d, J = 6.4 Hz, 1H, C1'-H), 5.50 (q, J = 5.1 Hz, 1H, N<u>H</u>CH_3), 4.72 (dd, J = 6.4, 5.0 Hz, 1H, C2'-H), 4.48 (td, J = 3.4, 1.2 Hz, 1H, C4'-H), 4.35 (dd, J = 5.0, 1.2 Hz, 1H, C3'-H), 3.75 (2 s, 6H, trityl-OCH_3), 3.43 (dd, J = 10.4, 3.6 Hz, 1H, C5'-H^a), 3.21 (dd, J = 10.5, 3.3 Hz, 1H, C5'-H^b), 3.05 (d, J = 5.1 Hz, 3H, NHC<u>H</u>$_3$).

^{13}C{^{1}H} NMR (100 MHz, $CDCl_3$): δ (ppm) = 158.58 (1C, trityl-C), 158.56 (1C, trityl-C), 147.96 (1C, C6), 145.91 (1C, C4), 145.17 (1C, C2), 144.42 (1C, trityl-C), 137.64 (1C, C8), 135.83 (1C, trityl-C), 135.62 (1C, trityl-C), 130.10 (2C, trityl-C), 130.05 (2C, trityl-C), 128.18 (2C, trityl-C), 127.95 (2C, trityl-C), 126.95 (1C, trityl-C), 124.05 (1C, C5), 113.23 (2C, trityl-C), 113.22 (2C, trityl-C), 98.33 (1C, C1), 91.31 (1C, C1'), 86.85 (1C, C4'), 86.51 (1C, trityl-C), 76.69 (1C, C2'), 73.28 (1C, C3'), 63.85 (1C, C5'), 55.31 (2C, trityl-OCH_3), 29.50 (1C, $NHCH_3$).

HR-ESI-MS: m/z calc. ($C_{33}H_{35}N_4O_6$ [M+H]$^+$): 583.2551, found: 583.2556.

5'-*O*-(4,4'-Dimethoxytrityl)-N^6-methyl-3-deazaadenosine (64)

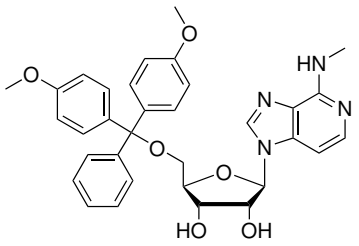

64
$C_{33}H_{34}N_4O_6$
582.66 g·mol^{-1}

Compound **15** (730 mg, 2.60 mmol, 1.00 eq.) was converted according to general procedure A and the crude product was purified by column chromatography (silica gel, CH_2Cl_2:MeOH = 98:2 + 2% NEt_3) to yield the product **64** as a colorless foam (1.02 g, 1.75 mmol, 67%).

^{1}H NMR (400 MHz, DMSO-d_6): δ (ppm) = 8.18 (s, 1H, C8-H), 7.62 (d, J = 5.8 Hz, 1H, C2-H), 7.39—7.33 (m, 2H, trityl-H), 7.31-–7.19 (m, 7H, trityl-H), 6.87—6.80 (m, 5H, C3-H, trityl-H), 6.74 (q, J = 4.7 Hz, 1H, N<u>H</u>CH_3), 5.81 (d, J = 5.3 Hz, 1H, C1'-H), 5.61 (d, J = 6.1 Hz, 1H, C2'-OH), 5.28 (d, J = 5.6 Hz, 1H, C3'-OH), 4.43 (q, J = 5.5 Hz, 1H, C2'-H), 4.18 (q, J = 5.1 Hz, 1H, C3'-OH), 4.08 (td, J = 4.6, 3.1 Hz, 1H, C4'-OH), 3.72 (s, 6H, trityl-OCH_3), 3.26—3.16 (m, 2H, C5-H), 2.91 (d, J = 4.7 Hz, 3H, NHC<u>H</u>$_3$).

^{13}C{^{1}H} NMR (100 MHz, DMSO-d_6): δ (ppm) = 158.08 (2C, trityl-C), 152.09 (1C, C6), 144.75 (1C, trityl-C), 140.55 (1C, C2), 139.30 (1C, C8), 136.75 (1C, C4), 135.41 (1C, trityl-C), 135.31 (1C, trityl-C), 129.76 (2C, trityl-C), 129.73 (2C, trityl-C), 127.87 (2C, trityl-C), 127.71 (2C, trityl-C), 127.34 (1C, C5), 126.73 (1C, trityl-C), 113.19 (4C, trityl-C), 96.92 (1C, C3), 88.94 (1C, C1'), 85.65 (1C, trityl-C), 83.34 (1C, C4'), 73.43 (1C, C2'), 70.08 (1C, C3'), 63.58 (1C, C5'), 55.03 (2C, trityl-OCH_3), 27.55 (1C, $NHCH_3$).

HR-ESI-MS: m/z calc. ($C_{33}H_{35}N_4O_6$ $[M+H]^+$): 583.2551, found: 583.2559.

5'-*O*-(4,4'-Dimethoxytrityl)-N^6-methyl-7-deazaadenosine (65)

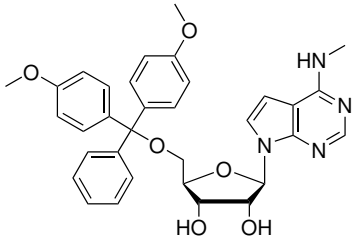

65
$C_{33}H_{34}N_4O_6$
582.66 g·mol^{-1}

Compound **17** (593 mg, 2.12 mmol, 1.00 eq.) was converted according to general procedure A with the following modifications: After addition of 4,4'-dimethoxytrityl chloride, the reaction mixture was stirred at ambient temperature for 20 h. An additional portion of 4,4'-dimethoxytrityl chloride (359 mg, 1.06 mmol, 0.50 eq.) was added and stirring was continued for 3 h before workup. After workup, the crude product was purified by column chromatography (silica gel, CH_2Cl_2:MeOH =

98:2 + 1% NEt_3 to 95:5 + 1% NEt_3) to yield the product **65** as a light yellow foam (742 mg, 1.27 mmol, 60%).

^{1}H NMR (400 MHz, $CDCl_3$): δ (ppm) = 8.25 (s, 1H, C2-H), 7.34 (d, J = 3.7 Hz, 1H, C8-H), 7.33—7.27 (m, 2H, trityl-H), 7.24-–7.14 (m, 7H, trityl-H), 6.77—6.70 (m, 4H, trityl-H), 6.38 (d, J = 3.7 Hz, 1H, C7-H), 6.04 (d, J = 6.2 Hz, 1H, C1'-H), 5.17 (s_{br}, 1H, N<u>H</u>CH_3), 4.67 (dd, J = 6.2, 5.1 Hz, 1H, C2'-H), 4.40 (td, J = 3.3, 1.9 Hz, 1H, C4'-H), 4.33 (dd, J = 5.2, 1.9 Hz, 1H, C3'-H), 3.76 (2 s, 6H, trityl-OCH_3), 3.47 (dd, J = 10.4, 3.3 Hz, 1H, C5'-H^a), 3.21-–3.17 (m, 4H, C5'-H^b, NHC<u>H</u>$_3$).

^{13}C{^{1}H} NMR (100 MHz, $CDCl_3$): δ (ppm) = 158.57 (2C, trityl-C, 157.33 (1C, C6), 151.26 (1C, C2), 148.66 (1C, C4), 144.58 (1C, trityl-C), 135.94 (1C, trityl-C), 135.71 (1C, trityl-C), 130.19 (2C, trityl-C), 130.12 (2C, trityl-C), 128.26 (2C, trityl-C), 127.93 (2C, trityl-C), 126.93 (1C, trityl-C), 122.00 (1C, C8), 113.19 (4C, trityl-C), 103.88 (1C, C5), 98.15 (1C, C7), 91.01 (C1'), 86.50 (1C, trityl-C), 85.85 (1C, C4'), 76.51 (1C, C2'), 73.29 (1C, C3'), 63.80 (1C, C5'), 55.33 (2C, trityl-OCH_3), 28.51 (1C, $NHCH_3$).

HR-ESI-MS: *m/z* calc. ($C_{33}H_{35}N_4O_6$ $[M+H]^+$): 583.25511, found: 583.25597.

General procedure B: 2'-TOM protection

2'-[(triisopropylsilyl)oxy]methyl (TOM) protection was performed according to a reported procedure.[261] A solution of compound **58** (286 mg, 490 µmol, 1.00 eq.) in dry 1,2-dichloroethane (DCE, 1.80 mL) under an inert gas atmosphere was treated with diisopropylethylamine (350 µL, 2.01 mmol, 4.10 eq.) and di-*tert*-butyltin dichloride (179 mg, 589 µmol, 1.20 eq.). The reaction mixture was stirred at 70 °C for 15 min and then allowed to cool to ambient temperature. [(triisopropylsilyl)oxy]methyl chloride (TOMCl, 131 mg, 588 µmol, 1.20 eq.) was added and the mixture was stirred at ambient temperature for 30 min. Methanol (120 µL) was added, the solution was diluted with dichloromethane (50 mL) and washed with sat. aq. $NaHCO_3$ solution (3 × 30 mL). The organic layer was separated, dried over Na_2SO_4 and the solvent was removed under reduced pressure. The residue was purified by column chromatography.

5'-*O*-(4,4'-Dimethoxytrityl)-2'-*O*-[[(triisopropylsilyl)oxy]methyl]-N^6-methyladenosine (66)

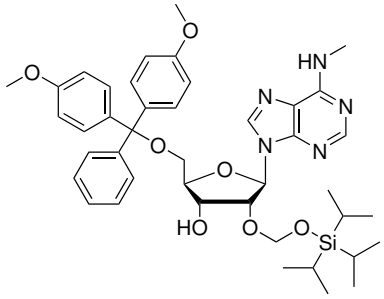

66
$C_{42}H_{55}N_5O_7Si$
770.02 g·mol^{-1}

Compound **58** (286 mg, 490 µmol, 1.00 eq.) was converted according to general procedure B and the crude product was purified by column chromatography (silica gel, *n*-hexane:EtOAc = 1:9 + 1% NEt_3) to yield the product **66** as a colorless foam (137 mg, 178 µmol, 36%). Analytical data agreed with reported values.[261]

^{1}H NMR (500 MHz, $CDCl_3$): δ (ppm) = 8.33 (s, 1H, C2-H), 7.94 (s, 1H, C8-H), 7.45—7.41 (m, 2H, trityl-H), 7.34—7.30 (m, 4H, trityl-H), 7.27-–7.23 (m, 2H, trityl-H), 7.22—7.18 (m, 1H, trityl-H), 6.81-–6.77 (m, 4H, trityl-H), 6.15 (d, *J* = 5.3 Hz, 1H, C1'-H), 5.77 (s_{br}, 1H, N<u>H</u>CH_3), 5.14 (d, *J* = 4.7 Hz, 1H, C2'-OCH_2^a), 4.98 (d, *J* = 4.7 Hz, 1H, C2'-OCH_2^b), 4.93 (t, *J* = 5.3 Hz, 1H, C2'-H), 4.52 (q, *J* = 4.2 Hz, 1H, C3'-H), 4.27 (q, *J* = 3.9 Hz, 1H, C4'-H), 3.78 (2 s, 6H, trityl-OCH_3), 3.49 (dd, *J* = 10.5, 3.6 Hz, 1H, C5'-H^a), 3.38 (dd, *J* = 10.5, 4.2 Hz, 1H, C5'-H^b), 3.19 (s_{br}, 3H, NHC<u>H</u>$_3$), 3.09 (s, 1H, C3'-OH), 1.11—1.00 (m, 21H, (C<u>H</u>$(CH_3)_2)_3$, ($CH(C\underline{H}_3)_2)_3$).

^{13}C{^{1}H} NMR (125 MHz, $CDCl_3$): δ (ppm) = 158.62 (2C, trityl-C), 155.57 (1C, C6), 153.40 (1C, C2), 148.88 (1C, C4), 144.73 (1C, trityl-C), 138.73 (1C, C8), 135.92 (1C, trityl-C), 135.88 (1C, trityl-C), 130.22 (4C, trityl-C), 128.33 (2C, trityl-C), 127.97 (2C, trityl-C), 127.00 (1C, trityl-C), 120.59 (1C, C5), 113.27 (4C, trityl-C), 90.98 (1C, C2'-O<u>C</u>H_2), 87.13 (1C, C1'), 86.64 (1C, trityl-C), 84.20 (1C, C4'), 82.25 (1C, C2'), 71.02 (1C, C3'), 63.54 (1C, C5'), 55.35 (2C, trityl-OCH_3), 27.65 (1C, $NHCH_3$), 17.90 (6C, $CH(\underline{C}H_3)_2$), 11.96 (3C, <u>C</u>$H(CH_3)_2$).

HR-ESI-MS: *m/z* calc. ($C_{42}H_{55}N_5NaO_7Si$ $[M+Na]^+$): 792.37630, found: 792.37626.

5'-*O*-(4,4'-Dimethoxytrityl)-2'-*O*-[[(triisopropylsilyl)oxy]methyl]-N^6-dimethyladenosine (67)

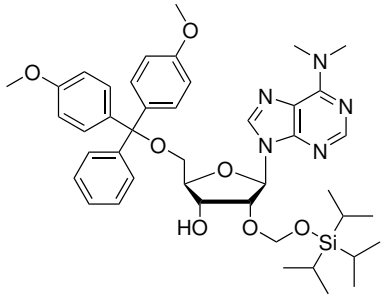

67
$C_{43}H_{57}N_5O_7Si$
784.04 g·mol^{-1}

Compound **59** (526 mg, 880 µmol, 1.00 eq.) was converted according to general procedure B and the crude product was purified by column chromatography (silica gel, *n*-hexane:EtOAc = 1:1 + 1% NEt_3) to yield the product **67** as a colorless foam (181 mg, 231 µmol, 26%). Analytical data agreed with reported values.[261]

^{1}H NMR (600 MHz, $CDCl_3$): δ (ppm) = 8.27 (s, 1H, C2-H), 7.92 (s, 1H, C8-H), 7.45—7.43 (m, 2H, trityl-H), 7.35—7.31 (m, 4H, trityl-H), 7.28—7.23 (m, 2H, trityl-H), 7.22-–7.18 (m, 1H, trityl-H), 6.81-–6.78 (m, 4H, trityl-H), 6.17 (d, *J* = 5.2 Hz, 1H, C1'-H), 5.14 (d, *J* = 4.8 Hz, 1H, C2'-OCH_2^a), 4.98 (d, *J* = 4.8 Hz, 1H, C2'-OCH_2^b), 4.87 (t, *J* = 5.2 Hz, 1H, C2'-H), 4.49 (q, *J* = 4.3 Hz, 1H, C3'-H), 4.25 (q, *J* = 4.0 Hz, 1H, C4'-H), 3.78 (2 s, 6H, trityl-OCH_3), 3.58—3.46 (m, 7H, C5'-H^a, $N(CH_3)_2$), 3.35 (dd, *J* = 10.5, 4.3 Hz, 1H, C5'-H^b), 3.07 (d, *J* = 4.1 Hz, 1H, C3'-OH), 1.13—0.98 (m, 21H, ($C\underline{H}(CH_3)_2)_3$, ($CH(C\underline{H}_3)_2)_3$).

^{13}C{^{1}H} NMR (125 MHz, $CDCl_3$): δ (ppm) = 158.53 (2C, trityl-C), 154.97 (1C, C6), 152.53 (1C, C2), 150.46 (1C, C4), 144.72 (1C, trityl-C), 136.92 (1C, C8), 135.94 (1C, trityl-C), 135.91 (1C, trityl-C), 130.16 (4C, trityl-C), 128.29 (2C, trityl-C), 127.90 (2C, trityl-C), 126.89 (1C, trityl-C), 120.79 (1C, C5), 113.25 (4C, trityl-C), 90.92 (1C, C2'-$O\underline{C}H_2$), 87.02 (1C, C1'), 86.59 (1C, trityl-C), 84.06 (1C, C4'), 82.11 (1C, C2'), 70.97 (1C, C3'), 63.61 (1C, C5'), 55.38 (2C, trityl-OCH_3), 38.73 (2C, $N(CH_3)_2$), 18.00 (6C, $CH(\underline{C}H_3)_2$), 12.11 (3C, $\underline{C}H(CH_3)_2$).

HR-ESI-MS: *m/z* calc. ($C_{43}H_{58}N_5O_7Si$ $[M+H]^+$): 784.4100, found: 784.4103.

5'-*O*-(4,4'-Dimethoxytrityl)-2'-*O*-[[(triisopropylsilyl)oxy]methyl]-O^6-methylinosine (68)

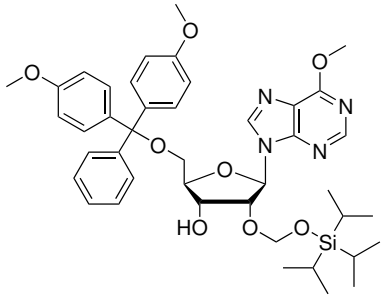

68
$C_{42}H_{54}N_4O_8Si$
771.00 g·mol^{-1}

Compound **60** (723 mg, 1.24 mmol, 1.00 eq.) was converted according to general procedure B and the crude product was purified by column chromatography (silica gel, *n*-hexane:EtOAc = 1:1 + 1% NEt_3) to yield the product **68** as a colorless foam (325 mg, 422 µmol, 34%).

^{1}H NMR (500 MHz, $CDCl_3$): δ (ppm) = 8.45 (s, 1H, C2-H), 8.10 (s, 1H, C8-H), 7.44–7.41 (m, 2H, trityl-H), 7.34–7.30 (m, 4H, trityl-H), 7.27–7.23 (m, 2H, trityl-H), 7.22–7.17 (m, 1H, trityl-H), 6.81–6.77 (m, 4H, trityl-H), 6.21 (d, *J* = 5.6 Hz, 1H, C1'-H), 5.12 (d, *J* = 4.8 Hz, 1H, C2'-OCH_2^a), 4.97–4.92 (m, 2H, C2'-OCH_2^b, C2'-H), 4.51 (dt, *J* = 5.1, 3.5 Hz, 1H, C3'-H), 4.30 (q, *J* = 3.7 Hz, 1H, C4'-H), 4.18 (s, 3H, OCH_3), 3.78 (s, 3H, trityl-OCH_3, 3.77 (s, 3H, trityl-OCH_3), 3.47 (dd, *J* = 10.5, 3.5 Hz, 1H, C5'-H^a), 3.40 (dd, *J* = 10.5, 4.3 Hz, 1H, C5'-H^b), 3.06 (d, *J* = 3.6 Hz, 1H, C3'-OH), 1.12–0.98 (m, 21H, ($C\underline{H}(CH_3)_2)_3$, ($CH(C\underline{H}_3)_2)_3$).

^{13}C{^{1}H} NMR (125 MHz, $CDCl_3$): δ (ppm) = 161.19 (1C, C6),158.64 (2C, trityl-C), 152.34 (1C, C2), 151.88 (1C, C4), 144.66 (1C, trityl-C), 141.22 (1C, C8), 135.84 (1C, trityl-C), 135.75 (2C, trityl-C), 130.21 (4C, trityl-C), 128.28 (2C, trityl-C), 128.00 (2C, trityl-C), 127.03 (1C, trityl-C), 122.23 (1C, C5), 113.28 (4C, trityl-C), 90.99 (1C, C2'-O$\underline{C}H_2$), 87.15 (1C, C1'), 86.73 (1C, trityl-C), 84.42 (1C, C4'), 82.34 (1C, C2'), 71.20 (1C, C3'), 63.61 (1 C, C5'), 55.34 (2C, trityl-OCH_3), 54.34 (1C, OCH_3), 17.89 (6C, ($CH(\underline{C}H_3)_2)_3$), 11.95 (3C, ($\underline{C}H(CH_3)_2)_3$).

HR-ESI-MS: *m/z* calc. ($C_{42}H_{55}N_4O_8Si$ $[M+H]^+$): 771.3784, found: 771.3767.

5'-*O*-(4,4'-Dimethoxytrityl)-2'-*O*-[[(triisopropylsilyl)oxy]methyl]-6-(methylthio)purine-9-riboside (69)

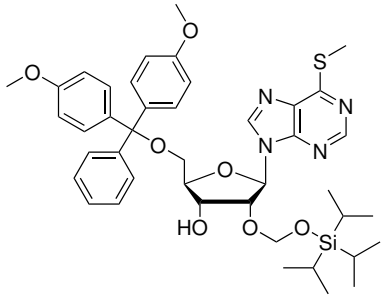

69
$C_{42}H_{54}N_4O_7SSi$
787.06 g·mol^{-1}

Compound **61** (749 mg, 1.25 mmol, 1.00 eq.) was converted according to general procedure B and the crude product was purified by column chromatography (silica gel, *n*-hexane:EtOAc = 6:4 + 2% NEt_3) to yield the product **69** as a colorless foam (184 mg, 234 µmol, 19%).

^{1}H NMR (600 MHz, $CDCl_3$): δ (ppm) = 8.63 (s, 1H, C2-H), 8.14 (s, 1H, C8-H), 7.44–7.40 (m, 2H, trityl-H), 7.33–7.29 (m, 4H, trityl-H), 7.27–7.23 (m, 2H, trityl-H), 7.22–7.18 (m, 1H, trityl-H), 6.81–6.77 (m, 4H, trityl-H), 6.20 (d, *J* = 5.6 Hz, 1H, C1'-H), 5.13 (d, *J* = 4.8 Hz, 1H, C2'-OCH_2^a), 4.97–4.94 (m, 2H, C2'-OCH_2^b, C2'-H), 4.55 (dd, *J* = 5.2, 3.0 Hz, 1H, C3'-H), 4.29 (q, *J* = 3.7 Hz, 1H, C4'-H), 3.78 (2s, 6H, trityl-OCH_3), 3.48 (dd, *J* = 10.5, 3.4 Hz, 1H, C5'-H^a), 3.39 (dd, *J* = 10.5, 4.2 Hz, 1H, C5'-H^b), 3.05 (d, *J* = 3.5 Hz, 1H, C3'-OH), 2.72 (s, 3H, SCH_3), 1.11–0.99 (m, 21H, $(CH(C\underline{H}_3)_2)_3$, $(C\underline{H}(CH_3)_2)_3$).

^{13}C{^{1}H} NMR (125 MHz, $CDCl_3$): δ (ppm) = 161.82 (1C, C6) 158.57 (2C, trityl-C), 152.05 (1C, C2), 148.11 (1C, C4), 144.58 (1C, trityl-C), 141.56 (1C, C8), 135.80 (1C, trityl-C), 135.74 (1C, trityl-C), 132.07 (1C, C5), 130.14 (2C, trityl-C), 130.11 (2C, trityl-C), 128.23 (2C, trityl-C), 127.92 (2C, trityl-C), 126.96 (1C, trityl-C), 113.27 (4C, trityl-C), 91.00 (1C, C2'-OCH_2), 87.15 (1C, C1'), 86.75 (1C, trityl-C), 84.48 (1C, C4'), 82.23 (1C, C2'), 71.18 (1C, C3'), 63.61 (1C, C5'), 55.39 (2C, trityl-OCH_3), 17.99 (6C, $(CH(\underline{C}H_3)_2)_3$), 12.09 (3C, $(\underline{C}H(CH_3)_2)_3$), 11.99 (1C, SCH_3).

HR-ESI-MS: *m/z* calc. ($C_{42}H_{55}N_4O_7SSi$ $[M+H]^+$): 787.3555, found: 787.3532.

5'-*O*-(4,4'-Dimethoxytrityl)-2'-*O*-[[(triisopropylsilyl)oxy]methyl]-6-ethylpurine-9-riboside (70)

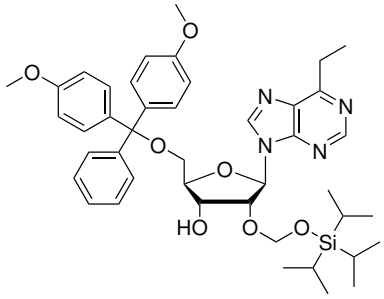

70
$C_{43}H_{56}N_4O_7Si$
769.03 g·mol^{-1}

Compound **61** (1.00 g, 1.72 mmol, 1.00 eq.) was converted according to general procedure B and the crude product was purified by column chromatography (silica gel, *n*-hexane:EtOAc = 1:1 + 1% NEt_3) to yield the product **70** as a colorless foam (488 mg, 635 µmol, 37%).

^{1}H NMR (400 MHz, $CDCl_3$): δ (ppm) = 8.78 (s, 1H, C2-H), 8.20 (s, 1H, C8-H), 7.46–7.39 (m, 2H, trityl-H), 7.36–7.28 (m, 4H, trityl-H), 7.29–7.16 (m, 3H, trityl-H), 6.83–6.75 (m, 4H, trityl-H), 6.23 (d, *J* = 5.7 Hz, 1H, C1'-H), 5.13 (d, *J* = 4.8 Hz, 1H, C3'-OCH_2^a), 5.01 (t, *J* = 5.4 Hz, 1H, C2'-H), 4.97 (d, *J* = 4.8 Hz, 1H, C3'-OCH_2^b), 4.56 (dt, *J* = 5.1, 3.4 Hz, 1H, C3'-H), 4.31 (q, *J* = 3.8 Hz, 1H, C4'-H), 3.78 (2s, *J* = 0.9 Hz, 6H, trityl-OCH_3), 3.49 (dd, *J* = 10.5, 3.6 Hz, 1H, C5'-H^a), 3.39 (dd, *J* = 10.5, 4.2 Hz, 1H, C5'-H^b), 3.22 (q, *J* = 7.6 Hz, 2H, $C\underline{H}_2CH_3$), 3.06 (d, *J* = 3.5 Hz, 1H, C3'-OH), 1.44 (t, *J* = 7.6 Hz, 3H, $CH_2C\underline{H}_3$), 1.12–0.93 (m, 21H, $(CH(C\underline{H}_3)_2)_3$, $(C\underline{H}(CH_3)_2)_3$).

^{13}C{^{1}H} NMR (100 MHz, $CDCl_3$): δ (ppm) = 164.16 (1C, C6), 158.66 (2C, trityl-C), 152.66 (1C, C2), 150.60 (1C, C4), 144.67 (1C, trityl-C), 142.76 (1C, C8), 135.86 (1C, trityl-C), 135.79 (1C, trityl-C), 133.10 (1C, C5), 130.21 (2C, trityl-C), 130.18 (2C, trityl-C), 128.27 (2C, trityl-C), 128.00 (2C, trityl-C), 127.04 (1C, trityl-C), 113.29 (4C, trityl-C), 90.98 (1C, C2'-$O\underline{C}H_2$), 87.07 (1C, C1'), 86.71 (1C, trityl-C), 84.42 (1C, C4'), 82.02 (121C, C2'), 71.15 (1C, C3'), 63.54 (1C, C5'), 55.35 (2C, trityl-OCH_3), 26.62 (1C, $\underline{C}H_2CH_3$), 17.88 (6C, $(CH(\underline{C}H_3)_2)_3$), 12.71 (1C, $CH_2\underline{C}H_3$), 11.93 (3C, $(\underline{C}H(CH_3)_2)_3$).

5'-*O*-(4,4'-Dimethoxytrityl)-2'-*O*-(triisopropylsilyl)-N^6-methyl-1-deazaadenosine (71)

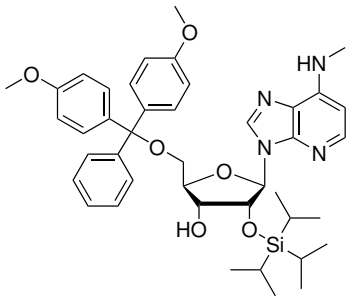

71
$C_{42}H_{54}N_4O_6Si$
739.00 g·mol^{-1}

A solution of compound **63** (750 mg, 1.29 mmol, 1.00 eq.) in dry pyridine (7 mL) under an inert gas atmosphere was treated with silver nitrate (875 mg, 5.15 mmol, 4.00 eq.) and stirred in the dark at ambient temperature for 30 min. Triisopropylsilyl chloride (1.10 mL, 5.15 mmol, 4.00 eq.) was added and stirring was continued in the dark for 22 h. The reaction mixture was diluted with dichloromethane (200 mL) and washed with sat. aq. $NaHCO_3$ solution (200 mL). The organic layer was separated, dried over Na_2SO_4 and the solvent was removed *in vacuo*. The residue was purified by column chromatography (silica gel, *n*-hexane:EtOAc = 2:1 + 1% NEt_3) to yield the product **71** as a colorless foam (333 mg, 451 µmol, 35%).

^{1}H NMR (400 MHz, $CDCl_3$): δ (ppm) = 7.93–7.89 (m, 2H, C2-H, C8-H), 7.46–7.41 (m, 2H, trityl-H), 7.35—7.30 (m, 4H, trityl-H), 7.29—7.14 (m, 3H, trityl-H), 6.81—6.76 (m, 4H, trityl-H), 6.27 (d, J = 5.5 Hz, 1H, C1-H), 6.01 (d, J = 5.7 Hz, 1H, C1'-H), 5.32 (dd, J = 5.8, 4.0 Hz, 1H, C2'-H), 5.18 (q, J = 5.2 Hz, 1H, N$\underline{H}$CH$_3$), 4.65 (dd, J = 4.1, 2.9 Hz, 1H, C3'-H), 4.27 (ddd, J = 5.6, 4.4, 2.8 Hz, 1H, C4'-H), 3.78 (2s, 6H, trityl-OCH$_3$), 3.57 (dd, J = 10.4, 5.7 Hz, 1H, C5'-H^a), 3.30 (dd, J = 10.3, 4.5 Hz, 1H, C5'-H^b), 3.00 (d, J = 5.2 Hz, 3H, NHC$\underline{H}_3$), 0.94—0.80 (m, 21H, (C$\underline{H}$(CH$_3$)$_2$)$_3$, CH(C$\underline{H}_3$)$_2$)$_3$).

^{13}C{^{1}H} NMR (100 MHz, $CDCl_3$): δ (ppm) = 158.51 (2C, trityl-C), 147.07 (1C, C6), 146.37 (1C, C4), 145.98 (1C, C2), 144.90 (1C, trityl-C), 139.72 (1C, C8), 136.15 (1C, trityl-C), 136.05 (1C, trityl-C), 130.25 (4C, trityl-C), 128.35 (2C, trityl-C), 127.88 (2C, trityl-C), 126.81 (1C, trityl-C), 124.43 (1C, C5), 113.16 (4C, trityl-C), 98.47 (1C, C1), 88.88 (1C, C1'), 86.56 (1C, trityl-C), 84.02 (1C, C4'), 74.73 (1C, C2'), 74.22 (1C, C3'), 63.88 (1C, C5'), 55.32 (2C, trityl-OCH$_3$), 29.50 (1C, NHCH$_3$), 18.16 (3C, CH(C$\underline{H}_3$)$_2$), 17.94 (3C, CH(C$\underline{H}_3$)$_2$), 12.74 (3C, C$\underline{H}$(CH$_3$)$_2$).

HR-ESI-MS: *m/z* calc. ($C_{42}H_{55}N_4O_6Si$ [M+H]$^+$): 739.3885, found: 739.3901.

5'-*O*-(4,4'-Dimethoxytrityl)-2'-*O*-(triisopropylsilyl)-N^6-methyl-3-deazaadenosine (72)

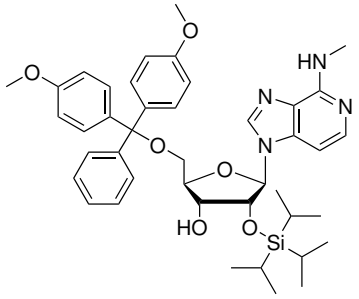

72
$C_{42}H_{54}N_4O_6Si$
739.00 g·mol^{-1}

A solution of compound **64** (678 mg, 1.17 mmol, 1.00 eq.) in dry pyridine (7 mL) under an inert gas atmosphere was treated with silver nitrate (791 mg, 4.66 mmol, 4.00 eq.) and stirred in the dark at ambient temperature for 30 min. Triisopropylsilyl chloride (994 µL, 4.66 mmol, 4.00 eq.) was added and stirring was continued in the dark for 22 h. The reaction mixture was diluted with dichloromethane (200 mL) and washed with sat. aq. $NaHCO_3$ solution (200 mL). The organic layer was separated, dried over Na_2SO_4 and the solvent was removed *in vacuo*. The residue was purified by column chromatography (silica gel, *n*-hexane:EtOAc = 1:2 + 1% NEt_3) to yield the product **72** as a colorless foam (320 mg, 433 µmol, 37%).

^{1}H NMR (400 MHz, $CDCl_3$): δ (ppm) = 7.92 (s, 1H, C8-H), 7.66 (d, J = 5.9 Hz, 1H, C2-H), 7.45–7.40 (m, 2H, trityl-H), 7.36—7.20 (m, 7H, trityl-H), 6.84–6.78 (m, 5H, C3-H, trityl-H), 5.78 (d, J = 6.9 Hz, 1H, C1'-H), 5.49 (s_{br}, 1H, N$\underline{H}$CH$_3$), 4.87 (dd, J = 6.9, 5.3 Hz, 1H, C2'-H), 4.38 (dd, J = 5.3, 2.0 Hz, 1H, C3'-H), 4.27 (q, J = 2.6 Hz, 1H, C4'-H), 3.78 (2s, 6H, trityl-OCH$_3$), 3.50 (dd, J = 10.7, 2.7 Hz, 1H, C5'-H^a), 3.42 (dd, J = 10.7, 3.1 Hz, 1H, C5'-H^b), 3.15 (d, J = 5.0 Hz, 3H, NHC$\underline{H}_3$), 2.93 (s, 1H, C3'-OH), 1.00—0.77 (m, 21H, (C$\underline{H}$(CH$_3$)$_2$)$_3$, CH(C$\underline{H}_3$)$_2$)$_3$).

^{13}C{^{1}H} NMR (100 MHz, $CDCl_3$): δ (ppm) = 158.77 (2C, trityl-C), 152.48 (1C, C6), 144.50 (1C, trityl-C), 141.43 (1C, C2), 139.15 (1C, C8), 137.20 (1C, C4), 135.46 (1C, trityl-C), 135.39 (1C, trityl-C), 130.30 (1C, trityl-C), 130.28 (1C, trityl-C), 128.27 (2C, trityl-C), 128.10 (4C, trityl-C), 127.98 (1C, C5), 127.21 (1C, trityl-C), 113.38 (4C, trityl-C), 97.67 (1C, C3), 89.24 (1C, C1'), 87.13 (1C, trityl-C), 84.19 (1C, C4'), 75.86 (1C, C2'), 71.92 (1C, C3'), 63.69 (1C, C5'), 55.36 (2C, trityl-OCH$_3$), 28.04 (1C, NHCH$_3$), 17.77 (3C, CH(C$\underline{H}_3$)$_2$), 17.56 (3C, CH(C$\underline{H}_3$)$_2$), 12.09 (3C, C$\underline{H}$(CH$_3$)$_2$).

HR-ESI-MS: *m/z* calc. ($C_{42}H_{55}N_4O_6Si$ [M+H]$^+$): 739.3885, found: 739.3889.

5'-*O*-(4,4'-Dimethoxytrityl)-2'-*O*-(*tert*-butyldimethylsilyl)-N^6-methyl-7-deazaadenosine (73)

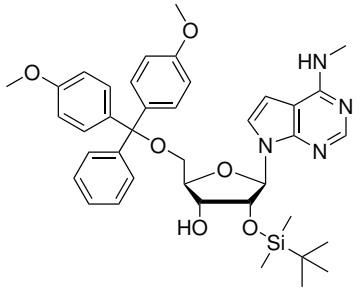

73
$C_{39}H_{48}N_4O_6Si$
696.92 g·mol^{-1}

Compound **73** (617 mg, 1.06 mmol, 1.00 eq.) was dissolved in dry pyridine (6 mL) under an inert gas atmosphere. Silver nitrate (719 mg, 4.23 mmol, 4.00 eq.) was added and the reaction mixture was stirred in the dark at ambient temperature for 30 min. *tert*-Butyldimethylsilyl chloride (192 mg, 1.27 mmol, 1.20 eq.) was added and the solution was stirred in the dark at ambient temperature for 15 h. Ethyl acetate (250 mL) was added, the resulting suspension was filtered through a pad of Celite and the filtrate was evaporated to dryness. Purification of the residue by column chromatography (silica gel, *n*-hexane:EtOAc = 1:3) yielded the product **73** as a colorless foam (243 mg, 365 µmol, 35%).

^{1}H NMR (400 MHz, $CDCl_3$): δ (ppm) = 8.33 (s, 1H, C2-H), 7.50—7.44 (m, 2H, trityl-H), 7.38—7.32 (m, 4H, trityl-H), 7.31—7.20 (m, 4H, C8-H, trityl-H), 6.85—6.78 (m, 4H, trityl-H), 6.34 (d, *J* = 3.7 Hz, 1H, C7-H), 6.31 (d, *J* = 5.9 Hz, 1H, C1'-H), 5.05 (s_{br}, 1H, N$\underline{H}$$CH_3$), 4.74 (t, *J* = 5.6 Hz, 1H, C2'-H), 4.29 (dd, *J* = 5.3, 3.1 Hz, 1H, C3'-H), 4.22 (q, *J* = 3.1 Hz, 1H, C4'-H), 3.78 (2s, 6H, trityl-OCH_3), 3.53 (dd, *J* = 10.5, 3.0 Hz, 1H, C5'-H^a), 3.30 (dd, *J* = 10.5, 3.4 Hz, 1H, C5'-H^b), 3.19 (d, *J* = 5.0 Hz, 3H, NHC$\underline{H}_3$), 2.83 (s_{br}, 1H, 3'-OH), 0.82 (s, 9H, $SiC(CH_3)_3$), -0.06 (s, 3H, $Si(CH_3)_2$^{a}), -0.19 (s, 3H, $Si(CH_3)_2$^{b}).

^{13}C{^{1}H} NMR (100 MHz, $CDCl_3$): δ (ppm) = 158.65 (2C, trityl-C), 157.16 (1C, C6), 152.21 (1C, C2), 150.69 (1C, C4), 144.90 (1C, trityl-C), 135.97 (1C, trityl-C), 135.89 (1C, trityl-C), 130.30 (4C, trityl-C), 128.37 (2C, trityl-C), 128.00 (2C, trityl-C), 127.01 (1C, trityl-C), 121.48 (1C, C8), 113.29 (4C trityl-C), 103.60 (1C, C5), 99.21 (1C, C7), 87.34 (1C, C1'), 86.61 (1C, trityl-C), 83.67 (1C, C4'), 76.31 (1C, C2'), 71.77 (1C, C3'), 63.85 (1H, C5'), 55.37 (2C, trityl-OCH_3), 28.50 (1H, $NHCH_3$), 25.73 (3C, $SiC(\underline{C}H_3)_3$), 18.07 (1C, $Si\underline{C}(CH_3)_3$), -4.94 (1C, $Si(CH_3)_2$^{a}), -5.27(1C, $Si(CH_3)_2^b$).

HR-ESI-MS: *m/z* calc. ($C_{39}H_{49}N_4O_6Si$ $[M+H]^+$): 697.3416, found: 697.3413.

5'-*O*-(4,4'-Dimethoxytrityl)-2'-*O*-[[(triisopropylsilyl)oxy]methyl]-N^6-methyladenosine 3'-*O*-(2-cyanoethyl)diisopropylphosphoramidite (74)

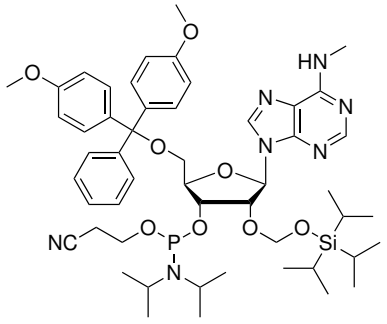

74
$C_{51}H_{72}N_7O_8PSi$
970.24 g·mol^{-1}

This compound was synthesized according to a reported procedure.[261] A solution of compound **66** (250 mg, 325 µmol, 1.00 eq.) in dry dichloromethane (2 mL) under an inert gas atmosphere was treated with ethyldimethylamine (350 µL, 3.23 mmol, 9.95 eq.). 2-Cyanoethyl *N,N*-diisopropylchlorophosphoramidite (CEPCl, 110 µL, 493 µmol, 1.52 eq.) was added and the resulting mixture was stirred at ambient temperature for 2.5 h. The solvent was removed under reduced pressure and the residue was purified by column chromatography (silica gel, *n*-hexane:EtOAc 3:2 + 1% NEt_3) to yield the product **74** as a colorless foam (238 mg, 245 µmol, 75%). Analytical data agreed with reported values.[261]

^{1}H NMR (500 MHz, $CDCl_3$): δ (ppm) = 8.30, 8.28 (2 s, 1H, C2-H), 7.92, 7.90 (2 s, 1H, C8-H), 7.42—7.38 (m, 2H, trityl-H), 7.32—7.15 (m, 7H, trityl-H), 6.81—6.74 (m, 4H, trityl-H), 6.14, 6.11 (2 d, J = 5.7 Hz, 1H, C1'-H), 5.72 (s_{br}, 1H, N$\underline{H}$$CH_3$), 5.19, 5.16 (2 t, J = 5.4 Hz, 1H, C2'-H), 5.00—4.91 (m, 2H, C2'-OCH_2), 4.75—4.65 (m, 1H, C3'-H), 4.37, 4.32 (2 q, J = 4.1 Hz, 1H, C4'-H), 3.98—3.84 (m, 1H, $POCH_2{}^a$), 3.78 (s, 3H, trityl-OCH_3), 3.77 (s, 3H, trityl-OCH_3), 3.71—3.48 (m, 4H, C5'-H^a, $POCH_2{}^b$, N(C$\underline{H}$$(CH_3)_2)_2$), 3.34—3.29 (m, 1H, C5'-H^b), 3.19 (s_{br}, 3H, NHC$\underline{H}_3$), 2.65 (td, J = 6.5, 3.8 Hz, 1H, $CH_2{}^aCN$), 2.37 (t, J = 6.6 Hz, $CH_2{}^bCN$), 1.18 (t, J = 6.5 Hz, 9H, N(CH(C$\underline{H}_3)_2)_3{}^{a,b,c}$), 1.07 (d, J = 6.8 Hz, 3H, N(CH(C$\underline{H}_3)_2)_3{}^d$), 0.94-–0.87 (m, 21H, Si(C$\underline{H}$$(CH_3)_2)_3$, Si(CH(C$\underline{H}_3)_2)_3$).

^{13}C{^{1}H} NMR (125 MHz, $CDCl_3$): δ (ppm) = 158.60, 158.58 (2C, trityl-C), 155.56 (1C, C6), 153.25, 153.23 (1C, C2), 148.95 (1C, C4), 144.76, 144.68 (1C, trityl-C), 139.31, 139.28 (1C, C8), 136.04, 135.95, 135.89 (2C, trityl-C), 130.25, 130.21, 130.18 (4C, trityl-C), 128.42, 128.36 (2C, trityl-C), 127.92 (2C, trityl-C), 126.98, 126.95 (1C, trityl-C), 120.68 (1C, C5), 117.82, 117.53 (1C, $CH_2\underline{C}N$), 113.21, 113.20 (4C, trityl-C), 89.75, 89.72, 89.39 (1C, C2'-O$\underline{C}H_2$), 87.50, 87.38 (1C, C1'), 86.61, 86.51 (1C, trityl-C), 84.05, 84.03, 83.94, 83.91 (1C, C4'), 77.69, 77.67, 77.04, 76.99 (1C, C2'), 71.93, 71.81, 71.42, 71.29 (1C, C3'), 63.46, 63.06 (1C, C5'), 59.23, 59.10, 58.32, 58.16 (1C, $POCH_2$), 55.35, 55.33 (2C, trityl-OCH_3), 43.54, 43.44, 43.37, 43.27 (2C, N$\underline{C}$H$(CH_3)_2$), 27.68 (1C, $NHCH_3$), 24.79, 24.74, 24.72, 24.68 (4C, NCH($\underline{C}H_3)_2$), 20.53, 20.43, 20.25, 20.20 (1C, $\underline{C}H_2CN$,) 17.83, 17.80 (6C, CH($\underline{C}H_3)_2$), 11.95 (3C, $\underline{C}$H$(CH_3)_2$).

^{31}P{^{1}H} NMR (202 MHz, $CDCl_3$): δ (ppm) = 150.56, 149.95.

HR-ESI-MS: *m/z* calc. ($C_{51}H_{73}N_7O_8PSi$ $[M+H]^+$): 970.50220, found: 970.50210.

5'-*O*-(4,4'-Dimethoxytrityl)-2'-*O*-[[(triisopropylsilyl)oxy]methyl]-*N*^{6}-dimethyladenosine 3'-*O*-(2-cyanoethyl)diisopropylphosphoramidite (75)

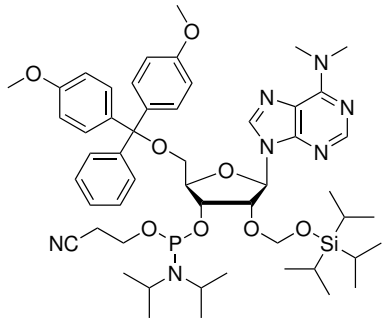

75
$C_{52}H_{74}N_7O_8PSi$
984.26 g·mol^{-1}

This compound was synthesized according to a reported procedure.[261] A solution of compound **67** (235 mg, 300 µmol, 1.00 eq.) in dry dichloromethane (3.5 mL) under an inert gas atmosphere was treated with ethyldimethylamine (330 µL, 3.05 mmol, 10.2 eq.). CEPCl (141 µL, 634 µmol, 2.11 eq.) was added and the resulting mixture was stirred at ambient temperature for 3.5 h. The solvent was removed under reduced pressure and the residue was purified by column chromatography (silica gel, *n*-hexane:EtOAc 5:2 + 2% NEt_3) to yield the product **75** as a colorless foam (265 mg, 269 µmol, 89%). Analytical data agreed with reported values.[261]

^{1}H NMR (500 MHz, $CDCl_3$): δ (ppm) = 8.23, 8.21 (2 s, 1H, C2-H), 7.90, 7.88 (2 s, 1H, C8-H), 7.43—7.38 (m, 2H, trityl-H), 7.32—7.15 (m, 7H, trityl-H), 6.81—6.74 (m, 4H, trityl-H), 6.16, 6.13 (2 d, *J* = 5.7 Hz, 1H, C1'-H), 5.15, 5.12 (2 t, *J* = 5.4 Hz, 1H, C2'-H), 5.00—4.90 (m, 2H, C2'-O$\underline{C}H_2$), 4.75—4.63 (m, 1H, C3'-H), 4.36, 4.31 (2 q, *J* = 3.8 Hz, 1H, C4'-H), 3.98—3.83 (m, 1H, $POCH_2{}^a$), 3.77 (2 s, 6H, trityl-OCH_3), 3.73—3.43 (m, 10H, C5'-H^a, $POCH_2{}^b$, $N(C\underline{H}(CH_3)_2)_2$), $N(CH_3)_2$), 3.32-–3.26 (m, 1H, C5'-H^b), 2.65 (td, *J* = 6.6, 3.8 Hz, 1H, $CH_2{}^aCN$), 2.36 (t, *J* = 6.6 Hz, $CH_2{}^bCN$), 1.18 (2 d, *J* = 6.6 Hz, 9H, $N(CH(C\underline{H}_3)_2)_3{}^{a,b,c}$), 1.05 (d, *J* = 6.7 Hz, 3H, $N(CH(C\underline{H}_3)_2)_3{}^d$), 0.95—0.87 (m, 21H, $Si(C\underline{H}(CH_3)_2)_3$, $Si(CH(C\underline{H}_3)_2)_3$).

^{13}C{^{1}H} NMR (125 MHz, $CDCl_3$): δ (ppm) = 158.57, 158.55 (2C, trityl-C), 155.04 (1C, C6), 152.48, 152.46 (1C, C2), 150.63, 150.60 (1C, C4), 144.78, 144.71 (1C, trityl-C), 137.62 (1C, C8), 136.09, 136.00, 135.96, 135.89 (2C, trityl-C), 130.25, 130.23, 130.21 (4C, trityl-C), 128.42, 128.35 (2C, trityl-C), 127.92 (2C, trityl-C), 126.94, 126.91 (1C, trityl-C), 120.85 (1C, C5), 117.84, 117.53 (1C, $CH_2\underline{C}N$), 113.21, 113.20 (4C, trityl-C), 89.78, 89.74, 89.41, 89.39 (1C, C2'-O$\underline{C}H_2$), 87.31, 87.13 (1C, C1'), 86.55, 86.45 (1C, trityl-C), 83.89, 83.88, 83.79, 83.76 (1C, C4'), 77.76, 77.74 (1C, C2'), 71.88, 71.76, 71.41, 71.27 (1C,

C3'), 63.48, 63.06 (1C, C5'), 59.25, 59.12, 58.33, 58.17 (1C, $POCH_2$), 55.34, 55.32 (2C, trityl-OCH_3), 43.52, 43.42, 43.35, 43.25 (2C, $N\underline{C}H(CH_3)_2$), 38.72 (2C, $N(CH_3)_2$), 24.78, 24.72, 24.66 (4C, $NCH(\underline{C}H_3)_2$), 20.52, 20.47, 20.23, 20.17 (1C, $\underline{C}H_2CN$), 17.84, 17.81 (6C, $CH(\underline{C}H_3)_2$), 11.97, 11.96 (3C, $\underline{C}H(CH_3)_2$).

$^{31}P\{^1H\}$ NMR (202 MHz, $CDCl_3$): δ (ppm) = 150.54, 149.91.

HR-ESI-MS: *m/z* calc. ($C_{52}H_{74}N_7NaO_8PSi$ $[M+Na]^+$): 1006.4998, found: 1006.4984.

5'-*O*-(4,4'-Dimethoxytrityl)-2'-*O*-[[(triisopropylsilyl)oxy]methyl]-O^6-methylinosine 3'-*O*-(2-cyanoethyl)diisopropylphosphoramidite (76)

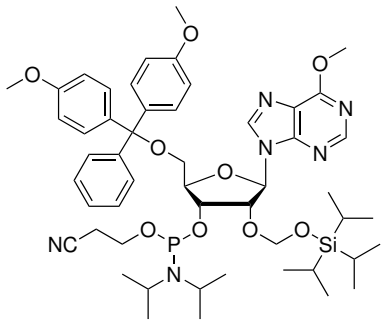

76
$C_{51}H_{71}N_6O_9PSi$
971.22 g·mol^{-1}

A solution of compound **68** (152 mg, 197 µmol, 1.00 eq.) in dry dichloromethane (2.3 mL) under an inert gas atmosphere was treated with ethyldimethylamine (220 µL, 2.04 mmol, 10.4 eq.). CEPCl (72.6 µL, 325 µmol, 1.65 eq.) was added and the resulting mixture was stirred at ambient temperature for 3 h. The solvent was removed under reduced pressure and the residue was purified by column chromatography (silica gel, *n*-hexane:EtOAc 3:2 + 1% NEt_3) to yield the product **76** as a colorless foam (154 mg, 159 µmol, 81%).

^1H NMR (500 MHz, $CDCl_3$): δ (ppm) = 8.42, 8.40 (2 s, 1H, C2-H), 8.10, 8.08 (2 s, 1H, C8-H), 7.43–7.38 (m, 2H, trityl-H), 7.33–7.16 (m, 7H, trityl-H), 6.81–6.74 (m, 4H, trityl-H), 6.19, 6.16 (2 d, J = 6.0 Hz, 1H, C1'-H), 5.20–5.14 (m, 1H, C2'-H), 4.99–4.89 (m, 2H, C2'-OCH_2), 4.71–4.63 (m, 1H, C3'-H), 4.40, 4.35 (2 q, J = 3.9 Hz, 1H, C4'-H), 4.18 (2 s, 3H, OCH_3), 3.97–3.84 (m, 1H, $POCH_2{}^a$), 3.78 (s, 3H, trityl-OCH_3), 3.77 (s, 3H, trityl-OCH_3), 3.72–3.46 (m, 4H, C5'-H^a, $POCH_2{}^b$, $N(C\underline{H}(CH_3)_2)_2$), 3.35, 3.33 (2 t, J = 4.3 Hz, 1H, C5'-H^b), 2.65 (td, J = 6.5, 3.1 Hz, 1H, $CH_2{}^aCN$), 2.38 (t, J = 6.5 Hz, 1H, $CH_2{}^bCN$), 1.19 (t, J = 6.6 Hz, 9H, $N(CH(C\underline{H}_3)_2)_3{}^{a,b,c}$), 1.08 (d, J = 6.8 Hz, 3H, $N(CH(C\underline{H}_3)_2)_3{}^d$), 0.95–0.84 (m, 21 H, $Si(C\underline{H}(CH_3)_2)_3$, $Si(CH(C\underline{H}_3)_2)_3$).

$^{13}C\{^1H\}$ NMR (125 MHz, $CDCl_3$): δ (ppm) = 161.17, 161.16 (1C, C6), 158.63, 158.61 (2C, trityl-C), 152.18(1C, C2), 151.90 (1C, C4), 144.69, 144.61 (1C, trityl-C), 141.69 (1C, C8), 135.96, 135.88, 135.85, 135.82 (2C, trityl-C), 130.24, 130.22, 130.18, 130.16 (4C,

trityl-C), 128.39, 128.31 (2C, trityl-C), 127.95 (2C, trityl-C), 127.02, 126.99 (1C, trityl-C), 122.35 (1C, C5), 117.77, 117.50 (1C, $CH_2\underline{C}N$), 113.21, 113.20 (4C, trityl-C), 89.67, 89.64, 89.28, 89.26 (1C, C2'-O$\underline{C}H_2$), 87.56, 87.44 (1C, C1'), 86.70, 86.60 (1C, trityl-C), 84.33, 84.32, 84.18, 84.14 (1C, C4'), 77.67, 77.64 (1C, C2'), 72.02, 71.89, 71.40, 71.27 (1C, C3'), 63.50, 63.12 (1C, C5'), 59.22, 59.09, 58.25, 58.10 (1C, $POCH_2$), 55.35, 55.33 (2C, trityl-OCH_3), 54.32 (1C, OCH_3), 43.56, 43.46, 43.37, 43.27 (2C, N$\underline{C}H(CH_3)_2$), 24.79, 24.73, 24.69 (4C, NCH($\underline{C}H_3)_2$), 20.53, 20.48, 20.27, 20.21 (1C, $\underline{C}H_2CN$), 17.81, 17.79, 17.77 (6C, CH($\underline{C}H_3)_2$), 11.92, 11.91 (3C, $\underline{C}H(CH_3)_2$).

$^{31}P\{^1H\}$ NMR (202 MHz, $CDCl_3$): δ (ppm) = 150.80, 150.00.

HR-ESI-MS: *m/z* calc. ($C_{51}H_{72}N_6O_9PSi$ $[M+H]^+$): 971.4862, found: 971.4853.

5'-*O*-(4,4'-Dimethoxytrityl)-2'-*O*-[[(triisopropylsilyl)oxy]methyl]-6-(methylthio)purine-9-riboside 3'-*O*-(2-cyanoethyl)diisopropylphosphoramidite (77)

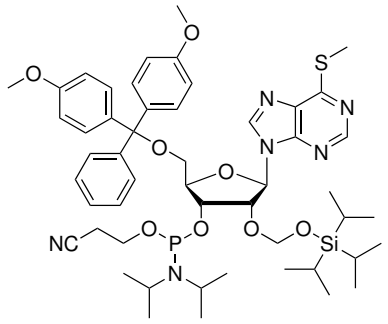

77
$C_{51}H_{71}N_6O_8PSSi$
987.28 g·mol^{-1}

A solution of compound **69** (180 mg, 229 µmol, 1.00 eq.) in dry dichloromethane (2.6 mL) under an inert gas atmosphere was treated with ethyldimethylamine (250 µL, 2.31 mmol, 10.1 eq.). CEPCl (86.6 µL, 388 µmol, 1.69 eq.) was added and the resulting mixture was stirred at ambient temperature for 3 h. The solvent was removed under reduced pressure and the residue was purified by column chromatography (silica gel, *n*-hexane:EtOAc 3:2 + 1% NEt_3) to yield the product **77** as a colorless foam (145 mg, 147 µmol, 64%).

^1H NMR (500 MHz, $CDCl_3$): δ (ppm) = 8.60, 8.58 (2 s, 1H, C2-H), 8.13, 8.11 (2 s, 1H, C8-H), 7.43–7.38 (m, 2H, trityl-H), 7.33–7.16 (m, 7H, trityl-H), 6.81–6.74 (m, 4H, trityl-H), 6.18, 6.15 (2 d, J = 5.9 Hz, 1H, C1'-H), 5.22–5.15 (m, 1H, C2'-H), 4.99–4.89 (m, 2H, C2'-OCH_2), 4.71–4.63 (m, 1H, C3'-H), 4.40, 4.35 (2 q, J = 4.3 Hz, 1H, C4'-H), 3.98–3.83 (m, 1H, $POCH_2{}^a$), 3.78 (s, 3H, trityl-OCH_3), 3.77 (s, 3H, trityl-OCH_3), 3.70–3.46 (m, 4H, C5'-H^a, $POCH_2{}^b$, N(C$\underline{H}(CH_3)_2)_2$), 3.35, 3.33 (2 dd, J = 4.5, 2.1 Hz, 1H, C5'-H^b), 2.68–2.63 (m, 1H, $CH_2{}^aCN$), 2.37 (t, J = 6.5 Hz, 1H, $CH_2{}^bCN$), 1.19 (dd, J = 6.8, 5.3 Hz, 9H, N(CH(C$\underline{H}_3)_2)_3{}^{a,b,c}$), 1.08 (d, J = 6.7 Hz, 3H, N(CH(C$\underline{H}_3)_2)_3{}^d$), 0.91–0.83

(m, 21H, Si(C<u>H</u>$(CH_3)_2)_3$, Si(CH(C<u>H</u>$_3)_2)_3$).

^{13}C{^{1}H} NMR (125 MHz, $CDCl_3$): δ (ppm) = 161.83, 161.78 (1C, C6), 158.62, 158.61 (2C, trityl-C), 152.02 (1C, C2), 148.16 (1C, C4), 144.67, 144.59 (1C, trityl-C), 142.13 (1C, C8), 135.95, 135.84, 135.81 (2C, trityl-C), 132.21 (1C, C5), 130.22, 130.15 (4C, trityl-C), 128.38, 128.30 (2C, trityl-C), 127.95 (2C, trityl-C), 127.02, 126.99 (1C, trityl-C), 113.23 (4C, trityl-C), 89.74 (1C, C2'-O<u>C</u>H_2), 87.63, 87.47 (1C, C1'), 86.69, 86.59 (1C, trityl-C), 84.38 (1C, C4'), 77.37, 77.36 (1C, C2'), 71.84 (1C, C3'), 60.55 (1C, C5'), 58.07 (1C, $POCH_2$), 55.34 (2C, trityl-OCH_3), 43.57, 43.38 (2C, N<u>C</u>H$(CH_3)_2$), 24.80, 24.72 (4C, NCH(<u>C</u>$H_3)_2$), 21.22 (1C, <u>C</u>H_2CN), 17.80, 17.79, 17.76 (6C, CH(<u>C</u>$H_3)_2$), 14.35 (1C, SCH_3), 11.93, 11.90 (3C, <u>C</u>H$(CH_3)_2$).

^{31}P{^{1}H} NMR (202 MHz, $CDCl_3$): δ (ppm) = 150.89, 150.08.

HR-ESI-MS: *m/z* calc. ($C_{51}H_{72}N_6O_8PSSi$ $[M+H]^+$): 987.46337, found: 987.46542.

5'-*O*-(4,4'-Dimethoxytrityl)-2'-*O*-[[(triisopropylsilyl)oxy]methyl]-6-ethylpurine-9-riboside 3'-*O*-(2-cyanoethyl)diisopropylphosphoramidite (78)

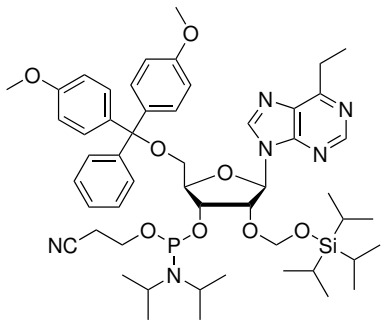

78
$C_{52}H_{73}N_6O_8PSi$
969.25 g·mol^{-1}

A solution of compound **70** (450 mg, 585 µmol, 1.00 eq.) in dry dichloromethane (5 mL) under an inert gas atmosphere was treated with ethyldimethylamine (634 µL, 5.85 mmol, 10.0 eq.). CEPCl (196 µL, 878 µmol, 1.50 eq.) was added and the resulting mixture was stirred at ambient temperature for 3 h. The solvent was removed under reduced pressure and the residue was purified by column chromatography (silica gel, *n*-hexane:EtOAc 3:2 + 1% NEt_3) to yield the product **78** as a colorless foam (465 mg, 480 µmol, 82%).

^{1}H NMR (400 MHz, $CDCl_3$): δ (ppm) = 8.74, 8.72 (2 s, 1H, C2-H), 8.19, 8.16 (2 s, 1H, C8-H), 7.44–7.37 (m, 2H, trityl-H), 7.36–.14 (m, 7H, trityl-H), 6.83–6.73 (m, 4H, trityl-H), 6.20, 6.17 (2 d, J = 6.2 Hz, 1H, C1'-H), 5.28–5.20 (m, 1H, C2'-H), 4.98–4.88 (m, 2H, C2'-OCH_2), 4.74–4.63 (m, 1H, C3'-H), 4.42, 4.36 (2 q, J = 4.2 Hz, 1H, C4'-H), 3.98–3.84 (m, 1H, $POCH_2$[a]), 3.78 (s, 3H, trityl-OCH_3), 3.77 (s, 3H, trityl-OCH_3), 3.74–3.48 (m, 4H, $POCH_2$[b], C5'-H[a], N(C<u>H</u>$(CH_text{ext}3)_2)_3$), 3.38–3.31 (m, 1H, C5'-H[b]), 3.25–3.17

(m, 2H, C6-CH_2), 2.68–2.62 (m, 1H, $CH_2{}^aCN$), 2.42–2.34 (m, 1H, $CH_2{}^bCN$), 1.46–1.40 (m, 3H, C6-$CH_2C\underline{H}_3$), 1.23–1.16 (m, 9H, $N(CH(C\underline{H}_3)_2)_3{}^{a,b,c}$), 1.09 (d, J = 6.7 Hz, 3H, $N(CH(C\underline{H}_3)_2)_3{}^d$), 0.88–0.81 (m, 21H, $Si(C\underline{H}(CH_3)_2)_3$, $Si(CH(C\underline{H}_3)_2)_3$).

$^{13}C\{^1H\}$ NMR (100 MHz, $CDCl_3$): δ (ppm) = 164.07, 164.03 (1C, C6), 158.65, 158.63 (2C, trityl-C), 152.52 (1C, C2), 150.62 (1C, C4), 144.62 (1C, trityl-C), 143.30 (1C, C8), 135.85 (2C, trityl-C), 133.18 (1C, C5), 130.24, 130.17 (4C, trityl-C), 128.38, 128.31 (2C, trityl-C), 127.95 (2C, trityl-C), 127.02 (1C, trityl-C), 113.24 (4C, trityl-C), 89.60 (1C, C2'-O$\underline{C}H_2$, 87.52, 87.38 (1C, C1'), 86.70, 86.60 (1C, trityl-C), 84.47, 84.30 (1C, C4'), 77.36 (1C, C2'), 63.60 (1C, C5'), 59.76, 57.69 (1C, $POCH_2$, 55.33 (2C, trityl-OCH_3, 43.38, 43.26 (2C, N$\underline{C}H(CH_3)_2$, 27.14 (1C, C6-$\underline{C}H_2$), 25.44 (4C, NCH($\underline{C}H_3)_2$), 20.49 (1C, $\underline{C}H_2CN$), 17.75, 17.72 (6C, CH($\underline{C}H_3)_2$), 13.64 (1C, C6-$CH_2\underline{C}H_3$), 11.88 (3C, $\underline{C}H(CH_3)_2$).

$^{31}P\{^1H\}$ NMR (162 MHz, $CDCl_3$): δ (ppm) = 150.84, 150.06.

5'-*O*-(4,4'-Dimethoxytrityl)-2'-*O*-(triisopropylsilyl)-N^6-methyl-1-deazaadenosine 3'-*O*-(2-cyanoethyl)diisopropylphosphoramidite (79)

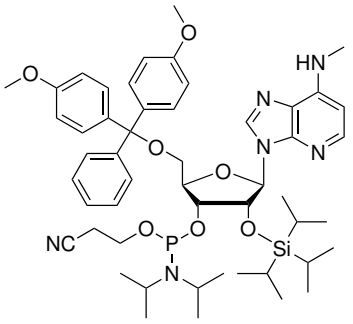

79
$C_{51}H_{71}N_6O_7PSi$
939.22 g·mol^{-1}

A solution of compound **71** (88.0 mg, 119 µmol, 1.00 eq.) in dry dichloromethane (1.4 mL) under an inert gas atmosphere was treated with ethyldimethylamine (130 µL, 1.19 mmol, 10.0 eq.). CEPCl (40.0 µL, 179 µmol, 1.51 eq.) was added and the resulting mixture was stirred at ambient temperature for 5 h. The solvent was removed under reduced pressure and the residue was purified by column chromatography (silica gel, *n*-hexane:EtOAc 2:1 + 1% NEt_3) to yield the product **79** as a colorless foam (57.0 mg, 60.7 µmol, 51%).

^1H NMR (400 MHz, $CDCl_3$): δ (ppm) = 7.99—7.91 (m, 2H, C2-H, C8-H), 7.50-–7.44 (m, 2H, trityl-H), 7.40—7.32 (m, 4H, trityl-H), 7.30—7.15 (m, 3H, trityl-H), 6.83-–6.75 (m, 4H, trityl-H), 6.29 (2 d, *J* = 4.8 Hz, 1H, C1-H), 6.04 (2 d, *J* = 6.3 Hz, 1H, C1'-H), 5.38 (2 dd, *J* = 6.3, 4.6 Hz, 1H, C2'-H), 5.28—5.20 (m, 1H, N$\underline{H}CH_3$), 4.53-–4.33 (m, 2H, C3'-H, C4'-H), 4.00—3.81 (m, 1H, $POCH_2{}^a$), 3.78 (2 s, 6H trityl-OCH_3), 3.70-–3.51 (m, 4H, C5'-H^a, $POCH_2{}^b$, N($C\underline{H}(CH_3)_2)_2$), 3.25 (2 dd, *J* = 10.4, 4.3 Hz, 1H, C5'-H^b), 3.01 (2

d, J = 5.2 Hz, 3H, NHC$\underline{H}_3$), 2.66—2.59 (m, 1H, $CH_2{}^aCN$), 2.30-–2.23 (m, 1H, $CH_2{}^bCN$), 1.17 (2 d, J = 6.8 Hz, 9H, N(CH(C$\underline{H}_3$)$_2$)$_2{}^{a,b,c}$), 1.07 (d, J = 6.8 Hz, 3H, N(CH(C$\underline{H}_3$)$_2$)$_2{}^d$), 0.99-–0.74 (m, 21H, Si(C$\underline{H}$(CH$_3$)$_2$)$_3$, Si(CH(C$\underline{H}_3$)$_2$)$_3$).

^{13}C{^{1}H} NMR (100 MHz, $CDCl_3$): δ (ppm) = 158.55 (2C, trityl-C), 147.14 (1C, C6), 146.54 (1C, C4), 146.08 (1C, C2), 144.83 (1C, trityl-C), 139.26 (1C, C8), 135.99, 135.96 (2C, trityl-C), 130.32, 130.30, 130.27 (4C, trityl-C), 128.47, 128.35 (2C, trityl-C), 127.93 (2C, trityl-C), 126.91, 126.89 (1C, trityl-C), 124.28, 123.98 (1C, C5), 117.77, 117.24 (1C, $CH_2\underline{C}N$), 113.22 (4C, trityl-C), 98.57 (1C, C1), 88.78, 88.32 (1C, C1'), 86.64, 86.53 (1C, trityl-C), 83.43, 82.97 (1C, C4'), 74.34, 74.16 (1C, C2'), 74.05 (1C, C3'), 63.63, 63.52 (1C, C5'), 58.99, 58.84, 57.79 (1C, $POCH_2$), 55.36, 55.33 (2C, trityl-OCH_3), 43.65, 43.52, 43.21, 43.09 (2C, N$\underline{C}$H(CH$_3$)$_2$), 29.51, 29.50 (1C, $NHCH_3$), 24.93, 24.91, 24.85, 24.70, 24.65, 24.59 (4C, NCH($\underline{C}$H$_3$)$_2$), 20.56, 20.49, 20.14, 20.06 (1C, $\underline{C}H_2CN$), 18.12, 17.84, 17.76 (6C, CH($\underline{C}$H$_3$)$_2$), 12.56, 12.42 (3C, $\underline{C}$H(CH$_3$)$_2$).

^{31}P{^{1}H} NMR (202 MHz, $CDCl_3$): δ (ppm) = 151.24, 148.58.

HR-ESI-MS: m/z calc. ($C_{51}H_{71}N_6NaO_7PSi$ [M+Na]$^+$): 961.4783, found: 961.4720.

5'-*O*-(4,4'-Dimethoxytrityl)-2'-*O*-(triisopropylsilyl)-*N*^{6}-methyl-3-deazaadenosine 3'-*O*-(2-cyanoethyl)diisopropylphosphoramidite (80)

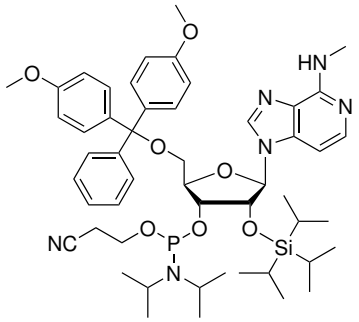

80
$C_{51}H_{71}N_6O_7PSi$
939.22 g·mol^{-1}

A solution of compound **72** (250 mg, 338 µmol, 1.00 eq.) in dry pyridine (1.4 mL) under an inert gas atmosphere was treated with diisopropylethylamine (590 µL, 3.38 mmol, 10.0 eq.). CEPCl (230 µL, 1.01 mmol, 3.00 eq.) was added and the resulting mixture was stirred at ambient temperature for 5 h. The mixture was diluted with acetonitrile (1.3 mL) and concentrated to a final volume of 0.6 mL under reduced pressure. The solution was diluted with acetonitrile (0.4 mL) and methyl di-*tert*-butyl ether (MTBE, 3.1 mL) and washed consecutively with water (1.1 mL), water/*N*,*N*-dimethylformamide (2 × 2.1 mL), water (1.1 mL) and 13% aq. NaCl solution (1.1 mL). The organic layer was dried over Na_2SO_4 and concentrated to a final volume of 0.7 mL under reduced pressure. The solution was added dropwise into *n*-heptane (6.3 mL). The volume was reduced to 2 mL under reduced pressure, *n*-heptane (4.2 mL) was added and the solu-

tion was stirred for 1.5 h. The precipitate was collected by filtration, washed with *n*-hexane (3 × 1.1 mL) and further purified by column chromatography (silica gel, *n*-hexane:EtOAc 1:1 + 1% NEt_3) to yield the product **80** as a colorless foam (185 mg, 197 µmol, 58%).

^{1}H NMR (400 MHz, $CDCl_3$): δ (ppm) = 7.98, 7.95 (2 s, 1H, C8-H), 7.72 (2 d, J = 5.9 Hz, 1H, C2-H), 7.48—7.39 (m, 2H, trityl-H), 7.38—7.17 (m, 7H, trityl-H), 6.88-–6.77 (m, 5H, C3-H, trityl-H), 5.85, 5.77 (2 d, J = 7.5 Hz, 1H, C1'-H), 5.44—5.35 (m, 1H, $N\underline{H}CH_3$), 4.86, 4.79 (2 dd, J = 7.5, 4.8 Hz, 1H, C2'-H), 4.50—4.28 (m, 2H, C3'-H, C4'-H), 4.00—3.82 (m, 2H, $POCH_2$), 3.78 (4 s, 6H, trityl-OCH_3), 3.71-–3.28 (m, 4H, C5'-H, $N(C\underline{H}(CH_3)_2)_2$), 3.15 (2 d, J = 5.1, 3H, $NHC\underline{H}_3$), 2.80—2.55 (m, 2H, CH_2CN), 1.31—1.15 (m, 9H, $N(CH(C\underline{H}_3)_2)_2$[a,b,c]), 1.07 (d, J = 6.7 Hz, 3H, $N(CH(C\underline{H}_3)_2)_2$[d]), 0.97—0.73 (m, 21H, $Si(C\underline{H}(CH_3)_2)_3$, $Si(CH(C\underline{H}_3)_2)_3$).

^{13}C{^{1}H} NMR (100 MHz, $CDCl_3$): δ (ppm) = 158.76 (2C, trityl-C), 152.48 (1C, C6), 144.48, 144.35 (1C, trityl-C), 141.42 (1C, C2), 139.09, 139.00 (1C, C8), 137.40 (1C, C4), 135.57, 135.39, 135.28 (2C, trityl-C), 130.34, 130.26 (4C, trityl-C), 128.38, 128.25, 128.09 (4C, trityl-C), 127.99 (1C, C5), 127.21 (1C, trityl-C), 117.63 (1C, $CH_2\underline{C}N$), 113.38 (4C, trityl-C), 97.87, 97.73 (1C, C3), 88.92, 88.75 (1C, C1'), 87.27, 87.12 (1C, trityl-C), 84.55, 83.68, 83.64 (1C, C4'), 75.90, 75.85 (1C, C2'), 73.78, 73.63 (1C, C3'), 63.67, 63.38 (1C, C5'), 58.99, 58.81 (1C, $POCH_2$), 55.36 (2C, trityl-OCH_3), 43.80, 43.67, 43.24, 43.12 (2C, $N\underline{C}H(CH_3)_2$), 28.00 (1C, $NHCH_3$), 24.90, 24.82, 24.71, 24.64 (4C, $NCH(\underline{C}H_3)_2$), 20.58, 20.52 (1C, $\underline{C}H_2CN$), 19.90, 18.03, 17.98, 17.69, 17.68, 17.66, 17.65 (6C, $CH(\underline{C}H_3)_2$), 12.46, 12.25 (3C, $\underline{C}H(CH_3)_2$).

^{31}P{^{1}H} NMR (162 MHz, $CDCl_3$): δ (ppm) = 152.48, 148.23.

HR-ESI-MS: *m/z* calc. ($C_{51}H_{72}N_6O_7PSi$ $[M+H]^+$): 939.4964, found: 939.4936.

5'-*O*-(4,4'-Dimethoxytrityl)-2'-*O*-(*tert*-butyldimethylsilyl)-N^6-methyl-7-deazaadenosine 3'-*O*-(2-cyanoethyl)diisopropylphosphoramidite (80)

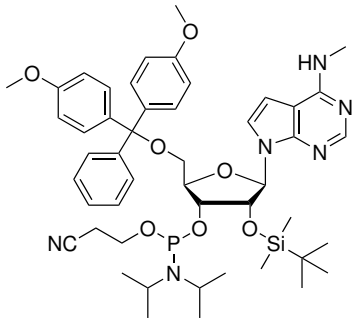

81
$C_{48}H_{65}N_6O_7PSi$
897.14 g·mol^{-1}

A solution of compound **73** (82.0 mg, 118 µmol, 1.00 eq.) in dry dichloromethane (1 mL) under an inert gas atmosphere was treated with ethyldimethylamine (120 µL, 1.11 mmol, 9.41 eq.). CEPCl (30.0 µL, 134 µmol, 1.14 eq.) was added in three portions over 1 h. The resulting mixture was stirred at ambient temperature for 3 h. The solvent was removed under reduced pressure and the residue was purified by column chromatography (silica gel, *n*-hexane:EtOAc 1:1 + 1% NEt_3) to yield the product **81** as a colorless foam (32.4 mg, 36.1 µmol, 31%).

^{1}H NMR (400 MHz, $CDCl_3$): δ (ppm) = 8.31, 8.28 (2s, 1H, C2-H), 7.51—7.43 (m, 2H, trityl-H), 7.41—7.31 (m, 4H, trityl-H), 7.32—7.17 (m, 3H, C8-H, trityl-H), 6.86—6.76 (m, 4H, trityl-H), 6.39—6.32 (m, 1H, C7-H), 6.29, 6.26 (2d, J = 6.6 Hz, 1H, C1'-H), 5.11 (s_{br}, 1H, N$\underline{H}CH_3$), 4.85, 4.79 (2 dd, J = 6.6, 4.7 Hz, 1H, C2'-H), 4.40—4.23 (m, 2H, C3'-H, C4'-H), 4.06—3.83 (m, 1H, $POCH_2{}^a$), 3.82—3.76 (m, 6H, trityl-OCH_3), 3.70—3.49 (m, 4H, N($C\underline{H}(CH_3)_2)_2$, C5'-H^a, $POCH_2{}^b$), 3.28-–3.15 (m, 4H, C5'-H^b, NH$C\underline{H}_3$), 2.70—2.64 (m, 1H, $CH_2{}^a$-CN), 2.31-–2.25 (m, 1H, $CH_2{}^b$-CN), 1.21-–1.13 (m, 9H, N(CH($C\underline{H}_3)_2)_2{}^{a,b,c}$), 1.00 (d, J = 6.7 Hz, 3H, N(CH($C\underline{H}_3)_2)_2{}^d$), 0.75 (d, J = 6.3 Hz, 9H, $Si(CH_3)_2(C(C\underline{H}_3)_3)$, -0.04, -0.09 (2 s, 3H, $Si(C\underline{H}_3)_2{}^a(C(CH_3)_3)$, -0.21, -0.23 (2 s, 3H, $Si(C\underline{H}_3)_2{}^b(C(CH_3)_3)$.

^{13}C{^{1}H} NMR (100 MHz, $CDCl_3$): δ (ppm) = 158.65 (2C, trityl-C), 157.09 (1C, C6), 152.02 (1C, C2), 150.85 (1C, C4), 144.90, 144.79 (1C, trityl-C), 136.07, 135.97, 135.88, 135.82 (2C, trityl-C), 130.37, 130.31, 130.27, 130.25 (4C, trityl-C), 128.47, 128.33 (2C, trityl-C), 128.01, 127.99 (2C, trityl-C), 127.01 (1C, trityl-C), 121.92, 121.87 (1C, C8), 117.95, 117.48 (1C, $CH_2\underline{C}N$), 113.30, 113.29, 113.26, 113.24 (4C, trityl-C), 103.75 (1C, C5), 99.06 (1C, C7), 87.61, 87.31 (1C, C1'), 86.69, 86.51 (1C, trityl-C), 83.45, 83.30 (1C, C4'), 75.86, 75.33 (1C, C2'), 72.93, 72.78 (1C, C3'), 63.76, 63.52 (1C, C5'), 59.63, 59.03, 57.88, 57.67 (1C, $POCH_2$), 55.38, 55.36 (2C, trityl-OCH_3), 43.54, 43.41, 43.05, 42.92 (2C, N$\underline{C}H(CH_3)_2$), 28.51, 27.40 (1C, $NHCH_3$), 25.82, 25.80, 25.77 (3C, $SiC(\underline{C}H_3)_3$), 24.91, 24.84, 24.76, 24.70, 24.64 (4C, $NCH(\underline{C}H_3)_2$), 20.65, 20.59, 20.19, 20.12 (1C, $\underline{C}H_2CN$), 18.16, 18.07 (1C, $Si\underline{C}(CH_3)_3$), -4.64, -4.68 (1C, $Si(CH_3)_2{}^a$), -5.03 (1C, $Si(CH_3)_2{}^b$).

$^{31}P\{^{1}H\}$ NMR (162 MHz, $CDCl_3$): δ (ppm) = 150.46, 148.71.

HR-ESI-MS: *m/z* calc. ($C_{48}H_{65}N_6NaO_7PSi$ $[M+Na]^+$): 919.43138, found: 919.43085.

5.3 Compounds described in Part II

1'-Cyano-5'-*O*-(4,4'-dimethoxytrityl)-N^6-dimethylformamidine-4-aza-7,9-dideazaadenosine (83)

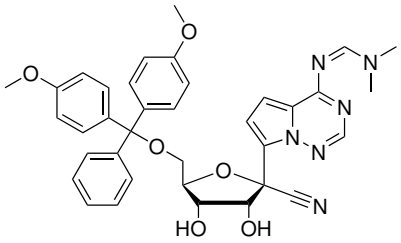

83
$C_{36}H_{36}N_6O_6$
648.72 g·mol^{-1}

Under an inert gas atmosphere, a suspension of 1'-Cyano-4-aza-7,9-dideazaadenosine (**82**, 400 mg, 1.37 mmol, 1.00 eq.) in pyridine (4 mL) was treated with *N*,*N*-dimethylformamide dimethyl acetal (550 µL, 4.12 mmol, 3.00 eq.) and stirred at ambient temperature for 18 h. Volatiles were removed *in vacuo* and the residue was re-dissolved in pyridine (4 mL). 4,4'-Dimethoxytrityl chloride (560 mg, 1.65 mmol, 1.20 eq.) was added. The resulting solution was stirred at ambient temperature for 3.5 h. Methanol (16 mL) was added and stirring was continued for 30 min. The solvent was removed under reduced pressure and the residue was purified by column chromatography (silica gel, CH_2Cl_2:MeOH = 98:2 + 2% NEt_3) to yield the product **83** as a colorless foam (830 mg, 1.28 mmol, 93%).

^{1}H NMR (400 MHz, $CDCl_3$): δ (ppm) = 8.89 (s_{br}, 1H, N^6-CH), 8.09 (s, 1H, C2-H), 7.27–7.23 (m, 2H, trityl-H), 7.21–7.13 (m, 7H, trityl-H), 7.04 (d, *J* = 4.6 Hz, 1H, C7-H), 7.00 (d, *J* = 4.6 Hz, 1H, C8-H), 6.77–6.70 (m, 4H, trityl-H), 4.78 (d, *J* = 5.3 Hz, 1H, C2'-H), 4.60 (td, *J* = 3.1, 1.7 Hz, 1H, C4'-H), 4.35 (dd, *J* = 5.3, 1.7 Hz, 1H, C3'-H), 3.77 (s, 3H, trityl-OCH_3), 3.75 (s, 3H, trityl-OCH_3), 3.50 (dd, *J* = 10.6, 3.1 Hz, 1H, C5'-H^a), 3.27 (d, *J* = 0.7 Hz, 3H, NCH_3 ^{a}), 3.25 (d, *J* = 0.5 Hz, 3H, $NCH_3{}^b$), 3.14 (dd, *J* = 10.6, 3.1 Hz, 1H, C5'-H^b).

$^{13}C\{^{1}H\}$ NMR (100 MHz, $CDCl_3$): δ (ppm) = 161.07 (1C, C6), 158.56 (2C, trityl-C), 158.08 (1C, N^6-CH), 147.91 (1C, C2), 144.57 (1C, trityl-C), 135.87 (1C, trityl-C), 135.51 (1C, trityl-C), 130.13 (2C, trityl-C), 130.09 (2C, trityl-C), 128.14 (2C, trityl-C), 127.91 (2C, trityl-C), 126.90 (1C, trityl-C), 125.69 (1C, C9), 122.53 (1C, C5), 116.78 (1C, CN), 113.23 (2C, trityl-C), 113.20 (2C, trityl-C), 111.46 (1C, C7), 103.87 (1C, C8), 87.20 (1C, C4'), 86.43 (1C, trityl-C), 79.24 (1C, C1'), 77.11 (1C, C2'), 73.49 (1C, C3'), 63.44 (1C,

C5'), 55.33 (1C, trityl-OCH_3), 55.31 (1C, trityl-OCH3), 41.76 ($NCH_3{}^a$), 35.54 ($NCH_3{}^b$).

HR-ESI-MS: *m/z* calc. ($C_{36}H_{37}N_6O_6$ $[M+H]^+$): 649.27691, found: 649.27836.

1'-Cyano-5'-*O*-(4,4'-dimethoxytrityl)-N^6-dimethylformamidine-3'-*O*-(*tert*-butyldimethylsilyl)-4-aza-7,9-dideazaadenosine (84)

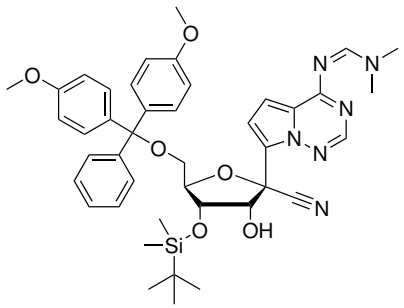

84
$C_{42}H_{50}N_6O_6Si$
762.98 g·mol^{-1}

Under an inert gas atmosphere, a solution of **83** (200 mg, 308 µmol, 1.00 eq.) in pyridine (2 mL) was treated with silver nitrate (209 mg, 1.23 mmol, 4.00 eq.) and stirred in the dark at ambient temperature for 30 min. *tert*-Butyldimethylsilyl chloride (55.8 mg, 370 µmol, 1.20 eq.) was added and stirring was continued in the dark for 22 h. The solvent was removed under reduced pressure. The residue was taken up in ethyl acetate and insoluble residues were removed by filtration through a pad of Celite. The filtrate was evaporated to dryness and the residue was purified by column chromatography (silica gel, *n*-hexane:EtOAc = 1:1 + 1% NEt_3 to 0:1 + 1% NEt_3) to yield the product **84** as a colorless foam (169 mg, 221 µmol, 72%).

^{1}H NMR (400 MHz, $CDCl_3$): δ (ppm) = 8.83 (s_{br}, 1H, N^6-CH), 8.04 (s, 1H, C2-H), 7.45–7.13 (m, 9H, trityl-H), 7.05 (d, *J* = 4.6 Hz, 1H, C7-H), 6.93 (d, *J* = 4.6 Hz, 1H, C8-H), 6.79–6.72 (m, 4H, trityl-H), 5.08 (dd, *J* = 9.1, 5.5 Hz, 1H, C2'-H), 4.39 (m, 1H, C4'-H), 4.34 (dd, *J* = 5.5, 2.3 Hz, 1H, C3'-H), 3.78–3.75 (m, 7H, (trityl-OCH_3)$_2$, C2'-OH), 3.50 (dd, *J* = 10.6, 4.2 Hz, 1H, C5'-H^a), 3.25 (d, *J* = 0.6 Hz, 3H, $NCH_3{}^a$), 3.22 (d, *J* = 0.5 Hz, 3H, $NCH_3{}^b$), 3.16 (dd, *J* = 10.6, 3.4 Hz, 1H, C5'-H^b), 0.93 (s, 9H, $SiC(CH_3)_3$), 0.09 (s, 3H, $SiCH_3$), 0.00 (s, 3H, $SiCH_3$).

^{13}C{^{1}H} NMR (100 MHz, $CDCl_3$): δ (ppm) = 160.73 (1C, C6), 158.46 (2C, trityl-C), 157.55 (1C, N^6-CH), 147.38 (1C, C2), 144.51 (1C, trityl-C), 135.84 (1C, trityl-C), 135.59 (1C, trityl-C), 130.02 (4C, trityl-C), 128.15 (2C, trityl-C), 127.79 (2C, trityl-C), 126.80 (1C, trityl-C), 123.60 (1C, C9), 123.45 (1C, C5), 116.53 (1C, CN), 113.08 (4C, trityl-C), 112.69 (1C, C7), 102.52 (1C, C8), 86.38 (1C, trityl-C), 86.21 (1C, C4'), 78.73 (1C, C1'), 74.69 (1C, C2'), 72.77 (1C, C3'), 62.53 (1C, C5'), 55.20 (2C, trityl-OCH_3), 41.46 (1C, $NCH_3{}^a$), 35.27 (1C, $NCH_3{}^b$), 25.61 (3C, $SiC(\underline{C}H_3)_3$), 17.99 (1C, $Si\underline{C}(CH_3)_3$), -4.63 (1C, $SiCH_3$), -4.99 (1C, $SiCH_3$).

HR-ESI-MS: *m/z* calc. ($C_{42}H_{51}N_6O_6Si$ $[M+H]^+$): 763.36339, found: 763.36464.

1'-Cyano-5'-*O*-(4,4'-dimethoxytrityl)-N^6-dimethylformamidine-2'-*O*-(*tert*-butyldimethylsilyl)-4-aza-7,9-dideazaadenosine (85)

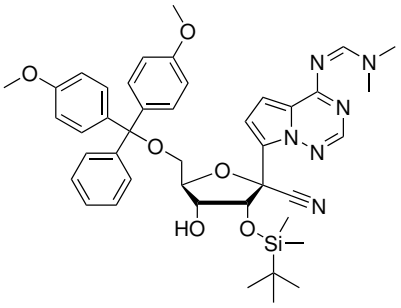

85
$C_{42}H_{50}N_6O_6Si$
762.98 g·mol^{-1}

Compound **84** (100 mg, 131 µmol, 1.00 eq.) was dissolved in a mixture of methanol (99 mL) and triethylamine (1 mL). After stirring at ambient temperature for 30 min the ratio of isomers **84** and **85** was ca. 1:1 (by TLC). After removal of the solvent under reduced pressure, separation of the isomers by column chromatography (*n*-hexane:EtOAc = 1:3), 30.0 mg (39.3 µmol, 30%) of pure product **85** were obtained as a colorless foam. The remaining mixture of isomers was isolated and again treated with trimethylamine in methanol.

^{1}H NMR (400 MHz, $CDCl_3$): δ (ppm) = 8.85–8.80 (m, 1H, N^6-CH), 7.79 (s, 1H, C2-H), 7.51–7.43 (m, 2H, trityl-H), 7.39–7.32 (m, 4H, trityl-H), 7.28–7.15 (m, 3H, trityl-H), 7.11 (d, *J* = 4.6 Hz, 1H, C7-H), 6.91 (d, *J* = 4.6 Hz, 1H, C8-H), 6.82–6.73 (m, 4H, trityl-H), 5.50 (d, *J* = 5.7 Hz, 1H, C2'-H), 4.45 (m, 1H, C4'-H), 4.34 (m, 1H, C3'-H), 3.77 (2s, 6H, trityl-OCH_3), 3.50 (dd, *J* = 10.4, 4.0 Hz, 1H, C5'-H^a), 3.34 (dd, *J* = 10.4, 4.4 Hz, 1H, C5'-H^b), 3.26 (d, *J* = 0.7 Hz, 3H, NCH_3), 3.22 (d, *J* = 0.4 Hz, 3H, NCH_3), 2.77 (d, *J* = 4.3 Hz, 1H, C3'-OH), 0.87 (s, 9H, $SiC(CH_3)_3$), -0.10 (s, 3H, $SiCH_3$), -0.15 (s, 3H, $SiCH_3$).

^{13}C{^{1}H} NMR (100 MHz, $CDCl_3$): δ (ppm) = 160.83 (1C, C6), 158.55 (1C, trityl-C), 158.53 (1C, trityl-C), 157.71 (1C, N^6-CH), 147.20 (1C, C2), 145.03 (1C, trityl-C), 136.22 (1C, trityl-C), 136.11 (1C, trityl-C), 130.28 (4C, trityl-C), 128.41 (2C, trityl-C), 127.87 (2C, trityl-C), 126.85 (1C, trityl-C), 123.86 (1C, C5), 122.29 (1C, C9), 117.10 (1C, CN), 114.81 (1C, C7), 113.18 (4C, trityl-C), 102.52 (1C, C8), 86.25 (1C, trityl-C), 85.43 (1C, C4'), 80.06 (1C, C1'), 73.61 (1C, C2'), 71.68 (1C, C3'), 63.02 (1C, C5'), 55.34 (2C, trityl-OCH_3), 41.62 (1C, $NCH_3{}^a$), 35.42 (1C, $NCH_3{}^b$), 25.75 (3C, $SiC(\underline{C}H_3)_3$), 18.11 (1C, $Si\underline{C}(CH_3)_3$), -4.91 (1C, $SiCH_3$), -5.12 (1C, $SiCH_3$).

HR-ESI-MS: *m/z* calc. ($C_{42}H_{51}N_6O_6Si$ $[M+H]^+$): 763.36339, found: 763.36413.

1'-Cyano-5'-*O*-(4,4'-dimethoxytrityl)-N^6-dimethylformamidine-2'-*O*-(*tert*-butyldimethylsilyl)-4-aza-7,9-dideazaadenosine 3'-β-cyanoethyl diisopropylphosphoramidite (86)

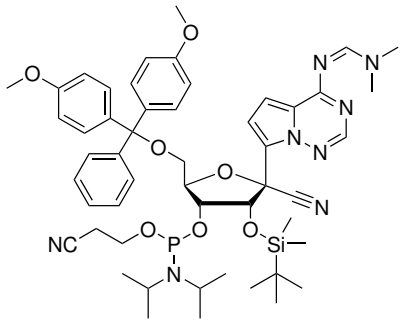

86
$C_{51}H_{67}N_8O_7PSi$
962.46 g·mol^{-1}

Under an inert gas atmosphere, a solution of **85** (110.0 mg, 144 µmol, 1.00 eq.) in dichloromethane (1.1 mL) was treated with *N*,*N*-dimethylethylamine (156 µL, 1.44 mmol, 10.0 eq.) and 2-cyanoethyl-*N*,*N*-diisopropylchlorophosphoramidite (40.9 mg, 173 µmol, 1.20 eq.) and stirred at ambient temperature for 5 h. The solvent was removed under reduced pressure and the residue was purified by column chromatography (silica gel, *n*-hexane:EtOAc = 1:3) to yield the product **86** as a colorless foam (104 mg, 108 µmol, 75%, isomer ratio at phosphorus 10:8).

^{1}H NMR (400 MHz, $CDCl_3$): δ (ppm) = 8.82, 8.81 (2s, N^6-CH), 7.68 (s, C2-H), 7.58 (s, C2-H), 7.54–7.45 (m, trityl-H), 7.43–7.33 (m, trityl-H), 7.27–7.18 (m, trityl-H), 7.16, 7.15 (2d, *J* = 4.6 Hz, C7-H), 6.92, 6.91 (2d, *J* = 4.6 Hz, C8-H), 6.83–6.72 (m, trityl-H), 5.63, 5.61 (2d, *J* = 5.3 Hz, C2'-H), 4.62 (q, *J* = 3.3 Hz, C4'-H), 4.58–4.51 (m, C4'-H), 4.45–4.34 (m, C3'-H), 4.20–4.09 (m, $POCH_2$), 3.98–3.88 (m, $POCH_2$), 3.78–3.75 (m, trityl-OCH_3), 3.66–3.52 (m, C5'-H, $N(C\underline{H}(CH_3)_2)_2$), 3.34 (dd, *J* = 10.3, 4.5 Hz, C5'-H), 3.28–3.23 (m, C5'-H, $N(CH_3)_2$), 3.21 (d, *J* = 0.9 Hz, $N(CH_3)_2$), 2.73–2.54 (m, CH_2CN), 2.24–2.18 (m, CH_2CN), 1.18 (d, *J* = 6.8 Hz, $N(CH(C\underline{H}_3)_2)_2$), 1.15 (d, *J* = 6.8 Hz, $N(CH(C\underline{H}_3)_2)_2$), 1.00 (d, *J* = 6.8 Hz, $N(CH(C\underline{H}_3)_2)_2$), 0.80 (s, $SiC(CH_3)_3$), 0.77 (s, $SiC(CH_3)_3$), -0.09 (s, $SiCH_3$), -0.18 (s, $SiCH_3$), -0.33 (s, $SiCH_3$), -0.40 (s, $SiCH_3$).

^{13}C{^{1}H} NMR (100 MHz, $CDCl_3$): δ (ppm) = 160.79 (C6), 158.55 (trityl-C), 157.67 (N^6-CH), 147.07 (C2), 146.98 (C2), 145.05 (trityl-C), 144.87 (trityl-C), 136.29 (trityl-C), 136.17 (trityl-C), 136.09 (trityl-C), 136.02 (trityl-C), 130.41 (trityl-C), 130.36 (trityl-C), 128.57 (trityl-C), 128.52 (trityl-C), 127.85 (trityl-C), 126.88 (trityl-C), 123.98 (C5), 123.81 (C5), 122.73 (C9), 122.22 (C9), 118.34 ($CH_2\underline{C}N$), 117.95 (C1'-$\underline{C}N$), 117.53 ($CH_2\underline{C}N$), 117.32 (C1'-$\underline{C}N$), 116.00 (C7), 115.46 (C7), 113.15 (trityl-C), 113.13 (trityl-C), 102.51 (C8), 86.43 (trityl-C), 86.24 (trityl-C), 85.79 (C4'), 79.90 (C1'), 79.69 (C1'), 73.45 (C2'), 72.46 (C3'), 72.35 (C3'), 63.32 (C5'), 63.04 (C5'), 59.26 ($POCH_2$), 59.14 ($POCH_2$), 57.78 ($POCH_2$), 57.59 ($POCH_2$), 55.35 (trityl-OCH_3), 43.55 ($N\underline{C}H(CH_3)_2$), 43.43 ($N\underline{C}H(CH_3)_2$), 43.04

($N\underline{C}H(CH_3)_2$), 42.91 ($N\underline{C}H(CH_3)_2$), 41.59 (NCH_3), 35.41 (NCH_3), 25.87 (Si-C($\underline{C}H_3)_3$) 25.85 (Si-C($\underline{C}H_3)_3$), 25.81 (Si-C($\underline{C}H_3)_3$), 24.93 (NCH($\underline{C}H_3)_2$), 24.85 (NCH($\underline{C}H_3)_2$), 24.75 (NCH($\underline{C}H_3)_2$), 24.69 (NCH($\underline{C}H_3)_2$), 24.63 (NCH($\underline{C}H_3)_2$), 20.88 ($\underline{C}H_2CN$), 20.83 ($\underline{C}H_2CN$), 18.11 ($Si\underline{C}(CH_3)_3$), 18.04 ($Si\underline{C}(CH_3)_3$), -4.64 ($SiCH_3$), -4.68 ($SiCH_3$), -5.37 ($SiCH_3$), -5.45 ($SiCH_3$).

$^{31}P\{^1H\}$ NMR (162 MHz, $CDCl_3$): δ (ppm) = 150.48, 147.94.

HR-ESI-MS: *m/z* calc. ($C_{51}H_{68}N_8O_7PSi$ $[M+H]^+$): 963.47124, found: 963.46940.

1'-Cyano-5'-*O*-(4,4'-dimethoxytrityl)-N^6-dimethylformamidine-3'-*O*-(*tert*-butyldimethylsilyl)-4-aza-7,9-dideazaadenosine 2'-β-cyanoethyl diisopropylphosphoramidite (87)

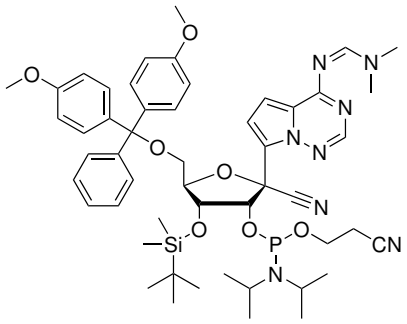

87
$C_{51}H_{67}N_8O_7PSi$
962.46 g·mol^{-1}

Under an inert gas atmosphere, a solution of **84** (50.0 mg, 65.5 µmol, 1.00 eq.) in dichloromethane (0.5 mL) was treated with *N*,*N*-dimethylethylamine (71.0 µL, 655 µmol, 10.0 eq.) and 2-cyanoethyl-*N*,*N*-diisopropylchlorophosphoramidite (18.6 mg, 78.6 µmol, 1.20 eq.) and stirred at ambient temperature for 5 h. The solvent was removed under reduced pressure and the residue was purified by column chromatography (silica gel, *n*-hexane:EtOAc = 1:2) to yield the product **87** as a colorless foam (54.0 mg, 56.1 µmol, 85%, isomer ratio at phosphorus 10:3).

^1H NMR (400 MHz, $CDCl_3$): δ (ppm) = 8.82 (s, N^6CH), 8.79 (t, *J* = 0.7 Hz, N^6CH), 7.92 (s, C2-H), 7.72 (s, C2-H), 7.46–7.16 (m, C7-H, trityl-H), 7.13 (dd, *J* = 4.6, 0.8 Hz, C7-H), 6.91 (d, *J* = 4.6 Hz, C8-H), 6.86 (d, *J* = 4.6 Hz, C8-H), 6.82–6.74 (m, trityl-H), 5.37 (dd, *J* = 12.6, 4.7 Hz, 1H, C2'-H), 5.28 (dd, *J* = 10.8, 4.1 Hz, 1H, C2'-H), 4.48–4.37 (m, 3'-H, 4'-H), 3.90-3.82 (m, $POCH_2$), 3.82–3.72 (m, (trityl-$OCH_3)_2$, $POCH_2$), 3.69–3.47 (m, $POCH_2$, N($C\underline{H}(CH_3)_2)_2$, C5'-H), 3.30 (dd, *J* = 10.2, 4.1 Hz, C5'-H), 3.26–3.19 (m, $N(CH_3)_2$, C5'-H), 2.78–2.31 (m, CH_2CN), 1.11 (d, *J* = 6.8 Hz, N(CH($C\underline{H}_3)_2)_2$), 1.05 (d, *J* = 6.7 Hz, N(CH($C\underline{H}_3)_2)_2$), 1.02–0.94 (m, N(CH($C\underline{H}_3)_2)_2$, $SiC(CH_3)_3$), 0.91 (s, $SiC(CH_3)_3$), 0.14 (s, $SiCH_3$), 0.12 (s, $SiCH_3$), 0.09 (s, $SiCH_3$), 0.00 (s, $SiCH_3$).

^{13}C{^{1}H} NMR (100 MHz, $CDCl_3$): δ (ppm) = 160.78 (C6), 158.58 (trityl-C), 158.56 (trityl-C), 157.63 (N^6-CH), 147.11 (C2), 144.82 (trityl-C), 136.07 (trityl-C), 135.92 (trityl-C), 130.28 (trityl-C), 130.24 (trityl-C), 130.16 (trityl-C), 128.46 (trityl-C), 128.40 (trityl-C), 127.93 (trityl-C), 127.89 (trityl-C), 126.92 (trityl-C), 123.65 (C5), 123.42 (C9), 117.75 ($CH_2\underline{C}N$), 117.07 (C1'-$\underline{C}N$), 114.03 (C7), 113.99 (C7), 113.21 (trityl-C), 113.19 (trityl-C), 102.44 (C8), 86.82 (trityl-C), 86.60 (trityl-C), 86.45 (C4'), 86.33 (C4'), 77.87 (C1'), 77.82 (C1'), 75.18 (C2'), 75.04 (C2'), 72.86 (C3'), 63.23 (C5'), 58.64 ($POCH_2$), 58.47 ($POCH_2$), 55.37 (trityl-OCH_3), 43.41 (N($\underline{C}H(CH_3)_2)_2$), 43.29 (N($\underline{C}H(CH_3)_2)_2$), 41.59 ($NCH_3$), 35.39 ($NCH_3$), 25.85 (SiC($\underline{C}H_3)_3$), 24.83 (N(CH($\underline{C}H_3)_2)_2$), 24.76 (N(CH($\underline{C}H_3)_2)_2$), 24.69 (N(CH($\underline{C}H_3)_2)_2$), 24.61 (N(CH($\underline{C}H_3)_2)_2$), 24.39 (N(CH($\underline{C}H_3)_2)_2$), 24.32 (N(CH($\underline{C}H_3)_2)_2$), 20.46 ($\underline{C}H_2CN$), 20.40 ($\underline{C}H_2CN$), 18.11 (Si$\underline{C}(CH_3)_3$), -4.33 ($SiCH_3$), -4.36 ($SiCH_3$), -4.40 ($SiCH_3$), -4.42 ($SiCH_3$).

^{31}P{^{1}H} NMR (162 MHz, $CDCl_3$): δ (ppm) = 149.92, 149.25.

HR-ESI-MS: *m/z* calc. ($C_{51}H_{68}N_8O_7PSi$ $[M+H]^+$): 963.47124, found: 963.47136.

4-Aza-7,9-dideazaadenosine 1'-(*N*-methyl)amidine (88)

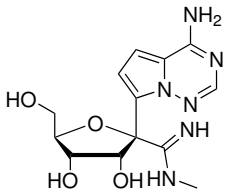

88
$C_{13}H_{18}N_6O_4$
322.33 g·mol^{-1}

1'-Cyano-4-aza-7,9-dideazaadenosine (**82**, 50 mg, 172 µmol, 1.00 eq.) was dissolved in methylamine (40% in water, 15 mL) and stirred at 37 °C for 5 h. The solvent was removed under reduced pressure, the residue was re-dissolved in water (30 mL) and freeze-dried. The crude product **88** was obtained as an off-white solid (55.2 mg, 95% purity by HPLC) and used without further purification for the next step.

^{1}H NMR (400 MHz, DMSO-d_6): δ (ppm) = 7.80 (s, 1H, C2-H), 6.84 (d, J = 4.5 Hz, 1H, C7-H), 6.62 (d, J = 4.6 Hz, 1H, C8-H), 4.88 (d, J = 4.8 Hz, 1H, C2'-H), 3.99 (q, J = 3.9 Hz, 1H, C4'-H), 3.93 (t, J = 4.7 Hz, 1H, C3'-H), 3.60 (dd, J = 11.8, 3.4 Hz, 1H, C5'-H^a), 3.46 (dd, J = 11.9, 3.9 Hz, 1H, C5'-H^b), 2.72 (d, J = 5.9 Hz, 3H, CH_3).

^{13}C{^{1}H} NMR (100 MHz, DMSO-d_6): δ (ppm) = 166.24 (1C, $\underline{C}$(NH)$NHCH_3$), 155.79 (1C, C6), 147.47 (1C, C2), 128.46 (1C, C9), 115.56 (1C, C5), 111.56 (1C, C7), 100.77 (1C, C8), 84.95 (1C, C4'), 82.99 (1C, C1'), 75.15 (1C, C2'), 71.59 (1C, C3'), 61.91 (1C, C5'), 30.05 (C(NH)NH$\underline{C}H_3$).

4-Aza-7,9-dideazaadenosine 1'-(*N*-methyl)amidine 5'-triphosphate (89)

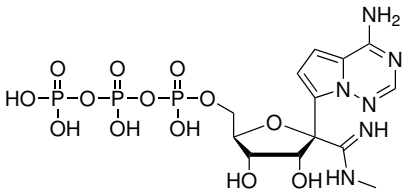

89
$C_{13}H_{21}N_6O_{13}P_3$
562.26 g·mol^{-1}

Compound **88** (20.0 mg, 62.1 µmol, 1.00 eq.) and proton sponge (18.6 mg, 86.9 µmol, 1.40 eq.) were dissolved in dry trimethyl phosphate (1.2 mL) under an inert gas atmosphere. The solution was cooled to -20 °C and freshly distilled phosphoryl chloride (6.38 µL, 68.3 µmol, 1.10 eq.) was added dropwise. The reaction mixture was stirred at -20 °C for 3 h. A solution of tributylamine (103 µL, 434 µmol, 7.00 eq.) and bis(tetrabutylammonium) pyrophosphate (279 mg, 422 µmol, 6.80 eq.) in dry *N*,*N*-dimethylformamide (500 µL) was added and the reaction mixture was stirred at 0 °C for 2 h. The reaction was quenched by addition of aq. triethylammonium bicarbonate (TEAB) buffer (1 M, pH = 7.7, 10 mL) and allowed to warm to ambient temperature. It was washed with ethyl acetate (2 × 10 mL) and the aqueous layer was lyophilized. The residue was dissolved in TEAB buffer (100 mM, pH = 7.7, 5 mL) and purified by anion exchange FPLC (DEAE Sephadex A-25, 15×120 mm, flow rate 1.5 mL/min, at 20 °C. Eluent A: 100 mM aq. TEAB, pH = 7.7. Eluent B: 1 M aq. TEAB, pH = 7.7. Gradient: 0% eluent B for 4.7 min, then 0–100 % eluent B in 40 min). The fractions containing the product were further purified by RP-HPLC (Nucleosil 8×250 mm, flow rate 2 mL/min, at 30 °C. Eluent A: 100 mM TEAA, pH = 7.0 in H_2O. Eluent B: 100 mM TEAA, pH = 7.0 in 90% aq. MeCN. Gradient: 2–12 % eluent B in 25 min). The fractions containing the product were lyophilized and reconstituted in water to yield 800 µL of a 3.2 mM aq. solution of **89** triethylammonium salt (2.56 µmol, 4%).

^{1}H NMR (400 MHz, D_2O): δ (ppm) = 7.82 (s, 1H, C2-H), 7.04 (d, J = 4.8 Hz, 1H, C7-H), 6.90 (d, J = 4.7 Hz, 1H, C8-H), 5.20 (d, J = 4.1 Hz, 1H, C2'-H), 4.52–4.41 (m, 2H, C3'-H, C4'-H), 4.10 (ddd, J = 11.7, 6.0, 2.9 Hz, 1H, C5'-H^a), 4.01 (ddd, J = 11.5, 7.1, 4.3 Hz, 1H, C5'-H^b), 2.95 (s, 3H, CH_3).

^{13}C{^{1}H} NMR (100 MHz, D_2O): δ (ppm) = 165.77 (1C, $\underline{C}$(NH)NHCH$_3$), 155.55 (1C, C6), 147.08 (1C, C2), 124.67 (1C, C9), 116.02 (1C, C5), 112.25 (1C, C7), 102.30 (1C, C8), 83.05 (1C, C4'), 82.66 (1C, C1'), 75.23 (1C, C2'), 71.06 (1C, C3'), 65.08 (1C, C5'), 28.30 (C(NH)NH$\underline{C}$H$_3$).

^{31}P{^{1}H} NMR (162 MHz, D_2O): δ (ppm) = -10.26 (d, J = 19.9 Hz, 1P, γ-P), -11.50 (d, J = 19.9 Hz, 1P, α-P), -23.21 (t, J = 19.9 Hz, 1P, β-P).

2,3,5-Tri-*O*-benzylribono-1,4-lactone (92)

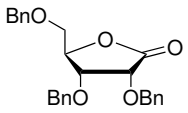

92
$C_{26}H_{26}O_5$
418.49 g·mol^{-1}

This compound was synthesized by modification of a reported procedure.[238] Acetyl chloride (3.60 mL, 50.6 mmol, 0.30 eq.) was dissolved in methanol (600 mL) and stirred at ambient temperature for 5 min. D-Ribose (25.0 g, 167 mmol, 1.00 eq.) was added and stirring was continued at ambient temperature for 16 h. The reaction was quenched by addition of solid $NaHCO_3$ (70 g), solids were removed by filtration and the filtrate was concentrated to dryness under reduced pressure. The residue was coevaporated twice with toluene and redissolved in *N*,*N*-dimethylformamide (750 mL). Benzyl bromide (83.0 mL, 698 mmol, 4.18 eq.) and tetrabutylammonium iodide (600 mg, 1.62 mmol, 0.01 eq.) were added, the mixture was cooled to 0 °C and treated with sodium hydride (60% in mineral oil, 28.0 g, 700 mmol, 4.19 eq.) in portions. The mixture was allowed to warm to ambient temperature and stirred for 16 h. The solvent was removed under reduced pressure, the residue was redissolved in diethyl ether (500 mL) and washed with 1 M hydrochloric acid (2 × 200 mL). The combined aqueous layers were extracted with diethyl ether (500 mL). The combined organic layers were dried over Na_2SO_4 and the solvent was removed *in vacuo*. The residue was dissolved in a mixture of acetic acid (500 mL) and water (125 mL) and stirred at 110 °C for 16 h. The mixture was concentrated under reduced pressure to a final volume of 100 mL and neutralized with 12 M aq. NaOH solution. The resulting solution was extracted with ethyl acetate (3 × 400 mL). The combined organic layers were dried over Na_2SO_4 and the solvent was removed *in vacuo*. The residue was dissolved in dimethylsulfoxide (240 mL), treated with acetic anhydride (81 mL, 869 mmol, 5.20 eq.) and stirred at ambient temperature for 16 h. The reaction mixture was poured into ice water (1.30 L), stirred for 20 min, and extracted with ethyl acetate (3 × 500 mL). The combined organic layers were washed with water (2 × 500 mL) and brine (500 mL) and dried over Na_2SO_4. The solvent was removed under reduced pressure and the residue was purified by column chromatography (silica gel, *n*-hexane:EtOAc = 1:0 to 4:1) to yield the product **92** as a light yellow viscous liquid, which slowly crystallized (38.8 g, 92.7 mmol, 55%). Analytical data agreed with reported values.[269]

^{1}H NMR (400 MHz, $CDCl_3$): δ (ppm) = 7.39—7.27 (m, 13H, benzyl-H), 7.22-–7.13 (m, 2H, benzyl-H), 4.95 (d, *J* = 12.0 Hz, 1H, C2-OCH_2^a), 4.74 (d, *J* = 12.0 Hz, 1H, C2-OCH_2^b), 4.70 (d, *J* = 11.9 Hz, 1H, C3-OCH_2^a), 4.59-–4.52 (m, 2H, C3-OCH_2^b, C4-H), 4.49 (d, *J* = 11.9 Hz, 1H, C5-OCH_2^a), 4.43—4.38 (m, 2H, C5-OCH_2^b, C2-H), 4.10 (dd, *J* = 5.7, 2.0 Hz,

1H, C3-H), 3.66 (dd, J = 11.0, 2.8 Hz, 1H, C5-H^a), 3.55 (dd, J = 11.0, 2.7 Hz, 1H, C5-H^b).

^{13}C{^{1}H} NMR (100 MHz, $CDCl_3$): δ (ppm) = 173.85 (1C, C1), 137.34 (1C, phenyl-C), 137.23 (1C, phenyl-C), 137.05(1C, phenyl-C), 128.67 (2C, phenyl-C), 128.64 (2C, phenyl-C), 128.62 (2C, phenyl-C), 128.40 (2C, phenyl-C), 128.25 (1C, phenyl-C), 128.19 (1C, phenyl-C), 128.12 (3C, phenyl-C), 127.72 (2C, phenyl-C), 81.90 (1C, C4), 75.47 (1C, C3), 73.81 (1C, C5-O<u>C</u>H$_2$), 73.77 (1C, C2), 72.84 (1C, C2-O<u>C</u>H$_2$), 72.52 (1C, C3-O<u>C</u>H$_2$), 68.85 (1C, C5).

HR-ESI-MS: m/z calc. ($C_{26}H_{26}NaO_5$ [M+Na]$^+$): 441.1672, found: 441.1668.

2,3,5-Tri-*O*-(*tert*-butyldimethylsilyl)ribono-1,4-lactone (93)

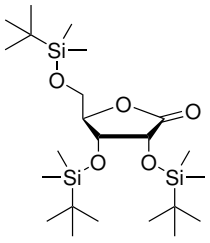

93
$C_{23}H_{50}O_5Si_3$
490.90 g·mol^{-1}

A solution of D-ribose (1.00 g, 6.66 mmol, 1.00 eq.) in water (10 mL) was treated with K_2CO_3 (1.10 g, 7.99 mmol, 1.20 eq.) in portions. The resulting solution was cooled to 0 °C and bromine (379 µL, 7.39 mmol, 1.11 eq.) was added dropwise. The mixture was stirred at ambient temperature for 16 h before the reaction was quenched by addition of sat. aq. $Na_2S_2O_3$ solution (10 mL). The solvent was removed under reduced pressure and the residue was dried *in vacuo*. The dried residue was dissolved in *N*,*N*-dimethylformamide (20 mL) and treated with imidazole (2.27 g, 33.3 mmol, 5.00 eq.) and *tert*-butyldimethylsilyl chloride (4.02 g, 26.6 mmol, 4.00 eq.). The reaction was stirred at ambient temperature for 24 h, before it was quenched by addition of water (50 mL). The aqueous layer was extracted with ethyl acetate (3 × 30 mL). The combined organic layers were washed with brine (50 mL) and dried over Na_2SO_4. The solvent was removed under reduced pressure and the residue was purified by column chromatography (silica gel, *n*-hexane:EtOAc = 2:1) to yield the product **93** as a colorless solid (883 mg, 1.80 mmol, 27%).

^{1}H NMR (400 MHz, $CDCl_3$): δ (ppm) = 4.57 (d, J = 5.1 Hz, 1H, C2-H), 4.31–4.24 (m, 2H, C3-H, C4-H), 3.86 (dd, J = 11.7, 3.1 Hz, 1H, C5-H^a), 3.78 (dd, J = 11.7, 2.1 Hz, 1H, C5-H^b), 0.94 (s, 9H, SiC(CH$_3$)$_3$), 0.89 (s, 9H, SiC(CH$_3$)$_3$), 0.88 (s, 9H, SiC(CH$_3$)$_3$), 0.18 (s, 3H, SiCH$_3$), 0.13 (s, 3H, SiCH$_3$), 0.10 (s, 3H, SiCH$_3$), 0.09 (s, 3H, SiCH$_3$), 0.07 (s, 3H, SiCH$_3$), 0.06 (s, 3H, SiCH$_3$).

$^{13}C\{^{1}H\}$ NMR (100 MHz, $CDCl_3$): δ (ppm) = 174.61 (1C, C1), 85.78 (1C, C2), 72.10(1C, C4), 71.12 (1C, C3), 62.54 (1C, C5), 25.99 (3C, $SiC(\underline{C}H_3)_3$), 25.97 (3C, $SiC(\underline{C}H_3)_3$), 25.83 (3C, $SiC(\underline{C}H_3)_3$), 18.58 (1C, $Si\underline{C}(CH_3)_3$), 18.45 (1C, $Si\underline{C}(CH_3)_3$), 18.32 (1C, $Si\underline{C}(CH_3)_3$), -4.42 (1C, $SiCH_3$), -4.48 (1C, $SiCH_3$), -4.69 (1C, S-CH_3), -4.90 (1C, $SiCH_3$), -5.38 (1C, $SiCH_3$), -5.51 (1C, $SiCH_3$).

HR-ESI-MS: *m/z* calc. ($C_{23}H_{50}NaO_5Si_3$ $[M+Na]^+$): 513.28637, found: 513.30858.

2-Cyanopyrrole (95)

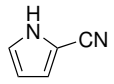

95
$C_5H_4N_2$
92.10 g·mol^{-1}

Under an inert gas atmosphere, dry *N*,*N*-dimethylformamide (250 mL, 3.23 mol, 7.90 eq.) was cooled to 0 °C and freshly distilled phosphoryl chloride (38.3 mL, 409 mmol, 1.10 eq.) was added slowly, so that the internal temperature did not exceed 15 °C. The reaction mixture was allowed to warm to ambient temperature and stirred for 30 min. The mixture was cooled to 0 °C and pyrrole (25.7 mL, 372 mmol, 1.00 eq.) was added slowly. The reaction mixture was allowed to warm to ambient temperature and stirred for 1 h. The solution was cooled to 0 °C and water (75 mL) was added slowly, so that the internal temperature did not exceed 15 °C. The reaction mixture was kept at this temperature for 5 min, before hydroxylamine hydrochloride (28.4 g, 409 mmol, 1.10 eq.), acetic anhydride (38.7 mL, 409 mmol, 1.10 eq.) and pyridine (150 mL, 1.86 mol, 5.00 eq.) were successively added, so that the internal temperature did not exceed 15 °C. The reaction was stirred at 90 °C for 72 h, then cooled to ambient temperature and diluted with water (250 mL). The aqueous layer was extracted with ethyl acetate (4 × 400 mL). The combined organic layers were washed with 1 M hydrochloric acid (300 mL) and brine (300 mL) and dried over Na_2SO_4. The solvent was removed under reduced pressure and the residue was purified by column chromatography (silica gel, *n*-hexane:EtOAc = 1:1 to yield the product **95** as a dark brown liquid (25.7 g, 279 mmol, 75%).

^{1}H NMR (400 MHz, $CDCl_3$): δ (ppm) = 9.30 (s_{br}, 1H, NH), 6.97 (td, J = 2.8, 1.4 Hz, 1H, C5-H), 6.88 (ddd, J = 3.9, 2.5, 1.4 Hz, 1H, C3-H), 6.28 (dt, J = 3.8, 2.6 Hz, 1H, C4-H).

$^{13}C\{^{1}H\}$ NMR (100 MHz, $CDCl_3$): δ (ppm) = 123.83 (1C, C5), 120.37 (1C, C3), 114.76 (1C, CN), 110.30(1C, C4), 100.94 (1C, C2).

HR-ESI-MS: *m/z* calc. ($C_5H_4N_2Na$ $[M+Na]^+$): 115.0272, found: 115.0267.

4-Aza-7,9-dideazaadenine (101)

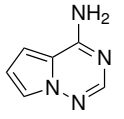

101
$C_6H_6N_4$
134.14 g·mol^{-1}

This compound was synthesized by modification of a reported procedure.[242] A suspension of ammonium chloride (14.8 g, 276 mmol) in methyl *tert*-butyl ether (198 mL) was cooled to -5 °C. 25% Aq. ammonia (22.8 mL) was slowly added. Aq. sodium hypochlorite solution (2.24 M, 258 mL) was added dropwise over 30 min. The mixture was stirred at -5 °C for 30 min. The two layers were separated and the organic layer was stored over finely ground $CaCl_2$ (9 g) at -20 °C for 1 h. The concentration of the ethereal solution of chloramine generated by this method was previously reported to be on average 740 mM.[242]

A solution of compound **95** (2.00 g, 21.7 mmol, 1.00 eq.) in methyl *tert*-butyl ether (20 mL) under an inert gas atmosphere was cooled to 0 °C and sodium hydride (60% in mineral oil, 1.26 g, 31.5 mmol, 1.45 eq.) was added in portions. The mixture was allowed to warm to ambient temperature and stirred for 30 min. Dry *N*,*N*-dimethylformamide (10 mL) was added and the methyl *tert*-butyl ether was removed by distillation at ambient temperature under reduced pressure. A solution of chloramine in methyl *tert*-butyl ether (ca. 740 mM, 40 mL, 29.6 mmol, 1.36 eq.) was added and the reaction was stirred at ambient temperature for 30 min before the methyl *tert*-butyl ether was removed by distillation at ambient temperature under reduced pressure. A second portion of chloramine in methyl *tert*-butyl ether (ca. 740 mM, 40 mL, 29.6 mmol, 1.36 eq.) was added and the reaction was stirred at ambient temperature for 30 min before the methyl *tert*-butyl ether was removed by distillation at ambient temperature under reduced pressure. A third portion of chloramine in methyl *tert*-butyl ether (ca. 740 mM, 40 mL, 29.6 mmol, 1.36 eq.) was added and the reaction was stirred at ambient temperature for 30 min. Dry *N*,*N*-dimethylformamide (10 mL) and formamidine acetate (6.56 g, 63.2 mmol, 2.91 eq.) were added and the methyl *tert*-butyl ether was removed by distillation at 1 bar, 95 °C. The mixture was stirred at 120 °C for 48 h. The solvent was removed under reduced pressure. The reaction mixture was adsorbed onto Celite and extracted by Soxhlet extraction with methyl *tert*-butyl ether. The solvent was removed *in vacuo* and the residue was purified by column chromatography (silica gel, EtOAc) to yield the product **101** as a light brown solid (1.68 g, 12.5 mmol, 58%). Spectroscopic data agreed with previous reports.[242]

^{1}H NMR (400 MHz, DMSO-d_6): δ (ppm) = 7.78 (s, 1H, C2-H), 7.69 (s_{br}, 2H, NH_2), 7.59 (dd, J = 2.6, 1.6 Hz, 1H, C9-H), 6.85 (dd, J = 4.4, 1.6 Hz, 1H, C7-H), 6.60 (dd, J =

4.3, 2.6 Hz, 1H, C8-H).

^{13}C{^{1}H} NMR (100 MHz, DMSO-d_6): δ (ppm) = 155.57 (1C, C6), 148.01 (1C, C2), 118.15 (1C, C9), 114.40 (1C, C5), 110.12 (1C, C8), 101.28 (1C, C7).

HR-ESI-MS: *m/z* calc. ($C_6H_7N_4$ $[M+H]^+$): 135.0670, found: 135.0674.

9-Bromo-4-aza-7,9-dideazaadenine (102)

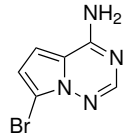

102
$C_6H_5BrN_4$
213.04 g·mol^{-1}

A solution of compound **101** (1.40 g, 10.4 mmol, 1.00 eq.) in *N*,*N*-dimethylformamide (14 mL) was cooled to 0 °C and *N*-bromosuccinimide (2.04 g, 11.5 mmol, 1.10 eq.) was added in portions. The reaction was stirred at 0 °C for 3 h before it was treated with 1 M aq. NaOH solution (115 mL, 115 mmol, 11.0 eq.). The solution was allowed to warm to ambient temperature and stirred for 3 h. The precipitate was collected by filtration, washed with water (30 mL) and dried to yield the product **102** as a light brown solid (2.07 g, 9.72 mmol, 93%). Analytical data agreed with previous reports.[270]

^{1}H NMR (400 MHz, DMSO-d_6): δ (ppm) = 7.92 (s, 1H, C2-H), 7.88 (s_{br}, 2H, NH_2), 6.99 (d, *J* = 4.5 Hz, 1H, C7-H)), 6.77 (d, *J* = 4.6 Hz, 1H, C8-H)).

^{13}C{^{1}H} NMR (100 MHz, DMSO-d_6): δ (ppm) = 155.28 (1C, C6), 148.83 (1C, C2), 115.81 (1C, C5), 112.41 (1C, C8), 102.63 (1C, C7), 99.58 (1C, C9).

HR-ESI-MS: *m/z* calc. ($C_6H_6BrN_4$ $[M+H]^+$): 212.9770, found: 212.9774.

2',3',5'-Tri-*O*-benzyl-1'-hydroxy-4-aza-7,9-dideazaadenosine (103)

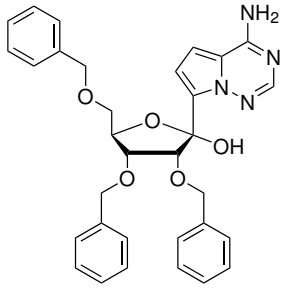

103
$C_{32}H_{32}N_4O_5$
552.63 g·mol-1

Method A:

This compound was synthesized by modification of a reported procedure.[246] A solution of compound **102** (1.00 g, 4.69 mmol, 1.00 eq.) in dry tetrahydrofuran (40 mL) under an inert gas atmosphere was treated with a solution of 1,2-bis(chlorodimethylsilyl)ethane (1.11 g, 5.16 mmol, 1.10 eq.) in dry tetrahydrofuran (5 mL). The reaction mixture was stirred at ambient temperature for 10 min. Diisopropylamine (724 µL, 5.16 mmol, 1.10 eq.) was added and stirring was continued for 10 min. The mixture was cooled to -78 °C and *n*-butyllithium (1.6 M in *n*-hexane, 12.6 mL, 20.2 mmol, 4.30 eq.) was added dropwise over 30 min. The solution was stirred at -78 °C for 15 min before a solution of compound **92** (3.93 g, 9.39 mmol, 2.00 eq.) in dry tetrahydrofuran (5 mL) was added dropwise over 10 min. The reaction was stirred at -78 °C for 2 h. It was allowed to warm to 0 °C, treated with 1 Maq. citric acid (50 mL) and stirring was continued for 15 min. The layers were separated and the aqueous layer was extracted with ethyl acetate (3 × 30 mL). The combined organic layers were washed with water (50 mL), sat. aq. $NaHCO_3$ solution and brine (50 mL), and dried over Na_2SO_4. The solvent was removed under reduced pressure and he residue was purified by column chromatography (silica gel, *N*-hexane:EtOAc = 1:2) to yield the product **103** as a colorless foam (1.54 g, 2.79 mmol, 59%).

Method B:

This compound was synthesized by modification of a reported procedure.[226] A solution of compound **104** (800 mg, 3.08 mmol, 1.00 eq.) in dry tetrahydrofuran (20 mL) under an inert gas atmosphere was treated with trimethylsilyl chloride (781 µL, 6.15 mmol, 2.00 eq.) and stirred at ambient temperature for 1 h. The mixture was cooled to 0 °C and phenylmagnesium chloride (2 M in tetrahydrofuran, 3.08 mL, 6.15 mmol, 2.00 eq.) was added dropwise over 30 min. The reaction mixture was stirred at 0 °C for 30 min. Isopropylmagnesium chloride lithium chloride complex solution (1.3 M in tetrahydrofuran, 3.55 mL, 4.61 mmol, 1.50 q.) was added dropwise over 30 min and stirring was continued at 0 °C for 12 h. The solution was cooled to -20 °C and a solution of compound **92** (1.48 g, 3.54 mmol, 1.15 eq.) in dry tetrahydrofuran (4 mL) was added dropwise over 30 min. The reaction mixture was stirred at -20 °C for 5 h. Acetic acid (10 mL) and water (10 mL) were added, the mixture

was allowed to warm to ambient temperature and the solvent was removed under reduced pressure. The residue was partitioned between ethyl acetate (200 mL) and 1 M hydrochloric acid (50 mL). The organic layer was separated, washed with sat. aq. $NaHCO_3$ solution (50 mL) and brine (50 mL) and dried over $Na-2SO_4$. The solvent was removed *in vacuo* and the residue was purified by column chromatography (silica gel, *n*-hexane:EtOAc = 1:2) to yield the product as a light yellow foam (425 mg, 769 µmol, 25%).

Analytical data agreed with previous reports.[246]

^{1}H NMR (400 MHz, DMSO-d_6): δ (ppm) = 8.08 (s_{br}, 2H, NH_2), 7.99 (s, 1H, C2-H), 7.45–7.22 (m, 12H, C7-H, benzyl-H), 7.17–7.08 (m, 3H, benzyl-H), 7.04–6.97 (m, 1H, benzyl-H), 6.94 (d, *J* = 4.8 Hz, 1H, C8-H), 5.38 (d, *J* = 5.9 Hz, 1H, C4'-H), 5.08 (d, *J* = 5.2 Hz, 1H, C4'-OH), 4.82-–4.24 (m, 6H, CH_2Bn), 4.01 (dt, *J* = 5.5, 2.9 Hz, 1H, C2'-H), 3.92 (dd, *J* = 5.9, 4.5 Hz, 1H, C3'-H), 3.68 (dd, *J* = 10.0, 3.4 Hz, 1H, C5'-H^a), 3.47 (dd, *J* = 10.0, 6.4 Hz, 1H, C5'-H^b).

^{13}C{^{1}H} NMR (100 MHz, DMSO-d_6): δ (ppm) = 188.03 (1C, C1'), 155.85 (1C, C6), 148.98 (1C, C2), 138.68 (1C, benzyl-C), 138.45 (1C, benzyl-C), 138.18 (1C, benzyl-C), 134.69 (1C, C9), 129.58 (1C, benzyl-C), 129.25 (1C, benzyl-C), 128.65 (1C, benzyl-C), 128.24 (1C, benzyl-C), 128.22 (1C, benzyl-C), 128.12 (1C, benzyl-C), 127.90 (1C, benzyl-C), 127.70 (1C, benzyl-C), 127.62 (1C, benzyl-C), 127.57 (1C, benzyl-C), 127.53 (1C, benzyl-C), 127.37 (1C, benzyl-C), 127.27 (1C, benzyl-C), 126.71 (1C, benzyl-C), 126.49 (1C, benzyl-C), 118.59 (1C, C5), 117.90 (1C, C7), 102.33 (1C, C8), 81.93 (1C, C3'), 80.85 (1C, C2'), 72.52 (1C, CH_2Bn), 72.34 (1C, CH_2Bn), 71.71 (1C, CH_2Bn), 71.43 (1C, C5'), 69.40 (1C, C4').

HR-ESI-MS: *m/z* calc. ($C_{32}H_{32}N_4NaO_5$ $[M+Na]^+$): 575.2265, found: 575.2269.

9-Iodo-4-aza-7,9-dideazaadenine (104)

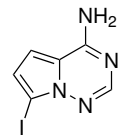

104
$C_6H_5IN_4$
260.04 g·mol^{-1}

A solution of compound **101** (1.50 g, 11.2 mmol, 1.00 eq.) in *N*,*N*-dimethylformamide (15 mL) was cooled to 0 °C and *N*-iodosuccinimide (2.89 g, 12.8 mmol, 1.14 eq.) was added in portions. The reaction was stirred at 0 °C for 3 h before it was treated with 1 M aq. NaOH solution (114 mL, 114 mmol, 10.2 eq.). The solution was allowed to warm to ambient temperature and stirred for

3 h. The precipitate was collected by filtration, washed with water (30 mL) and dried to yield the product **104** as a light brown solid (2.62 g, 10.1 mmol, 90%).

^{1}H NMR (400 MHz, DMSO-d_6): δ (ppm) = 7.91 (s, 1H, C2-H), 7.81 (s_{br}, 2H, NH_2), 6.99 (d, J = 4.4 Hz, 1H, C7-H), 6.83 (d, J = 4.4 Hz, 1H (C8-H)).

^{13}C{^{1}H} NMR (100 MHz, DMSO-d_6): δ (ppm) = 155.24 (1C, C6), 148.71 (1C, C2), 118.34 (1C, C8), 117.60 (1C, C5), 103.91 (1C, C7), 71.62 (1C, C9).

HR-ESI-MS: m/z calc. ($C_6H_6BrN_4$ $[M+H]^+$): 212.9770, found: 212.9774.

2',3',5'-Tri-*O*-(*tert*-butyldimethylsilyl)-1'-hydroxy-4-aza-7,9-dideazaadenosine (105)

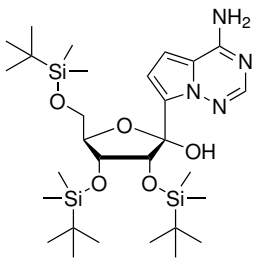

105
$C_{29}H_{56}N_4O_5Si_3$
625.05 g·mol-1

A solution of compound **102** (180 mg, 845 µmol, 1.00 eq.) in dry tetrahydrofuran (7.5 mL) under an inert gas atmosphere was treated with a solution of 1,2-bis(chlorodimethylsilyl)ethane (200 mg, 929 µmol, 1.10 eq.) in dry tetrahydrofuran (1 mL). The reaction mixture was stirred at ambient temperature for 10 min. Diisopropylamine (130 µL, 929 µmol, 1.10 eq.) was added and stirring was continued for 10 min. The mixture was cooled to -78 °C and *n*-butyllithium (1.6 M in *n*-hexane, 2.27 mL, 3.64 mmol, 4.30 eq.) was added dropwise over 30 min. The solution was stirred at -78 °C for 15 min before a solution of compound **93** (830 mg, 1.69 mmol, 2.00 eq.) in dry tetrahydrofuran (1 mL) was added dropwise over 10 min. The reaction was stirred at -78 °C for 2 h. It was allowed to warm to 0 °C, treated with 1 Maq. citric acid (10 mL) and stirring was continued for 15 min. The layers were separated and the aqueous layer was extracted with ethyl acetate (3 × 10 mL). The combined organic layers were washed with water (10 mL), sat. aq. $NaHCO_3$ solution and brine (10 mL), and dried over Na_2SO_4. The solvent was removed under reduced pressure and he residue was purified by column chromatography (silica gel, *N*-hexane:EtOAc = 1:2) to yield the product **105** as a colorless solid (317 mg, 507 µmol, 60%).

^{1}H NMR (400 MHz, $CDCl_3$): δ (ppm) = 7.85 (s, 1H, C2-H), 7.03–6.99 (m, 1H, C7-H), 6.73 (s, 1H, C8-H), 5.31 (s, 1H, C1'-OH), 5.18 (t, J = 4.0 Hz, 1H, C2'-H), 4.34 (dd, J = 4.5, 0.7 Hz, 1H, C3'-H), 4.26 (dd, J = 9.6, 4.8 Hz, 1H, C4'-H), 3.97 (td, J = 10.0,

2.2 Hz, 1H, C5'-H^a), 3.78 (dd, J = 10.6, 4.7 Hz, 1H, C5'-H^b), 0.95 (s, 9H, SiC(CH$_3$)$_3$), 0.94 (s, 9H, SiC(CH$_3$)$_3$), 0.76 (s, 9H, SiC(CH$_3$)$_3$), 0.17 (s, 3H, SiCH$_3$), 0.14 (s, 3H, SiCH$_3$), 0.11 (s, 3H, SiCH$_3$), 0.10 (s, 3H, SiCH$_3$), -0.23 (s, 3H, SiCH$_3$), -0.58 (s, 3H, SiCH$_3$).

HR-ESI-MS: m/z calc. ($C_{58}H_{112}N_8NaO_{10}Si_6$ [2M+Na]$^+$): 1271.7015, found: 1271.7577.

2',3',5'-Tri-*O*-benzyl-1'-(1-propynyl)-4-aza-7,9-dideazaadenosine (108)

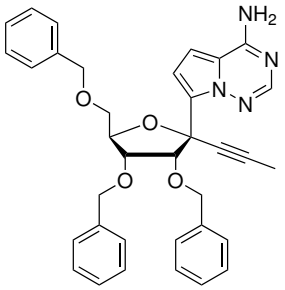

108
$C_{35}H_{34}N_4O_4$
574.68 g·mol-1

Under an inert gas atmosphere, a solution of lithium diisopropylamide (2 M in tetrahydrofuran/heptane/ethylbenzene, 25.4 mL, 50.8 mmol, 40.0 eq.) was cooled to -78°C and treated with 1,2-dibromopropane (1.77 mL, 16.9 mmol, 13.3 eq.) The mixture was stirred at -78 °C for 10 min, allowed to warm to 0 °C and stirring was continued for 30 min. The mixture was cooled to -78 °C and a solution of compond **103** (700 mg, 1.27 mmol, 1.00 eq.) in tetrahydrofuran (23 mL) was added. The reaction mixture was stirred at 0 °C for 4 h, quenched by addition of 1 M aq. citric acid (100 mL) and stirred for an additional 30 min. The organic layer was separated, the solvent was removed under reduced pressure and the intermediate **107** was isolated by column chromatography (silica gel, EtOAc). The fractions containing compound **107** were combined, the solvent was removed under reduced pressure and the residue was redissolved in dichloromethane (280 mL). Methanesulfonic acid (206 µL, 3.18 mmol, 2.50 eq.) was added and the solution was stirred at ambient temperature for 15 min. The reaction was quenched by addition of a solution of triethylamine (5 mL) in methanol (20 mL). The solvent was removed under reduced pressure and the residue was purified by column chromatography (silica gel, *n*-hexane:EtOAc = 1:2) to yield the product **108** as a colorless foam (307 mg, 533 µmol, 42%).

The product was isolated as an anomeric mixture (anomeric ratio at C1' = 1:0.36; thus, the NMR data could not be entirely assigned.

^{1}H NMR (400 MHz, $CDCl_3$): δ (ppm) = 7.88 (s, 0.36H, C2-H^{minor}), 7.80 (s, 1H, C2-H^{major}), 7.38—7.20 (m, 20.5H, benzyl-H), 7.00 (d, J = 4.6 Hz, 1H, C7-H^{major}), 6.94 (d, J = 4.5 Hz, 0.36H, C9-H^{minor}), 6.70 (d, J = 4.6 Hz, 0.36H, C8-H^{minor}), 6.55 (d, J = 4.6 Hz, 1H, C8-H^{major}), 4.93 (d, J = 12.2 Hz, 1H), 4.83–4.40 (m, 10H), 4.33 (d, J = 11.9 Hz, 1H), 4.19 (d, J = 11.7 Hz, 0.36H), 4.01 (dd, J = 7.6, 5.7 Hz, 1H), 3.88 (dd, J = 11.1,

2.9 Hz, 0.36H, C5'-$H^{a,minor}$), 3.81 (dd, *J* = 10.9, 3.4 Hz, 1H, C5'-$H^{a,major}$), 3.77 (dd, *J* = 11.1, 4.8 Hz, 0.36H, C5'-$H^{b,minor}$), 3.66 (dd, *J* = 10.9, 4.5 Hz, 1H, C5'-$H^{b,major}$), 1.94 (s, 3H, propynyl-$CH_3{}^{major}$), 1.72 (s, 1.08H propynyl-$CH_3{}^{minor}$).

$^{13}C\{^1H\}$ NMR (100 MHz, $CDCl_3$): δ (ppm) = 154.91 ($C6^{major}$), 154.49 ($C6^{minor}$), 145.86 ($C2^{major}$), 145.49($C2^{minor}$), 138.72, 138.54, 138.23, 137.96, 130.55 ($C7^{major}$), 130.16 ($C7^{minor}$), 128.52, 128.42, 128.37, 128.34, 128.31, 128.21, 128.03, 127.93, 127.82, 127.80, 127.69, 127.65, 127.63, 127.55, 127.48, 127.40, 127.28, 126.55, 126.30, 115.49, 114.16, 112.52 ($C9^{major}$), 111.41 ($C9^{minor}$), 101.07 ($C8^{minor}$), 100.04 ($C8^{major}$), 84.37, 83.65, 82.44, 80.33, 80.28, 79.59, 79.41, 78.62, 78.33, 76.96, 76.27, 73.65, 73.36, 73.34, 72.82, 72.68, 72.16, 70.22, 69.33, 4.43 (propynyl-$CH_3{}^{major}$), 4.11 (propynyl-$CH_3{}^{major}$).

HR-ESI-MS: *m/z* calc. ($C_{35}H_{34}N_4NaO_4$ $[M+Na]^+$): 597.2472, found: 597.2526.

2-Amino-4-aza-7,9-dideazaadenine (113)

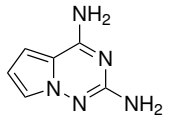

113
$C_6H_7N_5$
149.16 g·mol^{-1}

A suspension of ammonium chloride (7.90 g, 147 mmol) in methyl *tert*-butyl ether (100 mL) was cooled to -5 °C. 25% Aq. ammonia (11.9 mL) was slowly added. Aq. sodium hypochlorite solution (2.24 M, 130 mL) was added dropwise over 30 min. The mixture was stirred at -5 °C for 30 min. The two layers were separated and the organic layer was stored over finely ground $CaCl_2$ (4.5 g) at -20 °C for 1 h. The concentration of the ethereal solution of chloramine generated by this method was previously reported to be on average 740 mM.[242]

A solution of compound **95** (1.00 g, 10.8 mmol, 1.00 eq.) in methyl *tert*-butyl ether (10 mL) under an inert gas atmosphere was cooled to 0 °C and sodium hydride (60% in mineral oil, 630 mg, 15.7 mmol, 1.45 eq.) was added in portions. The mixture was allowed to warm to ambient temperature and stirred for 30 min. Dry *N*,*N*-dimethylformamide (5 mL) was added and the methyl *tert*-butyl ether was removed by distillation at ambient temperature under reduced pressure. A solution of chloramine in methyl *tert*-butyl ether (ca. 740 mM, 20 mL, 14.8 mmol, 1.36 eq.) was added and the reaction was stirred at ambient temperature for 30 min before the methyl *tert*-butyl ether was removed by distillation at ambient temperature under reduced pressure. A second portion of chloramine in methyl *tert*-butyl ether (ca. 740 mM, 20 mL, 14.8 mmol, 1.36 eq.) was added and the reaction was stirred at ambient temperature for 30 min before the methyl *tert*-butyl ether was removed

by distillation at ambient temperature under reduced pressure. A third portion of chloramine in methyl *tert*-butyl ether (ca. 740 mM, 20 mL, 14.8 mmol, 1.36 eq.) was added and the reaction was stirred at ambient temperature for 30 min. The mixture was passed through a pad of Celite and the solvent was removed under reduced pressure. The residue was redissolved in ethanol (45 mL), treated with triethylamine (7.50 mL, 53.8 mmol, 5.00 eq.) and guanidinium carbonate (5.86 g, 65.1 mmol, 6.00 eq.) and stirred in a sealed pressure tube at 125 °C for 2.5 d. solids were removed by filtration and the filtrate was evaporated to dryness. The residue was purified by column chromatography (silica gel, EtOAc) to yield the product **113** as a light brown solid (748 mg, 5.01 mmol, 47%). Analytical data agreed with previous reports.[240]

^{1}H NMR (400 MHz, DMSO-d_6): δ (ppm) = 7.26 (s_{br}, 2H, C6-NH_2), 7.19 (dd, J = 2.4, 1.7 Hz, 1H, C9-H), 6.65 (dd, J = 4.3, 1.7 Hz, 1H, C7-H), 6.30 (dd, J = 4.3, 2.4 Hz, 1H, C8-H), 5.39 (s, 2H, C2-NH_2).

^{13}C{^{1}H} NMR (100 MHz, DMSO-d_6): δ (ppm) = 157.31 (1C, C2), 155.57 (1C, C6), 116.51 (1C, C9), 111.85 (1C, C5), 107.97 (1C, C8), 100.48 (1C, C7).

HR-ESI-MS: m/z calc. ($C_6H_7N_5Na$ $[M+Na]^+$): 172.0599, found: 172.0578.

2-Amino-9-iodo-4-aza-7,9-dideazaadenine (114)

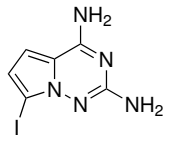

114
$C_6H_6IN_5$
275.05 g·mol^{-1}

A solution of compound **113** (748 mg, 5.05 mmol, 1.00 eq.) in *N*,*N*-dimethylformamide (7.5 mL) was cooled to 0 °C and *N*-iodosuccinimide (1.19 g, 5.30 mmol, 1.05 eq.) was added in portions. The reaction was stirred at 0 °C for 2 h before it was treated with 1 M aq. NaOH solution (60 mL, 60 mmol, 11.9 eq.). The solution was allowed to warm to ambient temperature and stirred for 16 h. The precipitate was collected by filtration, washed with water (15 mL) and dried to yield the product **114** as a light brown solid (990 mg, 3.61 mmol, 72%).

^{1}H NMR (400 MHz, DMSO-d_6): δ (ppm) = 7.35 (s_{br}, 2H, C6-NH_2), 6.81 (d, J = 4.5 Hz, 1H, C7-H), 6.52 (d, J = 4.4 Hz, 1H, C8-H), 5.64 (s, 2H, C2-NH_2).

^{13}C{^{1}H} NMR (100 MHz, DMSO-d_6): δ (ppm) = 157.96 (1C, C2), 155.36 (1C, C6), 115.95 (1C, C8), 115.04 (1C, C5), 103.21 (1C, C7), 69.15 (1C, C9).

HR-ESI-MS: *m/z* calc. ($C_6H_6IN_5Na$ $[M+Na]^+$): 297.9565, found: 297.6563.

1'-Cyano-4-aza-7,9-dideazainosine (120)

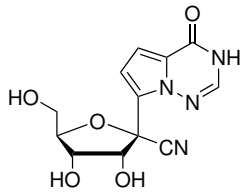

120
$C_{12}H_{12}N_4O_5$
292.25 g·mol^{-1}

A solution of compound **82** (40.0 mg, 137 µmol, 1.00 eq.) in a mixture of water (2.75 mL) and pyridine (442 µL, 5.49 mmol, 40.0 eq.) was treated with potassium isothiocyanate (267 mg, 2.75 mmol, 20.0 eq.) and diethyleneglycol dinitrite (**123**, 451 mg, 2.75 µmol, 20.0 eq.). The reaction mixture was stirred at 37 °C for 4 h. The solent was removed under reduced pressure and the residue was purified by reversed-phase HPLC (Phenomenex Synergi Fusion-RP 250×21.2 mm, flow rate 10 mL/min, at 25 °C. Eluent A: H_2O. Eluent B: MeCN. Gradient: 0–36 % eluent B in 18 min) to yield the product **120** as a colorless solid (39.8 mg, 136 µmol, 99%).

^{1}H NMR (400 MHz, DMSO-d_6): δ (ppm) = 11.91 (s_{br}, 1H, NH), 7.98 (s, 1H, C2-H), 6.91 (d, *J* = 4.5 Hz, 1H, C8-H), 6.81 (d, *J* = 4.5 Hz, 1H, C7-H), 6.16 (d, *J* = 6.1 Hz, 1H, C2'-OH), 5.24 (s, 1H, C3'-OH), 4.90 (s, 1H, C5'-OH), 4.55 (dd, *J* = 5.9, 2.9 Hz, 1H, C2'-H), 4.04 (ddd, *J* = 5.8, 4.5, 3.3 Hz, 1H, C4'-H), 3.95 (t, *J* = 5.5 Hz, 1H, C3'-H), 3.67-–3.57 (m, 1H, C5'-H^a), 3.53—3.46 (m, 1H, C5'-H^b), 3.34 (s, 3H).

^{13}C{^{1}H} NMR (100 MHz, DMSO-d_6): δ (ppm) = 153.89 (1C, C6), 138.49 (1C, C2), 126.90 (1C, C9), 122.19 (1C, C5), 117.19 (1C, CN), 110.29 (1C, C8), 106.78 (1C, C7), 85.35 (1C, C4'), 77.90 (1C, C1'), 75.14 (1C, C2'), 69.84 (1C, C3'), 60.64 (1C, C5').

HR-ESI-MS: *m/z* calc. ($C_{12}H_{12}N_4NaO_5$ $[M+Na]^+$): 315.0700, found: 315.0698.

1'-Cyano-4-aza-7,9-dideazainosine 5'-triphosphate (121)

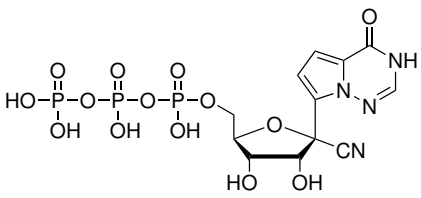

121
$C_{12}H_{15}N_4O_{14}P_3$
532.19 g·mol^{-1}

A solution of compound **120** (30.0 mg, 103 µmol, 1.00 eq.) in dry trimethyl phosphate (600 µL) under an inert gas atmosphere was cooled to 0 °C and freshly distilled phosphoryl chloride (23.5 µL, 252 µmol, 2.45 eq.) was added dropwise. The reaction mixture was stirred at 0 °C for 2 h. A solution of tributylamine (147 µL, 618 µmol, 6.00 eq.) and bis(tetrabutylammonium) pyrophosphate (171 mg, 258 µmol, 2.50 eq.) in dry ace-

tonitrile (450 µL) was added and the reaction mixture was stirred at 0 °C for 2 h. The reaction was quenched by addition of aq. triethylammonium bicarbonate (TEAB) buffer (1 M, pH = 7.7, 10 mL) and allowed to warm to ambient temperature. It was washed with ethyl acetate (2 × 10 mL) and the aqueous layer was lyophilized. The residue was dissolved in TEAB buffer (100 mM, pH = 7.7, 5 mL) and purified by anion exchange FPLC (DEAE Sephadex A-25 15×120 mm, flow rate 1.5 mL/min, at 20 °C. Eluent A: 100 mM aq. TEAB, pH = 7.7. Eluent B: 1 M aq. TEAB, pH = 7.7. Gradient: 0% eluent B for 4.7 min, then 0–100 % eluent B in 40 min). The fractions containing the product were further purified by RP-HPLC (Phenomenex Synergi Fusion-RP 250×21.2 mm, flow rate 5 mL/min, at 25 °C. Eluent A: 100 mM TEAA, pH = 7.0 in H_2O. Eluent B: 100 mM TEAA, pH = 7.0 in 90% aq. MeCN. Gradient: 0–10 % eluent B in 10 min, 10–25 % eluent B in 30 min). The fractions containing the product were lyophilized and reconstituted in water to yield an aq. solution of **121** triethylammonium salt (20.6 µmol, 20%). The product solution was lyophilized, redissolved in methanol (3 mL) and added dropwise to a solution of lithium perchlorate in acetone (5% *w*=w, 45 mL). The suspension was centrifuged at 4 °C for 15 min. The supernatant was discarded and the pellet was washed with acetone (3 mL) and dried *in vacuo* to yield the product **121** as lithium salt.

^{1}H NMR (400 MHz, D_2O): δ (ppm) = 7.86 (s, 1H, C2-H), 7.06 (d, J = 4.7 Hz, 1H, C7-H), 6.97 (d, J = 4.7 Hz, 1H, C8-H), 4.98 (d, J = 5.3 Hz, 1H, C2'-H), 4.57–4.46 (m, 2H, C3'-H, C4'-H), 4.19 (ddd, J = 11.8, 6.7, 3.4 Hz, 1H, C5'-H^a), 4.09 (ddd, J = 11.8, 5.2, 3.2 Hz, 1H, C5'-H^b).

^{13}C{^{1}H} NMR (100 MHz, D_2O): δ (ppm) = 157.11 (1C, C6), 137.12 (1C, C2), 125.98 (1C, C9), 121.18 (1C, C5), 115.35(1C, CN), 110.77 (1C, C8), 107.57 (1C, C7), 85.61 (1C, C4'), 77.20 (1C, C1'), 75.72 (1C, C2'), 70.11 (1C, C3'), 63.69 (1C, C5').

Diethyleneglycol dinitrite (123)

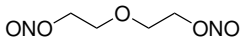

123
$C_4H_8N_2O_5$
164.12 g·mol^{-1}

This compound was synthesized according to a reported procedure.[251] A mixture of diethylene glycol (25.0 g, 236 mmol, 1.00 eq.), sodium nitrite (32.5 g, 471 mmol, 2.00 eq.) and ice (50 g) at 0 °C was treated dropwise with conc. hydrochloric acid (39.0 mL, 471 mmol, 2.00 eq.). The reaction mixture was stirred for 5 min before the organic layer was separated, washed with 10% aq. K_2CO_3 solution (50 mL) and dried over K_2CO_3 to yield the product **123** as a yellow oil (17.1 g, 104 mmol, 44%. Analytical data agreed with reported values.[251]

^{1}H NMR (400 MHz, $CDCl_3$): δ (ppm) = 4.83 (s_{br}, 4H, CH_2ONO), 3.74 (t, J = 4.8 Hz, 4H, $O(CH_2)_2$).

^{13}C{^{1}H} NMR (100 MHz, $CDCl_3$): δ (ppm) = 69.35 (2C, CH_2ONO), 67.27 (2C, $O(CH_2)_2$).

6 Solid-phase synthesis of oligonucleotides

6.1 Oligonucleotide synthesis and characterization

RNA oligonucleotides **R1**–**R10** were synthesized by automated solid phase synthesis using a Pharmacia LKB Gene Assembler Plus synthesizer. RNA oligonucleotides **R11**–**R15** were synthesized using an Applied Biosystems ABI 392 DNA/RNA synthesizer. The oligonucleotides were prepared on a 1000 ÅCPG support (20–25 µmol/g, 0.6 µmol scale) using 2'-*O*-TOM-protected N^6-acetyl-rA, N^4-acetyl-rC, N^2-acetyl-rG, and rU phosphoramidites (100 mM in acetonitrile). The modified phosphoramidites were used as 100 mM solutions in acetonitrile (**74**, **75**, **76**, **77**, **78**) or 1,2-dichloroethane (**79**, **80**, **81**, **87**, **86**), 5'-hexynyl phosphoramidite was used as a 100 mM solution in acetonitrile. Coupling was performed using 5-ethylthio-1*H*-tetrazole (ETT, 250 mM in acetonitrile) as activator, with 4 min coupling time for canonical phosphoramidites and 12 min coupling time for modified phosphoramidites. For Rem phosphoramidites **87** and **86**, coupling time was extended to 24 min. Detritylation was performed with 3% dichloroacetic acid (DCA) in 1,2-dichloroethane (DCE). Capping solutions contained 4-dimethylaminopyridine (0.5 M) in acetonitrile for Cap A, and acetic anhydride/*sym*-collidine/acetonitrile (2:3:5) for Cap B. Oxidation was performed with iodine (10 mM) in acetonitrile/*sym*-collidine/water (10:1:5).

The oligonucleotides were first cleaved from their solid support under basic conditions (**R1**–**R6**, **R9**–**R10**, **R14**–**R15**: 33% methylamine in ethanol/water (1:1) at 37 °C for 5 h; **R7**–**R8**: water/methanol/triethylamine (5:4:1) at 25 °C for 3 d; **R11**–**R13**: 25% aq. ammonia at 25 °C for 30 h), which simultaneously removed base-labile nucleobase protecting groups. 2'-Desilylation was achieved by 1 M tetrabutylammonium fluoride (TBAF) in tetrahydrofuran for 12 h. Crude oligonucleotides were desalted by size exclusion chromatography (GE Healthcare HiTRAP Desalting columns (3 × 5 mL), flow rate 2 mL/min, at ambient temperature).

Crude oligonucleotides were purified by denaturing polyacrylamide gel electrophoresis (20% acrylamide/bisacrylamide 19:1, 89 mM TRIS, 89 mM boric acid, 2 mM EDTA, 7 M urea, pH 8.0) in TBE buffer (89 mM TRIS, 89 mM boric acid, 2 mM EDTA, pH 8.0). Following excision of the oligonucleotide bands, the oligonucleotides were extracted into TEN buffer

(10 mM TRIS, 1 mM EDTA, 300 mM NaCl, pH 8.0) and precipitated by addition of 3-fold excess of ethanol.

Oligonucleotides were quantified by concentration measurements based on UV absorbance of the solution at 260 nm. Typical yields ranged from 100 nmol to 150 nmol of pure oligonucleotide per 0.6 µmol synthesis.

The purity of the RNA oligonucleotides was analyzed by anion-exchange HPLC (Dionex DNAPac PA200, 2 × 250 mm, flow rate 0.5 mL/min, at 60 °C; eluent A: 25 mM TRIS-HCl (pH 8.0), 6 M urea; eluent B: 25 mM TRIS-HCl (pH 8.0), 6 M urea, 0.5 M $NaClO_4$; gradient: 0—48% eluent B in 12 CV). The identities of all purified oligonucleotides were confirmed by HR-ESI-MS (Bruker micrOTOF-Q III, negative ion mode; monoisotopic masses of the oligonucleotides were obtained by charge deconvolution).

6.2 Fluorescent labeling of oligonucleotides

For fluorescent labeling, a solution of unlabeled, 5'-hexynyl-modified RNA oligonucleotide (625 µM, 1.00 eq.) in water/DMSO/*t*-BuOH 100:45:15 (1.0 mM, 10 µL) was treated with a solution of 6-FAM azide (50 mM, 6.25 eq) in DMSO. A solution of CuBr (33.3 mM, 12.5 eq.) and TBTA (66.6 mM, 25.0 eq.) in DMSO/*t*-BuOH 3:1 was added and the sample was incubated in the dark at 37 °C for 3 h. The labeled oligonucleotides were purified by denaturing gel electrophoresis; their purity and identity was confirmed by anion-exchange HPLC and HR-ESI-MS.

7 Spectroscopy

7.1 UV/Vis spectroscopy

7.1.1 Determination of molar extinction coefficients

Nucleoside stock solutions were prepared at 10 mM concentrations in DMSO and diluted with water to 80 µM as highest sample concentrations. Samples in the concetration range between 80 and 2.5 µM were prepared by serial 1:1 dilution with water. UV absorption spectra of each sample were recorded in quartz cuvettes (path length: d = 1 cm) using a Cary 100 Bio Spectrophotometer (spectral bandwidth: 2 nm; averaging time: 0.5 s; data interval: 0.5 nm) and blank-corrected by subtraction of absorption spectra of pure buffer in the same cuvettes. Molar extinction coefficients (ϵ) at the respective absorption maximum (λ_{max}) and at 260 nm were determined by plotting the sample absorbance (A) at the respective wavelength against the sample concentration (c) and fitting the data points according to Lambert-Beer's law:

$$A = \epsilon \cdot c \cdot d \tag{7.7}$$

For each compound, three individual dilution series were prepared and analyzed, the extinction coefficients were calculated as mean ± s.e.m of triplicates.

For determination of the molar extinction coefficient of hm^{6}A (compound **4**), the hm^{6}A nucleoside was prepared as described in Chapter 5. The resulting mixture of hm^{6}A and A as well as an unreacted A reference sample were analyzed by RP-HPLC. The molar fraction of hm^{6}A in the sample ($x_{\mathrm{hm^6A,sample}}$) was calculated based on the UV peak areas (A) of the substrate peaks in sample and unreacted reference:

$$x_{\mathrm{hm^6A,sample}} = 1 - \frac{A_{\mathrm{A,sample}}}{A_{\mathrm{A,ref}}} \tag{7.8}$$

The extinction coefficient of hm^{6}A was then determined from the hm^{6}A yield, the UV peak areas and the known extinction coefficient of the A nucleoside:

$$\epsilon_{\mathrm{hm^6A}} = \frac{A_{\mathrm{hm^6A,sample}} \cdot \epsilon_{\mathrm{A}}}{x_{\mathrm{hm^6A,sample}} \cdot A_{\mathrm{A,ref}}} \tag{7.9}$$

For determination of the molar extinction coefficient of f^{6}A (compound **5**), an f^{6}A sample was analyzed by RP-HPLC. Due to hydrolysis in aq. solution, the chromatogram showed

presence of adenosine. The concentration of adenosine in the f^{6}A sample was determined by comparison of the peak area with an adenosine reference sample of known concentration:

$$c_{\mathrm{A,\ sample}} = c_{\mathrm{A,\ ref}} \cdot \frac{A_{\mathrm{A,\ sample}}}{A_{\mathrm{A,\ ref}}} \tag{7.10}$$

The f^{6}A concentration followed as the difference between adenosine concentration and total nucleoside concentration in the sample:

$$c_{\mathrm{f^6A}} = c_{\mathrm{total}} - c_{\mathrm{A}} \tag{7.11}$$

Knowing concentration and UV peak area of f^{6}A in the sample, the molar extinction coefficient of f^{6}A was derived from the known extinction coefficient of adenosine:

$$\epsilon_{\mathrm{f^6A}} = \epsilon_{\mathrm{A}} \cdot \frac{c_{\mathrm{A}} \cdot A_{\mathrm{f^6A}}}{c_{\mathrm{f^6A}} \cdot A_{\mathrm{A}}} \tag{7.12}$$

7.1.2 pK_a titrations

The equilibrium between a weak acid HA and its conjugate base A$^-$

$$\mathrm{HA} \rightleftarrows \mathrm{A^-} + \mathrm{H^+} \tag{7.13}$$

at a specific pH is described by the Henderson-Hasselbalch equation

$$\mathrm{pH} = \mathrm{p}K_{\mathrm{a}} - \log\left(\frac{[\mathrm{HA}]}{[\mathrm{A^-}]}\right) \tag{7.14}$$

with [HA] and [A$^-$] being the concentrations of acid and conjugate base. In an equilibrium according to Equation (7.13), comprising only two species, the concentrations of acid and conjugate base can be translated into their molar fractions χ:

$$\chi_{\mathrm{HA}} = \frac{[\mathrm{HA}]}{[\mathrm{HA}] + [\mathrm{A^-}]} \tag{7.15}$$

$$\chi_{\mathrm{A^-}} = \frac{[\mathrm{A^-}]}{[\mathrm{HA}] + [\mathrm{A^-}]} \tag{7.16}$$

Thus, the Henderson-Hasselbalch Equation (7.14) can be rewritten as

$$\mathrm{pH} = \mathrm{p}K_{\mathrm{a}} - \log\left(\frac{\chi_{\mathrm{HA}}}{\chi_{\mathrm{A^-}}}\right) \tag{7.17}$$

The measured absorbance of a solution at any given pH results as the sum of the absorbances of protonated and deprotonated form of the solute weighted by their respective mole fractions:

$$A = A_{HA} \cdot \chi_{HA} + A_{A^-} \cdot \chi_{A^-} = A_{HA} \cdot \chi_{HA} + A_{A^-} \cdot (1 - \chi_{HA}) \tag{7.18}$$

Rearrangement of this equation leads to a mathematical expression for the mole fraction of the acid:

$$\chi_{HA} = \frac{A - A_{A^-}}{A_{HA} - A_{A^-}} \tag{7.19}$$

An analogous expression is obtained for the mole fraction of the conjugate base:

$$\chi_{A^-} = \frac{A_{HA} - A}{A_{HA} - A_{A^-}} \tag{7.20}$$

Insertion of these two expressions into Equation (7.17) results in

$$pH = pK_a - \log\left(\frac{A - A_{A^-}}{A_{HA} - A}\right) \tag{7.21}$$

Equation (7.21) can be rearranged to describe the experimentally measured absorbance A as a function of the pK_a value:

$$pK_a - pH = \log\left(\frac{A - A_{A^-}}{A_{HA} - A}\right) \tag{7.22}$$

$$10^{pK_a - pH} = \frac{A - A_{A^-}}{A_{HA} - A} \tag{7.23}$$

$$A = A_{HA} + \frac{A_{A^-} - A_{HA}}{1 + 10^{pK_a - pH}} \tag{7.24}$$

Samples containing 50 µM nucleoside in 30 mM Britton-Robinson buffer (30 mM AcOH, 30 mM H_3PO_4, 30 mM H_3BO_3) of respective pH were prepared at 13 pH values in the range between 4 and 10. UV absorption spectra of each sample were recorded in quartz cuvettes (path length: d = 1 cm) using an Agilent Cary Spectrophotometer (spectral bandwidth: 2 nm; averaging time: 20 ms; data interval: 0.5 nm) and blank-corrected by subtraction of absorption spectra of pure buffer in the same cuvettes. Sample absorbances at 260 nm and 277 nm, representing A_{HA} and A_{A^-}, respectively, were plotted against the pH value; fitting the data points according to Equation (7.24) yielded the pK_a value. All data points were collected as triplicates, pK_a values are given as mean ± s.e.m.

7.1.3 UV melting curves

In double-stranded oligonucleotide motifs, interactions between the transition dipole moments of stacked nucleobases lead to a decreased absorbance of the oligonucleotide sample; the absorbance of the duplex is therefore lower than the sum of absorbances of the two single strands.[271] As a result, thermal melting of a duplex structure gives rise to an increase in absorbance, which is commonly expressed as the percentage hyperchromicity H.

$$H = 100 \cdot \frac{A}{A - A_{\mathrm{min}}} \tag{7.25}$$

From the resulting sigmoidal melting curve, the melting temperature T_{m} (defined as the temperature at which 50% of the duplex structures are denatured) can be derived.[272]

After linear fitting of the upper and lower absorbance baselines

$$A_{\mathrm{U}} = m_{\mathrm{U}} \cdot T + b_{\mathrm{U}} \tag{7.26}$$

$$A_{\mathrm{L}} = m_{\mathrm{L}} \cdot T + b_{\mathrm{L}} \tag{7.27}$$

the fraction of intact duplex (α) at a given temperature T can be expressed as

$$\alpha = \frac{A_{\mathrm{U}} - A}{A_{\mathrm{U}} - A_{\mathrm{L}}} = \frac{m_{\mathrm{U}} \cdot T + b_{\mathrm{U}} - A}{(m_{\mathrm{U}} - m_{\mathrm{L}}) \cdot T + b_{\mathrm{U}} - b_{\mathrm{L}}} \tag{7.28}$$

At the melting temperature T_{m}, α is 0.5.

Thermal UV melting curves of 1, 2, 5, 10, and 20 µM RNA duplexes in PBS buffer (100 mM NaCl, 10 mM phosphate, pH 7.0) were recorded using an Agilent Cary UV-Vis Multicell Peltier spectrometer. Sample concentrations of 1, 2, and 5 µM M were measured in 10 mm semi-micro quartz cuvettes, whereas 10 and 20 µM samples were measured in 1 mm quartz cuvettes. The samples were overlaid with silicon oil to prevent evaporation during heating. Following an initial annealing ramp from 25 to 90 °C, four temperature ramps with a heating/cooling rate of 0.5 °C/min between 10 and 90 °C were recorded at wavelengths of 250, 260, and 280 nm. To determine the melting temperatures, the obtained melting curves were fit to a two-state transition model with upper and lower baselines according to Equation (7.28).

Thermodynamic parameters were obtained by van't Hoff analysis: For non-self-complementary duplexes, the relationship between free enthalpy ΔH^0 and the melting temperature is given

as

$$\frac{1}{T_m} = \frac{R}{\Delta H^0} \cdot \ln(c_{tot}) + \frac{\Delta S^0 - R \cdot \ln(4)}{\Delta H^0} \tag{7.29}$$

The concentration-dependent melting temperatures were plotted as $1/T_m$ vs. $\ln(c_{tot})$, with c_{tot} being the total oligonucleotide concentration. According to Equation (7.29), the slope m of a linear fit yields the free enthalpy ΔH^0 as

$$\Delta H^0 = \frac{R}{m} \tag{7.30}$$

while from the intercept b the entropy ΔS^0 is obtained:[272]

$$\Delta S^0 = \Delta H^0 \cdot b + R \cdot \ln(4) \tag{7.31}$$

Insertion of ΔH^0 and ΔS^0 into the Gibbs-Helmholtz equation allows determination of the Gibbs free energy ΔG^0, which was estimated at 298 K in this thesis.

$$\Delta G^0 = \Delta H^0 - T \cdot \Delta S^0 \tag{7.32}$$

7.2 Fluorescence spectroscopy

Fluorescence measurements were performed in Quartz SUPRASIL 10×2 and 3×3 mm High Precision Cell cuvettes (Hellma Analytics) at 25 °C, using a Jasco FP8300 spectrofluorometer. Fluorescence excitation and emission spectra were recorded at the respective emission and excitation maxima of the samples.

7.2.1 Fluorescence anisotropy assays

As outlined in Part I, Section 3.3, fluorophores preferentially absorb and emit light which is polarized in a plane parallel to the fluorophores' absorption and emission dipole, respectively.[188] Therefore, light emitted by a solid (e. g. frozen) sample will be anisotropic. In solution, this innate directivity of emission is mostly lost due to rotational diffusion of the fluorophore molecules during their excited state lifetime. The remaining anisotropic component of the emitted light is dependent on the rotational correlation time of the fluorophore, which in turn depends on the hydrodynamic radius. As a consequence, a solution of free fluorophores will display a lower fluorescence anisotropy than complexes of a fluorophore bound to a receptor (e. g. protein). This allows the determination of a complex dissociation constant (K_d) based on fluorescence anisotropy measurements.

For a reversible 1:1 binding model, a sample comprising a ligand L and a receptor R will eventually adopt an equilibrium

$$R_f + L_f \underset{k_{-1}}{\overset{k_1}{\rightleftarrows}} B \tag{7.33}$$

with R_f and L_f denoting the free ligand and receptor and B the bound complex. The equilibrium constant results as

$$K_D = \frac{k_{-1}}{k_1} = \frac{[L_f] \cdot [R_f]}{[B]} \tag{7.34}$$

The concentrations of free receptor and free ligand can be expressed based on the total receptor and ligand concentrations ([R] and [L]) in the sample:

$$[R_f] = [R] - [B] \tag{7.35}$$

$$[L_f] = [L] - [B] \tag{7.36}$$

Combination of Equation (7.35) and Equation (7.36) with Equation (7.34) and rearrangement yields an expression for the complex concentration:

$$[B] = \frac{[R] \cdot ([L] - [B])}{K_D + ([L] - [B])} \tag{7.37}$$

One real solution of this equation is

$$[B] = \frac{[L] + K_D + [R] + \sqrt{([L] + K_D + [R])^2 - 4[L][R]}}{2} \tag{7.38}$$

The relationship between the observed anisotropy r of the sample and the concentration of ligand-receptor complex [B] is given by

$$[B] = [L] \cdot \frac{r - r_f}{r_b - r_f} \tag{7.39}$$

where r_f and r_f are the anisotropy values of free ligand and bound complex, respectively. Insertion of Equation (7.39) in Equation (7.38) followed by rearrangement yields the following expression for the sample anisotropy r:

$$r = r_f + (r_b - r_f) \cdot \frac{[L] + K_D + [R] + \sqrt{([L] + K_D + [R])^2 - 4[L][R]}}{2[L]} \tag{7.40}$$

The recombinantly expressed YTH proteins used in this work (YTHDF2$^{380–579}$, YTHDC1$^{344–509}$ and YTHDC2$^{1277–1430}$, throughout this work referred to as YTHDF2,

YTHDC1 and YTHDC2) were provided by Jens Kretschmer in the working group of Prof. Dr. Markus Bohnsack, University Medical Center Göttingen, in an aqueous buffer containing 30 mM TRIS pH 7.4, 120 mM NaCl, 2 mM $MgCl_2$ and 20% glycerol. Fluorescence anisotropy measurements were performed using 20 nM of 6-FAM-labeled RNA in anisotropy buffer (30 mM TRIS pH 7.5, 120 mM NaCl). The samples were incubated with increasing concentrations of protein for 5 min at ambient temperature prior to the respective measurements. Measurements were performed at 25 °C, using manually operated polarization filters. The excitation and emission wavelengths were set to 470 and 520 nm, respectively.

Fluorescence anisotropy values were calculated as

$$r = \frac{I_{VV} - G \cdot I_{VH}}{I_{VV} + 2G \cdot I_{VH}} \tag{7.41}$$

where I_{VV} denotes emission intensity at vertical excitation/vertical emission and I_{VH} emission intensity at vertical excitation/horizontal emission. The grating factor G

$$G = \frac{I_{HV}}{I_{HH}} \tag{7.42}$$

is introduced as a correction factor to account for inherent unequal sensitivities of the spectrometer toward the different polarization planes. K_D values were obtained from nonlinear fitting of the anisotropy data according to Equation (7.40). In case of negligible binding at 10 µM protein, K_D values were not determined (n. d.). An overview of the binding isotherms and respective K_D values is shown in Part I, Section 3.3.

7.2.2 Fluorescence-based monitoring of exonuclease activity

The Rem nucleoside exhibits a highly environment-dependent fluorescence. Therefore, excision of the Rem nucleoside from an oligonucleotide can be detected based on an increase in fluorescence intensity (see Part II Section 3.3).

In a final volume of 55 µL, **R13** (2 µM) was incubated with snake venom phosphodiesterase (SVPD, 2 U/mL) in presence of $MgCl_2$ (6 mM) at 25 °C. Fluorescence emission intensity (λ_{ex} = 245 nm; λ_{em} = 418 nm) was monitored over 90 min in 30 s intervals.

8 HPLC-MS-based assays

The recombinantly expressed human m^6A eraser enzymes used in this work (FTO-His_6 and His_{10}-ALKBH5$^{66\text{-}292}$, in the following referred to as FTO and ALKBH5, as well as the fusion proteins His_{14}-MBP-FTO and His_{14}-MBP-ALKBH5$^{66\text{-}292}$) were provided by Nicole Kleiber in the group of Prof. Dr. Markus Bohnsack, University Medical Center Göttingen, in an aqueous buffer containing 30 mM phosphate buffer pH 7.3, 100 mM KCl, 50% (V/V) glycerol, 1 mM DTT and 100 µM ethylenediaminetetraacetic acid (EDTA) pH 8.0.

8.1 Demethylation assays

In a final volume of 10 µL, RNA oligonucleotide (20 µM) and demethylase (4 µM) were incubated in demethylation buffer (300 µM $Fe(NH_4)_2(SO_4)_2$, 300 µM α-ketoglutaric acid, 4 mM ascorbic acid, 100 mM KCl, 2 mM $MgCl_2$, 50 mM HEPES pH 7.0) at 25 °C for 2, 30, or 120 min. The reactions were stopped by snap-freezing in liquid nitrogen and the enzymes were denatured by three consecutive freeze-thaw cycles.

The samples were diluted to a volume of 20 µL and digested with 1 U Nuclease P1 (Sigma Aldrich) and 2 U Shrimp Alkaline Phosphatase (rSAP, New England BioLabs) at 37 °C for 20 min. The reactions were stopped by snap-freezing in liquid nitrogen. The samples were diluted to a total volume of 70 µL and the residual denatured protein was removed by extraction with $CHCl_3$ (2 × 70 µL). The aqueous layer was concentrated under reduced pressure at 35 °C for 20 min to remove residual $CHCl_3$ and adjusted to a final sample volume of 60 µL containing 10 mM NH_4OAc, pH 5.3.

The samples were analyzed by RP-HPLC (Phenomenex Synergi Fusion, 2 × 250 mm, flow rate 0.2 mL/min, at 25 °C. Eluent A: 10mM NH_4OAc in H_2O, pH 5.3. Eluent B: MeCN. Gradient: 0-–50% eluent B in 25 min.) coupled with ESI-MS (Bruker micrOTOF-Q III, positive ion mode). Chromatograms were recorded at 260 nm. Peaks in the UV chromatogram were identified based on the corresponding extracted ion chromatograms (EICs). Quantitative analysis was performed on the basis of the UV chromatograms: First, the area under the UV peak for each species (A) was calculated. To account for the extinction coefficients of the nucleosides at 260 nm (ϵ^{260}), the peak areas were normalized according to

$$A_{\text{norm}} = \frac{A}{\epsilon^{260}} \tag{8.43}$$

As the sum of methylated, demethylated and (if observed) oxidized intermediate species needs to amount to 100%, the percent fraction x of each species i is given as

$$x_i = \frac{A_{\mathrm{corr},i}}{\sum A_{\mathrm{corr}}} \tag{8.44}$$

8.2 Competitive demethylation assays

In a final volume of 10 µL, RNA oligonucleotide **R2** (20 µM) and a competitor oligonucleotide (**R1**, **R3**–**R5**) were incubated with FTO (4 µM) or ALKBH5 (2 µM) in demethylation buffer (300 µM $Fe(NH_4)_2(SO_4)_2$, 300 µM α-ketoglutaric acid, 4 mM ascorbic acid, 100 mM KCl, 2 mM $MgCl_2$, 50 m M HEPES pH 7.0) at 25 °C for 5 (ALKBH5) or 30 min (FTO). The reactions were stopped by snap-freezing in liquid nitrogen. The demethylase was denatured by heating the sample to 95 °C for 5 min.

The samples were diluted to a volume of 20 µL and digested with 0.2 U Snake Venom Phosphodiesterase (SVPD, Sigma Aldrich) and 2 U Shrimp Alkaline Phosphatase (rSAP, New England BioLabs) at 37 °C for 18 h. The enzymes were denatured by heating of the sample to 95 °C for 5 min. The samples were diluted to a total volume of 70 µL and the residual denatured protein was removed by extraction with $CHCl_3$ (2 × 70 µL). The aqueous layer was concentrated under reduced pressure at 35 °C for 20 min to remove residual $CHCl_3$ and adjusted to a final sample volume of 60 µL containing 10 mM NH_4OAc, pH 5.3.

The digested samples were analyzed and quantified by HPLC-MS as described in Section 8.1.

8.3 Photocatalytic demethylation

A solution of nucleoside (200 µM) and flavine mononucleotide (FMN, 100 µM) in sodium phosphate buffer (100 mM NaH_2PO_4/Na_2HPO_4 pH 7.0) was incubated under an O_2 atmosphere and irradiated with blue LED light (λ_{max} = 465 nm) at 25 °C for 2 h. The samples were analyzed and quantified by HPLC-MS as described in Section 8.1.

9 PAGE-based assays

9.1 Electrophoretic mobility shift assay (EMSA)

Electrophoretic mobility shift assays were performed to visualize the formation of covalent adducts between ALKBH5 and its RNA substrates.

Sample preparation, method A (native ALKBH5 cofactors):
In a final volume of 5 µL, 2 µM of 5'-FAM-labeled oligonucleotide were incubated with 5 µM of ALKBH5 in a buffer containing 50 mM HEPES pH 7.0, 300 µM $Fe(NH_4)_2(SO_4)_2$, 300 µM α-ketoglutaric acid, 4 m M ascorbic acid, 100 m M KCl, 2 m M $MgCl_2$ and 19.4% (V/V) glycerol at 25 °C for 1 h. As reference samples, 2 µM M of oligonucleotide were incubated in absence of ALKBH5 under the same conditions. 1.5 µL of sample were mixed with 1.5 µL of loading buffer (60 m M TRIS·HCl pH 6.8, 10% (V/V) glycerol) and analyzed by gel electrophoresis.

Sample preparation, method B (inactive cofactor surrogates):
In a final volume of 5 µL, 2 µM of 5'-FAM-labeled oligonucleotide were incubated with 5 µM of ALKBH5 in a buffer containing 50 m M HEPES pH 7.0, 300 µM $MnSO_4$, 300 µM *N*-oxalylglycine, 4 m M ascorbic acid, 100 m M KCl, 2 m M $MgCl_2$ and 19.4% (V/V) glycerol at 25 °C for 1 h. As reference samples, 2 µM of oligonucleotide were incubated in absence of ALKBH5 under the same conditions. 1.5 µL of sample were mixed with 1.5 µL of loading buffer (60 m M TRIS·HCl pH 6.8, 10% (V/V) glycerol) and analyzed by gel electrophoresis.

Sample preparation, method C (substrate pre-oxidation, native ALKBH5 cofactors):
In a final volume of 5 µL, 10 µM of 5'-FAM-labeled oligonucleotide were incubated with 2.5 µM of FTO in a buffer containing 50 mM HEPES pH 7.0, 300 µM $Fe(NH_4)_2(SO_4)_2$, 300 µM α-ketoglutaric acid, 4 mM ascorbic acid, 100 mM KCl, 2 mM $MgCl_2$ and 19.4% (V/V) glycerol at 25 °C for 30 min. The samples were snap-frozen in liquid nitrogen and thawed (3 freeze-thaw cycles) to denature FTO. 1 µL of sample was incubated in a final volume of 5µL with 5 µM of ALKBH5 in a buffer containing 50 m M HEPES pH 7.0, 300 µM $Fe(NH_4)_2(SO_4)_2$, 300 µM α-ketoglutaric acid, 4 mM ascorbic acid, 100 mM KCl, 2 mM $MgCl_2$ and 19.4% (V/V) glycerol at 25 °C for 1 h. As reference samples, 1 µL of FTO-treated sample was incubated in absence of ALKBH5 under the same conditions. 1.5 µL of sample were mixed with 1.5 µL of loading buffer (60 mM TRIS·HCl pH 6.8, 10%

(V/V) glycerol) and analyzed by gel electrophoresis.

Sample preparation, method D (substrate pre-oxidation, inactive cofactor surrogates):
In a final volume of 5 µL, 10 µM of 5'-FAM-labeled oligonucleotide were incubated with 2.5 µM of FTO in a buffer containing 50 m M HEPES pH 7.0, 300 µM $Fe(NH_4)_2(SO_4)_2$, 300 µM α-ketoglutaric acid, 4 m M ascorbic acid, 100 m M KCl, 2 m M $MgCl_2$ and 19.4% (V/V) glycerol at 25 °C for 30 min. The samples were snap-frozen in liquid nitrogen and thawed (3 freeze-thaw cycles) to denature FTO. 1 µL of sample was incubated in a final volume of 5 µL with 5 µM of ALKBH5 in a buffer containing 50 m M HEPES pH 7.0, 300 µM $MnSO_4$, 300 µM *N*-oxalylglycine, 4 m M ascorbic acid, 100 m M KCl, 2 m M $MgCl_2$ and 19.4% (V/V) glycerol at 25 °C for 1 h. As reference samples, 1 µL of FTO-treated sample was incubated in absence of ALKBH5 under the same conditions. 1.5 µL of sample were mixed with 1.5 µL of loading buffer (60 m M TRIS·HCl pH 6.8, 10% (V/V) glycerol) and analyzed by gel electrophoresis.

Native polyacrylamide gel electrophoresis was performed using 2-layer gels (stacking layer 8×1 mm, 5% acrylamide/bisacrylamide 19:1, 125 m M TRIS·HCl pH 6.8; resolving layer 54×1 mm, 15% acrylamide/bisacrylamide 19:1, 375 m M TRIS·HCl pH 8.8) in TRIS-glycine buffer (25 m M TRIS·HCl pH 8.3, 192 m M glycine). Gels were resolved at 200 V, 4 °C for 1 h. Fluorescent bands were detected on a Bio-Rad ChemiDoc MP Imaging System using Blue Epi illumination and 530/28 nm detection filters.

10 Computational Methods

All computations were performed on the level of density functional theory (DFT) using the ORCA 5.0 software package.[273]

10.1 Computations on nucleoside structures

10.1.1 Geometry optimizations

Molecule geometries were optimized using the B3LYP functional together with the def2-TZVPPD basis set.[274–277] To simplify calculations, the ribose was substituted for a methyl group at N9 of the nucleobases. Standard Gibbs energies ΔG^0 were obtained from thermodynamic calculations on the optimized geometries (using the FREQ keyword).

Exemplary ORCA input file for geometry optimization followed by thermodynamic analysis, starting from an xyz file containing an initial geometry:

```
! B3LYP def2-TZVPPD TightOpt KEEPDENS FREQ
*xyzfile 0 1 Initial_Geometry.xyz
```

10.1.2 Local nucleophilicities and electrophilicities

Several models have been developed to describe the nucleophilic and electrophilic behaviour of organic molecules, with the Fukui functions being the most frequently utilized. The Fukui functions f^- and f^+ describe the change in electron density ρ of a molecule (calculated on the density functional theory (DFT) level) upon removal or addition of an electron and therefore represent the nucleophilic and electrophilic character of the molecule, respectively.[278] They are defined as

$$f^- = \rho(n) - \rho(n\text{–}1) \tag{10.45}$$

and

$$f^+ = \rho(n\text{+}1) - \rho(n) \tag{10.46}$$

with n denoting the number of electrons in the molecule. Therefore, $(n\text{–}1)$ and $(n\text{+}1)$ correspond to the radical cationic and anionic species. Local maxima of f^- and f^+ mark nucleophilic and electrophilic sites in the molecule. As these functions in some cases fail to correctly predict the most reactive centers in a molecule, the Parr functions were proposed

as an alternative reactivity index, which is based on the electron spin density ρ_S rather than the electron density.[279]

$$P^- = \rho_S(n\text{–}1) \tag{10.47}$$

$$P^+ = \rho_S(n\text{+}1) \tag{10.48}$$

The local nucleophilicity N_k and electrophilicity ω_k at a specific atom k can be described as the product of the global nucleo- or electrophilicity of the molecule (N and ω) with the local Parr coefficient:

$$N_k = N \cdot P_k^- \tag{10.49}$$

$$\omega_k = \omega \cdot P_k^+ \tag{10.50}$$

As nucleophiles donate an amount of electron density during the reaction and thus obtain partially cationic character, the best nucleophiles are molecules which possess low ionization potentials. Since low ionization potentials are correlated with low HOMO energies,

$$N = E_{HOMO} - E_{HOMO,TCE} \tag{10.51}$$

has been proposed as a definition of the global nucleophilicity, which derives N from the HOMO energy (in eV) of the molecule and uses the HOMO energy of tetracyanoethylene (TCE) for standardization.[279] The global electrophilicity ω, in contrast, is linked to the chemical potential μ and the absolute hardness η of the molecule.[280]

$$\omega = \frac{\mu^2}{2\eta} \tag{10.52}$$

μ and η, in turn, are derived from the ionization energy I and the electron affinity A of a molecule as

$$\mu = -\frac{I + A}{2} \tag{10.53}$$

and

$$\eta = \frac{I - A}{2} \tag{10.54}$$

Thus, Equation (10.52) can be rewritten as

$$\omega = \frac{(I + A)^2}{4(I - A)} \tag{10.55}$$

Finally, expression of I and A based on the electronic energies E of neutral (n electrons), radical anionic (n+1) and radical cationic (n−1) species results in

$$I = E(n\text{−}1) - E(n) \tag{10.56}$$

and

$$A = E(n) - E(n\text{+}1) \tag{10.57}$$

Molecule geometries were optimized using the B3LYP functional together with the def2-TZVP basis set.[274–277] Besides the optimized geometry, the output of this computation contains the HOMO energy E_{HOMO} of the molecule, which was used to calculate the global nucleophilicity N according to Equation (10.51). Using the optimized geometries as input coordinates, single point energy calculations of the neutral, radical cationic and radical anionic species employing the spin-unrestricted Kohn-Sham formalism of the B3LYP functional (UB3LYP) were performed.[281] These yielded the single point energies $E(n)$, $E(n\text{−}1)$ and $E(n\text{+}1)$ as well as the local spin densities $\rho_{\mathrm{S}}(n\text{−}1)$ and $\rho_{\mathrm{S}}(n\text{+}1)$ of each atom. The single point energies were subsequently used to calculate the global electrophilicity ω according to Equations (10.55) to (10.57). Combination of N, ω, $\rho_{\mathrm{S}}(n\text{−}1)$ and $\rho_{\mathrm{S}}(n\text{+}1)$ finally allowed for determination of the local nucleophilicity (N_{k}) and electrophilicity (ω_{k}) according to Equations (10.47) to (10.50). Graphical visualization of the Parr functions on the molecular structure was achieved using the ChemCraft software package.

Exemplary ORCA input file for a spin-unrestricted single point energy calculation on a geometry-optimized radical cationic molecule:

```
! SPE UKS B3LYP def2-TZVP KEEPDENS
*xyzfile +1 2 Optimized_Structure.xyz
```

10.2 Computations on nucleoside–protein complexes

Minimized catalytically active structures of FTO and ALKBH5 in complex with m^6A atomic mutants were generated as described in Part I, Section 3.4.3.3. The resulting constructs were geometry-optimized using the spin-unrestricted UB3LYP functional together with the LANL2DZ basis set for iron and the 6-31G(d) basis set for all other atoms.[274–276,281–284] The LANL2DZ basis set for iron was obtained from the Basis Set Exchange database.[285] All geometry optimizations focused on the catalytically active quintet spin state of Fe(IV).[140]

During the geometry optimizations, bond lengths of heteroatom–proton bonds were constrained to prevent intra- or intermolecular proton transfers.

Exemplary ORCA input file for the geometry-optimization of the modeled FTO–m^{6}A complex (comprising a neutral active site):

```
! UKS B3LYP 6-31G(d) Opt FREQ
%basis
NewECP FE
N_core 10
lmax d
s 5
1 126.0571895 3.0000000 0
2 138.1264251 18.1729137 1
3 54.2098858 339.1231164 2
4 9.2837966 317.1068012 2
5 8.6289082 -207.3421649 2
p 5
1 83.1759490 5.0000000 0
2 106.0559938 5.9535930 1
3 42.8284937 294.2665527 2
4 8.7701805 154.4244635 2
5 8.0397818 -95.3164249 2
d 3
1 392.6149787 -10.0000000 1
2 71.1756979 -63.2667518 2
3 17.7320281 -10.9613338 2
end
end
%geom
Constraints
{B 6 13 C}
{B 8 14 C}
{B 8 15 C}
{B 9 16 C}
{B 9 17 C}
{B 64 74 C}
```

```
{B 2 3 C}
{B 2 4 C}
end
end
*xyzfile 0 5 FTO-m6A_initial.xyz
```

Exemplary ORCA input file for the geometry-optimization of the modeled ALKBH5–m^{6}A complex (comprising a monocationic active site):

```
! UKS B3LYP 6-31G(d) Opt FREQ
%basis
NewECP FE
N_core 10
lmax d
s 5
1 126.0571895 3.0000000 0
2 138.1264251 18.1729137 1
3 54.2098858 339.1231164 2
4 9.2837966 317.1068012 2
5 8.6289082 -207.3421649 2
p 5
1 83.1759490 5.0000000 0
2 106.0559938 5.9535930 1
3 42.8284937 294.2665527 2
4 8.7701805 154.4244635 2
5 8.0397818 -95.3164249 2
d 3
1 392.6149787 -10.0000000 1
2 71.1756979 -63.2667518 2
3 17.7320281 -10.9613338 2
end
end
%geom
Constraints
{B 82 83 C}
{B 82 84 C}
{B 16 22 C}
```

{B 61 70 C}
{B 3 7 C}
{B 3 8 C}
{B 3 9 C}
end
end
*xyzfile +1 5 FTO-m6A_initial.xyz

For modeling of complexes comprising the cationic form of the c^3m^6A nucleobase (protonated at N1), the system charge parameter consequently changes to +1 (FTO) or +2 (ALKBH5).

Appendix

1 Determination of molar extinction coefficients

Concentration-dependent absorption spectra of nucleoside solutions in water (left) and linear fits of the absorbances at 260 nm and the respective absorption maxima (right). Data points represent mean ± s.e.m of triplicates.

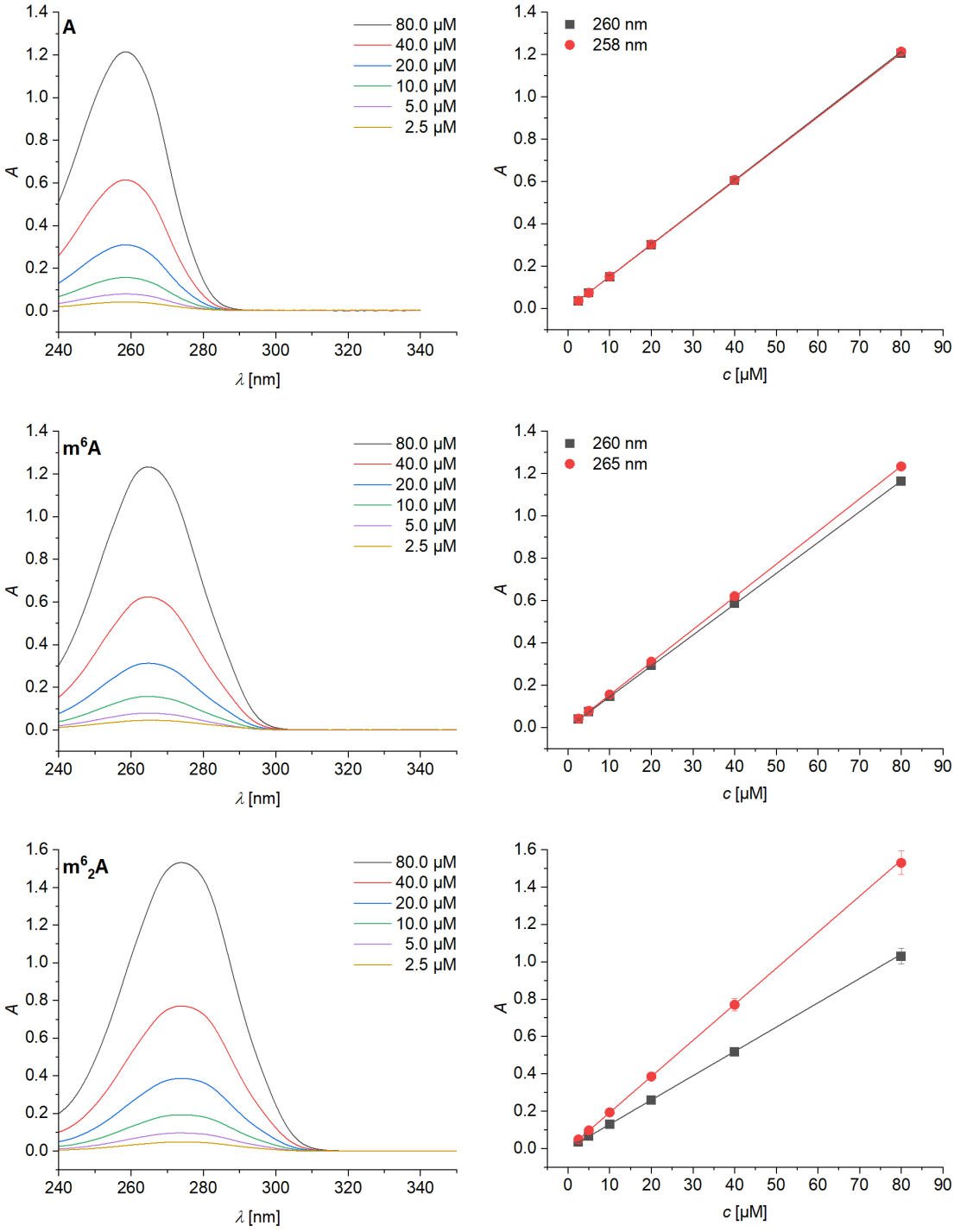

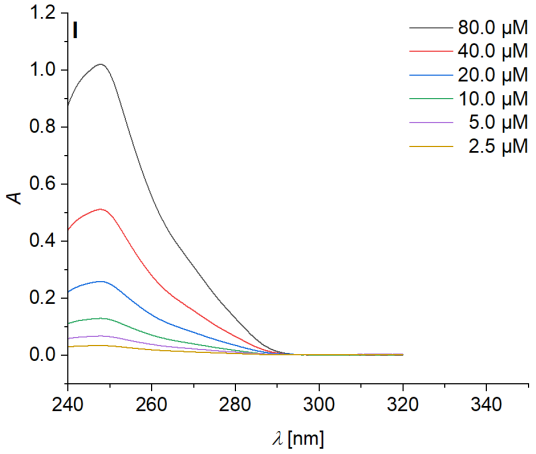
I
80.0 µM
40.0 µM
20.0 µM
10.0 µM
5.0 µM
2.5 µM
A
λ [nm]

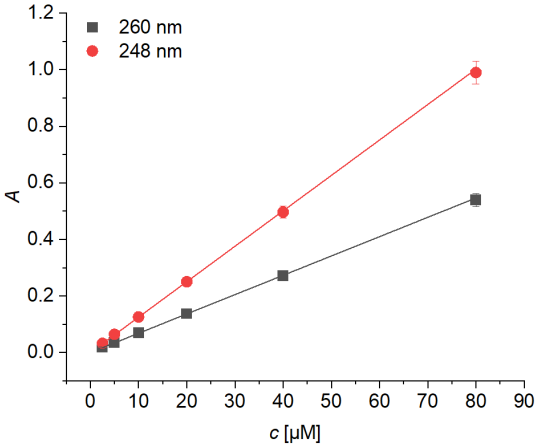
260 nm
248 nm
A
c [µM]

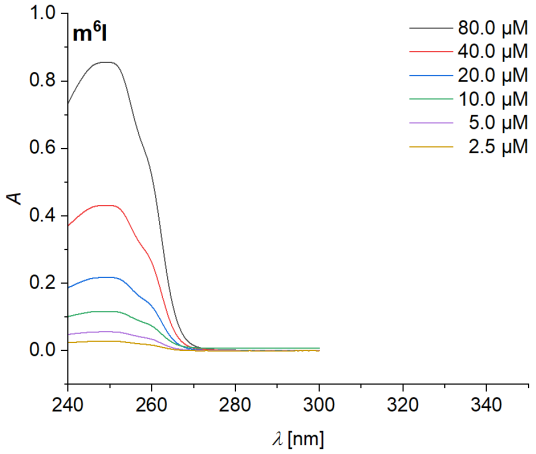
m6I
80.0 µM
40.0 µM
20.0 µM
10.0 µM
5.0 µM
2.5 µM
A
λ [nm]

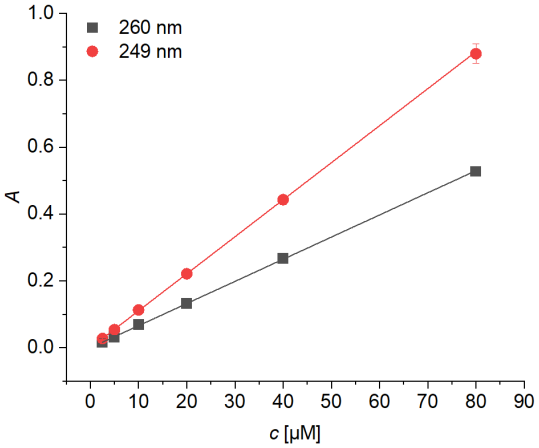
260 nm
249 nm
A
c [µM]

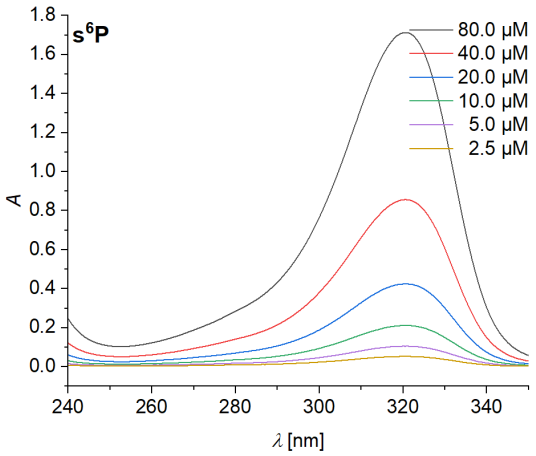
s6P
80.0 µM
40.0 µM
20.0 µM
10.0 µM
5.0 µM
2.5 µM
A
λ [nm]

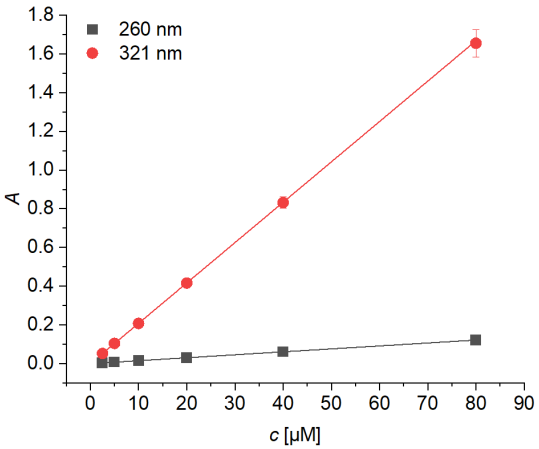
260 nm
321 nm
A
c [µM]

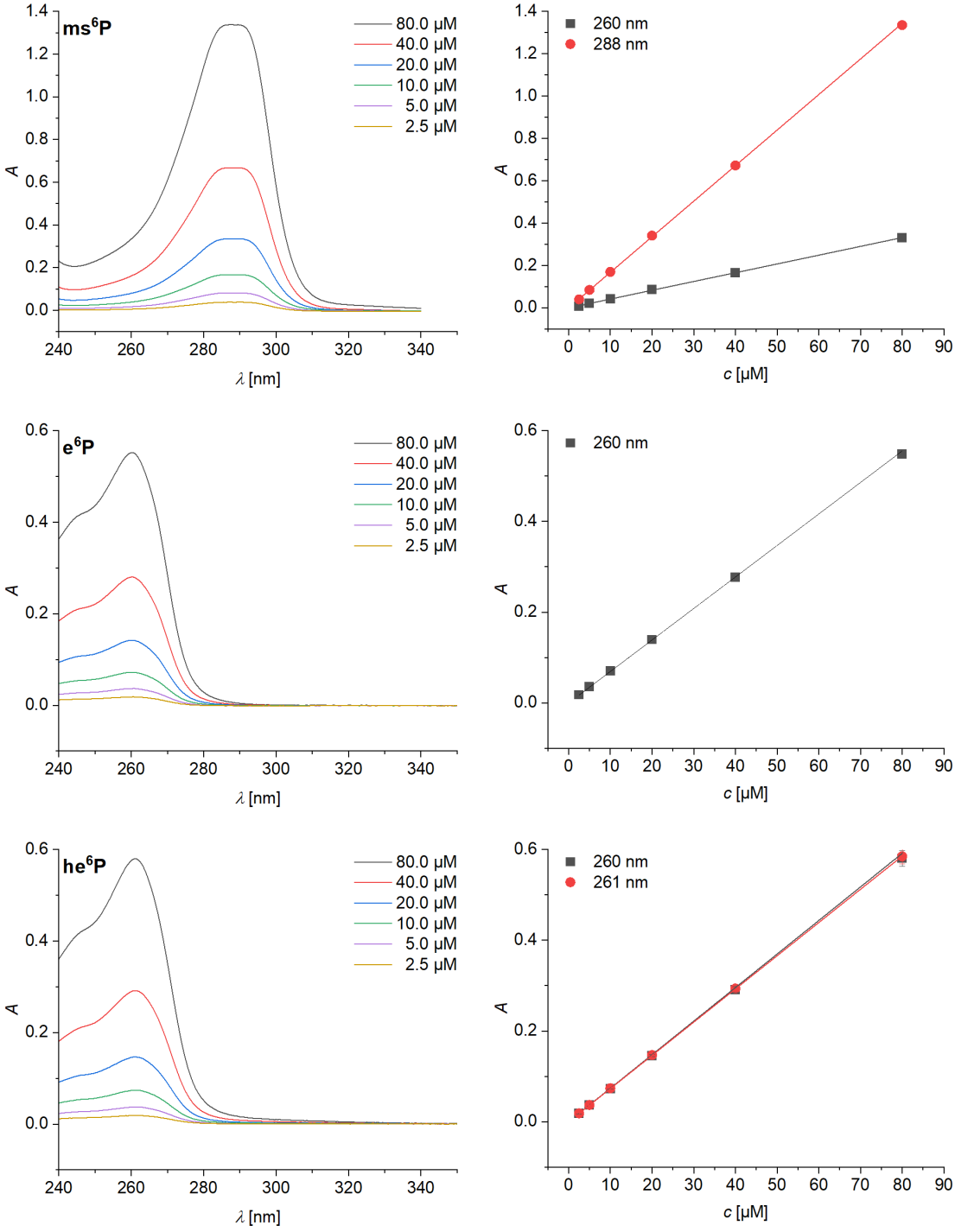
ms⁶P
80.0 µM
40.0 µM
20.0 µM
10.0 µM
5.0 µM
2.5 µM
A
λ [nm]
260 nm
288 nm
c [µM]
e⁶P
80.0 µM
40.0 µM
20.0 µM
10.0 µM
5.0 µM
2.5 µM
A
λ [nm]
260 nm
c [µM]
he⁶P
80.0 µM
40.0 µM
20.0 µM
10.0 µM
5.0 µM
2.5 µM
A
λ [nm]
260 nm
261 nm
c [µM]

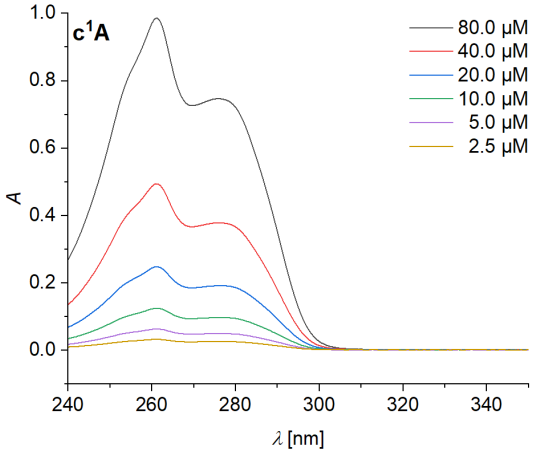
c¹A
80.0 µM
40.0 µM
20.0 µM
10.0 µM
5.0 µM
2.5 µM
A
λ [nm]

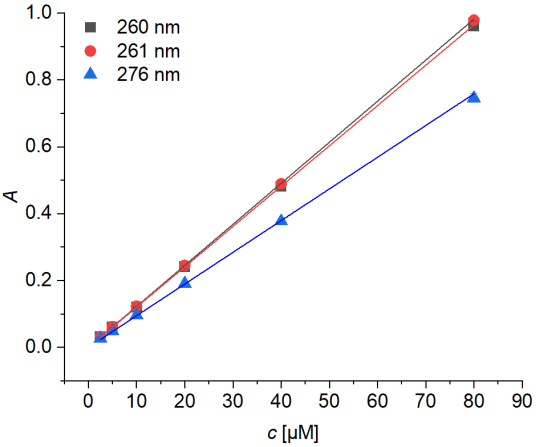
260 nm
261 nm
276 nm
A
c [µM]

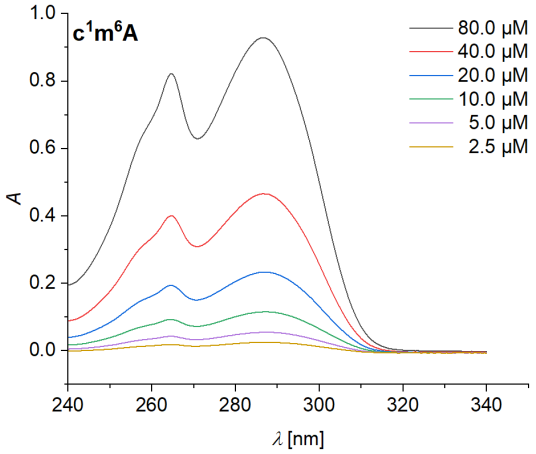
c¹m⁶A
80.0 µM
40.0 µM
20.0 µM
10.0 µM
5.0 µM
2.5 µM
A
λ [nm]

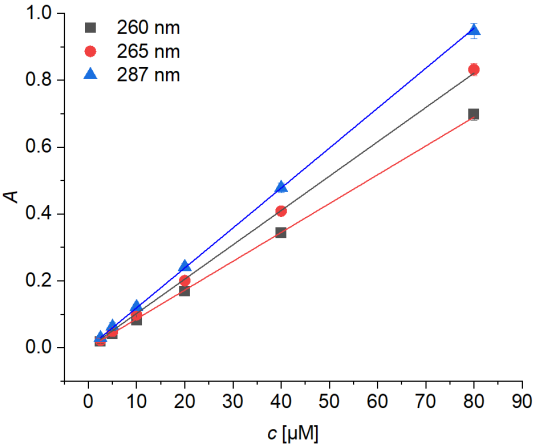
260 nm
265 nm
287 nm
A
c [µM]

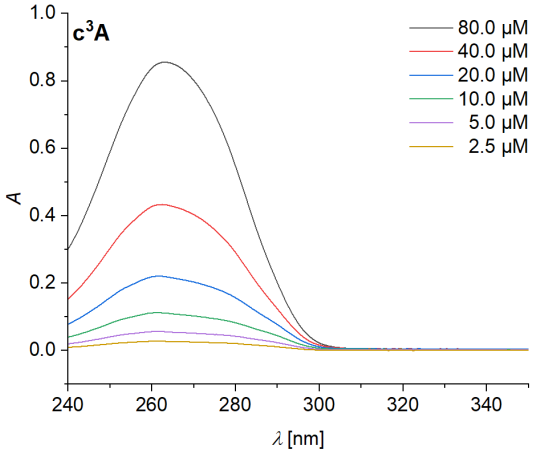
c³A
80.0 µM
40.0 µM
20.0 µM
10.0 µM
5.0 µM
2.5 µM
A
λ [nm]

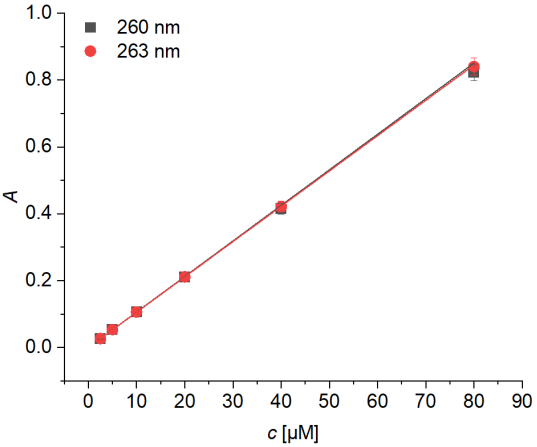
260 nm
263 nm
A
c [µM]

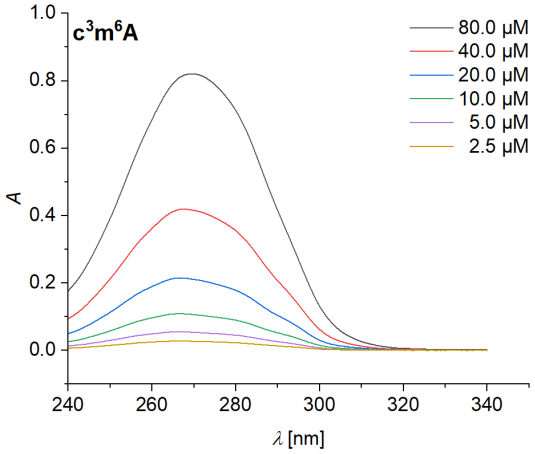
c³m⁶A
80.0 µM
40.0 µM
20.0 µM
10.0 µM
5.0 µM
2.5 µM
A
λ [nm]

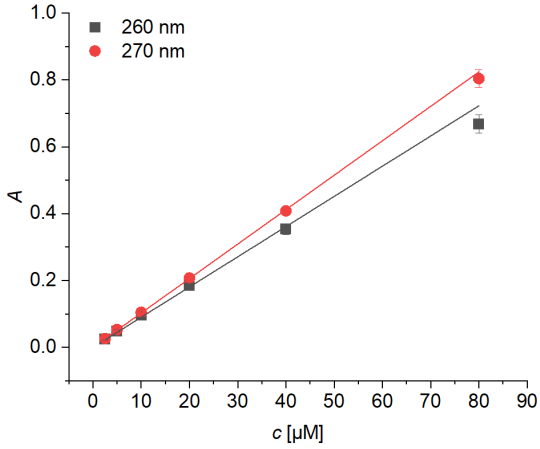
260 nm
270 nm
A
c [µM]

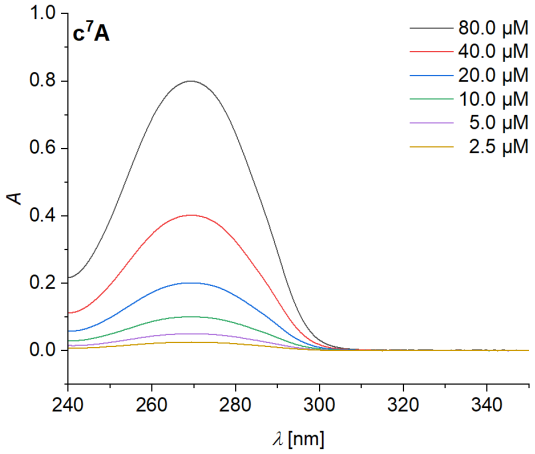
c⁷A
80.0 µM
40.0 µM
20.0 µM
10.0 µM
5.0 µM
2.5 µM
A
λ [nm]

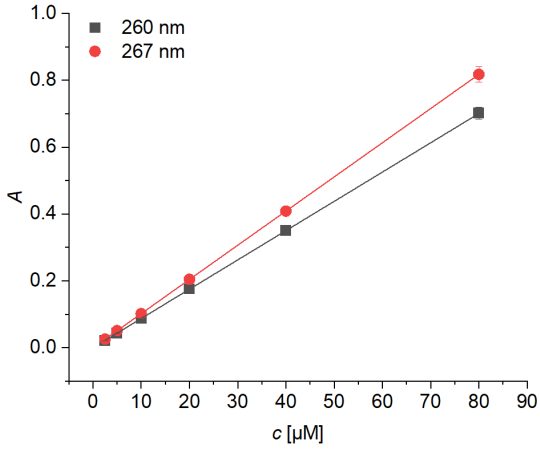
260 nm
267 nm
A
c [µM]

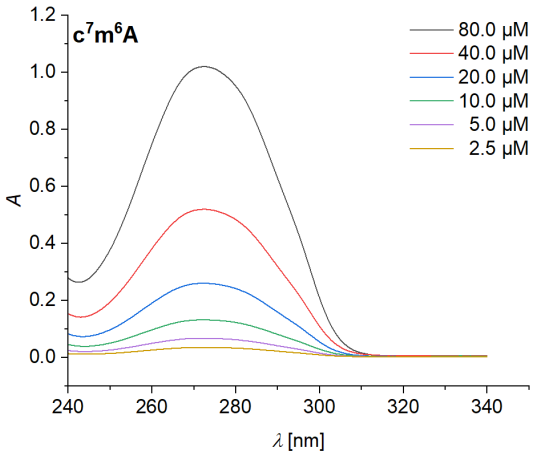
c⁷m⁶A
80.0 µM
40.0 µM
20.0 µM
10.0 µM
5.0 µM
2.5 µM
A
λ [nm]

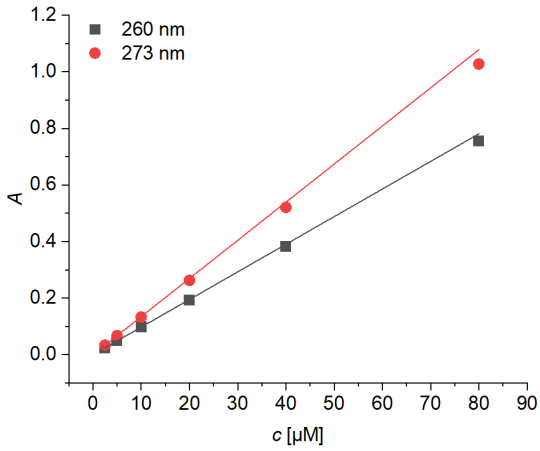
260 nm
273 nm
A
c [µM]

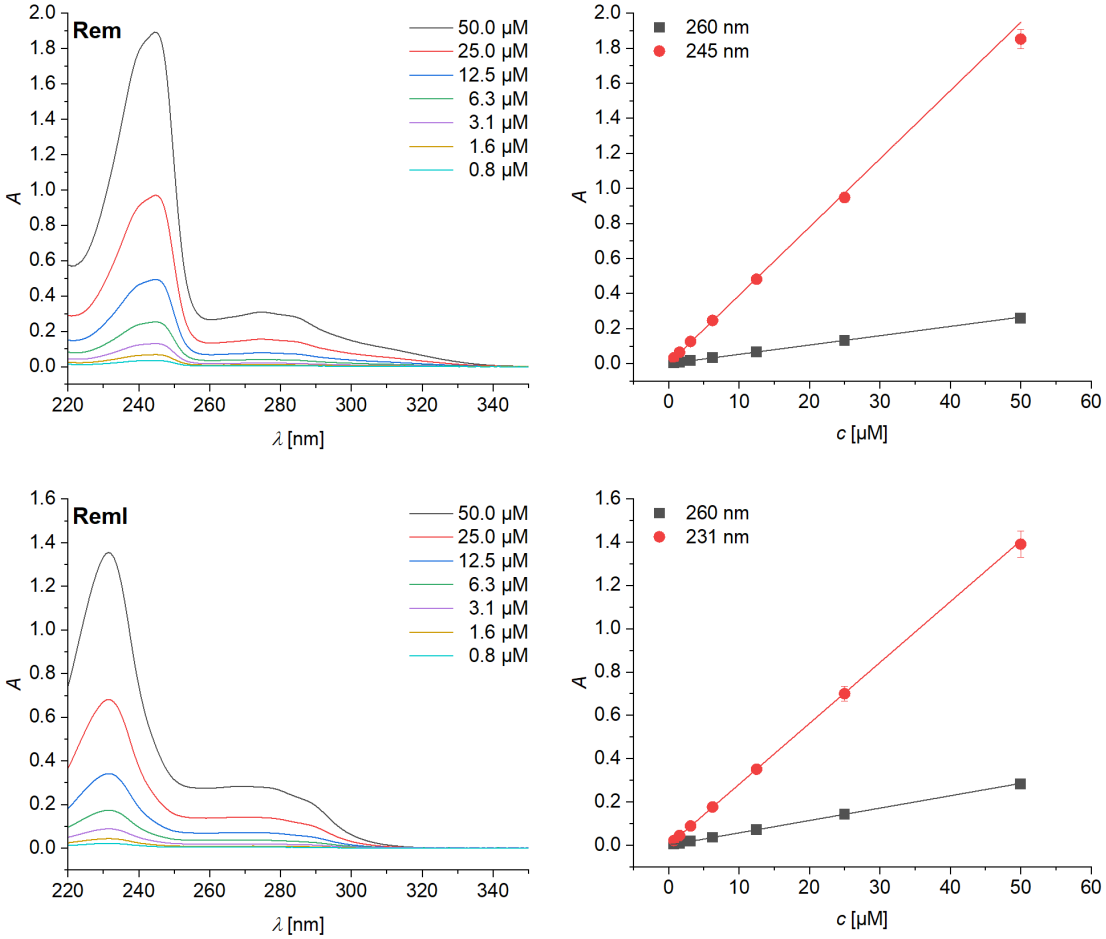
Rem
50.0 µM
25.0 µM
12.5 µM
6.3 µM
3.1 µM
1.6 µM
0.8 µM
A
λ [nm]
260 nm
245 nm
c [µM]
Reml
50.0 µM
25.0 µM
12.5 µM
6.3 µM
3.1 µM
1.6 µM
0.8 µM
A
λ [nm]
260 nm
231 nm
c [µM]

2 Supplementary UV melting curves

Thermal UV melting curves of 1, 2, 5, 10, and 20 µM RNA duplexes in PBS buffer (100 mM NaCl, 10 mM phosphate, pH 7.0) are shown next to the respective van't Hoff plots used for the determination of thermodynamic parameters.

2.1 RNA containing m^{6}A derivatives

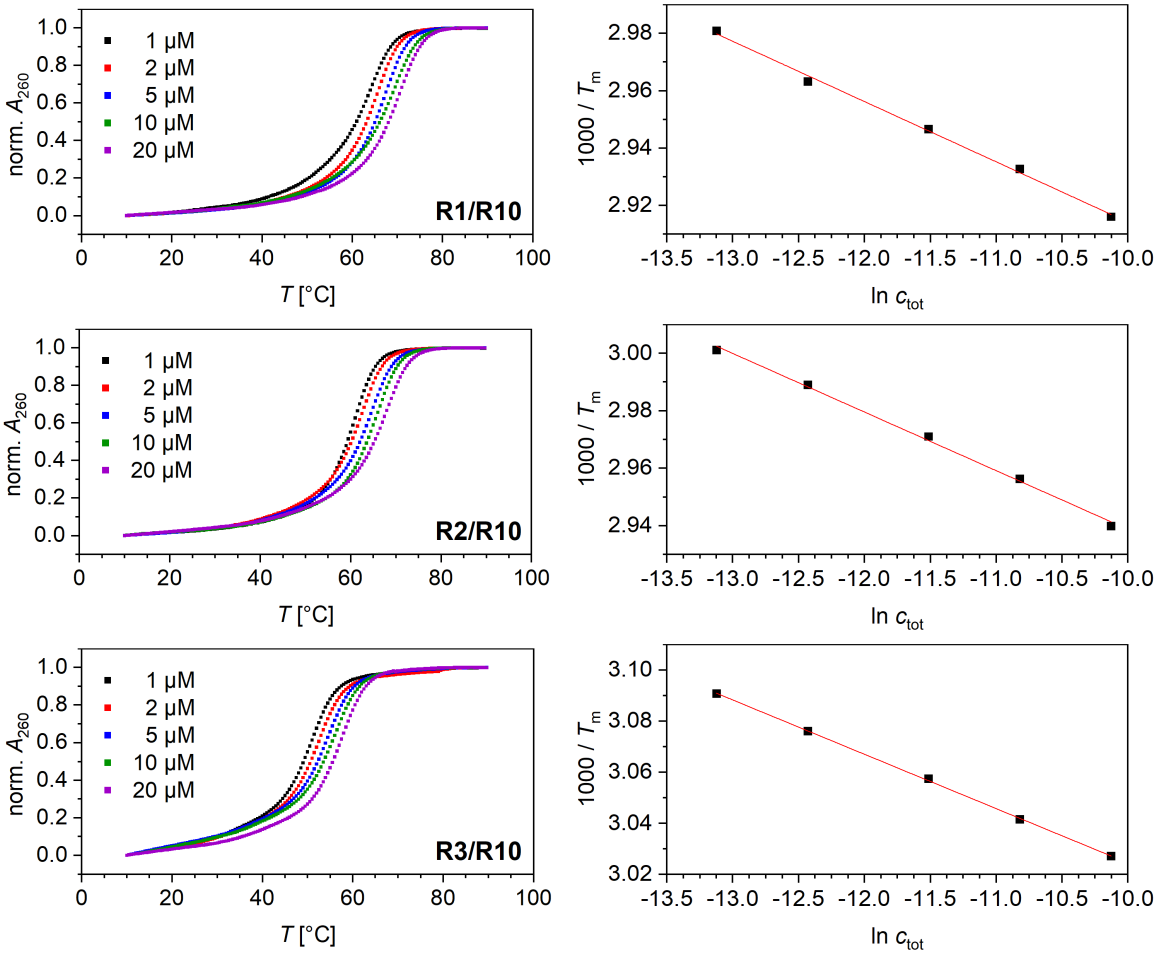

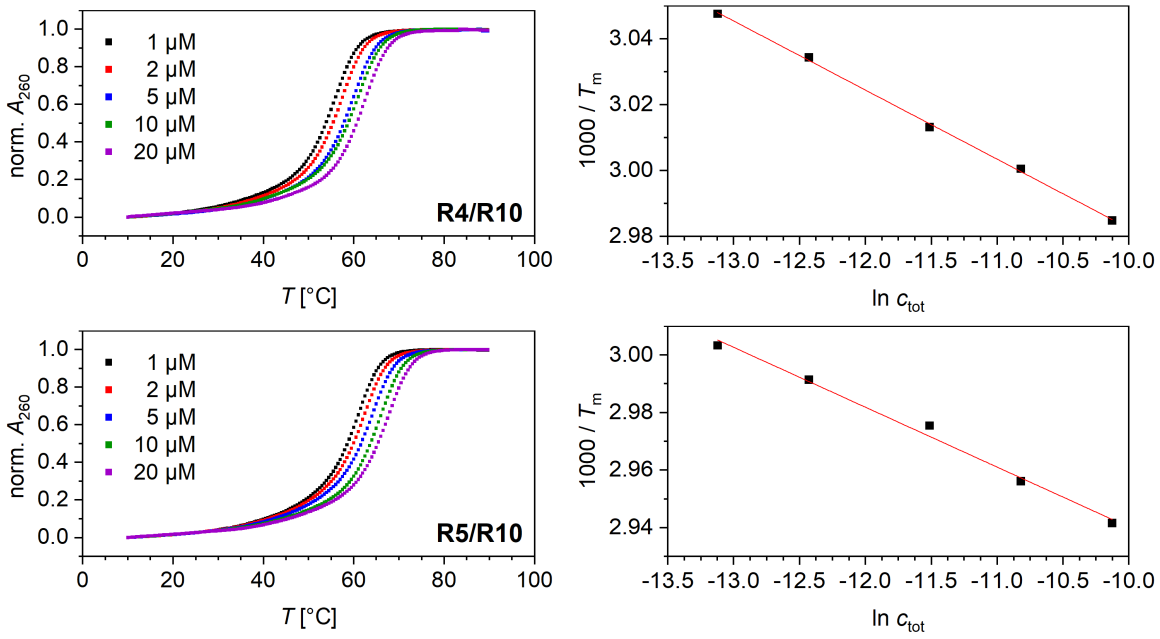

2.2 RNA containing Rem derivatives

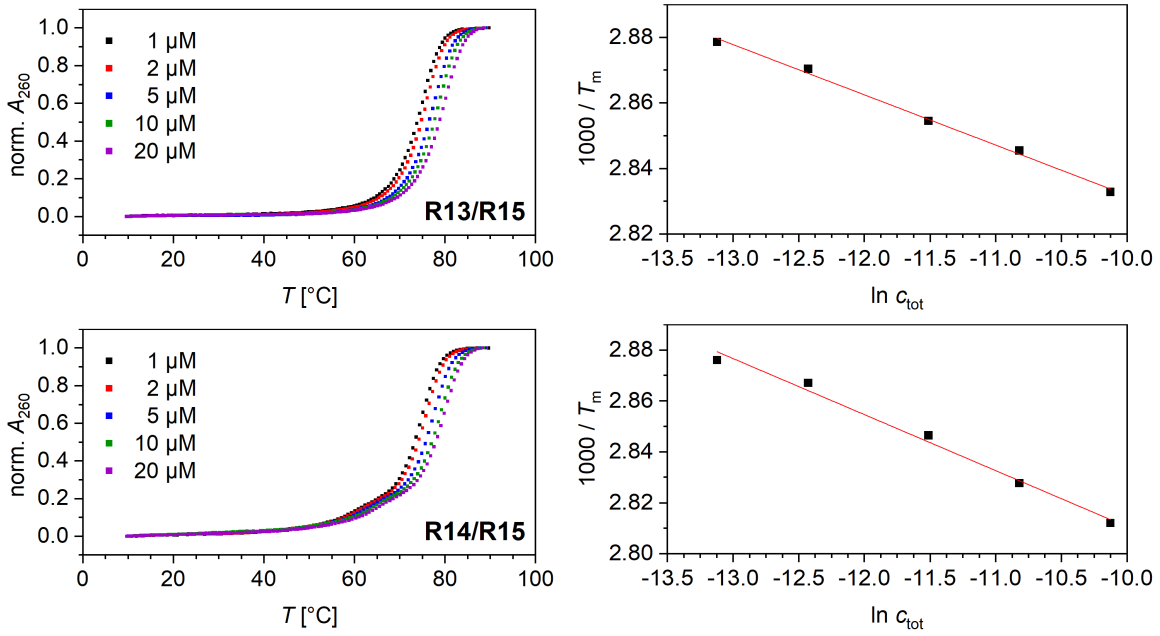

3 Supplementary HPLC-MS chromatograms

HPLC-MS analyses of digested oligonucleotide samples after incubation with m^6A demethylase enzymes (left: FTO; right: ALKBH5). The UV chromatograms (260 nm) are shown stacked on top of the nucleoside $[M+H]^+$ extracted ion chromatograms.

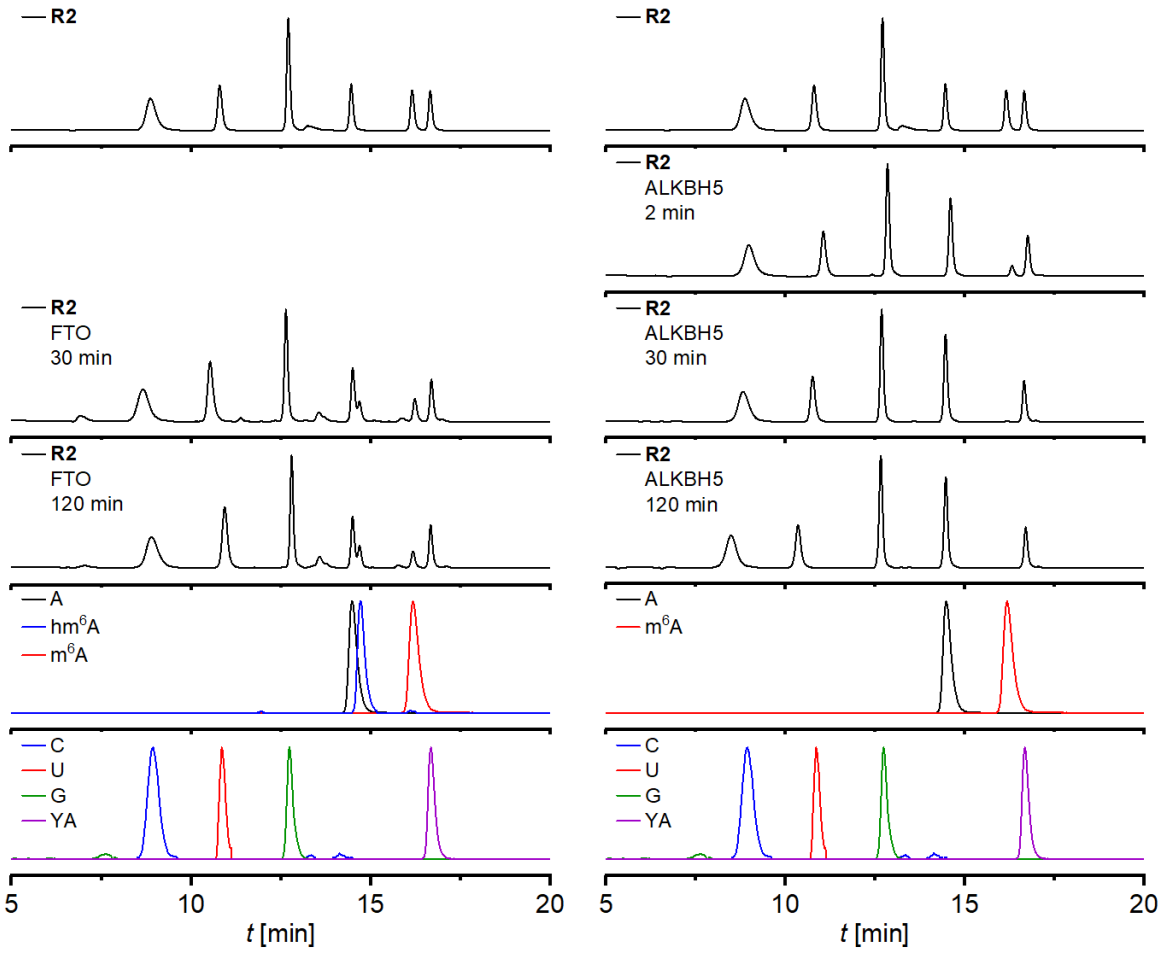

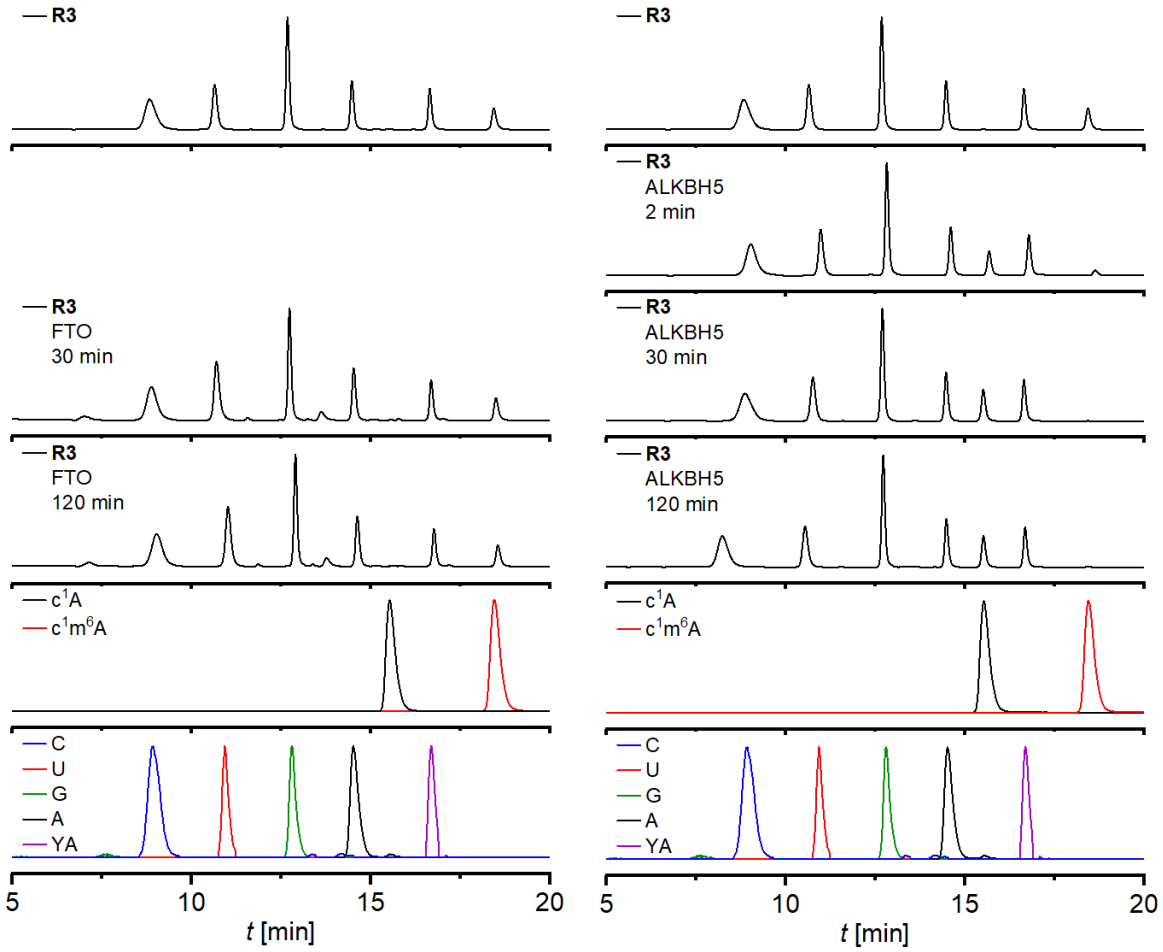
R3
R3
FTO
30 min
R3
FTO
120 min
c1A
c1m6A
C
U
G
A
YA
5
10
15
20
t [min]
R3
R3
ALKBH5
2 min
R3
ALKBH5
30 min
R3
ALKBH5
120 min
c1A
c1m6A
C
U
G
A
YA
5
10
15
20
t [min]

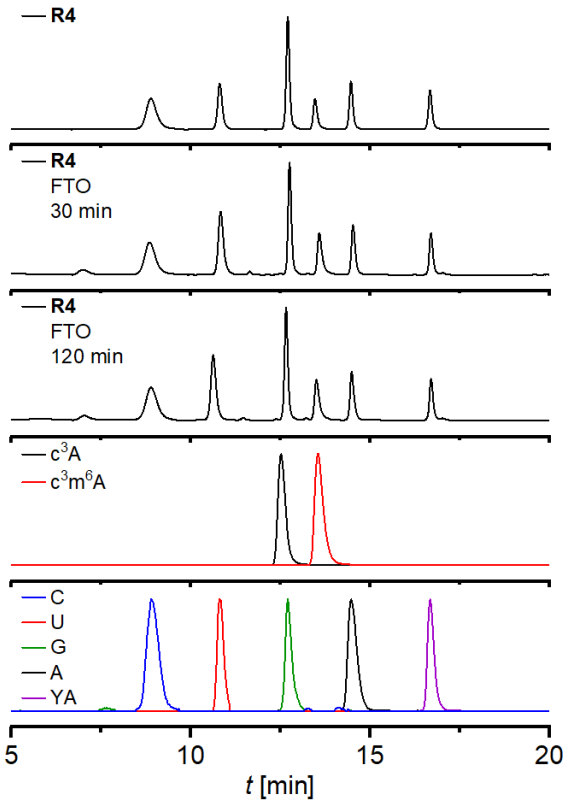
R4
R4
FTO
30 min
R4
FTO
120 min
c3A
c3m6A
C
U
G
A
YA
5
10
15
20
t [min]

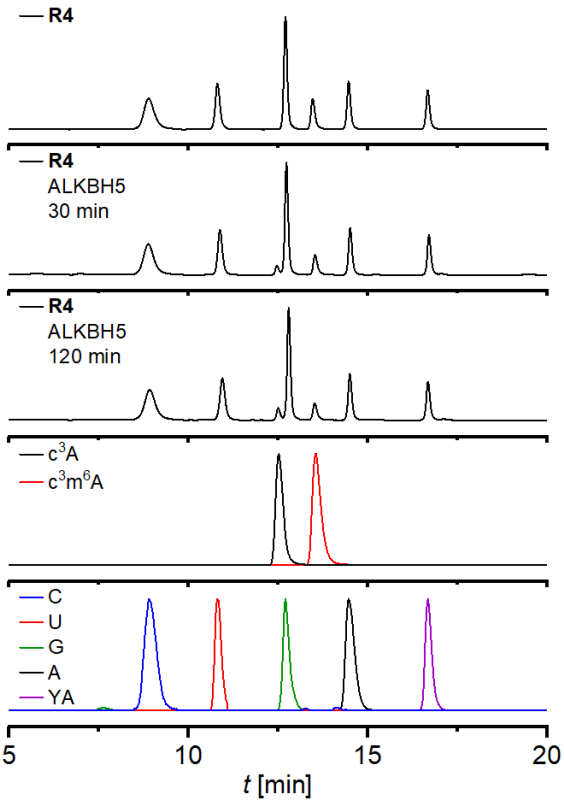
R4
R4
ALKBH5
30 min
R4
ALKBH5
120 min
c3A
c3m6A
C
U
G
A
YA
5
10
15
20
t [min]

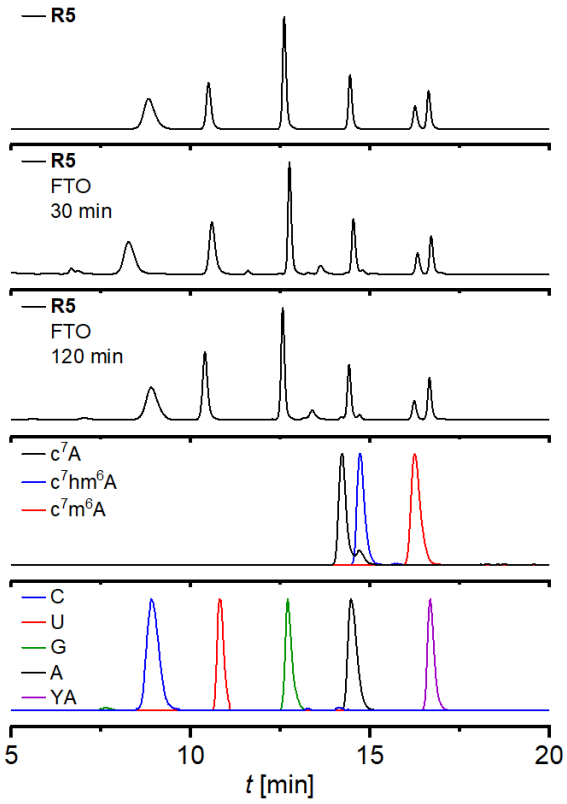
R5
R5
FTO
30 min
R5
FTO
120 min
c7A
c7hm6A
c7m6A
C
U
G
A
YA
5
10
15
20
t [min]

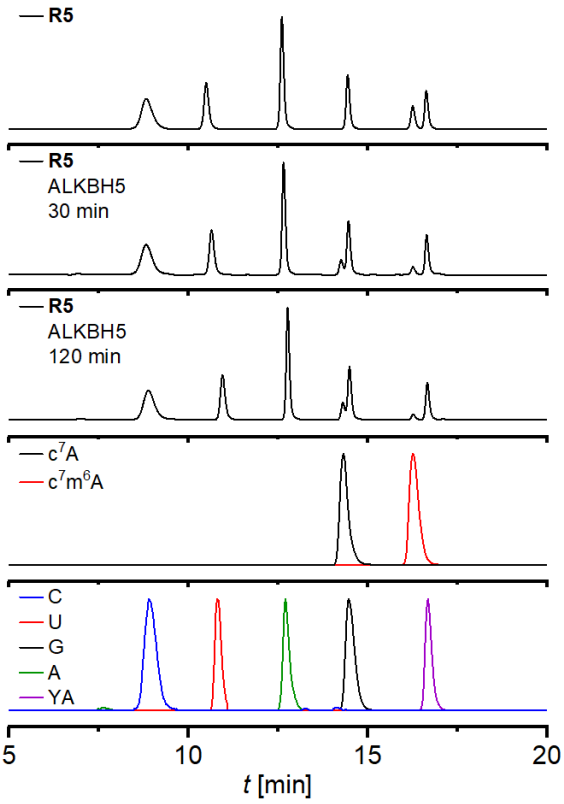
R5
R5
ALKBH5
30 min
R5
ALKBH5
120 min
c7A
c7m6A
C
U
G
A
YA
5
10
15
20
t [min]

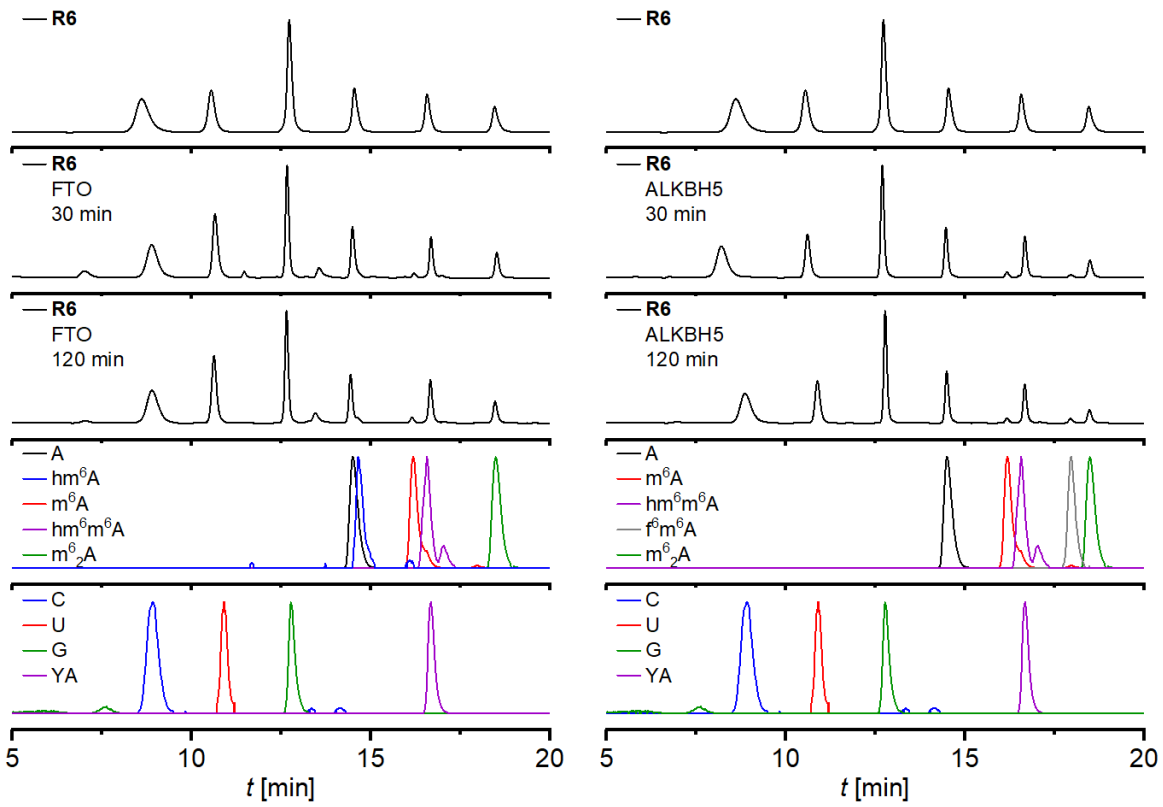
R6
R6
FTO
30 min
R6
FTO
120 min
A
hm6A
m6A
hm6m6A
m62A
C
U
G
YA
5
10
15
20
t [min]
R6
R6
ALKBH5
30 min
R6
ALKBH5
120 min
A
m6A
hm6m6A
fm6A
m62A
C
U
G
YA
5
10
15
20
t [min]

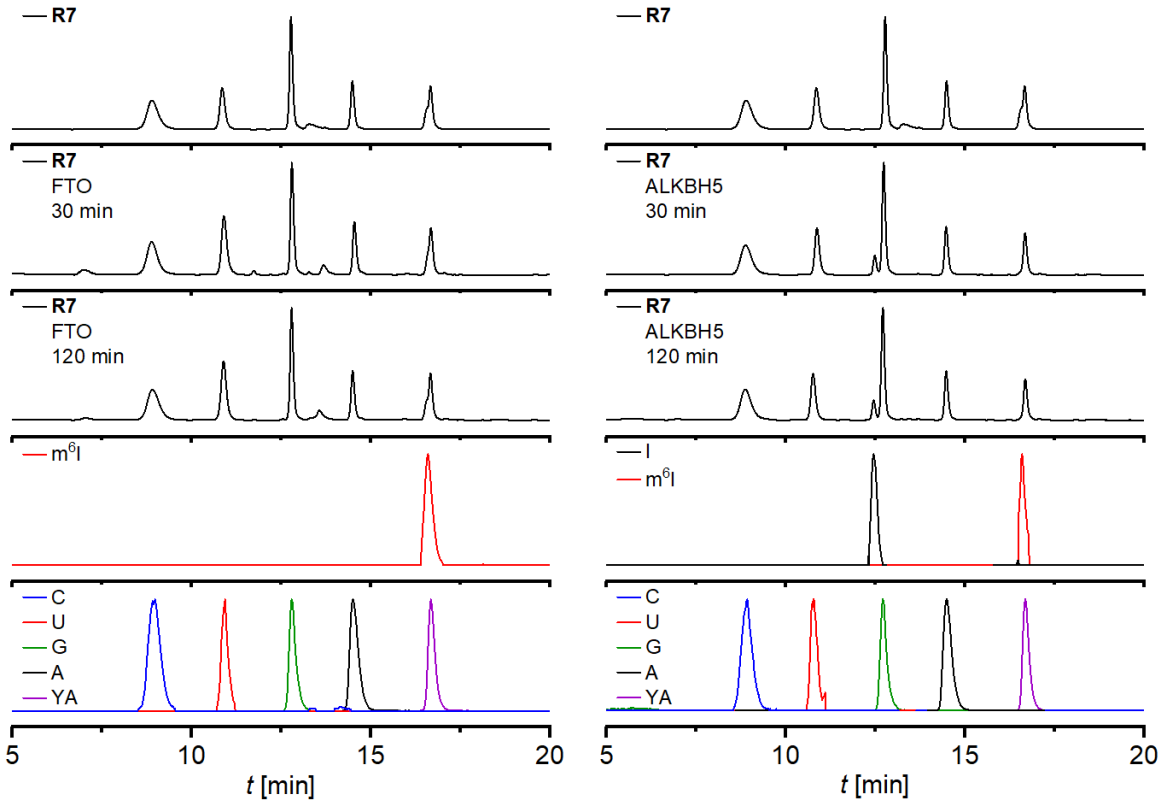
R7
R7
FTO
30 min
R7
FTO
120 min
m6I
C
U
G
A
YA
5
10
15
20
t [min]
R7
R7
ALKBH5
30 min
R7
ALKBH5
120 min
I
m6I
C
U
G
A
YA
5
10
15
20
t [min]

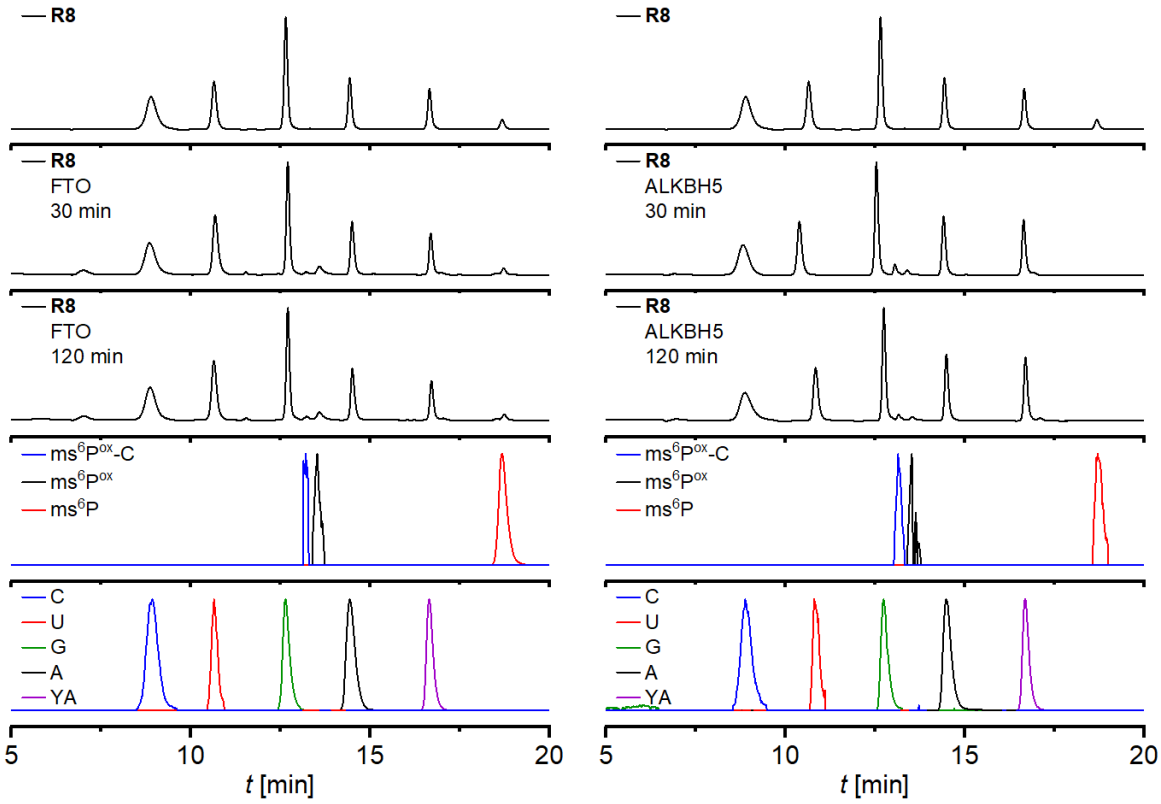
R8
R8
FTO
30 min
R8
FTO
120 min
ms6Pox-C
ms6Pox
ms6P
C
U
G
A
YA
5
10
15
20
t [min]
R8
R8
ALKBH5
30 min
R8
ALKBH5
120 min
ms6Pox-C
ms6Pox
ms6P
C
U
G
A
YA
5
10
15
20
t [min]

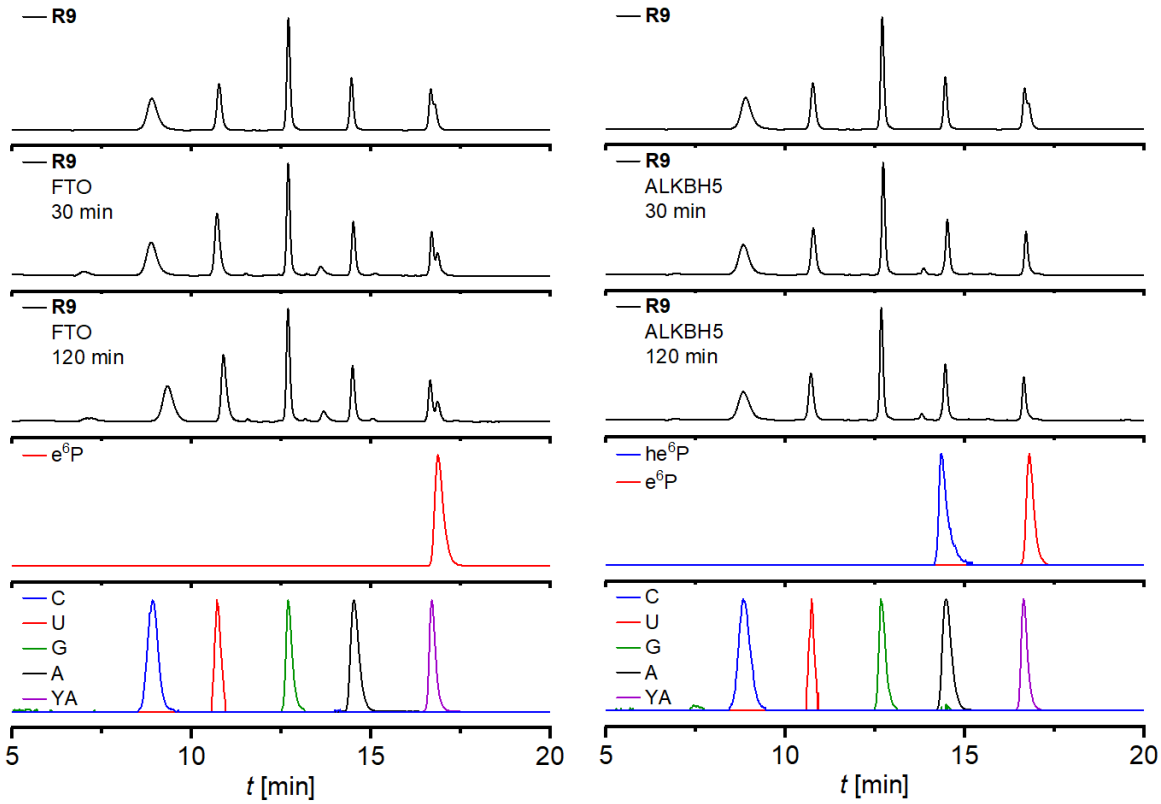
R9
R9
FTO
30 min
R9
FTO
120 min
e6P
C
U
G
A
YA
5
10
15
20
t [min]
R9
R9
ALKBH5
30 min
R9
ALKBH5
120 min
he6P
e6P
C
U
G
A
YA
5
10
15
20
t [min]

4 Abbreviations

ABCF1	ATP-binding cassette protein F1
ADA	adenosine deaminase
ADAR	adenosine deaminase acting on RNA
ADAT	adenosine deaminase acting on tRNA
ALKBH	AlkB homolog
α-KG	α-ketoglutarate
2-AP	2-aminopurine
aq.	aqueous
BAP	bacterial alkaline phosphatase
BCDSE	1,2-bis(chlorodimethylsilyl)ethane
BSA	*N*,*O*-bis(trimethylsilyl)acetamide
BTT	5-(benzylthio)-1*H*-tetrazole
CAPAM	cap-specific adenosine-N^6-MTase
CCR4-NOT	carbon catabolite repression—negative on TATA-less
cDNA	circular DNA
CDS	coding sequence
CEPCl	2-cyanoethyl *N*,*N*-diisopropylchlorophosphoramidite
COVID-19	coronavirus disease 2019
cryo-EM	cryogenic electron microscopy
DART	deamination adjacent to RNA modification targets
dba	dibenzylideneacetone
DBDMH	1,3-dibromo-5,5-dimethylhydantoin
DCA	dichloroacetic acid
DCE	1,2-dichloroethane
DCM	dichloromethane
DCP2	mRNA decapping enzyme 2
ddC	2',3'-dideoxycytidine
DEGDN	diethylene glycol dinitrite
DFT	density functional theory
DIPEA	*N*,*N*-diisopropylethylamine
DMAP	4-dimethylaminopyridine
DMF	*N*,*N*-dimethylformamide
DMFDMA	*N*,*N*-dimethylformamide dimethyl acetal
DMSO	dimethylsulfoxide
DMT	4,4'-dimethoxytrityl

DNA	deoxyribonucleic acid
EBOV	ebola virus
EC_{50}	half maximal effective concentration
EIC	extracted ion chromatogram
eIF	eukaryotic translation initiation factor
EMA	European Medicines Agency
EMSA	electrophoretic mobility shift assay
ESI	electrospray ionization
ETT	5-(ethylthio)-1*H*-tetrazole
ExoN	exonuclease
6-FAM	6-carboxyfluorescein
FDA	U.S. Food and Drug Administration
FMN	flavine mononucleotide
FTO	fat mass and obesity-associated
GDP	guanosine diphosphate
gRNA	genomic RNA
HCV	hepatitis C virus
HEPES	4-(2-hydroxyethyl)-1-piperazineethanesulfonic acid
HIV	human immunodeficiency virus
HNRNP	heterogeneous ribonucleoprotein
HPLC	high-performance liquid chromatography
HuR	human antigen R
IGF2BP	insuline-like growth factor 2 mRNA-binding protein
IMPDH	inosine monophosphate dehydrogenase
indels	insertion and deletion mutations
LDA	lithium diisopropylamide
LED	light-emitting diode
lncRNA	long non-coding RNA
MAC	m^6A-METTL complex
MACOM	m^6A-METTL-associated complex
MALAT1	metastasis-associated lung adenocarcinoma transcript 1
m^6A-REF-seq	m^6A-sensitive RNA-endoribonuclease-facilitated sequencing
MBP	maltose-binding protein
m-CPBA	4-chloroperbenzoic acid
MEP	molecular electrostatic potential

MeRIP-Seq	m^6A-specific methylated RNA immunoprecipitation with next-generation sequencing
MERS-CoV	Middle East respiratory syndrome-related coronavirus
METTL	methyltransferase-like protein
MHV	murine hepatitis virus
miCLIP	m^6A individual-nucleotide-resolution cross-linking and immunoprecipitation
miRNA	micro RNA
MMT	monomethoxytrityl / 4-methoxytrityl
MOA	mechanism of action
M^{pro}	main protease
mRNA	messenger RNA
MS	mass spectrometry
MTase	methyltransferase
MTBE	methyl *tert*-butyl ether
mt-mRNA	mitochondrial mRNA
NBS	*N*-bromosuccinimide
NCS	*N*-chlorosuccinimide
NDP	nucleoside diphosphate
NHC	N^4-hydroxycytidine
NiRAN	nidovirus RdRp-associated nucleotidyltransferase
NIS	*N*-iodosuccinimide
NMP	nucleoside monophosphate
NOG	*N*-oxalylglycine
nsp	non-structural protein
nt	nucleotide
NTA	nitrilotriacetic acid
NTP	nucleoside triphosphate
NXF1	nuclear export factor 1
ORF	open reading frame
OTf	trifluoromethanesulfonate / triflate
PA	phosphoramidite
PABP	poly-A binding protein
PAGE	polyacrylamide gel electrophoresis
PA-m^6A-seq	photo-crosslinking-assisted m^6A sequencing
P bodies	processing bodies

PBS	phosphate-buffered saline
PCIF1	phosphorylated CTD interacting factor 1
PDA	photodiode array
PL^{pro}	papain-like protease
pp	polyprotein
Rem	1'-cyano-4-aza-7,9-dideazaadenosine
RBM	RNA binding motif protein
RdRp	RNA-dependent RNA polymerase
RNA	ribonucleic acid
rRNA	ribosomal RNA
rSAP	shrimp alkaline phosphatase
rt	room temperature
RT	reverse transcription
SAM	*S*-adenosylmethionine
SARS-CoV	severe acute respiratory syndrome coronavirus
sat.	saturated
SATE	*S*-acyl-2-thioethyl
SCARLET	site-specific cleavage and radioactive-labeling followed by ligation-assisted extraction and thin-layer chromatography
siRNA	small interfering RNA
S_NAr	nucleophilic aromatic substitution
snRNA	small nuclear RNA
snoRNA	small nucleolar RNA
sno-RNP	small nucleolar ribonucleoprotein
SRSF	serine and arginine rich splicing factor
ss	single-stranded
SVPD	snake venom phosphodiesterase
TBAF	tetrabutylammonium fluoride
$TBAH_2F_3$	tetrabutylammonium dihydrogen trifluoride
TBAI	tetrabutylammonium iodide
TBDMS	*tert*-butyldimethylsilyl
TBDPS	*tert*-butyldiphenylsilyl
TBTA	tris[(1-benzyl-1*H*-1,2,3-triazol-4-yl)methyl]amine
TCA	trichloroacetic acid
TEAB	triethylammonium bicarbonate
TES	triethylsilyl

TFA	trifluoroacetic acid
THF	tetrahydrofuran
TIPS	triisopropylsilyl
TLC	thin-layer chromatography
TMS	trimethylsilyl
TOM	[(triisopropylsilyl)oxy]methyl
tRNA	transfer RNA
UTR	untranslated region
UV	ultraviolet
VIRMA	Vir like m^6A methyltransferase associated protein
WTAP	Wilms' tumor 1-associating protein
YTH	YT-521B homology
ZC3H13	zinc finger CCCH domain-containing protein 13

Bibliography

[1] Goodrich, J. A.; Kugel, J. F. Non-coding-RNA regulators of RNA polymerase II transcription. *Nat. Rev. Mol. Cell Biol* **2006**, *7*, 612–616.

[2] Bartel, D. P. Metazoan MicroRNAs. *Cell* **2018**, *173*, 20–51.

[3] Lan, M.-D.; Xiong, J.; You, X.-J.; Weng, X.-C.; Zhou, X.; Yuan, B.-F.; Feng, Y.-Q. Existence of Diverse Modifications in Small-RNA Species Composed of 16–28 Nucleotides. *Chem. Eur. J.* **2018**, *24*, 9949–9956.

[4] Carell, T.; Brandmayr, C.; Hienzsch, A.; Müller, M.; Pearson, D.; Reiter, V.; Thoma, I.; Thumbs, P.; Wagner, M. Structure and Function of Noncanonical Nucleobases. *Angew. Chem. Int. Ed.* **2012**, *51*, 7110–7131.

[5] Song, J.; Yi, C. Chemical Modifications to RNA: A New Layer of Gene Expression Regulation. *ACS Chem. Biol.* **2017**, *12*, 316–325.

[6] Duechler, M.; Leszczyńska, G.; Sochacka, E.; Nawrot, B. Nucleoside modifications in the regulation of gene expression: focus on tRNA. *Cell. Mol. Life Sci.* **2016**, *73*, 3075–3095.

[7] Yarian, C.; Townsend, H.; Czestkowski, W.; Sochacka, E.; Malkiewicz, A. J.; Guenther, R.; Miskiewicz, A.; Agris, P. F. Accurate Translation of the Genetic Code Depends on tRNA Modified Nucleosides. *J. Biol. Chem.* **2002**, *277*, 16391–16395.

[8] Urbonavičius, J.; Qian, Q.; Durand, J. M. B.; Hagervall, T. G.; Björk, G. R. Improvement of reading frame maintenance is a common function for several tRNA modifications. *EMBO J.* **2001**, *20*, 4863–4873.

[9] Haag, S.; Sloan, K. E.; Ranjan, N.; Warda, A. S.; Kretschmer, J.; Blessing, C.; Hübner, B.; Seikowski, J.; Dennerlein, S.; Rehling, P.; Rodnina, M. V.; Höbartner, C.; Bohnsack, M. T. NSUN3 and ABH1 modify the wobble position of mt-tRNA^{Met} to expand codon recognition in mitochondrial translation. *EMBO J.* **2016**, *35*, 2104–2119.

[10] Nobles, K. N.; Yarian, C. S.; Liu, G.; Guenther, R. H.; Agris, P. F. Highly conserved modified nucleosides influence Mg^{2+}-dependent tRNA folding. *Nucleic Acids Res.* **2002**, *30*, 4751–4760.

[11] Sampson, J. R.; Uhlenbeck, O. C. Biochemical and physical characterization of an unmodified yeast phenylalanine transfer RNA transcribed *in vitro*. *Proc. Natl. Acad. Sci. U. S. A.* **1988**, *85*, 1033–1037.

[12] Schöller, E.; Marks, J.; Marchand, V.; Bruckmann, A.; Powell, C. A.; Reichold, M.; Mutti, C. D.; Dettmer, K.; Feederle, R.; Hüttelmaier, S.; Helm, M.; Oefner, P.; Minczuk, M.; Motorin, Y.; Hafner, M.; Meister, G. Balancing of mitochondrial translation through METTL8-mediated m^3C modification of mitochondrial tRNAs. *Mol. Cell* **2021**, *81*, 4810–4825.

[13] Kleiber, N.; Lemus-Diaz, N.; Stiller, C.; Heinrichs, M.; Mai, M. M.-Q.; Hackert, P.; Richter-Dennerlein, R.; Höbartner, C.; Bohnsack, K. E.; Bohnsack, M. T. The RNA methyltransferase METTL8 installs m^3C_{32} in mitochondrial $tRNAs^{Thr/Ser(UCN)}$ to optimise tRNA structure and mitochondrial translation. *Nat. Commun.* **2022**, *13*, 209.

[14] Lentini, J. M.; Bargabos, R.; Chen, C.; Fu, D. Methyltransferase METTL8 is required for 3-methylcytosine modification in human mitochondrial tRNAs. *J. Biol. Chem.* **2022**, *298*, 101788.

[15] Morais, P.; Adachi, H.; Yu, Y.-T. Spliceosomal snRNA Epitranscriptomics. *Front. Genet.* **2021**, *12*, 652129.

[16] Sloan, K. E.; Warda, A. S.; Sharma, S.; Entian, K.-D.; Lafontaine, D. L. J.; Bohnsack, M. T. Tuning the ribosome: The influence of rRNA modification on eukaryotic ribosome biogenesis and function. *RNA Biol.* **2016**, *14*, 1138–1152.

[17] Decatur, W. A.; Fournier, M. J. rRNA modifications and ribosome function. *Trends Biochem. Sci.* **2002**, *27*, 344–351.

[18] Liang, X.-h.; Liu, Q.; Fournier, M. J. rRNA Modifications in an Intersubunit Bridge of the Ribosome Strongly Affect Both Ribosome Biogenesis and Activity. *Mol. Cell* **2007**, *28*, 965–977.

[19] King, T. H.; Liu, B.; McCully, R. R.; Fournier, M. J. Ribosome Structure and Activity Are Altered in Cells Lacking snoRNPs that Form Pseudouridines in the Peptidyl Transferase Center. *Mol. Cell* **2003**, *11*, 425–435.

[20] Zhao, B. S.; Roundtree, I. A.; He, C. Post-transcriptional gene regulation by mRNA modifications. *Nat. Rev. Mol. Cell Biol.* **2017**, *18*, 31–42.

[21] Adams, J. M.; Cory, S. Modified nucleosides and bizarre 5'-termini in mouse myeloma mRNA. *Nature* **1975**, *255*, 28–33.

[22] Muthukrishnan, S.; Both, G. W.; Furuichi, Y.; Shatkin, A. J. 5'-Terminal 7-methylguanosine in eukaryotic mRNA is required for translation. *Nature* **1975**, *255*, 33–37.

[23] Wei, C.-M.; Gershowitz, A.; Moss, B. N^6, $O^{2'}$-dimethyladenosine a novel methylated ribonucleoside next to the 5' terminal of animal cell and virus mRNAs. *Nature* **1975**, *257*, 251–253.

[24] Mauer, J.; Luo, X.; Blanjoie, A.; Jiao, X.; Grozhik, A. V.; Patil, D. P.; Linder, B.; Pickering, B. F.; Vasseur, J.-J.; Chen, Q.; Gross, S. S.; Elemento, O.; Debart, F.; Kiledjian, M.; Jaffrey, S. R. Reversible methylation of m^6A_m in the 5' cap controls mRNA stability. *Nature* **2017**, *541*, 371–375.

[25] Carlile, T. M.; Rojas-Duran, M. F.; Zinshteyn, B.; Shin, H.; Bartoli, K. M.; Gilbert, W. V. Pseudouridine profiling reveals regulated mRNA pseudouridylation in yeast and human cells. *Nature* **2014**, *515*, 143–146.

[26] Li, X.; Zhu, P.; Ma, S.; Song, J.; Bai, J.; Sun, F.; Yi, C. Chemical pulldown reveals dynamic pseudouridylation of the mammalian transcriptome. *Nat. Chem. Biol.* **2015**, *11*, 592–597.

[27] Karijolich, J.; Yu, Y.-T. Converting nonsense codons into sense codons by targeted pseudouridylation. *Nature* **2011**, *474*, 395–398.

[28] Li, X.; Xiong, X.; Wang, K.; Wang, L.; Shu, X.; Ma, S.; Yi, C. Transcriptome-wide mapping reveals reversible and dynamic N^1-methyladenosine methylome. *Nat. Chem. Biol.* **2016**, *12*, 311–316.

[29] Dominissini, D.; Nachtergaele, S.; Moshitch-Moshkovitz, S.; Peer, E.; Kol, N.; Ben-Haim, M. S.; Dai, Q.; Segni, A. D.; Salmon-Divon, M.; Clark, W. C.; Zheng, G.; Pan, T.; Solomon, O.; Eyal, E.; Hershkovitz, V.; Han, D.; Doré, L. C.; Amariglio, N.; Rechavi, G.; He, C. The dynamic N^1-methyladenosine methylome in eukaryotic messenger RNA. *Nature* **2016**, *530*, 441–446.

[30] Li, X.; Xiong, X.; Zhang, M.; Wang, K.; Chen, Y.; Zhou, J.; Mao, Y.; Lv, J.; Yi, D.; Chen, X.-W.; Wang, C.; Qian, S.-B.; Yi, C. Base-Resolution Mapping Reveals Distinct m^1A Methylome in Nuclear- and Mitochondrial-Encoded Transcripts. *Mol. Cell* **2017**, *68*, 993–1005.

[31] Safra, M.; Sas-Chen, A.; Nir, R.; Winkler, R.; Nachshon, A.; Bar-Yaacov, D.; Erlacher, M.; Rossmanith, W.; Stern-Ginossar, N.; Schwartz, S. The m^1A landscape on cytosolic and mitochondrial mRNA at single-base resolution. *Nature* **2017**, *551*, 251–255.

[32] Schwartz, S. m^1A within cytoplasmic mRNAs at single nucleotide resolution: a reconciled transcriptome-wide map. *RNA* **2018**, *24*, 1427–1436.

[33] Liu, N.; Pan, T. RNA epigenetics. *Transl. Res.* **2015**, *165*, 28–35.

[34] Meyer, K. D.; Saletore, Y.; Zumbo, P.; Elemento, O.; Mason, C. E.; Jaffrey, S. R. Comprehensive Analysis of mRNA Methylation Reveals Enrichment in 3' UTRs and near Stop Codons. *Cell* **2012**, *149*, 1635–1646.

[35] Wang, X.; Zhao, B. S.; Roundtree, I. A.; Lu, Z.; Han, D.; Ma, H.; Weng, X.; Chen, K.; Shi, H.; He, C. N^6-methyladenosine Modulates Messenger RNA Translation Efficiency. *Cell* **2015**, *161*, 1388–1399.

[36] Wang, X.; Lu, Z.; Gomez, A.; Hon, G. C.; Yue, Y.; Han, D.; Fu, Y.; Parisien, M.; Dai, Q.; Jia, G.; Ren, B.; Pan, T.; He, C. N^6-methyladenosine-dependent regulation of messenger RNA stability. *Nature* **2014**, *505*, 117–120.

[37] Liu, J.; Yue, Y.; Han, D.; Wang, X.; Fu, Y.; Zhang, L.; Jia, G.; Yu, M.; Lu, Z.; Deng, X.; Dai, Q.; Chen, W.; He, C. A METTL3–METTL14 complex mediates mammalian nuclear RNA N^6-adenosine methylation. *Nat. Chem. Biol.* **2014**, *10*, 93–95.

[38] Jia, G.; Fu, Y.; Zhao, X.; Dai, Q.; Zheng, G.; Yang, Y.; Yi, C.; Lindahl, T.; Pan, T.; Yang, Y.-G.; He, C. *N*6-Methyladenosine in nuclear RNA is a major substrate of the obesity-associated FTO. *Nat. Chem. Biol.* **2011**, *7*, 885–887.

[39] Zheng, G.; Dahl, J. A.; Niu, Y.; Fedorcsak, P.; Huang, C.-M.; Li, C. J.; Vågbø, C. B.; Shi, Y.; Wang, W.-L.; Song, S.-H.; Lu, Z.; Bosmans, R. P.; Dai, Q.; Hao, Y.-J.; Yang, X.; Zhao, W.-M.; Tong, W.-M.; Wang, X.-J.; Bogdan, F.; Furu, K.; Fu, Y.; Jia, G.; Zhao, X.; Liu, J.; Krokan, H. E.; Klungland, A.; Yang, Y.-G.; He, C. ALKBH5 Is a Mammalian RNA Demethylase that Impacts RNA Metabolism and Mouse Fertility. *Mol. Cell* **2013**, *49*, 18–29.

[40] Ianniello, Z.; Paiardini, A.; Fatica, A. N^6-Methyladenosine (m^6A): A Promising New Molecular Target in Acute Myeloid Leukemia. *Front. Oncol.* **2019**, *9*, 251.

[41] Zhang, B.; Jiang, H.; Dong, Z.; Sun, A.; Ge, J. The critical roles of m6A modification in metabolic abnormality and cardiovascular diseases. *Genes Dis.* **2021**, *8*, 746–758.

[42] Pruijssers, A. J.; Denison, M. R. Nucleoside analogues for the treatment of coronavirus infections. *Curr. Opin. Virol.* **2019**, *35*, 57–62.

[43] Zenchenko, A. A.; Drenichev, M. S.; Il'icheva, I. A.; Mikhailov, S. N. Antiviral and Antimicrobial Nucleoside Derivatives: Structural Features and Mechanisms of Action. *Mol. Biol.* **2021**, *55*, 786–812.

[44] Angusti, A.; Manfredini, S.; Durini, E.; Ciliberti, N.; Vertuani, S.; Solaroli, N.; Pricl, S.; Ferrone, M.; Fermeglia, M.; Loddo, R.; Secci, B.; Visioli, A.; Sanna, T.; Collu, G.; Pezzullo, M.; Colla, P. L. Design, Synthesis and Anti Flaviviridae Activity of N^6-, 5',3'-*O*- and 5',2'-*O*-Substituted Adenine Nucleoside Analogs. *Chem. Pharm. Bull.* **2008**, *56*, 423–432.

[45] Wray, S. K.; Gilbert, B. E.; Noall, M. W.; Knight, V. Mode of action of ribavirin: effect of nucleotide pool alterations on influenza virus ribonucleoprotein synthesis. *Antiviral Res.* **1985**, *5*, 29–37.

[46] Graci, J. D.; Cameron, C. E. Mechanisms of action of ribavirin against distinct viruses. *Rev. Med. Virol.* **2006**, *16*, 37–48.

[47] Sabariegos, R.; Ortega-Prieto, A. M.; Díaz-Martínez, L.; Grande-Pérez, A.; Crespo, C. G.; Gallego, I.; Ávila, A. I. de; Albentosa-González, L.; Soria, M. E.; Gastaminza, P.; Domingo, E.; Perales, C.; Mas, A. Guanosine inhibits hepatitis C virus replication and increases indel frequencies, associated with altered intracellular nucleotide pools. *PLoS Pathog.* **2022**, *18*, e1010210.

[48] Too, K.; Brown, D. M.; Bongard, E.; Yardley, V.; Vivas, L.; Loakes, D. Anti-malarial activity of N^6-modified purine analogues. *Bioorg. Med. Chem.* **2007**, *15*, 5551–5562.

[49] Seley-Radtke, K. L.; Yates, M. K. The evolution of nucleoside analogue antivirals: A review for chemists and non-chemists. Part 1: Early structural modifications to the nucleoside scaffold. *Antiviral Res.* **2018**, *154*, 66–86.

[50] Shannon, A.; Selisko, B.; Le, N.-T.-T.; Huchting, J.; Touret, F.; Piorkowski, G.; Fattorini, V.; Ferron, F.; Decroly, E.; Meier, C.; Coutard, B.; Peersen, O.; Canard, B. Rapid incorporation of Favipiravir by the fast and permissive viral RNA polymerase complex results in SARS-CoV-2 lethal mutagenesis. *Nat. Commun.* **2020**, *11*, 4682.

[51] Leś, A.; Adamowicz, L.; Rode, W. Structure and conformation of N^4-hydroxycytosine and N^4-hydroxy-5-fluorocytosine. A theoretical ab initio study. *Biochim. Biophys. Acta* **1993**, *1173*, 39–48.

[52] Kabinger, F.; Stiller, C.; Schmitzová, J.; Dienemann, C.; Kokic, G.; Hillen, H. S.; Höbartner, C.; Cramer, P. Mechanism of molnupiravir-induced SARS-CoV-2 mutagenesis. *Nat. Struct. Mol. Biol.* **2021**, *28*, 740–746.

[53] Baranovich, T.; Wong, S.-S.; Armstrong, J.; Marjuki, H.; Webby, R. J.; Webster, R. G.; Govorkova, E. A. T-705 (Favipiravir) Induces Lethal Mutagenesis in Influenza A H1N1 Viruses *In Vitro*. *J. Virol.* **2013**, *87*, 3741–3751.

[54] Olsen, D. B.; Eldrup, A. B.; Bartholomew, L.; Bhat, B.; Bosserman, M. R.; Ceccacci, A.; Colwell, L. F.; Fay, J. F.; Flores, O. A.; Getty, K. L.; Grobler, J. A.; LaFemina, R. L.; Markel, E. J.; Migliaccio, G.; Prhavc, M.; Stahlhut, M. W.; Tomassini, J. E.; MacCoss, M.; Hazuda, D. J.; Carroll, S. S. A 7-Deaza-Adenosine Analog Is a Potent and Selective Inhibitor of Hepatitis C Virus Replication with Excellent Pharmacokinetic Properties. *Antimicrob. Agents Chemother.* **2004**, *48*, 3944–3953.

[55] Cho, A.; Saunders, O. L.; Butler, T.; Zhang, L.; Xu, J.; Vela, J. E.; Feng, J. Y.; Ray, A. S.; Kim, C. U. Synthesis and antiviral activity of a series of 1′-substituted 4-aza-7,9-dideazaadenosine C-nucleosides. *Bioorg. Med. Chem. Lett.* **2012**, *22*, 2705–2707.

[56] Warren, T. K.; Wells, J.; Panchal, R. G.; Stuthman, K. S.; Garza, N. L.; Tongeren, S. A. V.; Dong, L.; Retterer, C. J.; Eaton, B. P.; Pegoraro, G.; Honnold, S.; Bantia, S.; Kotian, P.; Chen, X.; Taubenheim, B. R.; Welch, L. S.; Minning, D. M.; Babu, Y. S.; Sheridan, W. P.; Bavari, S. Protection against filovirus diseases by a novel broad-spectrum nucleoside analogue BCX4430. *Nature* **2014**, *508*, 402–405.

[57] Dominissini, D.; Moshitch-Moshkovitz, S.; Schwartz, S.; Salmon-Divon, M.; Ungar, L.; Osenberg, S.; Cesarkas, K.; Jacob-Hirsch, J.; Amariglio, N.; Kupiec, M.; Sorek, R.; Rechavi, G. Topology of the human and mouse m^{6}A RNA methylomes revealed by m^{6}A-seq. *Nature* **2012**, *485*, 201–206.

[58] Linder, B.; Grozhik, A. V.; Olarerin-George, A. O.; Meydan, C.; Mason, C. E.; Jaffrey, S. R. Single-nucleotide-resolution mapping of m6A and m6Am throughout the transcriptome. *Nat. Methods* **2015**, *12*, 767–772.

[59] Ke, S.; Alemu, E. A.; Mertens, C.; Gantman, E. C.; Fak, J. J.; Mele, A.; Haripal, B.; Zucker-Scharff, I.; Moore, M. J.; Park, C. Y.; Vågbø, C. B.; Kuśnierczyk, A.; Klungland, A.; Darnell, J. E.; Darnell, R. B. A majority of m^{6}A residues are in the last exons, allowing the potential for 3′ UTR regulation. *Genes Dev.* **2015**, *29*, 2037–2053.

[60] Chen, K.; Lu, Z.; Wang, X.; Fu, Y.; Luo, G.-Z.; Liu, N.; Han, D.; Dominissini, D.; Dai, Q.; Pan, T.; He, C. High-Resolution N^6-Methyladenosine (m^{6}A) Map Using Photo-Crosslinking-Assisted m^{6}A Sequencing. *Angew. Chem. Int. Ed.* **2015**, *54*, 1587–1590.

[61] Meyer, K. D. DART-seq: an antibody-free method for global m^{6}A detection. *Nat. Methods* **2019**, *16*, 1275–1280.

[62] Liu, N.; Parisien, M.; Dai, Q.; Zheng, G.; He, C.; Pan, T. Probing N^6-methyladenosine RNA modification status at single nucleotide resolution in mRNA and long noncoding RNA. *RNA* **2013**, *19*, 1848–1856.

[63] Csepany, T.; Lin, A.; Baldick, C. J.; Beemon, K. Sequence Specificity of mRNA N^6-Adenosine Methyltransferase. *J. Biol. Chem.* **1990**, *265*, 20117–20122.

[64] Aschenbrenner, J.; Werner, S.; Marchand, V.; Adam, M.; Motorin, Y.; Helm, M.; Marx, A. Engineering of a DNA Polymerase for Direct m^{6}A Sequencing. *Angew. Chem. Int. Ed.* **2018**, *57*, 417–421.

[65] Hong, T.; Yuan, Y.; Chen, Z.; Xi, K.; Wang, T.; Xie, Y.; He, Z.; Su, H.; Zhou, Y.; Tan, Z.-J.; Weng, X.; Zhou, X. Precise Antibody-Independent m6A Identification via 4SedTTP-Involved and FTO-Assisted Strategy at Single-Nucleotide Resolution. *J. Am. Chem. Soc.* **2018**, *140*, 5886–5889.

[66] Shu, X.; Cao, J.; Cheng, M.; Xiang, S.; Gao, M.; Li, T.; Ying, X.; Wang, F.; Yue, Y.; Lu, Z.; Dai, Q.; Cui, X.; Ma, L.; Wang, Y.; He, C.; Feng, X.; Liu, J. A metabolic labeling method detects m^{6}A transcriptome-wide at single base resolution. *Nat. Chem. Biol.* **2020**, *16*, 887–895.

[67] Hartstock, K.; Nilges, B. S.; Ovcharenko, A.; Cornelissen, N. V.; Püllen, N.; Lawrence-Dörner, A.-M.; Leidel, S. A.; Rentmeister, A. Enzymatic or In Vivo Installation of Propargyl Groups in Combination with Click Chemistry for the Enrichment and Detection of Methyltransferase Target Sites in RNA. *Angew. Chem. Int. Ed.* **2018**, *57*, 6342–6346.

[68] Islam, K.; Zheng, W.; Yu, H.; Deng, H.; Luo, M. Expanding Cofactor Repertoire of Protein Lysine Methyltransferase for Substrate Labeling. *ACS Chem. Biol.* **2011**, *6*, 679–684.

[69] Wang, R.; Zheng, W.; Yu, H.; Deng, H.; Luo, M. Labeling Substrates of Protein Arginine Methyltransferase with Engineered Enzymes and Matched *S*-Adenosyl-L-methionine Analogues. *J. Am. Chem. Soc.* **2011**, *133*, 7648–7651.

[70] Willnow, S.; Martin, M.; Lüscher, B.; Weinhold, E. A Selenium-Based Click AdoMet Analogue for Versatile Substrate Labeling with Wild-Type Protein Methyltransferases. *ChemBioChem* **2012**, *13*, 1167–1173.

[71] Shu, X.; Dai, Q.; Wu, T.; Bothwell, I. R.; Yue, Y.; Zhang, Z.; Cao, J.; Fei, Q.; Luo, M.; He, C.; Liu, J. N^6-Allyladenosine: A New Small Molecule for RNA Labeling Identified by Mutation Assay. *J. Am. Chem. Soc.* **2017**, *139*, 17213–17216.

[72] Garcia-Campos, M. A.; Edelheit, S.; Toth, U.; Safra, M.; Shachar, R.; Viukov, S.; Winkler, R.; Nir, R.; Lasman, L.; Brandis, A.; Hanna, J. H.; Rossmanith, W.; Schwartz, S. Deciphering the "m^{6}A Code" via Antibody-Independent Quantitative Profiling. *Cell* **2019**, *178*, 731–747.

[73] Zhang, Z.; Chen, L.-Q.; Zhao, Y.-L.; Yang, C.-G.; Roundtree, I. A.; Zhang, Z.; Ren, J.; Xie, W.; He, C.; Luo, G.-Z. Single-base mapping of m^{6}A by an antibody-independent method. *Sci. Adv.* **2019**, *5*, eaax0250.

[74] Imanishi, M.; Tsuji, S.; Suda, A.; Futaki, S. Detection of N^6-methyladenosine based on the methyl-sensitivity of MazF RNA endonuclease. *Chem. Commun.* **2017**, *53*, 12930–12933.

[75] Sednev, M. V.; Mykhailiuk, V.; Choudhury, P.; Halang, J.; Sloan, K. E.; Bohnsack, M. T.; Höbartner, C. N^6-Methyladenosine-Sensitive RNA-Cleaving Deoxyribozymes. *Angew. Chem. Int. Ed.* **2018**, *57*, 15117–15121.

[76] Wang, Y.; Xiao, Y.; Dong, S.; Yu, Q.; Jia, G. Antibody-free enzyme-assisted chemical approach for detection of N^6-methyladenosine. *Nat. Chem. Biol.* **2020**, *16*, 896–903.

[77] Wang, Y.; Li, Y.; Toth, J. I.; Petroski, M. D.; Zhang, Z.; Zhao, J. C. N^6-methyladenosine modification destabilizes developmental regulators in embryonic stem cells. *Nat. Cell Biol.* **2014**, *16*, 191–198.

[78] Meyer, K. D.; Patil, D. P.; Zhou, J.; Zinoviev, A.; Skabkin, M. A.; Elemento, O.; Pestova, T. V.; Qian, S.-B.; Jaffrey, S. R. 5' UTR m^{6}A Promotes Cap-Independent Translation. *Cell* **2015**, *163*, 999–1010.

[79] Bokar, J.; Rath-Shambaugh, M.; Ludwiczak, R.; Narayan, P.; Rottman, F. Characterization and partial purification of mRNA N^6-adenosine methyltransferase from HeLa cell nuclei. Internal mRNA methylation requires a multisubunit complex. *J. Biol. Chem.* **1994**, *269*, 17697–17704.

[80] Meyer, K. D.; Jaffrey, S. R. Rethinking m^{6}A Readers, Writers, and Erasers. *Annu. Rev. Cell Dev. Biol.* **2017**, *33*, 319–342.

[81] Akichika, S.; Hirano, S.; Shichino, Y.; Suzuki, T.; Nishimasu, H.; Ishitani, R.; Sugita, A.; Hirose, Y.; Iwasaki, S.; Nureki, O.; Suzuki, T. Cap-specific terminal N^6-methylation of RNA by an RNA polymerase II–associated methyltransferase. *Science* **2019**, *363*, eaav0080.

[82] Śledź, P.; Jinek, M. Structural insights into the molecular mechanism of the m^{6}A writer complex. *eLife* **2016**, *5*, e18434.

[83] Wang, X.; Feng, J.; Xue, Y.; Guan, Z.; Zhang, D.; Liu, Z.; Gong, Z.; Wang, Q.; Huang, J.; Tang, C.; Zou, T.; Yin, P. Structural basis of N^6-adenosine methylation by the METTL3–METTL14 complex. *Nature* **2016**, *534*, 575–578.

[84] Wang, P.; Doxtader, K. A.; Nam, Y. Structural Basis for Cooperative Function of Mettl3 and Mettl14 Methyltransferases. *Mol. Cell* **2016**, *63*, 306–317.

[85] Ping, X.-L.; Sun, B.-F.; Wang, L.; Xiao, W.; Yang, X.; Wang, W.-J.; Adhikari, S.; Shi, Y.; Lv, Y.; Chen, Y.-S.; Zhao, X.; Li, A.; Yang, Y.; Dahal, U.; Lou, X.-M.; Liu, X.; Huang, J.; Yuan, W.-P.; Zhu, X.-F.; Cheng, T.; Zhao, Y.-L.; Wang, X.; Danielsen, J. M. R.; Liu, F.; Yang, Y.-G. Mammalian WTAP is a regulatory subunit of the RNA N6-methyladenosine methyltransferase. *Cell Res.* **2014**, *24*, 177–189.

[86] Liu, K.; Ding, Y.; Ye, W.; Liu, Y.; Yang, J.; Liu, J.; Qi, C. Structural and Functional Characterization of the Proteins Responsible for N^6-Methyladenosine Modification and Recognition. *Curr. Protein Pept. Sci.* **2016**, *17*, 306–318.

[87] Schwartz, S.; Mumbach, M. R.; Jovanovic, M.; Wang, T.; Maciag, K.; Bushkin, G. G.; Mertins, P.; Ter-Ovanesyan, D.; Habib, N.; Cacchiarelli, D.; Sanjana, N. E.; Freinkman, E.; Pacold, M. E.; Satija, R.; Mikkelsen, T. S.; Hacohen, N.; Zhang, F.; Carr, S. A.; Lander, E. S.; Regev, A. Perturbation of m6A Writers Reveals Two Distinct Classes of mRNA Methylation at Internal and 5' Sites. *Cell Rep.* **2014**, *8*, 284–296.

[88] Bawankar, P.; Lence, T.; Paolantoni, C.; Haussmann, I. U.; Kazlauskiene, M.; Jacob, D.; Heidelberger, J. B.; Richter, F. M.; Nallasivan, M. P.; Morin, V.; Kreim, N.; Beli, P.; Helm, M.; Jinek, M.; Soller, M.; Roignant, J.-Y. Hakai is required for stabilization of core components of the m^{6}A mRNA methylation machinery. *Nat. Commun.* **2021**, *12*, 3778.

[89] Knuckles, P.; Lence, T.; Haussmann, I. U.; Jacob, D.; Kreim, N.; Carl, S. H.; Masiello, I.; Hares, T.; Villaseñor, R.; Hess, D.; Andrade-Navarro, M. A.; Biggiogera, M.; Helm, M.; Soller, M.; Bühler, M.; Roignant, J.-Y. Zc3h13/Flacc is required for adenosine methylation by bridging the mRNA-binding factor Rbm15/Spenito to the m^{6}A machinery component Wtap/Fl(2)d. *Genes Dev.* **2018**, *32*, 415–429.

[90] Yue, Y.; Liu, J.; Cui, X.; Cao, J.; Luo, G.; Zhang, Z.; Cheng, T.; Gao, M.; Shu, X.; Ma, H.; Wang, F.; Wang, X.; Shen, B.; Wang, Y.; Feng, X.; He, C.; Liu, J. VIRMA mediates preferential m^{6}A mRNA methylation in 3'UTR and near stop codon and associates with alternative polyadenylation. *Cell Discovery* **2018**, *4*, 10.

[91] Patil, D. P.; Chen, C.-K.; Pickering, B. F.; Chow, A.; Jackson, C.; Guttman, M.; Jaffrey, S. R. m^{6}A RNA methylation promotes *XIST*-mediated transcriptional repression. *Nature* **2016**, *537*, 369–373.

[92] Pendleton, K. E.; Chen, B.; Liu, K.; Hunter, O. V.; Xie, Y.; Tu, B. P.; Conrad, N. K. The U6 snRNA m^{6}A Methyltransferase METTL16 Regulates SAM Synthetase Intron Retention. *Cell* **2017**, *169*, 824–835.

[93] Shima, H.; Matsumoto, M.; Ishigami, Y.; Ebina, M.; Muto, A.; Sato, Y.; Kumagai, S.; Ochiai, K.; Suzuki, T.; Igarashi, K. *S*-Adenosylmethionine Synthesis Is Regulated by Selective *N*^{6}-Adenosine Methylation and mRNA Degradation Involving METTL16 and YTHDC1. *Cell Rep.* **2017**, *21*, 3354–3363.

[94] Warda, A. S.; Kretschmer, J.; Hackert, P.; Lenz, C.; Urlaub, H.; Höbartner, C.; Sloan, K. E.; Bohnsack, M. T. Human METTL16 is a *N*^{6} -methyladenosine (m^{6}A) methyltransferase that targets pre-mRNAs and various non-coding RNAs. *EMBO Rep.* **2017**, *18*, 2004–2014.

[95] Nance, D. J.; Satterwhite, E. R.; Bhaskar, B.; Misra, S.; Carraway, K. R.; Mansfield, K. D. Characterization of METTL16 as a cytoplasmic RNA binding protein. *PLOS ONE* **2020**, *15*, e0227647.

[96] Su, R.; Dong, L.; Li, Y.; Gao, M.; He, P. C.; Liu, W.; Wei, J.; Zhao, Z.; Gao, L.; Han, L.; Deng, X.; Li, C.; Prince, E.; Tan, B.; Qing, Y.; Qin, X.; Shen, C.; Xue, M.; Zhou, K.; Chen, Z.; Xue, J.; Li, W.; Qin, H.; Wu, X.; Sun, M.; Nam, Y.; Chen, C.-W.; Huang, W.; Horne, D.; Rosen, S. T.; He, C.; Chen, J. METTL16 exerts an m^{6}A-independent function to facilitate translation and tumorigenesis. *Nat. Cell Biol.* **2022**, *24*, 205–216.

[97] Boulias, K.; Toczydłowska-Socha, D.; Hawley, B. R.; Liberman, N.; Takashima, K.; Zaccara, S.; Guez, T.; Vasseur, J.-J.; Debart, F.; Aravind, L.; Jaffrey, S. R.; Greer, E. L. Identification of the m^{6}Am Methyltransferase PCIF1 Reveals the Location and Functions of m^{6}Am in the Transcriptome. *Mol. Cell* **2019**, *75*, 631–643.

[98] Zhou, K. I.; Pan, T. An additional class of m^{6}A readers. *Nat. Cell Biol.* **2018**, *20*, 230–232.

[99] Zhang, Z.; Theler, D.; Kaminska, K. H.; Hiller, M.; de la Grange, P.; Pudimat, R.; Rafalska, I.; Heinrich, B.; Bujnicki, J. M.; Allain, F. H.-T.; Stamm, S. The YTH Domain Is a Novel RNA Binding Domain. *J. Biol. Chem.* **2010**, *285*, 14701–14710.

[100] Li, F.; Zhao, D.; Wu, J.; Shi, Y. Structure of the YTH domain of human YTHDF2 in complex with an m^{6}A mononucleotide reveals an aromatic cage for m^{6}A recognition. *Cell Res.* **2014**, *24*, 1490–1492.

[101] Xu, C.; Wang, X.; Liu, K.; Roundtree, I. A.; Tempel, W.; Li, Y.; Lu, Z.; He, C.; Min, J. Structural basis for selective binding of m^{6}A RNA by the YTHDC1 YTH domain. *Nat. Chem. Biol.* **2014**, *10*, 927–929.

[102] Xu, C.; Liu, K.; Ahmed, H.; Loppnau, P.; Schapira, M.; Min, J. Structural Basis for the Discriminative Recognition of N^6-Methyladenosine RNA by the Human YT521-B Homology Domain Family of Proteins. *J. Biol. Chem.* **2015**, *290*, 24902–24913.

[103] Ma, C.; Liao, S.; Zhu, Z. Crystal structure of human YTHDC2 YTH domain. *Biochem. Biophys. Res. Commun.* **2019**, *518*, 678–684.

[104] Xiao, W.; Adhikari, S.; Dahal, U.; Chen, Y.-S.; Hao, Y.-J.; Sun, B.-F.; Sun, H.-Y.; Li, A.; Ping, X.-L.; Lai, W.-Y.; Wang, X.; Ma, H.-L.; Huang, C.-M.; Yang, Y.; Huang, N.; Jiang, G.-B.; Wang, H.-L.; Zhou, Q.; Wang, X.-J.; Zhao, Y.-L.; Yang, Y.-G. Nuclear m^{6}A Reader YTHDC1 Regulates mRNA Splicing. *Mol. Cell* **2016**, *61*, 507–519.

[105] Roundtree, I. A.; Luo, G.-Z.; Zhang, Z.; Wang, X.; Zhou, T.; Cui, Y.; Sha, J.; Huang, X.; Guerrero, L.; Xie, P.; He, E.; Shen, B.; He, C. YTHDC1 mediates nuclear export of N^6-methyladenosine methylated mRNAs. *eLife* **2017**, *6*, e31311.

[106] Li, A.; Chen, Y.-S.; Ping, X.-L.; Yang, X.; Xiao, W.; Yang, Y.; Sun, H.-Y.; Zhu, Q.; Baidya, P.; Wang, X.; Bhattarai, D. P.; Zhao, Y.-L.; Sun, B.-F.; Yang, Y.-G. Cytoplasmic m^{6}A reader YTHDF3 promotes mRNA translation. *Cell Res.* **2017**, *27*, 444–447.

[107] Shi, H.; Wang, X.; Lu, Z.; Zhao, B. S.; Ma, H.; Hsu, P. J.; Liu, C.; He, C. YTHDF3 facilitates translation and decay of N^6-methyladenosine-modified RNA. *Cell Res.* **2017**, *27*, 315–328.

[108] Huang, H.; Weng, H.; Chen, J. m^{6}A Modification in Coding and Non-coding RNAs: Roles and Therapeutic Implications in Cancer. *Cancer Cell* **2020**, *37*, 270–288.

[109] Du, H.; Zhao, Y.; He, J.; Zhang, Y.; Xi, H.; Liu, M.; Ma, J.; Wu, L. YTHDF2 destabilizes m^{6}A-containing RNA through direct recruitment of the CCR4–NOT deadenylase complex. *Nat. Commun.* **2016**, *7*, 12626.

[110] Zhou, J.; Wan, J.; Gao, X.; Zhang, X.; Jaffrey, S. R.; Qian, S.-B. Dynamic m^{6}A mRNA methylation directs translational control of heat shock response. *Nature* **2015**, *526*, 591–594.

[111] Tirumuru, N.; Zhao, B. S.; Lu, W.; Lu, Z.; He, C.; Wu, L. N^6-methyladenosine of HIV-1 RNA regulates viral infection and HIV-1 Gag protein expression. *eLife* **2016**, *5*, e15528.

[112] Kretschmer, J.; Rao, H.; Hackert, P.; Sloan, K. E.; Höbartner, C.; Bohnsack, M. T. The m^{6}A reader protein YTHDC2 interacts with the small ribosomal subunit and the 5'–3' exoribonuclease XRN1. *RNA* **2018**, *24*, 1339–1350.

[113] Hsu, P. J.; Zhu, Y.; Ma, H.; Guo, Y.; Shi, X.; Liu, Y.; Qi, M.; Lu, Z.; Shi, H.; Wang, J.; Cheng, Y.; Luo, G.; Dai, Q.; Liu, M.; Guo, X.; Sha, J.; Shen, B.; He, C. Ythdc2 is an N^6-methyladenosine binding protein that regulates mammalian spermatogenesis. *Cell Res.* **2017**, *27*, 1115–1127.

[114] Mao, Y.; Dong, L.; Liu, X.-M.; Guo, J.; Ma, H.; Shen, B.; Qian, S.-B. m^{6}A in mRNA coding regions promotes translation via the RNA helicase-containing YTHDC2. *Nat. Commun.* **2019**, *10*, 5332.

[115] Roost, C.; Lynch, S. R.; Batista, P. J.; Qu, K.; Chang, H. Y.; Kool, E. T. Structure and Thermodynamics of N^6-Methyladenosine in RNA: A Spring-Loaded Base Modification. *J. Am. Chem. Soc.* **2015**, *137*, 2107–2115.

[116] Liu, N.; Dai, Q.; Zheng, G.; He, C.; Parisien, M.; Pan, T. N^6-methyladenosine-dependent RNA structural switches regulate RNA–protein interactions. *Nature* **2015**, *518*, 560–564.

[117] Zhou, K. I.; Shi, H.; Lyu, R.; Wylder, A. C.; Matuszek, Ż.; Pan, J. N.; He, C.; Parisien, M.; Pan, T. Regulation of Co-transcriptional Pre-mRNA Splicing by m^{6}A through the Low-Complexity Protein hnRNPG. *Mol. Cell* **2019**, *76*, 70–81.

[118] Huang, H.; Weng, H.; Sun, W.; Qin, X.; Shi, H.; Wu, H.; Zhao, B. S.; Mesquita, A.; Liu, C.; Yuan, C. L.; Hu, Y.-C.; Hüttelmaier, S.; Skibbe, J. R.; Su, R.; Deng, X.; Dong, L.; Sun, M.; Li, C.; Nachtergaele, S.; Wang, Y.; Hu, C.; Ferchen, K.; Greis, K. D.; Jiang, X.; Wei, M.; Qu, L.; Guan, J.-L.; He, C.; Yang, J.; Chen, J. Recognition of RNA N^6-methyladenosine by IGF2BP proteins enhances mRNA stability and translation. *Nat. Cell Biol.* **2018**, *20*, 285–295.

[119] Lin, S.; Choe, J.; Du, P.; Triboulet, R.; Gregory, R. I. The m^{6}A Methyltransferase METTL3 Promotes Translation in Human Cancer Cells. *Mol. Cell* **2016**, *62*, 335–345.

[120] Coots, R. A.; Liu, X.-M.; Mao, Y.; Dong, L.; Zhou, J.; Wan, J.; Zhang, X.; Qian, S.-B. m^{6}A Facilitates eIF4F-Independent mRNA Translation. *Mol. Cell* **2017**, *68*, 504–514.

[121] Tanabe, A.; Tanikawa, K.; Tsunetomi, M.; Takai, K.; Ikeda, H.; Konno, J.; Torigoe, T.; Maeda, H.; Kutomi, G.; Okita, K.; Mori, M.; Sahara, H. RNA helicase YTHDC2 promotes cancer metastasis via the enhancement of the efficiency by which *HIF-1*α mRNA is translated. *Cancer Lett.* **2016**, *376*, 34–42.

[122] Frayling, T. M.; Timpson, N. J.; Weedon, M. N.; Zeggini, E.; Freathy, R. M.; Lindgren, C. M.; Perry, J. R. B.; Elliott, K. S.; Lango, H.; Rayner, N. W.; Shields, B.; Harries, L. W.; Barrett, J. C.; Ellard, S.; Groves, C. J.; Knight, B.; Patch, A.-M.; Ness, A. R.; Ebrahim, S.; Lawlor, D. A.; Ring, S. M.; Ben-Shlomo, Y.; Jarvelin, M.-R.; Sovio, U.; Bennett, A. J.; Melzer, D.; Ferrucci, L.; Loos, R. J. F.; Barroso, I.; Wareham, N. J.; Karpe, F.; Owen, K. R.; Cardon, L. R.; Walker, M.; Hitman, G. A.; Palmer, C. N. A.; Doney, A. S. F.; Morris, A. D.; Smith, G. D.; Hattersley, A. T.; McCarthy, M. I. A Common Variant in the *FTO* Gene Is Associated with Body Mass Index and Predisposes to Childhood and Adult Obesity. *Science* **2007**, *316*, 889–894.

[123] Dina, C.; Meyre, D.; Gallina, S.; Durand, E.; Körner, A.; Jacobson, P.; Carlsson, L. M. S.; Kiess, W.; Vatin, V.; Lecoeur, C.; Delplanque, J.; Vaillant, E.; Pattou, F.; Ruiz, J.; Weill, J.; Levy-Marchal, C.; Horber, F.; Potoczna, N.; Hercberg, S.; Stunff, C. L.; Bougnères, P.; Kovacs, P.; Marre, M.; Balkau, B.; Cauchi, S.; Chèvre, J.-C.; Froguel, P. Variation in *FTO* contributes to childhood obesity and severe adult obesity. *Nat. Genet.* **2007**, *39*, 724–726.

[124] Scuteri, A.; Sanna, S.; Chen, W.-M.; Uda, M.; Albai, G.; Strait, J.; Najjar, S.; Nagaraja, R.; Orrú, M.; Usala, G.; Dei, M.; Lai, S.; Maschio, A.; Busonero, F.; Mulas, A.; Ehret, G. B.; Fink, A. A.; Weder, A. B.; Cooper, R. S.; Galan, P.; Chakravarti, A.; Schlessinger, D.; Cao, A.; Lakatta, E.; Abecasis, G. R. Genome-Wide Association Scan Shows Genetic Variants in the *FTO* Gene Are Associated with Obesity-Related Traits. *PLoS Genetics* **2007**, *3*, e115.

[125] Gerken, T.; Girard, C. A.; Tung, Y.-C. L.; Webby, C. J.; Saudek, V.; Hewitson, K. S.; Yeo, G. S. H.; McDonough, M. A.; Cunliffe, S.; McNeill, L. A.; Galvanovskis, J.; Rorsman, P.; Robins, P.; Prieur, X.; Coll, A. P.; Ma, M.; Jovanovic, Z.; Farooqi, I. S.; Sedgwick, B.; Barroso, I.; Lindahl, T.; Ponting, C. P.; Ashcroft, F. M.; O'Rahilly, S.; Schofield, C. J. The Obesity-Associated *FTO* Gene Encodes a 2-Oxoglutarate-Dependent Nucleic Acid Demethylase. *Science* **2007**, *318*, 1469–1472.

[126] Jia, G.; Yang, C.-G.; Yang, S.; Jian, X.; Yi, C.; Zhou, Z.; He, C. Oxidative demethylation of 3-methylthymine and 3-methyluracil in single-stranded DNA and RNA by mouse and human FTO. *FEBS Lett.* **2008**, *582*, 3313–3319.

[127] Mauer, J.; Jaffrey, S. R. FTO, m^6A, m^6A_m, and the hypothesis of reversible epitranscriptomic mRNA modifications. *FEBS Lett.* **2018**, *592*, 2012–2022.

[128] Wei, J.; Liu, F.; Lu, Z.; Fei, Q.; Ai, Y.; He, P. C.; Shi, H.; Cui, X.; Su, R.; Klungland, A.; Jia, G.; Chen, J.; He, C. Differential m^6A, m^6A_m, and m^1A Demethylation

Mediated by FTO in the Cell Nucleus and Cytoplasm. *Mol. Cell* **2018**, *71*, 973–985.

[129] Gulati, P.; Avezov, E.; Ma, M.; Antrobus, R.; Lehner, P.; O'Rahilly, S.; Yeo, G. S. H. Fat mass and obesity-related (FTO) shuttles between the nucleus and cytoplasm. *Biosci. Rep.* **2014**, *34*, e00144.

[130] Thalhammer, A.; Bencokova, Z.; Poole, R.; Loenarz, C.; Adam, J.; O'Flaherty, L.; Schödel, J.; Mole, D.; Giaslakiotis, K.; Schofield, C. J.; Hammond, E. M.; Ratcliffe, P. J.; Pollard, P. J. Human AlkB Homologue 5 Is a Nuclear 2-Oxoglutarate Dependent Oxygenase and a Direct Target of Hypoxia-Inducible Factor 1α (HIF-1α). *PLoS ONE* **2011**, *6*, e16210.

[131] Ensfelder, T. T.; Kurz, M. Q.; Iwan, K.; Geiger, S.; Matheisl, S.; Müller, M.; Beckmann, R.; Carell, T. ALKBH5-induced demethylation of mono- and dimethylated adenosine. *Chem. Commun.* **2018**, *54*, 8591–8593.

[132] Feng, C.; Liu, Y.; Wang, G.; Deng, Z.; Zhang, Q.; Wu, W.; Tong, Y.; Cheng, C.; Chen, Z. Crystal Structures of the Human RNA Demethylase Alkbh5 Reveal Basis for Substrate Recognition. *J. Biol. Chem.* **2014**, *289*, 11571–11583.

[133] Zou, S.; Toh, J. D. W.; Wong, K. H. Q.; Gao, Y.-G.; Hong, W.; Woon, E. C. Y. N^6-Methyladenosine: a conformational marker that regulates the substrate specificity of human demethylases FTO and ALKBH5. *Sci. Rep.* **2016**, *6*, 25677.

[134] You, Z.; Omura, S.; Ikeda, H.; Cane, D. E.; Jogl, G. Crystal Structure of the Non-heme Iron Dioxygenase PtlH in Pentalenolactone Biosynthesis. *J. Biol. Chem.* **2007**, *282*, 36552–36560.

[135] Zheng, G.; Dahl, J. A.; Niu, Y.; Fu, Y.; Klungland, A.; Yang, Y.-G.; He, C. Sprouts of RNA epigenetics. *RNA Biol.* **2013**, *10*, 915–918.

[136] Fu, Y.; Jia, G.; Pang, X.; Wang, R. N.; Wang, X.; Li, C. J.; Smemo, S.; Dai, Q.; Bailey, K. A.; Nobrega, M. A.; Han, K.-L.; Cui, Q.; He, C. FTO-mediated formation of N^6-hydroxymethyladenosine and N^6-formyladenosine in mammalian RNA. *Nat. Commun.* **2013**, *4*, 1798.

[137] Zhang, X.; Wei, L.-H.; Wang, Y.; Xiao, Y.; Liu, J.; Zhang, W.; Yan, N.; Amu, G.; Tang, X.; Zhang, L.; Jia, G. Structural insights into FTO's catalytic mechanism for the demethylation of multiple RNA substrates. *Proc. Natl. Acad. Sci. U.S.A.* **2019**, *116*, 2919–2924.

[138] Xu, C.; Liu, K.; Tempel, W.; Demetriades, M.; Aik, W.; Schofield, C. J.; Min, J. Structures of Human ALKBH5 Demethylase Reveal a Unique Binding Mode for Specific Single-stranded N^6-Methyladenosine RNA Demethylation. *J. Biol. Chem.* **2014**, *289*, 17299–17311.

[139] Toh, J. D. W.; Crossley, S. W. M.; Bruemmer, K. J.; Ge, E. J.; He, D.; Iovan, D. A.; Chang, C. J. Distinct RNA *N*-demethylation pathways catalyzed by nonheme iron ALKBH5 and FTO enzymes enable regulation of formaldehyde release rates. *Proc. Natl. Acad. Sci. U.S.A.* **2020**, *117*, 25284–25292.

[140] Wang, B.; Cao, Z.; Sharon, D. A.; Shaik, S. Computations Reveal a Rich Mechanistic Variation of Demethylation of *N*-Methylated DNA/RNA Nucleotides by FTO. *ACS Catal.* **2015**, *5*, 7077–7090.

[141] Kaur, S.; Tam, N. Y.; McDonough, M. A.; Schofield, C. J.; Aik, W. S. Mechanisms of substrate recognition and N^6-methyladenosine demethylation revealed by crystal structures of ALKBH5–RNA complexes. *Nucleic Acids Res.* **2022**, *50*, 4148–4160.

[142] Balacco, D. L.; Soller, M. The m^6A Writer: Rise of a Machine for Growing Tasks. *Biochemistry* **2019**, *58*, 363–378.

[143] Li, H.; Ren, Y.; Mao, K.; Hua, F.; Yang, Y.; Wei, N.; Yue, C.; Li, D.; Zhang, H. FTO is involved in Alzheimer's disease by targeting TSC1-mTOR-Tau signaling. *Biochem. Biophys. Res. Commun.* **2018**, *498*, 234–239.

[144] Ziemkiewicz, K.; Warminski, M.; Wojcik, R.; Kowalska, J.; Jemielity, J. Quick Access to Nucleobase-Modified Phosphoramidites for the Synthesis of Oligoribonucleotides Containing Post-Transcriptional Modifications and Epitranscriptomic Marks. *J. Org. Chem.* **2022**, *87*, 10333–10348.

[145] Xu, X.; Zhang, J.; Xu, T. Chemoselective Perfluoromethylation of Thio- and Selenoamides. *Org. Lett.* **2020**, *22*, 8638–8642.

[146] Hassan, A. E. A.; Abou-Elkhair, R. A. I.; Riordan, J. M.; Allan, P. W.; Parker, W. B.; Khare, R.; Waud, W. R.; Montgomery, J. A.; Secrist, J. A. Synthesis and evaluation of the substrate activity of C-6 substituted purine ribosides with *E. coli* purine nucleoside phosphorylase: Palladium mediated cross-coupling of organozinc halides with 6-chloropurine nucleosides. *Eur. J. Med. Chem.* **2012**, *47*, 167–174.

[147] Hasník, Z.; Šilhár, P.; Hocek, M. Synthesis of (purin-6-yl)acetates and 6-(2-hydroxyethyl)purines via cross-couplings of 6-chloropurines with the Reformatsky reagent. *Tetrahedron Lett.* **2007**, *48*, 5589–5592.

[148] Hasník, Z.; Pohl, R.; Klepetářová, B.; Hocek, M. Synthesis of (purin-6-yl)acetates and their transformations to 6-(2-hydroxyethyl)- and 6-(carbamoylmethyl)purines. *Collect. Czech. Chem. Commun.* **2009**, *74*, 1035–1059.

[149] Brown, M. S.; Rapoport, H. The Reduction of Esters with Sodium Borohydride. *J. Org. Chem.* **1963**, *28*, 3261–3263.

[150] Bianco, A.; Passacantilli, P.; Righi, G. Improved Procedure for the Reduction of Esters to Alcohols by Sodium Borohydride. *Synth. Commun.* **1988**, *18*, 1765–1771.

[151] Traube, W. Ueber eine neue Synthese des Guanins und Xanthins. *Ber. Dtsch. Chem. Ges.* **1900**, *33*, 1371–1383.

[152] Traube, W. Der synthetische Aufbau der Harnsäure, des Xanthins, Theobromins, Theophyllins und Caffeïns aus der Cyanessigsäure. *Ber. Dtsch. Chem. Ges.* **1900**, *33*, 3035–3056.

[153] Robins, R. K.; Dille, K. J.; Willits, C. H.; Christensen, B. E. Purines. II. The Synthesis of Certain Purines and the Cyclization of Several Substituted 4,5-Diaminopyrimidines. *J. Am. Chem. Soc.* **1953**, *75*, 263–266.

[154] Fischer, E.; Helferich, B. Synthetische Glucoside der Purine. *Ber. Dtsch. Chem. Ges.* **1914**, *47*, 210–235.

[155] Davoll, J.; Lowy, B. A. A New Synthesis of Purine Nucleosides. The Synthesis of Adenosine, Guanosine and 2,6-Diamino-9-β-D-ribofuranosylpurine. *J. Am. Chem. Soc.* **1951**, *73*, 1650–1655.

[156] Niedballa, U.; Vorbrüggen, H. A General Synthesis of Pyrimidine Nucleosides. *Angew. Chem. Int. Ed.* **1970**, *9*, 461–462.

[157] Chiacchio, U.; Corsaro, A.; Pistarà, V.; Rescifina, A.; Iannazzo, D.; Piperno, A.; Romeo, G.; Romeo, R.; Grassi, G. Diastereoselective Synthesis of *N*,*O*-Psiconucleosides, a New Class of Modified Nucleosides. *Eur. J. Org. Chem.* **2002**, *2002*, 1206–1212.

[158] Bio, M. M.; Xu, F.; Waters, M.; Williams, J. M.; Savary, K. A.; Cowden, C. J.; Yang, C.; Buck, E.; Song, Z. J.; Tschaen, D. M.; Volante, R. P.; Reamer, R. A.; Grabowski, E. J. J. Practical Synthesis of a Potent Hepatitis C Virus RNA Replication Inhibitor. *J. Org. Chem.* **2004**, *69*, 6257–6266.

[159] Hirao, Y.; Seo, S.; Kubo, T. Self-Assembly of 1-Deazahypoxanthine: Cooperativity of Hydrogen-Bonding and Stacking Interactions. *J. Phys. Chem. C* **2019**, *123*, 20928–20935.

[160] Zeinyeh, W.; Xia, H.; Lawton, P.; Radix, S.; Marminon, C.; Nebois, P.; Walchshofer, N. Synthesis and modulation properties of imidazo[4,5-*b*]pyridin-7-one and indazole-4,7-dione derivatives towards the *Cryptosporidium parvum* CpABC3 transporter. *Eur. J. Med. Chem.* **2010**, *45*, 2480–2488.

[161] Seela, F.; Ming, X. 7-Functionalized 7-deazapurine β-D and β-L-ribonucleosides related to tubercidin and 7-deazainosine: glycosylation of pyrrolo[2,3-*d*]pyrimidines with 1-*O*-acetyl-2,3,5-tri-*O*-benzoyl-β-D or β-L-ribofuranose. *Tetrahedron* **2007**, *63*, 9850–9861.

[162] Ingale, S. A.; Leonard, P.; Seela, F. Glycosylation of Pyrrolo[2,3-*d*]pyrimidines with 1-*O*-Acetyl-2,3,5-tri-*O*-benzoyl-D -ribofuranose: Substituents and Protecting Groups Effecting the Synthesis of 7-Deazapurine Ribonucleosides. *J. Org. Chem.* **2018**, *83*, 8589–8595.

[163] Nauš, P.; Caletková, O.; Konečný, P.; Džubák, P.; Bogdanová, K.; Kolář, M.; Vrbková, J.; Slavětínská, L.; Tloušťová, E.; Perlíková, P.; Hajdúch, M.; Hocek, M. Synthesis, Cytostatic, Antimicrobial, and Anti-HCV Activity of 6-Substituted 7-(Het)aryl-7-deazapurine Ribonucleosides. *J. Med. Chem.* **2014**, *57*, 1097–1110.

[164] Kanie, K.; Mizuno, K.; Kuroboshi, M.; Hiyama, T. A Facile Synthesis of Trifluoromethylamines by Oxidative Desulfurization–Fluorination of Dithiocarbamates. *Bull. Chem. Soc. Jpn.* **1998**, *71*, 1973–1991.

[165] Milcent, T.; Crousse, B. The main and recent syntheses of the *N*-CF_3 motif. *C. R. Chim.* **2018**, *21*, 771–781.

[166] Werf, A. van der; Hribersek, M.; Selander, N. N-Trifluoromethylation of Nitrosoarenes with Sodium Triflinate. *Org. Lett.* **2017**, *19*, 2374–2377.

[167] Priewisch, B.; Rück-Braun, K. Efficient Preparation of Nitrosoarenes for the Synthesis of Azobenzenes. *J. Org. Chem.* **2005**, *70*, 2350–2352.

[168] Defoin, A. Simple Preparation of Nitroso Benzenes and Nitro Benzenes by Oxidation of Anilines with H_2O_2 Catalysed with Molybdenum Salts. *Synthesis* **2004**, *2004*, 706–710.

[169] Taylor, E. C.; Tseng, C. P.; Rampal, J. B. Conversion of a Primary Amino Group into a Nitroso Group. Synthesis of Nitroso-Substituted Heterocycles. *J. Org. Chem.* **1982**, *47*, 552–555.

[170] Xie, L.-J.; Wang, R.-L.; Wang, D.; Liu, L.; Cheng, L. Visible-light-mediated oxidative demethylation of N^6-methyl adenines. *Chem. Commun.* **2017**, *53*, 10734–10737.

[171] Xie, L.-J.; Yang, X.-T.; Wang, R.-L.; Cheng, H.-P.; Li, Z.-Y.; Liu, L.; Mao, L.; Wang, M.; Cheng, L. Identification of Flavin Mononucleotide as a Cell-Active Artificial N^6-Methyladenosine RNA Demethylase. *Angew. Chem. Int. Ed.* **2019**, *58*, 5028–5032.

[172] Gaied, N. B.; Glasser, N.; Ramalanjaona, N.; Beltz, H.; Wolff, P.; Marquet, R.; Burger, A.; Mély, Y. 8-vinyl-deoxyadenosine, an alternative fluorescent nucleoside analog to 2'-deoxyribosyl-2-aminopurine with improved properties. *Nucleic Acids Res.* **2005**, *33*, 1031–1039.

[173] Ward, D. C.; Reich, E.; Stryer, L. Fluorescence Studies of Nucleotides and Polynucleotides: I. Formycin, 2-Aminopurine Riboside, 2,6-Diaminopurine Riboside, and their Derivatives. *J. Biol. Chem.* **1969**, *244*, 1228–1237.

[174] Somoza, Á. Protecting groups for RNA synthesis: an increasing need for selective preparative methods. *Chem. Soc. Rev.* **2008**, *37*, 2668–2675.

[175] Oivanen, M.; Kuusela, S.; Lönnberg, H. Kinetics and Mechanisms for the Cleavage and Isomerization of the Phosphodiester Bonds of RNA by Brønsted Acids and Bases. *Chem. Rev.* **1998**, *98*, 961–990.

[176] Pitsch, S.; Weiss, P. A.; Jenny, L.; Stutz, A.; Wu, X. Reliable Chemical Synthesis of Oligoribonucleotides (RNA) with 2'-*O*-[(Triisopropylsilyl)oxy]methyl(2'-*O*-tom)-Protected Phosphoramidites. *Helv. Chim. Acta* **2001**, *84*, 3773–3795.

[177] Mairhofer, E.; Fuchs, E.; Micura, R. Facile synthesis of a 3-deazaadenosine phosphoramidite for RNA solid-phase synthesis. *Beilstein J. Org. Chem.* **2016**, *12*, 2556–2562.

[178] Saito-Tarashima, N.; Kira, H.; Wada, T.; Miki, K.; Ide, S.; Yamazaki, N.; Matsuda, A.; Minakawa, N. Groove modification of siRNA duplexes to elucidate siRNA–protein interactions using 7-bromo-7-deazaadenosine and 3-bromo-3-deazaadenosine as chemical probes. *Org. Biomol. Chem.* **2016**, *14*, 11096–11105.

[179] Hakimelahi, G. H.; Proba, Z. A.; Ogilvie, K. K. New catalysts and procedures for the dimethoxytritylation and selective silylation of ribonucleosides. *Can. J. Chem.* **1982**, *60*, 1106–1113.

[180] Tram, K.; Sanghvi, Y. S.; Yan, H. Further Optimization of Detritylation in Solid-Phase Oligodeoxyribonucleotide Synthesis. *Nucleosides Nucleotides Nucleic Acids* **2011**, *30*, 12–19.

[181] Gaur, R. K.; Paliwal, S.; Sharma, P.; Gupta, K. C. A simple and sensitive spectrophotometric method for the quantitative determination of solid supported amino groups. *J. Biochem. Biophys. Methods* **1989**, *18*, 323–329.

[182] Welz, R.; Müller, S. 5-(Benzylmercapto)-1*H*-tetrazole as activator for 2'-*O*-TBDMS phosphoramidite building blocks in RNA synthesis. *Tetrahedron Lett.* **2002**, *43*, 795–797.

[183] Chandra Vargeese, J. C.; Yegge, J.; Krivjansky, S.; Settle, A.; Kropp, E.; Peterson, K.; Pieken, W. Efficient activation of nucleoside phosphoramidites with 4,5-dicyanoimidazole during oligonucleotide synthesis. *Nucleic Acids Res.* **1998**, *26*, 1046–1050.

[184] Krotz, A. H.; Klopchin, P. G.; Walker, K. L.; Srivatsa, G.; Cole, D. L.; Ravikumar, V. T. On the formation of longmers in phosphorothioate oligodeoxyribonucleotide synthesis. *Tetrahedron Lett.* **1997**, *38*, 3875–3878.

[185] Ellington, A.; Pollard, J. D. Introduction to the Synthesis and Purification of Oligonucleotides. *Curr. Protoc. Nucleic Acid Chem.* **2000**, *00*, A.3C.1–A.3C.22.

[186] Seela, F.; Zulauf, M. Oligonucleotides Containing 7-Deazaadenines: The Influence of the 7-Substituent Chain Length and Charge on the Duplex Stability. *Helv. Chim. Acta* **1999**, *82*, 1878–1898.

[187] Bereiter, R.; Himmelstoß, M.; Renard, E.; Mairhofer, E.; Egger, M.; Breuker, K.; Kreutz, C.; Ennifar, E.; Micura, R. Impact of 3-deazapurine nucleobases on RNA properties. *Nucleic Acids Res.* **2021**, *49*, 4281–4293.

[188] Lenci, F.; Checcucci, G.; Sgarbossa, A.; Martin, M.; Plaza, P.; Angelini, N. in *Encyclopedia of Condensed Matter Physics*, Elsevier, **2005**, pp. 222–235.

[189] Kretschmer, J. Interactions and functions of RNA-binding proteins. Ph. D. Thesis, Georg-August-Universität Göttingen, Göttingen, **2016**.

[190] Scheitl, C. P. M.; Maghami, M. G.; Lenz, A.-K.; Höbartner, C. Site-specific RNA methylation by a methyltransferase ribozyme. *Nature* **2020**, *587*, 663–667.

[191] Müller, T. A.; Struble, S. L.; Meek, K.; Hausinger, R. P. Characterization of human AlkB homolog 1 produced in mammalian cells and demonstration of mitochondrial dysfunction in ALKBH1-deficient cells. *Biochem. Biophys. Res. Commun.* **2018**, *495*, 98–103.

[192] Tomczak, J. M.; Węglarz-Tomczak, E. Estimating kinetic constants in the Michaelis–Menten model from one enzymatic assay using Approximate Bayesian Computation. *FEBS Lett.* **2019**, *593*, 2742–2750.

[193] Itoh, T.; Kitano, S.; Mizuno, Y. Synthetic Studies of Potential Antimetabolites. XIII. Synthesis of 7-Amino-3-β-D-ribofuranosyl-3*H*-imidazo[4,5-*b*]pyridine (1-Deazaadenosine) and Related Nucleosides. *J. Heterocyclic Chem.* **1972**, *9*, 465–470.

[194] Martin, D. M. G.; Reese, C. B. Some Aspects of the Chemistry of *N*(1)- and *N*(6)-Dimethylallyl Derivatives of Adenosine and Adenine. *J. Chem. Soc. C* **1968**, 1731–1738.

[195] Jentoft, N.; Dearborn, D. G. Protein Labeling by Reductive Alkylation. *Methods Enzymol.* **1983**, *91*, 570–579.

[196] Orrillo, A. G.; Furlan, R. L. E. Sulfur in Dynamic Covalent Chemistry. *Angew. Chem. Int. Ed.* **2022**, *61*, e202201168.

[197] Szmant, H. H.; McIntosh, J. J. The Absorption Spectra of Some Phenyl Sulfides, Sulfoxides and Sulfones Containing Nitro and Amino Groups. *J. Am. Chem. Soc.* **1951**, *73*, 4356–4359.

[198] Ruscic, B. Active Thermochemical Tables: Sequential Bond Dissociation Enthalpies of Methane, Ethane, and Methanol and the Related Thermochemistry. *J. Phys. Chem. A* **2015**, *119*, 7810–7837.

[199] Wu, F.; Zhao, S.; Yu, B.; Chen, Y.-M.; Wang, W.; Song, Z.-G.; Hu, Y.; Tao, Z.-W.; Tian, J.-H.; Pei, Y.-Y.; Yuan, M.-L.; Zhang, Y.-L.; Dai, F.-H.; Liu, Y.; Wang, Q.-M.; Zheng, J.-J.; Xu, L.; Holmes, E. C.; Zhang, Y.-Z. A new coronavirus associated with human respiratory disease in China. *Nature* **2020**, *579*, 265–269.

[200] Zhou, P.; Yang, X.-L.; Wang, X.-G.; Hu, B.; Zhang, L.; Zhang, W.; Si, H.-R.; Zhu, Y.; Li, B.; Huang, C.-L.; Chen, H.-D.; Chen, J.; Luo, Y.; Guo, H.; Jiang, R.-D.; Liu, M.-Q.; Chen, Y.; Shen, X.-R.; Wang, X.; Zheng, X.-S.; Zhao, K.; Chen, Q.-J.; Deng, F.; Liu, L.-L.; Yan, B.; Zhan, F.-X.; Wang, Y.-Y.; Xiao, G.-F.; Shi, Z.-L. A pneumonia outbreak associated with a new coronavirus of probable bat origin. *Nature* **2020**, *579*, 270–273.

[201] Coronaviridae Study Group of the International Committee on Taxonomy of Viruses. The species *Severe acute respiratory syndrome-related coronavirus*: classifying 2019-nCoV and naming it SARS-CoV-2. *Nat. Microbiol.* **2020**, *5*, 536–544.

[202] Zhang, L.; Lin, D.; Sun, X.; Curth, U.; Drosten, C.; Sauerhering, L.; Becker, S.; Rox, K.; Hilgenfeld, R. Crystal structure of SARS-CoV-2 main protease provides a basis for design of improved α-ketoamide inhibitors. *Science* **2020**, *368*, 409–412.

[203] Snijder, E. J.; Bredenbeek, P. J.; Dobbe, J. C.; Thiel, V.; Ziebuhr, J.; Poon, L. L.; Guan, Y.; Rozanov, M.; Spaan, W. J.; Gorbalenya, A. E. Unique and Conserved Features of Genome and Proteome of SARS-coronavirus, an Early Split-off From the Coronavirus Group 2 Lineage. *J. Mol. Biol.* **2003**, *331*, 991–1004.

[204] Shah, A.; Rashid, F.; Aziz, A.; Jan, A. U.; Suleman, M. Genetic characterization of structural and open reading Fram-8 proteins of SARS-CoV-2 isolates from different countries. *Gene Rep.* **2020**, *21*, 100886.

[205] Hilgenfeld, R. From SARS to MERS: crystallographic studies on coronaviral proteases enable antiviral drug design. *FEBS J.* **2014**, *281*, 4085–4096.

[206] Ziebuhr, J. The Coronavirus Replicase. *Curr. Top. Microbiol. Immunol.* **2005**, *287*, 57–94.

[207] Ma, C.; Sacco, M. D.; Hurst, B.; Townsend, J. A.; Hu, Y.; Szeto, T.; Zhang, X.; Tarbet, B.; Marty, M. T.; Chen, Y.; Wang, J. Boceprevir, GC-376, and calpain inhibitors II, XII inhibit SARS-CoV-2 viral replication by targeting the viral main protease. *Cell Res.* **2020**, *30*, 678–692.

[208] Hu, Y.; Ma, C.; Szeto, T.; Hurst, B.; Tarbet, B.; Wang, J. Boceprevir, Calpain Inhibitors II and XII, and GC-376 Have Broad-Spectrum Antiviral Activity against Coronaviruses. *ACS Infect. Dis.* **2021**, *7*, 586–597.

[209] Owen, D. R.; Allerton, C. M. N.; Anderson, A. S.; Aschenbrenner, L.; Avery, M.; Berritt, S.; Boras, B.; Cardin, R. D.; Carlo, A.; Coffman, K. J.; Dantonio, A.; Di, L.; Eng, H.; Ferre, R.; Gajiwala, K. S.; Gibson, S. A.; Greasley, S. E.; Hurst, B. L.; Kadar, E. P.; Kalgutkar, A. S.; Lee, J. C.; Lee, J.; Liu, W.; Mason, S. W.; Noell, S.; Novak, J. J.; Obach, R. S.; Ogilvie, K.; Patel, N. C.; Pettersson, M.; Rai, D. K.; Reese, M. R.; Sammons, M. F.; Sathish, J. G.; Singh, R. S. P.; Steppan, C. M.; Stewart, A. E.; Tuttle, J. B.; Updyke, L.; Verhoest, P. R.; Wei, L.; Yang, Q.; Zhu, Y. An oral SARS-CoV-2 M^{pro} inhibitor clinical candidate for the treatment of COVID-19. *Science* **2021**, *374*, 1586–1593.

[210] Wen, W.; Chen, C.; Tang, J.; Wang, C.; Zhou, M.; Cheng, Y.; Zhou, X.; Wu, Q.; Zhang, X.; Feng, Z.; Wang, M.; Mao, Q. Efficacy and safety of three new oral antiviral treatment (molnupiravir, fluvoxamine and Paxlovid) for COVID-19: a meta-analysis. *Ann. Med.* **2022**, *54*, 516–523.

[211] Subissi, L.; Posthuma, C. C.; Collet, A.; Zevenhoven-Dobbe, J. C.; Gorbalenya, A. E.; Decroly, E.; Snijder, E. J.; Canard, B.; Imbert, I. One severe acute respiratory syndrome coronavirus protein complex integrates processive RNA polymerase and exonuclease activities. *Proc. Natl. Acad. Sci. U.S.A.* **2014**, *111*, E3900–E3909.

[212] Wang, Q.; Wu, J.; Wang, H.; Gao, Y.; Liu, Q.; Mu, A.; Ji, W.; Yan, L.; Zhu, Y.; Zhu, C.; Fang, X.; Yang, X.; Huang, Y.; Gao, H.; Liu, F.; Ge, J.; Sun, Q.; Yang, X.; Xu, W.; Liu, Z.; Yang, H.; Lou, Z.; Jiang, B.; Guddat, L. W.; Gong, P.; Rao, Z.

Structural Basis for RNA Replication by the SARS-CoV-2 Polymerase. *Cell* **2020**, *182*, 417–428.

[213] Hillen, H. S.; Kokic, G.; Farnung, L.; Dienemann, C.; Tegunov, D.; Cramer, P. Structure of replicating SARS-CoV-2 polymerase. *Nature* **2020**, *584*, 154–156.

[214] Dwivedy, A.; Mariadasse, R.; Ahmad, M.; Chakraborty, S.; Kar, D.; Tiwari, S.; Bhattacharyya, S.; Sonar, S.; Mani, S.; Tailor, P.; Majumdar, T.; Jeyakanthan, J.; Biswal, B. K. Characterization of the NiRAN domain from RNA-dependent RNA polymerase provides insights into a potential therapeutic target against SARS-CoV-2. *PLoS Comput. Biol.* **2021**, *17*, e1009384.

[215] Yin, W.; Mao, C.; Luan, X.; Shen, D.-D.; Shen, Q.; Su, H.; Wang, X.; Zhou, F.; Zhao, W.; Gao, M.; Chang, S.; Xie, Y.-C.; Tian, G.; Jiang, H.-W.; Tao, S.-C.; Shen, J.; Jiang, Y.; Jiang, H.; Xu, Y.; Zhang, S.; Zhang, Y.; Xu, H. E. Structural basis for inhibition of the RNA-dependent RNA polymerase from SARS-CoV-2 by remdesivir. *Science* **2020**, *368*, 1499–1504.

[216] Gao, Y.; Yan, L.; Huang, Y.; Liu, F.; Zhao, Y.; Cao, L.; Wang, T.; Sun, Q.; Ming, Z.; Zhang, L.; Ge, J.; Zheng, L.; Zhang, Y.; Wang, H.; Zhu, Y.; Zhu, C.; Hu, T.; Hua, T.; Zhang, B.; Yang, X.; Li, J.; Yang, H.; Liu, Z.; Xu, W.; Guddat, L. W.; Wang, Q.; Lou, Z.; Rao, Z. Structure of the RNA-dependent RNA polymerase from COVID-19 virus. *Science* **2020**, *368*, 779–782.

[217] Sangawa, H.; Komeno, T.; Nishikawa, H.; Yoshida, A.; Takahashi, K.; Nomura, N.; Furuta, Y. Mechanism of Action of T-705 Ribosyl Triphosphate against Influenza Virus RNA Polymerase. *Antimicrob. Agents Chemother.* **2013**, *57*, 5202–5208.

[218] Jin, Z.; Smith, L. K.; Rajwanshi, V. K.; Kim, B.; Deval, J. The Ambiguous Base-Pairing and High Substrate Efficiency of T-705 (Favipiravir) Ribofuranosyl 5′-Triphosphate towards Influenza A Virus Polymerase. *PLoS ONE* **2013**, *8*, e68347.

[219] Cai, Q.; Yang, M.; Liu, D.; Chen, J.; Shu, D.; Xia, J.; Liao, X.; Gu, Y.; Cai, Q.; Yang, Y.; Shen, C.; Li, X.; Peng, L.; Huang, D.; Zhang, J.; Zhang, S.; Wang, F.; Liu, J.; Chen, L.; Chen, S.; Wang, Z.; Zhang, Z.; Cao, R.; Zhong, W.; Liu, Y.; Liu, L. Experimental Treatment with Favipiravir for COVID-19: An Open-Label Control Study. *Engineering* **2020**, *6*, 1192–1198.

[220] Ruzhentsova, T. A.; Oseshnyuk, R. A.; Soluyanova, T. N.; Dmitrikova, E. P.; Mustafaev, D. M.; Pokrovskiy, K. A.; Markova, T. N.; Rusanova, M. G.; Kostina, N. E.; Agafina, A. S.; Brook, Y. F.; Bronov, O. Y.; Shults, E. I.; Filon, O. V. Phase 3 trial of coronavir (favipiravir) in patients with mild to moderate COVID-19. *Am. J. Transl. Res.* **2021**, *13*, 12575–12587.

[221] Agostini, M. L.; Pruijssers, A. J.; Chappell, J. D.; Gribble, J.; Lu, X.; Andres, E. L.; Bluemling, G. R.; Lockwood, M. A.; Sheahan, T. P.; Sims, A. C.; Natchus, M. G.; Saindane, M.; Kolykhalov, A. A.; Painter, G. R.; Baric, R. S.; Denison, M. R. Small-Molecule Antiviral β-D-N^4-Hydroxycytidine Inhibits a Proofreading-Intact Coronavirus with a High Genetic Barrier to Resistance. *J. Virol.* **2019**, *93*, e01348–19.

[222] Sheahan, T. P.; Sims, A. C.; Zhou, S.; Graham, R. L.; Pruijssers, A. J.; Agostini, M. L.; Leist, S. R.; Schäfer, A.; Dinnon, K. H.; Stevens, L. J.; Chappell, J. D.; Lu, X.; Hughes, T. M.; George, A. S.; Hill, C. S.; Montgomery, S. A.; Brown, A. J.; Bluemling, G. R.; Natchus, M. G.; Saindane, M.; Kolykhalov, A. A.; Painter, G.; Harcourt, J.; Tamin, A.; Thornburg, N. J.; Swanstrom, R.; Denison, M. R.; Baric, R. S. An orally bioavailable broad-spectrum antiviral inhibits SARS-CoV-2 in human airway epithelial cell cultures and multiple coronaviruses in mice. *Sci. Transl. Med.* **2020**, *12*, eabb5883.

[223] Zarenezhad, E.; Marzi, M. Review on molnupiravir as a promising oral drug for the treatment of COVID-19. *Med. Chem. Res.* **2022**, *31*, 232–243.

[224] Cavazzoni, P. Molnupiravir LOA 10272022. *U.S. Food and Drug Administration* **2022**, Accessed January 5, 2023. https://www.fda.gov/media/155053/download.

[225] Patil, S. A.; Otter, B. A.; Klein, R. S. 4-aza-7,9-dideazaadenosine, a new cytotoxic synthetic C-nucleoside analogue of adenosine. *Tetrahedron Lett.* **1994**, *35*, 5339–5342.

[226] Warren, T. K.; Jordan, R.; Lo, M. K.; Ray, A. S.; Mackman, R. L.; Soloveva, V.; Siegel, D.; Perron, M.; Bannister, R.; Hui, H. C.; Larson, N.; Strickley, R.; Wells, J.; Stuthman, K. S.; Tongeren, S. A. V.; Garza, N. L.; Donnelly, G.; Shurtleff, A. C.; Retterer, C. J.; Gharaibeh, D.; Zamani, R.; Kenny, T.; Eaton, B. P.; Grimes, E.; Welch, L. S.; Gomba, L.; Wilhelmsen, C. L.; Nichols, D. K.; Nuss, J. E.; Nagle, E. R.; Kugelman, J. R.; Palacios, G.; Doerffler, E.; Neville, S.; Carra, E.; Clarke, M. O.; Zhang, L.; Lew, W.; Ross, B.; Wang, Q.; Chun, K.; Wolfe, L.; Babusis, D.; Park, Y.; Stray, K. M.; Trancheva, I.; Feng, J. Y.; Barauskas, O.; Xu, Y.; Wong, P.; Braun, M. R.; Flint, M.; McMullan, L. K.; Chen, S.-S.; Fearns, R.; Swaminathan, S.; Mayers, D. L.; Spiropoulou, C. F.; Lee, W. A.; Nichol, S. T.; Cihlar, T.; Bavari, S. Therapeutic efficacy of the small molecule GS-5734 against Ebola virus in rhesus monkeys. *Nature* **2016**, *531*, 381–385.

[227] Mehellou, Y.; Balzarini, J.; McGuigan, C. Aryloxy Phosphoramidate Triesters: a Technology for Delivering Monophosphorylated Nucleosides and Sugars into Cells. *Chem. Med. Chem.* **2009**, *4*, 1779–1791.

[228] McGuigan, C.; Devine, K. G.; O'Connor, T. J.; Kinchington, D. Synthesis and anti-HIV activity of some haloalkyl phosphoramidate derivatives of 3'-azido-3'-deoxythymidine (AZT): potent activity of the trichloroethyl methoxyalaninyl compound. *Antiviral Res.* **1991**, *15*, 255–263.

[229] Sofia, M. J.; Bao, D.; Chang, W.; Du, J.; Nagarathnam, D.; Rachakonda, S.; Reddy, P. G.; Ross, B. S.; Wang, P.; Zhang, H.-R.; Bansal, S.; Espiritu, C.; Keilman, M.; Lam, A. M.; Steuer, H. M. M.; Niu, C.; Otto, M. J.; Furman, P. A. Discovery of a β-D-2'-Deoxy-2'-α-fluoro-2'-β-*C*-methyluridine Nucleotide Prodrug (PSI-7977) for the Treatment of Hepatitis C Virus. *J. Med. Chem.* **2010**, *53*, 7202–7218.

[230] Lee, W. A.; He, G.-X.; Eisenberg, E.; Cihlar, T.; Swaminathan, S.; Mulato, A.; Cundy, K. C. Selective Intracellular Activation of a Novel Prodrug of the Human Immunodeficiency Virus Reverse Transcriptase Inhibitor Tenofovir Leads to Preferential Distribution and Accumulation in Lymphatic Tissue. *Antimicrob. Agents Chemother.* **2005**, *49*, 1898–1906.

[231] Sheahan, T. P.; Sims, A. C.; Graham, R. L.; Menachery, V. D.; Gralinski, L. E.; Case, J. B.; Leist, S. R.; Pyrc, K.; Feng, J. Y.; Trantcheva, I.; Bannister, R.; Park, Y.; Babusis, D.; Clarke, M. O.; Mackman, R. L.; Spahn, J. E.; Palmiotti, C. A.; Siegel, D.; Ray, A. S.; Cihlar, T.; Jordan, R.; Denison, M. R.; Baric, R. S. Broad-spectrum antiviral GS-5734 inhibits both epidemic and zoonotic coronaviruses. *Sci. Transl. Med.* **2017**, *9*, eaal3653.

[232] Gordon, C. J.; Tchesnokov, E. P.; Feng, J. Y.; Porter, D. P.; Götte, M. The antiviral compound remdesivir potently inhibits RNA-dependent RNA polymerase from Middle East respiratory syndrome coronavirus. *J. Biol. Chem.* **2020**, *295*, 4773–4779.

[233] Gordon, C. J.; Tchesnokov, E. P.; Woolner, E.; Perry, J. K.; Feng, J. Y.; Porter, D. P.; Götte, M. Remdesivir is a direct-acting antiviral that inhibits RNA-dependent RNA polymerase from severe acute respiratory syndrome coronavirus 2 with high potency. *J. Biol. Chem.* **2020**, *295*, 6785–6797.

[234] Tchesnokov, E. P.; Gordon, C. J.; Woolner, E.; Kocinkova, D.; Perry, J. K.; Feng, J. Y.; Porter, D. P.; Götte, M. Template-dependent inhibition of coronavirus RNA-dependent RNA polymerase by remdesivir reveals a second mechanism of action. *J. Biol. Chem.* **2020**, *295*, 16156–16165.

[235] Jones, S. S.; Reese, C. B. Migration of t-Butyldimethylsilyl Protecting Groups. *J. Chem. Soc. Perkin Trans. 1* **1979**, 2762–2764.

[236] Kokic, G.; Hillen, H. S.; Tegunov, D.; Dienemann, C.; Seitz, F.; Schmitzova, J.; Farnung, L.; Siewert, A.; Höbartner, C.; Cramer, P. Mechanism of SARS-CoV-2 polymerase stalling by remdesivir. *Nat. Commun.* **2021**, *12*, 279.

[237] Nawale, G. N.; Gore, K. R.; Höbartner, C.; Pradeepkumar, P. I. Incorporation of 4'-*C*-aminomethyl-2'-*O*-methylthymidine into DNA by thermophilic DNA polymerases. *Chem. Commun.* **2012**, *48*, 9619–9621.

[238] Bouton, J.; Calenbergh, S. V.; Hullaert, J. Sydnone Ribosides as a Platform for the Synthesis of Pyrazole C-Nucleosides: A Unified Synthesis of Formycin B and Pyrazofurin. *Org. Lett.* **2020**, *22*, 9287–9291.

[239] Frédéric, C. J.-M.; Cornil, J.; Vandamme, M.; Dumitrescu, L.; Tikad, A.; Robiette, R.; Vincent, S. P. Highly (*Z*)-Diastereoselective Synthesis of Trifluoromethylated *exo*-Glycals via Photoredox and Copper Catalysis. *Org. Lett.* **2018**, *20*, 6769–6773.

[240] Patil, S. A.; Otter, B. A.; Klein, R. S. Synthesis of Pyrrolo[2,1-*f*][1,2,4]triazine Congeners of Nucleic Acid Purines *via N*-Amination of 2-Substituted Pyrroles. *J. Heterocyclic Chem.* **1994**, *31*, 781–786.

[241] O'Connor, S.; Dumas, J.; Lee, W.; Dixon, J.; Cantin, D.; Gunn, D.; Burke, J.; Phillips, B.; Lowe, D.; Shelekhin, T.; Wang, G.; Ma, X.; Ying, S.; McClure, A.; Achebe, F.; Lobell, M.; Ehrgott, F.; Iwuagwu, C.; Parcella, K. Pyrrolo[2,1-*f*][1,2,4]-triazin-4-ylamines IGF-1R Kinase Inhibitors for the Treatment of Cancer and Other Hyperproliferative Diseases. US 2011/0294776, **2011**.

[242] Paymode, D. J.; Cardoso, F. S. P.; Agrawal, T.; Tomlin, J. W.; Cook, D. W.; Burns, J. M.; Stringham, R. W.; Sieber, J. D.; Gupton, B. F.; Snead, D. R. Expanding Access to Remdesivir via an Improved Pyrrolotriazine Synthesis: Supply Centered Synthesis. *Org. Lett.* **2020**, *22*, 7656–7661.

[243] Butler, T.; Cho, A.; Kim, C. U.; Parrish, J.; Saunders, O. L.; Zhang, L. 1'-Substituted Carba-Nucleoside Analogs for Antiviral Treatment. US 2010/0021425, **2010**.

[244] Metobo, S. E.; Xu, J.; Saunders, O. L.; Butler, T.; Aktoudianakis, E.; Cho, A.; Kim, C. U. Practical synthesis of 1'-substituted Tubercidin C-nucleoside analogs. *Tetrahedron Lett.* **2012**, *53*, 484–486.

[245] Vieira, T.; Stevens, A. C.; Chtchemelinine, A.; Gao, D.; Badalov, P.; Heumann, L. Development of a Large-Scale Cyanation Process Using Continuous Flow Chemistry En Route to the Synthesis of Remdesivir. *Org. Process Res. Dev.* **2020**, *24*, 2113–2121.

[246] Xue, F.; Zhou, X.; Zhou, R.; Zhou, X.; Xiao, D.; Gu, E.; Guo, X.; Xiang, J.; Wang, K.; Yang, L.; Zhong, W.; Qin, Y. Improvement of the C-glycosylation Step for the Synthesis of Remdesivir. *Org. Process Res. Dev.* **2020**, *24*, 1772–1777.

[247] Xie, Y.; Hu, T.; Zhang, Y.; Wei, D.; Zheng, W.; Zhu, F.; Tian, G.; Aisa, H. A.; Shen, J. Weinreb Amide Approach to the Practical Synthesis of a Key Remdesivir Intermediate. *J. Org. Chem.* **2021**, *86*, 5065–5072.

[248] Dimitrov, V.; Kostova, K.; Genov, M. Anhydrous Cerium(III) Chloride – Effect of the Drying Process on Activity and Efficiency. *Tetrahedron Lett.* **1996**, *37*, 6787–6790.

[249] Siegel, D.; Hui, H. C.; Doerffler, E.; Clarke, M. O.; Chun, K.; Zhang, L.; Neville, S.; Carra, E.; Lew, W.; Ross, B.; Wang, Q.; Wolfe, L.; Jordan, R.; Soloveva, V.; Knox, J.; Perry, J.; Perron, M.; Stray, K. M.; Barauskas, O.; Feng, J. Y.; Xu, Y.; Lee, G.; Rheingold, A. L.; Ray, A. S.; Bannister, R.; Strickley, R.; Swaminathan, S.; Lee, W. A.; Bavari, S.; Cihlar, T.; Lo, M. K.; Warren, T. K.; Mackman, R. L. Discovery and Synthesis of a Phosphoramidate Prodrug of a Pyrrolo[2,1-f][triazin-4-amino] Adenine C-Nucleoside (GS-5734) for the Treatment of Ebola and Emerging Viruses. *J. Med. Chem.* **2017**, *60*, 1648–1661.

[250] Funder, T. Synthesis of antiviral nucleoside analogues as potential inhibitors of the SARS-CoV-2 polymerase. MA thesis, Julius-Maximilians-Universität Würzburg, **2022**.

[251] Werner, S.; Galliot, A.; Pichot, F.; Kemmer, T.; Marchand, V.; Sednev, M. V.; Lence, T.; Roignant, J.-Y.; König, J.; Höbartner, C.; Motorin, Y.; Hildebrandt, A.; Helm, M. NOseq: amplicon sequencing evaluation method for RNA m^6A sites after chemical deamination. *Nucleic Acids Res.* **2021**, *49*, e23.

[252] Cristalli, G.; Costanzi, S.; Lambertucci, C.; Lupidi, G.; Vittori, S.; Volpini, R.; Camaioni, E. Adenosine deaminase: Functional implications and different classes of inhibitors. *Med. Res. Rev.* **2001**, *21*, 105–128.

[253] Nishikura, K. Functions and Regulation of RNA Editing by ADAR Deaminases. *Annu. Rev. Biochem.* **2010**, *79*, 321–349.

[254] Rubio, M. A. T.; Pastar, I.; Gaston, K. W.; Ragone, F. L.; Janzen, C. J.; Cross, G. A. M.; Papavasiliou, F. N.; Alfonzo, J. D. An adenosine-to-inosine tRNA-editing enzyme that can perform C-to-U deamination of DNA. *Proc. Natl. Acad. Sci. U.S.A.* **2007**, *104*, 7821–7826.

[255] Bookser, B. C.; Raffaele, N. B. High-Throughput Five Minute Microwave Accelerated Glycosylation Approach to the Synthesis of Nucleoside Libraries. *J. Org. Chem.* **2006**, *72*, 173–179.

[256] Patching, S. G.; Baldwin, S. A.; Baldwin, A. D.; Young, J. D.; Gallagher, M. P.; Henderson, P. J. F.; Herbert, R. B. The nucleoside transport proteins, NupC and NupG, from *Escherichia coli*: specific structural motifs necessary for the binding of ligands. *Org. Biomol. Chem.* **2005**, *3*, 462–470.

[257] Miles, R. W.; Samano, V.; Robins, M. J. Nucleic Acid Related Compounds. 86. Nucleophilic Functionalization of Adenine, Adenosine, Tubercidin, and Formycin Derivatives via Elaboration of the Heterocyclic Amino Group into a Readily Displaced 1,2,4-Triazol-4-yl Substituent. *J. Am. Chem. Soc.* **1995**, *117*, 5951–5957.

[258] Cristalli, G.; Franchetti, P.; Grifantini, M.; Vittori, S.; Bordoni, T.; Geroni, C. Improved Synthesis and Antitumor Activity of 1-Deazaadenosine. *J. Med. Chem.* **1987**, *30*, 1686–1688.

[259] Mikhailopoulo, I. A.; Kalinichenko, E. N.; Podkopaeva, T. L.; Wenzel, T.; Rosemeyer, H.; Seela, F. L. Synthesis of 1-Deazaadenosine Analogues of (2'→5') ApApA. *Nucleosides and Nucleotides* **1996**, *15*, 445–464.

[260] Ali, M. A.; Yao, X.; Sun, H.; Lu, H. $[RhCp*Cl_2]_2$-Catalyzed Directed *N*-Boc Amidation of Arenes "on Water". *Org. Lett.* **2015**, *17*, 1513–1516.

[261] Höbartner, C.; Kreutz, C.; Flecker, E.; Ottenschläger, E.; Pils, W.; Grubmayr, K.; Micura, R. The Synthesis of 2'-*O*-[(Triisopropylsilyl)oxy]methyl (*TOM*) Phosphoramidites of Methylated Ribonucleosides (m^1G, m^2G, $m^2{}_2G$, m^1I, m^3U, m^4C, m^6A, $m^6{}_2A$) for Use in Automated RNA Solid-Phase Synthesis. *Monatsh. Chem.* **2003**, *134*, 851–873.

[262] Farrugia, M.; Trotter, N.; Vijayasarathy, S.; Salim, A. A.; Khalil, Z. G.; Lacey, E.; Capon, R. J. Isolation and synthesis of *N*-acyladenine and adenosine alkaloids from a southern Australian marine sponge, *Phoriospongia* sp.. *Tetrahedron Lett.* **2014**, *55*, 5902–5904.

[263] Tzvetkov, N. T.; Neumann, B.; Stammler, H.-G.; Antonov, L. A simple approach to multifunctionalized N1-alkylated 7-amino-6-azaoxindole derivatives using their in situ stabilized tautomer form. *Tetrahedron* **2016**, *72*, 6455–6466.

[264] Horatscheck, A.; Andrijevic, A.; Nchinda, A. T.; Manach, C. L.; Paquet, T.; Khonde, L. P.; Dam, J.; Pawar, K.; Taylor, D.; Lawrence, N.; Brunschwig, C.; Gibhard, L.; Njoroge, M.; Reader, J.; Watt, M. van der; Wicht, K.; Sousa, A. C. C. de; Okombo, J.; Maepa, K.; Egan, T. J.; Birkholtz, L.-M.; Basarab, G. S.; Wittlin, S.; Fish, P. V.; Street, L. J.; Duffy, J.; Chibale, K. Identification of 2,4-Disubstituted Imidazopyridines as Hemozoin Formation Inhibitors with Fast-Killing Kinetics and

In Vivo Efficacy in the *Plasmodium falciparum* NSG Mouse Model. *J. Med. Chem.* **2020**, *63*, 13013–13030.

[265] Yin, X.; Schneller, S. W. 1-Deaza-5'-noraisteromycin. *Nucleosides Nucleotides Nucleic Acids* **2004**, *23*, 67–76.

[266] Maiti, M.; Michielssens, S.; Dyubankova, N.; Maiti, M.; Lescrinier, E.; Ceulemans, A.; Herdewijn, P. Influence of the Nucleobase and Anchimeric Assistance of the Carboxyl Acid Groups in the Hydrolysis of Amino Acid Nucleoside Phosphoramidates. *Chem. Eur. J.* **2012**, *18*, 857–868.

[267] Xiao, Q.; Ju, Y.; Song, Y.; Ding, H.; Dou, Y.; Yang, R.; Sun, Q. Efficient and Practical Synthesis of 5'-Deoxytubercidin and Its Analogues via Vorbrüggen Glycosylation. *Synthesis* **2011**, *2011*, 1442–1446.

[268] Shen, W.; Kim, J.-S.; Hilfinger, J. Expedient Total Synthesis of Triciribine and Its Prodrugs. *Synth. Commun.* **2012**, *42*, 358–374.

[269] Alessandrini, L.; Casati, S.; Ciuffreda, P.; Ottria, R.; Santaniello, E. Synthesis of Differently Protected 1-*C*-Methyl-Ribofuranoses Intermediates for the Preparation of Biologically Active 1'-*C*-Methyl-Ribonucleosides. *J. Carbohydr. Chem.* **2008**, *27*, 332–344.

[270] Hill, M. D.; Fang, H.; King, H. D.; Iwuagwu, C. I.; McDonald, I. M.; Cook, J.; Zusi, F. C.; Mate, R. A.; Knox, R. J.; Post-Munson, D.; Easton, A.; Miller, R.; Lentz, K.; Clarke, W.; Benitex, Y.; Lodge, N.; Zaczek, R.; Denton, R.; Morgan, D.; Bristow, L.; Macor, J. E.; Olson, R. Development of 4-Heteroarylamino-1'-azaspiro[oxazole-5,3'-bicyclo[2.2.2]octanes] as α7 Nicotinic Receptor Agonists. *ACS Med. Chem. Lett.* **2016**, *8*, 133–137.

[271] Puglisi, J. D.; Tinoco, I. Absorbance Melting Curves of RNA. *Meth. Enzymol.* **1989**, *180*, 304–325.

[272] Plum, G. E. Optical Methods. *Curr. Protoc. Nucleic Acid Chem.* **2000**, *00*, 7.3.1–7.3.17.

[273] Neese, F.; Wennmohs, F.; Becker, U.; Riplinger, C. The ORCA quantum chemistry program package. *J. Chem. Phys.* **2020**, *152*, 224108.

[274] Becke, A. D. Density-functional thermochemistry. III. The role of exact exchange. *J. Chem. Phys.* **1993**, *98*, 5648–5652.

[275] Lee, C.; Yang, W.; Parr, R. G. Development of the Colle-Salvetti correlation-energy formula into a functional of the electron density. *Phys. Rev. B* **1988**, *37*, 785–789.

[276] Stephens, P. J.; Devlin, F. J.; Chabalowski, C. F.; Frisch, M. J. *Ab Initio* Calculation of Vibrational Absorption and Circular Dichroism Spectra Using Density Functional Force Fields. *J. Phys. Chem.* **1994**, *98*, 11623–11627.

[277] Weigend, F.; Ahlrichs, R. Balanced basis sets of split valence, triple zeta valence and quadruple zeta valence quality for H to Rn: Design and assessment of accuracy. *Phys. Chem. Chem. Phys.* **2005**, *7*, 3297–3305.

[278] Parr, R. G.; Yang, W. Density Functional Approach to the Frontier-Electron Theory of Chemical Reactivity. *J. Am. Chem. Soc.* **1984**, *106*, 4049–4050.

[279] Domingo, L. R.; Pérez, P.; Sáez, J. A. Understanding the local reactivity in polar organic reactions through electrophilic and nucleophilic Parr functions. *RSC Adv.* **2013**, *3*, 1486–1494.

[280] Pucci, R.; Angilella, G. G. N. Density functional theory, chemical reactivity, and the Fukui functions. *Found. Chem.* **2022**, *24*, 59–71.

[281] Jacob, C. R.; Reiher, M. Spin in Density-Functional Theory. *Int. J. Quantum Chem.* **2012**, *112*, 3661–3684.

[282] Hay, P. J.; Wadt, W. R. *Ab initio* effective core potentials for molecular calculations. Potentials for K to Au including the outermost core orbitals. *J. Chem. Phys.* **1985**, *82*, 299–310.

[283] Hehre, W. J.; Ditchfield, R.; Pople, J. A. Self–Consistent Molecular Orbital Methods. XII. Further Extensions of Gaussian–Type Basis Sets for Use in Molecular Orbital Studies of Organic Molecules. *J. Chem. Phys.* **1972**, *56*, 2257–2261.

[284] Hariharan, P. C.; Pople, J. A. The Influence of Polarization Functions on Molecular Orbital Hydrogenation Energies. *Theoret. Chim. Acta* **1973**, *28*, 213–222.

[285] Pritchard, B. P.; Altarawy, D.; Didier, B.; Gibson, T. D.; Windus, T. L. New Basis Set Exchange: An Open, Up-to-Date Resource for the Molecular Sciences Community. *J. Chem. Inf. Model.* **2019**, *59*, 4814–4820.